Mikhail G. Brik, Alok M. Srivastava (Eds.)

Luminescent Materials

Also of interest

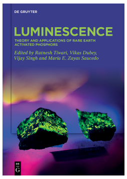
DE GRUYTER
LUMINESCENCE
THEORY AND APPLICATIONS OF RARE EARTH ACTIVATED PHOSPHORS
Edited by Ratnesh Tiwari, Vikas Dubey, Vijay Singh and Maria E. Zayas Saucedo

Luminescence.
Theory and Applications of Rare Earth Activated Phosphors
Ratnesh Tiwari, Vikas Dubey, Vijay Singh and
María Elena Zayas Saucedo (Eds.), 2021
ISBN 9783110676419, e-ISBN 9783110676457

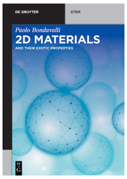
DE GRUYTER
STEM
Paolo Bondavalli
2D MATERIALS
AND THEIR EXOTIC PROPERTIES

2D Materials.
And Their Exotic Properties
Paolo Bondavalli, 2022
ISBN 9783110656329, e-ISBN 9783110656336

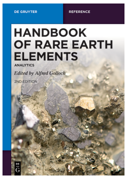
DE GRUYTER
REFERENCE
HANDBOOK OF RARE EARTH ELEMENTS
ANALYTICS
Edited by Alfred Golloch

Handbook of Rare Earth Elements.
Analytics
Alfred Golloch (Ed.), 2022
ISBN 9783110696363, e-ISBN 9783110696455

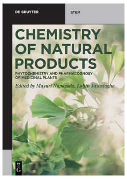
DE GRUYTER
STEM
CHEMISTRY OF NATURAL PRODUCTS
PHYTOCHEMISTRY AND PHARMACOGNOSY OF MEDICINAL PLANTS
Edited by Mayuri Napagoda, Lalith Jayasinghe

Chemistry of Natural Products.
Phytochemistry and Pharmacognosy of Medicinal Plants
Mayuri Napagoda and Lalith Jayasinghe (Eds.), 2022
ISBN 9783110595895, e-ISBN 9783110595949

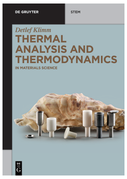
DE GRUYTER
STEM
Detlef Klimm
THERMAL ANALYSIS AND THERMODYNAMICS
IN MATERIALS SCIENCE

Thermal Analysis and Thermodynamics.
In Materials Science
Detlef Klimm, 2022
ISBN 9783110743777, e-ISBN 9783110743784

Luminescent Materials

Fundamentals and Applications

Edited by
Mikhail G. Brik, Alok M. Srivastava

DE GRUYTER

Editors
Prof. Dr. Mikhail G. Brik
Institute of Physics
University of Tartu
W. Ostwaldi 1
50411 Tartu, Estland
mikhail.brik@ut.ee

Alok M. Srivastava
GE Global Research
One Research Circle
K1-4A22
Niskayuna, NY 12309, USA
srivastaam@outlook.com

ISBN 978-3-11-060785-7
e-ISBN (PDF) 978-3-11-060787-1
e-ISBN (EPUB) 978-3-11-060822-9

Library of Congress Control Number: 2022949433

Bibliographic information published by the Deutsche Nationalbibliothek
The Deutsche Nationalbibliothek lists this publication in the Deutsche Nationalbibliografie; detailed bibliographic data are available on the Internet at http://dnb.dnb.de.

© 2023 Walter de Gruyter GmbH, Berlin/Boston
Cover image: Pavel Kostenko/iStock/Getty Images Plus
Typesetting: Integra Software Services Pvt. Ltd.
Printing and binding: CPI books GmbH, Leck

www.degruyter.com

Preface

Recent decades have witnessed rigorous research in the field of optical materials that have made possible the development of innovative luminescent materials for numerous practical applications. Advances in synthesizing, characterizing, and applying single crystals, polycrystalline powders, and functionalized nanoparticles have helped novel technologies as bioimaging, optical thermometry, photonics, and optoelectronics. Such research has also contributed to the development of commercially useful phosphors for white light light-emitting diodes (LEDs) and to persistent phosphors with high storage capacity.

The selection of luminescent material for practical applications starts by specifying the various requirements of a particular device. The selection of the optical material satisfying the pertinent requirements starts by the fundamental understanding of the enabling physical process. In recent years, researchers have been productive in advancing the fundamental understanding of structure–optical property relationships which serves as a practical guide to the selection of optical materials. The impetus for publishing this book emerged a few years back as we felt that researchers could benefit from an up-to-date review of optical materials in emerging fields along with advances in fundamental understanding of the physical process and spectroscopic properties. We approached this by inviting leading experts to write individual chapters on different topics, which are at the cutting edge of modern optical materials research. It is our sincere hope that the book will prove useful to both experienced and young researchers in understanding and designing luminescent materials and will help them in the different stages of their research careers.

The book consists of 11 chapters, which are authored by scientists with backgrounds in industry and academia. A short description of the chapters is given as follows:

Chapter 1 (M. G. Brik, A. M. Srivastava, and W. W. Beers) discusses some basic concepts and nomenclature or branches of luminescence by defining the terms that are used to identify various ways in which luminescence is generated with respect to the excitant. The chapter also briefly discusses a few examples of photoluminescence.

Chapter 2 (Israel F. Costa, Lucca Blois, Albano N. Carneiro Neto, Ercules E. S. Teotonio, Hermi F. Brito, Luís D. Carlos, Maria Claudia F. C. Felinto, Renaldo T. Moura Jr., Ricardo L. Longo, Wagner M. Faustino, and Oscar L. Malta) focuses on further developments of Judd–Ofelt theory in its application to the lanthanide ions and reinterpretation of the intensity parameters.

Chapter 3 (Markus Suta and Werner Urland) gives an overview of crystal and ligand field theories and explores the angular overlap model of the ligand field theory for the description of the electronic structure of coordination compounds.

Chapter 4 (Jiance Jin and Zhiguo Xia) is devoted to all-inorganic metal halide perovskites, their synthesis as nanocrystals and bulk crystals along with their luminescent property and mechanism, as well as applications in photonics.

https://doi.org/10.1515/9783110607871-202

Chapter 5 (A. Siva Sesha Reddy, M. Kostrzewa, N. Purnachand, G. Sahaya Bhaskaran, N. Venkatramaiah, V. Ravi Kumar, and N. Veeraiah) explores the influence of free volume space defects as estimated by positron annihilation spectroscopy on the luminescence efficiency of Ho^{3+} ions in Au_2O_3-doped $PbO–B_2O_3–SeO_2$ (PBS) glass ceramics.

Chapter 6 (Jumpei Ueda) discusses the fundamentals and applications of persistent luminescence in Ce^{3+}-doped garnets. Fundamental approaches to controlling and devising new persistent phosphors are presented.

Chapter 7 (Gabrielle A. Mandl, Gabriella Tessitore, Steven L. Maurizio, and John A. Capobianco) brings to the reader's attention the fundamental properties of luminescent nanoparticles based on lanthanide and transition metal ions for bioimaging applications. Imaging based on near-infrared emission, upconversion, and persistent luminescence is discussed.

Chapter 8 (Veeramani Rajendran, Ho Chang, and Ru-Shi Liu) is about the application of two transition metal ions with $3d^3$ electronic configuration, Mn^{4+} and Cr^{3+}, as generators of red and infrared phosphors in LED applications. The applications include general lighting and displays.

Chapter 9 (Florian Baur and Thomas Jüstel) deals with the fundamentals and uses of ultraviolet (UV)-emitting phosphors that are excitable by practical UV radiation sources such as Hg low-pressure discharge, excimer discharge, and LEDs. Phosphors for UVA, UVB, and UVC are discussed.

Chapter 10 (Philippe Boutinaud and Enrico Cavalli) discusses the advancements made in the fundamental understanding of the metal-to-metal charge transfer transitions between cations of oxidic hosts and Pr^{3+} or Tb^{3+} ions, when doped in oxidic compounds which are composed of cations with the d^0 and d^{10} electronic configurations. Application of such systems in optical thermometry is also discussed.

Chapter 11 (A. M. Srivastava, M. G. Brik, and W. W. Beers) presents and summarizes the considerable body of experimental and theoretical data that are available on the luminescence of the Bi^{3+} ion in materials with the orthorhombic perovskite and double perovskite structures. The chapter provides an understanding of the behavior of the Bi^{3+} ion in relation to the composition and electronic structure of the host crystal.

We would like to take this opportunity to express our sincere gratitude to all contributors to this book. Without their hard and intensely focused work, the book would not have become possible. We also thank the staff members at De Gruyter for their help and guidance during our collaborative efforts on this book. It has been an interesting and challenging adventure, and it is satisfying to reach the point at which the book is finalized and ready for production. We wish the readers an interesting journey through the book pages.

Mikhail G. Brik
Alok M. Srivastava

Contents

Preface —— V

List of contributors —— IX

Mikhail G. Brik, Alok M. Srivastava, William W. Beers
Chapter 1
Luminescence: basic definitions, processes, and properties —— 1

Israel F. Costa, Lucca Blois, Albano N. Carneiro Neto, Ercules E. S. Teotonio, Hermi F. Brito, Luís D. Carlos, Maria Claudia F. C. Felinto, Renaldo T. Moura Jr., Ricardo L. Longo, Wagner M. Faustino, Oscar L. Malta
Chapter 2
Reinterpreting the Judd–Ofelt parameters based on recent theoretical advances —— 19

Markus Suta, Werner Urland
Chapter 3
The angular overlap model: a chemically intuitive way to describe the ligand field of coordination compounds —— 63

Jiance Jin, Zhiguo Xia
Chapter 4
All-inorganic lead-free luminescent metal halide perovskite and perovskite derivatives —— 93

Annapureddy Siva Sesha Reddy, Marek Kostrzewa, Nalluri Purnachand, Gnanamuthu Sahaya Baskaran, Nutalapati Venkatramaiah, Vandana Ravi Kumar, Nalluri Veeraiah
Chapter 5
Influence of Au^0 particles on luminescence efficiency of Ho^{3+} ions in $PbO–B_2O_3–SeO_2$ glass ceramics: the role of free volume defects – exploration using PALS studies —— 115

Jumpei Ueda
Chapter 6
Garnet persistent phosphors —— 131

Gabrielle A. Mandl, Gabriella Tessitore, Steven L. Maurizio, John A. Capobianco
Chapter 7
Luminescent nanoparticles for bioimaging applications —— 155

Veeramani Rajendran, Ho Chang, Ru-Shi Liu
Chapter 8
Transition metal ion-based phosphors for LED applications —— 185

Florian Baur, Thomas Jüstel
Chapter 9
UV-emitting phosphors: from fundamentals to applications —— 221

Philippe Boutinaud, Enrico Cavalli
Chapter 10
Metal-to-metal charge transfer involving Pr^{3+} or Tb^{3+} ions in transition metal oxides and its consequences on the luminescence behaviors —— 239

Alok M. Srivastava, Mikhail G. Brik, William W. Beers
Chapter 11
Luminescence of Bi^{3+} in oxides with perovskite structures —— 271

Index —— 297

List of contributors

Dr. Gnamuttu Sahaya Baskaran
Department of Physics
Andhra Loyola College (Autonomous)
Vijayawada
Andhra Pradesh, India
sbalc@rediffmail.com
Chapter 5

Dr. Florian Baur
Department of Chemical Engineering
Münster University of Applied Sciences
Stegerwaldstrasse 39
48565 Steinfurt, Germany
florian.baur@fh-muenster.de
Chapter 9

Dr. William W. Beers
Current Lighting Solutions, LLC
1099 Ivanhoe Road
Cleveland, OH 44110, USA
william.beers@gecurrent.com
Chapter 2, 11

BSc Lucca Blois
Departamento de Química Fundamental
Instituto de Química
Universidade de São Paulo
Avenida Professor Lineu Prestes
748, B8T, Butantã
05508-000 São Paulo, Brazil
blois@iq.usp.br
Chapter 2

Prof. Philippe Boutinaud
Université Clermont Auvergne
Clermont Auvergne INP, CNRS, ICCF
63000 Clermont-Ferrand, France
boutinau@chimie.univ-bpclermont.fr
Chapter 10

Prof. Mikhail G. Brik
Institute of Physics
University of Tartu
W. Ostwaldi Str. 1
Tartu 50411, Estonia
mikhail.brik@ut.ee
Chapter 1, 11

Prof. Hermi F. Brito
Departamento de Química Fundamental
Instituto de Química
Universidade de São Paulo
Avenida Professor Lineu Prestes
748, B8T, Butantã
05508-000 São Paulo, Brazil
hefbrito@iq.usp.br
Chapter 2

Prof. John A. Capobianco
Department of Chemistry and Biochemistry
Centre for NanoScience Research
Concordia University
7141 Sherbrooke St W
Montreal, QC
Canada H4B 1R6
john.capobianco@concordia.ca
Chapter 7

Prof. Luís D. Carlos
Physics Department and CICECO – Institute
of Materials
University of Aveiro
Aveiro 3810-193, Portugal
lcarlos@ua.pt
Chapter 2

Prof. Enrico Cavalli
Department of Chemical Science, Life
and Environmental Sustainability
University of Parma
Parma, Italy
enrico.cavalli@unipr.it
Chapter 10

Prof. Ho Chang
Department of Mechanical Engineering and
Graduate Institute of Manufacturing Technology
National Taipei University of Technology
No. 1, Sec. 3, Zhongxiao East Road
Taipei 106, Taiwan
f10381@ntut.edu.tw
Chapter 8

https://doi.org/10.1515/9783110607871-204

Dr. Israel F. Costa
Departamento de Química Fundamental
Instituto de Química
Universidade de São Paulo
Avenida Professor Lineu Prestes
748, B8T, Butantã
05508-000 São Paulo, Brazil
israelfc@iq.usp.br
Chapter 2

Prof. Wagner M. Faustino
Departamento de Química
Universidade Federal da Paraíba
Centro de Ciências Exatas e da Natureza –
Campus I
Castelo Branco
58051-970 João Pessoa, Brazil
wmfaustino@quimica.ufpb.br
Chapter 2

Prof. Maria Claudia F. C. Felinto
Instituto de Pesquisas Energéticas e Nucleares
Centro de Química e Meio Ambiente
Av Professor Lineu Prestes 2242 Cidade
Universitária
Butantã, 05508-000 São Paulo, Brazil
mfelinto@ipen.br
Chapter 2

Dr. Jiance Jin
State Key Laboratory of Luminescent Materials
and Devices
South China University of Technology
Guangzhou 510641, P. R. China
chardking@163.com
Chapter 4

Prof. Thomas Jüstel
Department of Chemical Engineering
Münster University of Applied Sciences
Stegerwaldstrasse 39
48565 Steinfurt, Germany
tj@fh-muenster.de
Chapter 9

Prof. Marek Kostrzewa
Faculty of Physics
Opole University of Technology
Opole 45370, Poland
m.kostrzewa@po.opole.pl
Chapter 5

Dr. Vandana Ravi Kumar
Department of Physics
Acharya Nagarjuna University
Nagarjuna Nagar 522 510
Andhra Pradesh, India
vrksurya@rediffmail.com
Chapter 5

Prof. Ru-Shi Liu
Department of Chemistry
National Taiwan University
No. 1, Sec. 4, Roosevelt Road
Taipei 106, Taiwan
rsliu@ntu.edu.tw
Chapter 8

Prof. Ricardo L. Longo
Departamento de Química Fundamental
Universidade Federal de Pernambuco
Centro de Ciências Exatas e da Natureza
Av. Prof. Luiz Freire
s/n, Cidade Universitária
50740-540 Recife, Brazil
ricardo.longo@ufpe.br
Chapter 2

Prof. Oscar L. Malta
Departamento de Química Fundamental
Universidade Federal de Pernambuco
Centro de Ciências Exatas e da Natureza
Av. Prof. Luiz Freire
s/n, Cidade Universitária
50740-540 Recife, Brazil
oscar.malta@ufpe.br
Chapter 2

MSc Gabrielle A. Mandl
Department of Chemistry and Biochemistry
Centre for NanoScience Research
Concordia University
7141 Sherbrooke St W
Montreal, QC
Canada H4B 1R6
g_mandl@live.concordia.ca
Chapter 7

MSc Steven L. Maurizio
Department of Chemistry and Biochemistry
Centre for NanoScience Research
Concordia University
7141 Sherbrooke St W
Montreal, QC
Canada H4B 1R6
steven.maurizio@mail.concordia.ca
Chapter 7

Prof. Renaldo T. Moura Jr.
Departamento de Química e Física
Universidade Federal da Paraíba
Centro de Ciências Agrárias – Campus II
Rodovia PB 079 – km 12
Campus Universitário
58397-000 Areia, Brazil
renaldo.mourajr@cca.ufpb.br
Chapter 2

Dr. Albano N. Carneiro Neto
Physics Department and CICECO – Institute of Materials
University of Aveiro
Aveiro 3810-193, Portugal
albanoneto@ua.pt
Chapter 2

Dr. Nalluri Purnachand
School of Electronics Engineering
VIT-AP University
Inavolu 522 237
Andhra Pradesh, India
chanduinece@gmail.com
Chapter 5

MSc. Veeramani Rajendran
Materials Chemistry Laboratory
Department of Chemistry
National Taiwan University
No. 1, Sec. 4, Roosevelt Road
Taipei 106, Taiwan
veeramanir93@gmail.com
Chapter 8

Dr. Annapureddy Siva Sesha Reddy
Department of Physics
Krishna University
Machilipatnam 521003
Andhra Pradesh, India
shivasesshareddy@gmail.com
Chapter 5

Dr. Alok M. Srivastava
Current Lighting Solutions, LLC
1099 Ivanhoe Road
Cleveland, OH 44110, USA
srivastaam@outlook.com
Chapter 1, 11

Prof. Markus Suta
Inorganic Photoactive Materials
Institute of Inorganic Chemistry
Heinrich Heine University Düsseldorf
Universitätsstraße 1
40225 Düsseldorf, Germany
markus.suta@hhu.de
Chapter 3

Prof. Ercules E. S. Teotonio
Departamento de Química
Universidade Federal da Paraíba
Centro de Ciências Exatas e da Natureza – Campus I
Castelo Branco
58051-970 João Pessoa, Brazil
teotonioees@quimica.ufpb.br
Chapter 2

Prof. Gabriella Tessitore
Department of Chemistry
Université Laval
1045 Avenue de la Medicine
Quebec City, QC
Canada G1V 0A6
gabriella.tessitore@chm.ulaval.ca
Chapter 7

Prof. Jumpei Ueda
School of Material Science
Japan Advanced Institute of Science
and Technology
1-1 Asahidai, Nomi
Ishikawa 923-1292, Japan
ueda-j@jaist.ac.jp
Chapter 6

Prof. Werner Urland
Private Institute of Theoretical Chemical Physics
Via Dr. A. Sciaroni 2
6600 Muralto, Switzerland
werner.urland@gmail.com
Chapter 4

Prof. Nalluri Veeraiah
Department of Physics
Andhra Loyola College
Vijayawada 520008
Andhra Pradesh, India
and
Department of Physics
Acharya Nagarjuna University
Nagarjuna Nagar 522 510
Andhra Pradesh, India
profnvr@gmail.com
Chapter 5

Dr. Nutalapati Venkatramaiah
Department of Chemistry
SRM Institute of Science and Technology
Kattankulathur
Tamil Nadu, India
nvenkat83@gmail.com
Chapter 5

Prof. Zhiguo Xia
State Key Laboratory of Luminescent Materials
and Devices
South China University of Technology
Guangzhou 510641, P. R. China
xiazg@scut.edu.cn
Chapter 4

Mikhail G. Brik, Alok M. Srivastava, William W. Beers

Chapter 1
Luminescence: basic definitions, processes, and properties

1.1 Types of luminescence

Luminescence is a process of spontaneous emission of light by a substance (can be organic or inorganic, or even a living organism), in excess of the thermal radiation produced by heat in the substance. In other words, it is the emitted radiation not resulting from heat. As an example, the light emitted by the common incandescent light bulb arises due to the heating of a metal filament wire (tungsten) to a high temperature by passing electric current until it glows. In luminescence, the emission is excessive over thermal radiation, and its duration should be significantly longer than the period $T = 2\pi/\nu$ of the emitted light waves with frequency ν. This definition of luminescence was given by E. Wiedemann and extended (by highlighting importance of the timescale) by the Soviet academician S. I. Vavilov. The frequencies of light emitted as a result of luminescent processes in different substances ranging from infrared to ultraviolet spectral domains, including the visible light as well. The excess over blackbody or thermal radiation means that the luminescent object appears to be brighter (or produces a more intensive infrared or ultraviolet emission) than the ideal blackbody emitter, which has the same temperature as the luminescent medium. The ability of substances to produce luminescence does not depend on the aggregate state, that is, solids, liquids, and gases can luminesce. The phenomenon of luminescence should not, however, be understood as emission of a light by a substance without any reason. The luminescence is a way of conversion of excitation energy (which can be supplied to a luminescent object in various ways by external sources) into the energy of emitted light.

Examples of luminescence – although the origin of those was, of course, not understood at all and remained a mystery for centuries – were known to people since ancient times. Flying butterflies and beetles glowing in the nights, aurora borealis and aurora australis, the light of the seas, are those instances at which people were facing the luminescence processes without recognizing this fact. Already in the tenth century AC, Chinese artists were able to use special paints that were visible in the darkness and that were considered to be magic [1]. The first – or, at least, one of the first – example of luminescence of solids is the Bolognian stone (barite, $BaSO_4$), discovered in 1603, which could glow in the night after being reduced to BaS by heating in a charcoal furnace and exposing it to natural (sun) light. Later, in the same century, the chemical element phosphorus was isolated, and it is exactly this element, which gave the name to the term “phosphorescence,” which will be described later.

https://doi.org/10.1515/9783110607871-001

The advent of experimental spectroscopic techniques coupled with rapid progress in quantum mechanics and atomic physics led to the fundamental understanding of the luminescence-related phenomena and paved the way for scientists and engineers to develop luminescent materials for various applications.

In this chapter, we shall summarize the basic concepts and definitions of luminescence.

We start by defining some of the terminology of luminescence which is dependent on the means of excitation (excitant):

- Photoluminescence (PL): In PL, the emission occurs after the system has absorbed photons. The excitation is usually by low-energy light source emitting, for example, the ultraviolet and the visible photons. There are two categories of PL that are dependent on the duration of persistence (or afterglow) after cessation of excitation: phosphorescence (with lifetimes from microseconds to hours; it is named after the chemical element phosphorus) and fluorescence (with lifetimes less than microseconds).
- Thermoluminescence (TL) [2]: TL can be thought of as phosphorescence that is generated at various temperatures. TL involves the emission of light during heating of a substance which has absorbed energy from electromagnetic radiation. Usually, the material is preirradiated and the stored energy is emitted as light upon heating. It should be emphasized that such kind of luminescence (as a cold light emission) should not be confused with incandescence. Once the substance has been depleted of the stored energy, it must be re-irradiated to observe TL. A kind of opposite phenomenon, when the light is emitted upon cooling a luminescent substance, is called cryoluminescence.
- Electroluminescence (EL): EL is light emission as a result of applying an electric field to a substance. Again, this should not be confused with incandescence and the materials should have narrow bandgaps such as sulfides (ZnS).
- Cathodoluminescence (CL): In this case, the excitant is the beam of high-energy electrons (cathode rays).
- Chemiluminescence is the process when the visible light appears as a result of chemical reactions. Several kinds of chemiluminescence can be distinguished, such as (i) bioluminescence, when the light is produced by living organisms during biochemical reactions (insects glowing in the dark or the sea lights); (ii) electrochemiluminescence, caused by the electrochemical reactions, usually in solutions; (iii) lyoluminescence, which appears when a heavily irradiated solid (irradiated by cathode rays, for example) is dissolved in solvents; (iv) candoluminescence, when the light is given by substances upon heating and appears to be different from the blackbody radiation (an example is the limelight – Drummond light – luminescence of CaO after heating; it has been used for a long time for the stage lighting in theaters and music halls).
- Mechanoluminescence, when the light is produced after a mechanical action or impact on a solid. According to the type of mechanical impact, several mechanoluminescence subtypes are discerned: (i) piezoluminescence, when mechanical pressure applied

to some (not all!) solids can produce glowing light; (ii) fractoluminescence, when a solid is fractured, crashed, or broken and energy is released as a light; (iii) triboluminescence, when the light is produced by scratching or rubbing a luminescent material; (iv) sonoluminescence, when the light is produced after a collapse of a bubble in a liquid produced by an ultrasound wave.

- Radioluminescence, when the luminescent light is excited by ionizing radiation.
- Crystalloluminescence, when the luminescence light is produced during crystallization process from a solution.

To sum up, in all these cases, excitation energy is delivered to a luminescent medium by different ways – optical, mechanical, chemical, and so on – then, this energy is released in the form of emitted photons.

Main applications of luminescence are:

- Lighting industry (fluorescent lighting devices that are based on low-pressure mercury discharge, and light-emitting diodes (LED) that are based on EL)
- Phosphor materials, producing light via EL or radioluminescence mechanisms
- Sensing, that is, temperature and pressure measurements based on the detection of luminescence changes induced by varying the abovementioned parameters
- TL dosimetry, or measurements of the radiation doses through detection and analysis of TL

Since PL is the most widely studied and better understood phenomenon, we will focus our attention on this kind of luminescence (particularly in inorganic solids) in this chapter.

1.2 Main characteristics of luminescence

After N. Bohr developed his theory of hydrogen atom, which was later on confirmed theoretically by quantum-mechanical calculations, it has been widely recognized and accepted that all processes of absorption and emission of electromagnetic radiation correspond to the electron transitions between discrete energy levels of atoms and molecules, and the energy difference between which should be in resonance with or, at least, close enough to the energy of the absorbed photons.

The ability of a luminescent material to convert the absorbed energy into emitted energy is given by the quantum yield $\Phi(\lambda)$ [3]:

$$\Phi(\lambda) = \frac{\text{number of emitted photons}}{\text{number of absorbed photons}} \tag{1.1}$$

where λ indicates the wavelength of the absorbed photons. As a rule, in the luminescence excitation processes not all absorbed photons are transformed into the emitted ones, and the value of $\Phi(\lambda)$ is much less than unity. However, for some special cases, such as resonance absorption/emission, when only two energy levels are involved, $\Phi(\lambda)$ can approach the value of unity. Moreover, in the case of downconversion, which can be realized for some rare-earth ions, absorption of one photon can be followed by emission of two or more photons of smaller energy (longer wavelengths), thus resulting in the values of $\Phi(\lambda)$ greater than unity.

Another important parameter is the quantum efficiency η, defined as a ratio of the emitted energy to the absorbed energy [3]:

$$\eta = \frac{\text{emitted energy (output)}}{\text{absorbed energy (input)}} \tag{1.2}$$

At the first glance, it may seem that the quantum yield and quantum efficiency are equal, but this is true only for the resonance processes in a two-level system.

As a rule, the luminescence spectrum is redshifted with respect to the absorption (or luminescence excitation) spectrum. This is the so-called Stokes rule, and the Stokes shift is the difference in energy between the absorption and emission peaks, corresponding to the same electronic transition. The physical origin of the Stokes shift is better understood with the help of the single configuration coordinate model, whose foundations were laid in the pioneering works by J. Franck and E.U. Condon [4, 5] and have been described in various textbooks at different levels of depth since that time.

The model can be readily applied to the electronic transitions within a diatomic or polyatomic molecule and clusters formed by impurity ions in crystalline solids. It is based on the adiabatic approximation and assumption that the electronic energy levels versus coordinates in the harmonic approximation can be represented by parabolas. Usually, this coordinate is taken as the chemical bond length.

The atomic vibrations in a molecule or in a cluster are described as quantum-mechanical harmonic oscillators, whose energy levels form an equidistant discrete spectrum with the energy separation equal to the energy of the vibrational quantum $\hbar\omega$ (Figure 1.1).

At zero temperature, only the ground vibrational level $n = 0$ is occupied, and as the temperature increases, the higher vibrational levels become populated.

The positions of minima of the parabolas representing the ground and excited electronic states are shifted with respect to each other, which is well understood and explained by redistribution of the electron density upon electronic transitions (Figure 1.2).

The transitions between the electronic states are shown by the vertical arrows, which is a graphical representation of the Franck–Condon principle. It states that due to the large difference in masses of nuclei and electrons, the heavy nuclei do not change their position during an electronic transition (either in absorption or emission), which is realized very quickly, at the scale between milliseconds and nanoseconds.

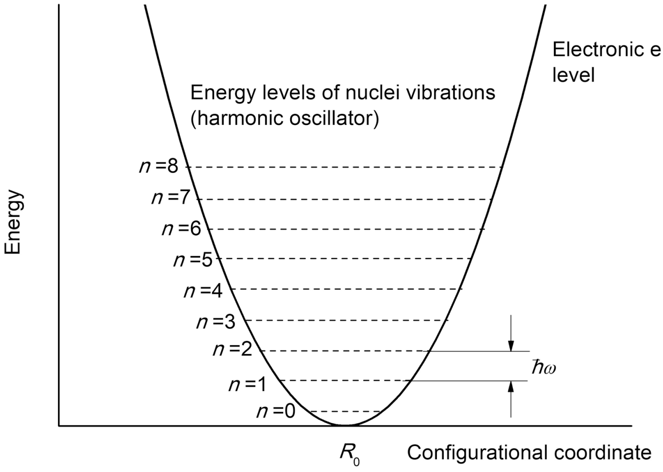

Figure 1.1: Representation of an electronic state and vibrational levels in a single configuration coordinate model.

The absorption process in Figure 1.2 is shown by an upward arrow. It reaches the parabola of the excited state at the point of excited vibrational state $m = 3$ in this particular example. Following the nonradiative relaxation to the ground vibrational state $m = 0$ of the excited electronic state, the emission process, that is, exhibited by the downward arrow, takes place. It reaches the ground state parabola at the point corresponding to the vibrational level $n = 1$ followed by the nonradiative relaxation to the ground vibrational state of the ground electronic state. It is easy to see that the lengths of the vertical arrows representing the electronic transitions are different; the emission arrow is shorter, which means that the emitted photon wavelength is red-shifted with respect to the absorbed photon. This is the explanation of the Stokes rule. The difference in energy between the absorbed and emitted photons is absorbed by the atomic vibrations in a molecule or a solid.

The magnitude of the parabolas' offset strongly depends on the considered system. For example, for the intraconfigurational $4f$–$4f$ transitions of the rare earth ions, the offset is practically zero because the $4f$ orbitals are the inner ones, screened by the completely filled $5s^2 5p^6$ orbitals, which results in a weak interaction of the $4f$ states with nearest neighbors. On the contrary, for the intraconfigurational $3d$–$3d$ transitions of the transition metal ions, the offset is much greater, since the open $3d$ orbitals are the external ones, strongly interacting with nearest neighbors and crystal lattice vibrations. Similarly, large shifts of the minima between the parabolas representing the ground and excited electronic states are observed in the case of the interconfigurational $4f$–$5d$ transitions of the rare earth ions, since in this case one of the states involved in the transition corresponds to the outer $5d$ orbitals, which is also strongly affected by the interaction with the nearest neighbors and local and collective vibrational modes.

Spectroscopically, the difference in the offsets values for the parabolas representing the electronic states that participate in the considered emission/absorption transitions is manifested in the widths of the corresponding spectroscopic features: the greater is the offset value (i.e., the stronger is the electron–vibrational interaction), the broader is the emission/absorption band.

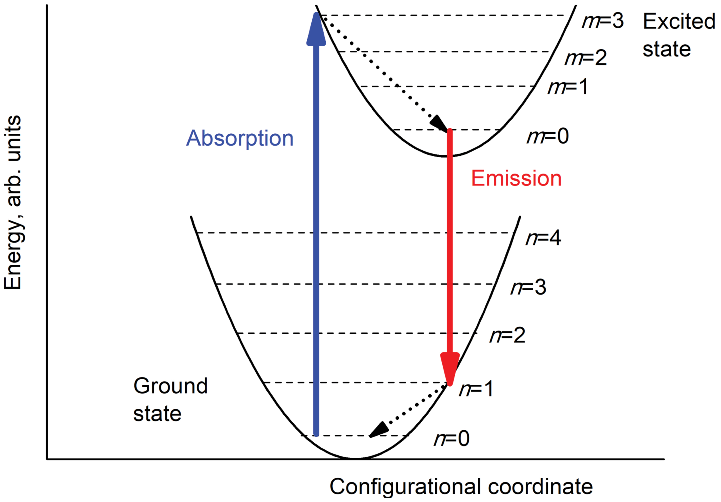

Figure 1.2: Representation of the absorption and emission transitions in a single configuration coordinate model. See text for more details.

Sometimes the anti-Stokes luminescence can be observed, when the emitting photons are blueshifted (i.e., they have a greater energy/frequency or a shorter wavelength) in comparison to the absorbed ones. Such situation can be realized at elevated temperatures, when higher vibrational levels of the ground electronic state are populated. Then some amount of vibrational energy can be taken from the luminescence medium and the arrow representing the emission transition will be longer, resulting in a blueshift of the luminescence spectra.

Another important property of the absorption and luminescence spectra (again, if they correspond to the same electronic transition) is the mirror symmetry of these spectra (Figure 1.3).

If these spectra are plotted in the same scale, they will intersect. The point of intersection corresponds to the zero-phonon line (ZPL) energy, which is the energy of pure electronic transition, without involvement of the vibrational subsystem.

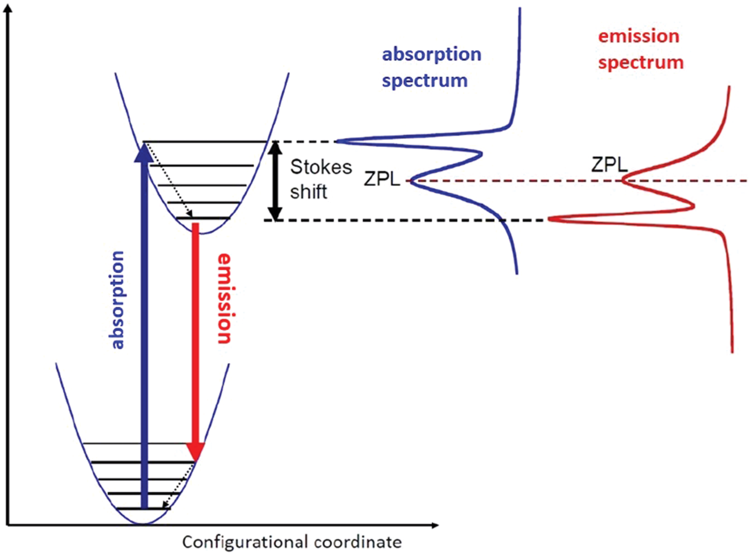

Figure 1.3: Illustration of mirror symmetry of the absorption and emission spectra corresponding to the same electronic transition.

1.3 A few examples of photoluminescence

In this section, we will consider several examples of the luminescence of intentionally introduced impurity ions in crystalline solids to highlight the main differences between optical spectra and provide explanation of the main physical reasons responsible for the differences.

1.3.1 Intraconfigurational 3*d*–3*d* transitions of Mn^{4+} and Cr^{3+} ions

Transition metal ions with unfilled 3*d* electron shell are used in various applications such as solid-state lasers [6], phosphor materials [7], and noncontact optical thermometry [8], to name a few. Their optical spectra arise from the electronic transitions between the states of their 3*d* electron configurations. Since these transitions are within the same electron configuration, they are parity forbidden. However, admixture of the high-lying 4*p* states and strong interaction with the crystal lattice vibrations partially removes this strict selection rule, making those transitions partially allowed and detectable in their excitation/emission spectra.

The first considered example is K_2SiF_6 doped with the Mn^{4+} ions. This is a commercial red phosphor material widely used for generating warm white light in white LEDs [9]. The Mn^{4+} ions substitute for the Si^{4+} ions in an ideal octahedral coordination. The Mn^{4+}

energy levels and corresponding spectra were analyzed in Ref. [10]. Figure 1.4 shows the energy-level scheme of the Mn^{4+} ions and main transitions that are responsible for their optical spectra. The attractive feature of the Mn^{4+} ion is that it can be excited by a blue LED emitting at about 450 nm (the $^4A_{2g} \rightarrow {}^4T_{2g}$ absorption transition, a broad upward arrow in Figure 1.4). This is a spin-allowed transition, which appears as a broad absorption band with a full width at half maximum of about several thousand cm^{-1}. After a nonradiative relaxation to the first excited state ^2E_g (a dashed arrow in Figure 1.4), the spin-forbidden $^2E_g \rightarrow {}^4A_{2g}$ emission transition manifests itself as a narrow emission line (which in different hosts may consist of an ZPL and several vibronic sidebands) in the red part of the visible spectra.

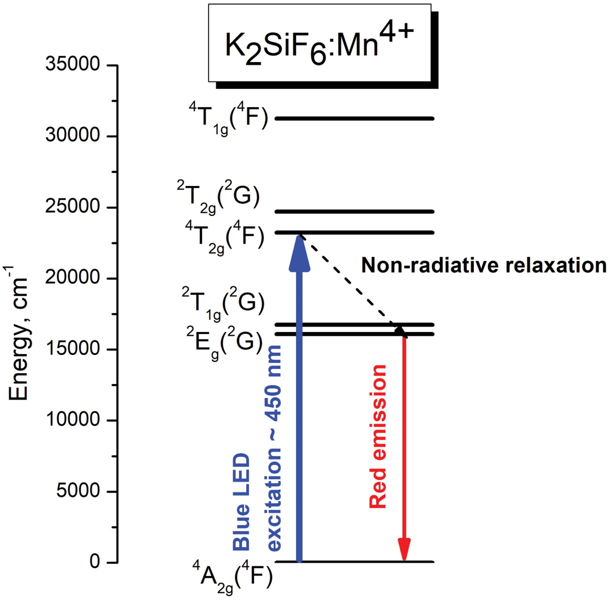

Figure 1.4: Energy level scheme of Mn^{4+} ions in K_2SiF_6. See text for more details.

Figure 1.5 shows the photoluminescence excitation (PLE) and PL spectra of $K_2SiF_6:Mn^{4+}$. The calculated Mn^{4+} energy levels are shown by the vertical lines; it can easily be seen that the agreement between the experimentally detected spectral features and calculated energy levels is good.

Although the energy level scheme of Cr^{3+} ion which is isoelectronic with the Mn^{4+} ion (both have the $3d^3$ electron configuration) is the same, there are important differences in the location of their energy levels. It was shown [11–13] that the Racah parameters for the isoelectronic ions increase linearly with the atomic number Z. Therefore, the Racah parameters for Cr^{3+} ($Z = 24$) are smaller than those for Mn^{4+} ($Z = 25$), which explains the redshift of all energy levels in the former case. To confirm

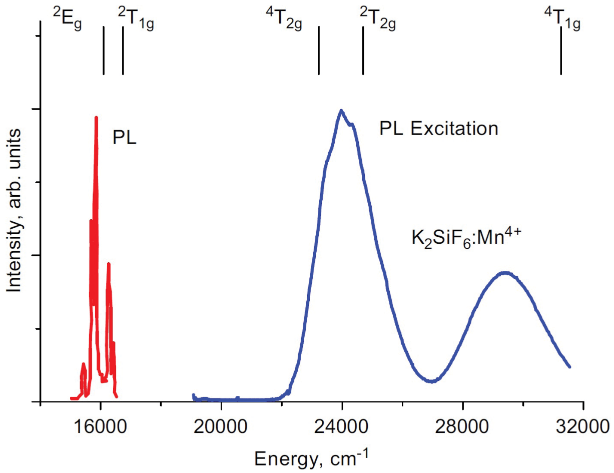

Figure 1.5: Excitation and photoluminescence spectra of Mn^{4+} ions in K_2SiF_6 (reproduced with permission from Ref. [10]).

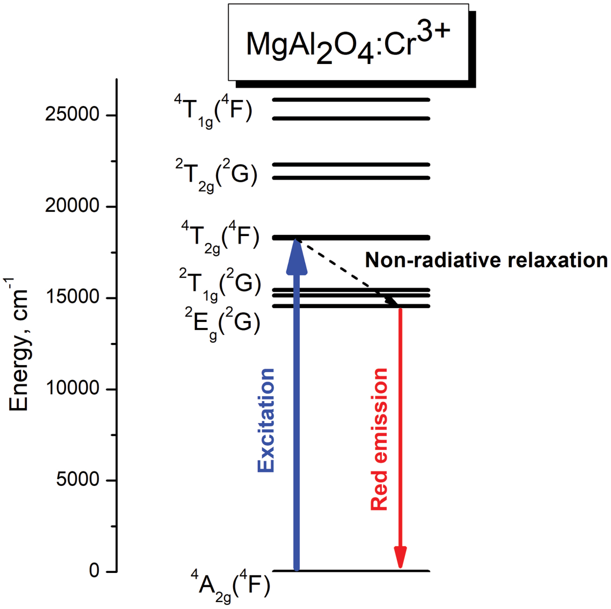
$MgAl_2O_4$:Cr^{3+}
$^4T_{1g}(^4F)$
$^2T_{2g}(^2G)$
$^4T_{2g}(^4F)$
$^2T_{1g}(^2G)$
$^2E_g(^2G)$
$^4A_{2g}(^4F)$
Non-radiative relaxation
Excitation
Red emission
Energy, cm^{-1}
25000
20000
15000
10000
5000
0

Figure 1.6: Energy level scheme of Cr^{3+} ions in $MgAl_2O_4$. See text for more details.

this trend, the energy level scheme of Cr^{3+} ions in $MgAl_2O_4$ (substituted at the Al^{3+} site with the D_{3d} trigonal symmetry) is shown (Figure 1.6) [14]. A quick comparison with Figure 1.4 shows that all energy levels are shifted down; the $^4T_{2g}$ level in this particular case is at about 18 300 cm^{-1} (corresponding to 546 nm), and a blue LED cannot be used for efficient excitation of the Cr^{3+} luminescence. The trigonal symmetry of the Cr^{3+} position in this $MgAl_2O_4$ spinel causes additional splitting of the orbital triplets into doublet and singlet states, and the detailed analysis of which was reported in Ref. [14].

The redshift of the Cr^{3+} energy levels in comparison with the Mn^{4+} ones is confirmed by Figure 1.7, in which the excitation and luminescence spectra of Cr^{3+} ions in $MgAl_2O_4$ are shown, together with the calculated Cr^{3+} energy levels [14].

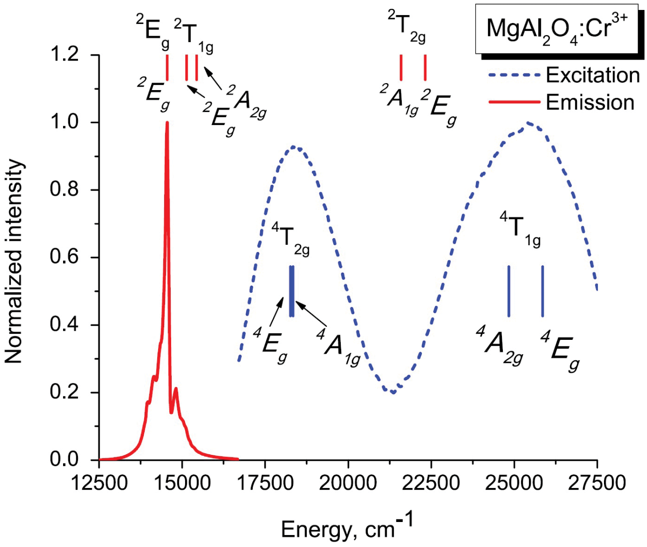

Figure 1.7: Excitation and photoluminescence spectra of Cr^{3+} ions in $MgAl_2O_4$ (reproduced with permission from Ref. [14]). The D_{3d} point group's irreducible representations are used to label the low-symmetry splitting of the orbital triplet states.

1.3.2 Intraconfigurational 4*f*–4*f* transitions of Eu^{3+} ions

Lanthanides (chemical elements with the unfilled 4*f* electron shell) are another group of activator ions with numerous optical applications. Similar to the case of the 3*d* ions, their unfilled electron shells are characterized by a large number of energy levels [15]. However, a very important difference is that the 4*f* electron shell is an inner one, which is located closer to the nuclei than the completely filled 5*s* and 5*p* shells. These completed shells act as a screen, which shields the 4*f* electrons from the nearest environment. As a result, the interaction between the 4*f* electrons of the lanthanide ions (Ln^{3+}) and nearest neighbors in crystal lattices and/or lattice vibrations is very weak. The optical absorption and emission spectra of the Ln^{3+} ions, which correspond to the 4*f*–4*f* transitions, consist of very sharp lines, whose positions almost do not vary significantly from one host material to another. The famous Dieke diagram is used in the interpretation of the absorption/emission spectra of trivalent lanthanide ions. An experimental evidence of very small variation of the lanthanide ion spectra in solids is given in Figures 1.8 and 1.9, where the PLE and PL spectra of Eu^{3+} ions in several crystalline materials are given [16].

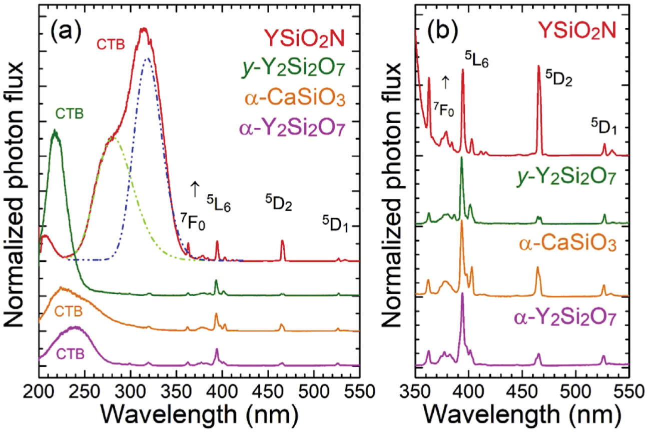

Figure 1.8: (a) Comparison of PLE spectra of Eu^{3+} ions in $YSiO_2N$, y-$Y_2Si_2O_7$, α-$CaSiO_3$, and α-$Y_2Si_2O_7$. CTB stands for the charge transfer band (from oxygen to europium). (b) Enlarged view of Figure 1.8(a) in the range between 350 and 550 nm (reproduced with permission from Ref. [16]).

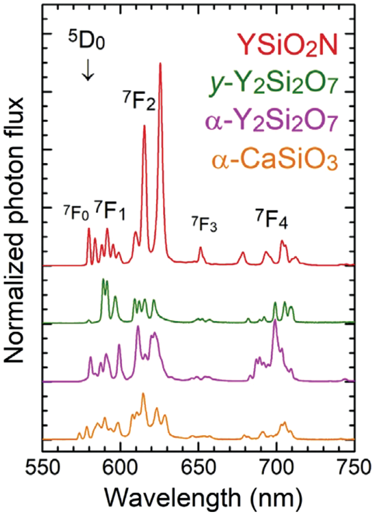

Figure 1.9: Comparison of PL spectra of Eu^{3+} ions in $YSiO_2N$, y-$Y_2Si_2O_7$, α-$CaSiO_3$, α-$Y_2Si_2O_7$ (reproduced with permission from Ref. [16]).

As shown in Figures 1.8 and 1.9, in spite of variation of chemical composition, the positions of the main spectral features associated with Eu^{3+} ions are very nearly the same.

Figure 1.10 shows the energy level scheme of Eu^{3+} ions in the energy interval from 0 to 40,000 cm^{-1}. It is seen that the $^5D_0$ level is separated by a wide gap (of about 15,000 cm^{-1}), which indicates that this is a potentially emitting energy level. Indeed, Figure 1.9 shows the emission spectra of the Eu^{3+} ions originating from the $^5D_0$ state to all lowest states ^7F_J ($J = 0, \ldots, 6$). These transitions are also shown in Figure 1.10 by downward arrows.

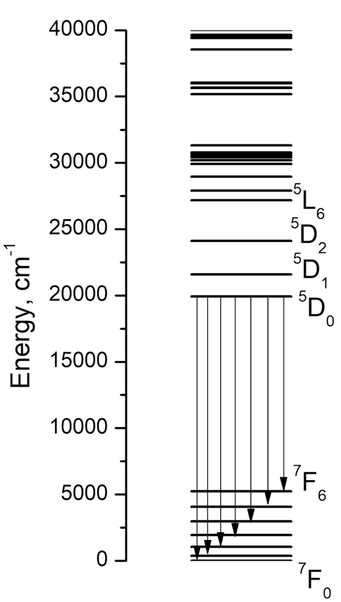

Figure 1.10: Energy level scheme of the Eu^{3+} ions. The downward arrows show the emission transition indicated in Figure 1.9. The ^7F_J ($J = 1.5$) levels are located between the $^7F_0$ and $^7F_6$.

The energy level scheme from Figure 1.10 suggests that the Eu^{3+} ions can be excited by the UV LED at about 330 nm, and this excitation, followed by the nonradiative relaxation to the $^5D_0$ level, will lead to the red emission with the ^7F_J ($J = 0, \ldots, 6$) terminating states.

1.3.3 Interconfigurational 5*d*–4*f* transitions of Ce^{3+} ($4f^1$) and Eu^{2+} ($4f^7$) ions

The 4*f*–5*d* absorption and 5*d*–4*f* emission transitions of the rare earth ions are parity allowed, and because of this, they have much greater intensities than the above-discussed intraconfigurational 3*d*–3*d* and 4*f*–4*f* transitions.

The 5*d* states of lanthanide ions are the outer ones interacting strongly with the crystalline lattice. As a result, their emissions can be varied from the UV to the red spectral region. The spectral bands corresponding to the 4*f*–5*d* transitions are very intensive and broad because of the strong interaction with the lattice.

Let us consider the optical properties of the Ce^{3+} ion with the $4f^1$ electronic configuration. The energy level structure of this ion is very simple, as exhibited schematically in Figure 1.11. The ground state is a doublet ($^2F_{5/2}$–$^2F_{7/2}$) separated by about 2,000 cm^{-1}, and the 5*d* excited states are located at about 33,000 cm^{-1}. Since the 4*f*→5*d* transition is allowed, a strong band is observed in the excitation/absorption spectrum. In crystal fields of low symmetry, the 5*d* states can be split into five energy levels as shown in Figure 1.11, and if all these five levels are in the host's bandgap, up to five absorption peaks can be observed in the 4*f*→5*d* excitation. The luminescence originates from the lowest Ce^{3+} 5*d* energy level. There are various commercial products that are based on the luminescence of the Ce^{3+} ion. Examples include the $Y_3Al_5O_{12}$:Ce^{3+} yellow phosphor used in the modern-day white LED and $(Y,Gd,Lu)_2SiO_5$ compounds that find application as PET scintillators.

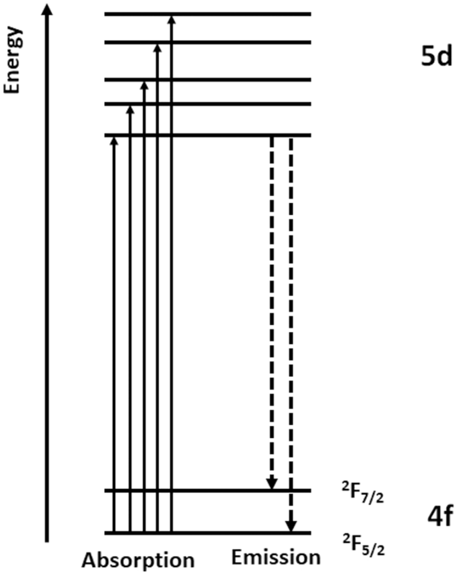

Figure 1.11: Schematic representation of the Ce^{3+} energy levels. The spin–orbit split ground states are separated by about 2,000 cm^{-1}. The emission is observed from the lowest 5*d* level split by the crystalline field.

Figure 1.12 shows the absorption spectrum of the Ce^{3+} ions in $YAlO_3$ [17], together with the calculated (from crystal field theory) 5*d* energy levels. This is a typical example of the 4*f*→5*d* excitation spectrum with broad absorption bands between 4 and 6 eV. Since the symmetry of the crystal lattice site occupied by the Ce^{3+} ion in this crystal is very low, all five 5*d* states are split, and their relative positions nicely correlate with the width of the absorption bands and their structure.

Another important rare earth ion for lighting application is the divalent europium (Eu^{2+}) ion with the $4f^7$ electronic configuration. Its $4f^7$ (ground) and $4f^65d^1$ (excited) electronic configurations (Figure 1.13) give rise to a very large number of possible energy

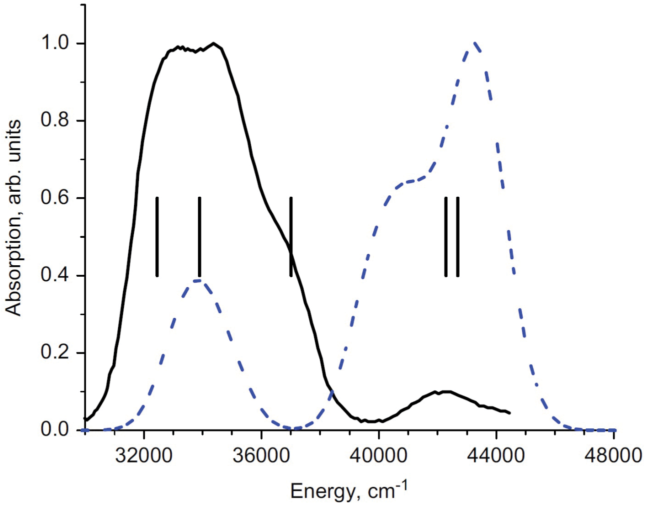

Figure 1.12: Calculated 5*d* energy levels (vertical lines) of Ce^{3+} in $YAlO_3$. The experimental spectrum is shown by a solid line, and the ab initio calculated spectrum by a dashed line (reproduced with permission from Ref. [17]).

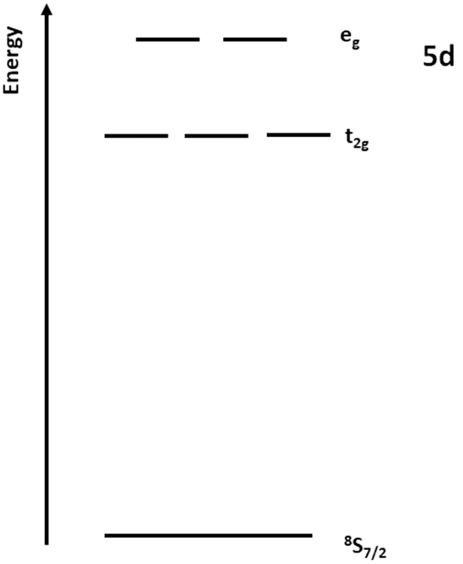

Figure 1.13: Schematic representation of the Eu^{2+} energy level scheme in an octahedral coordination.

levels, so the energy level scheme of this ion is very rich and complicated, with the lowest $4f^65d^1$ energy levels overlapping in energy with the states of the $4f^7$ configuration. The evolution of the energy level scheme is discussed in Ref. [18]. In the absence of any interaction between the $4f^6$ and $5d$ electrons, the excited state would be composed of seven levels ($^7F_0$–$^7F_6$) which is equivalent to the ground state of the Eu^{3+} ($4f^6$) ion. In an octahedral field, the states of the $5d^1$ electron will be split into a lower t_{2g} and an upper e_g states. The excitation spectrum of Eu^{2+} in an octahedral site is exhibited in Figure 1.14. The host is $Cs_2CaP_2O_7$. The low and high energy bands in the excitation spectra are associated with the $4f^7$ [$^8S_{7/2}$]→$4f^65d^1$[t_{2g}] and $4f^7$ [$^8S_{7/2}$]→$4f^65d^1$[e_g] transitions, respectively. Note that those superimposed on the lower t_{2g} bands are several sharp lines that are due to the seven $4f^6$ levels ($^7F_0$–$^7F_6$), as discussed previously. This so-called staircase spectrum is only observed when the interaction between the $5d$ and the $4f^6$ levels is weak.

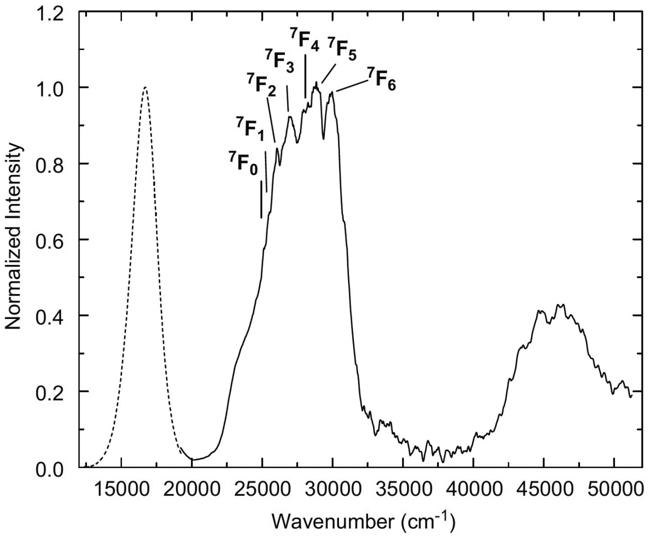

Figure 1.14: Excitation spectrum of Eu^{2+} in $Cs_2CaP_2O_7$ at $T = 80$ K (reproduced with permission from Ref. [19]).

Divalent europium-doped nitride and oxy-nitride compounds are important class of materials that are used to generate green and red photons in a modern-day white LED. Another important application of Eu^{2+} ion is in the field of persistent phosphors, which are capable of visible light emission long after (more than 8 h) the cessation of the excitation source. A much studied phosphor is $SrAl_2O_4$:Eu^{2+}, Dy^{3+} that is used to label safety signs to illuminate escape routes. The emission spectrum of this material consists of two broad bands, centered at about 520 nm (green) and 450 nm (blue), respectively. In this host, there are two nonequivalent Sr sites, Sr1 and Sr2, which are available for incorporation of Eu^{2+} ions; they are somewhat different in geometry, and Eu^{2+} ions in those two sites are responsible for the appearance of two different emission bands [20]. The crystal field calculations performed in Ref. [20] allowed to assign the observed emission bands at particular crystallographic sites occupied by the Eu^{2+} ion (Figure 1.15).

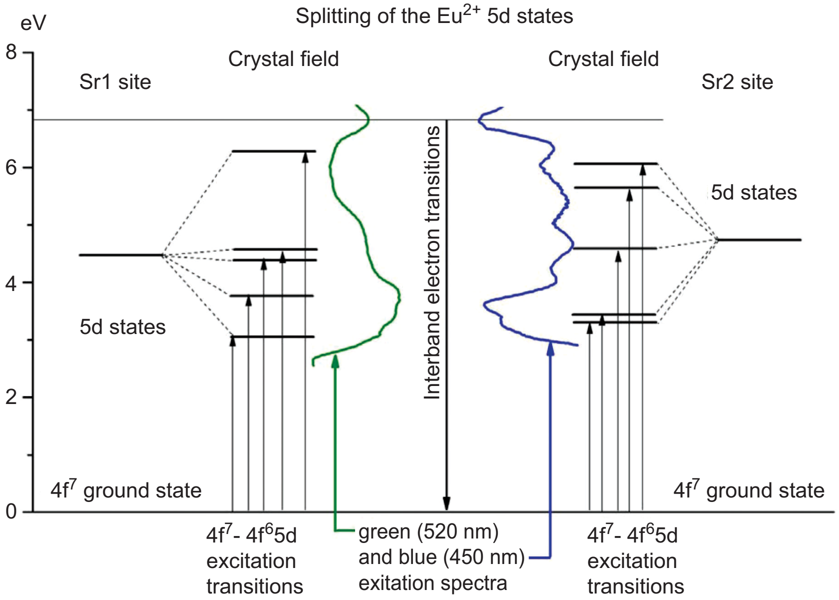
Splitting of the Eu2+ 5d states
eV
8
6
4
2
0
Crystal field
Crystal field
Sr1 site
Sr2 site
5d states
5d states
Interband electron transitions
4f7 ground state
4f7 ground state
4f7- 4f65d excitation transitions
green (520 nm) and blue (450 nm) exitation spectra
4f7- 4f65d excitation transitions

Figure 1.15: The $4f^7$–$4f^65d$ excitation spectra for green (520 nm) and blue (450 nm) bands in $SrAl_2O_4:Eu^{2+}$ (reproduced with permission from Ref. [20]).

1.4 Conclusions

A short summary of the main terms and definitions related to the luminescence of solids was summarized in this chapter. The introductory paragraph was followed by selected examples of luminescence of transition metal and rare earth ions in solids, with highlighted differences in the spectral appearance. For more details, the reader is kindly advised to read the original publications cited in this chapter.

References

[1] E.N. Harvey, A History of Luminescence from the Earliest Times until 1900, American Philosophical Society, Philadelphia, PA, USA (1957).
[2] R. Chen, S.W.S. McKeever, Theory of Thermoluminescence and Related Phenomena, World Scientific Publishing Co., Singapore (1997).
[3] K.-L. Wong, J.-C.G. Bünzli, P.A. Tanner, Quantum yield and brightness, J. Lumin. 224 (2020) 117256.
[4] J. Franck, Elementary processes of photochemical reactions, Trans. Faraday Soc. 21 (1926) 536–542.
[5] E.U. Condon, Nuclear motions associated with electron transitions in diatomic molecules, Phys. Rev. 32 (1928) 858–872.
[6] R.C. Powell, Physics of Solid-state Laser Materials, Springer New York, NY (1998).

[7] R.-S. Liu, X.-J. Wang, Eds., Phosphor Handbook, Third Edition, CRC Press (2022).

[8] L. Marciniak, K. Kniec, K. Elżbieciak-Piecka, K. Trejgis, J. Stefanska, M. Dramićanin, Luminescence thermometry with transition metal ions. A review, Coord. Chem. Rev. 469 (2022) 214671.

[9] E.V. Radkov, L.S. Grigorov, A.A. Setlur, A.M. Srivastava, United States Patent Application US2006/0169998A1.

[10] M.G. Brik, A.M. Srivastava, On the optical properties of the Mn^{4+} ion in solids, J. Lumin. 133 (2013) 69–72.

[11] M.G. Brik, A.M. Srivastava, Systematic analysis of the spectroscopic characteristics of 3d ions in a free state and some cubic crystals, Opt. Mater. 35 (2013) 1776–1782.

[12] C.-G. Ma, M.G. Brik, Systematic analysis of spectroscopic characteristics of heavy transition metal ions with $4d^N$ and $5d^N$ (N=1..10) electronic configurations in a free state, J. Lumin. 145 (2014) 402–409.

[13] M.G. Brik, C.-G. Ma, Theoretical Spectroscopy of Transition Metal and Rare Earth Ions: From Free State to Crystal Field, Jenny Stanford Publishing, Singapore (2020), 460 pages.

[14] M.G. Brik, J. Papan, D.J. Jovanović, M.D. Dramićanin, Luminescence of Cr^{3+} ions in $ZnAl_2O_4$ and $MgAl_2O_4$ spinels: Correlation between experimental spectroscopic studies and crystal field calculations, J. Lumin. 177 (2016) 145–151.

[15] M.G. Brik, A.M. Srivastava, Electronic properties of the lanthanide ions, in: R. Pöttgen, T. Jüstel, C.A. Strassert (Eds.), Rare Earth Chemistry, De Gruyter, Berlin/Boston (2020), pp. 83–96.

[16] Y. Kitagawa, J. Ueda, M.G. Brik, S. Tanabe, Intense hypersensitive luminescence of Eu^{3+}-doped $YSiO_2N$ oxynitride with near-UV excitation, Opt. Mater. 83 (2018) 111–117.

[17] M.G. Brik, I. Sildos, V. Kiisk, Calculations of physical properties of pure and doped crystals: Ab initio and semi-empirical methods in application to $YAlO_3$:Ce^{3+} and TiO_2, J. Lumin. 131 (2011) 396–403.

[18] F.M. Ryan, W. Lehmann, D.W. Feldman, J. Murphy, Fine structure in the optical spectra of divalent europium in the alkaline earth sulfates, J. Electrochem. Soc. 121 (1974) 1476.

[19] A.M. Srivastava, H.A. Comanzo, S. Camardello, S.B. Chaney, M. Aycibin, U. Happek, Unusual luminescence of octahedrally coordinated divalent europium ion in $Cs_2M^{2+}P_2O_7$ (M^{2+}=CaSr), J. Lumin. 129 (2009) 919–925.

[20] M. Nazarov, M.G. Brik, D. Spassky, B. Tsukerblat, Crystal field splitting of 5d states and luminescence mechanism in $SrAl_2O_4$: Eu^{2+}phosphor, J. Lumin. 182 (2017) 79–86.

Israel F. Costa, Lucca Blois, Albano N. Carneiro Neto,
Ercules E. S. Teotonio, Hermi F. Brito, Luís D. Carlos,
Maria Claudia F. C. Felinto, Renaldo T. Moura Jr.,
Ricardo L. Longo, Wagner M. Faustino, Oscar L. Malta

Chapter 2
Reinterpreting the Judd–Ofelt parameters based on recent theoretical advances

2.1 Introduction

Lanthanide (or lanthanoid, Ln)-based complexes and materials hold a special place among luminescent systems, for example, (bio)organic systems (molecules and crystals [1–7], covalent organic frameworks [8, 9], hydrogen-bonded organic frameworks [10], green fluorescent proteins [11–14]), transition metals (coordination compounds [15–20], inorganic matrices [21, 22], and metal-organic frameworks [23–29]), inorganic (binary and ternary), quantum, and carbon dots [30–32], due to their unique and peculiar characteristics. One of the most attractive features of lanthanide ions (particularly, trivalent lanthanides – Ln(III)) is the predictability of their spectroscopic and photophysical properties. For instance, their special electronic structure shields the effects of the environment (e.g., ligands, lattice, and solvent) on the $4f^N$ electrons resulting in $4f$–$4f$ transitions with almost invariant energies. This spectroscopic behavior was realized several decades ago, and the energy level diagrams of all Ln(III), known as Dieke's diagram [33–35], have been developed and improved. These diagrams are a powerful predicting tool and allow the design of luminescent complexes and materials with remarkable accuracy of their absorption, excitation, and emission wavelengths or wave numbers. In addition, the Ln(III) series spans a wide and nearly continuous spectral range from the near-infrared (ca. 2,000 cm^{-1}), through the visible (e.g., red, pink, green, yellow, and blue), up to ultraviolet (ca. 100,000 cm^{-1}) [36–40].

In designing new luminescent materials, not only the spectral positions or regions of transitions are relevant, but their intensities also play a crucial role. These intensities (or, e.g., absorption cross section and spontaneous emission coefficient) can be related to the symmetry and its consequences onto the selection rules, especially the Laporte's rule, as well as the ligand field strength, particularly its odd components, and the properties of the ligating atoms (or ions) of the coordination polyhedron [41, 42], and even long-range interactions [43, 44]. In this regard, Ln(III) ions are also unique because, for each ion in a given environment, the intensities of $4f$–$4f$ transitions can be fully described and quantified by only three quantities known as intensity or Judd–Ofelt parameters denoted as Ω_λ with $\lambda = 2$, 4, and 6. The brightness, or more specifically luminance [45], of a given transition at a known wavelength, can be quantified by the Ω_λ's and the

https://doi.org/10.1515/9783110607871-002

population of the emitting level, so a key component of luminescence becomes accessible. Indeed, for most applications, the brightness should be the figure of merit for comparing luminescent materials because it considers absorption and emission properties simultaneously. However, due to the difficulties in measuring the (absolute) value of brightness, the comparison of quantum yields of such materials and compounds is widespread, even though high quantum yields do not necessarily reflect high luminance because the absorption cross section is also relevant. In this sense, comparisons of Ω_λ's may be more suitable for quantifying the luminescent properties of lanthanides. Several other photophysical properties such as emission lifetimes, branching ratios, radiative rates, and nonradiative energy transfer rates can be related to the intensity parameters. Given their relevance in the luminescence of lanthanides, values of Ω_λ's have been experimentally determined for many systems, and several models have been proposed to describe and calculate them. Indeed, at the turn of the century, Ω_λ's of about 800 Ln(III) in various host matrices (mostly crystals and glasses) were reported and grouped in tables of ref. [46] for each ion and increasing values of Ω_2. The (relative) values of Ω_λ's have been interpreted based on bonding properties and environment of Ln(III) ions. Empirical observations performed several decades ago suggested that Ω_2 is related to covalency, while Ω_6 to the viscosity (or rigidity) of the medium [47]. However, these interpretations were amended or improved, for instance, by considering the effects of the local asymmetry on Ω_2, the ionic packing ratio of the host on Ω_6, and the number of $4f$ electrons on both Ω_4 and Ω_6, or are even being challenged by systematic measurements and quantitative models [41, 47–58].

In this context, we intend to present a brief review of expressions of Ω_λ's within the framework of the Judd–Ofelt theory and some of its extensions. The interpretations of the intensity parameters are presented from a historical perspective, emphasizing the trends and patterns observed for Ln(III) in several environments. We shall focus on models such as the simple overlap model (SOM) [59, 60] and the recent bond overlap model (BOM) [41, 61], as well as approaches available in computational tools freely available such as JOYSpectra web platform [62]. Despite not being explicitly dependent on the temperature, thermal effects on the Ω_λ's could be relevant, particularly for optical thermometry at the nanoscale. A review of models to account for these effects shall be discussed [63–65]. These models are based upon the fact that the intensity parameters depend strongly on the structure around Ln(III), especially of the coordination polyhedron [65, 66]. Individual atomic thermal vibrations in this polyhedron affect the structure and, therefore, the values of Ω_λ's. The thermal effects are then considered by tuning the amplitudes of these vibrations. Tutorial-like applications of the JOYSpectra web-based platform are presented for selected compounds, including the effects of temperature.

2.2 *4f–4f* transition characteristics

The 4*f*–4*f* transitions of Ln(III) ions occur in a spectral region that spans from the ultraviolet up to the near-infrared, with several of them occurring in the visible range. Unlike *nd*–*nd* transitions of the *d* metal ions, the emission and absorption spectra of the 4*f*–4*f* transitions are much more structured because of their narrower bands (atomic-like spectra), with typical oscillator strengths in the range of 10^{-7} to 10^{-5}. Furthermore, depending on the temperature and the nature of the chemical environment, the full width at half maximum (FWHM) of the 4*f*–4*f* transitions has values of 10 up to 100 cm^{-1}, while *nd*–*nd* transitions show typical values for FWHM larger than 1,000 cm^{-1}.

Such spectroscopic features reflect the weak interactions of the electrons in the 4*f* orbitals with the chemical environment, which make lanthanide ions unique systems and very attractive in terms of technological applications. Despite these weak interactions, the environment around the lanthanide ion is essential for 4*f*–4*f* intensities, especially because its symmetry defines the selection rules, and the strengths of these transitions are dependent on the nature and local symmetry of the Ln(III) site. As an example, consider Ln(III) in the crystalline environment of yttrium oxychloride, as illustrated in Figure 2.1a. This system is interesting because the Ln(III) ion, for instance, Eu(III), replaces the Y(III) ion with $C_{4\text{v}}$ point group symmetry, as depicted in Figure 2.1b and c, for the coordination polyhedron. The structural data play an essential role in the 4*f*–4*f* intensities. Thus, choosing another Ln(III) or other crystalline environments will change the luminescent behavior of the material.

The 4*f*–4*f* transitions are mainly described by the forced electric dipole (FED), via the odd component of the ligand field, and dynamic coupling (DC) mechanisms, followed by the magnetic dipole (MD), relevant to some intraconfigurational transitions, and the vibronic mechanisms (generally much less relevant [48, 57, 67, 68]). The two latter mechanisms become dominant for Ln(III) ions at a chemical environment with a center of inversion because both FED and DC mechanisms are null in such symmetries.

2.2.1 The electric dipole mechanism: the Judd–Ofelt theory

In the absence of a center of inversion, the ligand field Hamiltonian can be split into two parts with opposite parity. The odd part is responsible for the mixing of the electronic configurations of opposite parity. This mixing has been conveniently treated through time-independent perturbation theory using the approximation introduced by Judd and Ofelt [67, 68], in which the intraconfigurational energy differences are much smaller than the interconfigurational energy differences as illustrated in Figure 2.2. In addition, the latter is taken as being the difference between the centroids of the electronic configurations, that is:

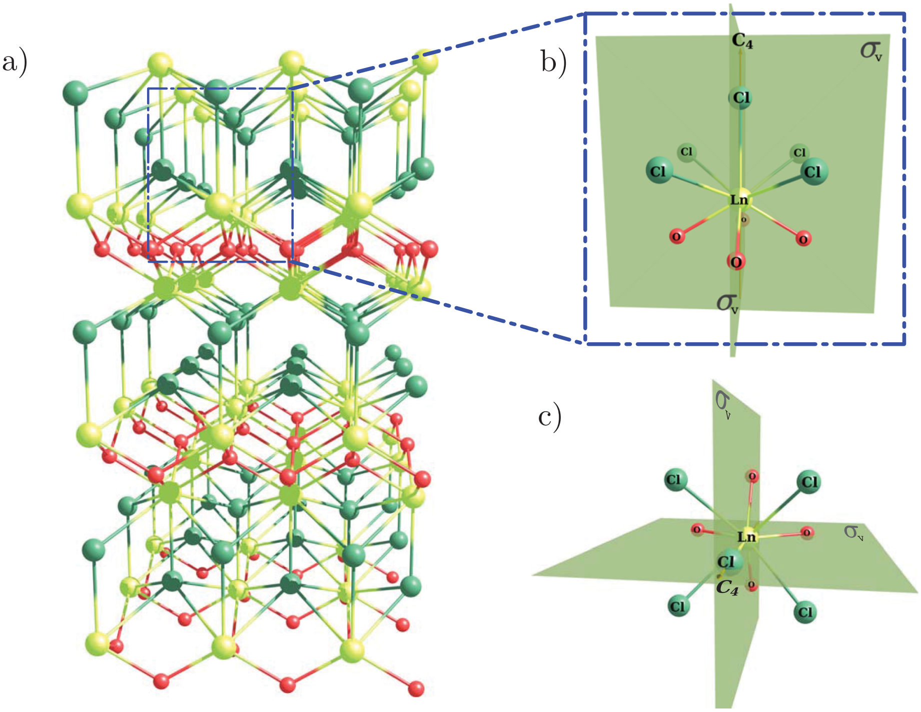
a)
b)
c)
C_4
σ_v
Cl
Ln
O

Figure 2.1: (a) Crystallographic structure of an expanded 3 × 3 × 3 cell of YOCl. The purple sphere represents a Ln(III) = Eu(III) ion replacing a Y(III) ion (yellow spheres). Cl^- and O^{2-} ions are represented by green and red spheres, respectively. (b) Magnification of the first coordination sphere of the Ln(III) ion situated at a site with C_{4v} point group symmetry (the two σ_d planes were omitted for a clear view). (c) View along the C_4 symmetry axis.

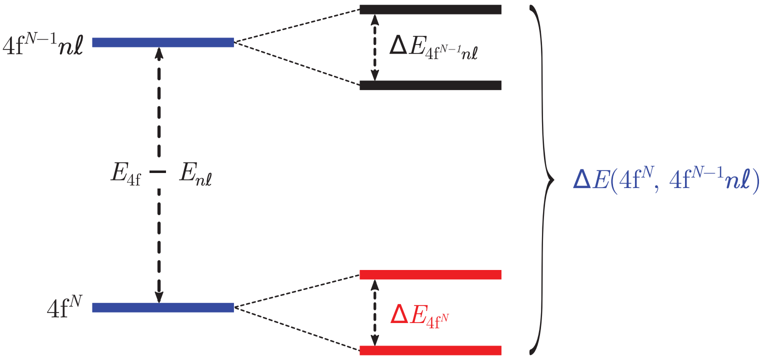
$4f^{N-1}n\ell$
$4f^N$
$E_{4f} - E_{n\ell}$
$\Delta E_{4f^{N-1}n\ell}$
ΔE_{4f^N}
$\Delta E(4f^N, 4f^{N-1}n\ell)$

Figure 2.2: Schematic energy levels of the ground and excited configurations illustrating the Judd–Ofelt approximations. The color scheme refers to the quantities in eq. (2.1).

$$\left|\Delta E_{4f^N}\right| \ll \left|\Delta E\left(4f^N, 4f^{N-1}n\ell\right)\right| \cong \left|E_{4f} - E_{n\ell}\right| \tag{2.1}$$

The configurations with opposite parity to that $4f^N$ are the following: $4f^{N-1}n\ell$ with $\ell = f \pm 1$ (or d and g orbitals) and $\left(n'\ell'\right)^{4\ell'+1}4f^{N+1}$, corresponding to core excitations with $n'\ell' =$ $3d$ and $4d$. Such excited configurations correspond to single-particle excitations once the ligand field Hamiltonian is a sum over single-particle operators. In the configuration mixing process, it is expected that the $4f^{N-1}n\ell$ configurations play a much more relevant role given that the core excitations are highly energetic.

The contribution of a certain excited configuration B to the electric dipole operator between two states $|A\alpha\rangle$ and $\left|A\alpha'\right\rangle$ of the ground configuration $4f^N$ (represented by A) is given by

$$\frac{1}{E_A - E_B}\sum_{\beta}\left(\langle A\alpha'|\vec{\mu}|B\beta\rangle\langle B\beta|H_{\mathrm{LF}}^{\mathrm{odd}}|A\alpha\rangle + \langle A\alpha'|H_{\mathrm{LF}}^{\mathrm{odd}}|B\beta\rangle\langle B\beta|\vec{\mu}|A\alpha\rangle\right) \tag{2.2}$$

where $E_A - E_B = E_{4f} - E_{n\ell}$ is the energy difference between the barycenters (or centroids) of both electronic configurations.

In terms of irreducible tensor operators, the electric dipole operator is represented as [69]

$$\vec{\mu} = -e\sum_{i}\vec{r}_i = -e\sum_{q,i} r_i C_q^{(1)}(i)\vec{e}_q^{\,*} \tag{2.3}$$

where e is the elementary charge; thus, $-e$ is the charge of the electron and the components described by $q = 0, \pm 1$ are the polarization components, which may represent the relative orientation of the dipole moment and the electromagnetic fields [46].

As in the Judd–Ofelt theory [67, 68], one obtains the following structure in the cases of d and g configurations with $n > 4$:

$$\begin{aligned}
&\frac{-e}{E_{4f} - E_{n\ell}}\sum_{t,p,q}\sum_{\lambda,\rho}(-1)^{\rho}(2\lambda+1)\\
&\left[\langle 4f|r|n\ell\rangle\langle n\ell|r^t|4f\rangle\left\langle f\|C^{(1)}\|\ell\right\rangle\left\langle \ell\|C^{(t)}\|f\right\rangle\begin{pmatrix} t & 1 & \lambda\\ p & q & \rho\end{pmatrix}\begin{Bmatrix} f & 1 & \ell\\ t & f & \lambda\end{Bmatrix}\right.\\
&\left.+\langle 4f|r^t|n\ell\rangle\langle n\ell|r|4f\rangle\langle f\|C^{(t)}\|\ell\rangle\langle \ell\|C^{(1)}\|f\rangle\begin{pmatrix} 1 & t & \lambda\\ q & p & \rho\end{pmatrix}\begin{Bmatrix} f & t & \ell\\ 1 & f & \lambda\end{Bmatrix}\right]\\
&\gamma_p^t\left\langle A\alpha'\middle|U_{-\rho}^{(\lambda)}\middle|A\alpha\right\rangle\vec{e}_q^{\,*}
\end{aligned} \tag{2.4}$$

For the case of core excitations ($\ell' = 2$ and $n' = 3$ and 4), we have a similar equation except for a minus sign because the core excitations have an opposite contribution as that of $4f^{N-1}n\ell$.

From both terms in the brackets in eq. (2.4), the 3–j symbols differ only in their signal:

$$\begin{pmatrix} 1 & t & \lambda \\ q & p & \rho \end{pmatrix} = (-1)^{1+t+\lambda} \begin{pmatrix} t & 1 & \lambda \\ p & q & \rho \end{pmatrix} \tag{2.5}$$

because t is odd, eq. (2.4) is null for odd values of λ. Therefore, λ must be an even number. In addition, from the triangularity relations of the 6–j symbols [70, 71], we have that $\lambda \leq f + f = 6$. For $\lambda = 0$, the unitary irreducible tensor operator $\hat{U}^{(0)}$ is a constant and because the states $|A\alpha\rangle$ and $|A\alpha'\rangle$ are orthogonal, the values for λ of interest in eq. (2.4) are 2, 4, and 6. Therefore, the rank $t \leq 7$.

Summing over all possible excited electronic configurations, the matrix element of the electric dipole operator between the initial and final states can be expressed as follows:

$$\langle A\alpha' | \vec{\mu}_{\text{eff}} | A\alpha \rangle = -e \sum_{\lambda,\rho,q} \sum_{t,p} (-1)^{\rho} (2\lambda + 1) \begin{pmatrix} t & 1 & \lambda \\ p & q & \rho \end{pmatrix} B_{\lambda,t,p} \langle A\alpha' | U^{(\lambda)}_{-\rho} | A\alpha \rangle \vec{e}^{\,*}_{q} \tag{2.6}$$

where $\vec{\mu}_{\text{eff}}$ is an effective dipole operator acting within the $4f^N$ configuration and

$$B_{\lambda,t,p} = \Xi\,(t,\lambda)\gamma^t_p \tag{2.7}$$

where

$$\Xi\,(t,\lambda) = \sum_{n,\ell} \frac{2}{E_{4f} - E_{n\ell}} \langle 4f|r|n\ell\rangle \langle n\ell|r^t|4f\rangle \left\langle f \| C^{(1)} \| \ell \right\rangle \left\langle \ell \| C^{(t)} \| f \right\rangle \begin{Bmatrix} f & 1 & \ell \\ t & f & \lambda \end{Bmatrix} \tag{2.8}$$

and γ^t_p are the parameters in the odd part of the ligand field Hamiltonian according to

$$H^{\text{odd}}_{\text{LF}} = \sum_{t,p,i} \gamma^t_p r^t_i C^{(t)}_p(i), \qquad \gamma^t_p = \left(\frac{4\pi}{2t+1}\right)^{1/2} \sum_j g_j \rho_j \left(2\beta_j\right)^{t+1} \frac{Y^{t\,*}_p\left(\theta_j, \phi_j\right)}{R^{t+1}_j} \tag{2.9}$$

where g_j, ρ_j, and β_j are quantities related to the chemical bonds that appear in the framework of the ligand field SOM [59, 60].

If we are interested in the total transition intensity between two J multiplets, we can consider that J and M_J are, in a crude approximation, good quantum numbers and use the $4f$ eigenfunctions in the intermediate coupling: $|A\alpha\rangle \cong \left|\left(4f^N\right)\psi J M_J\right\rangle$, to perform a sum over different M_J and $M_{J'}$. This is equivalent to considering that the $M_{J'}$'s are approximately equally populated or degenerated. Note that this summation should be performed over the absolute square of the dipole operator matrix element, and it should be divided by the degeneracy of the initial state once the transition starts from a given M_J (the initial M_J's are equally populated) and may end up in any of the final $M_{J'}$. Moreover, before performing this summation, we apply the Wigner–Eckart theorem to the matrix element of the unit tensor operator $\boldsymbol{U}^{(\lambda)}$ in eq. (2.6). Finally, by using the orthonormality relations for both the 3–j symbols and the spherical unit vectors, together with a sum over the three components of the dipole operator, it can be shown that

$$\left|\langle \psi' J' \| \vec{\mu}_{\text{eff}} \| \psi J \rangle\right|^2 = \frac{e^2}{(2J+1)} \sum_{\lambda} \Omega_\lambda \left\langle (4f^N)\psi' J' \| U^{(\lambda)} \| (4f^N)\psi J \right\rangle^2 \tag{2.10}$$

where

$$\Omega_\lambda = (2\lambda+1) \sum_{t,p} \frac{\left|B_{\lambda,t,p}\right|^2}{(2t+1)} \tag{2.11}$$

In this way, it is possible to treat 4f–4f intensities for a given Ln(III) ion in different chemical environments by only three parameters, Ω_λ, $\lambda = 2$, 4, and 6, which are known as the Judd–Ofelt intensity parameters, and the promoting mechanism of electronic transitions associated with this theory is known as the FED mechanism. This has been a successful approach in the field of lanthanide spectroscopy. It is important to emphasize that this description by only three parameters is a direct consequence of the approximations discussed earlier.

The theoretical calculation of the Judd–Ofelt Ω_λ parameters, considering only the FED mechanism, involves two difficulties. The first one is the choice of an appropriate ligand field model that leads to reliable values for the γ_p^t quantities that appear in eq. (2.9), which will be discussed later. We stress that, in contrast to the case of the so-called B_q^k ligand field parameters in the even component of the ligand field, the γ_p^t parameters cannot be obtained experimentally from the splitting of the J manifolds in Stark components. The second difficulty consists in obtaining the values for the radial integrals and energy differences to perform the sum over n and ℓ in eq. (2.8). Hartree–Fock and relativistic Hartree–Fock methods have been employed to yield widely used values for these quantities [72, 73].

2.2.2 The average energy denominator approach

In 1966, Bebb and Gold employed the average energy denominator method in the treatment of ionization processes by multiphoton absorption in hydrogen and noble gases [74]. In perturbation theory, it is common to have sums over excited configurations of the type

$$Q = \sum_{x} \frac{\langle a|\hat{T}|x\rangle \langle x|\hat{P}|b\rangle}{\Delta E_x} \tag{2.12}$$

where $\hat{T}$ and $\hat{P}$ are Hermitian operators and ΔE_x is the energy difference between the ground and excited states. Notice that eq. (2.2) is an example of such a case. In general,

$\langle a|\hat{T}|x\rangle$ and $\langle x|\hat{P}|b\rangle$ are nonzero only for certain states x. For example, when the parity is well-defined and the operators $\hat{T}$ and $\hat{P}$ have odd parity, only opposite parity states will have nonvanishing matrix elements. In this case, $|x\rangle$ must have the same parity that is opposite to $|a\rangle$ and $|b\rangle$. Let a set of states $\{|m\rangle\}$ be orthonormal and complete, and to include the $|a\rangle$, $|b\rangle$, and $|x\rangle$ states, the summation in eq. (2.12) can be expressed as follows:

$$Q = \frac{1}{\overline{\Delta E}}\langle a|\hat{T}\hat{P}|b\rangle \tag{2.13}$$

where the so-called average energy denominator, $\overline{\Delta E}$, was introduced and the closure relation was employed. Thus, if $\overline{\Delta E}$ is known, the sum Q can be exactly determined by eq. (2.13). However, the situation is not that simple due to the physical meaning and value of $\overline{\Delta E}$ for a given system.

In the case of 4*f*–4*f* intensities, in the present framework employing eq. (2.2), the operators $\hat{T}$ and $\hat{P}$ correspond to the electric dipole operator and the odd component of the ligand field, respectively, and eq. (2.13) can be seen as a justification of the approximation employed by Judd and Ofelt for the energy denominators. As for the physical meaning, it was shown that $\overline{\Delta E}$ can be expressed as the energy difference between the first excited electronic configuration with opposite parity to the ground state, for $\hat{T}$ and $\hat{P}$ with odd parity. For Ln(III) ions, this result can also be applied by considering [75]

$$\overline{\Delta E} \cong E_{4f} - E_{5d} \tag{2.14}$$

According to this method, the $B_{\lambda,t,p}$ quantities in eq. (2.7) are given by [76]

$$B_{\lambda,t,p} = \frac{2}{\overline{\Delta E}}\langle 4f|r^{t+1}|4f\rangle\theta(t,\lambda)\gamma_p^t \tag{2.15}$$

where the numerical factors $\theta(t,\lambda)$ are given by

$$\theta(t,\lambda) = \left\langle f\|C^{(1)}\|g\right\rangle\left\langle g\|C^{(t)}\|f\right\rangle\begin{Bmatrix} f & t & g \\ 1 & f & \lambda \end{Bmatrix} + (1-2\delta_t)\left\langle f\|C^{(1)}\|d\right\rangle\left\langle d\|C^{(t)}\|f\right\rangle\begin{Bmatrix} f & t & d \\ 1 & f & \lambda \end{Bmatrix} \tag{2.16}$$

and

$$\delta_t = \frac{\sum_{n'=3,4}\langle 4f|r|n'd\rangle\langle n'd|r^t|4f\rangle}{\langle 4f|r^{t+1}|4f\rangle} \tag{2.17}$$

which represents the participation of core excitations in the closure relation for a given value of t. For the Eu(III) ion, Hartree–Fock calculations [72] give the following values: $\delta_1 = 0.539$, $\delta_3 = 0.223$, $\delta_5 = 0.082$, and $\delta_7 \cong 0$. As it is a relationship between different radial integrals, these values should not be significantly different for the other lanthanide ions. They indicate that the average energy denominator method overestimates, especially for $t = 1$, the contribution of core excitations to the FED mechanism. This was already expected because the core excitations present very high energies, and in this method, they are considered as close to the ground configuration as the first excited $4f^{N-1}5d$ one, even though such effect is partially compensated because other excited configuration contributions are also overestimated, but with the opposite signal.

The numerical values $\theta(t,\lambda)$ for the Eu(III) ion are: $\theta(1,2) = -0.17$, $\theta(3,2) = 0.34$, $\theta(3,4) = 0.18$, $\theta(5,4) = -0.24$, $\theta(5,6) = -0.24$, and $\theta(7,6) = 0.24$. Such values should be similar for the rest of the lanthanide series. Theoretical calculations for the Eu(III) ion in various compounds show that the values of $B_{\lambda,t,p}$ given by eq. (2.15) are close to those given by eq. (2.7) [76].

2.2.3 The dynamic coupling mechanism

Despite the success of the original J-O theory, it was noticed that the FED and MD (allowed by parity) are not the only operative mechanisms in 4*f*–4*f* transitions. In an attempt to explain the very large variations of the intensity of some 4*f*–4*f* transitions due to the chemical environment around the Ln(III) ion, the so-called hypersensitive transitions, a mechanism was proposed 2 years after the J-O theory in a seminal paper by Jørgensen and Judd [77], which became known as the DC mechanism. Figure 2.3a displays a simplified visualization of the original DC mechanism.

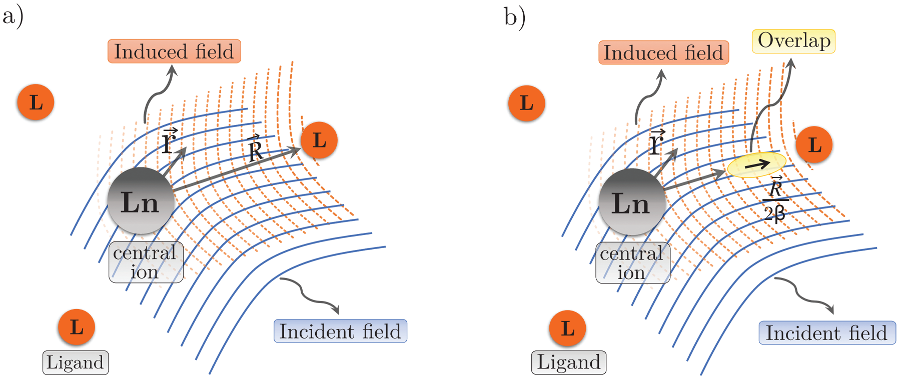

Figure 2.3: Pictorial representations of (a) the original dynamic coupling (DC) mechanism [77, 78] and (b) the bond overlap model (BOM) [41, 61].

The incident radiation field, $\vec{E}_{\text{incident}}$, induces oscillating dipoles in the atoms or ions surrounding the lanthanide ion, and, consequently, an additional oscillating electric field is produced. This electric field presents enormous gradients close to the lanthanide ion and can induce 4*f*–4*f* transitions with oscillator strengths in the order of 10^{-6}. In a first approximation, the induced oscillating dipoles depend on the isotropic dipolar polarizability of the atoms or ions that surround the Ln(III) ion in the following way:

$$\vec{\mu}_j = \alpha_j \vec{E}_{\text{incident}} \tag{2.18}$$

where α_j is the polarizability of the *j*th surrounding atom or ion.

The interaction energy, H_{DC}, of the 4*f* electrons is given by

$$H_{\text{DC}} = -\vec{\mu}_{\text{DC}} \cdot \vec{E}_{\text{incident}} \tag{2.19}$$

where

$$\vec{\mu}_{\text{DC}} = -e \sum_{i,j} \alpha_j \frac{\left(\vec{r}_i - \vec{R}_j\right)}{\left|\vec{r}_i - \vec{R}_j\right|^3} \tag{2.20}$$

Considering that $|\vec{r}_i| < \left|\vec{R}_j\right|$ and using the following multipole expansion [71]

$$\frac{\left(\vec{r}_i - \vec{R}_j\right)}{\left|\vec{r}_i - \vec{R}_j\right|^3} = \sum_{\lambda,Q,\rho,p} (-1)^{\lambda+\rho}[4\pi(\lambda+1)(2\lambda+1)]^{1/2} \times \frac{Y_p^{\lambda+1*}\left(\theta_j, \phi_j\right)}{R_j^{\lambda+2}} \begin{pmatrix} \lambda+1 & 1 & \lambda \\ p & Q & \rho \end{pmatrix} r_i^{\lambda} C_{-\rho}^{(\lambda)}(i)\, \vec{e}_Q^{\,*} \tag{2.21}$$

the dipole moment operator $\vec{\mu}_{\text{DC}}$ can be written as

$$\vec{\mu}_{\text{DC}} = -e \sum_{\lambda,\rho,Q,p,i} (-1)^{\lambda+\rho}(2\lambda+1) \times \left[\frac{(\lambda+1)(2\lambda+3)}{(2\lambda+1)}\right]^{1/2} \Gamma_p^t \delta_{t,\lambda+1} \begin{pmatrix} t & 1 & \lambda \\ p & Q & \rho \end{pmatrix} r_i^{\lambda} C_{-\rho}^{(\lambda)}(i)\, \vec{e}_Q^{\,*} \tag{2.22}$$

where the Γ_p^t quantities are

$$\Gamma_p^t = \left(\frac{4\pi}{2t+1}\right)^{1/2} \sum_j \alpha_j \frac{Y_p^{t*}\left(\theta_j, \phi_j\right)}{R_j^{t+1}} \tag{2.23}$$

The dipole operator $\vec{\mu}_{\text{DC}}$ leads to nonzero matrix elements between the states of the $4f^N$ configurations for $\lambda = 2$, 4, or 6. Therefore, the 4*f*–4*f* transitions are allowed by the DC mechanism, but not for $\lambda = 1$, which would require mixing of opposite parity configurations, leading to oscillator strengths much smaller than the contributions from the FED mechanism (comparison not shown in this chapter). From eq. (2.22), the following quantities are similarly defined for the DC mechanism:

$$B_{\lambda,t,p}^{\text{DC}} = -\left[\frac{(\lambda+1)(2\lambda+3)}{(2\lambda+1)}\right]^{1/2} \left\langle 4f|r^{\lambda}|4f\right\rangle \left\langle f\middle\|C^{(\lambda)}\middle\|f\right\rangle \Gamma_p^t \delta_{t,\lambda+1} \tag{2.24}$$

As described earlier, the additional field in the DC mechanism is produced by oscillating dipoles, which do not consider the effects of chemical bonding. An approximated manner to consider these effects consists in multiplying the expression for $B_{\lambda,t,p}^{\mathrm{DC}}$ in eq. (2.24) by the shielding factor $(1-\sigma_\lambda)$. This factor is not included in the $B_{\lambda,t,p}^{\mathrm{FED}}$ within the framework of SOM [59, 60] because it already considers the overlaps between 4*f* orbitals and ligating atom valence shell orbitals, which intrinsically contain the shielding effects. Similarly, within the BOM framework [41, 61], this shielding factor is not included in the $B_{\lambda,t,p}^{\mathrm{DC}}$ because the overlaps are considered explicitly as depicted in Figure 2.3b.

Theoretical calculations have shown that the $B_{\lambda,t,p}^{\mathrm{DC}}$ are as important as the $B_{\lambda,t,p}^{\mathrm{FED}}$, or even more relevant in some cases such as for hypersensitive transitions [41]. It is noteworthy that the DC mechanism, according to eq. (2.23), depends on structural factors (coordination geometry) and it is expected to be very sensitive to the nature of the chemical environment through the polarizabilities, α_j, of the ligating atom or ion [41, 61, 79].

An analysis of the typical values of the quantities appearing in both DC and FED mechanisms shows that, in general, they contribute with opposite signs and, therefore, the effects of interference can be relevant. Both γ_p^t (ligand field) and Γ_p^t (polarizability-dependent term) parameters contain the same kind of summation over the neighboring atoms. Consequently, they contain the same information on symmetry. The only difference is that Γ_p^t does not involve the rank 1 spherical harmonics Y_p^1, as it can be seen from the Krönecker delta in eqs. (2.22) and (2.24). As the site occupied by the Ln(III) ion becomes more and more symmetric, tending to a site symmetry with a center of inversion, the γ_p^t and Γ_p^t of lower ranks go to zero faster than the higher rank ones [80]. Thus, the lower rank functions are more sensitive to changes in symmetry than the higher ranked ones, even though the latter is more sensitive to changes in the Ln-ligating atom distances, R_j, as expressed in eq. (2.23) and depicted in Figure 2.3. As will be discussed later, this behavior follows the correct direction for the comprehension of the hypersensitive transitions that are, in general, those dominated by the Ω_2 intensity parameter.

2.2.4 Summarizing the theory

By considering both FED and DC mechanisms, eq. (2.11) should be rewritten as follows:

$$\Omega_\lambda = (2\lambda+1)\sum_{t,p}\frac{\left|B_{\lambda,t,p}\right|^2}{(2t+1)}, B_{\lambda,t,p} = B_{\lambda,t,p}^{\mathrm{FED}} + B_{\lambda,t,p}^{\mathrm{DC}} \tag{2.25}$$

where $B_{\lambda,t,p}^{\mathrm{FED}}$ and $B_{\lambda,t,p}^{\mathrm{DC}}$ are given, respectively, in eqs. (2.7) and (2.24). It is worthy to emphasize that the assumptions that were made in the derivation of the $B_{\lambda,t,p}^{\mathrm{FED}}$, and consequently the Ω_λ parameters, lead to limitations in the applications of the theory for systems in which the lowest opposite parity configuration $4f^{N-1}5d$ lies close to the ground $4f^N$ one. In this case, the lowest $4f^{N-1}5d$ states may even overlap excited states of the $4f^N$ configuration, and the approximation $\left|\Delta E_{4f^N}\right| \ll \left|\Delta E\left(4f^N, 4f^{N-1}5d\right)\right| \cong \left|E_{4f} - E_{5d}\right|$ becomes questionable (Figure 2.2), as well as the use of first-order time-independent perturbation theory to reach the form as given by eq. (2.10). This reasoning also applies to the average energy denominator method, leading to eq. (2.15) [74, 75]. Furthermore, because the states $\left|\left(4f^N\right)\psi J M_J\right\rangle$ and $\left|\left(4f^N\right)\psi J' M_{J'}\right\rangle$ were considered equally populated (or, equivalently, degenerate for the purpose of summation over the M_J's) with respect to M_J and $M_{J'}$, respectively, care should be taken in applying the theory to model systems at low temperatures. In this later issue, as the main emitting level of the Eu(III) ion ($^5D_0$) is nondegenerate, this ion does not present limitation in this regard when the Ω_λ parameters are evaluated from the emission spectra.

If one is interested in evaluating the intensities of Stark-to-Stark transitions (from the fine structures of J levels), the $B_{\lambda,t,p}$ quantities should be used instead of Ω_λ [81, 82]. In this case, the M_J's should no longer be considered as good quantum numbers and the Stark levels are now labeled by irreducible representations of the point symmetry group in which the Ln(III) ion is located.

Before closing this section, it should be called attention to the fact that, starting from eqs. (2.7), (2.9), (2.23), and (2.25), the symmetry aspects, involving summations over the ligating atoms or ions in the first coordination sphere, appeared before taking the squared modulus of the $B_{\lambda,t,p}$ parameters. Therefore, the $4f$–$4f$ oscillator strengths or the transition rates cannot be separated into a sum of contributions from each ligating atom or ion as reported in ref. [83]. Otherwise, not only symmetry effects, which are crucial, would be completely lost but also numerical values of transition rates would be wrongly evaluated.

2.3 A brief review of correlations and interpretations of the intensity parameters

In lanthanide ion spectroscopy, the treatment of $J \rightarrow J'$ transitions in terms of three parameters, Ω_2, Ω_4, and Ω_6, has been since 1962 a successful procedure widely used in many areas of chemistry and physics involved with the optical features of lanthanide compounds. Soon after the J-O theory pointed toward the relevance of the intensity parameters, attempts were made to interpret them in terms of the properties of the Ln (III) ion and its environment. For instance, while explaining the origins of hypersensitive transitions, relationships of Ω_2 with the local structure were observed [77].

In the following decades, enough experimental data were gathered and theoretical approaches matured to allow more detailed and direct interpretations of the

Ω_λ's.[1] Indeed, a very influential interpretation was based on the trends observed for Ω_λ's of Er(III) in 17 local environments, including solids (crystal and glass), liquids (water and alcohols), and gas [47]. For Er(III) in solution, the values of Ω_2 (in units of 10^{-20}cm^2) increased as 1.59 in water < 3.2 in CH_3OH < 5.0 in CH_3CH_2OH < 5.5 in n-$CH_3CH_2CH_2OH$, while in the gas phase increased as 25.8 for $ErCl_3$ < 60 for $ErBr_3$ < 100 for ErI_3 [47]. It was suggested that Ω_2 increases with the covalency of the lanthanide ion. Interpreting the trends of Ω_2 by the covalency of the bonds of the lanthanide ion with its environment is very appealing, despite being described by a difficult concept. Indeed, covalency is not a uniquely quantifiable descriptor of chemical bonds, especially for lanthanide ions. Because the chemical behaviors of Ln(III) are very similar, the covalency or degree of covalence will be mostly dictated by the nature of the ligands and can be related qualitatively to their polarizabilities or sizes or hardness or electronegativities. In fact, within the formalism of the density functional theory, these properties are interrelated and can be partially quantified. From an experimental perspective, there are different methods to estimate the covalency between the lanthanide ion and its ligands. One of the earliest approaches and still widely employed is based on the nephelauxetic effect [84, 85]. This effect is quantified by the nephelauxetic ratio of the electron repulsion parameters (or Slater integrals) F_k ($k = 2, 4, 6$) of the ion surrounded by the ligands (i.e., complex) to that of the free ion [84–86], namely,

$$\beta_k = \frac{F_k(\text{complex})}{F_k(\text{free ion})} \tag{2.26}$$

The reasoning is that the covalency of Ln(III)–ligand bonds would spread or expand the electron density of the ion, thus decreasing the electronic repulsion. It is usually assumed that this ratio does not vary with k [84], namely, $\beta_k \cong \beta$, so a single value of the nephelauxetic ratio is estimated. This approximation can be justified theoretically by considering that only the $4f$ radial function, $R_{4f}(r)$, is modified during the Ln(III)–ligand bonding such as [58]

$$R_{4f}(r) = (1-b)^{1/2} R^{\circ}_{4f}(r) - b^{1/2} R_{\mathrm{L}}(r) \tag{2.27}$$

where $R^{\circ}_{4f}(r)$ is the radial function of the free ion and $R_{\mathrm{L}}(r)$ is the ligand's radial function redefined relative to an origin located at the ion, which is mixed by the "covalency" descriptor b [58]. When the repulsion integrals are calculated with this modified radial function and after neglecting all terms involving products of $4f$, $R^{\circ}_{4f}(r)$, and ligand, $R_{\mathrm{L}}(r)$, radial functions as well as all terms involving b^2, the ratio becomes $\beta_k \cong \beta = 1 - 2b$, which is independent of k and the (degree of) covalency can be calculated as [58]

---

[1] The intensity parameters are usually reported as Ω_λ; however, there are also other representations such as T_λ and $T_\lambda \equiv \tau_\lambda$, whose relationships with Ω_λ are given in ref. [46]. In fact, several of the Ω_λ values listed in this page were reported originally as τ_λ, which were accordingly transformed to Ω_λ.

$$b = (1 - \beta)/2 \tag{2.28}$$

However, experimental results and calculations do not corroborate such an approximation. For instance, $LaCl_3$- and $LaBr_3$-doped crystals with Pr(III) presented ratios β_k of ca. 0.95, 1.01, and 1.03 for $k = 2$, 4, 6, respectively [58]. Despite these and other evidences, the nephelauxetic effect ratio is considered independent of k and the (degree of) covalency calculated as $b = (1 - \beta)/2$. The complexity of extracting F_k from spectra as well as obtaining these parameters for the free ion prompted the proposal and acceptance of an approximated method for determining the nephelauxetic effect as the ratio of the wave numbers of the Ln(III) 4*f*–4*f* transitions surrounded by ligands (i.e., complex), $\tilde{\nu}_{\text{comp}}$, to that of the aqua-ion, $\tilde{\nu}_{\text{aqua}}$, namely [85],

$$\beta \cong \frac{\tilde{\nu}_{\text{comp}}}{\tilde{\nu}_{\text{aqua}}} \tag{2.29}$$

This quantity is also known as Sinha's parameter.

Other approaches to quantify the covalency of lanthanide ion–ligand bonds have been proposed such as that based on the parameter e_σ of the angular overlap model [87–89]. An analysis of a series of anhydrous Eu(III) phosphates corroborated the relation between the parameter e_σ of the Eu−O bond and its distance, $e_\sigma(\text{Eu} - \text{O}) \sim d_{\text{Eu-O}}^{-7}$, and showed that $e_\sigma(\text{Eu} - \text{O})$ is strongly dependent on the polarizabilities of the oxygen ligating atoms, which, on the other hand, can be related to the optical basicity of the ligands [88, 89]. Interestingly, these correlations and trends were obtained for this series of anhydrous Eu(III) phosphates employing a unit nephelauxetic ratio, $\beta = 1.0$, so the free ion parameters were not scaled in describing the properties in the complexes [88]. Considering the dependence of Ω_2 on the covalency of Ln−ligand bonds, it was recently proposed that a correlation between the parameter e_σ and Ω_2 would be expected [89]; however, it still has not been corroborated by experimental data. Another approach for quantifying the covalency of Ln−ligand bonds is based on the overlap properties of these bonds and will be presented further in more detail.

The relevance of Ln(III) ions in optical fiber communications has prompted detailed studies of their photophysical properties in glasses. These studies provided a correlation between the magnitude of Ω_2 and the symmetry of the coordination polyhedron surrounding the ion [50, 51]. Several years before, by analyzing the expressions for the Ω_λ within the J-O theory, it was suggested that symmetry should play a significant role in their values [48, 49]. However, the lack of experimental data for well-defined structures at that time hindered the corroboration of such a suggestion. A more detailed analysis of the symmetry effects of the coordination polyhedron proposed a dimensionless quantity Θ_t expressed as a summation over the ligating atoms (L, L') of the Legendre polynomial of degree t, P_t, with the cosine of the angle between the ligating atoms and the lanthanide ion $\theta_{\text{LL}'} \equiv \angle(\text{L}-\text{Ln}-\text{L}')$ as argument [90]:

$$\Theta_t = \sum_{\mathrm{L,L'}} P_t\left(\cos\theta_{\mathrm{LL'}}\right) \tag{2.30}$$

This quantity Θ_t has interesting properties [90] and was employed to explain the different values of Ω_2 of lanthanide trihalides in the gas phase (LnX_3(g) with a shallow C_{3v} pyramidal structure) and the crystal (LnX_3(s) nine coordination with D_{3h} local symmetry). Setting an angle of 100° for LnX_3(g) and of 42° for LnX_3(s), Θ_3 is 5.68 for LnX_3(g) and 0.88 for LnX_3(s), which gives an enhancement factor of 6.5 that is consistent with experimental observations; however, the experimental ratios $\Omega_2(\mathrm{gas})/\Omega_2(\mathrm{crystal})$ for LnX_3 are quite larger than 6.5 [90]. These and other analyses and results point to the relevance of the symmetry onto the intensity parameters, especially on Ω_2.

The symmetry of a polyhedron is quantifiable by order of its point group symmetry as well as by the degree of distortion concerning a given perfect (or undistorted or ideal) polyhedron. Thus, as the coordination polyhedron changes, it is said to become more asymmetric as the order of the point group decreases or the degree of distortion increases. It was then observed and proposed that the value of Ω_2 strongly increases by lowering the symmetry (or increasing the asymmetry) of the coordination polyhedron [50, 51]. This proposal has become a powerful tool to probe the local environment of Ln (III) ions and to rationalize changes of their photophysical properties upon thermal treatments of prepared samples or modifications of glass composition, for instance. It has also been applied quite successfully to complexes with organic ligands as well as inorganic crystalline systems. At first glance, it seems that the dependence of Ω_2 on the covalency and the symmetry is unrelated and may exclude each other. However, to account for covalency, the orbitals must overlap, and because they are directional, the overlaps and covalency of bonds will depend on the arrangement of the ligating atoms around the lanthanide ion. In addition, the orbitals of the ligating atoms will combine according to their arrangement and provide interferences that will affect the behavior of the Ln–ligand bonds. Thus, covalency and symmetry are intrinsically related. However, it seems that by using the lowest energy Tb(III) $4f^8 \rightarrow 4f^7 5d^1$ transition as a measure of covalency, these two effects were separated [56]. Indeed, a linear relationship between the Eu(III) Ω_2 values and the peak wavelength of the Tb(III) $4f^8 \rightarrow 4f^7 5d^1$ absorption band at 200–220 nm found for the fluoride, fluoride phosphate, and phosphate glasses. This observation is consistent with the J-O theory that predicts that Ω_λ's are proportional to the inverse of the energy of the f–d transition, so they are proportional to the wavelength of this transition. In addition, because the energy of the f–d transition is affected by the polarizability of the ligating atoms [56], it can be used as a measure of covalency, and the observed linear trend in the values of Ω_2 is attributed to changes in the covalency. As a result, the deviations observed for ultraphosphate glasses were attributed to variations of the asymmetry [56], and the effects of covalency and symmetry were separated.

The trends observed for the values of Ω_6 of Er(III) in those 17 environments [47] suggested that it could be correlated to the rigidity of the system. Grouping these systems according to their rigidity, the values of Ω_6 (in units of 10^{-20}cm^2) for Er(III) were in the crystalline phase (0.48 and 0.57), glasses (0.90, 1.14, 1.19, 2.2, and 7), molten salt (1.4), solution (0.6, 0.7, 0.8, 1.4, and 1.90), and vapor (1.7, 2.0, and 3.7). Despite the wide range of variation and overlapping values, it was suggested that Ω_6 increases as the rigidity of the medium decreases [47]. The concept of rigidity is somewhat abstract, and it has been proposed to quantify rigidity by the viscosity of the medium or by its order of crystallinity. For lanthanide ions in solvents, there seems to be a decrease in the values of Ω_6 with an increase of the viscosity of the medium [47]. In glasses, systematic studies indicated that Ω_4 and Ω_6 are insensitive to the local structures but they increase when the covalency of the lanthanide site decreases [50–53]. It was also observed that Ω_4 and Ω_6 increase with ionic packing ratio of the host matrix, and that both Ω_4 and Ω_6 decrease with the increase in the number of 4*f* electrons [54, 55, 57, 86]. These assertions are based on several correlations and trends: the determination of Ω_λ of Nd (III) in 90 samples of silicate, borate, and phosphate glasses showed that Ω_4 and Ω_6 increased systematically as the radius of the network modifier increased, for example, from Li(I) to Cs(I) and from Mg(II) to Ba(II). Indeed, quantitative relationships of the increase of Ω_4 and Ω_6 with the ionic packing ratio V_p were observed [54, 55], with $V_\text{p} = V_\text{ion}/V_\text{m}$, where V_ion is the ionic volume:

$$V_\text{ion} = \sum_i \frac{4}{3}\pi r_i^3 x_i N_\text{A} \tag{2.31}$$

where r_i and x_i are the ionic radius and the molar fraction, respectively, of component *i* of the glass host, and N_A is the Avogadro number, whereas V_m is the molar volume expressed as the ratio of the molar mass (M) to the measured density (ρ) of the glass host: $V_\text{m} = M/\rho$ [54]. On the other hand, the values of Ω_4 and Ω_6 for Pr(III), Nd(III), Sm (III), Tb(III), Dy(III), Ho(III), Er(III), and Tm(III) in alkali and/or alkaline-earth silicate, borate, and phosphate glasses decreased systematically along with this series, thus with the increase in the number of 4*f* electrons, while Ω_2 did not present such systematic variations [55]. Another interesting correlation was found between the values of Ω_6 for Nd(III) in phosphate and silicate glasses and Er(III) in oxide glasses with the isomer shift in the Mössbauer spectra of ^{151}Eu(III) in the same matrices [52, 53]. For oxide glasses, Ω_6 decreased with the isomer shift, which is proportional to the 6*s* electron density. This trend was explained by the stronger dependence of Ω_6 on the overlaps between 4*f* and 5*d* orbitals, which should increase with an increase of these overlaps. On the other hand, these overlaps should decrease when the 6*s* electron density becomes larger because it shields the 5*d* orbitals, thus decreasing their overlaps with the 4*f* orbitals [52, 53].

2.3.1 A brief review of gaseous lanthanide halide complexes

Lanthanide trihalide complexes (LnX_3, X = F, Cl, Br, I) in crystal and gaseous forms have played a relevant role in the development of models and interpretation of the intensity parameters Ω_λ [47, 91]. Therefore, some studies of LnX_3 and other gaseous complexes [90, 92–97] will be briefly reviewed. The relevance of LnX_3 complexes is due to their simplicity (monoatomic ligands and trigonal planar D_{3h} or pyramidal C_{3v} structures), measurements of Ω_λ in the gas phase (nearly isolated systems), and systematic trends.

Early on, the values of Ω_2 (in units of 10^{-20}cm^2) for gaseous LnX_3 were determined [92, 93] and follow the trend $\Omega_2(LnI_3) \cong 1.6 \times \Omega_2(LnBr_3)$. More specifically, Ω_2 (in units of 10^{-20}cm^2) values were ~ 90 and ~ 45 for PrI_3 and $PrBr_3$, 270 and 180 for NdI_3 and $NdBr_3$, 95 and 58 for ErI_3 and $ErBr_3$, and 88 and 53 for TmI_3 and $TmBr_3$. Notice that these values of Ω_2 for NdI_3 and $NdBr_3$ were adjusted considering the values of Ω_4 and Ω_6 equal to those in solution, namely, $\Omega_4 = \Omega_6 = 9 \times 10^{-20}\text{cm}^2$ [93]. In fact, the values of Ω_4 and Ω_6 for these gaseous complexes could not be properly determined (some of them were negative) because of the appearance of a broad band at around 28,000 cm^{-1}. For PrI_3 and $PrBr_3$, only lower limits of Ω_4 and Ω_6 were obtained, whereas a nonphysical negative value of Ω_6 was obtained for ErI_3, and negative values Ω_4 were also reported for TmI_3 and $TmBr_3$. It is noteworthy to set the values of Ω_4 and Ω_6 as those for TmI_3 and $TmBr_3$ in solution, namely, $\Omega_4 = \Omega_6 = 27 \times 10^{-20}\text{cm}^2$, then the adjusted values of Ω_2 become 37 and 41 $\times 10^{-20}\text{cm}^2$, so the trend $\Omega_2(LnI_3) > 1.6 \cdot \Omega_2(LnBr_3)$ in the gas phase is not observed [93]. This discussion regarding the relative values of Ω_2 is relevant because for gaseous LnX_3, the trend of Ω_2 increasing with the atomic number of the halide X has been decisive to attribute the increase of covalency [47, 48]. The values of Ω_λ were obtained by adjusting them to reproduce the experimentally observed oscillator strengths, which were determined by integrating the molar absorptivity $\varepsilon_{\tilde{\nu}}$ over the wave number $\tilde{\nu}$ range of the absorption band. The $\varepsilon_{\tilde{\nu}}$ quantity is obtained from the measured absorbance $A_{\tilde{\nu}}$ at $\tilde{\nu}$, divided by the optical path length l and the molar concentration of the vapor complex $[LnX_3]$, or $\varepsilon_{\tilde{\nu}} = A_{\tilde{\nu}}/(l \cdot [LnX_3])$ [92, 93]. Notice that only in the case of $ErBr_3$, enough 4*f*–4*f* transitions were available to perform a rigorous analysis of the absorption spectrum and to obtain reliable values of Ω_λ [93]. For the other trihalide complexes, some adjusted values of Ω_4 and/or Ω_6 were negative because the appearance of a broad band at around 28,000 cm^{-1} precluded the observation of many 4*f*–4*f* transitions associated with these intensity parameters. The origin of this broad absorption band was unknown, but its intensity increased with time and temperature. An error of ±25% was reported for the values of the oscillator strengths; however, the relative intensities are known within ±5%, which determine the relative magnitudes of Ω_λ, except for weak transitions of less volatile PrX_3 and NdX_3 complexes, for which the errors are ±25% [93]. However, regarding the relative values of Ω_2 for $LnBr_3$ and LnI_3, an essential source of error is their concentrations $[LnX_3]$ in the gas phase because it directly affects the oscillator strengths. The determination of $[LnX_3]$ requires some assumptions and several thermochemical values, which some were not known at that time [92, 93]. An analysis of the errors of the oscillator strengths and of Ω_λ's associated with the uncertainties on the concentrations was not performed, and an error of ±25% was guessed for the molar absorptivity [93].

Values of Ω_2, Ω_4, and Ω_6 (in units of $10^{-20}\mathrm{cm}^2$) for gaseous $ErCl_3(AlCl_3)_x$ were determined as 25.8, 2.7, and 2.0, respectively [98–100], and compared those of $ErBr_3$ and ErI_3 [47]. The value of Ω_2 for $ErCl_3(AlCl_3)_x$ is less than half of that for $ErBr_3$ and it is tempting to attribute to a decrease of covalency. However, the $ErCl_3(AlCl_3)_x$ complex does not correspond to an isolated $ErCl_3$ species, and because $x \sim 3.5$ for the $NdCl_3$–$AlCl_3$ system, a six-coordinated $LnCl_6$ complex was suggested with a distorted octahedral structure and Ln–Cl–Al bridging-type coordination [98], which precludes direct comparisons with $ErBr_3$ and ErI_3.

These experimental results motivated several studies on lanthanide complexes in the gas phase [101, 102] as well as theoretical modeling of the intensity parameters, especially in measuring, calculating, and explaining the high intensities of the hypersensitive 4*f* transitions. The temperatures required to produce viable quantities of gaseous LnX_3 are quite high, namely, 1,046–1,195 °C for $LnBr_3$ and 942–1,190 °C for LnI_3, with Ln = Pr, Nd, Er, and Tm [93]. This thermal feature limited the studies to lanthanide tribromide and triiodide complexes, whereas gaseous $LnCl_3$ complexes were studied using evaporation under the atmosphere of $ACl_3(g)$ (A = Al, Ga, In) at temperatures in the range of ca. 230–730 °C [101]. Lanthanide trihalide complexes (e.g., NdI_3 and $HoCl_3$) were also studied under MCl(g) (M = Li, Cs, Tl) [101, 102]. These studies are interesting because they provide information regarding the structural effects on the intensities of 4*f*–4*f* transitions, once LnX_3, LnX_3–AX_3, and LnX_3–MX systems have different structures, namely, gaseous LnX_3 has trigonal planar (D_{3h}) or pyramidal (C_{3v}) structure. In contrast, the lanthanide ion in LnX_3–AX_3 systems has distorted octahedral coordination, while the LnX_3–MX systems are better represented as a distorted tetrahedral $MLnX_4$ with M(I) coordinated to one of the vertices of the polyhedral [102].

Several experimental techniques have pointed to a trigonal planar (D_{3h}) structure for gaseous LnX_3, which has been the source of some interesting discussions [103, 104]. Indeed, the normal mode associated with the inversion of the pyramidal (C_{3v}) structure has a very low vibrational frequency, which suggests that the C_{3v} structure is highly fluxional. It has then been argued that some observed planar D_{3h} structure could in fact be an average fluxional pyramidal structure. It is expected that changing the symmetry from D_{3h} to C_{3v} would greatly affect the intensities of the 4*f*–4*f* transitions; however, the effects of fluxionally on these intensities are still unexplored. Tetratomic systems such as LnX_3 can have structures with symmetries D_{3h}, C_{3v}, C_{2v}, C_s, and C_1; however, comprehensive reviews of the structural and vibrational features of gaseous LnX_3 indicated either D_{3h} or C_{3v} structures [103, 104]. Despite the several advances in experimental methods, analysis techniques, and quantum chemical calculations, there are still some ambiguities and controversies regarding the gaseous structures of LnX_3 [103, 104]. It has been proposed that all LnF_3 have pyramidal structures with recommended equilibrium

F−Ln−F angles increasing systematically in the interval of 109.0–116.0° for La to Lu [104]. The X−Ln−X angles increase to 118.0−119.0° for Ln = La, Ce, Pr, and Nd and X = Cl, Br, and I, whereas for the remaining LnX_3 complexes the structures are trigonal planar with X−Ln−X angles of 120.0°. The observed trend consists of an increase of X−Ln−X angles from F to I and from La to Lu, which has been attributed to the decreasing polarizability of Ln from La to Lu and the weakening polarization ability of the X from F to I [104]. It is important to emphasize that the analysis of the experimental data to extract structural information depends on the vibrational frequencies. The normal modes of LnX_3 molecules are represented by $2A_1 + 2E$ for a C_{3v} symmetry and by $A'_1 + A''_2 + 2E'$ for a D_{3h} one, where A'_1 can be assigned to the symmetric stretch, A''_2 to the out-of-plane bending or pyramidalization mode, E' to asymmetric bending, and asymmetric stretch [95]. The recommended vibrational frequencies of LnX_3 systematically increase from La to Lu; for example, for $LnCl_3$, the wave numbers of A'_1 vary from 318 to 345 cm^{-1}, A''_2 from ca. 59 to 69 cm^{-1}, E'_{bend} from 84 to 98 cm^{-1}, and $E_{\mathrm{str}}{}'$ from 317 to 351 cm^{-1} [104]. On the other hand, for ErX_3, the wave numbers systematically decrease for X = F to I; for example, A'_1 mode from 576 to 168 cm^{-1}, A''_2 from 98 to 29 cm^{-1}, E'_{bend} from 142 to 44 cm^{-1}, and $E_{\mathrm{str}}{}'$ from 556 to 197 cm^{-1} [104]. These trends can be promptly rationalized by the smooth increase of the masses from La to Lu and their drastic increase from F to I. The small wave numbers ($< 100 cm^{-1}$) of the A''_2 mode suggests that the inversion of the pyramidal structure would have a small barrier. For LnX_3 with X = Cl, Br, and I, barriers smaller than 1 kJ/mol were estimated from experimental data and ab initio quantum chemical calculations, while DFT methods overestimated these barriers [104]. Nevertheless, these are highly fluxional structures with energy barriers, for the heavier species, so low that are close or below the zero-point vibrational energy of the inversion mode, rendering an effectively planar geometry. It is thus expected that these low vibrational frequency modes can affect many molecular properties, particularly the intensities of 4*f*–4*f* transitions. These effects can be inferred from the dipole moments of LnX_3 molecules. For GdX_3, the calculated electric dipole moments are 3.4 and 2.1 D for X = F and Cl (C_{3v} symmetry), respectively, and 0.0 D for both Br and I (D_{3h} symmetry) [105]. Averaging the dipole moment over the vibrational modes at 0 K causes a decrease to 3.0 D and 1.1 D for X = F and Cl, while an increase to 0.3 and 0.2 D for Br and I [105], which shows the relevance of the inversion of the pyramidal structure and the pyramidalization of the planar one. Higher vibrational levels become populated for temperatures above 0 K, and larger amplitude motions start taking effect. Indeed, for temperatures near those employed in the gaseous measurements, that is, at 1,000 K, the average dipole moments become 2.8, 2.1, 1.4, and 1.1 D for X = F, Cl, Br, and I, respectively, in GdX_3 [105].

The reports of very intense hypersensitive transitions for gaseous LnI_3 and $LnBr_3$, where Ln = Pr, Nd, Er, and Tm [92, 93], triggered immediate attempts [90, 93–97] to explain those results. A symmetry analysis [106] indicated that a D_{3h} environment around the lanthanide ion could not account for hypersensitive transitions. It was proposed that the hypersensitivity was due to the molecular vibrations [93], especially the out-of-plane bending normal mode that leads to a C_{3v} structure that satisfies the symmetry requirements for hypersensitive transitions [106]. However, this vibronic mechanism [93] was strongly criticized due to its estimated negligible contribution to the oscillator strengths of 4*f*–4*f* transitions [90, 91]. Covalency was then introduced in the model to explain the hypersensitivity, once the (degree of) covalency depends on the surrounding ligands. Because the properties of charge-transfer transitions are very sensitive to the nature of the ligands and metal ion, the covalency effects were also considered by mixing charge-transfer states in the description of the 4*f*–4*f* intensities [107]. However, when this modified model was applied to an isostructural series of lanthanide compounds, it was found that charge-transfer mixing has negligible contribution to the intensities of hypersensitive transitions in Ln(III) [108].

Only after the development of the DC mechanism [78, 90, 109–119], some hypersensitivity of some 4*f*–4*f* transitions in LnX_3(g) were adequately explained and quantified [90, 109]. This model describes these transitions by the interactions of the electric dipoles in the ligands induced by the radiation field with the electronic density (multipole moments) of the metal ion *f*-orbitals. It was shown that the hypersensitive transitions are restricted to the quadruple moment of the *f*-electronic density [78], originating the former designations of "pseudo-quadrupole mechanism" [77] or "pseudo-multipolar field" [112–114], and DC mechanism yields contribution to 4*f*–4*f* transitions in Ln(III) within environments belonging to the point groups: D_n and C_{nv} (for any *n*), C_{3h}, D_{3h}, T_d, and their subgroups [78], with C_{3v} and D_{3h} being particularly relevant to LnX_3(g). However, despite the (semi)quantitative agreements and explanations, these models rely on (semi)empirical parameters that may require values that are unusual or even unphysical, most likely because in these calculations of Ω_λ for LnX_3(g), the vibrational and thermal averaging effects have not been considered.

From a quantum chemistry perspective, the intensities of the 4*f*–4*f* transitions can be calculated by the expectation value of the dipole moment operator with respect to the wave functions describing the initial and final states. These calculations are quite challenging for lanthanide complexes and materials because of the open-shell configurations, the spin multiplets, the electronic correlation effects, and relativistic effects, particularly spin–orbit (SO) coupling. Thus, the application of quantum chemical methods is restricted to small systems, and gaseous LnX_3 complexes have been studied in detail [95–97]. As noticed previously, vibrational and thermal effects are relevant for molecular properties and should be considered when calculating transition dipole moment. Given the very weak interaction of the 4*f*-electrons with their environment, it can be considered that the same coordinates $\boldsymbol{Q}_i$ of the *i*th normal mode can be used to describe the potential energy surfaces of the initial I and final F electronic states in 4*f*–4*f* transitions [95]. Under this approximation, the vibrationally and thermally averaged oscillator strength f_{FI_i} can be calculated as,

$$\langle f_{\mathrm{FI}i} \rangle = \int^{\mathrm{d}} \boldsymbol{Q}_i f_{\mathrm{FI}}(\boldsymbol{Q}_i) \sum_{\upsilon} \left| \chi_{\upsilon}^{I}(\boldsymbol{Q}_i) \right|^2 W_{\upsilon}(T) \tag{2.32}$$

where I is the initial and F the final electronic states in $4f$–$4f$ transitions, $\boldsymbol{Q}_i$ is the coordinate of the ith normal mode, $f_{\mathrm{FI}}(\boldsymbol{Q}_i)$ is the oscillator strength calculated at normal mode coordinate $\boldsymbol{Q}_i$, χ_{υ}^{I} is the vibrational wave function of the initial electronic state at quantum vibrational number υ, and W_{υ} is the Boltzmann distribution factor of the vibrational state υ at the initial electronic state calculated at temperature T [95]. The vibrational wave functions χ_{υ}^{I} were determined numerically by finite difference grid method on a potential energy curve determined by the model core potential (MCP) approach, and the vibrational eigenvalues were used to compute the thermal weighting factor W_{υ} at 1,000 K. The electronic wave functions of the initial and final states were calculated with the multireference SO configuration interaction (MR-SOCI) method using the one-electron SO Hamiltonian with effective nuclear charge adjusted to reproduce the SO splittings of the Ln(III) ion and the halide atoms. Two relativistic effective core potentials and the MCP were used to describe the inner electrons of Ln and halide atoms. The SOCI method employed the state-averaged molecular orbitals obtained by averaging over all configurations generated by the $4f^2$ or $4f5d$ of LnX$_3$ with Ln = Pr and Tm. The singlet and triplet configuration state functions were generated with the reference of $4f^2$ or $4f5d$ in the first- and second-order CI. A large external space consisting of all the SCF virtual orbitals was used to account for all relevant one-electron excitations for Ln, f–d mixing, ligand-to-metal charge transfer (LMCT), and intraligand excitations [95]. The calculations were performed for the PrBr$_3$, PrI$_3$, TmBr$_3$, and TmI$_3$ complexes at the $D_{3\mathrm{h}}$ geometry at the experimental bond lengths. The calculated oscillator strengths at the $D_{3\mathrm{h}}$ structure agreed well with the experimental data. For instance, the hypersensitive $^3\mathrm{H}_4 \rightarrow {}^3\mathrm{F}_2$ transition was calculated with an oscillator strength of 28.1×10^{-6} and 52.9×10^{-6} for PrBr$_3$ and PrI$_3$, respectively, which compares well with the experimental values 20.0×10^{-6} and 40.0×10^{-6} for combined $^3\mathrm{H}_4 \rightarrow ({}^3\mathrm{H}_6,{}^3\mathrm{F}_2)$ transitions. Similar trends and even better agreement were obtained for TmBr$_3$ and TmI$_3$ complexes. Based on symmetry analysis, these results suggest that the DC mechanism is dominant for gaseous LnX$_3$. It is noteworthy that the vibrational and thermal effects have negligible contributions to the oscillator strength of the hypersensitive transition, corroborating earlier estimations based on semiempirical models. As expected, the more significant contributions arose from the lowest wave number normal modes: A_2'' out-of-plane bending (35 cm^{-1}) and E' asymmetric bending (46 cm^{-1}). The oscillator strength of the hypersensitive $^3\mathrm{H}_4 \rightarrow {}^3\mathrm{F}_2$ transition in PrBr$_3$ decreased from 28.1×10^{-6} to 26.4×10^{-6} after being vibrationally and thermally averaged with respect to the A_2'' normal mode and to 26.3×10^{-6} for the E' mode, which amounts to a relative variation of only ca. −6% [95]. These results can be contrasted to the large vibrational and thermal effects on the electric dipole moments of GdX$_3$, where X = F, Cl, Br, and I [105].

By analyzing the transition dipole moment in the atomic basis and classifying the contribution of each configuration to the transition, it was possible to quantify the weight of intra-Ln, *f–d* mixing, LMCT, and intraligand excitations [95]. Both intra-Ln and *f–d* mixing contributions can be associated with the FED mechanism, whereas LMCT excitations are related to the covalency model, while the intraligand excitations represent the DC mechanism. For all transitions in $PrBr_3$ and $TmBr_3$, the contributions from the *f–d* mixing were negligible, while the intraligand excitations dominated most transitions, including the hypersensitive ones, except the very weak $^3H_4 \rightarrow {}^3P_{0,1,2}$ transitions in $PrBr_3$ that were dominated intra-Ln contributions, as well as sizeable contributions from the LMCT excitations to most transitions in $TmBr_3$ [95].

The same ab initio method (MR-SOCI) was employed in the studies of a wider number of LnX_3 complexes, where Ln = Pr, Nd, Pm, Sm, Eu, Tb, Dy, Ho, Er, Tm and X = Cl, Br, I [96, 97]. In general, these results corroborated earlier assertions that the contribution of the DC mechanism dominates the intensities of the hypersensitive transitions, with some contributions of the covalency effects, depending on the Ln (III) ion. The theoretical intensity parameter $\Omega_2(\mathrm{ab})$ was determined from the ab initio calculated oscillator strength and from available matrix elements of $\boldsymbol{U}^{(2)}$ [96]. In addition, a model for the DC contribution was used to calculate $\Omega_2(\mathrm{DC})$ based on the polarizability of the halide, the Ln−X distance, the matrix elements of $C^{(2)}$, and the expectation value of r^2, $\langle 4f|r^2|4f\rangle$, with respect to the 4*f* orbitals of Ln(III). The values of $\Omega_2(\mathrm{DC})$ are systematically higher than $\Omega_2(\mathrm{ab})$, and $\Omega_2(\mathrm{DC})$ decreases smoothly with the increase of the atomic number of Ln because the $\langle 4f|r^2|4f\rangle$ decreases along with the series. In addition, $\Omega_2(\mathrm{DC})$ follows the order $LnI_3 > LnBr_3 > LnCl_3$ because the polarizability of the halide also follows the same order. The ab initio calculated $\Omega_2(\mathrm{ab})$ displays a more complex pattern with respect to the atomic number of Ln because it includes all contributions to the oscillator strength, especially the LMCT excitations that are significant for Eu(III) and cause a break along with the series. These similarities between $\Omega_2(\mathrm{ab})$ and $\Omega_2(\mathrm{DC})$ indicate the dominance of the DC mechanism to the 4*f*–4*f* intensities of LnX_3 complexes, whereas the differences between $\Omega_2(\mathrm{ab})$ and $\Omega_2(\mathrm{DC})$ can be correlated and explained by the weight of the LMCT configurations in the final states of hypersensitive transition, particularly for EuX_3 that have a much larger contribution than TbX_3 [97].

2.3.2 Selected experimental intensity parameters

Nearly 800 values of the intensity parameters Ω_λ for Pr(III) through Tm(III), except Gd(III), mainly in crystalline and glass matrices, have already been reported [46]. Therefore, a few selected examples of experimental intensity parameters are presented in Tables 2.1 and 2.2 for systems with well-defined structures. For instance, Ω_λ's for Nd(III) in 22 environments, for example, coordination compounds (β-diketonates, carboxylates, and perchlorates) and inorganic matrices (molybdates, vanadates, silicates, niobates, and phosphates), are presented in 5 groups according to the relative values of Ω_2, Ω_4, and Ω_6. This aims at observing possible trends, which could be relevant in the interpretations of intensity parameters in terms of covalency, symmetry, polarizability, and so on. The Nd(III) ion was selected because data are extensively known as the experimental intensity parameters. A significant amount of data on Ω_λ for Nd(III) different chemical environments are reported in the literature, and a selection was necessary.

Table 2.1: Intensity parameters Ω_λ (in units of 10^{-20}cm^2) for Nd(III) materials.

Compound	Medium	Ω_2	Ω_4	Ω_6	Trend	Reference
$[Nd(DBM)_3 \cdot H_2O]$	Single crystal	44.7	11.9	1.25	$\Omega_2 > \Omega_4 > \Omega_6$	[120]
$[Nd(TTA)_3(TPPO)_2]$	PMMA	37.0	9.58	6.72	$\Omega_2 > \Omega_4 > \Omega_6$	[121]
$[Nd(DBM)_3(TPPO)_2]$	MMA	30.7	10.5	5.12	$\Omega_2 > \Omega_4 > \Omega_6$	[122]
$[Nd(DBM)_3(TPPO)_2]$	PMMA	30.3	9.65	4.31	$\Omega_2 > \Omega_4 > \Omega_6$	[122]
$[Nd(BDPZ)_3(PHEN)]$	Single crystal	28.8	5.65	5.31	$\Omega_2 > \Omega_4 > \Omega_6$	[123]
$[N(C_2H_5)_4)][Nd(HFA)_4(H_2O)]$	Single crystal	15.3	7.3	3.90	$\Omega_2 > \Omega_4 > \Omega_6$	[124]
$[Nd_2(MAN)_6(H_2O)_4 \cdot 3H_2O]$	Single crystal[a]	7.72	7.31	6.18	$\Omega_2 > \Omega_4 > \Omega_6$	[125]
$[Nd(bpyO_2)_4](ClO_4)_3$	Single crystal	2.18	1.10	0.41	$\Omega_2 > \Omega_4 > \Omega_6$	[79]
$Nd(III){:}CsGd(MoO_4)_2$	Crystal	26.7	12.7	17.8	$\Omega_2 > \Omega_6 > \Omega_4$	[126]
$[Nd(BDPZ)_3(EtOH)]$	Single crystal	22.7	5.32	5.36	$\Omega_2 > \Omega_6 > \Omega_4$	[123]
$Nd(III){:}YNbO_4$	Crystal	14.2	4.3	6.40	$\Omega_2 > \Omega_6 > \Omega_4$	[127]
$Nd(III){:}YVO_4$	Crystal	12.0	6.3	10.1	$\Omega_2 > \Omega_6 > \Omega_4$	[128]
$[Nd_2(MAN)_6(H_2O)_4 \cdot 3H_2O]$	Single crystal[b]	6.82	3.64	5.79	$\Omega_2 > \Omega_6 > \Omega_4$	[125]
$Nd(HCC(CH_2)_2COO)_3 \cdot 2H_2O$	Crystal	4.44	2.02	5.42	$\Omega_6 > \Omega_2 > \Omega_4$	[129]
$Nd(III){:}YAsO_4$	Crystal	4.20	2.70	7.00	$\Omega_6 > \Omega_2 > \Omega_4$	[128]
$Na_3[Nd(TTHA)]2.5NaClO_47.617\ H_2O$	Single crystal	4.57	5.82	6.84	$\Omega_6 > \Omega_4 > \Omega_2$	[130]
$Nd(III){:}YSiO_5$	Crystal	3.34	4.35	5.60	$\Omega_6 > \Omega_4 > \Omega_2$	[131]
$[Nd(C_4O_4H_3)_3] \cdot 8H_2O$	Single crystal	2.82	3.33	10.3	$\Omega_6 > \Omega_4 > \Omega_2$	[132]
$[C(NH_2)_3]_2[Nd(DTPA)(H_2O)] \cdot 7H_2O$	Single crystal	1.40	3.18	7.88	$\Omega_6 > \Omega_4 > \Omega_2$	[133]
$[Nd(C_4H_5O_6)(C_4H_4O_6)][3H_2O]$	MOF solid	0.83	9.51	10.2	$\Omega_6 > \Omega_4 > \Omega_2$	[134]
$Nd(III){:}YPO_4$	Crystal	0.40	4.80	9.60	$\Omega_6 > \Omega_4 > \Omega_2$	[128]
$Nd(III){:}Y_3Al_5O_{12}$	Crystal	0.00	3.20	4.30	$\Omega_6 > \Omega_4 > \Omega_2$	[128]

[a] Horizontal polarization; [b] vertical polarization.

In general, Nd(III) β-diketonate complexes show the following trend: $\Omega_2 > \Omega_4 > \Omega_6$. However, crystalline $[Nd(BDPZ)_3(PHEN)]$ and $[Nd(BDPZ)_3(EtOH)]$ complexes were assigned to different groups in Table 2.1 due to an inversion of the relative values of Ω_4 and Ω_6. These differences are very small, and they should be grouped together. For these compounds, the differences of Ω_2 are meaningful and could be attributed to the ancillary ligands PHEN and EtOH. Most likely, because PHEN is larger and more rigid than EtOH, it causes more distortions of the coordination polyhedron that could explain the higher value of Ω_2 for $[Nd(BDPZ)_3(PHEN)]$. The importance of ancillary ligands can also be verified for the $[Nd(DBM)_3 \cdot H_2O]$ and $[Nd(DBM)_3(TPPO)_2]$ compounds, with a decrease of Ω_2 and increase of Ω_6. In addition, slight changes of the medium from MMA to PMMA cause a small systematic decrease of Ω_λ for $[Nd(DBM)_3(TPPO)_2]$.

Regarding the inorganic matrices, despite having oxygen as the ligating atom, no systematic behavior or trends were promptly observed. The values of Ω_2 can vary by more than one order of magnitude by changing the Nd(III) inorganic environment, with molybdates yielding the largest values of Ω_λ, while phosphates and aluminates are the smallest. Notice, however, that Ω_6 is always sizable and shows at most a fourfold variation. So, any conclusion regarding the effects of the chemical environment on the intensity parameters needs to be carefully verified. In general, inorganic systems doped with Nd(III) ions show lower values of Ω_2 compared to coordination complexes with organic ligands, showing a reversal in the trend of the intensity parameters: $\Omega_6 > \Omega_4 > \Omega_2$.

Unusual results were reported for $[Nd_2(MAN)_6(H_2O)_4 \cdot 3H_2O]$ using polarized incident radiation in the absorption spectrum [125]. In fact, the values of the adjusted Ω_λ are classified into different groups due to a significant inversion of the values of Ω_4 and Ω_6 when the incident radiation has horizontal or vertical polarization. As commented earlier, provided nonpolarized light is incident (except if the crystal is, for example, birefringent), individual (fine structure) Stark-to-Stark transitions should be treated individually. Notice that there are no differences in the local environment of Nd(III), so these marked differences of Ω_λ cannot be explained by the usual concepts. The refractive index could be dependent on the polarization, which would cause distinct local field effects and two different sets of dipole strengths [46]. From a statistical point of view, the observed different oscillator strengths for both horizontal and vertical polarizations can be adjusted by two independent sets of Ω_λ as reported in ref. [125]. However, it should be investigated if these reported values Ω_λ are meaningful within the J-O framework. In fact, the explanation of the 4*f*–4*f* intensities by three even parameters, Ω_2, Ω_4, and Ω_6 is only achieved within the J-O theory when the summation over the polarizations of the incident radiation, described by the polarization numbers $q = 0, \pm 1$ in eq. (2.4), is performed. Because of this averaging, the J-O theory does not consider different polarizations of the incident radiation separately. So, the experimental dipole strength should properly average the polarizations (e.g., σ and π for uniaxial crystals) [46] to provide a single set of oscillator strengths to be used in the fitting procedure to produce the intensity parameters.

In this context, the rationalization, quantification, and interpretation of intensity parameters do require suitable models that consider all relevant effects. However, these models should be able to separate the effects, so comparisons between them can be performed to quantify their relative contributions to Ω_λ, as will be shown with the BOM theoretical model.

On the other hand, the effects of the nature of the lanthanide ion on the intensity parameters were considered for the almost complete series: Pr(III), Nd(III), Sm(III), Eu (III), Tb(III), Dy(III), Ho(III), Er(III), and Tm(III), in the same chemical environment, as presented in Table 2.2.

Table 2.2: Intensity parameters Ω_λ (in units of 10^{-20}cm^2) for Ln(III) doped in two different matrices.

Ln(III)	Matrix	Medium	Ω_2	Ω_4	Ω_6	Trend	Reference
Pr(III)	$LiYF_4$	Crystal	4.1	3.7	7.9	$\Omega_6 > \Omega_2 > \Omega_4$	[135]
	LaF_3	Crystal	0.1	1.8	4.8	$\Omega_6 > \Omega_4 > \Omega_2$	[136]
Nd(III)	$LiYF_4$	Crystal	0.4	4.0	4.8	$\Omega_6 > \Omega_4 > \Omega_2$	[137]
	LaF_3	Nanoparticles	1.9	9.6	5.2	$\Omega_4 > \Omega_6 > \Omega_2$	[138]
Sm(III)	$LiYF_4$	Crystal	0.5	2.4	1.7	$\Omega_4 > \Omega_6 > \Omega_2$	[139]
	LaF_3	Crystal	6.8	9.0	4.0	$\Omega_4 > \Omega_2 > \Omega_6$	[140]
Eu(III)	$NaYF_4$	Nanocrystals	1.8	1.6	–	$\Omega_2 > \Omega_4$	[141]
	LaF_3	Nanoparticles	1.4	2.2	–	$\Omega_4 > \Omega_2$	[142]
Tb(III)	$LiTbF_4$	Crystal	1.5	2.2	2.0	$\Omega_4 > \Omega_6 > \Omega_2$	[143]
	LaF_3	Crystal	1.1	1.4	0.9	$\Omega_4 > \Omega_2 > \Omega_6$	[144]
Dy(III)	$LiYF_4$	Crystal	2.0	1.3	2.4	$\Omega_6 > \Omega_2 > \Omega_4$	[145]
	LaF_3	Crystal	2.4	1.8	2.1	$\Omega_2 > \Omega_6 > \Omega_4$	[45]
Ho(III)	$Na_{0.4}Y_{0.6}F_{2.2}$	Crystal	1.0	1.7	1.1	$\Omega_4 > \Omega_6 > \Omega_2$	[146]
	LaF_3	Nanocrystals	1.9	4.0	4.7	$\Omega_6 > \Omega_4 > \Omega_2$	[147]
Er(III)	β-$NaYF_4$	Crystal	2.4	0.2	1.2	$\Omega_2 > \Omega_6 > \Omega_4$	[148]
	LaF_3	Crystal	1.1	0.3	0.6	$\Omega_2 > \Omega_6 > \Omega_4$	[149]
Tm(III)	$Na_{0.4}Y_{0.6}F_{2.2}$	Crystal	1.9	2.2	1.4	$\Omega_4 > \Omega_2 > \Omega_6$	[150]
	LaF_3	Crystal	0.5	1.1	0.8	$\Omega_4 > \Omega_6 > \Omega_2$	[151]

Notice in Table 2.2 that despite the Ln(III) ions being at the same fluoride environment, the values of Ω_λ change significantly from an YF_4^- to LaF_3 environment. These differences are due to changes of coordination number and symmetry from a crystal lattice to the other. So, to explain and quantify these differences, additional information regarding the coordination polyhedron is required.

Considering that the sites in YF_4^- or LaF_3 are the same for any of the doping lanthanide ions, there are no clear systematic trends in the values of Ω_λ by varying Ln (III) from Pr(III) to Tm(III). Any trend can be better visualized graphically as shown in Figure 2.4a for Ln(III): YF_4^- and Figure 2.4b for Ln(III): LaF_3.

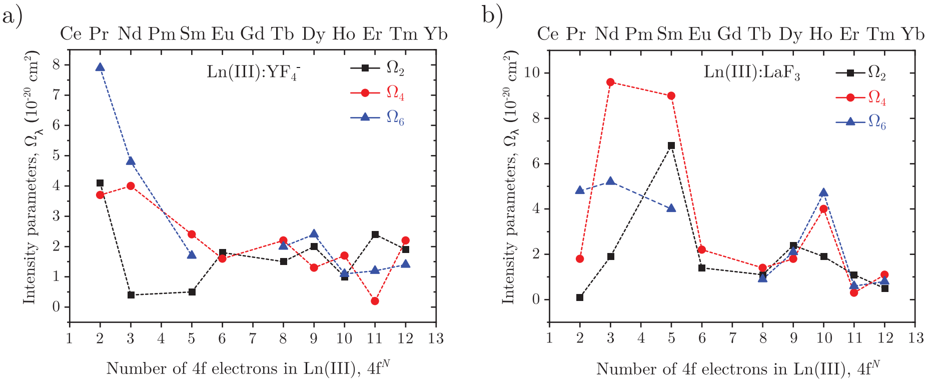

Figure 2.4: Variation of the experimental intensity parameters, Ω_λ, for Ln(III) in (a) YF_4^- and (b) LaF_3 environments with respect to the number of electrons in the 4*f* subshell.

From Figure 2.4 it can be observed that, from Eu(III) up to the end of the series, Ω_λ becomes small and practically constant (ca. 1.5×10^{-20} cm^2), except for Er(III) in β-$NaYF_4$ and Ho(III) in LaF_3. For the lighter lanthanide ions, the variations of Ω_λ are more drastic, most likely due to the hypersensitive nature of some transitions in these ions. In the $LiYF_4$ environment, Ω_2 and Ω_6 decrease sharply from Pr(III) to Sm(III), while Ω_4 decreases less drastically. This behavior is very different in LaF_3, where Ω_2 and Ω_4 increase significantly, whereas Ω_6 remains almost constant. Similar observations and trends have been reported in the literature [46], which has also emphasized the difficulties in fitting a single set of intensity parameters for all transitions of Pr(III) [46].

Despite the great efforts in measuring the intensity parameters, their values, comparisons, and trends should be viewed critically and with care. Indeed, there are several experimental variables that can affect the fitted values, from the uncertainties in the oscillator strengths to the choices of the transitions employed in the fitting procedure [46]. The physical state of the sample, for example, solid (powder, single crystal), liquid, or gas, as well as the refractive index of the medium and its dependence with the wavelength also play important roles.

2.4 JOYSpectra functionalities for intensity parameters

The JOYSpectra web platform is a tool for theoretical calculations of Judd–Ofelt intensity parameters using the SOM and BOM approaches [41, 59–61] as well as other quantities such as ligand–Ln(III) and Ln(III)–Ln(III) energy transfer rates [152–154], radiative rates, and other features that will be implemented soon [62]. The platform can be freely accessed through http://slater.cca.ufpb.br/joyspectra or http://app.uabj.ufrpe.br/joyspectra.

The covalency contribution on the Ω_λ parameters is considered, within BOM, using the overlap polarizability α_{OP}, as an indicator of covalency, written as [41, 59–61]

$$\alpha_{OP} = \frac{e^2 \rho^2 R^2}{2\Delta\varepsilon} \tag{2.33}$$

where e is the electron charge, ρ is the magnitude of the overlap between the $4f$ orbitals and the valence of the ligand, R is the length of the chemical bond, and $\Delta\varepsilon$ is a parameter related to the Ln–ligating atom's first excitation energy [41, 155]. Values of ρ and $\Delta\varepsilon$ are available as a function of distance, within the JOYSpectra program [62], for all lanthanide ions and most ligating atoms inside and will be discussed later. Within the framework of the BOM (Figure 2.3b), the α_{OP} is included explicitly in the DC mechanism, inside the Γ_p^t term (eq. (2.23)), which becomes

$$\Gamma_p^t = \left(\frac{4\pi}{2t+1}\right)^{1/2} \sum_j \left(\alpha'_j + (2\beta)^{t+1}\alpha_{OP,j}\right) \frac{Y_p^{t*}\left(\theta_j, \phi_j\right)}{R_j^{t+1}} \tag{2.34}$$

where α' are the effective ligand polarizabilities, which can be fitted (to reproduce experimental Ω_λ values) or calculated with localized molecular orbitals [41–43, 156]. As mentioned, the α_{OP}'s are calculated within JOYSpectra as a function of Ln–ligating atom distances using eq. (2.33) [157].

The JOYSpectra was developed using a variety of computational languages (C/C++, PHP, HTML, Python, and Unix-based Shellscript), and its structure is separated into front-end and back-end modules. The front-end constituted PHP/HTML codes and includes an interactive web browser object for molecular structure visualization. The front-end is a user-friendly interface that allows the easy use of JOYSpectra. The back-end is written in C/C++, Python, and Unix-based Shellscript, and is the module that runs all the calculations available in the JOYSpectra. For a more detailed presentation and discussion of the JOYSpectra web platform, see ref. [62].

2.4.1 Covalency and intensity parameters: selected cases

Aiming at the discussions regarding interpretations of Ω_λ, some examples of intensity parameter calculations will be presented, from which the covalency effects can be quantified and rationalized. The [Nd(DBM)$_3$•H$_2$O] [120] and [Nd(BDPZ)$_3$(EtOH)] [123] compounds were chosen because they have similar ligands (β-diketonates), however, with very distinct values of intensity parameters (see Table 2.1). In addition, [Nd(bpyO$_2$)$_4$](ClO$_4$)$_3$ and [Pr(bpyO$_2$)$_4$](ClO$_4$)$_3$ complexes were investigated because despite having the same environment, they present very different values of experimental Ω_λ.

This section presents some practical examples of the JOYSpectra application. As illustrative examples, theoretical values of Ω_λ for the [Nd(DBM)$_3$•H$_2$O] [120] and [Nd(BDPZ)$_3$(EtOH)] [123] compounds were calculated using the JOYSpectra fitting procedure,[2] which requires the geometry and the experimental Ω_λ's as input data. From these calculations, the intensity parameters can be interpreted in terms of structural and chemical bond properties.

Figure 2.5 depicts the structures of [Nd(DBM)$_3$•H$_2$O] and [Nd(BDPZ)$_3$(EtOH)], and their coordination polyhedra. Both complexes are seven-coordinated; however, they have different point group symmetry of the coordination polyhedron, namely, [Nd (DBM)$_3$•H$_2$O] is close to C_{3v} and [Nd(BDPZ)$_3$(EtOH)] is close to C_s.

By fitting the theoretical Ω_λ to the experimental values, the polarizabilities α' and α_{OP}, within the BOM framework, and the charge factors g, within the SOM framework, can be determined for each ligating atom (Table 2.3). The fitting procedure in JOYSpectra was performed by setting each ancillary ligand O$_1$ as independent, that is, H$_2$O for [Nd(DBM)$_3$•H$_2$O] and EtOH for [Nd(BDPZ)$_3$(EtOH)]. The main ligating atoms, labeled O$_2$ to O$_7$, were treated slightly differently for each compound. DBM ligands were treated by considering equivalent one oxygen ligating atom in each ligand, which were grouped as {O$_2$, O$_4$, O$_6$} and {O$_3$, O$_5$, O$_7$}, as shown in Figure 2.5a,b. On the other hand, BDPZ ligand oxygens were treated by grouping each ligand molecule separately as {O$_2$, O$_3$}, {O$_4$, O$_5$}, and {O$_6$, O$_7$}, as shown in Figure 2.5c,d. This choice of groupings reflects some aspects of the coordination polyhedron symmetry and is important for the fitting procedure. The setup used in JOYSpectra for these fitting procedures is highlighted in Table 2.3 as "JOYSpectra FIT#" columns.

Table 2.3: Chemical bond parameters for the [Nd(DBM)$_3$•H$_2$O] and [Nd(BDPZ)$_3$(EtOH)] complexes.

Ligating atom	[Nd(DBM)$_3$•H$_2$O]					[Nd(BDPZ)$_3$(EtOH)]				
	JOYSpectra FIT no.	R	α'	α_{OP}	g	JOYSpectra FIT#	R	α'	α_{OP}	g
O$_1$	FIT1	2.467	2.015	2.014	0.968	FIT1	2.532	0.066	1.778	0.077
O$_2$	FIT2	2.393	0.248	2.314	0.073	FIT2	2.357	0.168	2.477	1.066
O$_3$	FIT3	2.368	0.851	2.428	0.050	FIT2	2.396	0.168	2.304	1.066
O$_4$	FIT2	2.393	0.248	2.314	0.073	FIT3	2.392	1.583	2.323	0.067
O$_5$	FIT3	2.368	0.851	2.428	0.050	FIT3	2.346	1.583	2.527	0.067
O$_6$	FIT2	2.393	0.248	2.314	0.073	FIT4	2.353	0.167	2.495	0.101
O$_7$	FIT3	2.368	0.851	2.428	0.050	FIT4	2.356	0.167	2.479	0.101

Bond distances R in Å. α' (in Å^3) and α_{OP} (in 10^{-3} Å^3) are the effective and overlap polarizabilities according to the BOM framework (DC mechanism), respectively. g (dimensionless) is the charge factor in the SOM framework (FED mechanism). JOYSpectra FIT no. columns indicate the group to which each ligating atom belongs, as depicted in Figure 2.5, being the information inserted into the web platform.

---

[2] The JOYSpectra fitting is a procedure based on a metaheuristic optimization method. A set of random points (typically ca. 10^5 points) is generated considering predefined optimization limits (α' and g in acceptable ranges). Then, a best individual subset (typically with ca. 500 points) is used to iteratively narrow the limits until a convergence threshold is reached.

The program separates the calculated values of Ω_λ into FED and DC contributions. Consequently, the covalency contribution to each Ω_λ (quantified by α_{OP}) can be calculated, at the same structure of the complex, by setting α' and g to zero. This ensures that the FED and DC (only the α' term) contributions are null. The result of this procedure provides only the α_{OP} contribution to the intensity parameters, $\Omega_\lambda^{\alpha_{\mathrm{OP}}}$, which can be compared to the sum of the FED, $\Omega_\lambda^{\mathrm{FED}}$, and DC, $\Omega_\lambda^{\mathrm{DC}}$, contributions. These $\Omega_\lambda^{\mathrm{FED}}$ and $\Omega_\lambda^{\mathrm{DC}}$ are determined with the fitted values of g and α', respectively. Thus, the relative (percentage) contribution of the covalency to the intensity parameters can be determined as [41]

$$\%\alpha_{\mathrm{OP}}(\Omega_\lambda) = \frac{\Omega_\lambda^{\alpha_{\mathrm{OP}}}}{\Omega_\lambda^{\mathrm{FED}} + \Omega_\lambda^{\mathrm{DC}}} \times 100\% \tag{2.35}$$

which are depicted in Figure 2.6a.

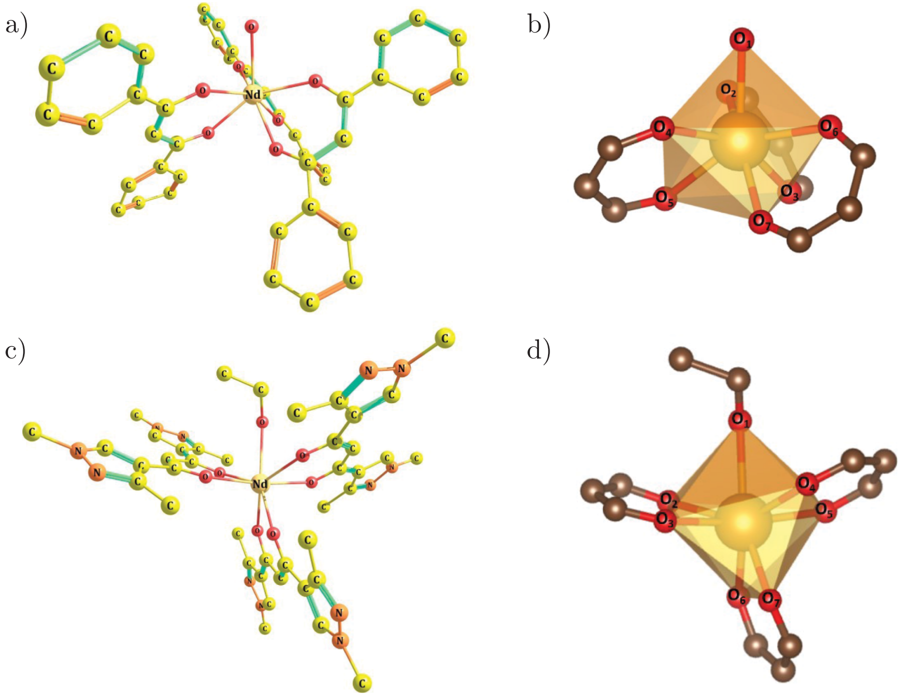

Figure 2.5: Crystallographic structures of (a) [Nd(DBM)$_3$•H$_2$O] (CCDC number: 1101179) and (c) [Nd(BDPZ)$_3$(EtOH)] (CCDC number: 1842471) compounds and their respective coordination polyhedron (b) and (d) with the same labels as used for the Ω_λ calculations (Table 2.3). Hydrogen atoms were omitted.

Table 2.3 shows the fitted effective ligand polarizabilities, α', and the charge factors, g, for each Ln–O$_i$ bond in the [Nd(DBM)$_3$•H$_2$O] and [Nd(BDPZ)$_3$(EtOH)] complexes. The first line, Ln–O$_1$ bond, represents oxygen in H$_2$O and EtOH ligands. It is observed that despite DBM and BDPZ being symmetric ligands (see Figure 2.5a,c), the bond distances of Ln–O$_i$, $i = 2$, 4, and 6 ($R = 2.393$ Å), and Ln–O$_i$, $i = 3$, 5, and 7 ($R = 2.368$ Å), are equivalent in the [Nd(DBM)$_3$•H$_2$O] complex. On the other hand, for the [Nd(BDPZ)$_3$(EtOH)] complex, the bond distances of Ln–O$_i$ are all different from each other. These structural features justify the groupings for the fitting procedure and reinforce the relevance of a proper choice.

In both complexes, the Ln–O$_1$ (H$_2$O or EtOH ligand) bond has the smallest value of α_{OP} because of its distance and the nature of the ligating atom. The overlap polarizabilities for all compounds are within the range of values found for β-diketone ligands [41, 42, 156]. The values of α' and g for the Ln–O$_1$(EtOH) bond in [Nd(BDPZ)$_3$(EtOH)] complex are much smaller than the Ln–O$_1$(H$_2$O) bond in [Nd(DBM)$_3$•H$_2$O] complex, most likely due to the larger Ln–O$_1$(EtOH) distance.

It is important to emphasize that the adjusted parameters depend on the chemical criterion adopted in the optimization procedure, which is relevant for the dimensions of the parameter spaces of α' and g. For the [Nd(DBM)$_3$•H$_2$O] compound, three different types of bonds that yield a six-dimensional space for α' and g independent were selected, while an eight-dimensional space was employed in the [Nd(BDPZ)$_3$(EtOH)] case because four different types of bonds were chosen. On the other hand, if all bonds were considered nonequivalent, a 14-dimensional parameter space for α' and g would be involved, which certainly has a different response surface. Constraining the optimization space by limiting the subset of the Euclidean space (decreasing the number of variables) imposes restrictions on the optimization paths and directs the result to similar minima, being an effective strategy. However, this strategy does not guarantee a global minimum search or the uniqueness of the fitted parameters, as proposed in [158]. Thus, the relevance of developing quantitative models for these parameters (α', α_{OP}, and g) and for Ω_λ's is to ascertain the physical reasonableness of the fitted parameters and the fitting procedure.

Table 2.4 summarizes the experimental and theoretical Ω_λ for the selected cases. The three different Nd(III) complexes with DBM, BDPZ, and bpyO$_2$ main ligands exhibit variations of an order of magnitude in the values of Ω_λ. It is difficult to assign a single quantity as responsible for this order of magnitude differences, and a more detailed analysis would be required, which is beyond the scope of this contribution. Additionally, the effects of the lanthanide ions were investigated for the [Ln(bpyO$_2$)$_4$](ClO$_4$)$_3$, where Ln = Nd(III) and Pr(III), complexes. Despite these two complexes having the same coordination polyhedron, they present quite different values of Ω_λ. As can be observed in Table 2.3, these values are systematically larger (nearly one order of magnitude) for the Pr(III) complex compared to the Nd(III) analogue [79]. Thus, it is noteworthy that distinct Ln(III) ions interact quite differently with the chemical environment, leading to differences in the values of g, α', α_{OP}, overlap integrals ρ, and distances R. The overlap integrals, ρ, appearing in the expression of α_{OP}, eq. (2.33), are a quantity related to chemical bond covalency within the scope of BOM [41, 155, 159].

Table 2.4: Experimental and fitted theoretical intensity parameters (in units of 10^{-20} cm^2) for selected cases.

Complex	**Ω_2**		**Ω_4**		**Ω_6**	
	Exp.	**Theor.**	**Exp.**	**Theor.**	**Exp.**	**Theor.**
[Nd(DBM)$_3$•H$_2$O]	44.7	44.9	11.9	11.6	1.25	1.76
[Nd(BDPZ)$_3$(EtOH)]	22.7	22.8	5.32	7.81	5.36	4.89
[Nd(bpyO$_2$)$_4$](ClO$_4$)$_3$[a]	2.18	2.18	1.10	1.10	0.41	0.53
[Pr(bpyO$_2$)$_4$](ClO$_4$)$_3$[a]	14.1	14.1	16.8	16.8	12.5	12.4

[a] Reference [79].

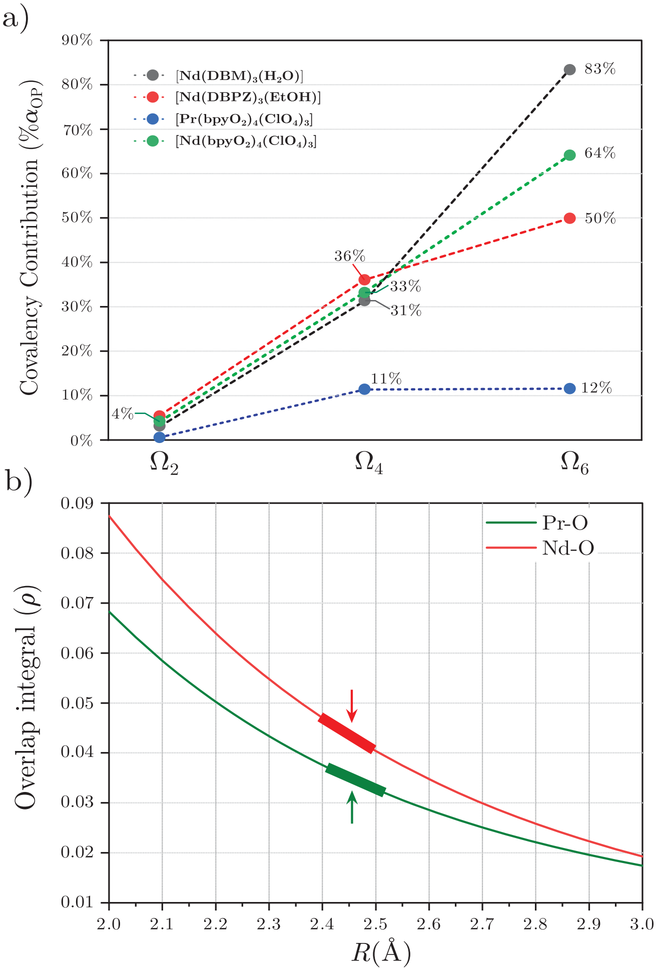

Figure 2.6: (a) Covalency contribution (through the overlap polarizability α_{OP}) in the Ω_λ for various Ln-based compounds. (b) Overlap integral ρ as a function of Ln–O distance. The intervals indicated in red and green illustrate Ln–O distance range considered for the [Ln(bpyO$_2$)$_4$](ClO$_4$)$_3$ complexes.

Figure 2.6 depicts the covalency contributions (through the overlap polarizability α_{OP}) for each Ω_λ in the selected cases. The observed trend for all cases is that covalency contribution increases with the λ value, being most important in the description of Ω_6 and Ω_4 than for Ω_2. Interestingly, the $\%\alpha_{OP}(\Omega_\lambda)$ values do not even follow the same trends of Ω_λ, namely, the [Nd(DBM)$_3$•H$_2$O] compound with the biggest $\Omega_2 = 44.7 \times 10^{-20}\text{cm}^2$ exhibits a smaller $\%\alpha_{OP}(\Omega_2)$ than in the [Nd(BDPZ)$_3$(EtOH)] complex, which has $\Omega_2 = 22.7 \times\ 10^{-20}\text{cm}^2$. The same is observed in Ω_4 of these two compounds. However, the DBM compound with a smaller $\Omega_6 = 1.25 \times 10^{-20}\text{cm}^2$ than the BDPZ compound ($\Omega_6 = 5.36 \times\ 10^{-20}\text{cm}^2$) has the largest $\%\alpha_{OP}(\Omega_6) = 83\%$ value among the investigated compounds.

The covalency contributions for the [Nd(bpyO$_2$)$_4$](ClO$_4$)$_3$ and [Pr(bpyO$_2$)$_4$](ClO$_4$)$_3$ compounds are also depicted in Figure 2.6a. It is observed that the Pr(III) complex exhibits the smallest $\%\alpha_{OP}(\Omega_\lambda)$ values, even with much higher Ω_λ values than Nd(III). This behavior is a consequence of the overlap integral ρ(Pr–O) being smaller than ρ(Nd–O), as can be seen in Figure 2.6b, leading to very small values of α_{OP} in Pr(III) compounds, and hence smaller $\%\alpha_{OP}(\Omega_\lambda)$ contributions. In addition, due to the lanthanide contraction, Ln(III)–O distance is slightly smaller for Nd(III) than Pr(III) compounds, which also contributes to the larger overlap integral of Nd–O bond.

These and other results available in the literature showed the very diverse contributions of covalency, $\%\alpha_{OP}$, for distinct Ω_λ and compounds, which clearly indicate that the total value of the intensity parameters Ω_λ cannot be a proper descriptor of covalency, specifically for Ω_2. Indeed, the parameters Ω_4 and Ω_6 are more dependent on covalency (through α_{OP}) than Ω_2 (Figure 2.6a). Thus, reinterpretations of the intensity parameters in terms of covalency and other effects (e.g., symmetry, distances and angles, and nature of ligating atoms – g and α', lanthanide ion – ρ) are necessary.

2.4.2 Thermal effects on structures and intensity parameters

Small variations of the interatomic distances during vibrational motions have additional effects on the electronic transitions. Such effects have a strong dependence on the material in which the transitions occur and are particularly important in cases in which the site symmetry occupied by the ion has a center of inversion without distortions since FED and DC mechanisms have a null contribution because the sum over odd-rank spherical harmonics is null, and there is no mixture of opposite parity configurations. Thus, the 4*f* states remain with their parities well defined and Laporte's rule is not relaxed. However, some asymmetrical vibrational modes momentarily break the symmetry and lead to a Laporte's rule relaxation. It is important to note that this so-called vibronic mechanism is also operative even in the absence of a center of inversion, even though it leads to oscillator strengths around 10^{-8}, which is much smaller than the other mechanisms, for example, FED and DC.

Under the theoretical formalism presented here, the intensity parameters are independent of the temperature, except for the weak vibronic interaction described above that is not taken into consideration. However, thermal effects can induce distortions of the coordination polyhedron that may allow centrosymmetric systems (for which $\Omega_\lambda = 0$) to access geometries in which the inversion center is absent and thus $\Omega_\lambda > 0$.

Previous works [63–65] treated the thermal effects as random distortions of the equilibrium ligand positions in inorganic lanthanide compounds by assuming that each distorted geometry contributes equally to the averaged intensity parameters $\langle\Omega_\lambda\rangle$. These random distorted geometries were obtained by a Monte Carlo-like approach, in which the Cartesian coordinates of the ligating atoms were randomly changed, within certain limits proportional to the Boltzmann factor, to calculate $\langle\Omega_\lambda\rangle$ as

$$\langle\Omega_\lambda\rangle = \sum_{i}^{M} \frac{p_i}{p_{\text{total}}}\Omega_{\lambda,i}, \quad p_{\text{total}} = \sum_{j}^{M} p_j \tag{2.36}$$

where p_i is the population of the ith configuration with intensity parameter $\Omega_{\lambda,i}$. In the case of equally weighted intensity parameters, then $p_i = 1$. The summation in eq. (2.36) runs over the total number of configurations (M), and the maximum displacement of the atomic coordinates was initially defined using X-ray crystallography data [160]. Another approach considers the limits of the displacements through a Bose–Einstein population distribution [65], which reasonably reproduced the experimental results of elpasolite photophysical properties [65, 66]. Figure 2.7 shows that the elpasolite experimental value of Ω_2 increases when the temperature rises, being $0.534 \times 10^{-20}\,\text{cm}^2$ at 77 K and $1.881 \times 10^{-20}\,\text{cm}^2$ at 300 K. By allowing small displacements (10^6 random configurations) around the equilibrium geometry with maximum displacements of 0.089 Å at 77 K and of 0.158 Å at 300 K, the intensity parameters averaged over these displaced structures, $\langle\Omega_2\rangle$, become nonzero and in good agreement with the experimental ones: $\langle\Omega_2\rangle = 0.408 \times 10^{-20}\,\text{cm}^2$ at 77 K and $1.277 \times 10^{-20}\,\text{cm}^2$ at 300 K.

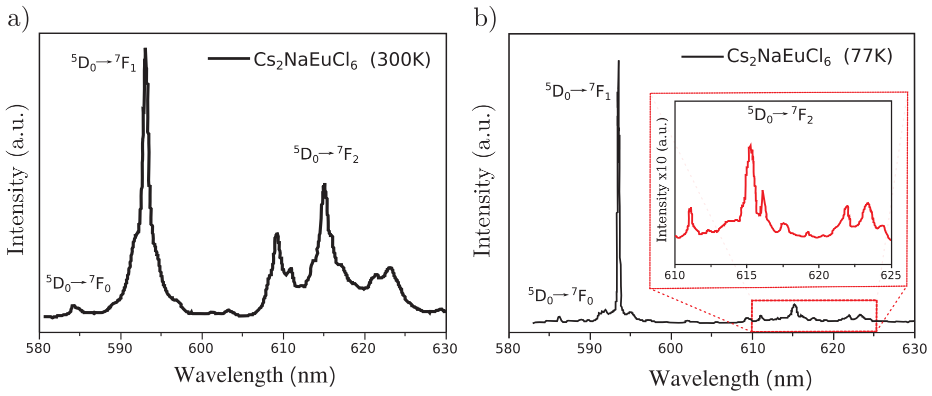

Figure 2.7: Emission spectra of $Cs_2NaEuCl_6$ elpasolite at (a) room temperature and (b) 77 K (reproduced with permission from ref. [65]).

Notice that these approaches are different from the vibrational and thermal averaging procedures employed for the oscillator strengths [95] as described in eq. (2.32).

Notice that "thermal effects" available in the JOYSpectra, via the "Bose–Einstein Population" option, employ distortions of the coordination polyhedron (default value: 10,000), which are carried out into the intensity parameters. Although satisfactory, this approach does not consider geometric configurations that represent large-amplitude deformations of the equilibrium geometry, which may be thermally inaccessible. Furthermore, random dispersions do not allow mapping of which normal modes most effectively contribute to vibrational and thermal changes in photophysical properties. Indeed, vibrational and Boltzmann-like thermal averaging procedures are being implemented and will soon be available in the JOYSpectra web platform.

2.5 Concluding remarks

Using irreducible tensor operator techniques, in 1962 Judd and Ofelt, working independently, have shown that most of the intraconfigurational electronic transitions in Ln (III) compounds (4*f*–4*f* transitions) could be described by the electric dipole mechanism, provided Laporte's rule would be relaxed by a mixing of opposite parity electronic configurations of the ions induced by odd-parity components of the ligand field (or crystal field). A process that became known as the Judd–Ofelt theory, or the FED mechanism, leads to oscillator strengths of the order of 10^{-6}, as observed experimentally. In the following years, it was noticed that localized inhomogeneities of the external incident electromagnetic field (high field gradients produced by the ligands) could also induce 4*f*–4*f* transitions with oscillator strengths of the order of 10^{-6}. This mechanism became nowadays called the ligating atom (ion) polarizability-dependent DC mechanism. These two mechanisms have precisely the same form and cannot be distinguished experimentally, implying the emergence of theoretical calculations relevance.

This chapter presented a brief review of the expressions of Ω_λ's within the framework of the Judd–Ofelt theory and some of its extensions. Gathering Ln(III) spectroscopy and theoretical chemistry, as well as the trends and patterns observed for Ln(III) ions in several environments, the chapter describes in detail the scheme we developed in the past decades that allowed a new interpretation of the 4*f*–4*f* intensity parameters. Taking into account that the intensity parameters depend strongly on the structure around the Ln(III) ions (especially of the coordination polyhedron), the developed scheme encompasses the theoretical description of the ligand field and both FED and DC mechanisms, using models such as SOM and BOM, and computational tools such as JOYSpectra.

To discuss the interpretation of the intensity parameters, these recent theoretical developments were used to perform intensity parameter calculations in illustrative examples of Nd(III) compounds from which the covalency effects can be quantified, rationalized, and compared with experimental data. These calculations showed very diverse contributions of covalency for the selected compounds, which clearly indicate that the values of the intensity parameters Ω_λ cannot be a proper descriptor of covalency, specifically for Ω_2, showing that a reinterpretation of the intensity parameters in terms of covalency and other effects (e.g., symmetry, distances and angles, and nature of ligating atoms) is mandatory. However, overall, from the present model, we conclude that the Ω_4 and, mainly, Ω_6 parameters are more sensitive to covalency than Ω_2. On the other hand, Ω_2 is more sensitive to the angular part of the local coordination geometry than Ω_4 and Ω_6; it has already brought attention in 1979 by Judd [90]. The Ln(III)–ligating atom (ion) distance plays a role of paramount importance in the case of the Ω_6 parameter.

We expect that this contribution will catalyze the generation of reliable databases of intensity parameters Ω_λ, for a wide range of lanthanide complexes and materials with well-defined structures. The predictions by the theoretical and computational models could then be validated by these databases, and they could provide training and test sets for methods based on QSPR (quantitative structure–property relationship). Applications of artificial intelligence (AI) techniques on these databases could emerge novel and unprecedented trends and patterns as well as set the foundations for developing predictive AI-based methods for designing new and improved lanthanide materials for distinct applications such as luminescent micro- and nanothermometers (as far as the thermal effects on the intensity parameters may be quantitatively treated).

References

[1] K.-H. Hellwege, A.M. Hellwege, Eds., Luminescence of Organic Substances, Springer-Verlag, Berlin/Heidelberg (1967). https://doi.org/10.1007/b86158.

[2] W.M. Yen, S. Shionoya, H. Yamamoto, Eds., Fundamentals of Phosphors, CRC Press (2018). https://doi.org/10.1201/9781315219981.

[3] J. Yang, M. Fang, Z. Li, Organic luminescent materials: The concentration on aggregates from aggregation-induced emission, Aggregate 1 (2020) 6–18. https://doi.org/10.1002/agt2.2.

[4] J.M. Ha, S.H. Hur, A. Pathak, J.-E. Jeong, H.Y. Woo, Recent advances in organic luminescent materials with narrowband emission, NPG Asia Mater. 13 (2021) 53. https://doi.org/10.1038/s41427-021-00318-8.

[5] J. Gierschner, J. Shi, B. Milián-Medina, D. Roca-Sanjuán, S. Varghese, S. Park, Luminescence in crystalline organic materials: From molecules to molecular solids, Adv. Opt. Mater. 9 (2021) 2002251. https://doi.org/10.1002/adom.202002251.

[6] P. Xue, P. Wang, P. Chen, B. Yao, P. Gong, J. Sun, Z. Zhang, R. Lu, Bright persistent luminescence from pure organic molecules through a moderate intermolecular heavy atom effect, Chem. Sci. 8 (2017) 6060–6065. https://doi.org/10.1039/C5SC03739E.

[7] Y. Gao, C. Ren, X. Lin, T. He, The progress and perspective of organic molecules with switchable circularly polarized luminescence, Front. Chem. 8 (2020). https://doi.org/10.3389/fchem.2020.00458.

[8] Y. Liu, X. Yan, H.-S. Lu, W.-D. Zhang, Y.-X. Shi, Z.-G. Gu, A three-dimensional covalent organic framework with turn-on luminescence for molecular decoding of volatile organic compounds, Sens. Actuators B Chem. 323 (2020) 128708. https://doi.org/10.1016/j.snb.2020.128708.

[9] Y. Xiang, X. Yu, Y. Li, J. Chen, J. Wu, L. Wang, D. Chen, J. Li, Q. Zhang, Covalent organic framework as an efficient fluorescence-enhanced probe to detect aluminum ion, Dye. Pigment. 195 (2021) 109710. https://doi.org/10.1016/j.dyepig.2021.109710.

[10] M.R. Di Nunzio, I. Hisaki, A. Douhal, HOFs under light: Relevance to photon-based science and applications, J. Photochem. Photobiol. C Photochem. Rev. 47 (2021) 100418. https://doi.org/10.1016/j.jphotochemrev.2021.100418.

[11] R.Y. Tsien, The green fluorescent protein, Annu. Rev. Biochem. 67 (1998) 509–544. https://doi.org/10.1146/annurev.biochem.67.1.509.

[12] N.C. Shaner, P.A. Steinbach, R.Y. Tsien, A guide to choosing fluorescent proteins, Nat. Methods 2 (2005) 905–909. https://doi.org/10.1038/nmeth819.

[13] R.M. Hoffman, Fluorescent Proteins, in: Comprehensive Biomedical Physics, Elsevier (2014), 27–32. https://doi.org/10.1016/B978-0-444-53632-7.00403-2.

[14] G. Cox, Ed., Fundamentals of Fluorescence Imaging, Jenny Stanford Publishing (2019). https://doi.org/10.1201/9781351129404.

[15] J.N. Demas, B.A. DeGraff, Design and applications of highly luminescent transition metal complexes, Anal. Chem. 63 (1991) 829A–837A. https://doi.org/10.1021/ac00017a719.

[16] D.-L. Ma, H.-Z. He, K.-H. Leung, D.S.-H. Chan, C.-H. Leung, Bioactive luminescent transition-metal complexes for biomedical applications, Angew. Chemie Int. Ed. 52 (2013) 7666–7682. https://doi.org/10.1002/anie.201208414.

[17] C.-N. Ko, G. Li, C.-H. Leung, D.-L. Ma, Dual function luminescent transition metal complexes for cancer theranostics: The combination of diagnosis and therapy, Coord. Chem. Rev. 381 (2019) 79–103. https://doi.org/10.1016/j.ccr.2018.11.013.

[18] F.N. Castellano, Making iron glow, Nature 543 (2017) 627–628. https://doi.org/10.1038/543627a.

[19] P. Chábera, Y. Liu, O. Prakash, E. Thyrhaug, A. El Nahhas, A. Honarfar, S. Essén, L.A. Fredin, T.C.B. Harlang, K.S. Kjær, K. Handrup, F. Ericson, H. Tatsuno, K. Morgan, J. Schnadt, L. Häggström, T. Ericsson, A. Sobkowiak, S. Lidin, P. Huang, S. Styring, J. Uhlig, J. Bendix, R. Lomoth, V. Sundström, P. Persson, K. Wärnmark, A low-spin Fe(iii) complex with 100-ps ligand-to-metal charge transfer photoluminescence, Nature 543 (2017) 695–699. https://doi.org/10.1038/nature21430.

[20] C. Wegeberg, O.S. Wenger, Luminescent first-row transition metal complexes, JACS Au. 1 (2021) 1860–1876. https://doi.org/10.1021/jacsau.1c00353.

[21] G. Blasse, B.C. Grabmaier, Luminescent Materials, Springer Berlin Heidelberg, Berlin, Heidelberg (1994). https://doi.org/10.1007/978-3-642-79017-1.

[22] C. Fouassier, Luminescent materials, Curr. Opin. Solid State Mater. Sci. 2 (1997) 231–235. https://doi.org/10.1016/S1359-0286(97)80071-X.

[23] M.D. Allendorf, C.A. Bauer, R.K. Bhakta, R.J.T. Houk, Luminescent metal–organic frameworks, Chem. Soc. Rev. 38 (2009) 1330. https://doi.org/10.1039/b802352m.

[24] Y. Cui, Y. Yue, G. Qian, B. Chen, Luminescent functional metal–organic frameworks, Chem. Rev. 112 (2012) 1126–1162. https://doi.org/10.1021/cr200101d.

[25] H. Kaur, S. Sundriyal, V. Pachauri, S. Ingebrandt, K.-H. Kim, A.L. Sharma, A. Deep, Luminescent metal-organic frameworks and their composites: Potential future materials for organic light emitting displays, Coord. Chem. Rev. 401 (2019) 213077. https://doi.org/10.1016/j.ccr.2019.213077.

[26] R. Haldar, S. Bhattacharyya, T.K. Maji, Luminescent metal–organic frameworks and their potential applications, J. Chem. Sci. 132 (2020) 99. https://doi.org/10.1007/s12039-020-01797-y.

[27] Y. Zheng, F. Sun, X. Han, J. Xu, X. Bu, Recent progress in 2D metal-organic frameworks for optical applications, Adv. Opt. Mater. 8 (2020) 2000110. https://doi.org/10.1002/adom.202000110.

[28] M. Huangfu, M. Wang, C. Lin, J. Wang, P. Wu, Luminescent metal–organic frameworks as chemical sensors based on “mechanism–response”: A review, Dalt. Trans. 50 (2021) 3429–3449. https://doi.org/10.1039/D0DT04276E.

[29] C. Cong, H. Ma, Photonic metal-organic frameworks, Adv. Opt. Mater. 9 (2021) 2100733. https://doi.org/10.1002/adom.202100733.

[30] W.R. Algar, M. Massey, K. Rees, R. Higgins, K.D. Krause, G.H. Darwish, W.J. Peveler, Z. Xiao, H.-Y. Tsai, R. Gupta, K. Lix, M.V. Tran, H. Kim, Photoluminescent nanoparticles for chemical and biological analysis and imaging, Chem. Rev. 121 (2021) 9243–9358. https://doi.org/10.1021/acs.chemrev.0c01176.

[31] J.K. Molloy, C. Lincheneau, M.M. Karimdjy, F. Agnese, L. Mattera, C. Gateau, P. Reiss, D. Imbert, M. Mazzanti, Sensitisation of visible and NIR lanthanide emission by InPZnS quantum dots in bi-luminescent hybrids, Chem. Commun. 52 (2016) 4577–4580. https://doi.org/10.1039/C6CC01182A.

[32] M. Fang, A.N.C. Neto, L. Fu, R.A.S. Ferreira, V. DeZeaBermudez, L.D. Carlos, A hybrid materials approach for fabricating efficient WLEDs based on di-ureasils doped with carbon dots and a europium complex, Adv. Mater. Technol. 7 (2021) 2100727. https://doi.org/10.1002/admt.202100727.

[33] G.H. Dieke, H.M. Crosswhite, The spectra of the doubly and triply ionized rare earths, Appl. Opt. 2 (1963) 675. https://doi.org/10.1364/AO.2.000675.

[34] G.H. Dieke, R.A. Satten, Spectra and energy levels of rare earth ions in crystals, Am. J. Phys. 38 (1970) 399–400. https://doi.org/10.1119/1.1976350.

[35] W.T. Carnall, G.L. Goodman, K. Rajnak, R.S. Rana, A systematic analysis of the spectra of the lanthanides doped into single crystal LaF_3, J. Chem. Phys. 90 (1989) 3443–3457. https://doi.org/10.1063/1.455853.

[36] K. Rademaker, W.F. Krupke, R.H. Page, S.A. Payne, K. Petermann, G. Huber, A.P. Yelisseyev, L.I. Isaenko, U.N. Roy, A. Burger, K.C. Mandal, K. Nitsch, Optical properties of Nd^{3+}- and Tb^{3+}-doped KPb_2Br_5 and $RbPb_2Br_5$ with low nonradiative decay, J. Opt. Soc. Am. B 21 (2004) 2117. https://doi.org/10.1364/JOSAB.21.002117.

[37] U.N. Roy, R.H. Hawrami, Y. Cui, S. Morgan, A. Burger, K.C. Mandal, C.C. Noblitt, S.A. Speakman, K. Rademaker, S.A. Payne, Tb^{3+}-doped KPb_2Br_5: Low-energy phonon mid-infrared laser crystal, Appl. Phys. Lett. 86 (2005) 151911. https://doi.org/10.1063/1.1901815.

[38] J. An, C.M. Shade, D.A. Chengelis-Czegan, S. Petoud, N.L. Rosi, Zinc-adeninate metal−organic framework for aqueous encapsulation and sensitization of near-infrared and visible emitting lanthanide cations, J. Am. Chem. Soc. 133 (2011) 1220–1223. https://doi.org/10.1021/ja109103t.

[39] A. D’Aléo, F. Pointillart, L. Ouahab, C. Andraud, O. Maury, Charge transfer excited states sensitization of lanthanide emitting from the visible to the near-infra-red, Coord. Chem. Rev. 256 (2012) 1604–1620. https://doi.org/10.1016/j.ccr.2012.03.023.

[40] K. Lunstroot, P. Nockemann, K. Van Hecke, L. Van Meervelt, C. Görller-Walrand, K. Binnemans, K. Driesen, Visible and near-infrared emission by samarium(III)-containing ionic liquid mixtures, Inorg. Chem. 48 (2009) 3018–3026. https://doi.org/10.1021/ic8020782.

[41] R.T. Moura, A.N. Carneiro Neto, R.L. Longo, O.L. Malta, On the calculation and interpretation of covalency in the intensity parameters of 4f-4f transitions in Eu^{3+} complexes based on the chemical bond overlap polarizability, J. Lumin. 170 (2016) 420–430. https://doi.org/10.1016/j.jlumin.2015.08.016.

[42] G.B.V. Lima, J.C. Bueno, A.F. da Silva, A.N. Carneiro Neto, R.T. Moura, E.E.S. Teotonio, O.L. Malta, W.M. Faustino, Novel trivalent europium β-diketonate complexes with N-(pyridine-2-yl)amides and N-(pyrimidine-2-yl)amides as ancillary ligands: Photophysical properties and theoretical structural modeling, J. Lumin. 219 (2020) 116884. https://doi.org/10.1016/j.jlumin.2019.116884.

[43] I.P. Assunção, A.N. Carneiro Neto, R.T. Moura, C.C.S. Pedroso, I.G.N. Silva, M.C.F.C. Felinto, E.E.S. Teotonio, O.L. Malta, H.F. Brito, Odd-even effect on luminescence properties of europium

aliphatic dicarboxylate complexes, ChemPhysChem. 20 (2019) 1931–1940. https://doi.org/10.1002/cphc.201900603.

[44] Y. Kitagawa, M. Kumagai, P.P. Ferreira da Rosa, K. Fushimi, Y. Hasegawa, Long-range LMCT coupling in Eu^{III} coordination polymers for an effective molecular luminescent thermometer, Chem. – Eur. J. 27 (2021) 264–269. https://doi.org/10.1002/chem.202002628.

[45] K.-L. Wong, J.-C.G. Bünzli, P.A. Tanner, Quantum yield and brightness, J. Lumin. 224 (2020) 117256. https://doi.org/10.1016/j.jlumin.2020.117256.

[46] C. Görller-Walrand, K. Binnemans, Spectral intensities of f-f transitions, in: K.A. Gschneidner Jr., L. Eyring (Eds.), Handbook Physics and Chemistry Rare Earths, Vol. 25, Elsevier (1998), pp. 101–264. https://doi.org/10.1016/S0168-1273(98)25006-9.

[47] C.K. Jørgensen, R. Reisfeld, Judd-Ofelt parameters and chemical bonding, J. Less-Common Met. 93 (1983) 107–112. https://doi.org/10.1016/0022-5088(83)90454-X.

[48] R.D. Peacock, The intensities of lanthanide f ↔ f transitions, in: Rare Earths, Springer Berlin Heidelberg, Berlin, Heidelberg (n.d.), pp. 83–122. https://doi.org/10.1007/BFb0116556.

[49] R. Reisfeld, Radiative and non-radiative transitions of rare-earth ions in glasses, in: Rare Earths, Springer Berlin Heidelberg, Berlin, Heidelberg (n.d.), pp. 123–175. https://doi.org/10.1007/BFb0116557.

[50] S. Tanabe, T. Ohyagi, N. Soga, T. Hanada, Compositional dependence of Judd-Ofelt parameters of Er^{3+} ions in alkali-metal borate glasses, Phys. Rev. B 46 (1992) 3305–3310. https://doi.org/10.1103/PhysRevB.46.3305.

[51] S. Tanabe, T. Hanada, Effect of ligand field on branching ratio of ultraviolet and blue upconversions of Tm^{3+} ions in halide and oxide glasses, J. Appl. Phys. 76 (1994) 3730–3734. https://doi.org/10.1063/1.357444.

[52] S. Tanabe, T. Ohyagi, S. Todoroki, T. Hanada, N. Soga, Relation between the Ω_6 intensity parameter of Er^{3+} ions and the ^{151}Eu isomer shift in oxide glasses, J. Appl. Phys. 73 (1993) 8451–8454. https://doi.org/10.1063/1.353417.

[53] S. Tanabe, T. Hanada, T. Ohyagi, N. Soga, Correlation between ^{151}Eu Mössbauer isomer shift and Judd-Ofelt Ω_6 parameters of Nd^{3+} ions in phosphate and silicate laser glasses, Phys. Rev. B 48 (1993) 10591–10594. https://doi.org/10.1103/PhysRevB.48.10591.

[54] Y. Nageno, H. Takebe, K. Morinaga, Correlation between radiative transition probabilities of Nd^{3+} and composition in silicate, borate, and phosphate glasses, J. Am. Ceram. Soc. 76 (1993) 3081–3086. https://doi.org/10.1111/j.1151-2916.1993.tb06612.x.

[55] H. Takebe, Y. Nageno, K. Morinaga, Compositional dependence of Judd-Ofelt parameters in silicate, borate, and phosphate glasses, J. Am. Ceram. Soc. 78 (1995) 1161–1168. https://doi.org/10.1111/j.1151-2916.1995.tb08463.x.

[56] H. Ebendorff-Heidepriem, D. Ehrt, Tb^{3+} f-d absorption as indicator of the effect of covalency on the Judd-Ofelt Ω_2 parameter in glasses, J. Non. Cryst. Solids 248 (1999) 247–252. https://doi.org/10.1016/S0022-3093(99)00243-4.

[57] M.P. Hehlen, M.G. Brik, K.W. Krämer, 50th anniversary of the Judd-Ofelt theory: An experimentalist's view of the formalism and its application, J. Lumin. 136 (2013) 221–239. https://doi.org/10.1016/j.jlumin.2012.10.035.

[58] D.E. Henrie, Per cent 'covalency' and the nephelauxetic effect in lanthanide complexes, Mol. Phys. 28 (1974) 415–421. https://doi.org/10.1080/00268977400102941.

[59] O.L. Malta, Theoretical crystal-field parameters for the YOCl: Eu^{3+}system. A simple overlap model, Chem. Phys. Lett. 88 (1982) 353–356. https://doi.org/10.1016/0009-2614(82)87103-0.

[60] O.L. Malta, A simple overlap model in lanthanide crystal-field theory, Chem. Phys. Lett. 87 (1982) 27–29. https://doi.org/10.1016/0009-2614(82)83546-X.

[61] A.N. Carneiro Neto, R.T. Moura, E.C. Aguiar, C.V. Santos, M.A.F.L.B. de Medeiros, Theoretical study of geometric and spectroscopic properties of Eu(III) complexes with Ruhemann's Purple ligands, J. Lumin. 201 (2018) 451–459. https://doi.org/10.1016/j.jlumin.2018.05.014.

[62] R.T. Moura Jr., A.N. Carneiro Neto, E.C. Aguiar, C.V. Santos-Jr., E.M. de Lima, W.M. Faustino, E.E.S. Teotonio, H.F. Brito, M.C.F.C. Felinto, R.A.S. Ferreira, L.D. Carlos, R.L. Longo, O.L. Malta, JOYSpectra: A web platform for luminescence of lanthanides, Opt. Mater. X 11 (2021) 100080. https://doi.org/10.1016/j.omx.2021.100080.

[63] T. Grzyb, A. Szczeszak, A. Shyichuk, R.T. Moura, A.N.C. Neto, N. Andrzejewska, O.L. Malta, S. Lis, Comparative studies of structure, spectroscopic properties and intensity parameters of tetragonal rare earth vanadate nanophosphors doped with Eu(III), J. Alloys Compd. 741 (2018) 459–472. https://doi.org/10.1016/j.jallcom.2018.01.095.

[64] A. Shyichuk, R.T. Moura, A.N. Carneiro Neto, M. Runowski, M.S. Zarad, A. Szczeszak, S. Lis, O.L. Malta, Effects of dopant addition on lattice and luminescence intensity parameters of Eu(III)-doped lanthanum orthovanadate, J. Phys. Chem. C 120 (2016). https://doi.org/10.1021/acs.jpcc.6b10778.

[65] A.N. Carneiro Neto, R.T. Moura, O.L. Malta, On the mechanisms of non-radiative energy transfer between lanthanide ions: Centrosymmetric systems, J. Lumin. 210 (2019) 342–347. https://doi.org/10.1016/j.jlumin.2019.02.049.

[66] O.A. Serra, L.C. Thompson, Emission Spectra of Cs2NaEuCls and CszNa(Eu,Y)Ck 0, Inorg. Chem. 15 (1976) 504–507. https://doi.org/10.1021/ic50157a002.

[67] B.R. Judd, Optical absorption intensities of rare-earth ions, Phys. Rev. 127 (1962) 750–761. https://doi.org/10.1103/PhysRev.127.750.

[68] G.S. Ofelt, Intensities of crystal spectra of rare-earth ions, J. Chem. Phys. 37 (1962) 511–520. https://doi.org/10.1063/1.1701366.

[69] A.R. Edmonds, Angular Momentum in Quantum Mechanics, 1st ed., Princeton University Press, New Jersey (1957).

[70] A. Messiah, Quantum Mechanics, Dover Publications (1962).

[71] B.R. Judd, Operator Techniques in Atomic Spectroscopy, McGraw-Hill Book Company, New York (1998).

[72] L. Smentek, Theoretical description of the spectroscopic properties of rare earth ions in crystals, Phys. Rep. 297 (1998) 155–237. https://doi.org/10.1016/S0370-1573(97)00077-X.

[73] S. Edvardsson, M. Klintenberg, Role of the electrostatic model in calculating rare-earth crystal-field parameters, J. Alloys Compd. 275–277 (1998) 230–233. https://doi.org/10.1016/S0925-8388(98)00309-0.

[74] H.B. Bebb, A. Gold, Multiphoton ionization of hydrogen and rare-gas atoms, Phys. Rev. 143 (1966) 1–24. https://doi.org/10.1103/PhysRev.143.1.

[75] O.L. Malta, E.A. Gouveia, Comment on the average energy denominator method in perturbation theory, Phys. Lett. A 97 (1983) 333–334. https://doi.org/10.1016/0375-9601(83)90655-2.

[76] O.L. Malta, S.J.L. Ribeiro, M. Faucher, P. Porcher, Theoretical intensities of 4f-4f transitions between stark levels of the Eu^{3+} ion in crystals, J. Phys. Chem. Solids 52 (1991) 587–593. https://doi.org/10.1016/0022-3697(91)90152-P.

[77] C.K. Jørgensen, B.R. Judd, Hypersensitive pseudoquadrupole transitions in lanthanides, Mol. Phys. 8 (1964) 281–290. https://doi.org/10.1080/00268976400100321.

[78] S.F. Mason, R.D. Peacock, B. Stewart, Ligand-polarization contributions to the intensity of hypersensitive trivalent lanthanide transitions, Mol. Phys. 30 (1975) 1829–1841. https://doi.org/10.1080/00268977500103321.

[79] A.N. Carneiro, E. Huskowska, P. Gawryszewska, J. Legendziewicz, O.L. Malta, Modeling 4*f*–4*f* intensity parameters as a function of structural distortions in Ln (2,2′-bipyridine-1,1′-dioxide)$_4$(ClO$_4$)$_3$

complexes (Ln=Pr^{3+}, Nd^{3+}), J. Lumin. 169 (2016) 454–457. https://doi.org/10.1016/j.jlumin.2015.02.028.

[80] M. Bettinelli, A. Speghini, F. Piccinelli, A.N.C. Neto, O.L. Malta, Luminescence spectroscopy of Eu^{3+} in $Ca_3Sc_2Si_3O_{12}$, J. Lumin. 131 (2011) 1026–1028. https://doi.org/10.1016/j.jlumin.2011.01.016.

[81] P. Porcher, P. Caro, Crystal field parameters for Eu^{3+} in KY_3F_{10}. II. Intensity parameters, J. Chem. Phys. 68 (1978) 4176–4182. https://doi.org/10.1063/1.436279.

[82] M.F. Reid, Transition intensities, in: R. Hull, J. Parisi, R.M. Osgood, H. Warlimont, G. Liu, B. Jacquier (Eds.), Spectroscopic Properties Rare Earths in Optical Materials Springer Series in Materials Science, Vol. 83, Springer, Berlin, Heidelberg (2005), pp. 95–129. https://doi.org/10.1007/3-540-28209-2_2.

[83] N.B.D. Lima, J.D.L. Dutra, S.M.C. Gonçalves, R.O. Freire, A.M. Simas, Chemical partition of the radiative decay rate of luminescence of europium complexes, Sci. Rep. 6 (2016) 21204. https://doi.org/10.1038/srep21204.

[84] C.K. Jørgensen, The Nephelauxetic Series (2007), pp. 73–124. https://doi.org/10.1002/9780470166055.ch2.

[85] S.P. Sinha, H.-H. Schmidtke, The nephelauxetic effect in rare earth complexes illustrated for praseodymium (III), Mol. Phys. 10 (1965) 7–11. https://doi.org/10.1080/00268976600100021.

[86] P.D. Dragic, M. Cavillon, J. Ballato, Materials for optical fiber lasers: A review, Appl. Phys. Rev. 5 (2018) 041301. https://doi.org/10.1063/1.5048410.

[87] A. Bronova, N. Kannengießer, R. Glaum, Optical spectra and magnetic behavior of a wide range of europium(iii) oxo-compounds: Analysis of the ligand-field effects, Inorg. Chem. 56 (2017) 9235–9246. https://doi.org/10.1021/acs.inorgchem.7b01287.

[88] R. Glaum, W. Grunwald, N. Kannengießer, A. Bronova, Analysis of ligand field effects in europium (III) phosphates, Z. Anorg. Allg. Chem. 646 (2020) 184–192. https://doi.org/10.1002/zaac.202000019.

[89] M. Suta, F. Cimpoesu, W. Urland, The angular overlap model of ligand field theory for f elements: An intuitive approach building bridges between theory and experiment, Coord. Chem. Rev. 441 (2021) 213981. https://doi.org/10.1016/j.ccr.2021.213981.

[90] B.R. Judd, Ionic transitions hypersensitive to environment, J. Chem. Phys. 70 (1979) 4830. https://doi.org/10.1063/1.437372.

[91] R.D. Peacock, The intensities of lanthanide f ↔ f transitions, Struct. Bond. 22 (1975) 83–122. https://doi.org/10.1016/B978-0-444-62735-3.00019-X.

[92] D.M. Gruen, C.W. DeKock, Absorption spectra of gaseous $NdBr_3$ and NdI_3, J. Chem. Phys. 45 (1966) 455–460. https://doi.org/10.1063/1.1727588.

[93] D.M. Gruen, C.W. DeKock, R.L. McBeth, Electronic Spectra of Lanthanide Compounds in the Vapor Phase, in: Advances in Chemistry (1967), pp. 102–121. https://doi.org/10.1021/ba-1967-0071.ch008.

[94] S.F. Mason, The ligand polarization model for the spectra of metal complexes: The dynamic coupling transition probabilities, in: Structure and Bonding (1980), pp. 43–81. https://doi.org/10.1007/3-540-09787-2_2.

[95] M. Hatanaka, S. Yabushita, Theoretical study on the f−f transition intensities of lanthanide trihalide systems, J. Phys. Chem. A 113 (2009) 12615–12625. https://doi.org/10.1021/jp9049507.

[96] M. Hatanaka, S. Yabushita, An ab initio study on the f-f hypersensitive transition intensities of lanthanide tribromide molecules, Chem. Phys. Lett. 504 (2011) 193–198. https://doi.org/10.1016/j.cplett.2011.01.077.

[97] M. Hatanaka, S. Yabushita, Mechanisms of f–f hypersensitive transition intensities of lanthanide trihalide molecules: A spin–orbit configuration interaction study, Theor. Chem. Acc. 133 (2014) 1517. https://doi.org/10.1007/s00214-014-1517-2.

[98] W.T. Carnall, J.P. Hessler, H.R. Hoekstra, C.W. Williams, The absorption spectra and excited state relaxation properties of lanthanide and actinide halide vapor complexes. I. $ErCl_3(AlCl_3)_x$, J. Chem. Phys. 68 (1978) 4304. https://doi.org/10.1063/1.436299.

[99] G.N. Papatheodorou, R.W. Berg, Laser-induced fluorescence of high-temperature vapor complexes of $ErCl_3$ with $AlCl_3$, $GaCl_3$ and $InCl_3$, Chem. Phys. Lett. 75 (1980) 483–487. https://doi.org/10.1016/0009-2614(80)80560-4.

[100] R.W. Berg, G.N. Papatheodorou, Vapor complexes of erbium(III) chloride with aluminum(III), gallium(III) and indium(III) chlorides, Inorg. Chim. Acta 45 (1980) L211–L213. https://doi.org/10.1016/S0020-1693(00)80149-8.

[101] S. Boghosian, G.N. Papatheodorou, Halide vapors and vapor complexes, in: K.A. Gschneidner Jr., L. Eyring (Eds.), Handbook Physics and Chemistry Rare Earths, Vol. 23, Elsevier B.V. (1996), pp. 435–496. https://doi.org/10.1016/S0168-12739623008-9.

[102] A.G. Kalampounias, G.N. Papatheodorou, Spectrophotometric study of the gaseous species over molten $HoCl_3$, LiCl-$HoCl_3$ and CsCl-$HoCl_3$ at temperature up to 1500K, J. Mol. Struct. 1206 (2020) 127707. https://doi.org/10.1016/j.molstruc.2020.127707.

[103] M. Hargittai, The molecular geometry of gas-phase metal halides, Coord. Chem. Rev. 91 (1988) 35–88. https://doi.org/10.1016/0010-8545(88)80013-4.

[104] A. Kovács, R.J.M. Konings, Structure and vibrations of lanthanide trihalides: An assessment of experimental and theoretical data, J. Phys. Chem. Ref. Data 33 (2004) 377–404. https://doi.org/10.1063/1.1595651.

[105] C. Adamo, V. Barone, Structures and properties of lanthanide and actinide complexes by a new density functional approach: Lanthanum, gadolinium, lutetium, and thorium halides as case studies, J. Comput. Chem. 21 (2000) 1153–1166. https://doi.org/10.1002/1096-987X(200010)21:13<1153::AID-JCC4>3.0.CO;2-V.

[106] B.R. Judd, Hypersensitive transitions in rare-earth ions, J. Chem. Phys. 44 (1966) 839–840. https://doi.org/10.1063/1.1726774.

[107] D.E. Henrie, R.L. Fellows, G.R. Choppin, Hypersensitivity in the electronic transitions of lanthanide and actinide complexes, Coord. Chem. Rev. 18 (1976) 199–224. https://doi.org/10.1016/S0010-8545(00)82044-5.

[108] R.D. Peacock, The charge-transfer contribution to the intensity of hypersensitive trivalent lanthanide transitions, Mol. Phys. 33 (1977) 1239–1246. https://doi.org/10.1080/00268977700101051.

[109] S.F. Mason, R.D. Peacock, B. Stewart, Dynamic coupling contributions to the intensity of hypersensitive lanthanide transitions, Chem. Phys. Lett. 29 (1974) 149–153. https://doi.org/10.1016/0009-2614(74)85001-3.

[110] D.J. Newman, G. Balasubramanian, Parametrization of rare-earth ion transition intensities, J. Phys. C Solid State Phys. 8 (1975) 37–44. https://doi.org/10.1088/0022-3719/8/1/008.

[111] R.D. Peacock, The intensities of Laporte forbidden transitions of the d- and f-block transition metal ions, J. Mol. Struct. 46 (1978) 203–227. https://doi.org/10.1016/0022-2860(78)87144-0.

[112] O.L. Malta, G.F. de Sá, Explanation of the anomalous hypersensitive $^3H_4 \rightarrow {}^3P_2$ transition in Pr^{3+}, Phys. Rev. Lett. 45 (1980) 890–893. https://doi.org/10.1103/PhysRevLett.45.890.

[113] O.L. Malta, G.F. De Sá, Hypersensitivity of the $^4I_{9/2} \rightarrow {}^4G_{5/2}, {}^2G_{7/2}$ transition of Nd^{3+} in the Y_2O_3 and $CaWO_4$ hosts, Chem. Phys. Lett. 74 (1980) 101–104. https://doi.org/10.1016/0009-2614(80)85023-8.

[114] O.L. Malta, Lanthanide f↔f transitions hypersensitive to the environment, Mol. Phys. (1981) 65–72. https://doi.org/10.1080/00268978100100051.

[115] F.S. Richardson, On the calculation of electric dipole strengths of 4f→4f transitions in lanthanide complexes, Chem. Phys. Lett. 86 (1982) 47–50. https://doi.org/10.1016/0009-2614(82)83114-X.

[116] M.F. Reid, F.S. Richardson, Anisotropic ligand polarizability contributions to lanthanide 4f → 4f intensity parameters, Chem. Phys. Lett. 95 (1983) 501–506. https://doi.org/10.1016/0009-2614(83)80341-8.

[117] M.F. Reid, F.S. Richardson, Electric dipole intensity parameters for lanthanide 4f→4f transitions, J. Chem. Phys. 79 (1983) 5735–5742. https://doi.org/10.1063/1.445760.

[118] M.F. Reid, J.J. Dallara, F.S. Richardson, Comparison of calculated and experimental 4f→4f intensity parameters for lanthanide complexes with isotropic ligands, J. Chem. Phys. 79 (1983) 5743–5751. https://doi.org/10.1063/1.445761.

[119] M.F. Reid, F.S. Richardson, Lanthanide 4f → 4f electric dipole intensity theory, J. Phys. Chem. 88 (1984) 3579–3586. https://doi.org/10.1021/j150660a041.

[120] A.F. Kirby, R.A. Palmer, Hypersensitive transition probability in tris(1,3-diphenyl-1,3-propanedionato) aquolanthanides (III), Inorg. Chem. 20 (1981) 4219–4222. https://doi.org/10.1021/ic50218a016.

[121] J. Lu, K. Yu, H. Wang, J. He, G. Cheng, C. Qin, J. Lin, W. Wei, B. Peng, Optical properties of Nd(TTA)$_3$ (TPPO)$_2$ doped polymer and its potential laser application, Opt. Mater. (Amst). 30 (2008) 1531–1537. https://doi.org/10.1016/j.optmat.2007.09.009.

[122] B. Chen, J. Xu, N. Dong, H. Liang, Q. Zhang, M. Yin, Spectra analysis of Nd(DBM)$_3$(TPPO)$_2$ in MMA solution and PMMA matrix, Spectrochim. Acta – Part A Mol. Biomol. Spectrosc. 60 (2004) 3113–3118. https://doi.org/10.1016/j.saa.2004.02.023.

[123] D.A. Metlina, M.T. Metlin, S.A. Ambrozevich, I.V. Taydakov, K.A. Lyssenko, A.G. Vitukhnovsky, A.S. Selyukov, V.S. Krivobok, D.F. Aminev, A.S. Tobokhova, Luminescence and electronic structure of Nd^{3+} complex with pyrazole-substituted 1,3-diketone and 1,10-phenanthroline, J. Lumin. 203 (2018) 546–553. https://doi.org/10.1016/j.jlumin.2018.07.005.

[124] A. Mech, Crystal structure and optical properties of novel (N(C$_2$H$_5$)$_4$)[Nd(hfa)$_4$(H$_2$O)] tetrakis complex, Polyhedron 27 (2008) 393–405. https://doi.org/10.1016/j.poly.2007.09.031.

[125] M. Babij, P. Starynowicz, A. Mondry, Structural and spectroscopic studies of neodymium complexes with S(+)-mandelic acid, J. Mol. Struct. 1006 (2011) 672–677. https://doi.org/10.1016/j.molstruc.2011.10.031.

[126] P. Loiko, A. Pavlyuk, S. Slimi, R.M. Solé, E. Ben Salem, E. Dunina, A. Kornienko, P. Camy, U. Griebner, V. Petrov, F. Díaz, M. Aguiló, X. Mateos, Growth, spectroscopy and laser operation of monoclinic Nd: CsGd(MoO4)$_2$crystal with a layered structure, J. Lumin. 231 (2021) 117793. https://doi.org/10.1016/j.jlumin.2020.117793.

[127] S. Ding, Q. Zhang, J. Gao, J. Luo, W. Liu, X. Wang, G. Sun, D. Sun, Energy-level structure and spectral analysis of Nd^{3+} in GdNbO$_4$ crystal, Opt. Mater. (Amst). 64 (2017) 474–478. https://doi.org/10.1016/j.optmat.2017.01.021.

[128] O. Guillot-Noel, B. Bellamy, B. Viana, D. Gourier, Correlation between rare-earth oscillator strengths and rare-earth–valence-band interactions in neodymium-doped YMO$_4$ (M=V, P, As), Y$_3$Al$_5$O$_{12}$, and LiYF$_4$ matrices, Phys. Rev. B 60 (1999) 1668–1677. https://doi.org/10.1103/PhysRevB.60.1668.

[129] G. Oczko, Investigation of lanthanide(III) coordination compounds with 4-pentynoic acid, J. Mol. Struct. 979 (2010) 136–143. https://doi.org/10.1016/j.molstruc.2010.06.016.

[130] A. Mondry, P. Starynowicz, Crystal structure and absorption spectroscopy of a neodymium(III) complex with triethylenetetraaminehexaacetic acid, Na$_3$[Nd(TTHA)]·2.5NaClO$_4$·7.617H$_2$O, Inorg. Chem. 36 (1997) 1176–1180. https://doi.org/10.1021/ic9604728.

[131] R. Beach, M.D. Shinn, L. Davis, R.W. Solarz, W.F. Krupke, Optical absorption and stimulated emission of neodymium in yttrium orthosilicate, IEEE J. Quantum Electron. 26 (1990) 1405–1412. https://doi.org/10.1109/3.59689.

[132] G. Oczko, J. Legendziewicz, M.S. Wickleder, G. Meyer, Crystal structure, magnetism and photophysics of the lanthanide maleates RE(C$_4$O$_4$H$_3$)$_3$·8H$_2$O (RE=Nd, Sm), J. Alloys Compd. 341 (2002) 255–262. https://doi.org/10.1016/S0925-8388(02)00092-0.

[133] A. Mondry, A. Starynowicz, Optical spectroscopy of neodymium(III) complexes with diethylenetriaminepentaacetic acid in solution and in [C(NH$_2$)$_3$]$_2$[Nd(dtpa)(H$_2$O)]·7H$_2$O single crystal, Polyhedron 19 (2000) 771–777. https://doi.org/10.1016/S0277-5387(00)00308-9.

[134] B.Z. Ahmad, B. Want, Spectroscopic properties of lanthanide based metal-organic framework [Nd (C$_4$H$_5$O$_6$)(C$_4$H$_4$O$_6$)][3H$_2$O]: Theoretical and experimental approaches, J. Lumin. 198 (2018) 378–383. https://doi.org/10.1016/j.jlumin.2018.02.052.

[135] G.Q. Wang, Y.P. Lin, Y.N. Feng, L.Y. Li, Environmentally friendly growth of fluoride crystal $LiYF_4$: Pr $^{3+}$with broadband near-infrared emission from $^1D_2$ manifolds, J. Cryst. Growth 520 (2019) 27–32. https://doi.org/10.1016/j.jcrysgro.2019.05.023.

[136] W.F. Krupke, Optical absorption and fluorescence intensities in several rare-earth-doped Y_2O_3 and LaF_3 single crystals, Phys. Rev. 145 (1966) 325–337. https://doi.org/10.1103/PhysRev.145.325.

[137] J.R. Ryan, R. Beach, Optical absorption and stimulated emission of neodymium in yttrium lithium fluoride, J. Opt. Soc. Am. B 9 (1992) 1883. https://doi.org/10.1364/JOSAB.9.001883.

[138] X. Cui, J. She, K. Cui, C. Gao, C. Hou, W. Wei, B. Peng, Nd^{3+}-doped LaF_3 nanoparticles with a larger emission cross-section, Chem. Phys. Lett. 489 (2010) 191–194. https://doi.org/10.1016/j.cplett.2010.02.066.

[139] G.Q. Wang, Y.F. Lin, X.H. Gong, Y.J. Chen, J.H. Huang, Z.D. Luo, Y.D. Huang, Polarized spectral properties of Sm^{3+}: $LiYF_4$crystal, J. Lumin. 147 (2014) 23–26. https://doi.org/10.1016/j.jlumin.2013.10.058.

[140] H.M. Ha, T.T.Q. Hoa, L. Van Vu, N.N. Long, Optical properties and Judd–Ofelt analysis of Sm ions in Lanthanum trifluoride nanocrystals, J. Mater. Sci. Mater. Electron. 28 (2017) 884–891. https://doi.org/10.1007/s10854-016-5603-1.

[141] P. Du, J.S. Yu, Facile hydrothermal synthesis of Eu^{3+}-activated $NaYF_4$ nanocrystals and their Judd-Ofelt analysis, photoluminescence and cathodoluminescence properties, Curr. Appl. Phys. 17 (2017) 1662–1669. https://doi.org/10.1016/j.cap.2017.09.011.

[142] A. Ćirić, S. Stojadinović, M.D. Dramićanin, Approximate prediction of the CIE coordinates of lanthanide-doped materials from the Judd-Ofelt intensity parameters, J. Lumin. 213 (2019) 395–400. https://doi.org/10.1016/j.jlumin.2019.05.052.

[143] V. Vasyliev, E.G. Víllora, Y. Sugahara, K. Shimamura, Judd-Ofelt analysis and emission quantum efficiency of Tb-fluoride single crystals: $LiTbF_4$ and $Tb_{0.81}Ca_{0.19}F_{2.81}$, J. Appl. Phys. 113 (2013) 203508. https://doi.org/10.1063/1.4807649.

[144] W.T. Carnall, H. Crosswhite, H.M. Crosswhite, Energy level structure and transition probabilities in the spectra of the trivalent lanthanides in LaF_3, Argonne, IL, United States (1978). https://doi.org/10.2172/6417825.

[145] M.G. Brik, T. Ishii, A.M. Tkachuk, S.E. Ivanova, I.K. Razumova, Calculations of the transitions intensities in the optical spectra of Dy^{3+}:$LiYF_4$, J. Alloys Compd. 374 (2004) 63–68. https://doi.org/10.1016/j.jallcom.2003.11.142.

[146] A.M. Tkachuk, S.E. Ivanova, A.A. Mirzaeva, F. Pellé, Study of spectroscopic characteristics of holmium-doped double sodium-yttrium fluoride crystals $Na_{0.4}Y_{0.6}F_{2.2}$: Ho^{3+}, Opt. Spectrosc. 111 (2011) 919–935. https://doi.org/10.1134/S0030400X11130248.

[147] H.M. Ha, T.T.Q. Hoa, L. Van Vu, N.N. Long, Radiative transition dynamics of holmium ions-doped LaF_3 nanocrystals, J. Mater. Sci. Mater. Electron. 29 (2018) 1607–1613. https://doi.org/10.1007/s10854-017-8071-3.

[148] G. Yao, C. Lin, Q. Meng, P. Stanley May, M.T. Berry, Calculation of Judd-Ofelt parameters for Er^{3+} in β-$NaYF_4$: Yb^{3+}, Er^{3+} from emission intensity ratios and diffuse reflectance spectra, J. Lumin. 160 (2015) 276–281. https://doi.org/10.1016/j.jlumin.2014.12.025.

[149] G.G. Demirkhanyan, R.B. Kostanyan, Spectroscopic capabilities of LaF_3: Er^{3+} crystals for MIR lasers cascade operation, J. Contemp. Phys. (Armenian Acad. Sci. 55 (2020) 306–313. https://doi.org/10.3103/S1068337220040076.

[150] S.E. Ivanova, A.M. Tkachuk, A. Mirzaeva, F. Pellé, Spectroscopic study of thulium-activated double sodium yttrium fluoride $Na_{0.4}Y_{0.6}F_{2.2}$: Tm^{3+}crystals: I. Intensity of spectra and luminescence kinetics, Opt. Spectrosc. 105 (2008) 228–241. https://doi.org/10.1134/S0030400X08080110.

[151] J. Hong, L. Zhang, M. Xu, Y. Hang, Optical characterization of Tm^{3+} in LaF_3 single crystal, Infrared Phys. Technol. 82 (2017) 50–55. https://doi.org/10.1016/j.infrared.2017.02.012.

[152] O.L. Malta, Ligand – Rare-earth ion energy transfer in coordination compounds. A theoretical approach, J. Lumin. 71 (1997) 229–236. https://doi.org/10.1016/S0022-23139600126-3.

[153] O.L. Malta, F.R. Gonçalves E Silva, A theoretical approach to intramolecular energy transfer and emission quantum yields in coordination compounds of rare earth ions, Spectrochim. Acta Part A Mol. Biomol. Spectrosc. 54 (1998) 1593–1599. https://doi.org/10.1016/S1386-14259800086-9.

[154] A.N. Carneiro Neto, E.E.S. Teotonio, G.F. de Sá, H.F. Brito, J. Legendziewicz, L.D. Carlos, M.C.F.C. Felinto, P. Gawryszewska, R.T. Moura Jr., R.L. Longo, W.M. Faustino, O.L. Malta, Modeling intramolecular energy transfer in lanthanide chelates: A critical review and recent advances, in: J.-C.G. Bünzli, V.K. Pecharsky (Eds.), Handbook Physics and Chemistry Rare Earths, Vol. 56, Elsevier (2019), pp. 55–162. https://doi.org/10.1016/bs.hpcre.2019.08.001.

[155] O.L. Malta, H.J. Batista, L.D. Carlos, Overlap polarizability of a chemical bond: A scale of covalency and application to lanthanide compounds, Chem. Phys. 282 (2002) 21–30. https://doi.org/10.1016/S0301-0104(02)00631-6.

[156] P.R.S. Santos, D.K.S. Pereira, I.F. Costa, I.F. Silva, H.F. Brito, W.M. Faustino, A.N. Carneiro Neto, R.T. Moura, M.H. Araujo, R. Diniz, O.L. Malta, E.E.S. Teotonio, Experimental and theoretical investigations of the $[Ln(\beta\text{-dik})(NO_3)_2(phen)_2]\ H_2O$ luminescent complexes, J. Lumin. 226 (2020) 117455. https://doi.org/10.1016/j.jlumin.2020.117455.

[157] A.N. Carneiro Neto, R.T. Moura Jr., Overlap integrals and excitation energies calculations in trivalent lanthanides 4f orbitals in pairs Ln-L (L = Ln, N, O, F, P, S, Cl, Se, Br, and I), Chem. Phys. Lett. 757 (2020) 137884. https://doi.org/10.1016/j.cplett.2020.137884.

[158] J.D.L. Dutra, N.B.D. Lima, R.O. Freire, A.M. Simas, Europium luminescence: Electronic densities and superdelocalizabilities for a unique adjustment of theoretical intensity parameters, Sci. Rep. 5 (2015) 13695. https://doi.org/10.1038/srep13695.

[159] R.T. Moura, A.N. Carneiro Neto, O.L. Malta, R.L. Longo, Overlap properties of chemical bonds in generic systems including unusual bonding situations, J. Mol. Model 26 (2020) 301. https://doi.org/10.1007/s00894-020-04535-w.

[160] A. Shyichuk, R.T. Moura, A.N.C. Neto, M. Runowski, M.S. Zarad, A. Szczeszak, S. Lis, O.L. Malta, Effects of dopant addition on lattice and luminescence intensity parameters of Eu(III)-doped lanthanum orthovanadate, J. Phys. Chem. C 120 (2016) 28497–28508. https://doi.org/10.1021/acs.jpcc.6b10778.

Markus Suta, Werner Urland

Chapter 3
The angular overlap model: a chemically intuitive way to describe the ligand field of coordination compounds

3.1 Introductory remarks

This chapter aims at giving an overview of crystal and ligand field theories. We wanted to give a generalized overview to the often-reported formulas of crystal field calculations in literature, motivate their advantages, indicate limitations, and then introduce the angular overlap model (AOM) of ligand field theory as an alternative equivalent approach to the description of the electronic structure of coordination entities. Based on our experience with the communities of optical spectroscopy and magnetochemistry, we devoted this chapter to the description of the interpretational content of the key formulas instead of focusing on a very thorough theoretical derivation to avoid distraction from the main statements. Readers who are interested in those technical details are invited to read a recently published review by us for a more complete derivation and explanation of the mathematical details [1]. Although we tried to minimize the amount of necessary background to keep the ideas still intuitive, a certain preliminary knowledge is recommended for a better understanding. Crystal and ligand field theories deal with the description of coordination compounds in solids or solution and are among the fundamental teaching topics of compounds in chemistry. In addition, a background in orbital theory, the concepts of coordination number and geometry, as well as some familiarity with the description of symmetry by groups such as irreducible representations may be helpful, although we tried to avoid using technical terminology or explained in more detail for the sake of a general understanding.

3.2 Crystal field theory: the symmetry approach to coordination compounds

3.2.1 Qualitative description of the splitting of orbitals in crystal fields

Inorganic transition metal and lanthanoid compounds play an important role in our daily lives. They are most prominent for their beautiful colors, bright photoluminescence, and strong magnetic features [2]. It comes as no surprise that these physical properties

https://doi.org/10.1515/9783110607871-003

are used in modern devices such as light-emitting devices, windmills, hard drive disks, or smartphones [3]. In addition, they are crucial for many biochemical processes and the function of enzymes. While hemoglobin with Fe(II) as the metal center in the active site is probably the best-known example, also Co (cobalamines, vitamin B_{12}) and Cu (plastocyanine) play vital roles as metal centers in enzymes. Since 2014, it has also been elucidated that lanthanoids also play an important role in methylotrophic bacteria [4].

The variation in the optical and magnetic properties of transition metal and lanthanoid compounds is determined by their chemical environment. Usually, the metal atoms or ions are *coordinated* by a set of surrounding atoms, ions, or even molecules in a specific geometry. It is customary to refer to the metal center as the *central atom* or *ion*, while the surrounding atoms, ions, or molecules are called the *ligands*. Altogether, the entity of central atom/ion and ligands is called a *coordination compound*. It was already realized early on by Alfred Werner, one of the pioneers of coordination chemistry, that the beautiful colors of transition metal coordination compounds are controlled by the type and number of ligands around a central metal atom. In 1929, Hans Bethe published an extensive model that could explain the differences in colors of many transition metal coordination compounds, in principle [5]. It was realized by John Hasbrouck van Vleck that this theoretical approach could also account for the differences in observable magnetic moments of many transition metal coordination compounds [6]. Nowadays, their ideas are classic teaching elements of chemistry undergraduate courses.

Bethe's original theoretical framework treated the surrounding ligands as repulsive point charges. That means that within this framework, the formation of a coordination compound is considered to be purely based on electrostatic interaction. Given the name of Bethe's original publication in German (*Termaufspaltung in Kristallen*, English: Term splitting in crystals), his approach is commonly known as *crystal field theory*. The crystal field refers to the electrostatic field produced by the approaching ligands around a central atom or ion. We want to introduce the elements of this theory and the relevance for chemistry in more detail.

A key element to crystal field theory is *symmetry*. Symmetry denotes whether an object remains invariant under certain transformations such as rotation or reflection. Symmetry plays an important role in physical theories quite generally. Noether's theorem (after Emmy Noether, 1918) [7] states that any (so-called global) symmetry is fundamentally connected to a conserved physical quantity and is the underlying principle for, for example, energy (time invariance), momentum (translational invariance), or angular momentum (isotropy of three-dimensional space) conservation, especially energy and angular momentum conservation will be important throughout this chapter.

From the quantum-mechanical treatment of free atoms, it is known that the electron wave functions can be classified into different sets according to their orbital angular momentum quantum number ℓ, which are called *orbitals*: *s* orbitals are characterized by

$\ell = 0$, *p* orbitals by $\ell = 1$, *d* orbitals by $\ell = 2$, and *f* orbitals by $\ell = 3$.[1] A set of orbitals for a given ℓ is always $(2\ell+1)$-fold energetically degenerate in a spherically symmetric atom. This is a consequence of the symmetry of the atomic Hamiltonian governing the dynamics of electrons in a free atom: A free atom is spherically symmetric, and so is the Hamiltonian.

In a crystal field, this situation changes. When the point charge-like ligands approach a free central atom or ion in a specific geometrical fashion, the corresponding electrostatic potential *breaks* the spherical symmetry of the atom and becomes anisotropic. In that case, there are certain spatial regions that are energetically more favorable for the electrons of the central atom to be located at than others, namely those at which the spatial electron density of the central atom within the orbitals avoids the approaching point charges as much as possible. Consequently, the orbitals will *split* and sacrifice degeneracy: some orbitals of a given ℓ are energetically favored in a crystal field of a specific symmetry. This is a consequence of the fact that the Hamiltonian shares the symmetry of the coordination compound. We will demonstrate that for the different types of orbitals on a set of exemplary coordination geometries.

Example:

***s* orbitals:** *s* orbitals are only singly degenerate and spherically symmetric wave functions. For them, there is no preferred direction, and therefore, they do not split up irrespective of the symmetry of the coordination compound.

***p* orbitals:** For *p* orbitals, the situation already changes. For example, in the case of octahedrally coordinated central atoms, *p* orbitals will retain their degeneracy. Each *p* orbital points to the direction of one of the Cartesian axes *x*, *y*, *z*. It is always possible to set the central atom into the origin of the coordinate system and rotate the coordinate system such that there are two ligands approaching along one of these axes, while the four other ligands approach along the other two axes. This is equivalent for all three spatial directions. Therefore, *p* orbitals will retain their degeneracy in an octahedral coordination compound. Similar arguments can be found for a tetrahedrally or cubically coordinated compound. In contrast, a square-planar coordination geometry leads to a splitting of *p* orbitals into a doubly degenerate set (p_x, p_y) that is in the plane of approaching ligands, while the *p* orbital perpendicular to the plane (p_z) constitutes a singly degenerate state. Given the lower degree of electronic repulsion in that direction, the singly degenerate state should have a lower energy than the doubly degenerate set from an electrostatic point of view. The same type of splitting holds for any other planar configuration (e.g., trigonal planar, pentagonal planar, and hexagonal planar).

***d* orbitals:** The *d* orbitals are probably the most familiar example to chemists, for which they encounter the effect of a crystal field. It is also good to demonstrate the relevance of the coordination geometry and the related symmetry group here. For example, *d* orbitals of a central would retain their complete fivefold degeneracy in an icosahedrally coordinated geometry (coordination number of 12). In the case of an octahedral coordination geometry with the six ligands approaching along the three Cartesian axes x, y, z, the electrostatic repulsion for the d orbitals oriented along the three axes ($d_{x^2-y^2}$, d_{z^2}) is higher than for the other three d orbitals in between the Cartesian axes (d_{xy}, d_{xz}, d_{yz}). Consequently, the originally fivefold degenerate d orbitals split into a set of energetically more favorable triply degenerate wave functions and a set of energetically more unfavorable doubly degenerate wave functions. In the case of a tetrahedral or cubic coordination geometry, the splitting pattern is similar, but the energetic order of the d orbitals is reversed: the doubly degenerate set of wave functions becomes energetically stabilized, while the triply degenerate set is energetically more unfavorable. This is related to the different situation that upon definition of the same Cartesian coordinate system as for an octahedron (pointing along the three fourfold rotation axes), the ligands approach in between the Cartesian axes, in contrast to the case of an octahedron. This last example also shows an important difference between symmetry analysis and energy accounting: Symmetry analysis can only explain the general splitting pattern (in the previous example, the splitting into doubly and triply degenerate sets of wave functions) but make no statement about the energetic order of the states described by the respective wave functions. This can only be done by electrostatic considerations or by solving Schrödinger's equation.

---

[1] In the language of group theory, the mathematical description of symmetries, the different sets of orbitals form so-called $(2\ell+1)$-dimensional *irreducible representations* of the three-dimensional rotational symmetry group. A *group* is a set of *symmetry elements* that fulfill special mathematical properties that define it as such.

***f* orbitals:** *f* orbitals already have more complex shapes and a total degeneracy of 7 in a free atom. This degeneracy is not completely retained in the commonly known coordination geometries. For the sake of clarity, we will restrict ourselves to the familiar case of an octahedral coordination geometry. Among the seven *f* orbitals, three point along one of the three Cartesian axes ($f_{x^3}, f_{y^3}, f_{z^3}$), three other orbitals lie on two of the three Cartesian axes ($f_{x(z^2-y^2)}, f_{y(z^2-x^2)}, f_{z(x^2-y^2)}$), and one points in between all three axes (f_{xyz}). It is then simple to deduce the splitting pattern by electrostatic arguments and *f* orbitals split into a set of an energetically favorable singly degenerate (f_{xyz}), one sets of a slightly less favorable triply degenerate set ($f_{x(z^2-y^2)}, f_{y(z^2-x^2)}, f_{z(x^2-y^2)}$) and a set of an energetically more unfavorable triply degenerate set ($f_{x^3}, f_{y^3}, f_{z^3}$) of wave functions. Again, this situation reverses in the case of a cubically coordinated[2] central atom.

The previous examples also show that lower symmetries remove more of the degeneracy of the states. A lower symmetry is characterized by fewer symmetry elements that are available in an object. It is also important to note that the splitting of the orbitals in a crystal field is not symmetrical. In the framework of crystal field theory, the central atom is only prone to a nonspherical electrostatic charge distribution due to the ligands that break its spherical symmetry. The splitting neither creates nor destroys energy because of energy conservation. Since the orbitals typically split into sets of states with mutually different degeneracies, only the energy barycenter remains a conserved quantity.

---

[2] This formally also applies to a tetrahedral coordination. However, the lanthanides and actinides are already so large that they are never encountered in coordination geometries with a low coordination number of 4.

3.2.2 The Wybourne parametrization of the crystal field potential

The previous example demonstrates that many independent parameters are required to fully describe the various energy differences between the split states from an originally degenerate set of orbitals. A technically well-established way of generalizing this approach to all point symmetries was originally developed by Brian G. Wybourne [8]. It is based on the conceptual idea that the tip of every coordination polyhedron can be placed on the surface of a sphere that incorporates this polyhedron (see Figure 3.1). This allows to expand every geometrical set of point charges in terms of the orthogonal basis functions of the spherical surface, the *spherical harmonics* $Y_\ell^m(\varphi, \theta)$, irrespective of the exact form of the charge density distribution. The crystal field potential can thus be formally written as

$$V_{\mathrm{CF}}(r, \varphi, \theta) = \sum_{\ell=0}^{\infty} \sum_{m=-\ell}^{+\ell} V_m^\ell(r) Y_\ell^m(\varphi, \theta) \tag{3.1}$$

with distance-dependent expansion coefficients $V_m^\ell(r)$ for a given ℓ. Approach (3.1) is called a *spherical multipole expansion*.

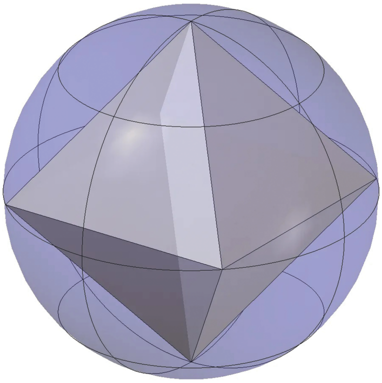

Figure 3.1: Octahedron inscribed into a sphere motivating the possibility of a spherical multipole expansion of the crystal field potential.

In a quantum-mechanical interpretation, the crystal field potential takes the role of a Hamiltonian and is thus regarded as an operator. An operator basically just transforms one state vector into another. From linear algebra, such an action is known from *tensors*. In operator form, it is conventional to write the upper potential symbolically as

$$\hat{\mathcal{H}}_{CF} = \sum_{\ell=0}^{\infty} \sum_{m=-\ell}^{+\ell} \hat{\mathcal{B}}_m^\ell(r) \hat{\mathcal{C}}_\ell^m(\varphi, \theta) \tag{3.2}$$

with

$$\hat{\mathcal{C}}_{\ell}^{m}(\varphi,\theta)=\sqrt{\frac{4\pi}{2\ell+1}}Y_{\ell}^{m}(\varphi,\theta) \tag{3.3}$$

as so-called *spherical tensor operators* or *multipole moments* to stress their transformation role. While operators only represent a physical observable, their measurable values are given by *matrix elements*, which depend on the choice of a state vectors as a basis. As already indicated, conventional crystal field theory is typically focused on the *perturbation* of the states of the central atom by the electrostatic potential generated by the approach of the surrounding ligands. As a simple demonstrative example for the reader,[3] we will consider the simple case of atomic orbitals of a free central atom, which can be characterized by the *principal quantum number n*, the *orbital angular momentum quantum number ℓ*, and the *magnetic quantum number m*. In position space representation, the respective (stationary) wave functions read

$$\psi_{n\ell m}(r,\varphi,\theta)=\langle r\varphi\theta|n\ell m\rangle=R_{n\ell}(r)Y_{\ell}^{m}(\varphi,\theta) \tag{3.4}$$

In contrast to hydrogenic one-electron systems, the radial functions $R_{n\ell}(r)$ of a many-electron system are not known analytically and must be determined by numerical solution of the Schrödinger equation of the free central atom. Once the wave functions of the atomic states of interest are known to a desired level of accuracy, they can serve as the basis for the calculation of the so-called *crystal field matrix elements*,

$$\left\langle\psi_{n\ell m}|\hat{\mathcal{H}}_{\mathrm{CF}}|\psi_{n\ell m'}\right\rangle=\sum_{k=0}^{\infty}\sum_{k=-q}^{+q}\left\langle R_{n\ell}|\hat{\mathcal{B}}_{q}^{k}|R_{n\ell}\right\rangle\left\langle Y_{\ell}^{m}|\hat{\mathcal{C}}_{k}^{q}|Y_{\ell}^{m'}\right\rangle\equiv\sum_{k=0}^{\infty}\sum_{k=-q}^{+q}B_{q}^{k}C_{k}^{q} \tag{3.5}$$

Note that the operator hats are missing now on the right-hand side to stress that these are numerical (expectation) values. The B_q^k are called *Wybourne parameters* of the crystal field potential. It should be noted that eq. (3.5) is basically nothing less than the first-order perturbation correction to the energy eigenvalues of the central atom by the perturbing crystal field potential.

Equations (3.1)–(3.5) may appear like a complicated way to describe the crystal field potential. The benefit of this approach will become evident in the following. The C_q^k are called *Gaunt integrals* and can be explicitly calculated or are tabulated. For two orbitals with the same *n* and *ℓ*, they read

---

[3] This is actually a crude approximation in practice and should now be only considered for demonstrative purpose. Typically, mutual electron repulsion and spin–orbit coupling cannot be neglected anymore, and the atomic states need to be described with different quantum numbers such as overall orbital angular momentum *L*, spin *S*, and total angular momentum *J* (dependent on the relative magnitude of electron repulsion and spin–orbit coupling). The procedure then gets slightly more complicated and requires usage of the *Wigner–Eckart theorem*, but does not change in its general essence.

$$C_k^q = \left\langle Y_\ell^m | \hat{\mathcal{C}}_k^q | Y_\ell^{m'} \right\rangle = (-1)^m (2\ell+1) \begin{pmatrix} \ell & k & \ell \\ 0 & 0 & 0 \end{pmatrix} \begin{pmatrix} \ell & k & \ell \\ -m & q & m' \end{pmatrix} \tag{3.6}$$

The six-entry objects on the right-hand side are so-called *Wigner 3j symbols*. They are only nonzero under very restrictive conditions. Two of these are that k needs to be $2(t-\ell)$ with t as any positive integer, as well as $0 \leq k \leq 2\ell$. That means that k is restricted to any even integer positive value up to 2ℓ. For crystal field matrix elements involving solely p orbitals, the Gaunt integrals (3.6) are thus only nonzero for $k = 0, 2$; for d orbitals, $k = 0, 2, 4$; and for f orbitals, $k = 0, 2, 4, 6$. The second Wigner 3j symbol in eq. (3.6) is additionally nonzero, if $q = m - m'$. Thus, for a given k, there are only limited values of q (since ℓ restricts the values of m) possible, for which the C_k^q is nonzero. For two-open shell configurations such as the $4f^{N-1}5d^1$ configuration of trivalent or divalent lanthanoid ions, there are also odd values of k possible since ℓ_1 is different from ℓ_2 (typically $\ell_2 = \ell_1 + 1$).

Despite the reduction of necessary terms in expansion (3.5) to just a few values, there are still quite some possibilities for independent nonzero Wybourne parameters B_q^k given a specific k. Since the crystal field potential is a real-valued function, the crystal field matrix composed of the elements (3.5) must be symmetric with respect to its main diagonal. Thus, out of the $(2\ell+1) \times (2\ell+1)$ possible entries, only $(2\ell+1)$ (from the main diagonal) + $\frac{1}{2}(2\ell+1) \cdot 2\ell$ (from the upper triangle) are independent. Thus, for a given type of orbital with quantum number ℓ in an open-shell configuration prone to a crystal field potential, there are at maximum $(\ell+1)(2\ell+1)$ independent Wybourne parameters B_q^k possible. While there is always *1* spherical B_0^0 parameter that is typically incorporated into the free-atom Hamiltonian as a constant energy shift, there are 5 more B_q^2 parameters for p electrons, *9* additional B_q^4 parameters for d electrons (i.e., in total 14 independent Wybourne parameters), and 13 additional B_q^6 parameters for f electrons (i.e., in total 27 independent Wybourne parameters).

Fortunately, the actual point symmetry of the coordination polyhedron helps reduce the number of independent nonzero Wybourne parameters further. This is another consequence of Noether's theorem: Since the electrostatic charge density due to the surrounding ligands is time-invariant (this is why it is referred to as *static*), the theorem states that there must be a correspondingly conserved quantity. As we have indicated in Section 2.1, this quantity is the energy, which is just represented by the Hamiltonian. For a given coordination polyhedron, the Hamiltonian needs to remain invariant under each of the possible symmetry transformations within the symmetry point group of the polyhedron. Now the benefit of the multipole expansion (3.5) comes to real action: The higher the symmetry of the coordination polyhedron (i.e., the more symmetry elements are contained therein or the higher the order of the respective point group), the more restrictions there are on the Wybourne parameters B_q^k in order to fulfill the requirement of an invariant crystal field Hamiltonian and thus, the less nonzero, independent Wybourne parameters at all. Table 3.1 gives an

Table 3.1: Number of independent Wybourne parameters (B_0^0 excluded) for *d* orbitals ($\ell = 2$) or *f* orbitals ($\ell = 3$) for the 32 different crystallographic three-dimensional point groups (given in Schönflies notation).

***d* orbitals ($\ell = 2$)**		***f* orbitals ($\ell = 3$)**	
No. of independent B_q^k	**Point groups**	**No. of independent B_q^k**	**Point groups**
14	C_1, C_i	27	C_1, C_i
8	C_2, C_s, C_h	15	C_2, C_s, C_h
5	C_{2v}, D_{2h}, D_2		
4	C_3, C_4, C_{4h}, S_4, S_6	9	C_{2v}, C_3, D_2, D_{2h}, S_6
3	C_{3v}, C_{4v}, D_{2d}, D_3, D_{3d}, D_4, D_{4h}	7	C_4, $C_{4\mathrm{h}}$, S_4
		6	C_{3v}, D_3, D_{3d}
2	C_6, C_{6v}, C_{3h}, C_{6h}, D_{3h}, D_6, D_{3h}, D_{6h}, D_{4d}, D_{6d}, $C_{\infty v}$, $D_{\infty h}$	5	C_6, C_{4v}, C_{3h}, C_{6h}, D_{2d}, D_4, D_{4h}
		4	C_{6v}, D_6, D_{3h}, D_{6h}
		3	D_{4d}, D_{6d}, $C_{\infty v}$, $D_{\infty h}$
1*	T_d, O_h	2*	T_d, O_h
0	I_h	1*	I_h

*The Wybourne parameters are not unique here and depend on the reference coordinate system.

overview over the number of independent Wybourne parameters for the relevant cases of *d* orbitals and *f* orbitals.

It is helpful to consider the cases of highest symmetry for a better insight. As indicated in our earlier example, *d* orbitals retain their complete fivefold degeneracy in an icosahedral symmetry (I_h), while *f* orbitals split into a set of fourfold degenerate and triply degenerate states. It comes as no surprise that no Wybourne parameter (apart from B_0^0) is required in the case of *d* orbitals, while exactly one Wybourne parameter (B_0^6) is needed to describe the splitting of *f* orbitals. The same holds of the cubic symmetries T_d or O_h. The *d* orbitals split into a set of triply and doubly degenerate states in that case, which requires one Wybourne parameter (B_0^4) to describe this splitting. In fact, B_0^4 and the conventionally used parameter $10Dq$ in octahedral crystal fields are only related by a simple factor, $10Dq = \left(10/21\right)B_0^4$. In contrast, *f* orbitals split into a singly degenerate state and two sets of triply degenerate states, which makes two independent splitting parameters or, alternatively, two independent Wybourne parameters (B_0^4 and B_0^6) for the full description of the crystal field splitting necessary. For the lower symmetries, successively more parameters are required.

3.2.3 Limitations of crystal field theory and the symmetry-based approach

The crystal field model by Bethe works qualitatively well for small negatively charged ligands. Ligands are typically, however, extended molecules that cannot be simply approximated by a point charge. A particularly important realization of this fact is the *spectrochemical series* of ligands originally established by Tsuchida, which compares the impact of different types of ligands on the splitting of the *d* orbitals of a common transition metal center in octahedral coordination geometry. It is an experimental fact that many molecular neutral ligands such as H_2O, NH_3, or CO lead to a much higher splitting between the *d* orbitals than charged ligands such as F^-. This observation is incompatible with the assumptions of Bethe's classical crystal field theory that would predict exactly the opposite trend of charged ligands inducing a stronger crystal field splitting. Even among anions, there are certain differences that are not fully covered in a simple approximation of point charges. For example, nitride ions, N^{3-}, have a higher charge than oxide ions, O^{2-}. Yet, nitride ions are at most comparable, if not actually weaker ligands than O^{2-}. Another example is the hydride anion, H^-, that should expectedly be comparable in the crystal field splitting strength compared to simple halide anions such as F^-. Nonetheless, it is known from Eu^{2+} with an excited $4f^65d^1$ configuration that it typically absorbs/emits in the violet/blue range in the case of CaF_2 ($\lambda_{em} = 425$ nm) [9], while it absorbs/emits in the green/red range in CaH_2 ($\lambda_{em} = 764$ nm) [10]. These examples all indicate that a pure electrostatic model of the chemical bond between central atom and ligands may work well in many instances but is not sufficient to fully cover all effects that determine the physical properties of coordination compounds.

There is, however, an additional subtlety related to the exploitation of symmetry and the description of the crystal field potential by means of the Wybourne formalism. Transition metal atoms with specific d^N configurations are particularly often encountered in octahedral, tetrahedral, or tetragonally distorted coordination geometries due to a thermodynamic stabilization. For example, Cr^{3+} and Mn^{4+} (d^3) generally prefer a surrounding octahedral coordination geometry, while Co^{2+} (d^7) often favors tetrahedral coordination with weak-field ligands based on the additional contribution of a crystal field stabilization energy. Zn^{2+} and Cd^{2+} (d^{10}) also gain a thermodynamic stabilization upon tetrahedral coordination because of additional admixture of their higher energetic *p* orbitals. Finally, Cu^{2+} (d^9) or Mn^{3+} (d^4) in weak fields are often found in tetragonally distorted octahedral coordination because of an energy gain by symmetry reduction due to the Jahn–Teller effect. In such high symmetries of coordination polyhedra, the *d* orbitals retain a large amount of their original degeneracy. Thus, the crystal field splitting among the arising states can already be described by just a few Wybourne parameters (see Table 3.1, left column).

In contrast, the larger lanthanides with their chemically well-shielded 4*f* orbitals only weakly interact with the surrounding ligands, and thus, do not typically show such a pronounced thermodynamically preference for high coordination geometries. Therefore, especially coordination compounds of the early and larger lanthanides tend to be characterized by high coordination numbers and connected low symmetries. This is particularly often realized in the structure of crystalline solids of the rare-earth ions. For example, the orthophosphates of the larger rare-earth ions, $RE\text{PO}_4$ (RE = La–Gd), crystallize in the monoclinic monazite structure type ($P2_1/n$, no. 14), while the orthophosphates of the smaller rare-earth ions (RE = Tb–Lu, Y, Sc) crystallize in the more symmetric, tetragonal xenotime or zircon-type structure ($I4_1/amd$, no. 141). In the monazite-type structure, the rare-earth ions are ninefold coordinated by the oxygen atoms in the form of a pentagonal interpenetrating tetrahedral polyhedron and become eightfold coordinated in the xenotime-type structure by the oxygen atoms in a distorted dodecahedral fashion. The symmetry of both coordination polyhedra is not very high and would already require 15 (monazite-type $RE\text{PO}_4$) or 5 (xenotime-type $RE\text{PO}_4$) independent Wybourne parameters to fully parametrize the crystal field potential acting on the trivalent rare-earth ion.

3.3 The angular overlap model of ligand field theory: exploiting the coordination geometry and chemical intuition

3.3.1 Foundations of the angular overlap model and conceptual difference to the Wybourne parametrization

The purely electrostatic and symmetry-motivated approach to parametrize the crystal field works technically very well and can already explain quite some observed trends in the features of coordination compounds. In chemistry, however, it is much more common to think in terms of bonds and orbital overlap. Thus, instead of exploiting the symmetry of a coordination polyhedron, one could also envision it as a collection of linear metal-ligand bonds that are arranged in the right *geometry*. It is common to refer to *ligand field theory* if the ligand orbitals are explicitly included into the model of a coordination compound. Since a linear metal–ligand bond has a cylindrical symmetry ($C_{\infty v}$), the originally $(2\ell+1)$-fold degenerate orbitals in spherical symmetry will also split in this lower symmetry. This decomposition is, however, very intuitive to chemists. The resulting orbitals are simply denoted by the bonding symmetry of the orbitals with respect to the metal–ligand bond axis z.[4] An s orbital can only give rise to a σ-type orbital in $C_{\infty v}$ that has cylindrical symmetry and lies on the bond axis of the metal–ligand bond. The p orbitals split into a cylindrically symmetric σ-type orbital (p_z) and a set of degenerate π-type orbitals (p_x, p_y) that are perpendicularly oriented with respect to the bond axis.

---

[4] These are the irreducible representations of $C_{\infty v}$.

The d orbitals also split into one σ-type orbital (d_{z^2}), a set of degenerate π-type orbitals (d_{xz}, d_{yz}), and a set of degenerate so-called δ-type orbitals (d_{xy}, $d_{x^2-y^2}$). Finally, f orbitals give rise to a σ-type orbital (f_{z^3}), a set of degenerate π-type orbitals (f_{x^3}, f_{y^3}), δ-type orbitals ($f_{x\left(z^2-y^2\right)}, f_{y\left(z^2-x^2\right)}$), and even so-called ϕ-type orbitals ($f_{z\left(x^2-y^2\right)}, f_{xyz}$). Table 3.2 compiles the splitting of the chemically relevant orbitals again.

Table 3.2: Splitting of atomic orbitals in $C_{\infty v.}$

ℓ	**Decomposition in $C_{\infty v.}$**
0 (s)	0 (σ)
1 (p)	0 (σ) ⊕ ±1 (π)
2 (d)	0 (σ) ⊕ ±1 (π) ⊕ ±2 (δ)
3 (f)	0 (σ) ⊕ ±1 (π) ⊕ ±2 (δ) ⊕ ±3 (ϕ)

The benefit of this approach is that it allows to readily incorporate ligand-related orbitals and consider the *effective orbital overlap* between the metal- and ligand-centered orbitals. From the reference perspective of the central atom, this effective overlap can be evaluated if the metal-centered orbitals are appropriately rotated into each of the frames of the ligands, respectively, that are all positioned at specific distances and angular positions dependent on the coordination geometry. This approach is called the *angular overlap model* of ligand field theory and was majorly developed by Schäffer and Jørgensen [11], and later also Urland [12]. Recalling from eq. (3.4) that the atomic orbitals can be decomposed into a radial and angular part, we basically have to simply project the spherical harmonic functions $Y_\ell^m(\varphi, \theta)$ into the respective ligand frame. This can be achieved by the so-called *Wigner D rotation matrices* that rotate the spherical harmonics. We refer to our review for a detailed derivation [1] and restrict ourselves to this statement within this chapter. If we denote the bonding type with λ ($\lambda = \sigma$, π, δ, etc.), we can translate this task into a mathematical formula. Using again the demonstrative example of atomic orbitals (see eq. (3.4)), the ligand field matrix elements within the framework of the AOM read

$$\begin{aligned} \left\langle \psi_{n\ell m} | \hat{\mathcal{H}}_{\mathrm{LF}} | \psi_{n\ell m'} \right\rangle &= \sum_{j=0}^{N} \sum_{\lambda=0}^{\pm\ell} D_{m\lambda}^{(\ell)*}\left(\varphi_j, \theta_j\right) D_{\lambda m'}^{(\ell)}\left(\varphi_j, \theta_j\right) \left\langle n\ell\lambda | \hat{\mathcal{H}}_{\mathrm{LF}} | n\ell\lambda \right\rangle \\ &\equiv \sum_{j=0}^{N} \sum_{\lambda=0}^{\pm\ell} D_{\lambda m'}^{(\ell)}\left(\varphi_j, \theta_j\right) D_{\lambda m'}^{(\ell)}\left(\varphi_j, \theta_j\right) e_\lambda^j(\ell) \end{aligned} \tag{3.7}$$

where j denotes one of the N ligands at the angular positions (φ_L, θ_L). The $e_\lambda^j(\ell)$ are the so-called *angular overlap parameters* of the different metal–ligand bonds and depend on the type of bonding, amd the type of involved central atom orbitals. They also implicitly bear a distance dependence (due to the radial functions, see eq. (3.4)). It is important to realize that eq. (3.7) basically represents the same ligand field matrix elements as eq. (3.5) but only in a different parametrization scheme. This indicates a one-to-one connection between the Wybourne parameters and the angular overlap parameters. Like it was the case for the C_k^q in eq. (3.6), the Wigner D matrix elements are tabulated and can be analytically calculated depending on the explicit angular positions $\left(\varphi_j, \theta_j\right)$ and the values for ℓ, m, and λ. A crucial difference between eqs. (3.5) and (3.7) is, however, that the number of independent parameters $e_\lambda^j(\ell)$ solely depends on the desired bonding level irrespective of the symmetry of the coordination polyhedron! For example, if it is desirable to calculate the ligand field matrix elements for a set of six equidistant ligands of the same type surrounding a central atom and solely consider the σ- and π-type orbital overlap between the metal- and ligand-centered orbitals, the number of independent angular overlap parameters is three (one $e_\sigma^j(\ell)$, two $e_{\pi\pm}^j(\ell)$ parameters), irrespective of the symmetry if the coordination polyhedron is O_h or C_1. This would not be the case in a Wybourne parametrization scheme. While the Wybourne methodology focusses on the symmetry of the coordination polyhedron with the geometry merely naturally resulting out of that, the AOM approach focusses on the explicit geometrical/structural information of the coordination polyhedron with the symmetry naturally arising out of the arrangement of the different ligands around the central atom.

In the context of eq. (3.7), the parameters $e_\lambda^j(\ell)$ are interpreted as leading-order perturbative corrections to the free atomic states of the central atom, similar to the content of eq. (3.5). The true power of the AOM comes, however, from a chemically even more intuitive interpretation, which will be presented in the following section.

3.3.2 Interpretation of the angular overlap parameters in chemical context

Bethe's original crystal field approach is electrostatic, and thus, treats the metal–ligand bonds as purely ionic. Chemical bonds do, however, also have a covalent nature, which is dominated by the constructive orbital overlap and consequent delocalization of charge density. Intuitively, one would thus expect the ligand field strength to correlate with the metal–ligand orbital overlap integral S_{ML}. Since the atomic orbitals of the central atom/ion, $|\phi_{\mathrm{M}}\rangle$, should be described by a (not analytically known) radial part $R_{n\ell}(r)$ and an angular part $Y_{\ell m}(\vartheta, \theta)$ (see eq. (3.4)), a reasonable starting point is that the overlap integral is similarly factorizable into radial and angular parts:

$$S_{\mathrm{ML}}(r) = \langle\phi_{\mathrm{M}}|\phi_{\mathrm{L}}\rangle :\ = s_\lambda(r) \cdot f_\lambda(\vartheta, \varphi) \tag{3.8}$$

where λ again labels the different types of bonding. The ligand orbitals, $|\phi_\mathrm{L}\rangle$, do not necessarily have to be atomic orbitals but can be simply symmetry-adapted linearly combined molecular orbitals.

From a quantum-chemical perspective, a metal–ligand bond can be described in a molecular orbital picture. The wave function of the M–L moiety is then given by the following linear combination of (atomic) orbitals:

$$|\psi_\mathrm{ML}\rangle = c_\mathrm{M}|\phi_\mathrm{M}\rangle + c_\mathrm{L}|\phi_\mathrm{L}\rangle \tag{3.9}$$

where c_M and c_L are mixing coefficients with the normalization condition

$$|c_\mathrm{L}|^2 + |c_\mathrm{M}|^2 = 1 \tag{3.10}$$

The wave function of the M–L entity obeys the time-independent Schrödinger equation:

$$\hat{\mathcal{H}}|\psi_\mathrm{ML}\rangle = E|\psi_\mathrm{ML}\rangle \tag{3.11}$$

Insertion of eq. (3.4) into eq. (3.11) and action with $\langle\phi_j|$ ($j = \{\mathrm{L}, \mathrm{M}\}$) from the left transforms the Schrödinger equation to a coupled matrix equation of the form

$$\left(\mathcal{H} - E\mathrm{S}\right)c = 0 \tag{3.12}$$

where $\mathcal{H}$ is the Hamiltonian matrix, c is the coefficient vector containing the orbital contributions of the ligand and central atom/ion to the overall wave function, and S is the overlap matrix with diagonal entries of 1. The upper equation is solved for nonzero entries of c if the secular determinant vanishes:

$$\begin{vmatrix} \mathcal{H}_\mathrm{M} - E & \mathcal{H}_\mathrm{LM} - ES \\ \mathcal{H}_\mathrm{LM} - ES & \mathcal{H}_\mathrm{L} - E \end{vmatrix} = 0 \tag{3.13}$$

where $\mathcal{H}_\mathrm{M} = \langle\phi_\mathrm{M}|\hat{\mathcal{H}}|\phi_\mathrm{M}\rangle$ and $\mathcal{H}_\mathrm{L} = \langle\phi_\mathrm{L}|\hat{\mathcal{H}}|\phi_\mathrm{L}\rangle$ denote the energy eigenvalues of the free metal and ligand orbitals, respectively. $\mathcal{H}_\mathrm{LM} = \langle\phi_\mathrm{L}|\hat{\mathcal{H}}|\phi_\mathrm{M}\rangle = \mathcal{H}_\mathrm{ML} = \langle\phi_\mathrm{M}|\hat{\mathcal{H}}|\phi_\mathrm{L}\rangle$ denotes a nonspecified electronic coupling. Equation (3.13) can be solved for the energy eigenvalues and with a Taylor expansion of the respective root, the eigenvalues of the perturbed metal–ligand entity are given by

$$E_- \approx \mathcal{H}_\mathrm{L} - \frac{\mathcal{H}_\mathrm{LM}^2 - 2\mathcal{H}_\mathrm{LM}\mathcal{H}_\mathrm{L}S + \mathcal{H}_\mathrm{L}^2 S^2}{\mathcal{H}_\mathrm{M} - \mathcal{H}_\mathrm{L}} \tag{3.14}$$

and

$$E_{+} \approx \mathcal{H}_{\mathrm{M}} + \frac{\mathcal{H}_{\mathrm{LM}}^2 - 2\mathcal{H}_{\mathrm{LM}}\mathcal{H}_{\mathrm{M}}S + \mathcal{H}_{\mathrm{M}}^2 S^2}{\mathcal{H}_{\mathrm{M}} - \mathcal{H}_{\mathrm{L}}} \tag{3.15}$$

where it is implicitly assumed that $\mathcal{H}_{\mathrm{L}} < \mathcal{H}_{\mathrm{M}}$, which is reasonable as the ligands typically act as Lewis bases, and thus, have lower molecular orbital energies. Typically, $\mathcal{H}_{\mathrm{L}}$ differs much from $\mathcal{H}_{\mathrm{M}}$, that is, the metal–ligand bond is supposed to have an appreciable polar character. This allows to identify the right-hand terms of eqs. (3.14) and (3.15) as small perturbative corrections to the energies of the free orbitals of the central atom/ion and ligand due to the (covalent) bond formation. It should be noted that these conditions are very well fulfilled for lanthanoids with their shielded $4f$ orbitals that do not allow much orbital overlap and whose chemical bonds are typically regarded as almost purely ionic or nonbonding.

The next step is the specification of electronic coupling element $\mathcal{H}_{\mathrm{LM}}$. In the Wolfsberg–Helmholz approximation [13], it is assumed that this coupling can be related to the overlap integral S,

$$\mathcal{H}_{\mathrm{LM}} \approx k\frac{\mathcal{H}_{\mathrm{L}} + \mathcal{H}_{\mathrm{M}}}{2}S \tag{3.16}$$

where $k \sim 1.75–2$. This gives

$$E_{-} \approx \mathcal{H}_{\mathrm{L}} - \frac{\mathcal{H}_{\mathrm{M}}^2}{\mathcal{H}_{\mathrm{M}} - \mathcal{H}_{\mathrm{L}}}S^2 = \mathcal{H}_{\mathrm{L}} - \Delta\varepsilon \tag{3.17}$$

and

$$E_{+} \approx \mathcal{H}_{\mathrm{M}} + \frac{\mathcal{H}_{\mathrm{L}}^2}{\mathcal{H}_{\mathrm{M}} - \mathcal{H}_{\mathrm{L}}}S^2 = \mathcal{H}_{\mathrm{M}} + \Delta\varepsilon^{*} \tag{3.18}$$

In practice, the energy perturbation $\Delta\varepsilon^{*}$ to the central atom-based orbitals is of interest. If we now simply superimpose the contribution from each of the ligands, that is, the overall perturbation energy is simply the sum of the energies from each contributing M–L bond and uses the factorization of the overlap integral S into a radial and angular part (see eq. (3.8)), the total perturbative correction ΔE^{*} with antibonding character to the central atom-based orbital may be written as follows:

$$\begin{aligned}\Delta E^{*} &= \sum_{j=1}^{N}\Delta\varepsilon_j^{*} = \sum_{j=1}^{N}\sum_{\lambda=0}^{\pm\ell}\frac{\mathcal{H}_{\mathrm{L}}^2}{\mathcal{H}_{\mathrm{M}} - \mathcal{H}_{\mathrm{L}}}S_{j\lambda}^2 = \sum_{j=1}^{N}\sum_{\lambda=0}^{\pm\ell}\frac{\mathcal{H}_{\mathrm{L}}^2}{\mathcal{H}_{\mathrm{M}} - \mathcal{H}_{\mathrm{L}}}s_\lambda^2(r_j)f_\lambda^2\left(\varphi_j, \vartheta_j\right)\\ &\equiv \sum_{j=1}^{N}\sum_{\lambda=0}^{\pm\ell}e_\lambda(r_j)f_\lambda^2\left(\varphi_j, \vartheta_j\right)\end{aligned} \tag{3.19}$$

with $f_\lambda^2(\vartheta_j, \varphi_j)$ containing the angular information of the overlap between central atom/ion and ligand j. It is insightful to regard the previous section now: eq. (3.19) is in fact analogous to the expression of the AOM ligand field matrix elements in eq. (3.7). However, this derivation shows the power of the AOM: The AO parameters $e_\lambda(r_j)$ can be, in fact, interpreted as measures for the bond strength between the central atom/ion and ligands and are immediately connected to orbital overlap (see Figure 3.2). It should be noted that the AOM has not been developed to predict precise results but is rather to be understood as an effective theory aiming at semiquantitative results with strong chemical insight.

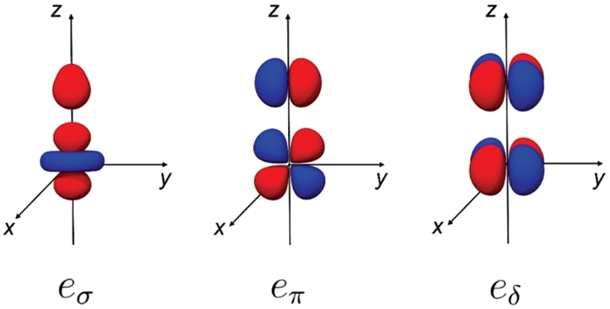

Figure 3.2: Pictorial representation of the interpretation of the angular overlap parameters in the context of orbital overlap and formation of a covalent metal–ligand bond.

It is also helpful to interpret the different impacts upon the AO parameters e_λ according to eq. (3.19). The main contribution comes from a necessary overlap between metal- and ligand-centered orbitals (encoded in the overlap contribution $S_{j\lambda}^2$). This factor also explains the order of the AO parameters dependent on the bonding type as σ-type bonding is connected to higher overlap integrals than π-type bonding. Thus, it is usually $e_\sigma > e_\pi \gg e_\delta \gg e_\phi$, and consequently, in most practical calculations, the δ- and ϕ-type contributions are even disregarded (although sometimes important such as in $[Cr(OAc)_2]_2 \cdot 2H_2O$ with OAc = acetate, O_2CCH_3).

The energy difference between metal- and ligand-centered orbitals, $\mathcal{H}_\mathrm{M} - \mathcal{H}_\mathrm{L}$, is also important: The more polar the M–L bond is, the smaller is e_λ. This demonstrates again that this interpretation of the AO parameters treats the degree of covalency as a perturbation to the otherwise ionic M–L bond in the context of the Wolfsberg–Helmholz approximation (see eq. (3.16)). Equation (3.19) also implies that the AO parameters should be implicitly dependent on the metal–ligand distance based on the radial part of the overall wave function. In fact, pressure-dependent experiments on coordination compounds showed that the distance dependence of the e_σ parameters for d orbitals roughly scales as R^{-5} [14], while an approximate R^{-7} dependence is found for these parameters for bonds involving f orbitals [15]. This allows to estimate AO parameters for a series of isotypic compounds given they are known for one representative of the compound class. In that regard, the AOM is an easily generalizable model.

3.3.3 Ligand field splitting in octahedral coordination compounds: the angular overlap model in action

3.3.3.1 Definition of σ donors, π donors, and π acceptors

In the interpretatory scheme of the Wolfsberg–Helmholz approximation, the AOM relates the splitting of orbitals in a ligand field with explicit bonding contributions from the surrounding ligands. This allows to intuitively access the well-known (empirical) spectrochemical series of ligands [16]. The spectrochemical series orders the ligands in terms of the induced size of the ligand field splitting in an octahedrally coordinated entity, given a specific reference central atom/ion. Ligands are typically considered Lewis bases donating electron pairs to the central atom/ion, thereby forming chemical bonds. This is incorporated in a positive parameter $e_\sigma(\ell)$: the larger e_σ for a given metal–ligand bond, the stronger a ligand acts as a Lewis base. Such a ligand is referred to as a *σ donor*. It should be noted that within the interpretation of e_σ as a measure for the overlap between metal- and ligand-centered orbitals (and thus a measure for covalency), the size of e_σ reflects the increase of metal-centered orbitals due to an increasingly antibonding character (see eq. (3.19)). Thus, strong σ donors expectedly give rise to a large ligand field splitting since they induce a more antibonding character of the metal-centered orbitals oriented along the M–L bond axis and shift them toward higher energies. In the case of an octahedrally coordinated central atom/ion with *d* orbitals, these would be the e_g-transforming states (see Figure 3.3).

The type of interacting orbitals is relevant for the size of the AO parameters: For spatially extended orbitals, e_σ is usually large (in the order of 10,000 cm^{-1} for *d* orbitals increasing from 3*d* over 4*d* to 5*d*), while it is comparably small for shielded orbitals like the *f* orbitals (order of 500 cm^{-1} for 4*f* orbitals to ~ 1,000 cm^{-1} for 5*f* orbitals). The stronger influence of the ligand field on the 5*f* orbitals compared to the 4*f* orbitals has also been experimentally confirmed [17]. It is interesting to realize that the perturbative definition of the AOM indicates that the e_σ parameters for *d* orbitals may already hint toward a limiting case of the validity regime of this theoretical framework. That depends, however, upon the relative size between e_σ and the energy separation between metal- and ligand-centered orbitals, $\mathcal{H}_\text{M} - \mathcal{H}_\text{L}$. If $e_\sigma \ll \mathcal{H}_\text{M} - \mathcal{H}_\text{L}$, the AOM offers a reasonable description. Especially the *f* elements fulfill this condition very well and thus are ideal candidates for which ligand field effects can be described accurately within the AOM.

It is noteworthy that the AOM description does in principle also allow the chemically rather unusual situation that ligands could act σ acids. These are usually additional neighboring metal ions in the second coordination sphere that can withdraw electron density from the central atom/ion of interest and thereby stabilize the antibonding metal-localized orbitals. The corresponding $e_\sigma(\ell)$ parameters are then negative. Such examples are known for the lipscombite/lazulite-type oxidophosphates $\text{MTi}_2\text{O}_2(\text{PO}_4)_2$ (M = Fe, Co, Ni)

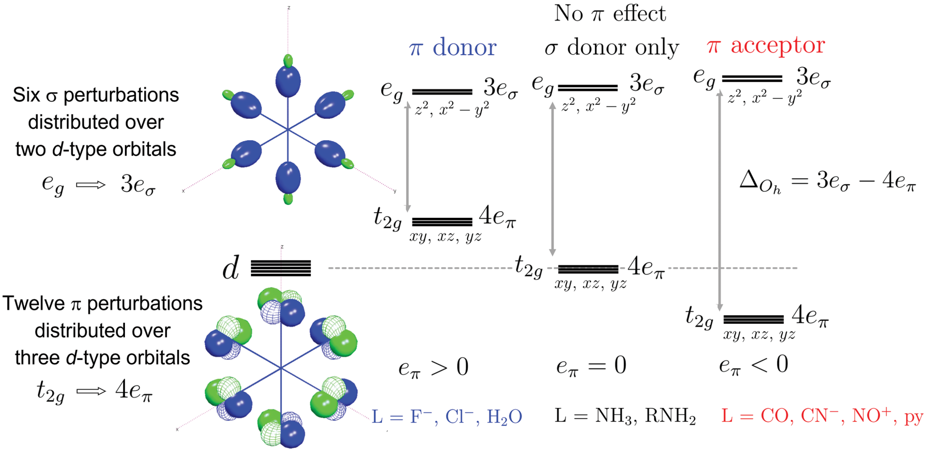
Six σ perturbations distributed over two d-type orbitals
$e_g \Longrightarrow 3e_\sigma$
Twelve π perturbations distributed over three d-type orbitals
$t_{2g} \Longrightarrow 4e_\pi$
d
π donor
No π effect
σ donor only
π acceptor
e_g $3e_\sigma$
z^2, x^2-y^2
t_{2g} $4e_\pi$
xy, xz, yz
$\Delta_{O_h} = 3e_\sigma - 4e_\pi$
$e_\pi > 0$
$e_\pi = 0$
$e_\pi < 0$
L = F⁻, Cl⁻, H₂O
L = NH₃, RNH₂
L = CO, CN⁻, NO⁺, py

Figure 3.3: Scheme of the origin and trends in the octahedral ligand field splitting within the AOM framework. The doubly degenerate e_g set is solely affected by the σ-type interactions, as is suggested on the left-hand side. The energy of the triply degenerate t_{2g} set is solely affected by π-type interacting ligand orbitals. Note that there are always two contributions from either p_x-like (meshed) or p_y-like (solid) ligand orbitals perpendicular to the respective bonding axis. The right-hand side indicates the dependence of the octahedral ligand field splitting of d orbitals on the type of bonding interaction of the approaching ligands that intuitively explains weak and strong field ligands encountered in the spectrochemical series (adapted from Putz et al. [18] © Springer International Publishing AG, p. 534).

with small M–Ti distances (~ 2.90 Å) [19], the green-emitting hexagonal perovskite-derived $CsMgBr_3$:Eu^{2+} with correspondingly small Eu–Mg distances (~ 3.25 Å) [20], and have also been recently anticipated for the red-emitting UCr_4C_4-type phosphor $Sr[Li_2Al_2O_2N_2]$:Eu^{2+} (SALON:Eu^{2+}) with small Eu–Sr distances (~ 3.18 Å) [21] within the so-called *vierer ring* channels containing the large Sr^{2+} and Eu^{2+} ions, respectively.

Most ligands also effectively interact via π bonding next to σ interaction perpendicular to the metal–ligand bond axis. This can occur in two ways. Ligands with more than one lone pair can have an additional donating electron density by a π interaction and act as so-called *π donors* or π bases. This is characterized by a positive value of $e_\pi(\ell)$. According to eq. (3.19), this means that such an interaction increases the energy of the metal-centered orbitals with π-type symmetry again inducing a more antibonding character of the otherwise nonbonding orbitals (see Figure 3.3). In the case of an octahedral coordination compound, these are the t_{2g}-transforming orbitals. Typical representatives of π donors are the halide anions with two additional π-type lone pairs. Qualitatively, one would expect an increasing π donating trend from the hard F^- to the soft I^- anion based on the effectively decreasing energy difference between metal- and halide-based atomic orbitals. This can be related to the decreasing electronegativity of the halide ions. The very electronegative F^- anion has a strong tendency to retain its localized $2p$ electrons, that is, it requires much energy to shift the electron density toward a metal cation. In contrast, the weakly electronegative I^- anion with its diffuse and spatially extended $5p$ valence orbitals can be easily polarized, and thus, the energy difference between metal- and I^--based orbitals is expectedly small. In contrast, the overlap integral s_π^F is expectedly larger than s_π^I because of the smaller metal–ligand distance. In total, it depends on the interplay between $\left(s_\pi^L\right)^2$ and $\mathcal{H}_\mathrm{M} - \mathcal{H}_\mathrm{L}$ (see eq. (3.19)) what precise value $e_\pi(\ell)$ will take.

Some molecular ligands internally also exhibit π bonds, and thus, have available π-symmetric lowest unoccupied molecular orbitals (LUMOs) at sufficiently low energies. Such ligands can act as *π acceptors* or *π acids* and accept electron density from the central atom/ion upon formation of a coordinative bond. Very prominent examples for this type of interaction are the isoelectronic molecules NO^+, CN^-, or CO. Removal of electron density from the metal atom/ion stabilizes the metal-centered orbitals (in the case of *d* orbitals, these are the t_{2g}-type orbitals; see Figure 3.3), and thus, makes them less antibonding. Correspondingly, this negative inductive effect and the π Lewis acidic character of ligands is encoded in a negative $e_\pi(\ell)$ value (i.e., the difference $\mathcal{H}_\mathrm{M} - \mathcal{H}_\mathrm{L}$ becomes actually negative because of the higher energetic unoccupied π-symmetric MOs of the ligands). In chemical textbooks and literature, this situation is usually referred to as *π backbonding*. Ligands with this property bind particularly strongly to a metal atom/ion. The withdrawal of electron density from the metal ion should in turn destabilize the internal molecular bond within the ligands because they interact via their usually slightly antibonding LUMOs, and additional electron density also leads to higher repulsion. This is in fact evidenced by vibrational spectroscopy in carbonyl complexes of transition metal ions. The strong π acidic character of CO leads to a weakening of the internal carbon–oxygen bond, and the characteristic C–O stretching vibration shifts to lower energies compared to that in free CO.

3.3.3.2 Ligand field splitting of *d* and *f* orbitals in the Wybourne and AOM parametrization scheme

As indicated in Section 3.1, the equivalence of the crystal/ligand field matrix elements within the Wybourne or AOM parametrization scheme should allow to describe common coordination situations in both pictures and unambiguously translate in between them. In this chapter, we will focus on the most commonly known example of an octahedral coordination geometry within a homoleptic complex, that is, the six ligands are assumed to be identical. In the case of *d* orbitals, group theory then dictates the well-known result that these orbitals transform like the irreducible representations t_{2g} and e_g in a coordination geometry with octahedral symmetry. Within the framework of the Wybourne parametrization, the splitting between the two sets of orbitals is parameterized by the parameter B_0^4 or, more commonly, $10Dq = (10/21)B_0^4$. In the context of AOM, this splitting can be expressed in terms of parameters $e_\lambda(d)$. In general, it is necessary to set up the angular overlap matrix composed by the Wigner matrices according to eq. (3.7), identify the angular positions of each of the ligands, and finally establish the effective contribution of each ligand to a specific type of binding mode between metal and ligand. In the case of coordination geometries with high symmetry such as an octahedron, this can often be, however, visualized more intuitively.[5] We will thus demonstrate the latter approach to explain the principle.

A σ-type interaction is only possible along the M–L bond axis. Thus, only the two e_g-transforming orbitals can participate in this type of interaction. Since there are six ligands approaching the central atom/ion in an octahedral geometry interacting with two *d* orbitals, the overall energy increase of the e_g-transforming orbitals in the ligand field compared to the free central atom/ion is $(6/2)e_\sigma(d) = 3e_\sigma(d)$. The three t_{2g}-transforming orbitals interact with six ligands each being able to interact via two π binding modes (each perpendicular to the M–L axis). This gives a total ligand-induced energy increase of $((6 \cdot 2)/3)e_\pi(d) = 4e_\pi(d)$. The ligand field splitting of $10Dq$ *d* orbitals is then given by

$$\Delta_{O_h} = 10Dq = \frac{10}{21}B_0^4 = 3e_\sigma(d) - 4e_\pi(d) \tag{3.20}$$

up to π bonding level. Usually, it is $e_\sigma(d) > |e_\pi(d)|$. An additionally possible δ interaction can also be incorporated but is comparably much weaker and only present for very special ligands. Therefore, it is usually a very good approximation to neglect these contributions. Equation (3.20) therefore represents the translation scheme between the Wybourne and AOM description of the ligand field splitting in an octahedral coordination geometry.

Equation (3.20) allows to understand the previous influences of σ donors, π donors, or π acceptors straightforwardly (see Figure 3.3). σ donors increase the ligand field splitting because of the energy gain of the e_g-transforming orbitals by means of the positive parameter $e_\sigma(d)$. π donors are characterized by a positive $e_\pi(d)$ value, and thus, effectively decrease the ligand field splitting according to eq. (3.20). π acceptors in turn are characterized by negative $e_\pi(d)$ values (see Section 3.3.1), and thus, lead to an increase of the ligand field splitting in the case of *d* elements. By inspection of eq. (3.20), the spectrochemical series of ligands for a given central atom/ion can therefore be readily explained. Weak ligands such as I^- are good π donors and weak σ donors. Intermediate ligands such as H_2O or NH_3 are usually considered pure σ donors with very weak (H_2O) or without (NH_3) any π donating effects. The strongest ligands are those that are both good σ donors and π acceptors such as CN^- or CO. A rigorous treatment shows that also other established relations of the ligand field splitting in different geometries for a given type of central atom/ion and ligands hold within the AOM framework [22], that is, for a tetrahedral complex, one finds $\Delta_{T_d} = -4/9\Delta_{O_h}$ both in the Wybourne and AOM parametrization scheme up to π bonding level.

---

[5] This works so well because an octahedral coordination compound is *orthoaxial*: The ligands only approach along the three reference axes. This is a somewhat special case. In most common coordination geometries, an explicit calculation of the Wigner *D* matrix elements is unavoidable.

An analogously simple treatment of the ligand field splitting of *f* orbitals in an octahedral coordination geometry is not as intuitive anymore. This is already evident from their dictated splitting pattern according to group theory that states that *f* orbitals transform like the irreducible representations a_{2u}, t_{1u}, and t_{2u} in an octahedral ligand field (see Figure 3.4). In the Wybourne parametrization scheme, the two energy differences are described by the two parameters B_0^4 and B_0^6 [23, 24]. An explicit calculation with eq. (3.7) leads to the relations [12, 25]

$$\begin{aligned} E(t_{2u}) - E(a_{2u}) &= \frac{10}{33}B_0^4 - \frac{140}{143}B_0^6 = \frac{5}{2}e_\pi(f) \\ E(t_{1u}) - E(a_{2u}) &= \frac{6}{11}B_0^4 - \frac{140}{429}B_0^6 = 2e_\sigma(f) + \frac{3}{2}e_\pi(f) \end{aligned} \tag{3.21}$$

with the singly degenerate a_{2u}-transforming orbital (f_{xyz}) that is predicted to be nonbonding at least up to the π bonding mode within the AOM. The $e_\sigma(f)$ contribution to the second splitting derives from the fact that the triply degenerate t_{1u}-transforming *f* orbitals (f_{x^3}, f_{y^3}, f_{z^3}) are oriented along the three coordinate axes, respectively. With six approaching ligands interacting via a σ-type interaction, the overall energy increase is $(6/3)e_\sigma(f) = 2e_\sigma(f)$. The $e_\pi(f)$ contributions are, however, not as evident, acting in both the t_{1u} and t_{2u} sets. They cannot be obtained by symmetry-based shortcuts and have to be derived explicitly from evaluation of eq. (3.7). This is a consequence of the specific form and spatial orientation of the *f* orbitals.

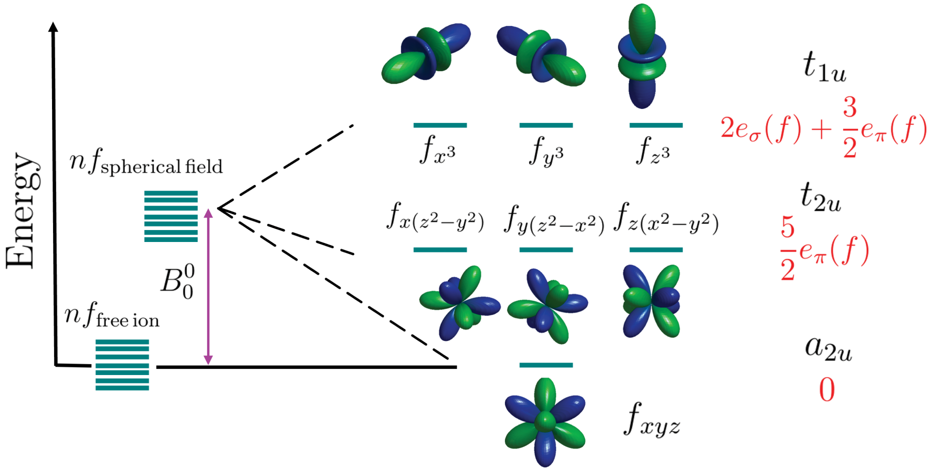

Figure 3.4: Scheme of the ligand field splitting of *f* orbitals in octahedral [ML$_6$] complexes and the relative energies within the AOM (published by Elsevier B.V under the Creative Commons Attribution License 4.0) [1].

3.4 The angular overlap model in action – applications in magnetism and optical spectroscopy

3.4.1 Quenching of paramagnetism of lanthanoid ions due to the ligand field – case study of Pr^{3+}

Lanthanoid ions with their partially filled 4*f* valence shell are generally known to give rise to large magnetic moments that exceed the usually encountered spin-only moments of the transition metal ions. This physical property also explains some of the typical application areas of the trivalent lanthanoid ions. Nd^{3+} ($4f^3$) has a room-temperature magnetic moment of $3.62\mu_B$ with μ_B as Bohr's magneton ($\mu_B = 9.274 \times 10^{-24}$ JT^{-1}) and is used in modern wind turbines or in the Nd–Fe–B alloys in permanent magnets. Gd^{3+} with its $4f^7$-related $^8S_{7/2}$ ground level has a room-temperature magnetic moment of $7.94\mu_B$ and is a common contrast agent for magnetic resonance imaging. Dy^{3+} ($4f^9$) and Ho^{3+} ($4f^{10}$) have room-temperature magnetic moments of $10.64\mu_B$ (Dy^{3+}) and $10.61\mu_B$ (Ho^{3+}) and have become prominent in single-molecule magnets for information storage [26].

Due to the shielded nature of the 4*f* orbitals, the ligand field splitting of the resulting spin–orbit ground levels is usually rather small, in the order of around 100 cm^{-1}. This is in the order of thermal energies ($k_BT \sim 215$ cm^{-1} at $T = 300$ K). Thus, at room temperature, there is thermalization among the different ligand field states of a spin–orbit multiplet $^{2S+1}L_J$ and the magnetic moment reaches the expected value

$$\mu = \mu_B g_J \sqrt{J(J+1)} \tag{3.22}$$

where g_J is Landé's *g* factor:

$$g_J = \frac{3}{2} + \frac{S(S+1) - L(L+1)}{2J(J+1)} \tag{3.23}$$

This situation changes at low temperatures since then thermal energy is too low to ensure a thermal Boltzmann equilibrium among the different ligand field levels. The size of the magnetic moment will then depend on the fact if a resulting ligand field state has a well-defined nonzero projection of the total angular momentum. Thus, the magnetic moment of many lanthanoid ions is usually strongly temperature dependent. It becomes evident that the ligand field strength has a crucial impact on this temperature dependence. An illustrative example in that regard is Pr^{3+}, which will be discussed further.

Pr^{3+} ($4f^2$) has a $^3H_4$ spin–orbit ground level according to Hund's rules and should be characterized by a magnetic moment of around $3.58\mu_B$. This value is also typically observed at room temperature. However, upon cooling the cubic fluoridoelpasolites

Cs_2APrF_6 (A = K, Rb), a gradual decrease of the magnetic moment down to a temperature-independent paramagnetic threshold of around $0.40\mu_B$ at 4 K was observed [27]. In these compounds, Pr^{3+} is octahedrally coordinated by six F^- ligands. A similar behavior was already reported in the pioneering work by Penney and Schlapp on $Pr_2(SO_4)_3{\cdot}8H_2O$ [28]. Since the 4f orbitals are very shielded and the mutual Pr–Pr distances within these elpasolites are in the order of around 7 Å [27], collective antiferromagnetic interactions can be excluded as an underlying reason. In fact, this observation is a consequence of the splitting of the $^3H_4$ level in an octahedral ligand field (see Figure 3.5). According to group theory, the originally (2•4 + 1) = 9-fold degenerate $^3H_4$ level (according to the different values for $M_J = -4, \ldots, +4$) splits into ligand field states that transform like $A_{1g} \oplus E_g \oplus T_{1g} \oplus T_{2g}$. In a spherically symmetric ion, the different degenerate eigenstates can be distinguished by the different values of M_J meaning that the projection of the total angular momentum, $\hat{J}_z$, commutes with the free-ion Hamiltonian. In that case, the energy eigenstates can also be described by the quantum numbers of the total angular momentum, which are defined sharply.

This situation changes in an octahedral ligand field (and generally any ligand field Hamiltonian) since the spherical symmetry is broken then, and the components of the angular momentum are no longer conserved quantities. A ligand field calculation shows that the energetic order of the arising states from the $^3H_4$ ground multiplet is A_{1g}, T_{1g}, E_g, T_{2g}. This energetic order allows to understand the observed temperature dependence of the magnetic moment and is most easily approached from a symmetry perspective. In O_h symmetry, the three components of the orbital angular momentum transform as the irreducible representation T_{1g}. The magnetic moment is proportional to this orbital angular momentum. Thus, a magnetic contribution of a pure state transforming with a generalized irreducible representation Γ is expected if the respective transition matrix element does not vanish, which is the case if the direct product $\Gamma \otimes \Gamma\left(L_j\right) \otimes \Gamma$ contains the totally symmetric irreducible representation of the group (i.e., the same representation as the Hamiltonian). For the example of the $^3H_4$ multiplet, this is only the case for the T_{1g}- and T_{2g}-transforming crystal field states. Thus, one would also formally expect a vanishing orbital magnetic moment for the lowest energetic A_{1g} crystal field component from a symmetry analysis. This is usually referred to as *orbital angular momentum quenching* by the ligand field and is particularly prominent in d elements. Van Vleck derived, however, that such nonmagnetic states can acquire a nonvanishing orbital magnetic moment upon mixing with a higher excited magnetic state by the presence of an external magnetic field. This is a second-order perturbation effect and is called *van Vleck paramagnetism* [6, 29]. As a perturbative effect, the magnetic moment will depend on the energy difference ΔE between the nonmagnetic and magnetic states as ΔE^{-1}, that is, the lower the energy difference, the higher the magnetically induced mixing. The corresponding direct product $\Gamma \otimes \Gamma\left(L_j\right) \otimes \Gamma$ will then contain the totally symmetric irreducible representation of the respective point group, and thus, the states with representation Γ have a nonzero contribution to the orbital magnetic moment.

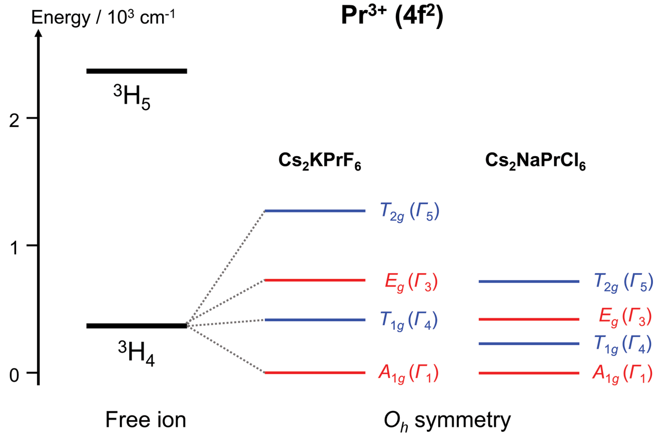

Figure 3.5: Splitting of the lowest $^3H_4$ spin–orbit multiplet of Pr^{3+} in an octahedral ligand field. The differences in ligand field strength are demonstrated for the explicit cases of Cs_2KPrF_6 ($[PrF_6]^{3-}$ octahedra) and $Cs_2NaPrCl_6$ ($[PrCl_6]^{3-}$ octahedra). Nonmagnetic ligand field states are depicted in red color, and ligand field states with magnetic contribution in blue color. The irreducible representations are given both in Mulliken–Herzberg and Bethe notation.

In Cs_2KPrF_6, the energy separation between the nonmagnetic A_{1g} and adjacent magnetic T_{1g} states was experimentally found to be around 400 cm^{-1} [27, 30], which is sufficiently low to yet induce a small temperature-independent paramagnetism at low temperatures. In the chloride $Cs_2NaPrCl_6$, the respective ligand field-induced splitting between the A_{1g} and T_{1g} state is only 236–241 cm^{-1} [30, 31]. Expectedly, this should result in a slightly higher effective temperature-independent magnetic moment of $0.56\mu_B$ at low temperatures in the chloride (compared to $0.40\mu_B$ in Cs_2KPrF_6) since the lower splitting enables more effective mixing of the two states [23]. Moreover, the onset of the inverse susceptibility toward conventional Curie behavior lies at around 130 K for Cs_2KPrF_6 [27], while it already sets in at around 78 K for $Cs_2NaPrCl_6$ [23] (see also Figure 3.6). Within the context of ligand field theory, this is also intuitive. A chloride ligand is softer and has a weaker σ-donating nature than a fluoride ligand. Consequently, the ligand field splitting of any spin–orbit multiplet of the lanthanoid ions is expectedly smaller in a more covalent chloride. This led to the formulation of a so-called magnetochemical series of ligands, in analogy to the well-known spectrochemical series [32].

3.4.2 Modeling of subtle ligand field effects on the optical spectra of Sm^{3+} and Eu^{3+} in inorganic compounds with the AOM

Lanthanoid ions are particularly prominent for their bright photoluminescence and colorful compounds. Most of the trivalent but also several divalent lanthanoid ions show intraconfigurational $4f^N$–$4f^N$ ($N = 1, \ldots, 13$) transitions in the UV, visible, and

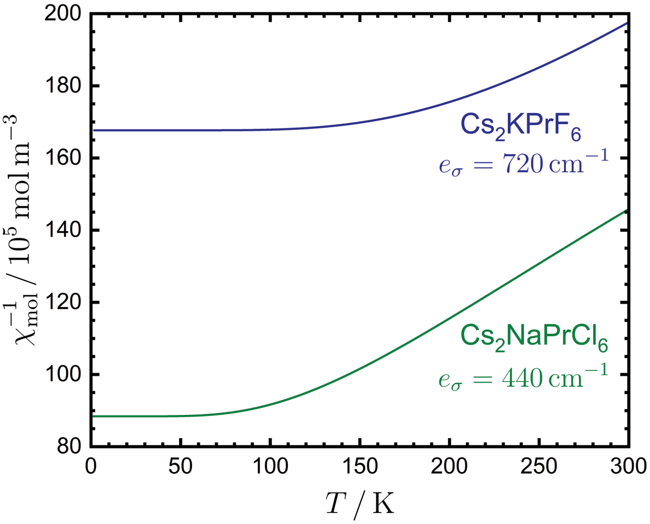

Figure 3.6: Simulated temperature evolution of the inverse molar magnetic susceptibilities of the cubic elpasolite-type crystallizing halides Cs_2KPrF_6 (blue) and $Cs_2NaPrCl_6$ (green). The dominant angular overlap parameters e_σ are also given [27, 30]. Note the differences in magnitude of the temperature-independent (inverse) susceptibilities and the different onset temperatures to the conventional Curie behavior ($\chi_{\mathrm{mol}}^{-1} \propto T$).

NIR range that are characteristically narrow and are typically considered independent from the host material the lanthanide ions are embedded into based on the shielded character of 4*f* orbitals by the outer 5*s* and 5*p* electrons of the [Xe] core configuration of the lanthanoid ions. The $4f^N$– $4f^N$ transitions also show characteristic splitting patterns that often contain delicate information about the local structure and ligand field around the lanthanide ions. This fact is particularly often exploited in the case of Eu^{3+} ($4f^6$), given the single degeneracy of both its lowest ground level $^7F_0$ and the lowest excited level $^5D_0$ [33, 34], which simplifies symmetry analyses enormously. As such, Eu^{3+} has often been used as a local optical symmetry probe, for example, for compounds with limited or lacking long-range order such as glasses [35].

As already indicated in Section 2.2, the large size of the early lanthanoids (La–Gd) usually induces the crystallization of thermodynamically stable compounds that crystallize in low symmetric structures for the sake of higher coordination numbers around the lanthanoid ions. For these cases, the Wybourne parametrization scheme was almost exclusively used due to the straightforward technical implementation [8, 33]. Besides the pioneering works by Urland in the case of UCl_3-type $LaCl_3$ [36], or (anti-)scheelite-type $LiYF_4$ [37], it has been recently successfully demonstrated by Glaum et al. with the computer program *BonnMag* [38] that it is possible to account for the splitting of the different electronic spin–orbit levels of Eu^{3+} [39, 40] and Sm^{3+} [41] in any ligand field very accurately by means of the AOM (see Figure 3.7).

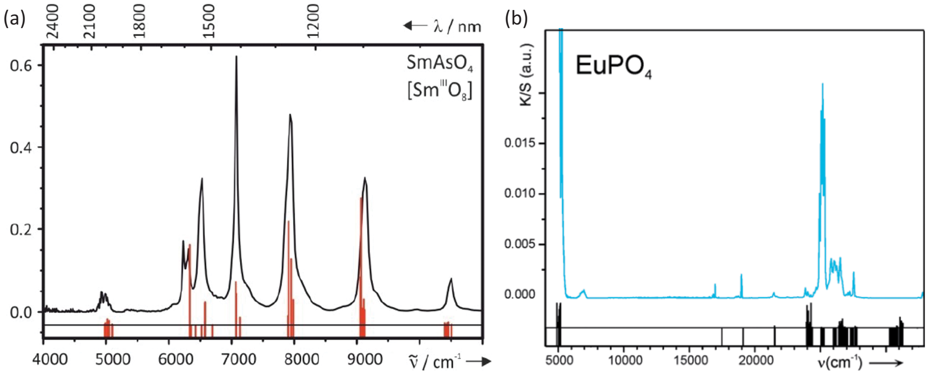

Figure 3.7: Experimental Kubelka–Munk spectra (obtained from diffuse reflectance on powders) and AOM simulations (bars) of $SmAsO_4$ (a) (*European Journal of Inorganic Chemistry* published by Wiley-VCH GmbH under the Creative Commons Attribution Non-Commercial License 4.0) and $EuPO_4$ (b) (published by Wiley-VCH Verlag GmbH & Co. KGaA under the Creative Commons Attribution Non-Commercial License 4.0) [39–41]. The line strengths were modeled by means of the Judd–Ofelt intensity theory for $4f^N \leftrightarrow 4f^N$ transitions.

The huge advantage of this approach is that the experimentally accessible crystallographic structure input based on single-crystal X-ray diffraction can be exploited for that. By that methodology, even two crystallographically very similar but inequivalent sites can be distinguished with an independent comparison between optical absorption and theoretically covered assignment of the different Stark states from a given spin–orbit level [40]. It is important to note that while the AOM and programs like *BonnMag* can independently predict the splitting pattern and the corresponding energies, intensities of the transitions are covered by the Judd–Ofelt theory for $4f^N – 4\,f^N$ transitions and are not an explicit part of the AOM [42].

An interesting recently demonstrated implication was a linear correlation between the AOM parameter e_σ and the optical basicity of ligands in the case of Eu(III) phosphates [40]. Optical basicity is a concept that was originally introduced for luminescent s^2 ions (e.g., Sn^{2+}, Pb^{2+}, or Bi^{3+}) [43] and also later transition metals [44] to quantify the influence of the surrounding host matrix in a chemically intuitive way. It is a relative measure of the Lewis basicity of the surrounding ligands of a luminescent ion taking CaO as an (idealized ionic) reference with $\Lambda = 1.0$, and thus, serves as an indicator for the covalency of the metal–ligand bond. It was shown by Duffy that it scales linearly with the reciprocal of the ligand polarizability, that is, the higher the optical basicity, the more polarizable a ligand should be, which agrees with the Lewis acidity/basicity concept [45]. The very sensitive distance dependence of $e_\sigma(f)$ ($\sim R^{-7}$) makes it intuitively clear that subtle changes in the surrounding ligand field can induce notable changes in the size of the parameters, and thus, also chemical bonding situation offers a new direction in the assessment of covalency by means of optical measurements of optical spectra. Also the Ω_2 Judd–Ofelt parameter for lanthanides is known to be related to the covalence of a lanthanide–ligand bond [46]. A correlation between the e_σ parameter and Ω_2 is also expected, which can be tested by, for example, the selection of hypersensitive luminescent transitions. This hypothesis still needs to be verified although there are already indications for its validity [40].

3.4.3 Perspective on ab initio ligand field theory – towards a prediction of AOM parameters?

Despite its long history as a semiempirical model, the continuous improvement of computational facilities and performance has recently motivated developing ab initio ligand field theory with the ultimate desire to predict the ligand field strength and energy splittings of electronic states of transition metal and lanthanoid complexes independently from experiment. The chemically intuitive interpretation of the AOM parameters offers a way to put these ab initio approaches to ligand field theory to a test and to immediately compare experimental values obtained from either optical or magnetic data. This has been recently developed by Atanasov and coworkers for the cubic lanthanoid and actinoid chloridoelpasolites $Cs_2NaLnCl_6$ (Ln = Ce–Yb) [47] and $Cs_2NaAnCl_6$ (An = Pa–No) [48] but also for cases such as hexahalidochromates(III), $[CrX_6]^{3-}$ (X = F, Cl, Br, I) [49], emerald ($Be_3Al_2[SiO_3]_6:Cr^{3+}$) [50], or also the tetrahalidocobaltates(II) $[CoX_4]^{2-}$ in the recent works of the Krewald group [51]. The electronic structure within the ab initio ligand field theory approach is usually treated on an advanced spin–orbit complete active space self-consistent field and second-order *N*-electron valence state perturbation theory level (i.e., a wave function-based approach), which allows to derive the otherwise experimentally accessible ligand field parameters from theory itself [52]. These can be directly compared with the derived ligand field parameters from experimental data. Ab initio ligand field theory is currently implemented in the ORCA quantum chemistry package and constantly improved [53]. The future development in this direction will become exciting.

References

[1] M. Suta, F. Cimpoesu, W. Urland, The angular overlap model of ligand field theory for f elements: An intuitive approach building bridges between theory and experiment, Coord. Chem. Rev. 441 (2021) 213981. https://doi.org/10.1016/j.ccr.2021.213981.

[2] R. Pöttgen, T. Jüstel, C.A. Strassert, Rare Earth Chemistry, De Gruyter (2020).

[3] T. Cheisson, E.J. Schelter, Rare earth elements: Mendeleev's bane, modern marvels, Science 363 (2019) 489–493. https://doi.org/10.1126/science.aau7628.

[4] a) J.T. Keltjens, A. Pol, J. Reimann, H.J.M. Op den Camp, PQQ-dependent methanol dehydrogenases: Rare-earth elements make a difference, Appl. Microbiol. Biotechnol. 98 (2014) 6163–6183. https://doi.org/10.1007/s00253-014-5766-8 b) J.A. Cotruvo, E.R. Featherston, J.A. Mattocks, J.V. Ho, T.N. Laremore, Lanmodulin: A highly selective lanthanide-binding protein from a lanthanide-utilizing bacterium, J. Am. Chem. Soc. 140 (2018) 15056–15061. https://doi.org/10.1021/jacs.8b09842;

c) L.J. Daumann, Essential and ubiquitous: The emergence of lanthanide metallobiochemistry, Angew. Chem. Int. Ed. 58 (2019) 12795–12802. https://doi.org/10.1002/anie.201904090;
d) L.J. Daumann, A natural lanthanide-binding protein facilitates separation and recovery of rare earth elements, ACS Cent. Sci. 7 (2021) 1780–1782. https://doi.org/10.1021/acscentsci.1c01247.

[5] H. Bethe, Termaufspaltung in Kristallen, Ann. Phys. 395 (1929) 133–208. https://doi.org/10.1002/andp.19293950202.

[6] J.H. van Vleck, The Theory of Electric and Magnetic Susceptibilities, Oxford University Press, New York (1932).

[7] E. Noether, Invariante Variationsprobleme, Nachr. D. König. Gesellsch. D. Wiss. Gött., Math-phys. Klasse (1918) 235–257.

[8] B.G. Wybourne, Spectroscopic Properties of Rare Earths, Jon Wiley & Sons, New York, (1965).

[9] W. Kaiser, C.G.B. Garrett, Two-photon excitation in CaF_2: Eu^{2+}, Phys. Rev. Lett. 7 (1961) 229–231. https://doi.org/10.1103/PhysRevLett.7.229.

[10] N. Kunkel, H. Kohlmann, A. Sayede, M. Springborg, Alkaline-earth metal hydrides as novel host lattices for Eu^{II} luminescence, Inorg. Chem. 50 (2011) 5873–5875. https://doi.org/10.1021/ic200801x.

[11] a) C.K. Jørgensen, R. Pappalardo, H.-H. Schmidtke, Do the "Ligand Field" parameters in lanthanides represent weak covalent bonding? J. Chem. Phys. 39 (1963) 1422–1430. https://doi.org/10.1063/1.1734458; b) C.E. Schäffer, C.K. Jørgensen, The angular overlap model, an attempt to revive the ligand field approaches, Mol. Phys. 9 (1965) 401–412. https://doi.org/10.1080/00268976500100551.

[12] W. Urland, On the ligand-field potential for f electrons in the angular overlap model, Chem. Phys. 14 (1976) 393–401. https://doi.org/10.1016/0301-0104(76)80136-X.

[13] M. Wolfsberg, L. Helmholz, The spectra and electronic structure of the tetrahedral ions $MnO4^-$ $CrO4^-$ and $ClO4^-$, J. Chem. Phys. 20 (1952) 837–843. https://doi.org/10.1063/1.1700580.

[14] a) J.D. Axe, G. Burns, Influence of covalency upon rare-earth ligand field splittings, Phys. Rev. 152 (1966) 331–340. https://doi.org/10.1103/PhysRev.152.331; b) G. Burns, J.D. Axe, Pressure dependence of ligand field splittings (10*Dq*), J. Chem. Phys. 45 (1966) 4362–4363. https://doi.org/10.1063/1.1727505; c) M. Bermejo, L. Pueyo, On the R_{ML} dependence of 10*Dq*, J. Chem. Phys. 78 (1983) 854–857. https://doi.org/10.1063/1.444786.

[15] W. Urland, The assessment of the crystal field parameters for f^n-electron systems by the angular overlap model. Rare-earth ions in $CaWO_4$, Chem. Phys. 38 (1979) 407–412. https://doi.org/10.1016/0301-0104(79)89013-8.

[16] a) R. Tsuchida, Absorption spectra of co-ordination compounds. I, Bull. Chem. Soc. Jpn. 13 (1938) 388–400. https://doi.org/10.1246/bcsj.13.388; b) R. Tsuchida, Absorption spectra of co-ordination compounds. II, Bull. Chem. Soc. Jpn. 13 (1938) 436–450. https://doi.org/10.1246/bcsj.13.436;
c) R. Tsuchida, M. Kobayashi, Absorption spectra of co-ordination compounds. III. Special bands of chromium complexes, Bull. Chem. Soc. Jpn. 13 (1938) 471–480. https://doi.org/10.1246/bcsj.13.471;
d) K. Hisao, R. Tsuchida, Absorption spectra of co-ordination compounds. IV. Ethylenediamine cobaltic complexes, Bull. Chem. Soc. Jpn. 15 (1940) 427–439. https://doi.org/10.1246/bcsj.15.427.

[17] a) J.M. Sperling, E.J. Warzecha, C. Celis-Barros, D.-C. Sergentu, X. Wang, B.E. Klamm, C.J. Windorff, A.N. Gaiser, F.D. White, D.A. Beery et al., Compression of curium pyrrolidine-dithiocarbamate enhances covalency, Nature 583 (2020) 396–399. https://doi.org/10.1038/s41586-020-2479-2;
b) J.M. Sperling, E. Warzecha, C.J. Windorff, B.E. Klamm, A.N. Gaiser, M.A. Whitefoot, F.D. White, T.N. Poe, T.E. Albrecht-Schönzart, Pressure-induced spectroscopic changes in a californium 1D material are twice as large as found in the holmium analog, Inorg. Chem. 59 (2020) 10794–10801. https://doi.org/10.1021/acs.inorgchem.0c01290.

[18] M.V. Putz, F. Cimpoesu, M. Ferbinteanu, Structural Chemistry – Principles, Methods, and Case Studies, Springer International Publishing AG, Cham, Switzerland (2018), p. 534.

[19] M. Schöneborn, R. Glaum, Crystal growth, single-crystal structure refinement and unusual ligand-field splittings of lazulite-type oxidephosphates $MTi_2O_2(PO_4)_2$ (M = FeII, CoII, NiII), Z. Anorg. Allg. Chem. 633 (2007) 2568–2578. https://doi.org/10.1002/zaac.200700293.

[20] H. Ramanantoanina, F. Cimpoesu, C. Göttel, M. Sahnoun, B. Herden, M. Suta, C. Wickleder, W. Urland, C. Daul, Prospecting lighting applications with ligand field tools and density functional theory: A first-principles account of the $4f^7$-$4f^6$5d luminescence of $CsMgBr_3$:Eu_{2+}, Inorg. Chem. 54 (2015) 8319–8326. https://doi.org/10.1021/acs.inorgchem.5b00988.

[21] a) G.J. Hoerder, M. Seibald, D. Baumann, T. Schröder, S. Peschke, P.C. Schmid, T. Tyborski, P. Pust, I. Stoll, M. Bergler et al., $Sr[Li_2Al_2O_2N_2]$:Eu^{2+}-A high performance red phosphor to brighten the future, Nat. Commun. 10 (2019) 1824. https://doi.org/10.1038/s41467-019-09632-w; b) J. Bouquiaux, S. Poncé, Y. Jia, A. Miglio, M. Mikami, X. Gonze, Importance of long-range channel Sr displacements for the narrow emission in $Sr[Li_2Al_2O_2N_2]$:Eu^{2+} phosphor, Adv. Opt. Mater. 9 (2021) 2100649. https://doi.org/10.1002/adom.202100649.

[22] H.-H. Schmidtke, Die Relationen zwischen den kubischen Ligandenfeldparametern und ihre Ableitung auf gruppentheoretischer Grundlage, Z. Naturforsch. A 19 (1964) 1502–1510. https://doi.org/10.1515/zna-1964-1312.

[23] H. Lueken, Magnetochemie, Vieweg & Teubner, Stuttgart, Leipzig (1999).

[24] B.N. Figgis, M.A. Hitchman, Ligand Field Theory and Its Applications, Wiley-VCH, New York (2000).

[25] M. Atanasov, C. Daul, H.U. Güdel, T.A. Wesolowski, M. Zbiri, Ground states, excited states, and metal-ligand bonding in rare earth hexachloro complexes: A DFT-based ligand field study, Inorg. Chem. 44 (2005) 2954–2963. https://doi.org/10.1021/ic040105t.

[26] a) F.-S. Guo, B.M. Day, Y.-C. Chen, M.-L. Tong, A. Mansikkamäki, R.A. Layfield, A dysprosium metallocene single-molecule magnet functioning at the axial limit, Angew. Chem. Int. Ed. 56 (2017) 11445–11449. https://doi.org/10.1002/anie.201705426; b) C.A.P. Goodwin, F. Ortu, D. Reta, N.F. Chilton, D.P. Mills, Molecular magnetic hysteresis at 60 kelvin in dysprosocenium, Nature 548 (2017) 439–442. https://doi.org/10.1038/nature23447; c) Y.-C. Chen, J.-L. Liu, W. Wernsdorfer, D. Liu, L.F. Chibotaru, X.-M. Chen, M.-L. Tong, Angew. Chem. Int. Ed. 56 (2017) 4996.

[27] W. Urland, K. Feldner, R. Hoppe, Über das magnetische Verhalten von Cs_2KPrF_6 und Cs_2RbPrF_6, Z. Anorg. Allg. Chem. 465 (1980) 7–14. https://doi.org/10.1002/zaac.19804650102.

[28] W.G. Penney, R. Schlapp, The influence of crystalline fields on the susceptibilities of salts of paramagnetic ions. I. The rare earths, especially Pr and Nd, Phys. Rev. 41 (1932) 194–207. https://doi.org/10.1103/PhysRev.41.194.

[29] J.H. Van Vleck, On dielectric constants and magnetic susceptibilities in the new quantum mechanics Part III - Application to dia- and paramagnetism, Phys. Rev. 31 (1928) 587–613. https://doi.org/10.1103/PhysRev.31.587.

[30] H.-D. Amberger, Zur Elektronenstruktur hochsymmetrischer Verbindungen der f-Elemente XI (1) elektronisches Raman-Spektrum und Kristallfeld-Aufspaltungsmuster der Grundmannigfaltigkeit $3H_4$ von $Cs_2KPr^{III}F_6$, Inorg. Nucl. Chem. Lett. 14 (1978) 491–495. https://doi.org/10.1016/0020-1650(78)80020-8.

[31] H.-D. Amberger, Zur Elektronenstruktur hochsymmetrischer Verbindungen der Lanthanoiden und Actinoiden. X [1]. Das Kristallfeld-Aufspaltungsmuster von $Cs_2NaPr^{III}Cl_6$ im Niederenergiebereich, Z. Anorg. Allg. Chem. 439 (1978) 48–56. https://doi.org/10.1002/zaac.19784390105.

[32] W. Urland, “Magnetochemical series” for Lanthanoid compounds, Angew. Chem. Int. Ed. 20 (1981) 210–211. https://doi.org/10.1002/anie.198102101.

[33] C. Görller-Walrand, K. Binnemans, Rationalization of crystal-field parametrization, in: K.A. Gschneidner Jr., L. Eyring (Eds.), Handbook on the Physics and Chemistry of Rare Earths, Elsevier, Amsterdam (1996), pp. 121–283.

[34] K. Binnemans, Interpretation of europium(III) spectra, Coord. Chem. Rev. 295 (2015) 1–45. https://doi.org/10.1016/j.ccr.2015.02.015.

[35] a) R. Reisfeld, E. Zigansky, M. Gaft, Europium probe for estimation of site symmetry in glass films, glasses and crystals, Mol. Phys. 102 (2004) 1319–1330. https://doi.org/10.1080/00268970410001728609. b) F. Durville, G. Boulon, R. Reisfeld, H. Mack, C.K. Jørgensen, Site-selective fluorescence of europium(III) in vitrous and partly crystallized phospho-tungstate glass, Chem. Phys. Lett. 102 (1983) 393–398. https://doi.org/10.1016/0009-2614(83)87430-2; c) R. Reisfeld, R.A. Velapoldi, L. Boehm, M. Ish-Shalom, Transition probabilities of europium in phosphate glasses, J. Phys. Chem. 75 (1971) 3980–3983. https://doi.org/10.1021/j100695a012.

[36] W. Urland, The interpretation of the crystal field parameters for f^n-electron systems by the angular overlap model. Rare-earth ions in $LaCl_3$, Chem. Phys. Lett. 53 (1978) 296–299. https://doi.org/10.1016/0009-2614(78)85400-1.

[37] W. Urland, The assessment of the crystal-field parameters for f^n-electron systems by the angular overlap model: Rare-earth ions M_{3+} in $LiMF_4$ and substituted in $LiYF_4$, Chem. Phys. Lett. 77 (1981) 58–62. https://doi.org/10.1016/0009-2614(81)85599-6.

[38] A. Bronova, T. Bredow, R. Glaum, M.J. Riley, W. Urland, BonnMag: Computer program for ligand-field analysis of f^n systems within the angular overlap model, J. Comput. Chem. 39 (2018) 176–186. https://doi.org/10.1002/jcc.25096.

[39] A. Bronova, N. Kannengießer, R. Glaum, Optical spectra and magnetic behavior of a wide range of europium(III) oxo-compounds: Analysis of the ligand-field effects, Inorg. Chem. 56 (2017) 9235–9246. https://doi.org/10.1021/acs.inorgchem.7b01287.

[40] R. Glaum, W. Grunwald, N. Kannengießer, A. Bronova, Analysis of ligand field effects in europium(III) phosphates, Z. Anorg. Allg. Chem. 646 (2020) 184–192. https://doi.org/10.1002/zaac.202000019.

[41] N. Kannengießer, M. Jähnig, R.K. Kremer, R. Glaum, Understanding optical absorption spectra and magnetic behavior of a wide range of samarium(III) oxo-compounds: Analysis of the ligand-field effects, Eur. J. Inorg. Chem. 2021 (2021) 1722–1735. https://doi.org/10.1002/ejic.202001115.

[42] a) B.R. Judd, Optical absorption intensities of rare-earth ions, Phys. Rev. 127 (1962) 750–761. https://doi.org/10.1103/PhysRev.127.750; b) G.S. Ofelt, Intensities of crystal spectra of rare-earth ions, J. Chem. Phys. 37 (1962) 511–520. https://doi.org/10.1063/1.1701366.

[43] a) J.A. Duffy, M.D. Ingram, Establishment of an optical scale for Lewis basicity in inorganic oxyacids, molten salts, and glasses, J. Am. Chem. Soc. 93 (1971) 6448–6454. https://doi.org/10.1021/ja00753a019; b) J.A. Duffy, M.D. Ingram, An interpretation of glass chemistry in terms of the optical basicity concept, J. Non-Cryst. Solids 21 (1976) 373–410. https://doi.org/10.1016/0022-3093(76)90027-2.

[44] J.A. Duffy, Optical electronegativity, X^*, of transition-metal ions in simple compounds, J. Chem. Soc., Dalton Trans. (1983) 1475–1478. https://doi.org/10.1039/DT9830001475.

[45] J.H. Binks, J.A. Duffy, A molecular orbital treatment of the basicity of oxyanion units, J. Non-Cryst. Solids 37 (1980) 387–400. https://doi.org/10.1016/0022-3093(80)90074-5.

[46] a) C.K. Jørgensen, B.R. Judd, Hypersensitive pseudoquadrupole transitions in lanthanides, Mol. Phys. 8 (1964) 281–290. https://doi.org/10.1080/00268976400100321; b) C.K. Jørgensen, R. Reisfeld, Judd-Ofelt parameters and chemical bonding, J. Less-Common Met. 93 (1983) 107–112. https://doi.org/10.1016/0022-5088(83)90454-X.

[47] D. Aravena, M. Atanasov, F. Neese, Periodic trends in lanthanide compounds through the eyes of multireference ab initio theory, Inorg. Chem. 55 (2016) 4457–4469. https://doi.org/10.1021/acs.inorgchem.6b00244.

[48] J. Jung, M. Atanasov, F. Neese, Ab initio ligand-field theory analysis and covalency trends in actinide and lanthanide free ions and octahedral complexes, Inorg. Chem. 56 (2017) 8802–8816. https://doi.org/10.1021/acs.inorgchem.7b00642.

[49] S.K. Singh, J. Eng, M. Atanasov, F. Neese, Covalency and chemical bonding in transition metal complexes: An ab initio based ligand field perspective, Coord. Chem. Rev. 344 (2017) 2–25. https://doi.org/10.1016/j.ccr.2017.03.018.

[50] M. Atanasov, E.-L. Andreici Eftimie, N.M. Avram, M.G. Brik, F. Neese, First-principles study of optical absorption energies, ligand field and spin-Hamiltonian parameters of Cr^{3+} ions in emeralds, Inorg. Chem. 61 (2022) 178–192. https://doi.org/10.1021/acs.inorgchem.1c02650.

[51] M. Buchhorn, R.J. Deeth, V. Krewald, Revisiting the fundamental nature of metal-ligand bonding: An impartial and automated fitting procedure for angular overlap model parameters, Chem. Eur. J. 28 (2022) e202103775. https://doi.org/10.1002/chem.202103775.

[52] M. Atanasov, D. Ganyushin, K. Sivalingam, F. Neese, A modern first-principles view on ligand field theory through the eyes of correlated multireference wavefunctions, Struct. Bond. 143 (2012) 149–220. https://doi.org/10.1007/430_2011_57.

[53] a) F. Neese, The ORCA program system, WIREs Comput. Mol. Sci. 2 (2012) 73–78. https://doi.org/10.1002/wcms.81; b) F. Neese, F. Wennmohs, U. Becker, C. Riplinger, The ORCA quantum chemistry program package, J. Chem. Phys. 152 (2020) 224108. https://doi.org/10.1063/5.0004608.

Jiance Jin, Zhiguo Xia

Chapter 4
All-inorganic lead-free luminescent metal halide perovskite and perovskite derivatives

4.1 Introduction

Recently, metal halide perovskites (MHPs) in the form of nanocrystals and bulk crystals receive broad interests as a kind of emerging luminescence materials for optoelectronic applications. These new materials also provide a versatile platform for manipulating tunable photoluminescence (PL) behaviors due to their variable crystal structures, chemical compositions, and morphologies. Among them, luminescent organic–inorganic hybrid metal halides (OIMHs) represented by $CH_3NH_3PbBr_3$ nanocrystals (NCs) have firstly received attention, also including some famous two-dimensional (2D) perovskite bulk microcrystals such as $R_2PbBr_{4-x}Cl_x$ ($R = C_4H_9NH_3^+$, $C_6H_5CH_3NH_3^+$, etc.) [1]. However, one vital shortcoming is that OIMHs suffer from thermal instability, that is, the organic part will decompose at around 200 °C. Undoubtedly, all inorganic cesium lead halide ($CsPbX_3$, X = Cl, Br, or I) NCs and bulk crystals have recently drawn much attention because of the relatively high stability compared to that of the hybrid compounds. In fact, before the emergence of OIMHs, all-inorganic metal halides appeared in the glass crystallization process were earlier found and explored, which also possess excellent optical properties. Nowadays, these all-inorganic metal halides can gain great reputations in the applications of light-emitting devices, display, and luminescent sensors. Considering the rigid crystal structure and chemical composition of ABX_3 (X = Cl, Br, I)-type perovskite compound, typical all-inorganic metal halides discussed herein contain traditional MHPs and their derivatives. Moreover, we will just focus on the lead-free MHPs and their derivatives considering the toxicity of lead in lead-based MHPs, which enables the long-term environmental impact of the final devices. These lead-free luminescence materials will then have the positions in the future development compared to the rare earth luminescence materials used in the daily life.

Accordingly, in this chapter, the definition of all-inorganic lead-free MHPs and their derivatives will be firstly introduced, followed by the synthetic method for the NCs and bulk crystals, luminescent property, and mechanism for these materials. Then, some recent examples on these luminescent materials will be summarized, and

---

Acknowledgment: Our work was supported by the National Natural Science Foundations of China (grant no. 51961145101) and the Local Innovative and Research Teams Project of Guangdong Pearl River Talents Program (2017BT01X137).

https://doi.org/10.1515/9783110607871-004

the related luminescent applications will be concluded. Finally, an outlook will be proposed discussing the future prospect for these luminescence materials.

4.2 Definition of all-inorganic MHPs and their derivatives

The definition of MHPs can be tracked to the perovskite oxides named after the Russian geologist Lev Perovski with the formula ABO_3, whose famous representative is $CaTiO_3$. The formula for the classic all-inorganic MHPs herein belongs to the three-dimensional (3D) ABX_3, and the A-site represents the monovalent inorganic alkali cation, namely Li^+, Na^+, K^+, Rb^+, and Cs^+. Note that these inorganic cations can also be replaced by methylamine, ethylamine, and so on, leading to the formation of OIMHs, which however will not be discussed in this chapter. The B-site elements are divalent metal ions (e.g., Pb^{2+}, Sn^{2+}). The X represents the halogen ligand (F^-, Cl^-, Br^-, and I^-). In fact, the cation and anion strictly follow a rule (i.e., the Goldschmidt's tolerance rule) which strongly limits their ion radii in order to stabilize the 3D structure of ABX_3. The tolerance rule is listed as follows:

$$t = \frac{R_A + R_X}{\sqrt{2}(R_B + R_X)}$$

where t is the tolerance factor, and R_A, R_X, R_B refers to the ionic radius of A, X, and B, respectively [2].

Owing to the different coordination methods for B and X, diversified low-dimensional all-inorganic perovskites can be realized including 2D layer, one-dimensional (1D) chain, and zero-dimensional (0D) structure, leading to various luminescent properties. Additionally, when the B-site expands to high-valent metal ions such as trivalent metals of Sb^{3+}, Bi^{3+}, and In^{3+}, and tetravalent metals of Sn^{4+} and Te^{4+}, the dimension and formula for these all-inorganic MHP derivatives also vary [3, 4]. On the other hand, another monovalent metal ion (B^{I}) could replace partial trivalent B^{III}-site ions to eventually form a double perovskite with a formula of $A_2B^{I}B^{III}X_6$. These MHPs and their derivatives possess colorful luminescent properties, owing to their different crystal structures and chemical compositions, as will be discussed further [3, 4].

4.3 Syntheses of MHPs and their derivatives: single crystals and nanocrystals

4.3.1 MHPs and their derivatives: single crystal

The synthetic methods of single crystal can be divided into the following types: solid-state method, hydrothermal/solvothermal method, and solution evaporation method.

4.3.1.1 Solid-state method

For solid-state method, the solid crystals or powder agents are mixed and grounded together. Then they are transferred to a quartz tube. The quartz tube is sealed or just put together and heated under a high temperature for a controlled time. Finally, the crystal or sometimes powder can be obtained.

4.3.1.2 Hydrothermal/solvothermal method

Water/organic solvent is needed in the hydrothermal/solvothermal method. All the reagents solve in the water or organic solvent, and the solution is sealed in a Teflon container that is transferred in stainless autoclave. The autoclave is heated at a certain temperature. The single crystals can be formed when the temperature slowly cools down. Note that glass bottle can also be utilized for such method.

4.3.1.3 Solution evaporation method

The solution evaporation method refers to the slow evaporation of the solution containing reagents. Sometimes heating is needed for the quick evaporation. The volatile organic solvent is also a good candidate in this method, such as acetonitrile and acetone.

4.3.2 MHPs and their derivatives: nanocrystals

As for NCs, the synthetic methods mainly focus on hot-injection method, antisolvent recrystallization method, and vapor-phase epitaxial method.

4.3.2.1 Hot-injection method

Hot-injection method is a classic method for the preparation of NCs. A short burst of nucleation can be realized by the rapid injection of organometallic precursors into hot coordinating solvents at a higher temperature under N atmosphere protection, and then the nucleation gradually grows up when the temperature reaches the lower value [5]. The morphology and optical property are affected by the solvent ratio, temperature, ion concentration, and so on.

4.3.2.2 Antisolvent recrystallization method

The hot-injection method, however, suffers from the complex manipulation and uncontrollable swift injection, leading to the difficult preparation in large scale. Antisolvent recrystallization method, however, can overcome such problems. This method is conducted under room temperature (RT), which can be described as follows: the reagents are dissolved in the solvent with good solubility, and then the poor solvent is added to generate a highly supersaturated state, in which the NCs can be formed.

4.3.2.3 Vapor-phase epitaxial method

Recently, vapor-phase epitaxial method has been utilized to prepare NCs. This method is usually conducted in a chemical vapor deposition setup equipped with a mass flow controller and pressure control. As shown in Figure 4.1, Jin et al. have utilized vapor-phase epitaxial method to obtain $CsSnX_3$ (X = Br, I) nanowires [6].

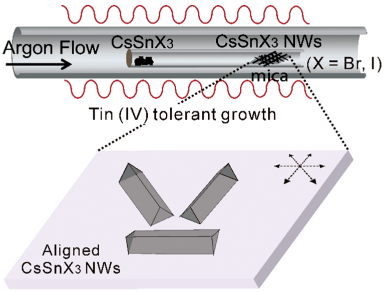

Figure 4.1: Vapor-phase epitaxial method for the synthesis of $CsSnX_3$ (X = Br, I) nanowires on a chemical vapor deposition device (reprinted with permission from ref. [6], Copyright 2019, the American Chemical Society).

4.4 Examples of all-inorganic MHPs and their derivatives

Given that the flexibility of the formula of MHPs, other ions with different valence can be employed to replace the divalent B-sites to form MHP derivatives (Figure 4.2). In this respect, different cations, such as monovalent ions of Cu^+, divalent ions of Zn^{2+}, Mn^{2+}, and Cd^{2+}, trivalent ions of In^{3+}, Sb^{3+}, and Bi^{3+}, and tetravalent ions of Te^{4+}, Zr^{4+}, and Sn^{4+}, have been used as B-sites to form MHP derivatives with the formula of $A_xM_yX_z(H_2O)_n$ ($n \geq 0$). Additionally, double perovskites can also be realized by introducing two different B-site ions. As a result, the family of MHP can be greatly enlarged. Moreover, the doping of Sb^{3+} and Bi^{3+} ions into these materials is also attractive to improve the luminescence property [7, 8]. Note that only MHPs and MHP derivatives with reported luminescence are included in this chapter.

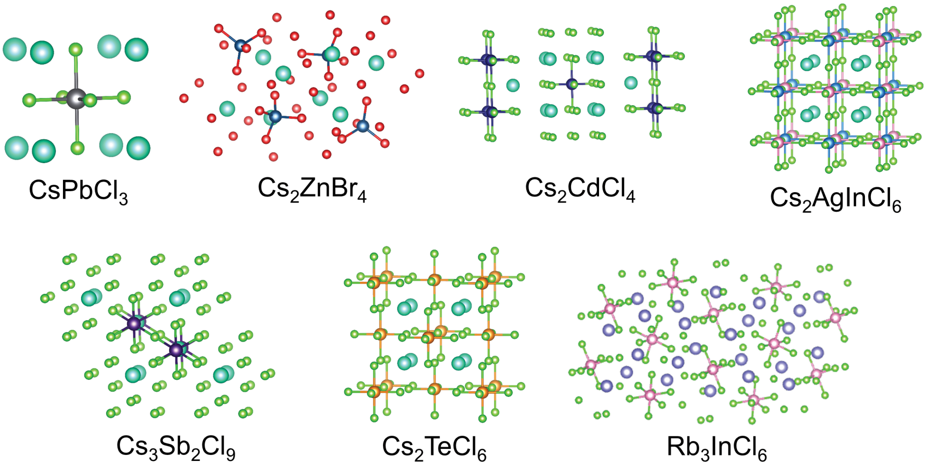

Figure 4.2: Selected crystal structure of MHP and MHP derivatives.

4.4.1 The ABX_3 type

The classical ABX_3 MHP is $CsPbX_3$ with bright green emission at around 520 nm, in which the adjacent $[PbX_6]$ octahedra links together by donor-sharing halogens to finally form a 3D structure. The lead MHPs, especially 3D $CsPbX_3$ and 0D Cs_4PbX_6, have received tremendous investigation, owing to their excellent luminescent property. However, the toxicity of lead materials severely hinders the development of lead MHPs in many cases and applications. Therefore, the luminescent studies based on lead-free MHPs have received massive attention. Tin(II), possessing the same lone-pair s orbital, remains the obvious candidate for the replacement of lead(II). In this respect, MHPs of $CsSnX_3$ have been studied for the luminescent property.

The earlier luminescent study of $CsSnX_3$ can be tracked to 1981 when Donaldson and coworkers [9] studied the emission property of cubic $CsSnBr_3$ at different temperatures. It possesses red emission at 1.78 eV at 300 K and slightly redshifts to 1.72 eV at 80 K. When the temperature is lower, a second intense emission at near-infrared (NIR) region of 1.26 eV was detected. This second emission cannot be detected by the optical excitation at RT but electron beam. The change of halogen from Br to Cl for cubic $CsSnBr_{3-x}Cl_x$ can lead to the shift of emission's maximum peak to a higher energy. The increase of x can bring about the decrease in the luminescent intensity, and the emission is undetectable when $x = 2$. The materials with $x > 2$ are monoclinic phase with no emission at RT. Additionally, both $CsSnF_3$ and $CsSnI_3$ are not emissive at 80 K.

Later in 1994, Voloshinovskii's group investigated the different structure of $CsSnCl_3$ (cubic and monoclinic phases) and corresponding luminescence at 77 K [10]. The cubic phase possesses emission at 555 nm and excitation at 368 nm, while the monoclinic phase possesses emission at 493 nm and excitation at 313 nm. These emissions can be attributed to the self-localized excitons, of which the electron moiety is mainly localized on the Sn atoms. Interestingly, the air moisture can lead to the redshift of emission at 582 nm, which can be attributed to the radiation from the oxygen-containing luminescent centers, considering these centers can be excited under 278 nm. The distinct luminescence can be applied for the determination of different phases of $CsSnCl_3$.

Owing to the easy hygroscopicity and oxidation in air for $CsSnX_3$, it remains difficult to study the property of $CsSnX_3$, which means that a strict protection is needed. However, the other type of tin(II)-based MHP derivative, Cs_4SnX_6, with lower hygroscopicity and uneasy oxidation property is employed as adjuvant to study the property of $CsSnX_3$. In 2008, for instance, Myagkota et al. [11] studied the cathodoluminescence of $CsSnBr_3$ in Cs_4SnBr_6 matrix.

In comparison of these star materials of $CsSnX_3$ in solar cell, the study of luminescence for these materials has been paid less attention. Until recently, the study in PL of their nano/micromaterials and the electroluminescence of these type MHPs have emerged. In 2020, Mu group [12] has successfully fabricated $CsSnBr_3$-based perovskite light-emitting diodes by thermal evaporation. The as-prepared $CsSnBr_3$ films possess different emissions depending on the annealing temperatures. It possesses 675 nm red emission at RT annealing temperature, while the emission maximum peak redshifts to 680 nm along with the great enhancement in the intensity at 85 °C annealing temperature. The enhancement PL can also be observed by the increasing PL quantum yield (PLQY) from 0.62% at RT annealing temperature to 3.76% at 85 °C annealing temperature. The as-fabricated perovskite light-emitting diode with 85 °C annealing temperature also possesses the highest external quantum efficiency (EQE) value of 0.16%. As for micromaterials, in 2021, Hsu group studied the thermal PL quenching property of $CsSnBr_3$ microsquares and micropyramids, which belong to the cubic crystalline structure [13]. The studies show that $CsSnBr_3$ microsquares and micropyramids possess great thermal stability, endowing them with great potential in optical devices at high temperature.

The substitution of B-site element by doping other metal ions could enhance the luminescent property. For instance, in 2019, Mi's group succeeded in doping In^{3+} and Mn^{2+} into $CsSnCl_3$, respectively [14]. The doped materials possess red emission at 645 nm for the Mn^{2+} ion doping and blue emission at 484 nm for the In^{3+} ion doping, and the intensity of which is significantly enhanced compared to the host's original $CsSnCl_3$. The enhanced luminescence of Mn^{2+}-doped sample can be ascribed to the energy transfer process while the In^{3+}-doped one is attributed to the created B-site vacancies that contribute to the band-to-band recombination of charge carriers.

As mentioned earlier, the tin(II)-based MHP are air-sensitive, which would be oxidated into tin(IV) under air atmosphere. Therefore, some other divalent metal ions have been employed to replace Sn^{2+}, such as Mn^{2+} and Cd^{2+}. Earlier in 1982, McPherson et al. investigated the PL property of $AMnX_3$ (A = Rb, Cs; X = Cl, Br, I) [15]. They possess orange-to-red emissions varying from 608 to 678 nm depending on the A-site ions and halogen ions. The PL decay at low temperature of 77 K and at RT of 296 K are also tested, showing the microsecond-level lifetime. Later in 2000 and 2002, the Yb^{3+}-doped $CsMnCl_3$ and $RbMnCl_3$ materials were studied by Valiente et al., which show the upconversion luminescence [16, 17]. The upconversion luminescence can be attributed to the interactions between Yb^{3+} and Mn^{2+}. In fact, a water-coordinated structure is easily formed for $CsMnCl_3$-type material, namely $CsMnCl_3 \cdot 2H_2O$. The structure of $CsMnCl_3 \cdot 2H_2O$ is slightly different from ABX_3 MHP; thus, the related studies will be discussed in the other sections as all Mn(II)-based MHP derivatives.

The luminescent study based on $ACdX_3$ is very rare. Except the luminescent study of $CsCdCl_3$ host in 1984 and 1985 [18, 19], and $TlCdCl_3$ in 1998 [20], the subsequent researches of luminescence are basically based on the doping of other ions into $CsCdX_3$.

For instance, in 2005, Valiente group reported on the Ni^{2+}-, Yb^{3+}-codoped $CsCdBr_3$ material [21]. The excitation at the absorption wavelength of Yb^{3+} results in the visible upconversion luminescence from Ni^{2+} $^1T_{2g} \rightarrow {}^3A_{2g}$ at low temperature. They also mentioned that the introduction of Yb^{3+} plays a significant role for the energy transfer between Ni^{2+} and Yb^{3+} ions.

In 2007, U^{3+} was doped into $CsCdCl_3$, resulting in the emission of 1,470 and 2,350 nm at NIR region under the excitation of 514 nm [22]. Besides, the dopant of Bi^{3+} into $CsCdX_3$ (X = Cl and Br) could bring about NIR emission [23]. The $CsCdBr_3$:Bi^{3+} possesses emission of 1,078 nm at 77 K and 1,056 nm at 300 K, while the $CsCdCl_3$:Bi^{3+} possesses emission centered at 1,032 nm at 77 K and 980 nm at 300 K.

The luminescent study of different types of lead-free MHPs remains more explorations, compared with the massive investigation of $CsPbX_3$ MHPs.

4.4.2 The A_2BX_4 type

The A_2BX_4 type mainly focuses on the divalent metal ions such as Zn^{2+} and Cd^{2+}. The study of Cs_2ZnCl_4 can be tracked to 2012, when auger-free luminescence for Cs_2ZnCl_4 was investigated [24]. Then, Cs_2ZnCl_4 has been utilized as the host material, into which different metal ions have been doped. Doping Te^{4+} into Cs_2ZnCl_4 host could lead to broadband yellow emission at 570 nm [25]. The yellow emission is attributed to the self-trapped excitons (STEs), and the concentration of Te^{4+} can affect the intensity of PL and the decay lifetime. Sb^{3+} has also been utilized to be doped into A_2ZnX_4 (A = Cs, Cs/Rb, Cs/K; X = Cl, Br) by Xia group [26]. Taking Cs_2ZnCl_4: Sb^{3+} as an example, one can find that the deep red to NIR emission can be realized by the doping of Sb^{3+} with the emission peaking at 745 nm and the decay lifetime of 12.8 μs under RT. Transition metal ion of Cu^+ was doped into A_2ZnX_4 (A = Cs, Rb; X = Cl, Br) [27]. A blue emission peaking at 465 nm with PLQY of 65.3% was obtained for Cs_2ZnBr_4: Cu^+ sample. This blue emission is attributed to the STEs. Additionally, A_2ZnCl_4: Cu^+ (A = Cs, Rb) were synthesized in order to further study the role of the A-site cation and halogen, which were found to possess sky blue emission with PLQY up to 73.1%. In 2021, PL of Sn^{2+}-doped Cs_2ZnCl_4 crystal has been investigated and discussed [28]. An emission peaking at 648 nm at 270 K can be observed, which can be ascribed to the STEs of $[SnCl_4]^{2-}$ units. Recently, nanomaterial of Cs_2ZnCl_4 has also been studied [29]. A series of Cs_2ZnCl_4, $Cs_2ZnBr_2Cl_2$, and $Cs_2ZnCl_2I_2$ NCs with blue emission were synthesized. The highest PLQY can reach 51.93%.

The luminescent study based on A_2CdX_4 is very rare. In 2018, $Rb_2CdCl_2I_2$ was reported to possess warm white light with a high color rendering index (CRI) of 88 [30]. In 2020, Sb^{3+} was incorporated into Cs_2CdCl_4:Sb^{3+} NCs to bring cyan emission with a PLQY of 20% [31].

4.4.3 The A_2BX_6 type

The B-site metal ion in A_2BX_6 type with luminescent property is usually composed of tetravalent Te^{4+}, Hf^{4+}, Zr^{4+}, and Sn^{4+}. The tetravalent ion of Te^{4+}-based MHP derivatives focuses on A_2TeX_6 (A = K, Rb, Cs, Tl; X = Br, I). Basically, the yellow emission peaking at 580 nm for Cs_2TeCl_6 was observed at 300 K, while only red emission at around 670 nm was found at 77 K for Cs_2TeBr_6 and Cs_2TeI_6 [32]. Recently, Zhang group successfully obtained $Cs_2Hf_{1-x}Te_xCl_6$ via ion-exchange method [33]. Cs_2HfCl_6 possesses a 450 nm emission originating from STEs, while Cs_2TeCl_6 possesses 578 nm emission from Te^{4+}. The coexistence of Hf^{4+} and Te^{4+} in $Cs_2Hf_{1-x}Te_xCl_6$ would bring about a dual emission with white emission, whose luminescent mechanism can be attributed not only to the STEs from $[HfCl_6]^{2-}$ moiety but to the Te^{4+}. A PLQY of 83.46% can be realized for $Cs_2Hf_{0.99}Te_{0.01}Cl_6$ under 306 nm excitation.

Owing to the blue emission nature of Cs_2ZrCl_6, scientists made endeavor to introduce yellow emission ions Sb^{3+} or Te^{4+} into the host of Cs_2ZrCl_6 to bring about the white emission in a single component recently. The as-prepared sample Cs_2ZrCl_6: Sb^{3+} is capable of emitting dual emission at different excitations: the blue one from the host and the yellow-to-orange one from Sb^{3+} dopant [34, 35]. In this respect, the appropriate choice of excitation could induce white emission. For Te doping material, the blue emission from Cs_2ZrCl_6 cannot be realized, owing to the lack of excitation at high energy for Te^{4+}. The as-prepared $Cs_2Zr_{1-x}Te_xCl_6$ microcrystals exhibit broad and strong yellow emission with high PLQY up to 79.46% [36]. However, the white emission devices can still be obtained by coating $Cs_2Zr_{1-x}Te_xCl_6$ on a 450 nm blue chips.

Cs_2SnCl_6 MHP derivative, in which the Sn^{4+} is much more stable than Sn^{2+}, has also been utilized for the luminescent study. However, the single crystal of host itself possesses poor luminescence. Therefore, introducing emissive ions such as Sb^{3+}, Bi^{3+}, and Te^{4+} as the dopant is thought to enhance the luminescence. For instance, in 2018, Tang and coworkers [37] studied the Bi^{3+}-doped Cs_2SnCl_6. The doping of Bi^{3+} could turn the originally nonluminous Cs_2SnCl_6 to exhibit a highly efficient deep blue emission at 455 nm, with a Stokes shift of 106 nm and a high PLQY close to 80%. In 2019, Tang and coworkers studied the luminescence of Sb-doped Cs_2SnCl_6 single crystal, which turns out to possess a broadband orange-red emission peaking at around 601 nm [38]. The concentration of Sb^{3+} would affect the luminescent intensity without changing the peak position. The highest PLQY can reach 37% when 0.59% Sb^{3+} was introduced. Later in the same year, Xia group successfully synthesized Cs_2SnCl_6 NCs and Sb-doped Cs_2SnCl_6 NCs [39]. The NCs of host sample possess blue emission peaking at 438 nm, and the doping of Sb^{3+} could bring about a broadband emission peaking at 615 nm. In 2020, Xiao et al. reported on the Te^{4+}-doped Cs_2SnCl_6 single crystal [40]. The introduction of Te^{4+} would lead to a strong Jahn–Teller distortion, capable of bringing about Jahn–Teller-like STEs. The as-prepared sample possesses 580 nm yellow emission with a very high PLQY of 95.4%. The luminescent mechanism can be ascribed to Te luminescent center and the STEs. Interestingly, Cs_2SnCl_6: Te^{4+} could withstand the water condition without quenching its emission, which may be due to the formation of amorphous alteration phase as mentioned by authors. In 2021, Du group has introduced Bi^{3+} and Te^{4+} into Cs_2SnCl_6 host to obtain sample with dual emission [41]. The blue emission at 450 nm comes from the doping of Bi^{3+} while the yellow emission at 575 nm comes from Te^{4+}. The dopant concentration will affect the PL property for as-synthesized compound, and a white emission was obtained when the ratio of Te reaches 0.049%. This compound was also water-stable and can emit light under water condition. Later in 2022, the Bi^{3+}/Te^{4+} co-doped Cs_2SnCl_6 microcrystal was prepared by Chen et al. [42]. The luminescent mechanism was thoroughly revealed, that is, the interconfigurational $^3P_{0,1} \rightarrow {}^1S_0$ transitions of Bi^{3+} and Te^{4+}, in which an energy transfer was involved from Bi^{3+} to Te^{4+}.

4.4.4 The $A_3B_2X_9$ type

The B-site metal ions in $A_3B_2X_9$ type are mainly trivalent Sb^{3+} and Bi^{3+}. The structure study for such MHP derivatives can be tracked back to 2016, when Chang et al. synthesized $Rb_3Sb_2Br_9$, $Rb_3Sb_2I_9$, $Rb_3Bi_2Br_9$, $Rb_3Bi_2I_9$, and $Tl_3Bi_2Br_9$ [43]. It is interesting that $Rb_3Sb_2Br_9$, $Rb_3Sb_2I_9$, and $Rb_3Bi_2I_9$ belong to the space group of $P2_1/n$, which can be regarded as $Tl_3Bi_2I_9$ type, while $Rb_3Bi_2Br_9$ and $Tl_3Bi_2Br_9$ crystallize in a slightly different type space group, that is, $P2_1/a$. Double layers with corner-sharing $[MX_6]$ octahedra can be found in both types of structures. Later, the PL property for such $A_3M_2X_9$ (A = Cs, Rb; M = Sb, Bi; X = Cl, Br, I) MHP derivatives was investigated. In 2017, Wessels synthesized $A_3M_2I_9$ (A = Cs, Rb; M = Bi, Sb), and their luminescence was studied [44]. PL at both low temperature and RT was tested. $Cs_3Sb_2I_9$ and $Rb_3Sb_2I_9$ possess broad PL emission bands peaking at 1.96 and 1.92 eV, respectively, while PL spectra of $Cs_3Bi_2I_9$ exhibited broad emission consisting of several overlapping bands in the 1.65–2.2 eV range. The PL was ascribed to the electron–phonon interaction, which is also the factor resulting in the broad PL. In the same year, Nag et al. reported on the luminescence of $Cs_3Sb_2I_9$ and $Rb_3Sb_2I_9$ NCs [45]. They also found that the nanoshape of such samples will affect their optical properties. The $Cs_3Sb_2I_9$ nanoplatelets possess yellow emission while $Cs_3Sb_2I_9$ nanorods (NRs) have orange emission. Additionally, the optical property of $Rb_3Sb_2I_9$ NCs was reported to be similar to $Cs_3Sb_2I_9$ NCs. Moreover, $Cs_3Sb_2Br_9$ quantum dots (QDs) were synthesized by Song group, which possess blue emission at 410 nm with a high PLQY of 46% [46]. The PL from 370 to 560 nm can also be tuned for $Cs_3Sb_2X_9$ by simply changing the halogen anion. In 2019, Shan et al. further investigated the electroluminescence for $Cs_3Sb_2Br_9$ QDs [47]. The EQE of 0.206% can be realized. As for bismuth MHP derivatives, in 2018, Tang and coworkers reported on $Cs_3Bi_2Br_9$ QDs with blue emission at 410 nm and a PLQY up to 19.4% [48]. In 2019, Kanatzidis and coworkers reported on the enhanced electron–phonon coupling by introducing Cl into 0D $Cs_3Bi_2I_9$ to form a 2D $Cs_3Bi_2I_6Cl_3$ [49]. The 2D structure compound possesses similar emission compared with $Cs_3Sb_2I_9$, that is, a single broad peak at 1.94 eV with a low-energy tail under 405 nm excitation.

4.4.5 Other Sb(III)- and Bi(III)-based MHP derivatives

Instead of the study based on $A_3M_2X_9$ (A = Cs, Rb; M = Sb, Bi; X = Cl, Br, I), the luminescence research on $Rb_7M_3X_{16}$ (M = Sb, Bi; X = Cl, Br) has also been involved. For instance, in 2019, Song and coworkers reported on the structure of $Rb_7Bi_3Cl_{16}$ single crystal and PL for $Rb_7Bi_3Cl_{16}$ NCs [50]. It is found that $Rb_7Bi_3Cl_{16}$ NCs possess a blue emission at 437 nm with a PLQY of 28.43%, and a good moisture stability for 1 month. Later in 2020, Kovalenko group studied the luminescence of $Rb_7Sb_3Cl_{16}$, which has PL peaking at 560 nm and a PLQY of around 3.8% [51]. Additionally, they also discovered that the substitution of Sb^{3+} by Bi^{3+} will result in the blueshift of PL peak. $Rb_7M_3X_{16}$

(M = Sb, Bi; X = Br, I) was also synthesized by Kovalenko group, and they found that a dual emission exists for $Rb_7Sb_3Br_{16}$, that is, 612 nm (2.03 eV) and 650 nm (1.91 eV) at 12 K [52].

4.4.6 All Mn(II)-based MHP derivatives

While limited luminescent researches have been conducted on $AMnX_3$ (A = Rb, Cs; X = Cl, Br, I), the luminescent study based on $CsMnCl_3 \cdot 2H_2O$ is relatively large. The early study can be reached in 1993 when Eremenko et al. investigated the luminescent QY and PL decay of $CsMnCl_3 \cdot 2H_2O$ from 6 to 30 K [53]. Notably, the luminescence property for Cu^{2+}-doped $CsMnCl_3 \cdot 2H_2O$ has also been studied [54]. In 2000, Eremenko et al. also found the anti-Stokes excitation of the fluorescence of Mn^{2+} ions in $CsMnCl_3 \cdot 2H_2O$ [55]. In 2020, Lin et al. discovered that the 1D $CsMnCl_3 \cdot 2H_2O$ can be transformed into 0D Cs_3MnCl_5 and eventually into 0D $Cs_2MnCl_4 \cdot 2(H_2O)$ [56]. The luminescence is switched with the red emission of $CsMnCl_3 \cdot 2H_2O$ to green emission of Cs_3MnCl_5 and finally red emission of $Cs_2MnCl_4 \cdot 2(H_2O)$. In 2020, Han and coworkers reported on the bromide NCs with structural transformation and PL switching [57]. The red emission $CsMnBr_3$ NCs can be transformed to green emission Cs_3MnBr_5 NCs triggered by isopropanol. Moreover, the humid atmosphere could further induce $CsMnBr_3$ NCs and Cs_3MnBr_5 NCs to be transformed into $Cs_2MnCl_4 \cdot 2(H_2O)$ NCs with blue emission. The thermal annealing dehydration can lead to inverse transformation. In 2021, Du group reported on the PL switching between $CsMnCl_3$ and $CsMnCl_3 \cdot 2H_2O$ [58]. They discovered that moisture could induce a structural change from $CsMnCl_3$ to $CsMnCl_3 \cdot 2H_2O$, leading to an enhancement of luminescence.

Cs_3MnBr_5 MHP derivative was also studied to possess green emission at 520 nm under 460 nm excitation with the PLQY of 49% by Xia group [59]. Additionally, Zn^{2+} has been introduced into Cs_3MnBr_5 host to enhance the thermal stability, that is, the luminescence improved from 82% for Cs_3MnBr_5 to 87% for Cs_3MnBr_5: Zn^{2+} with the intensity values at 423 K compared to that at 298 K.

4.4.7 All Cu(I)-based MHP derivatives

The Cu^{+}-based all-inorganic metal halides can be summarized into $CsCu_2I_3$, $Cs_3Cu_2I_5$, and Rb_2CuX_3 (X = Cl and Br). In 2018, $Cs_3Cu_2I_5$ was reported to possess very high PLQY of 90% and blue emission at around 445 nm [60]. The fabricated film based on $Cs_3Cu_2I_5$ also possesses 60% PLQY. In 2019, Huang et al. reported on the yellow emission of $CsCu_2I_3$ with PLQY of 15.7% [61]. This emission originates from the STEs. Later, the NCs of 0D $Cs_3Cu_2I_5$ and 1D $CsCu_2I_3$ were also synthesized. The reduction in dimensionality causes the enhancement of PLQY from 5% for 1D $CsCu_2I_3$ NRs to 67% for 0D $Cs_3Cu_2I_5$ NCs [62]. The pressure-induced PL of $CsCu_2I_3$ crystal has also been investigated [63].

The high-pressure compression leads to the strong STE emission for 1D $CsCu_2I_3$ crystal. In 2020, Yuan reported the scintillation property of $Cs_3Cu_2I_5$ and the doping of Tl^+ into $Cs_3Cu_2I_5$ can increase the scintillation light yield [64]. The PL properties of Rb_2CuX_3 (X = Cl and Br) have been reported in 2019 and 2020 [65–67]. The chloride material possesses 99.4% PLQY [66], while the bromide one has PLQY of 98.6% [67]. The scintillation properties for both of them are investigated.

4.4.8 $A_2InX_5{\cdot}H_2O$ and A_3InX_6

Different from the MHP derivatives based on trivalent ions of Sb^{3+} and Bi^{3+}, the MHP derivatives comprising In^{3+} mainly focus on A_3InX_6 and $A_2InX_5{\cdot}H_2O$ (A = Cs, Rb). The host materials of A_3InX_6 and $A_2InX_5{\cdot}H_2O$ (A = Cs, Rb) are reported to be nonemissive or weak emission, until recently Wang et al. found that $Cs_2InCl_5{\cdot}H_2O$ possess two different emissions (orange and blue) [68, 69]. The main researches for these indium perovskite derivatives lie in the PL of Sb^{3+}-doped materials. In 2019, Su et al. reported on the red emission with PLQY of 33% for Sb^{3+}-doped $Cs_2InBr_5{\cdot}H_2O$ [70]. Later in 2020, Han group reported on the Sb^{3+}-doped $A_2InCl_5{\cdot}H_2O$ and A_3InCl_6 (A = Cs, Rb) [69]. The water-coordinated one possesses yellow emission with PLQY of 90%, while the six Cl atom-coordinated one possesses green emission with PLQY of 95%. Their emissions are attributed to STEs, and Sb^{3+}-doped Cs_3InCl_6 can be easily transformed into Sb^{3+}-doped $Cs_2InCl_5{\cdot}H_2O$ when exposed in air for 1 month. The transformation between Sb^{3+}-doped Rb_3InCl_6 and $Rb_2InCl_5{\cdot}H_2O$ is much tougher. Woodward group has studied the transformation and PL switching between Sb^{3+}-doped Rb_3InCl_6 and $Rb_2InCl_5{\cdot}H_2O$ [71]. Xia group investigated Sb^{3+}-doped $Cs_2InCl_5{\cdot}H_2O$ and influence of halogens to the luminescence property [72]. Except the dopant Sb^{3+}, Te^{4+} and Cu^+ have also been utilized to be doped into $Cs_2InCl_5{\cdot}H_2O$ and Rb_3InCl_6, respectively [73, 74]. The $Cs_2InCl_5{\cdot}H_2O$: Te^{4+} possesses a 660 nm emission while the Rb_3InCl_6: Cu^+ has PL at 398 nm.

4.4.9 Double perovskites

All-inorganic double perovskite halides are usually in the form of $Cs_2M^IM^{III}X_6$ (X = Cl, Br). However, the host double perovskites are commonly poorly emissive. In 2018, Tang and coworkers studied the luminescence property for $Cs_2AgInCl_6$ theoretically and experimentally [75]. The dark transition of free excitons (FEs) and STEs in $Cs_2AgInCl_6$ strongly affect its luminescence property, leading to a quite low PLQY of <0.1%. One way to improve PLQY is to manipulate the symmetry of the STE wave function so that the parity-forbidden transition can be broken. The broadband emission (typically STE emission) for $Cs_2NaInCl_6$ inspired them to introduce Na^+ into the host of $Cs_2AgInCl_6$. As a result, the luminescence of $Cs_2Na_xAg_{1-x}InCl_6$ powder has been enhanced with a display of white emission. Moreover, they also found that the doping of Bi^{3+} can further increase the PLQY for such $Cs_2Na_xAg_{1-x}InCl_6$ double perovskite. In 2021, Xia group summarized a review about the synthesis and optical property for $Cs_2AgInCl_6$-based single crystal and NCs, in which many luminescent studies based on the doped $Cs_2AgInCl_6$ are involved [76].

Given that the host of such double perovskite bulk materials is commonly nonluminous at RT, therefore, the luminescence studies for such double perovskites lie in the doping of luminous metal ions such as Sb^{3+} and Mn^{2+}. In 2020, Kovalenko group successfully doped Sb^{3+} into $Cs_2NaInCl_6$ and Cs_2KInCl_6 single crystals, resulting in the bright broadband blue and green emissions, respectively, and the PLQYs can reach up to 93% [77]. The luminescent mechanism can be attributed to STEs from the Sb(III)-hosted moiety. The doping of Cr^{3+} can realize the NIR emission for $Cs_2AgInCl_6$: Cr^{3+} [78]. The nanomaterial for $Cs_2NaInCl_6$ has also been prepared. For instance, Han group has doped Ag^+ into the nearly nonluminous $Cs_2NaInCl_6$ NCs [79]. The as-prepared $Cs_2NaInCl_6$: Ag^+ exhibits broadband emission peaking at 535 nm. The concentration of Ag^+ dopant plays a significant role in the luminescent intensity, and the highest PLQY can reach 31.1% when 10% Ag^+ has been added.

Except In^{3+} as M^{III}-site ion, the double perovskites based on Bi^{3+} have also been studied. The typical materials are Cs_2AgBiX_6. $Cs_2AgBiCl_6$ has been reported to possess weak emission at 575 nm when deposited on a glass [80]. In 2017, Mitzi et al. study the electronic structure by $Cs_2AgBiBr_6$ alloying of In^{3+}/Sb^{3+} [81]. The luminescence property has also been altered. The In-alloyed samples yield different PL intensities with 75.0% substitution the smallest, and 25.0% the largest. The PL for Sb substituted material is weaker and obviously shifted to longer wavelength compared to the analogous spectrum for $Cs_2AgBiBr_6$ host. In 2021, Yuan et al. reported on the pressure-induced emission based on $Cs_2NaBiCl_6$ crystal [82]. The originally nonluminous $Cs_2NaBiCl_6$ crystal is capable of exhibiting an unexpected broadband dual-color emission when the external pressure is increased to 6.77 GPa. Such emission is attributed to the singlet STEs and triplet STEs, and the twisted $[BiCl_6]^{3-}$ plays an important role in such emission.

Moreover, in the same year, an air-stable, all-inorganic Sc-based double perovskite $Cs_2NaScCl_6$ is reported by Han group [83]. This perovskite exhibits blue emission peaking at 445 nm with PLQY of 29.05%. Notably, such PLQY value remains the highest for pristine halide double perovskite. They also successfully doped Mn^{2+} into $Cs_2NaScCl_6$. The as-prepared material possesses tunable dual broadband emission. One emission is the blue emission (450 nm) from the host and the other is red emission (635 nm) from Mn^{2+} *d–d* transitions.

Other double perovskites such as $Cs_4CdSb_2Cl_{12}$, $Rb_4MnSb_2Cl_{12}$, $Rb_4CuSb_2Cl_{12}$, $Cs_4MnBi_2Cl_{12}$, and $Cs_4CdBi_2Cl_{12}$ have also been synthesized by Solis-Ibarra group [84]. Except $Rb_4CuSb_2Cl_{12}$, other four double perovskites possess very broad emission peak. $Cs_4CdSb_2Cl_{12}$ particularly has a broadband emission that can span all visible spectra from 400 to 800 nm with a wide full width at half maxima (FWHM) of 220 nm. These broad PL emissions can be attributed to STEs. In 2020, the same group studied Sb^{3+}

substitution in $Cs_4Cd_{1-x}Mn_xBi_2Cl_{12}$ [85]. They found that $Cs_4Cd_{1-x}Mn_xSb_2Cl_{12}$ exhibits emission peaking at 605 nm, which can be ascribed to Mn^{2+} centers. The PLQY reaches up to 28.5%. In addition, the variation of Sb^{3+} and Bi^{3+} concentrations would affect the emission property. A decreased efficiency of the $Cs_4Cd_{1-x}Mn_xSb_2Cl_{12}$ family compared with $Cs_4Cd_{1-x}Mn_xBi_2Cl_{12}$ can be observed. This decreased efficiency can be attributed to a decreased spin–orbit and Jahn–Teller couplings in Sb, thus leading to electronic delocalization and affecting the energy transfer to Mn^{2+} centers.

4.5 Luminescent mechanism of MHPs and their derivatives

As another hot topic, the luminescent mechanisms for all-inorganic MHPs and their derivatives have been widely discussed. When the B-sites are metal ions with ns^2 electronic shell, the luminescence is commonly attributed to the STE emission. The STE emission is strongly related to the electron–phonon interaction and lattice softness, which usually results in a broad emission, that is, large FWHM. The FWHM can be investigated by the following equation:

$$\mathrm{FWHM} = 2.36\sqrt{S}\hbar\omega_{\mathrm{phonon}}\sqrt{\coth\frac{\hbar\omega_{\mathrm{phonon}}}{2k_{\mathrm{B}}T}}$$

where S refers to the Huang–Rhys factor, $\hbar$ is the reduced Planck constant, ω is the phonon frequency, k_{B} is the Boltzmann constant, and T is the temperature. S is strongly related to the formation of STEs and the FWHM value. Larger S may lead to more nonradiation transition [86].

In some cases, luminescence from FE can also be observed with relatively narrow emission peak. Smith and Karunadasa [87] have proposed an intuitive representation with ball interacting with a rubber sheet to show three luminescent mechanisms (Figure 4.3): (1) intrinsic self-trapping; (2) defect trapping; and (3) extrinsic self-trapping.

Other luminescent mechanism based on *s*–*p* electrical theory has also been utilized to explain the origin of different emissions for ns^2-type B-site ions [88]. In this respect, the energy level is composed of ground state of $^1S_0$ and excited states of $^3P_2$, $^3P_1$, $^3P_0$, and $^1P_1$ [89]. The photoexcitation leads to the rapid formation of singlet state ^1P and triplet states of ^3P via electron–electron interaction-induced Coulomb repulsion and exchange interaction. Then the existence of spin–orbit coupling (SOC) causes the split of the ^3P state into nondegenerate states, that is, $^3P_2$, $^3P_1$, and $^3P_0$. The electronic transition from $^1P_1$ to $^1S_0$ could lead to the singlet fluorescent emission while transition from $^3P_{2,1}$ to $^1S_0$ could bring about the triplet phosphorescent emission. Notably

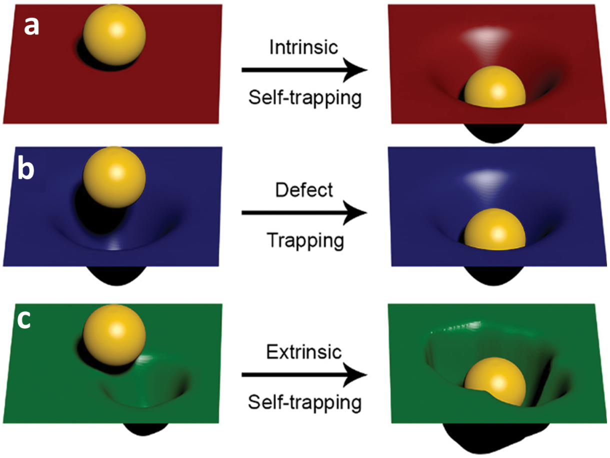

Figure 4.3: The ball and rubber sheet model for (a) intrinsic self-trapping, (b) defect trapping, and (c) extrinsic self-trapping (reprinted with permission from ref. [87], Copyright 2018, the American Chemical Society).

the $^1S_0$ to $^3P_0$ transition is strongly forbidden, but can be partially allowed in the case of SOC.

Given that the energy state will be influenced by the coordination of halogen ligands, another mechanism has been proposed by Kovalenko's group, namely molecular orbital (MO) theory [90]. In this case, the atomic term symbols could be replaced by the molecular ones, that is, a_1g replaces $^1S_0$. Additionally, the molecular term symbols are related to the molecular geometries such as octahedral, square pyramidal, and disphenoidal, which were summarized by Vogler and Nikol in 1993 [91]. Therefore, the MO theory could not only explain the origin of luminescence but also shows the different molecular geometries, especially in the 0D structure with various geometries.

For transition metal ions that form all-inorganic MHPs, the luminescence can also be derived by the special *d*–*d* electron transition (e.g., Mn^{2+} [92]). It should be mentioned that when the other metal ions have been doped into all-inorganic MHPs, the luminescence will be altered. In some cases, the luminescence is complex with the mixture of the abovementioned mechanisms.

4.6 Photonic applications of MHPs and their derivatives

The colorful PL emission from visible light region to NIR light region endows MHPs and MHP derivatives with great potentiality in many fields. First, light-emitting devices, including photoluminescent one and electroluminescent one, are mainly and frequently reported. Among different light-emitting devices, white light-emitting devices (WLED) are significant in our daily life. Based on the white emission devices rule, blue chips with yellow phosphor, or blue chips with red and green phosphors, or blue chips with red and yellow phosphors can lead to the white emission. Therefore, broadband yellow emission that could be excited by blue light can be adopted to fabricate WLED. For instance, $Cs_2Hf_{0.99}Te_{0.01}Cl_6$ has been coated on a blue chip (named as WLED1, Figure 4.4a) and a UV chip mixing blue phosphor (named as WLED2, Figure 4.4b), respectively [33]. The former possesses CRI of 73.6, while the latter has CRI of 81.9. Notably, high CRI WLED can be applied to the illumination. Moreover, materials with narrow emission peak can be utilized to fabricate into WLEDs as backlights. These materials are usually mixed with commercial phosphors with narrow PL peak. Green emission Mn^{2+}-based halides usually possess a relatively narrow PL peak with FWHM reaching from 40 to 50 nm. Such materials are good candidates because they emit green light (one of the tricolor), and can be excited by blue lights. In 2019, Xia group reported on the WLED fabricated by blue chips, Cs_3MnBr_5 or $Cs_3Mn_{0.96}Zn_{0.04}Br_5$ (green emission) and K_2SiF_6: Mn^{4+} (KSF:Mn^{4+}, red emission) phosphor [59]. The WLED exhibits a high luminous efficiency of 108.88 and 107.76 lm/W, respectively. Two WLEDs also have wide color gamut of 104% and 101% National Television System Committee standard in Commission Internationale de L'Eclairage (CIE) 1931 color space, respectively.

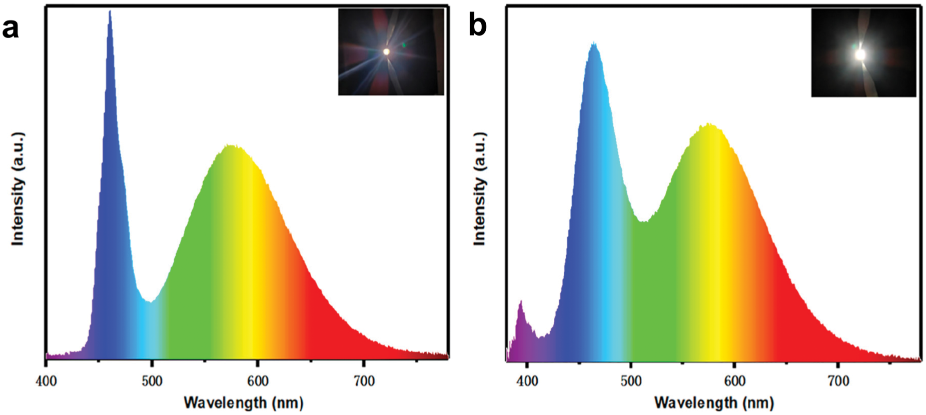

Figure 4.4: PL spectra of fabricated (a) WLED1 (blue chip and yellow emission $Cs_2Hf_{0.99}Te_{0.01}Cl_6$) and (b) WLED2 (UV chip, blue phosphor, and $Cs_2Hf_{0.99}Te_{0.01}Cl_6$) (reprinted with permission from ref. [33], Copyright 2021, the American Chemical Society).

Other photoluminescent light-emitting devices have also been investigated, such as NIR light-emitting device (NILED). $Cs_2AgIn_{0.9}Cl_6$: $0.1Cr^{3+}$ phosphor was coated on a 405 nm chip to fabricate NILED [78]. As for electroluminescent light-emitting device, $Cs_3Cu_2I_5$ NCs have been prepared to form an electroluminescent light-emitting device with the device heterostructure comprising Al/LiF/TPBi/$Cs_3Cu_2I_5$ NCs/NiO/ITO [93]. The as-prepared device possesses the highest EQE of around 1.12%, almost reaching the optimal performance in lead halide perovskite or perovskite derivative-based blue light-emitting devices. Additionally, excellent operation stability is realized because the electroluminescence performance could be restored to the original state after 1 h relaxation and the half-lifetime could reach 108 h.

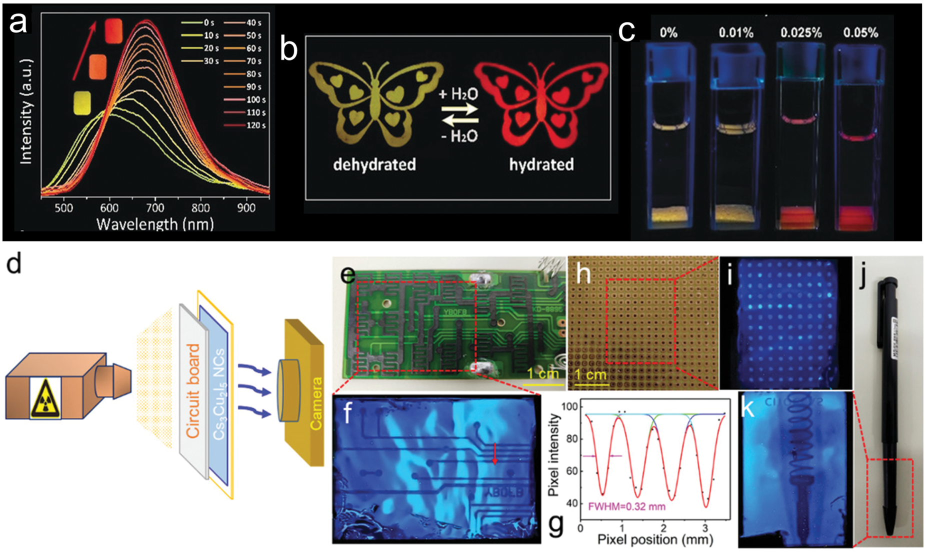

Figure 4.5: (a) PL spectra collected immediately after exposing the dehydrated to the air (80% humidity). (b) Photographs of etched butterfly patterns prepared by the hydrated and dehydrated materials under UV light showing the PL switching. (c) The dehydrated mixture in tetrahydrofuran solutions containing different amounts of water (0–0.05% v/v) (reprinted with permission from ref. [70], Copyright 2019, Wiley-VCH). (d) View of the prototype projection system for X-ray imaging, where the objects from left to right are an X-ray source, a circuit board, $Cs_3Cu_2I_5$ NC scintillators, and a smartphone camera. (e) The photograph of a circuit board under daylight. (f) X-ray image of a circuit board. (g) Point spread function (red arrow in (f)) of the intensity profile is fitted with Gaussian function, and the FWHM is obtained as the spatial resolution. (h) The photograph of a universal board under daylight. (i) X-ray image of a universal board. (j) The photograph of a ballpoint pen with an encapsulated metallic spring. (k) X-ray image of a ballpoint pen with an encapsulated metallic spring (reprinted with permission from ref. [94], Copyright 2020, Wiley-VCH).

The luminescence property endows some materials with the probability of probing and sensing. Changes or quenches in luminescence will occur under a certain circumstance (temperature difference, atmosphere change, etc.), thus leading to an “ON/OFF” mode or luminescent peak shifting. $Cs_2InBr_5{\cdot}H_2O$ with red emission was reported to possess luminescent probing property under water condition [70]. Heating $Cs_2InBr_5{\cdot}H_2O$ to around 125 °C would lead to the dehydration of $Cs_2InBr_5{\cdot}H_2O$, whose PL turns to yellow one. When the dehydrated mixture was put under 80% humidity, the yellow emission can be reversely turned back to red emission (Figure 4.5a,b). Such material also possesses remarkable recyclability with no obvious change in PL intensity after 20 cycles. Water detection test was performed by adding water into the tetrahydrofuran solution containing dehydrated material (Figure 4.5c). It can be noticed that the different content of water will lead to different PL property. The more water is added, the clearer the red emission is observed. As for temperature sensor, Cs_4SnBr_6 was reported to possess the appropriate sensitivity from −30 to 40 °C considering its temperature-dependent PL lifetimes when compared to other tin(II) halides of $[C(NH_2)_3]_2SnBr_4$ and $(C_4N_2H_{14}I)_4SnI_6$ [95]. The lifetime of Cs_4SnBr_6 undergoes an apparent decrease from −30 to 40 °C, during which the lifetime is still capable of being detected. Thus, high-resolution remote thermometry and thermography can be realized by using Cs_4SnBr_6. Moreover, traditional time-resolved measurement techniques suffer from the drawback of single channel detectors. Therefore, a frequency-domain time-resolved technique named as time-of-flight fluorescence lifetime imaging was chosen for thermographic imaging, which leads to a higher lateral thermographic resolution.

Recently, the emerging application of MHP and their derivatives in scintillation has received great attention for luminescent materials. These materials could absorb high-energy rays or particles and yield visible or NIR emission. One important characteristic for scintillator is that heavy atom plays a significant role in absorbing rays. The main scintillators focus on copper(I)-based MHP derivatives. For instance, $Cs_3Cu_2I_5$ and $Cs_3Cu_2I_5$: Tl^+ are reported in possessing scintillation [64]. Rb_2CuX_3 (X = Cl and Br) has also been reported by Tang group with scintillation property [66, 67]. In 2020, Zhang's group obtained $Cs_3Cu_2I_5$ NCs, which possess high PLQY of 73.7% and exhibit strong scintillation under X-ray irradiation [94]. The $Cs_3Cu_2I_5$ NCs can be applied to the X-ray imaging (Figure 4.5d–j).

4.7 Conclusion and outlook

Lead-free all-inorganic MHPs and MHP derivatives have been reported to possess various luminescence properties and emerging photonic applications. In this chapter, we summarized different types for MHPs and MHP derivatives and explicated the syntheses, luminescent property, mechanism, and their applications. Compared with the luminescence from MHP or MHP derivative hosts themselves, we find that the emission from doped materials receives more attention. The doping techniques have introduced luminescent ions with different luminescent mechanisms into host to bring various materials with different emissions. Moreover, the strategies of tailoring of dimensionality, hybridization of halogens, and change in A-site ions further enrich the family of MHPs and MHP derivatives with colorful and tunable luminescence. Finally, the applications are also displayed in this chapter. Up to now, MHPs and MHP derivatives have been utilized to integrate into optoelectronic devices in the fields of light-emitting devices, luminescent sensors, thermometers, and scintillations.

However, some challenges still need to be fixed. (1) The specific relationships between luminescence and the chemical component of MHPs and MHP derivatives remain unsolved. (2) The application in scintillation, sensors, and thermometers requires more exploration. Up to now, the appropriate candidates of MHPs and MHP derivatives in such fields still need to be explored and investigated. (3) As for the fabrication of WLED, a full spectrum emission is still in vacancy. Future study should also focus on the single component material with full-spectrum white emission.

References

[1] J.-C. Jin, N.-N. Shen, Z.-P. Wang, Y.-C. Peng, X.-Y. Huang, Coordin. Chem. Rev. 448 (2021) 214185.
[2] V.M. Goldschmidt, Naturwissenschaften 14 (1926) 477–485.
[3] M. Lyu, J.-H. Yun, P. Chen, M. Hao, L. Wang, Adv. Energy Mater. 7 (2017) 1602512.
[4] Z. Xiao, Z. Song, Y. Yan, Adv. Mater. 31 (2019) 1803792.
[5] T. Xuan, R.-J. Xie, Chem. Eng. J. 393 (2020) 124757.
[6] J. Chen, Z. Luo, Y. Fu, X. Wang, K.J. Czech, S. Shen, L. Guo, J.C. Wright, A. Pan, S. Jin, ACS Energy Lett. 4 (2019) 1045–1052.
[7] H. Arfin, A.S. Kshirsagar, J. Kaur, B. Mondal, Z. Xia, S. Chakraborty, A. Nag, Chem. Mater. 32 (2020) 10255–10267.
[8] Y. Jing, Y. Liu, M. Li, Z. Xia, Adv. Opt. Mater. 9 (2021) 2002213.
[9] S.J. Clark, C.D. Flint, J.D. Donaldson, J. Phys. Chem. Solids 42 (1981) 133–135.
[10] A.S. Voloshinovskii, S.V. Myagkota, N.S. Pidzyrailo, M.V. Tokarivskii, J. Appl. Spectrosc. 60 (1994) 226–228.
[11] S.V. Myagkota, P.V. Savchin, A.S. Voloshinovskii, T.M. Demkiv, Y.V. Boiko, R.S. Vus, L.S. Demkiv, Phys. Solid State 50 (2008) 1473–1476.
[12] H. Mu, F. Hu, R. Wang, J. Jia, S. Xiao, J. Lumin. 226 (2020) 117493.
[13] Z.Y. Wu, J.-H. Zhuang, Y.-T. Lin, Y.-H. Chou, P.C. Wu, C.-L. Wu, P. Chen, H.-C. Hsu, ACS Nano 15 (2021) 19613–19620.
[14] Z. Wu, Q. Zhang, B. Li, Z. Shi, K. Xu, Y. Chen, Z. Ning, Q. Mi, Chem. Mater. 31 (2019) 4999–5004.
[15] G.L. McPherson, K. Talluto, R.A. Auerbach, Solid State Commun. 43 (1982) 817–819.
[16] R. Valiente, O.S. Wenger, H.U. Gudel, Chem. Phys. Lett. 320 (2000) 639–644.
[17] R. Valiente, O.S. Wenger, H.U. Gudel, J. Chem. Phys. 116 (2002) 5196–5204.
[18] V.N. Vishnevskii, N.S. Pidzyrailo, Z.A. Khapko, Sov. Phys. Solid State (USA) 26 (1984) 322–324.
[19] N.S. Pidzyrailo, Z.A. Khapko, Ukrayins'kyi Fizychnyi Zhurnal 30 (1985) 189–192.
[20] M.V. Kutsyk, M.S. Pidzyrailo, J. Lumin. 79 (1998) 135–141.
[21] S. Garcia-Revilla, P. Gerner, O.S. Wenger, H.U. Gudel, R. Valiente, Chem. Phys. Lett. 401 (2005) 492–496.
[22] M. Sobczyk, J. Drozdznski, Mater. Lett. 61 (2007) 2319–2321.
[23] D.N. Vtyurina, I.A. Kaurova, G.M. Kuz'micheva, V.B. Rybakov, D.Y. Chernyshov, E.V. Khramov, S.V. Firstov, V.N. Korchak, J. Alloy. Compd. 803 (2019) 912–921.
[24] A. Ohnishi, M. Kitaura, M. Itoh, M. Sasaki, J. Phys. Soc. Jpn. 81 (2012) 114704.
[25] X. Liu, C. Peng, L. Zhang, D. Guo, Y. Pan, J. Mater. Chem. C 10 (2022) 204–209.
[26] B. Su, M. Li, E. Song, Z. Xia, Adv. Funct. Mater. 31 (2021) 2105316.
[27] P. Cheng, L. Feng, Y. Liu, D. Zheng, Y. Sang, W. Zhao, Y. Yang, S. Yang, D. Wei, G. Wang, K. Han, Angew. Chem. Int. Ed. 59 (2020) 21414–21418.

[28] X. Wang, Q. Shen, Y. Chen, N. Ali, Z. Ren, G. Bi, H. Wu, Nanoscale 13 (2021) 15285–15291.

[29] H. Shankar, S. Ghosh, P. Kar, J. Alloy. Compd. 844 (2020) 156148.

[30] X. Li, S. Wang, S. Zhao, L. Li, Y. Li, B. Zhao, Y. Shen, Z. Wu, P. Shan, J. Luo, Chem. Eur. J. 24 (2018) 9243–9246.

[31] F. Locardi, M. Samoli, A. Martinelli, O. Erdem, D.V. Magalhaes, S. Bals, Z. Hens, ACS Nano 15 (2021) 17729–17737.

[32] T.V. Sedakova, A.G. Mirochnik, Opt. Spectrosc. 120 (2016) 268–273.

[33] R. Liu, J. Yang, D. Zhao, W. Liu, G. Li, W. Yan, W. Zhang, Inorg. Chem. 60 (2021) 17878–17888.

[34] B. Chen, Y. Guo, Y. Wang, Z. Liu, Q. Wei, S. Wang, A.L. Rogach, G. Xing, P. Shi, F. Wang, J. Am. Chem. Soc. 143 (2021) 17599–17606.

[35] R. Liu, W. Zhang, G. Li, W. Liu, Inorg. Chem. Front. 8 (2021) 4035–4043.

[36] Z. Li, Z. Rao, Q. Li, L. Zhou, X. Zhao, X. Gong, Adv. Opt. Mater. 9 (2021) 2100804.

[37] Z. Tan, J. Li, C. Zhang, Z. Li, Q. Hu, Z. Xiao, T. Kamiya, H. Hosono, G. Niu, E. Lifshitz, Y. Cheng, J. Tang, Adv. Funct. Mater. 28 (2018) 1801131.

[38] J. Li, Z. Tan, M. Hu, C. Chen, J. Luo, S. Li, L. Gao, Z. Xiao, G. Niu, J. Tang, Front. Optoelectron. 12 (2019) 352–364.

[39] Y. Jing, Y. Liu, J. Zhao, Z. Xia, J. Phys. Chem. Lett. 10 (2019) 7439–7444.

[40] Z. Tan, Y. Chu, J. Chen, J. Li, G. Ji, G. Niu, L. Gao, Z. Xiao, J. Tang, Adv. Mater. 32 (2020) 2002443.

[41] Y. Zhong, Y.-E. Huang, T. Deng, Y.-T. Lin, X.-Y. Huang, Z.-H. Deng, K.-Z. Du, Inorg. Chem. 60 (2021) 17357–17363.

[42] W. Zhang, W. Zheng, L. Li, P. Huang, Z. Gong, Z. Zhou, J. Sun, Y. Yu, X. Chen, Angew. Chem. Int. Ed. 61 (2022) e202116085.

[43] J.-H. Chang, T. Doert, M. Ruck, Z. Anorg. Allg. Chem. 642 (2016) 736–748.

[44] K.M. McCall, C.C. Stoumpos, S.S. Kostina, M.G. Kanatzidis, B.W. Wessels, Chem. Mater. 29 (2017) 4129–4145.

[45] J. Pal, S. Manna, A. Mondal, S. Das, K.V. Adarsh, A. Nag, Angew. Chem. Int. Ed. 56 (2017) 14187–14191.

[46] J. Zhang, Y. Yang, H. Deng, U. Farooq, X. Yang, J. Khan, J. Tang, H. Song, ACS Nano 11 (2017) 9294–9302.

[47] Z. Ma, Z. Shi, D. Yang, F. Zhang, S. Li, L. Wang, D. Wu, Y. Zhang, G. Na, L. Zhang, X. Li, Y. Zhang, C. Shan, ACS Energy Lett. 5 (2019) 385–394.

[48] M. Leng, Y. Yang, K. Zeng, Z. Chen, Z. Tan, S. Li, J. Li, B. Xu, D. Li, M.P. Hautzinger, Y. Fu, T. Zhai, L. Xu, G. Niu, S. Jin, J. Tang, Adv. Funct. Mater. 28 (2018) 1704446.

[49] K.M. McCall, C.C. Stoumpos, O.Y. Kontsevoi, G.C.B. Alexander, B.W. Wessels, M.G. Kanatzidis, Chem. Mater. 31 (2019) 2644–2650.

[50] J.-L. Xie, Z.-Q. Huang, B. Wang, W.-J. Chen, W.-X. Lu, X. Liu, J.-L. Song, Nanoscale 11 (2019) 6719–6726.

[51] B.M. Benin, K.M. McCall, M. Worle, V. Morad, M. Aebli, S. Yakunin, Y. Shynkarenko, M.V. Kovalenko, Angew. Chem. Int. Ed. 59 (2020) 14490–14497.

[52] K.M. McCall, B.M. Benin, M. Wörle, T. Vonderach, D. Günther, M.V. Kovalenko, Helv. Chim. Acta 104 (2020) e2000206.

[53] V.V. Eremenko, V.A. Karachevtsev, A.R. Kazachkov, V.V. Shapiro, V.V. Slavin, Solid State Commun. 87 (1993) 1027–1029.

[54] V.V. Eremenko, V.A. Karachevtsev, I.S. Kachur, N.Y. Nedbailo, V.G. Piryatinskaya, V.V. Slavin, V.V. Shapiro, J. Lumin. 92 (2000) 35–42.

[55] V.V. Eremenko, V.I. Fomin, V.S. Kumosov, Low Temp. Phys. 26 (2000) 479–483.

[56] H. Xiao, P. Dang, X. Yun, G. Li, Y. Wei, X. Xiao, Y. Zhao, M.S. Molokeev, Z. Cheng, J. Lin, Angew. Chem. Int. Ed. 60 (2020) 3699–3707.

[57] Q. Kong, B. Yang, J. Chen, R. Zhang, S. Liu, D. Zheng, H. Zhang, Q. Liu, Y. Wang, K. Han, Angew. Chem. Int. Ed. 60 (2021) 19653–19659.

[58] Y.P. Lin, L.C. Rao, M.J. Zhao, X.Y. Huang, K.Z. Du, Dalton Trans. 50 (2021) 2001–2006.

[59] B. Su, M.S. Molokeev, Z. Xia, J. Mater. Chem. C 7 (2019) 11220–11226.

[60] T. Jun, K. Sim, S. Iimura, M. Sasase, H. Kamioka, J. Kim, H. Hosono, Adv. Mater. 30 (2018) 6.

[61] R.C. Lin, Q.L. Guo, Q. Zhu, Y.M. Zhu, W. Zheng, F. Huang, Adv. Mater. 31 (2019) 7.

[62] P. Cheng, L. Sun, L. Feng, S. Yang, Y. Yang, D. Zheng, Y. Zhao, Y. Sang, R. Zhang, D. Wei, W. Deng, K. Han, Angew. Chem. Int. Ed. 58 (2019) 16087–16091.

[63] Q. Li, Z. Chen, B. Yang, L. Tan, B. Xu, J. Han, Y. Zhao, J. Tang, Z. Quan, J. Am. Chem. Soc. 142 (2020) 1786–1791.

[64] D. Yuan, ACS Appl. Mater. Interfaces 12 (2020) 38333–38340.

[65] T.D. Creason, A. Yangui, R. Roccanova, A. Strom, M.-H. Du, B. Saparov, Adv. Opt. Mater. 8 (2020) 1901338.

[66] X. Zhao, G. Niu, J. Zhu, B. Yang, J.-H. Yuan, S. Li, W. Gao, Q. Hu, L. Yin, K.-H. Xue, E. Lifshitz, X. Miao, J. Tang, J. Phys. Chem. Lett. 11 (2020) 1873–1880.

[67] B. Yang, L. Yin, G. Niu, J.-H. Yuan, K.-H. Xue, Z. Tan, X.-S. Miao, M. Niu, X. Du, H. Song, E. Lifshitz, J. Tang, Adv. Mater. 31 (2019) 1904711.

[68] C. Yang, F. Guo, Y. Zhang, X. Zhong, J. Feng, N. Wang, J. Wang, Chem. Asian J. 16 (2021) 1619–1625.

[69] P. Han, C. Luo, S. Yang, Y. Yang, W. Deng, K. Han, Angew. Chem. Int. Ed. 59 (2020) 12709–12713.

[70] L. Zhou, J.F. Liao, Z.G. Huang, J.H. Wei, X.D. Wang, W.G. Li, H.Y. Chen, D.B. Kuang, C.Y. Su, Angew. Chem. Int. Ed. 58 (2019) 5277–5281.

[71] J.D. Majher, M.B. Gray, T. Liu, N.P. Holzapfel, P.M. Woodward, Inorg. Chem. 59 (2020) 14478–14485.

[72] Y. Jing, Y. Liu, X. Jiang, M.S. Molokeev, Z. Lin, Z. Xia, Chem. Mater. 32 (2020) 5327–5334.

[73] J.-H. Wei, J.-B. Luo, J.-F. Liao, W.-T. Ou, D.-B. Kuang, Sci. China Mater. 65 (2021) 764–772.

[74] C. Zhang, X. Feng, Q. Song, C. Zhou, L. Peng, J. Chen, X. Liu, H. Chen, J. Lin, X. Chen, J. Phys. Chem. Lett. 12 (2021) 7928–7934.

[75] J. Luo, X. Wang, S. Li, J. Liu, Y. Guo, G. Niu, L. Yao, Y. Fu, L. Gao, Q. Dong, C. Zhao, M. Leng, F. Ma, W. Liang, L. Wang, S. Jin, J. Han, L. Zhang, J. Etheridge, J. Wang, Y. Yan, E.H. Sargent, J. Tang, Nature 563 (2018) 541–545.

[76] Y. Liu, A. Nag, L. Manna, Z. Xia, Angew. Chem. Int. Ed. 60 (2021) 11592–11603.

[77] A. Noculak, V. Morad, K.M. McCall, S. Yakunin, Y. Shynkarenko, M. Worle, M.V. Kovalenko, Chem. Mater. 32 (2020) 5118–5124.

[78] F. Zhao, Z. Song, J. Zhao, Q. Liu, Inorg. Chem. Front. 6 (2019) 3621–3628.

[79] P. Han, X. Mao, S. Yang, F. Zhang, B. Yang, D. Wei, W. Deng, K. Han, Angew. Chem. Int. Ed. 58 (2019) 17231–17235.

[80] G. Volonakis, M.R. Filip, A.A. Haghighirad, N. Sakai, B. Wenger, H.J. Snaith, F. Giustino, J. Phys. Chem. Lett. 7 (2016) 1254–1259.

[81] K. Du, W. Meng, X. Wang, Y. Yan, D.B. Mitzi, Angew. Chem. Int. Ed. 56 (2017) 1–6.

[82] J. Jiang, G. Niu, L. Sui, X. Wang, Y. Zhang, L. Che, G. Wu, K. Yuan, X. Yang, J. Phys. Chem. Lett. 12 (2021) 7285–7292.

[83] R. Zhang, Z. Wang, X. Xu, X. Mao, J. Xiong, Y. Yang, K. Han, Adv. Opt. Mater. 9 (2021) 2100689.

[84] B. Vargas, R. Torres-Cadena, D.T. Reyes-Castillo, J. Rodríguez-Hernández, M. Gembicky, E. Menéndez-Proupin, D. Solis-Ibarra, Chem. Mater. 32 (2019) 424–429.

[85] B. Vargas, E. Coutiño-Gonzalez, O. Ovalle-Encinia, C. Sánchez-Aké, D. Solis-Ibarra, J. Phys. Chem. Lett. 11 (2020) 10362–10367.

[86] S. Li, J. Luo, J. Liu, J. Tang, J. Phys. Chem. Lett. 10 (2019) 1999–2007.

[87] M.D. Smith, H.I. Karunadasa, Acc. Chem. Res. 51 (2018) 619–627.

[88] M. Li, Z. Xia, Chem. Soc. Rev. 50 (2021) 2626–2662.

[89] A. Vogler, A. Paukner, H. Kunkely, Coordin. Chem. Rev. 97 (1990) 285–297.

[90] K.M. McCall, V. Morad, B.M. Benin, M.V. Kovalenko, ACS Mater. Lett. 2 (2020) 1218–1232.

[91] A. Vogler, H. Nikol, Comments Inorg. Chem. 14 (1993) 245–261.

[92] P. Tao, S.J. Liu, W.Y. Wong, Adv. Opt. Mater 8 (2020) 2000985.

[93] L. Wang, Z. Shi, Z. Ma, D. Yang, F. Zhang, X. Ji, M. Wang, X. Chen, G. Na, S. Chen, D. Wu, Y. Zhang, X. Li, L. Zhang, C. Shan, Nano Lett. 20 (2020) 3568–3576.

[94] L. Lian, M. Zheng, W. Zhang, L. Yin, X. Du, P. Zhang, X. Zhang, J. Gao, D. Zhang, L. Gao, G. Niu, H. Song, R. Chen, X. Lan, J. Tang, J. Zhang, Adv. Sci. 7 (2020) 2000195.

[95] S. Yakunin, B.M. Benin, Y. Shynkarenko, O. Nazarenko, M.I. Bodnarchuk, D.N. Dirin, C. Hofer, S. Cattaneo, M.V. Kovalenko, Nat. Mater. 18 (2019) 846–852.

Annapureddy Siva Sesha Reddy, Marek Kostrzewa, Nalluri Purnachand,
Gnanamuthu Sahaya Baskaran, Nutalapati Venkatramaiah,
Vandana Ravi Kumar, Nalluri Veeraiah

Chapter 5

Influence of Au^0 particles on luminescence efficiency of Ho^{3+} ions in $PbO–B_2O_3–SeO_2$ glass ceramics: the role of free volume defects – exploration using PALS studies

5.1 Introduction

Selenium oxide (SeO_2) is an interesting chalcogenide oxide. It involves in glass formation with isolated selenite $[SeO_3]^{2-}$ as well as selenate $[SeO_4{}^{2-}]$ structural units. The selenite units occupy modifying positions and deaugment the host glass network by creating dangling bonds and free oxygen ions; due to these reasons, a decrement in the phonon losses that facilitates the improvement of luminescence efficiency (LE) of dopant RE (rare-earth) ions is expected [1]. The selenate groups, however, do participate in the glass formation and increase the glass-forming ability. In $[SeO_3]^{2-}$ units, two of the 4*p* electrons link with covalent bonding while the third *p* orbital consists of a couple of electrons that can easily be dislodged. For this reason, these structural groups do possess high electronic polarizability and as a result the materials containing SeO_2 do find applications in nonlinear optical and several semiconducting devices [2].

With the addition of lead oxide to SeO_2 glass system, the density as well as refractive index are expected to be enhanced and pave the way to increase the LE of the lasing dopant RE ions [3, 4]. A small content of borate was also added to this glass composition in order to improve glass formation of lead selenate since SeO_2 is an incipient glass former.

Among different RE ions, Ho^{3+} is an attractive luminescent ion; its emission spectra consist of sharp emission peaks spreading over a wide wavelength region with a large number of excited states. Laser action of Ho^{3+} ions is expected to be due to multiple processes of cross-relaxation (with self-upconversion) [5–7]. Because of such intense PL emission, the Ho^{3+}-doped glasses do find potential applications, to mention a few, for the storage of optical data, as optical sensors, in 3D display systems, and so on. As mentioned earlier, holmium ions do have a large number of intermediate levels (which normally do not get affected by multiple phonon decay process) and hence facilitate multilasing transition probabilities which spread over a broad spectral region. Additionally, the $^5I_7$ energy of holmium ions emits strong near-infrared (NIR) band at nearly 2.0 μm by de-excitation to $^5I_8$ energy state. The $^5I_7$ energy level is a long-lasting

https://doi.org/10.1515/9783110607871-005

energy state with larger stimulated σ^E. For this reason, this emission of Ho^{3+} mixed glasses is considered useful for chromospheres of NIR lasers. Despite the fact that a considerable investigation on luminescence characteristics of Ho^{3+} ions in conventional glass systems was available [5–7], such studies on the fascinating incipient glass systems like selenium oxide were hardly investigated.

By incorporating small concentrations of noble metal ions/metallic particles (MPs), for example, Au^0 along with Ho^{3+} ions into the PBS glass system, it is possible for the enhancement of LE of green emission of Ho^{3+} ions. This is possible because the Au^0 MPs also exhibit luminescence in these regions with significant intensity. Due to the interaction of noble metal ions in glasses with electromagnetic (e.m.) waves, these ions form clusters and emit radiation [8–10]. To be precise, the e.m. beam stimulates the coupled oscillations of outer most electrons of gold metallic particles, inculcates surface plasmon resonance (SPR), and produces E-field around Au ions [11]. This electric field causes enhancement of luminescence in the spectral range of 400–600 nm. To be specific, the Au^0 particles sensitize the RE ions and increase their luminescence emission by transferring energy. A considerable number of studies were already reported with Au ions as sensitizers that activate RE ions in different glass systems [9, 12].

In the current investigation, a small quantity of gold oxide (≤0.1 mol%) is chosen to sensitize Ho^{3+} ions. Au_2O_3 is an extremely unstable compound and fractures into divalent and monovalent oxides and also into metallic particles during synthesis and annealing of the glasses. For obtaining a considerable concentration of Au^0 MPs (that are predicted to exhibit PL in the visible range as mentioned earlier) by reducing Au^{3+} ions (according to the reduction: $Au^{3+}\ (5d^8) \rightarrow Au^{2+}(5d^9) \rightarrow Au^{+}(5d^{10}) \rightarrow Au^0$), in this study, the fabricated glasses were heated at T_c (temperature of crystallization) for about 24 h. This type of heat treatment causes the conversion of Au^{3+} ions into Au^0 MPS and further paves the way for the creation of $Au_2(SeO_3)_3$ and $Au_2(SeO_3)_2(SeO_4)$ anisotropic crystallites [13, 14] along with Au^0 MPs in these samples. The presence of such crystalline phases is expected to have a strong bearing on LE of the doped Ho^{3+} ions.

As mentioned earlier, the selenite, namely, $[SeO_3]^{2-}$ ions, and also Au^0 MPs take part in modifying positions and introduce several kinds of defects like voids (of nano-size) and floating bonds in the glass matrix. Such defects will have strong bearing on PL efficiency of dopant RE ions. Hence, assessment (size, concentration, etc.) of such defects is highly important for understanding the increase in PL output of doped Ho^{3+} ions.

To assess the information on exceptionally small point imperfections in the glass matrix we have used a fascinating technique known as positron annihilation lifetime spectroscopy (PALS). It is a highly subtle method to assess the volume of such imperfections and also f_v fraction trapped in the bulk sample up to the scale of nanodimensions [15–21]. The details of this technique can be found in our earlier report [19].

It is possible to estimate τ_3 (the third component of decay time) by deconvoluting the decay profiles of the positron in the samples. With this τ_3 value, radius (R) of free cavities was estimated in these samples with the expression [22, 9]:

$$\tau_3 = \frac{1}{2}\left[1 - \frac{R}{R_0} + \frac{1}{2\pi}\sin\left(\frac{2\pi R}{R_0}\right)\right]^{-1} \tag{5.1}$$

In eq. (5.1), $R_0 = R + \Delta R$ ($\Delta R = 1.66$ Å) is estimated by fitting these τ_3 values (evaluated for a sample containing voids of known dimensions). Compared to τ_1 and τ_2, τ_3 can be estimated precisely because it is larger with respect to τ_1 and τ_2. With I_3 and the free void radius R, f_V (free volume fraction) trapped in the samples can be calculated using the equation:

$$f_V = A \cdot I_3(\%) \cdot \left(\frac{4}{3}\pi R^3\right) \tag{5.2}$$

The objective of this investigation is to compute the size of imperfections and f_v (space stuck in titled samples) in terms of Au_2O_3 content and to investigate their impact on the PL efficacy of holmium ions in $PbO–B_2O_3–SeO_2$ glass ceramics. Recently, we have reported the results of our studies on the bearing of Au^0 MPs on PL efficacy of holmium ions in the lead boroselenate glass (PBSG) system [10]. This report is, however, devoted to the studies on the effect of nanosized defects estimated by PALS studies on emission characteristics of PBSG ceramics.

5.2 Experimental

Within the approximate region of glass formation [9], the $40PbO–10B_2O_3–(49.5–x)SeO_2–0.5Ho_2O_3{:}xAu_2O_3$ ($x = 0$ (HA_0), 0.025 (HA_{25}), 0.050 (HA_{50}), 0.075 (HA_{75}), and 0.1 (HA_{100}) mol%) composition was selected for this investigation. The samples were synthesized by melting the appropriate amounts of chemicals in the range of 1,000–1,050 °C for about 40 min. The fabricated samples were heat-treated for 24 h at T_c (about 630 °C evaluated from thermal analysis). Other information regarding the fabrication methods and characterization of these glasses (X-ray diffraction (XRD) and scanning electron microscopy (SEM)) were reported earlier [9, 10].

X-ray photoelectron spectra (XPS) were recorded on PHI 5000 Versa Probe ULVAC Al Kα source of X-rays. Electron emission angle was 45° and the analyzed area was 100 μm. The stage was enclosed in the double-sided carbon tape and the sample was kept on this tape and at the entry point of the compartment for 12 h. Spectra were recorded with C 1*s* peak (284.6 eV) as reference [23–25]. The details of recording transmission electron microscopy (TEM) images were reported in ref. [9].

The optical absorption spectra were recorded on a JASCO V–670 spectrometer and PL spectra on Horiba Jobin-Yvon Fluorolog-3 spectrophotometer as reported in ref. [9].

For recording positron annihilation lifetime (PAL) spectra, ^{22}Na isotope (100 kBq) was used as a positron source. The source was draped with Kapton foil ($t = 12.5$ μm).

The lifetime (τ) is estimated to a precession of 230 ps at ambient conditions, with a ^{60}Co source prompt curve. These spectral profiles were recorded using Ortec PAL system. γ-Rays were captured using two XP 2020Q PM tubes (which were coupled by barium fluoride scintillators, ∅ 2.54 cm, 1.0 cm). The sensors of these tubes were arranged such that the first one was ON at 1,274.6 keV, whereas the second one was ON at 511.0 keV.

Nearly 10^6 annihilations were captured for calculating τ and I of decay components. Losses due to absorption of Kapton wafer were assessed as approximately 12%. LT 9.0 program was used to analyze raw PAL spectra, and the three intensity components I_1, I_2, and I_3 [26] were obtained by deconvolution. Using these exponentials, the corresponding components of lifetimes τ_1, τ_2, and τ_3 were determined.

5.3 Results and discussion

The pure glasses or glass ceramics (free from Au_2O_3 and Ho_2O_3) were observed to be colorless. As Au_2O_3 was increased gradually, the glasses were observed to turn slowly into ruby color (this color is predicted to be of Au^0 nano-MPs). Obviously, the observed change of color of the glass ceramics indicates the reduction of Au^{3+} ions into Au^0 MPs [12, 27]. Se^{4+} ions are expected to act as reductants for this reduction since the net potential variation necessary for selenium oxide-based amorphous systems is ~0.348 eV only [28, 29]. Hence, it is possible for such reduction during the course of preparation of glass ceramics.

XRD patterns of as-prepared samples exhibited virtually no crystalline peaks. It indicates the glassy nature of these samples. Patterns of heat-treated glasses, however, indicated two narrow peaks at 29.9° and 44.0° due to the reflections from $Au_2(SeO_3)_3$ crystalline phase and Au^0 MPs, respectively [13, 14, 28]. With an increase in Au_2O_3 concentration, a peak connected with the reflections from Au^0 MPs exhibited an increasing tendency. Such an increase confirms the hike in the concentration of Au^0 MPs as Au_2O_3 concentration is increased. As a whole, variations in the intensity of both peaks in the diffractograms with Au_2O_3 concentration suggest possible increased formation of Au^0 particles with an increase of Au_2O_3 concentration in the presence of SeO_2 in the glass ceramic. Figure 5.1 shows the diffractogram of HA_{50} glass ceramic, and in the inset, the intensity of the peak connected with Au^0 MPs versus concentration of Au_2O_3 was presented.

For having further evidence of entrenchment of gold MPs in these glasses, the XPS was registered with C 1*s* as a reference peak; spectra showed a pair of peaks at 85.8 and 89.6 eV (representing the binding energy (B.E.) in the 4*f* region of Au^{3+} ions) and yet two more peaks were detected at 84.0 and 87.6 eV due to Au^0 MPs [30, 31]. In Figure 5.2, the spectrum of HA_{50} glass was shown, and in its inset, the intensities of

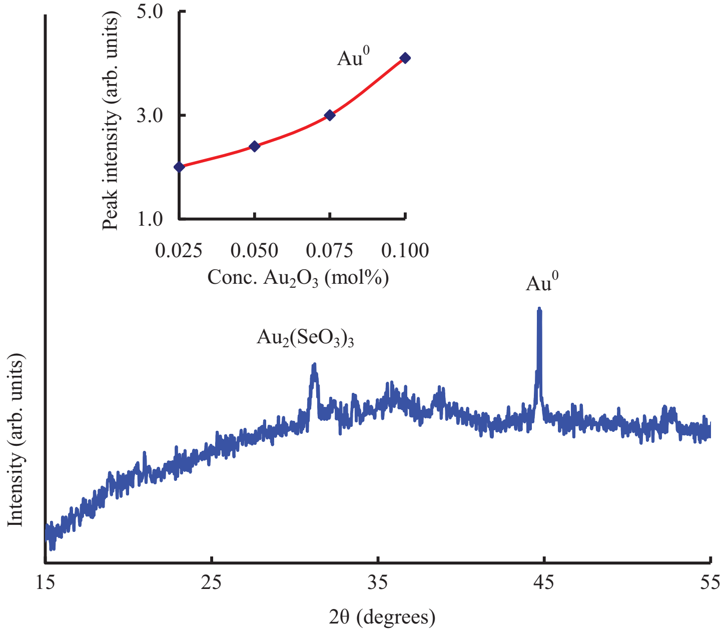

Figure 5.1: Diffraction pattern of HA_{50} glass ceramic. In the inset, the peak intensity of Au^0 peak versus Au_2O_3 content is plotted.

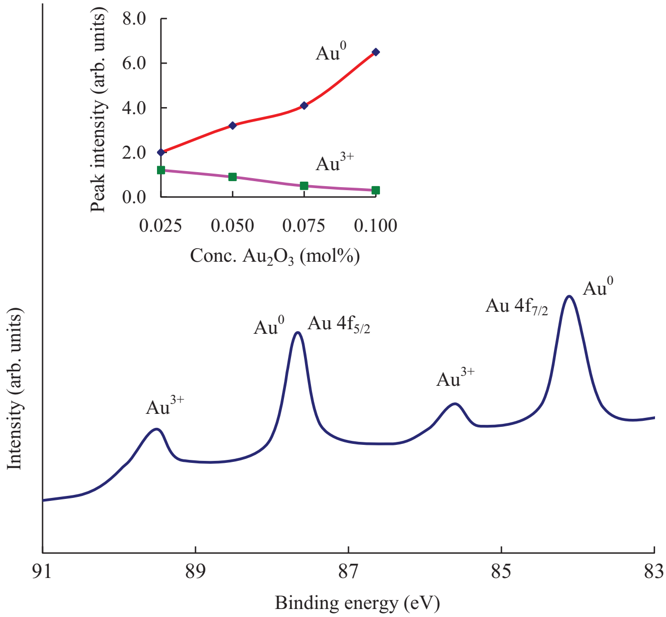

Figure 5.2: XPS of HA_{50} sample. In the inset, intensities of Au^{3+} and Au^0 peaks versus Au_2O_3 content were plotted.

84.0 eV (Au^0 MPs) and 85.8 eV (of Au^{3+} ions) peaks were plotted as a function of Au_2O_3 concentration. The plots suggested an increase in the concentration of Au^0 MPs and a decrease in the concentration of Au^{3+} ions with an increase of Au_2O_3 content.

In Figure 5.3(a), we have presented the SEM photograph of the sample, namely, HA_{50}. The SEM photograph of the as-prepared glass did not indicate any crystalline behavior. The SEM picture of the heated samples shows embedment of tiny crystallites (with growing sizes ranging from 0.1 to 0.5 µm) in residual phase of glass. Pictures of other glasses were found to be similar. The comparison, however, showed a gradual hike in the fraction of the crystallites with enlarged size as Au_2O_3 concentration was raised. The elemental composition of the samples was verified with EDS. EDS for HA_{50} (Figure 5.3(b)) indicated that all the expected elements were intact in the glass ceramic.

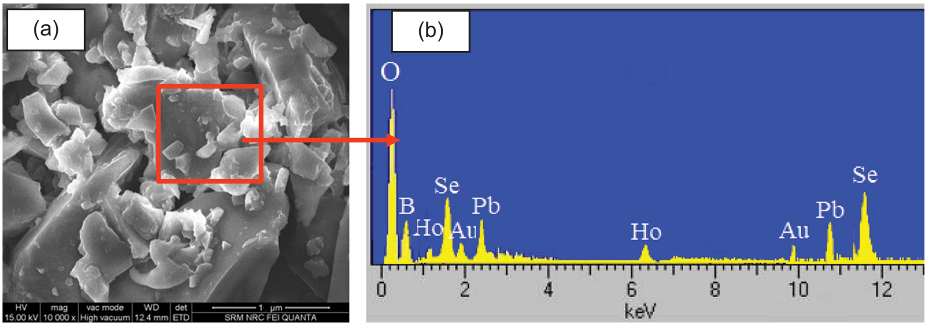

Figure 5.3: (a) SEM photograph of the sample HA_{50} and (b) EDS spectrum.

For assessing information on entrenched f_v defects in glass ceramics, TEM photographs for HA_{25} and HA_{100} were recorded with different magnifications. The images (Figure 5.4) suggested amorphous like phase segregates with insertions of voids (of nm scale) amid crystalline grains.

PAL decay profiles of HA_{25} and HA_{100} samples were presented in Figure 5.5. We have decomposed the profiles into three decay curves by least-square fitting. Values of I and τ components obtained were presented in Table 5.1.

In these components, I_1 and I_2 (which normally arise due to the contributions from the edge dislocation and vacancies) were observed to be dominant (Figure 5.6(a) and (b)). By analyzing these components, one cannot obtain quantitative information on nanosized defects entrenched in the material; however, such analysis gives some averaged information about the imperfections.

Hence, the emphasis was made on the third component, which gives the quantitative information on the dimensions of the free cavities (in which annihilation took place) so as to obtain a correlation between PAL results with luminescence properties. However, it is worth mentioning here that the I_3 component is feeble and its magnitude

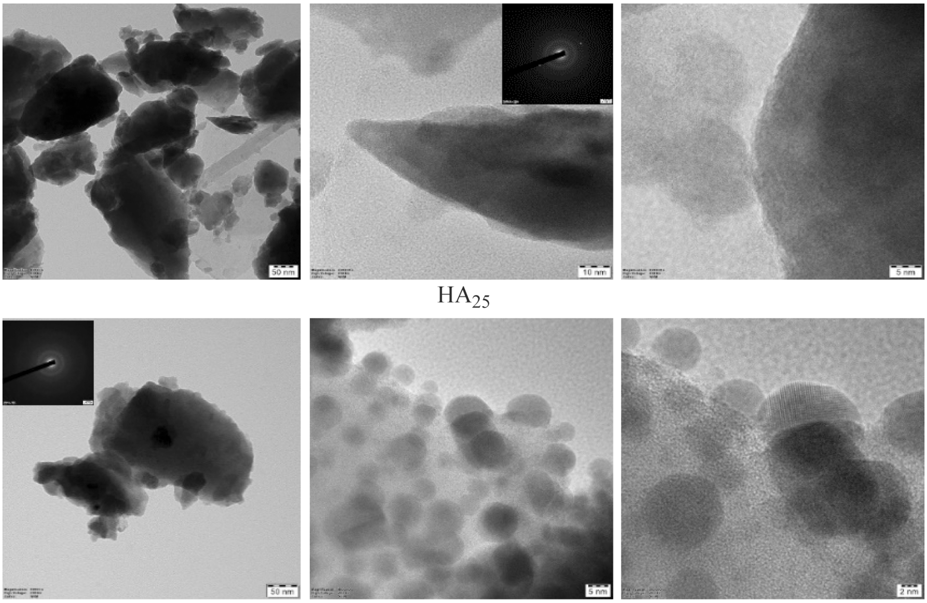

HA$_{25}$

HA$_{100}$

Figure 5.4: TEM photographs of HA$_{25}$ and HA$_{100}$ glass ceramics captured with various magnifications.

Table 5.1: Brief summary of intensity and lifetime components evaluated from PAL decay profiles of Ho^{3+} ions doped with lead boroselenate glass ceramics containing varied contents of Au$_2$O$_3$.

Sample	I_1 (%)	I_2 (%)	I_3 (%)	τ_1 (ns)	τ_2 (ns)	τ_3 (ns)
HA$_0$	29.49	67.71	2.80	0.17	0.33	1.74
HA$_{25}$	31.98	65.13	2.89	0.17	0.33	1.78
HA$_{50}$	29.28	67.81	2.91	0.18	0.333	1.78
HA$_{75}$	29.84	67.18	2.981	0.17	0.32	1.84
HA$_{100}$	27.51	69.02	3.47	0.18	0.33	1.90

Note: The deviations are shown in Figures 5.5 and 5.6.

is greatly dependent on the fraction of f_v space available in the samples (Figure 5.6(c)). Despite the fact that it is a weak component, its lifetime (τ_3) is very high compared to that of other two components.

The obtained values of three lifetime components and τ_{avg} were plotted against the concentration of Au$_2$O$_3$ in Figure 5.7(a–d), respectively. Cavities entrenched in these samples were evaluated using the value of τ_3 with eq. (5.1). The dependence of R and $\Delta f/f_0$ (free volume fraction evaluated using eq. (5.2)) on the concentration of Au$_2$O$_3$ is shown in Figure 5.8(a) and (b), respectively.

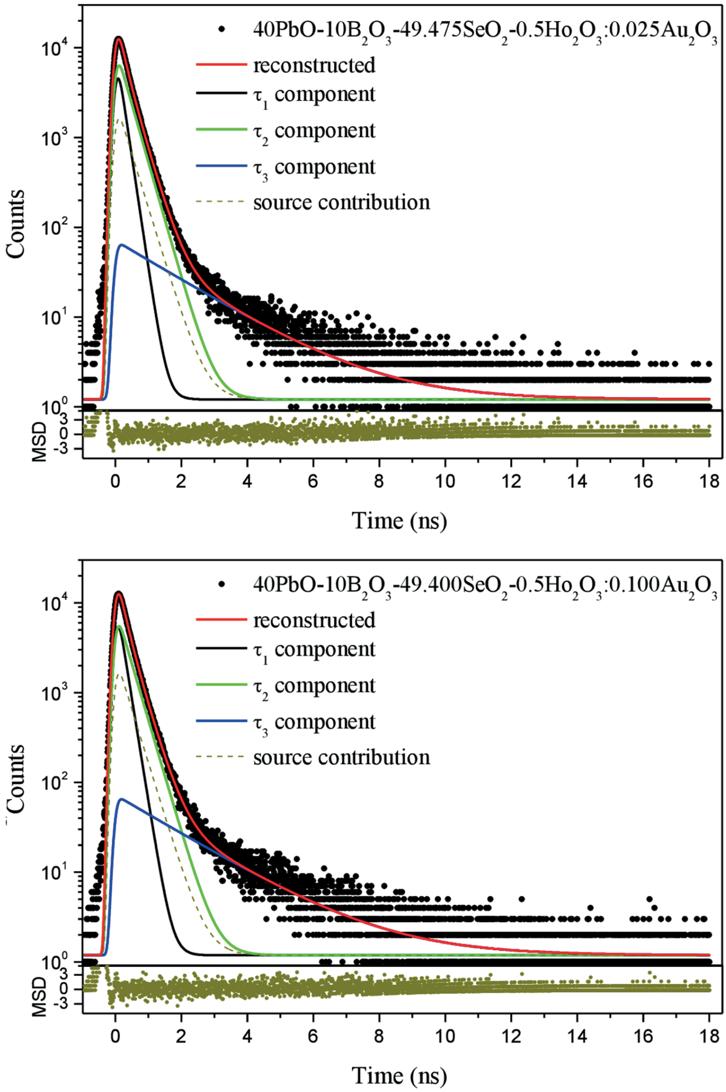

Figure 5.5: PAL decay profiles of HA_{25} and HA_{100} glass ceramics.

Both the parameters have shown a rising trend with Au_2O_3 content. Such an increase of f_v space causes to decrease the phonon losses and rise the PL efficiency of Ho^{3+} ions with an increase of Au_2O_3 concentration.

For additional support of this conclusion, the results of OA spectra and PL efficiency of these samples were analyzed in terms of Au_2O_3 concentration. Figure 5.9 represents the OA spectrum of the glass ceramic HA_{50} recorded in the visible region.

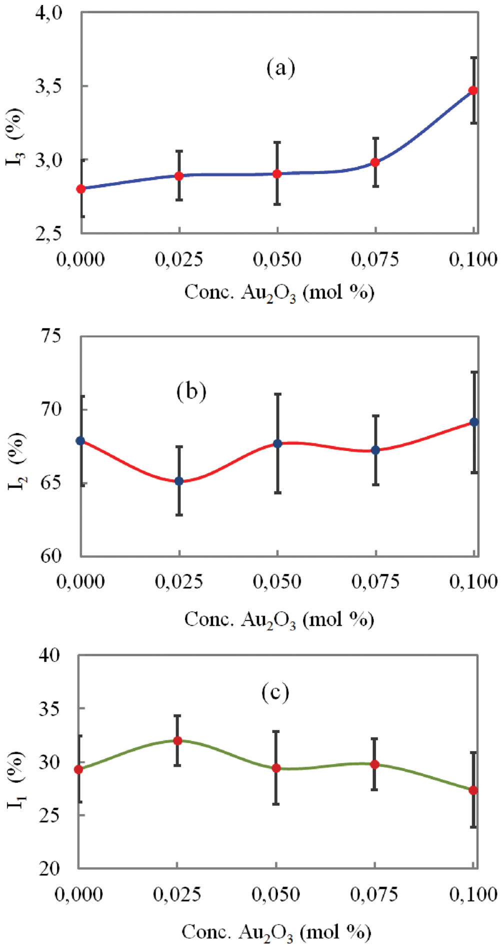

Figure 5.6: The plots of intensity components (a) I_3, (b) I_2, and (c) I_1 versus Au_2O_3 concentration.

The spectrum exhibited the following OA bands originated from $^5I_8$ ground state of holmium ions:

$$^5I_8 \longrightarrow {}^5G_6 + {}^5F_1 + {}^3K_8, {}^5F_{2,3}, {}^5F_4 + {}^5S_2, {}^5F_5$$

Among these, the band due to $^5I_8 \rightarrow {}^5F_4 + {}^5S_2$ transition was observed to be hypersensitive, possibly because of low shielding effect. The spectra of all other glass ceramics exhibited these bands; however, a considerable growing of these bands was observed with Au_2O_3 content. In the inset (a) of Figure 5.9, the intensity of $^5I_8 \rightarrow {}^5F_4 + {}^5S_2$ band with the concentration Au_2O_3 was presented.

It is worth mentioning here that in the spectral range of 520–620 nm ($^5I_8 \rightarrow {}^5F_4 + {}^5S_2$ transition region), a band due to SPR of Au^0 MPs was reported earlier [9, 10]. Using this

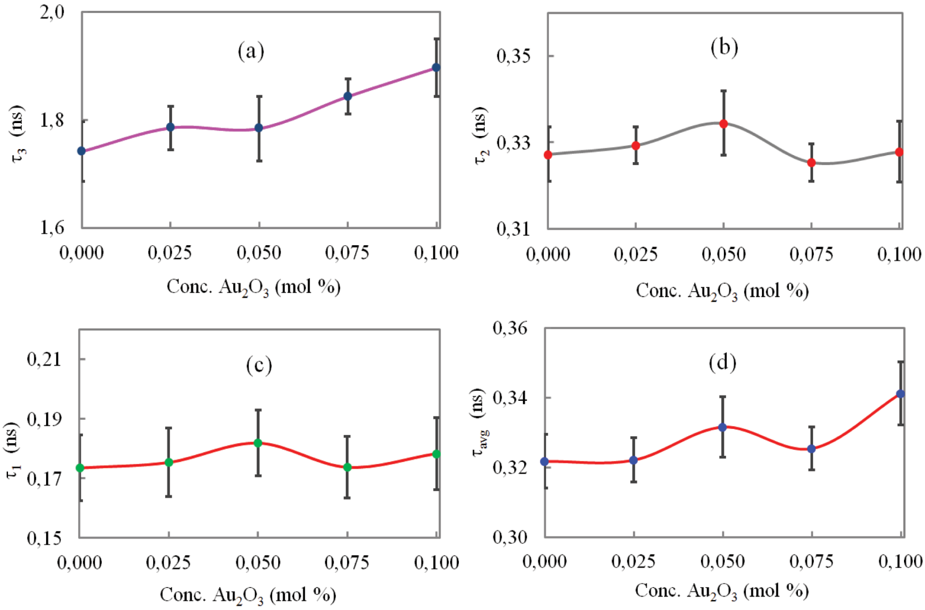

Figure 5.7: Plots of lifetime components (a) τ_3, (b) τ_2, (c) τ_1, and (d) (τ_{avg}) with Au_2O_3 concentration. The parameters suggested a growth with the concentration of gold oxide.

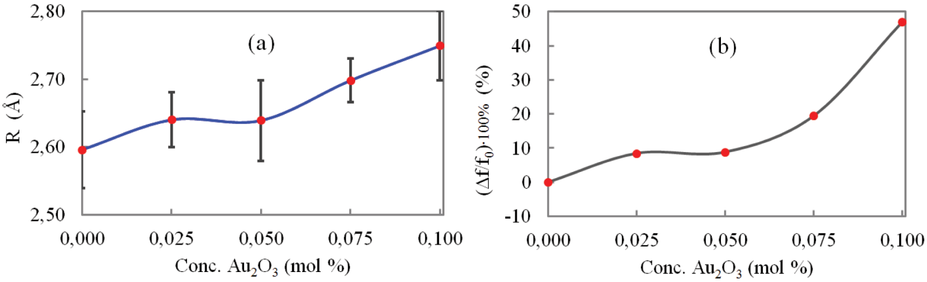

Figure 5.8: Variations of (a) R and (b) $\Delta f/f_0$ of Ho^{3+} ions versus the content of Au_2O_3 for PBSH glass ceramics.

band, the size (R_G) of Au metallic particle was also evaluated approximately with the relation $R_G = \left(\left(V_F\lambda^2\right)/2\pi c\Delta\lambda\right)$, where V_F denotes the Fermi velocity (139 × 10^6 cm/s) in gold metal and c represents the velocity of light. The value of R_G estimated from this relation was found to vary from nearly 30 to 45 nm with an increase of gold oxide up to 0.1 mol%. As discussed earlier, these particles emit green to orange radiations and enrich PL output of Ho^{3+} ions in these regions. Further, these particles decompose $Au_2(SeO_3)_3$ phase [9] by acting as modifiers and also breaks the Se–O–Se linkages in glass network.

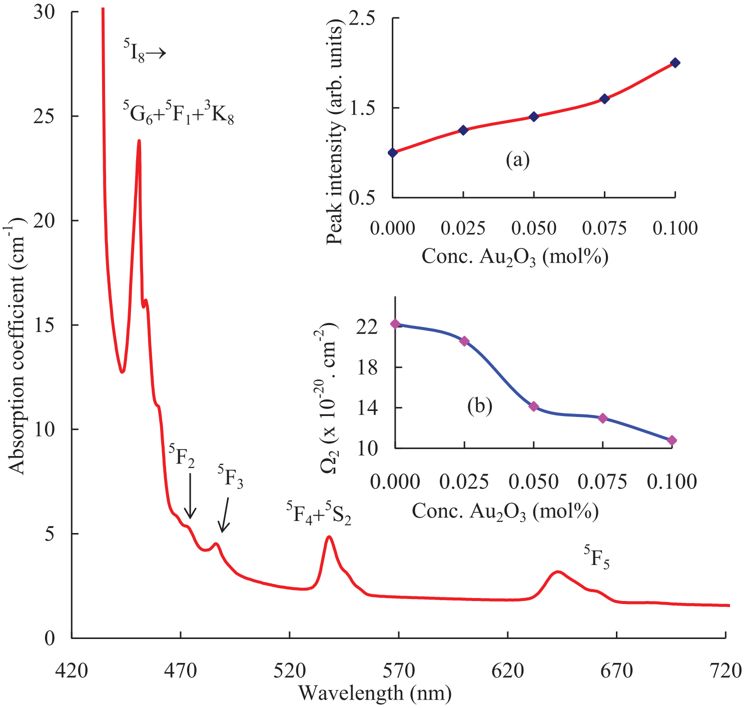

Figure 5.9: OA spectrum of HA$_{50}$ glass ceramic. In the inset (a), the intensity of $^5I_8 \rightarrow ^5F_4 + ^5S_2$ transition of Ho^{3+} versus Au$_2$O$_3$ is plotted, and in the inset (b), the magnitude of Ω_2 versus the content of Au$_2$O$_3$ is plotted.

Using an area under OA bands of the observed transitions of Ho^{3+} ions, the f_{exp} (expt. oscillator strengths) was estimated with the equation $f_{\mathrm{exp}\,\dot{\times}} = 4.319 \times 10^{-9} * \int^{\varepsilon}(\nu)d\nu$, where $\varepsilon(\nu)$ is the molar absorption coefficient. Oscillator strengths corresponding to different transitions were also calculated theoretically as per J-O theory with the following expression:

$$f_{\mathrm{cal}} = \frac{8\pi^2 mc\,\nu\chi}{3h(2J+1)} \sum_{\lambda=2,4,6} \Omega_\lambda \left\langle f^N[\gamma, S, L]J||U^\lambda||f^N[\gamma' S', L']J' \right\rangle^2 \tag{5.3}$$

Description of the standard terms in eq. (5.3) can be found in refs. [32, 33].

Out of three J-O coefficients calculated, the Ω_2 value was found to decrease with Au$_2$O$_3$ concentration (inset (b) of Figure 5.9). In these samples, the gold ions (with multivalent states) with varied concentrations get inserted along the chains of SeO$_4$ groups; as a result, magnitudes of symmetry and covalency around Ho^{3+} ions would change with the content of Au$_2$O$_3$. Such variations in the symmetry around Ho^{3+} ions influence the LE of Ho^{3+} ions. Even if CN of holmium ions in the network of this glass unchanged, the varied contents of gold metallic particles, the relative changes in the fractions of $[SeO_3]^{2-}$, and $[SeO_4]^{2-}$ structural units introduce different magnitudes of disorders in the samples at Ho^{3+} positions. Such disruptions may cause nonuniformity in the crystal field of holmium ions and change the Ω_2 value. The estimated value of Ω_2 suggested a decrement with an increase of Au_2O_3 content. This observation suggested the minimal covalent behavior of the sample HA_{100} due to higher magnitude of internal disturbances because of the largest proportions of gold MPs [12, 27]. To say it another way, the variation of Ω_2 with Au_2O_3 content suggested an increased concentration of imperfections that include voids (or cavities) in these glass ceramics.

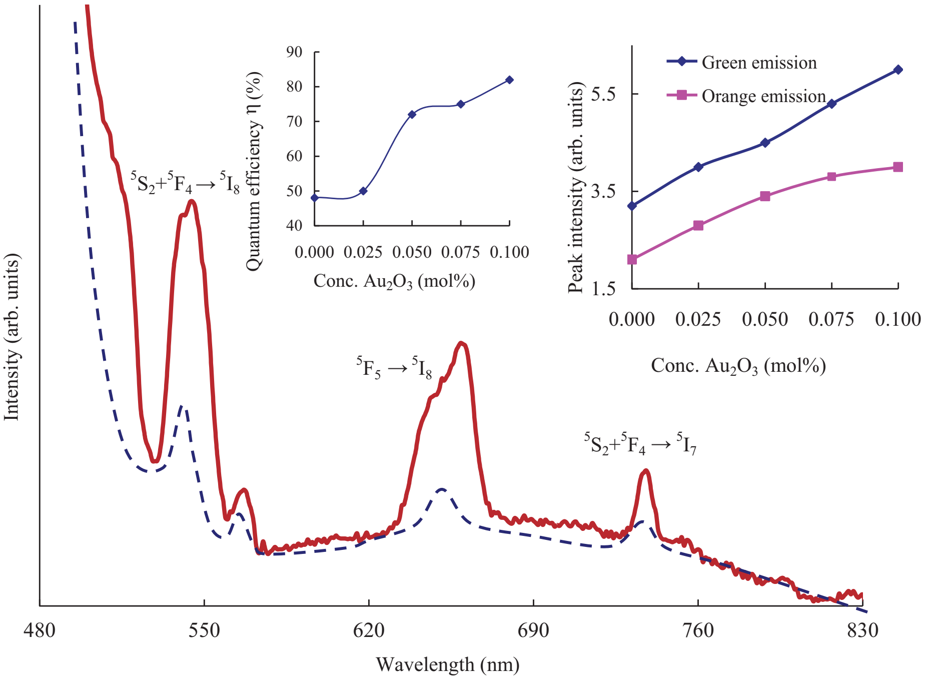

Figure 5.10: PL spectrum of HA_{50} sample. In the inset (a), relative intensities of G and O bands versus the content of gold oxide are plotted. In inset (b), quantum efficiency, η, versus the content of Au_2O_3 is plotted.

To strengthen this argument further, the results of luminescence studies were also used. PL spectrum obtained in the visible region for the sample HA_{50} recorded at $\lambda_{exe} = 450$ nm was shown in Figure 5.10. Blue (B), green (G), orange (O), and red (R) emission bands of holmium ions, connected with $^5F_3 \rightarrow {}^5I_8$, $^5S_2 + {}^5F_4 \rightarrow {}^5I_8$, $^5F_5 \rightarrow {}^5I_8$, and $^5S_2 + {}^5F_4 \rightarrow {}^5I_7$ transitions, were observed in these spectra [34]. The figure also contained the spectrum of samples with no Au_2O_3. The close look of the spectra suggested a threefold increase of intensity of the abovementioned bands due to Au_2O_3 doping. The intensity variation of G and O emission bands with gold oxide content was plotted and presented in inset (a) of Figure 5.10. The intensity of the bands was observed to grow with Au_2O_3 concentration.

Moreover, the change of quantum efficiency (τ_{meas}/τ_{calc}) of green band with Au_2O_3 content indicated a raising trend (inset (b) of Figure 5.10). This observation revealed the decreased magnitude of phonon losses (because of increasing presence of the concentration of defects like voids) as Au_2O_3 content was increased in these glass ceramics.

Thus, the assessment of results of OA and PL measurements suggested an increased fraction of defects in the PBSH glass ceramics with an increase of Au_2O_3 content. These results were well in accordance with the conclusions drawn from PAL spectral results.

5.4 Conclusions

In this work, the impact of f_v defects on LE of Ho^{3+} ions in PBS glass ceramics doped with gold oxide was reported. The PALS results suggested an increased magnitude of f_v with an increase of Au_2O_3 concentration. PL spectra of these glass ceramics exhibited intense G and O bands, and the bands were observed to grow as Au_2O_3 concentration increased. The observed increase of LE was attributed to the increased fraction of f_v defects that were prophesied to have lowered the phonon losses. A reasonable agreement between the variations of f_v fraction and the LE of Ho^{3+} ions with the Au_2O_3 content could be arrived. Small concentrations (~0.1 mol%) of Au_2O_3 were, therefore, considered a good sensitizer for increasing the LE of the holmium ions in the studied glass ceramics.

References

[1] Y. Dimitriev, A. Bachvarova-Nedelcheva, R. Iordanova, Glass formation tendency in the system SeO_2-Ag_2O-B_2O_3, Mater. Res. Bull. 43 (2008) 1905–1910.

[2] A. Bachvarova-Nedelcheva, R. Iordanova, S. Yordanov, Y. Dimitriev, Optical properties of selenite glasses, J. Non-Cryst. Solids 355 (2009) 2027–2030.

[3] R. El-Mallawany, E. Kavaz, U. Perişanoğlu, H.O. Tekin, S.H. Alazoumi, S.A. Umar, F.I. El-Agawany, Y.S. Rammah, New shielding ZnO-PbO-TeO_2 glasses, Optik 243 (2021) 167483.

[4] J. Schwarz, H. Ticha, Thermal expansion and structural properties of some $(PbO)_x(ZnO)_{35-x}(TeO_2)_{65}$ glasses, SN Appl. Sci. 3 (2021) 484.

[5] B. Suresh, Y. Zhydachevskii, M.G. Brik, A. Suchocki, M. Srinivasa Reddy, M. Piasecki, N. Veeraiah, Amplification of green emission of Ho^{3+} ions in lead silicate glasses by sensitizing with Bi^{3+} ions, J. Alloys Compd. 683 (2016) 114–122.

[6] K. Damak, E.S. Yousef, A.S. Al-Shihri, H.J. Seo, C. Rüssel, R. Maâlej, Quantifying Raman and emission gain coefficients of Ho^{3+} doped $TeO_2{\cdot}ZnO{\cdot}PbO{\cdot}PbF_2{\cdot}Na_2O$ (TZPPN) tellurite glass, Solid State Sci. 28 (2014) 74–80.

[7] V.R. Kumar, G. Giridhar, V. Sudarsan, N. Veeraiah, Influence of red lead on the intensity of green and orange emissions of Sm^{3+} and Ho^{3+} co-doped ZnO -SrO -P_2O_5 glass system, J. Alloys Compd. 695 (2017) 668–681.

[8] M. Pattabi, R.M. Pattabi, Photoluminescence from gold and silver nanoparticles, Nano Hybrids 6 (2014) 1–35.

[9] A. Siva Sesha Reddy, V.R. Kumar, G. Lakshminarayana, N. Purnachand, N. Venkatramaiah, V.R. Kumar, N. Veeraiah, Influence of gold ions on visible and NIR luminescence features of Er^{3+} ions in lead boroselenate glass ceramics, J. Lumin. 226 (2020) 117481.

[10] A. Siva Sesha Reddy, N. Purnachand, M. Kostrzewa, M.G. Brik, N. Venkatramaiah, V.R. Kumar, N. Veeraiah, The role of gold metallic particles on improving green and NIR emissions of Ho^{3+} ions in non-conventional SeO_2 based glass ceramics, J. Non-Cryst. Solids 576 (2022) 121240.

[11] M. Eichelbaum, K. Rademann, A. Hoell, G. Pacchioni, Photoluminescence of atomic gold and silver particles in soda-lime silicate glasses, Nanotechnology 19 (2008) 135701.

[12] R. Rajaramakrishna, S. Karuthedath, R.V. Anavekar, H. Jain, Nonlinear optical studies of lead lanthanum borate glass doped with Au nanoparticles, J. Non-Cryst. Solids 358 (2012) 1667–1672.

[13] P.G. Jones, G.M. Sheldrick, E. Schwarzmann, A. Vielmäder, Preparation and crystal structure of di-gold(III) bis(selenite)oxide, $Au_2(SeO_3)_2O$, Z. Naturforsch. 38 (1983) 10–11.

[14] M.S. Wickleder, O. Buchner, C. Wickleder, S. Sheik, G. Brunklaus, H. Eckert, $Au_2(SeO_3)_2(SeO_4)$: Synthesis and characterization of a new non-centrosymmetric selenite-selenate, Inorg. Chem. 43 (2004) 5860–5864.

[15] O. Shpotyuk, V. Adamiv, I. Teslyuk, A. Ingram, P. Demchenko, Probing vacancy-type free-volume defects in $Li_2B_4O_7$ single crystal by positron annihilation lifetime spectroscopy, J. Phys. Chem. Solids 112 (2018) 8–13.

[16] O. Shpotyuk, V. Adamiv, I. Teslyuk, A. Ingram, Positron lifetime spectroscopy of lithium tetraborate $Li_2B_4O_7$ glass, J. Non-Cryst. Solids 471 (2017) 338–343.

[17] Y. Shpotyuk, A. Ingram, O. Shpotyuk, PAL spectroscopy of rare-earth doped Ga -Ge -Te/Se glasses, J. Phys. Chem. Solids 91 (2016) 76–79.

[18] P. Horodek, Positron annihilation studies of irradiation-induced defects with swift heavy ions in gold, Vacuum 164 (2019) 421–427.

[19] A. Siva Sesha Reddy, M. Kostrzewa, A. Ingram, N. Purnachand, P. Bragiel, V.R. Kumar, I.V. Kityk, N. Veeraiah, Positron annihilation exploration of voids in zinc zirconium borate glass ceramics entrenched with $ZnZrO_3$ perovskite crystal phases, J. Eur. Ceram. Soc. 38 (2018) 2010–2016.

[20] A. Ingram, R. Golovchak, M. Kostrzewa, S. Wacke, M. Shpotyuk, O. Shpotyuk, Compositional dependences of average positron lifetime in binary As -S/Se glasses, Physica B 407 (2012) 652–655.

[21] E. Golis, E.S. Yousef, M. Reben, K. Kotynia, J. Filipecki, Measurements of defect structures by positron annihilation lifetime spectroscopy of the tellurite glass TeO_2 -P_2O_5 -ZnO -$LiNbO_3$ doped with ions of rare earth elements: Er^{3+}, Nd^{3+} and Gd^{3+}, Solid State Sci. 50 (2015) 81–84.

[22] M. Eldrup, D. Lighbody, J.N. Sherwood, The temperature dependence of positron lifetimes in solid pivalic acid, Chem. Phys. 63 (1981) 51–58.

[23] G. Greczynski, L. Hultman, X-ray photoelectron spectroscopy: Towards reliable binding energy referencing, Prog. Mater. Sci. 107 (2020) 100591.

[24] G. Greczynski, L. Hultman, The same chemical state of carbon gives rise to two peaks in X-ray photoelectron spectroscopy, Sci. Rep. 11 (2021) 11195.

[25] G. Greczynski, L. Hultman, Compromising science by ignorant instrument calibration-need to revisit half a century of published XPS data, Angew. Chem. Int. Ed. 59 (2020) 5002–5006.

[26] J. Kansy, Microcomputer program for analysis of positron annihilation lifetime spectra, Nucl. Instr. Methods A 374 (1996) 235–244.

[27] R.H. Lambertson, C.A. Lacy, S.D. Gillespie, M.C. Leopold, R.H. Coppage, Gold nanoparticle colorants as traditional ceramic glaze alternatives, J. Am. Ceram. Soc. 100 (2017) 3943–3951.

[28] K. Virender Sharma, T.J. Mc-Donald, M. Sohn, G.A.K. Anquandah, M. Pettine, R. Zbořil, Biogeochemistry of selenium. A review, Environ. Chem. Lett. 13 (2014) 49–58.

[29] P. Kumar, M.C. Mathpal, G. Jagannath, J. Prakash, J.-R. Maze, W.D. Roos, H.C. Swart, Optical limiting applications of resonating plasmonic Au nanoparticles in a dielectric glass medium, Nanotechnology 32 (2021) 345709.

[30] Y. Mikhlin, M. Likhatski, Y. Tomashevich, A. Romanchenko, S. Erenburg, S. Trubina, XAS and XPS examination of the Au-S nanostructures produced via the reductionof aqueous gold (III) by sulfide ions, J. Electron. Spectrosc. Relat. Phenom. 177 (2010) 24–29.

[31] M. Zacharska, A.L. Chuvilin, V.V. Kriventsov, S. Beloshapkin, M. Estrada, A. Simakov, D.A. Bulushev, Support effect for nanosized Au catalysts in hydrogen production from formic acid decomposition, Catal. Sci. Technol. 6 (2016) 6853–6860.

[32] B.R. Judd, Optical absorption intensities of rare-earth ions, Phys. Rev. 127 (1962) 750.

[33] G.S. Ofelt, Intensities of crystal spectra of rare-earth ions, J. Chem. Phys. 37 (1962) 511.

[34] M. Azam, V.K. Rai, Ho^{3+}-Yb^{3+}codoped tellurite-based glasses in visible lasers and optical devices: Judd-Ofelt analysis and frequency upconversion, Solid State Sci. 66 (2017) 7–15.

Jumpei Ueda

Chapter 6
Garnet persistent phosphors

6.1 Introduction

Oxide garnets are the most prominent optical host materials for lanthanoid and transition metal ions. For instance, $Y_3Al_5O_{12}$:Ce^{3+} yellow phosphors are widely used as white LED (light-emitting diode) phosphors, owing to their excellent spectral conversion characteristics, high stability under the extremely high photon flux, and operating temperature [1, 2]. $Y_3Al_5O_{12}$:Nd^{3+} single crystals and transparent ceramics exhibit excellent NIR (near-infrared) laser performance due to the good thermo-mechanical properties of the garnet host material [3, 4]. Recently, Cr^{3+}-doped garnets can become promising wide band NIR phosphors [5, 6]. So far, many garnet-based materials have been applied to optical devices. Also, the garnet compounds are suitable for persistent phosphors with unique and excellent luminescent properties [7, 8]. The advantages of garnet materials as a luminescent host are the solubility of luminescence ions and the tunability of host composition, which enable to control the optical properties. Since 2010, various Ce^{3+}-doped garnet persistent phosphors have been developed [9–16], and then persistent luminescence centers have been extended to other lanthanoid and transition metal ions such as Pr^{3+}, Tb^{3+}, Cr^{3+}, Er^{3+}, and Nd^{3+} [17–23]. In this section, the garnet crystal structure and electronic structure are introduced first, and then the optical properties of Ce^{3+} in the garnet compounds are explained. Subsequently, it summarizes what persistent phosphors are and how to control and design Ce^{3+}-doped garnet persistent phosphors and non-Ce^{3+}-doped garnet persistent phosphors.

6.2 Garnet structure

6.2.1 Unit lattice

In 1929, the garnet structure in several minerals was determined as $Ia\bar{3}d$ space group by Menzer [24]. Figure 6.1a shows a unit cell of a general cubic garnet structure. The chemical formula of general oxide garnet compounds can be written as $\{A\}_3[B]_2(C)_3O_{12}$. The garnet crystal belongs to $Ia\bar{3}d$ (no. 230) space group. The {A} represents a cation in the dodecahedral (eightfold) site with D_2 symmetry, which is 24c as Wyckoff position. The [B] and (C) represent cations in the octahedral (sixfold) site (16a) with C_{3i} symmetry and in the tetrahedral (fourfold) site (24d) with S_4 symmetry, respectively. The oxygen anion occupies the tetrahedral site (96 h) with C_i symmetry. In the unit cell, 160 atoms exist. The lattice constant (a_0) is around 12 Å. Considering the garnet

https://doi.org/10.1515/9783110607871-006

crystal which is consisted of {A^{3+}}, [B^{3+}], (C^{3+}), and O^{2-}, the bond strengths of {A^{3+}}–O^{2-}, [B^{3+}]–O^{2-}, and (C^{3+})–O^{2-} are 3/8, 3/6, and 3/4, respectively. The O^{2-} site is coordinated by two {A^{3+}} ions, one [B^{3+}] ion, and one (C^{3+}) ion. Thus, Pauling's second rule is satisfied by the bond sums $3/8 \times 2 + 3/6 \times 1 + 3/4 \times 1 = 2$. Also, this rule is applied in {A^{2+}}$_3$ [B^{3+}]$_2$ (C^{4+})$_3O_{12}$ garnets.

However, understanding the garnet structure is slightly difficult from this description in Figure 6.1a. When we focus on the (C) tetrahedron and [B] octahedron, it is seen that both polyhedrons are connected by the corner and form a 3D framework as shown in Figure 6.1b. Thus, the octahedral [B] site is completely isolated from other [B] octahedral sites; similarly to this, the tetrahedral (C) sites are also isolated from each other. The {A} cation is just located in the space of the 3D framework of [B] and (C) sites. For a better understanding of the garnet structure, the octahedral [B] lattice is described in Figure 6.1c. It can be seen that the octahedral [B] sites are located at the corners of the unit cell and are regularly aligned. Checking a small cubic lattice with $1/2a_0$ length, we find the octahedral [B] sites are aligned by a body-centered cubic (BCC) sublattice as described by the black dashed line in Figure 6.1c. The unit cell is formed by eight BCC sublattices. The enlarged BBC sublattices with [A] and [C] cations are shown in Figure 6.1d. On the centerline of each square plane of BBC sublattice, one dodecahedral {A} site and one tetrahedral [C] site are aligned at 1/4 and 3/4 height with respect to an edge. As shown by a black arrow in Figure 6.1d, the body diagonal of BBC sublattice is a threefold rotational axis. The threefold rotational axis in each BBC sublattice has a different direction in the unit cell. Figure 6.1e shows the unit cell projected from the [001] direction. Solid arrows are the threefold rotational axes in upper BCC sublattices ($1/2 \le z \le 1$) and the dashed arrows are the axes in lower BCC sublattices ($0 \le z \le 1/2$). The up and down arrows are expressed by an additional triangle which shows a higher level.

Figure 6.2 shows the sequential atomic layers parallel to the (001) plane of the unit cell at height increments of 1/8 a_0 along the z-axis. At 0 a_0, the dodecahedral and tetrahedral sites are alternately located at ({$1/4x$, $3/4x$}, {$1/8y$, $3/8y$, $5/8y$, $7/8y$}). In the chain of alternate dodecahedral {A} site and tetrahedral {C} site in parallel to y-axis, one dodecahedral site shared two edges with two tetrahedral sites and vice versa. The neighbor chain of {A} and (C) sites at 180° turns in the opposite direction. On the plane at 1/8 a_0 height, {A} and (C) sites are located above the BCC sublattice edges as shown in Figure 6.2. On the plane at 2/8 a_0 height, [B] sites are located in the center of each BCC sublattices, and the {A} and (C) sites are located alternately at ({$1/8x$, $3/8x$, $5/8x$, $7/8x$}, {$0y$, $1/2y$, ($1y$)}). In this plane, the chains of alternate {A} and (C) sites are parallel to the x-axis. The plane at 3/8 a_0 is similar to that at 1/8 a_0, but the positions of {A} and (C) sites are opposite. The plane at 5/8 a_0 is similar to that at 1/8 a_0, but the direction of {A} and (C) polyhedrons is different. The same relationship between 7/8 a_0 and 3/8 a_0 can be observed. The planes at 4/8 a_0 and 6/8 a_0 are similar to that at 0 a_0 and 2/8 a_0, respectively, but the {A} and (C) positions are opposite.

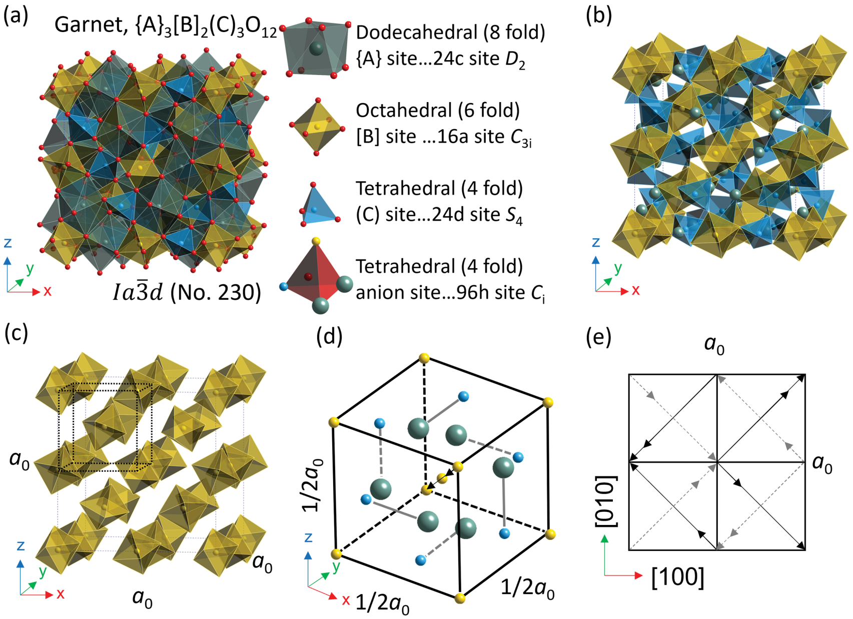
(a)
Garnet, {A}3[B]2(C)3O12
Dodecahedral (8 fold)
{A} site...24c site D2
Octahedral (6 fold)
[B] site ...16a site C3i
Tetrahedral (4 fold)
(C) site...24d site S4
Tetrahedral (4 fold)
anion site...96h site Ci
Ia3̄d (No. 230)
z
y
x
(b)
(c)
a0
(d)
1/2a0
(e)
[010]
[100]

Figure 6.1: (a) Unit cell of garnet structure with gray dodecahedron {A} site, yellow octahedral [B] site, blue tetrahedral (C) site, and red spherical anion. (b) A unit cell represented using the framework of the yellow octahedron and blue tetrahedron. (c) Octahedral [B] site lattice without {A} and (C) cations. (d) Body-centered cubic (BCC) sublattice by [B] cation with {A} and [C] cations. (e) Projection image from [001] direction of BCC lattice assembly. Solid arrows and dashed arrows represented the three-rotational axes in upper and lower BCC lattices, respectively. The triangle in the midpoint of arrows shows the higher position (the crystal structures are drawn by VESTA [25]).

6.2.2 Dodecahedral {A} site and octahedral [B] site for luminescence ions

The lanthanoid ion generally occupies the {A} site, whose environment affects to the optical properties significantly. Here, we focus on the dodecahedral site on 4/8 a_0 plane which is highlighted by some colored dots as shown in Figure 6.2. The enlarged dodecahedral site is also shown in Figure 6.3a (the neighbor dodecahedral sites are not shown to avoid the complex structure). The dodecahedral {A} site shares two edges with two tetrahedral (C) sites and two edges with two octahedral [B] sites on the plane at 4/8 a_0, and also shares extra two edges with two octahedral [B] sites on 2/8 a_0 and 6/8 a_0. In addition, the dodecahedral {A} site shares four corners (as shown in blue, green, yellow, and red dots of Figure 6.2) with tetrahedral (C) sites on 2/8, 3/8, 5/8, 6/8 a_0. And more, the {A} site shares four edges with other four dodecahedral sites on 2/8, 3/8, 5/8, 6/8 a_0. Here, we refer that the shared edge between tetrahedral and dodecahedral sites is d_{48}, the edge between octahedral and dodecahedral

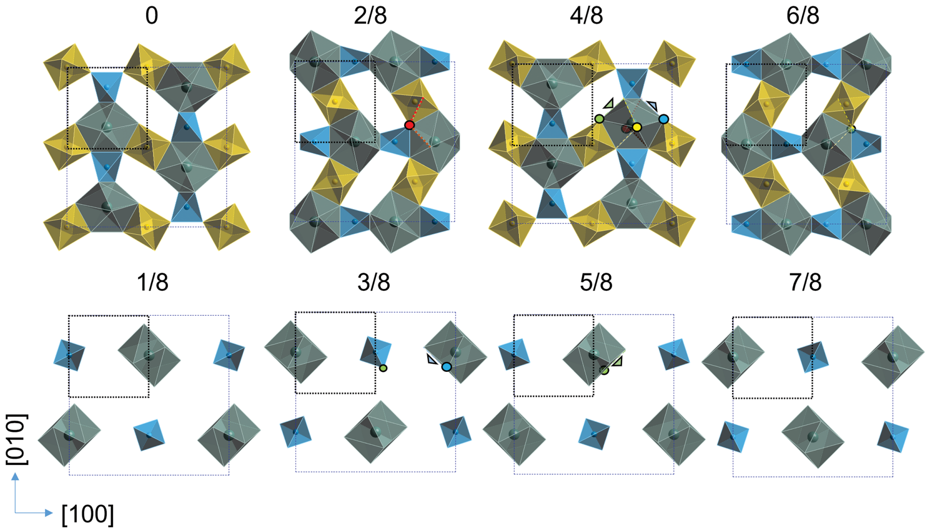

Figure 6.2: Sequential atomic layers of the garnet structure parallel to the (001) plane (the crystal structures are drawn by VESTA [25]).

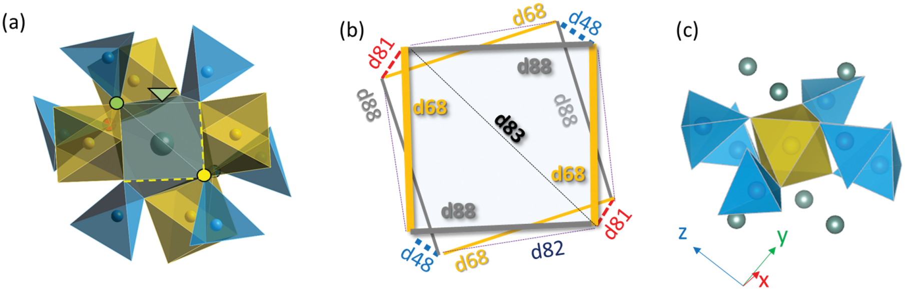

Figure 6.3: (a) Local structure around dodecaheral site (four nearest dodecahedral sites are not depicted); (b) schematic local structure of dodecahedral site with sharing edge and nonsharing edges [26] (reproduced from Ref. [26] with permission from the Elsevier); (c) local structure around the octahedral site ({A}, [B], and (C) ions are shown by gray, yellow, and blue spheres, respectively) [13].

sites is d_{68}, and the edge between dodecahedral and dodecahedral sites is d_{88} [27]. Three different unshared edges are represented as d_{81}, d_{82}, and d_{83}. Figure 6.3b shows the dodecahedral site formed by the edges defined earlier: 18 edges of $2\times d_{48}$, $4\times d_{68}$, $4\times d_{88}$, $2\times d_{81}$, $4\times d_{82}$, $2\times d_{83}$. The transition metal ion prefers to occupy the octahedral [B] site and its optical property can be varied by the environment. Figure 6.3c shows the nearest cation sites around the octahedral [B] site. The octahedral site shares corners with six tetrahedral sites and edges with six dodecahedral sites.

6.2.3 Electronic structure of garnet compounds

The garnet compounds have a wide solid solution region, which leads to various electronic structures. For instance, the dodecahedral {A} site can be occupied by rare earth ions and alkaline earth ions; the octahedral [B] site can be substituted by Al^{3+}, Ga^{3+}, In^{3+}, Sc^{3+}; the tetrahedral (C) site can be done by Al^{3+}, Ga^{3+}, Si^{4+}, and Ge^{4+}. The combination of cations in {A}, [B], and (C) sites can be tailored within the limitations of the proper ionic radius and valence states for the net charge neutrality. Figure 6.4 shows the stacked vacuum-referred binding energy (VRBE) diagram of various garnet compounds [26]. Changing the garnet compositions, the VRBE of the valence band and conduction band is largely changed. Also, the VRBE of 4*f* and 5*d* levels of Ce^{3+} ions is altered. As a result, Ln^{3+}-doped garnet compounds as well as Ce^{3+}-doped garnets show interesting tunability for optical and optoelectronic properties.

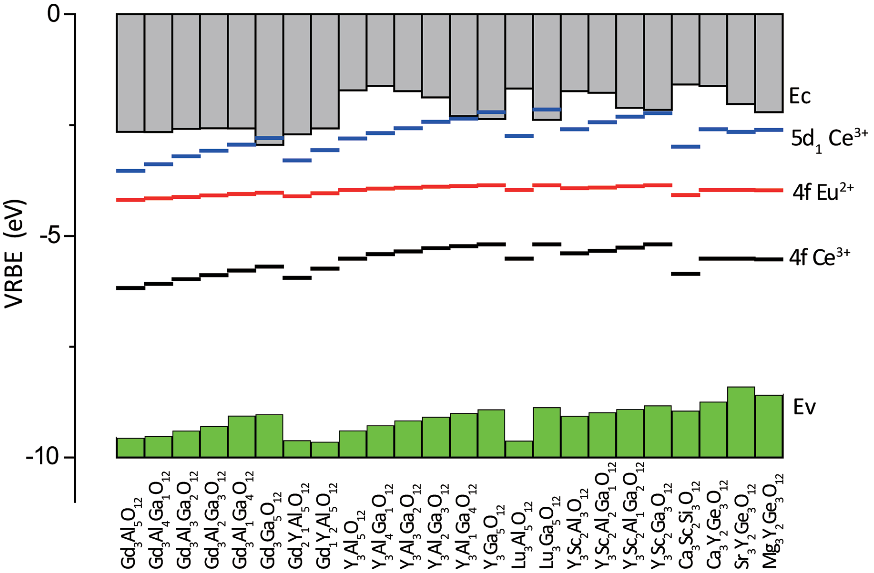

Figure 6.4: Stacked VRBE diagram of various garnet compounds [26] (reproduced from Ref. [26] with permission from Elsevier).

6.3 Ce^{3+}:5*d* energy level in garnet

Ce^{3+} ion (atomic number: 58) belongs to the lanthanoid group and its electronic configuration is $[Xe]4f^1$. There are two 4*f* levels of $^2F_{5/2}$ and $^2F_{7/2}$ generated by the spin–orbit coupling. The Ce^{3+} ion also has the transition from $[Xe]4f^1$ to $[Xe]4f^05d^1$ electronic configuration. In the free ion, this 4*f*–5*d* absorption is located around 6 eV. The 5*d* excited state is separated into $^2D_{3/2}$ and $^2D_{5/2}$ by the spin–orbit coupling; the absorption energies from the ground state to $^2D_{3/2}$ and to the centroid energy of $^2D_{3/2}$ and $^2D_{5/2}$ are 6.12 and 6.35 eV, respectively [28, 29]. On the other hand, the strong 4*f*–5*d* absorption and 5*d*–4*f* luminescence of Ce^{3+} can be observed in compounds from UV to visible range [29–32]. The wavelength variation in different host compounds is caused by shifting the 5*d* energy levels. Figure 6.5 shows the Ce^{3+} energy levels (4*f* and 5*d*) in different environments. Assuming Ce^{3+} ion in the spherical electrostatic field caused by anion coordination, the 5*d* states degenerate, but the 5*d* energy can be shifted by the centroid shift, which is defined as the lowering of the average energy of the Ce^{3+} 5*d* configuration relative to the value as a free ion (6.35 eV) [33]. The centroid shift is related to the physical (polarizability) and chemical (covalence) properties of the anions coordinating Ce^{3+}. In a specific anion polyhedron site, the crystal field splitting, which is determined by the size and shape of the first anion coordination polyhedron, varies the Ce^{3+} 5*d* energy levels. For instance, the t_{2g} and e_g orbitals are unstabilized and stabilized, respectively, in the cubic polyhedron. For the dodecahedral polyhedron of the garnet structure, the eight oxide ions around Ce^{3+} ion slightly move from the cubic positions and then become a disordered square anti-prism, which leads to larger crystal field splitting. The crystal field splitting between the lowest $5d_1$ and the highest $5d_5$ is referred to as ε_{cfs} and the splitting between the $5d_1$ and the second lowest $5d_2$ is referred to as Δ_{12} [34]. Subsequently, the Ce^{3+}-doped garnet-type structure shows a significant redshifting of the 4*f*–5*d* absorption.

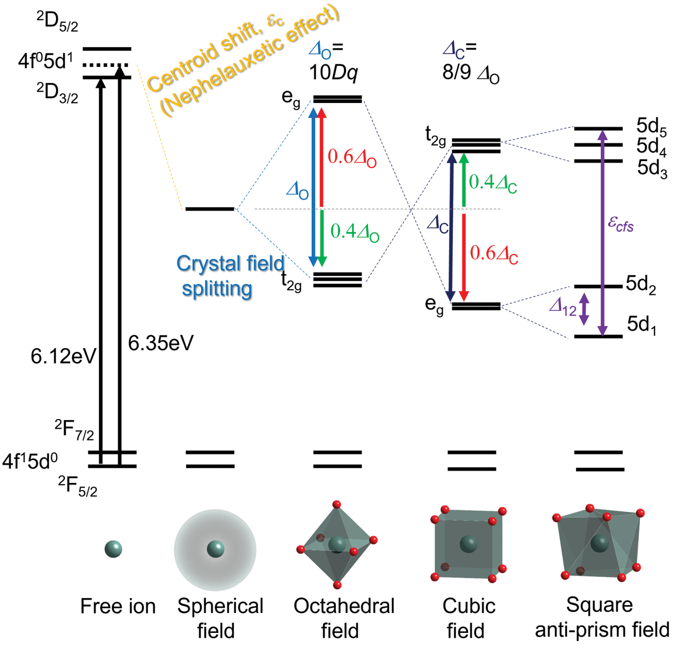
$^2D_{5/2}$
$4f^05d^1$
$^2D_{3/2}$
Centroid shift, ε_c
(Nephelauxetic effect)
Δ_O= 10Dq
Δ_C= 8/9 Δ_O
e_g
t_{2g}
$0.6\Delta_O$
Δ_O
$0.4\Delta_O$
Crystal field splitting
$0.4\Delta_C$
Δ_C
$0.6\Delta_C$
$5d_5$
$5d_4$
$5d_3$
ε_{cfs}
$5d_2$
Δ_{12}
$5d_1$
6.12eV
6.35eV
$^2F_{7/2}$
$4f^15d^0$
$^2F_{5/2}$
Free ion
Spherical field
Octahedral field
Cubic field
Square anti-prism field

Figure 6.5: Schematic Ce^{3+} energy diagram in various coordinations [26] (reproduced from Ref. [26] with permission from the Elsevier).

6.3.1 Variation of Ce^{3+}:5*d*–4*f* energy in garnet

Although the 5*d* energy shifting of Ce^{3+} in the garnet structure is explained in the previous section, the contributions of the centroid shift and the crystal field to the redshifting of $5d_1$ energy had not been well understood. Dorenbos collected the spectroscopic data of $(Gd, Y, Lu)_3(Al_{1-x}Ga_x)_5O_{12}$:$Ce^{3+}$ and plotted the $5d_1$ and $5d_2$ energies as a function of redshifting (*D*(1, 3+,A)), finding a clear trend between *D*(1,3+,A) and Δ_{12} [34]. Here, the *D* (1, 3+,A) is expressed by

$$D(1,3+,A)=E_{fd\text{ave},\text{free}}-E_{f5d1,A}-0.23 \tag{6.1}$$

where $E_{fd\text{ave},\text{free}}$ is the average energy of 4*f*–5*d* absorption in the free ion (6.35 eV), $E_{f5d1,A}$ is the lowest 4*f*–5*d* absorption energy (eV) in compound *A*, 0.23 eV is the difference between $E_{fd\text{ave},\text{free}}$ and the lowest 4*f*–5*d*($^2D_{3/2}$) energy in the free ion as shown in Figure 6.5.

Dorenbos introduced the effective polarizability [29] that is named as spectroscopic polarizability (α_{sp}), and reported in the following equation:

$$\varepsilon_c=1.79\times10^{13}\alpha_{sp}\sum_{i=1}^{N}\frac{1}{(R_i-0.6\Delta R)^6} \tag{6.2}$$

where R_i is the distance from Ce^{3+} ion to the ligand *i* in pm, the centroid shift energy is in eV, α_{sp} is in Å^3, and $\Delta R=R_M-R_{Ce}$, R_M is the ionic radius of the cation that is replaced by Ce^{3+} with ionic radius R_{Ce}, and $0.6\Delta R$ is the estimated amount of bond length relaxation. The spectroscopic polarizability can characterize the chemical property of the anion ligand and the cations that bind with the anion ligands [35]. One may relate the average bond strength of the ligand electrons to the average electronegativity α_{av} of the cations in the compound. However, in the garnet compounds, the electronegativity is not good to estimate the centroid shift energy [26]. Dorenbos also investigated the correlation between α_{sp} and the optical basicity (Λ) [36]. The optical basicity is the electron donating power of oxygen ligands, and it was firstly estimated from the energy shifting of $^1S_0$–$^3P_1$ transition of Pb^{2+}, Bi^{3+}, and Tl^+ [37–39]. The optical basicity can be calculated from the chemical composition as follows [37–39]:

$$\Lambda_{\text{cal}}=\frac{1}{2N_a}\sum_{i}^{N_c}\frac{z_i}{\gamma_i} \tag{6.3}$$

where N_a is the number of oxygen anions in the compound's formula. The summation is over all the N_c cations in the compound's formula, where z_i is the charge of cation *i*, and γ_i is the optical basicity moderating parameter belonging to cation *i*. The optical basicity moderating parameter estimated from the experimental data is more effective than that from the electronegativity in the garnet compounds [26]. The optical basicity moderating parameter of several atoms are shown in Table 6.1. Based on the plot between α_{sp} obtained by the centroid shift of Ce^{3+} in garnet and optical basicity, it was proposed that α_{sp} in the Ce^{3+}-doped garnets can be estimated from the following equation [26]:

$$\alpha_{sp} = 10.34 \times \Lambda_{\text{cal\_RI}} - 5.36 \tag{6.4}$$

Therefore, in the Ce^{3+}-doped garnet, α_{sp} as well as centroid shift can be estimated from the optical basicity (Λ_{cal}), which is calculated from the optical basicity moderating parameter and the chemical composition.

Table 6.1: Basicity moderating parameters [40].

M^{1+}	γ	M^{2+}	γ	M^{3+}	γ	$M^{4+/5+}$	γ
Li	1.23	Mg	1.15	B	2.47	Si	2.1
Na	0.905	Ca	1.00	Al	1.65	Ge	1.64
K	0.76	Sr	0.95	Ga	1.4	P	2.1 or 2.8
Rb	0.70	Ba	0.75	In	1.05		
Cs	0.65			Sc	1.1		
				Y	1.0		
				La	0.85		
				Lu	1.03		

6.3.2 Relationship between crystal field splitting and crystal structure

Ce^{3+}-doped garnets show strong crystal field splitting. As shown in Figure 6.3a, b, the dodecahedral site has a disordered square anti-prism structure, whose distorted structure induces the extra crystal filed splitting of Δ_{12} [34]. In general, the crystal field splitting ε_{cfs} becomes larger with decreasing the cation site size. Dorenbos reported the general tendency between ε_{cfs} and the average bond length modified by the lattice relaxation (R_{av}). The R_{av} is defined as

$$R_{av} = \frac{1}{N}\sum_{i=1}^{N}(R_i - 0.6\,\Delta R) \tag{6.5}$$

where R_i are the individual bond lengths to the N coordinating anions in the unrelaxed lattice [33]. $\Delta R = R_M - R_{Ln}$ with R_M the ionic radius of the cation that is replaced by the lanthanide Ln with ionic radius R_{Ln}, and $0.6\Delta R$ is the estimated amount of bond length relaxation. In the octahedral, cubic, and cuboctahedral coordination, crystal field splitting appeared to behave the following relationship:

$$\varepsilon_{\text{cfs}} = \beta_{\text{poly}}^{Q} R_{\text{av}}^{-2} \tag{6.6}$$

where β_{poly}^{Q} is a constant that depends on the type of coordination polyhedron and whether the lanthanide is trivalent ($Q = 3+$) or divalent ($Q = 2+$) [30–32, 41]. However, in the garnet structure, we could not find a suitable β_{poly}^{Q} [26]. This is because the crystal field splitting of the dodecahedral site in the garnet crystals are largely changed by distortion. Wu et al. showed a tendency between the luminescence wavelength and the distortion factor defined as the ratio of edge lengths of dodecahedral, d_{88}/d_{81} [42]. We found that the ratio of d_{83}/d_{48} is a much better parameter to predict Δ_{12} as attested by the good linearity [26]. The d_{83} is the non-sharing edge of the dodecahedral site which is the approximate diagonal of the square formed by two d_{88} and two d_{86} edges (Figure 3b). The ratio d_{83}/d_{48} is the parameter to describe the distortion of the dodecahedral site, but it does not fully consider the contribution of the size of the dodecahedral site. In order to include this contribution, a new parameter dividing d_{83}/d_{48} by the R_{av} was proposed [26]. Based on the linear fit (Figure 6.6), the Δ_{12} can be estimated empirically by the crystal structure data of garnet as follows:

$$\Delta_{12} = 942 \times \frac{d_{83}}{d_{48}} \frac{1}{R_{\text{av}}} - 4.78 \tag{6.7}$$

Here, Δ_{12} is in eV unit and R_{av} is in pm unit.

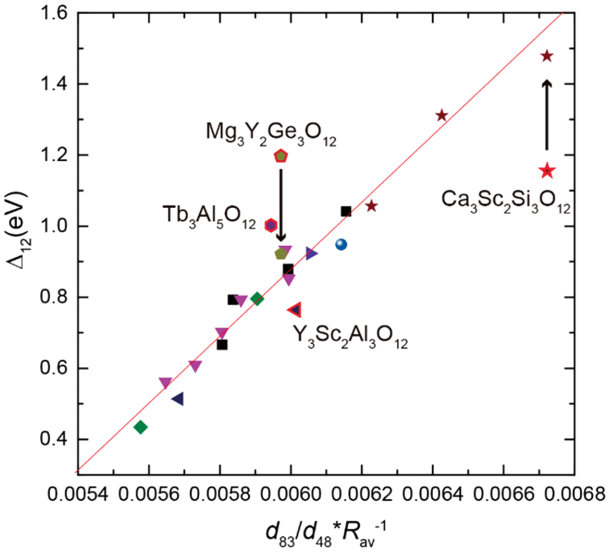

Figure 6.6: Δ_{12} against $d_{83}/(d_{48}{}^{*}R_{\text{av}})$ of various Ce^{3+}-doped garnets. The red line is a fitting result. For $Mg_3Y_2Ge_3O_{12}$ and $Ca_3Sc_2Si_3O_{12}$, two different data from the different group were plotted [26] (reproduced from ref. [26] with permission from Elsevier).

6.4 Persistent luminescence mechanism

6.4.1 Carrier generation, trapping, and detrapping

Persistent luminescence is continuous luminescence even after ceasing excitation. This phenomenon is caused by carrier generation by light, carrier trapping, carrier detrapping, and recombination processes [8, 43]. These processes are schematically depicted in Figure 6.7. When samples are illuminated by excitation light with photon energy above bandgap, the electron–hole pair can be generated (1. carrier generation). The generated carriers can be captured by electron traps and hole traps, respectively (2. carrier trapping). These carriers are not released if the trap depths are deep enough relative to the thermal energy at a given temperature (3. storage). To cause persistent luminescence, either electron or hole must be de-trapped by thermal energy at a given temperature (detrapping process). Although the detrapping carrier is determined by the relationship of carrier trap depth, many persistent phosphors follow the electron detrapping process. In the condition that the electron trap depth (E_{e_trap}) is shallower than the hole trap depth (E_{h_trap}), the electrons are firstly detrapped (4. electron detrapping). The detrapped electrons transfer to the hole traps (hole trapping luminescence centers) and recombine with them. In general, luminescence is caused from the individual excited state of the luminescence center through the recombination process (5. luminescence).

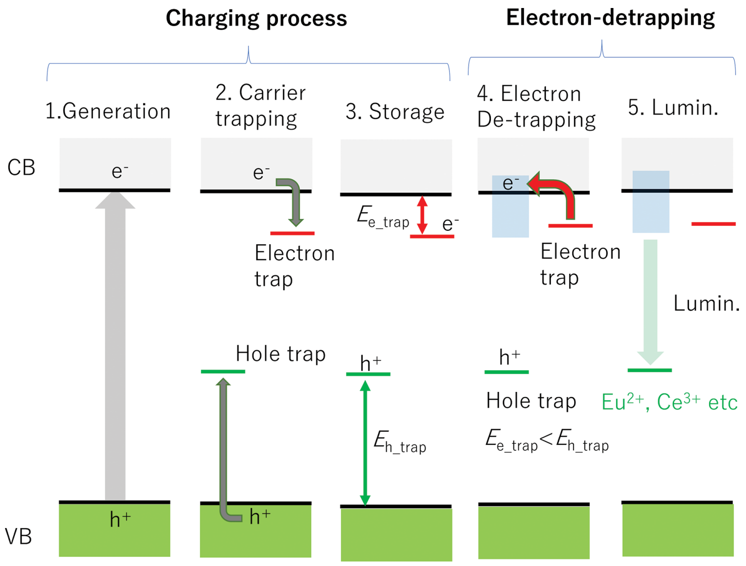

Figure 6.7: Persistent luminescence mechanism with different processes (generation, trapping, storage, electron detrapping or hole detrapping, and luminescence) [8] (reproduced from Ref. [8] with permission from the Chemical Society of Japan).

6.5 Design of persistent phosphors

6.5.1 VRBE diagram

For the persistent phosphors based on the electron detrapping model, the luminescence center should keep a hole before the recombination phase. This means that the condition of $E_{\text{h\_trap}}>E_{\text{e\_trap}}$ should be satisfied. When the electron trap depth is ranged between ~0.5 and ~1.0 eV, the persistent phosphors based on the electron detrapping mechanism can be obtained at ambient temperature. To predict the hole and electron traps, the VRBE diagram becomes a powerful tool.

The VRBE of Ln-doped compounds can be constructed using spectroscopic data according to the method proposed by Dorenbos, who studied the energy levels of lanthanoid ions and transition metal ions in different host compounds with respect to the valence band top (so-called host-referred binding energy, HRBE) or to the vacuum level (so-called VRBE) for the recent 20 years [33, 44–50]. Figure 6.8 shows the VRBE diagram of $Y_3Al_2Ga_3O_{12}$ garnet compound, in which the VRBE with Ln ions is shown by the number of 4*f* electrons of Ln^{3+} ion as *x*-axis and the VRBE of the electron in a compound as *y*-axis. According to the proposed chemical shift model [33, 46, 51], we can predict the VRBE of Ln ion with several parameters, such as host exciton creation energy (E^{ex}), charge transfer energy of Ln^{3+}, and the $U(6,A)$ parameter that is the energy difference between Eu^{2+} and Eu^{3+} energy levels as shown in Figure 6.8. These parameters can be obtained by simple spectroscopy. Although it is not easy to obtain the $U(6,A)$ value directly, the $U(6,A)$ can be estimated using the centroid shift (ε_c) of 5*d* energy level of Ce^{3+} [51] and the VRBE of Eu^{2+} ($E_{4f}(7,2+,A)$) can be determined by the $U(6,A)$ as follows [46]:

$$U(6,A)=5.44+2.834\exp(-\varepsilon_c/2.2) \tag{6.8}$$

$$E_{4f}(7,2+,A)=-24.92+\frac{18.05-U(6,A)}{0.777-0.0353U(6,A)} \tag{6.9}$$

The zigzag curves of 4*f* electron energy with respect to the vacuum level for Ln^{2+} and Ln^{3+} ions as a function of the 4*f* electron number are not largely changed by the composition of compounds due to the insensitivity of the 4*f* electrons for the environments. Thus, after determining the VRBE of Eu^{2+} from the $U(6,A)$, all VRBEs of Ln^{2+} and Ln^{3+} can be estimated from the universal character of the zigzag curves [46]. Strictly, the zigzag curves of Ln^{3+} and Ln^{2+} are shifted to lower energy by the nephelauxetic effect by increasing the number of 4*f* electrons [49, 50]. In Figure 6.8, the VRBEs of several transition metal ions are also shown based on the charge transfer absorption energy, the trap depth, and the ab initio calculation [47, 48, 52–54].

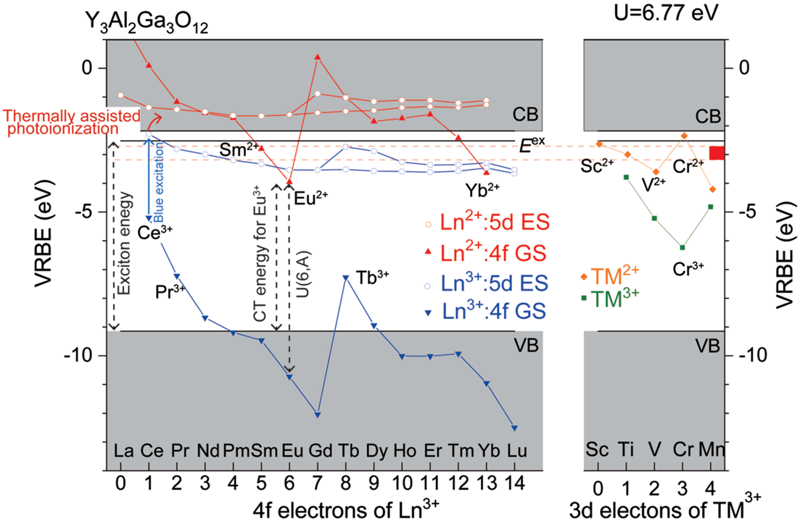

Figure 6.8: VRBE diagram with Ln^{2+}, Ln^{3+}, TM^{2+}, and TM^{3+} in $Y_3Al_2Ga_3O_{12}$ host [8] (reproduced from ref. [8] with permission from the Chemical Society of Japan).

6.5.2 Ce^{3+}-doped garnet persistent phosphors

Figure 6.8 shows the VRBE diagram of the $Y_3Al_2Ga_3O_{12}$ garnet compound. The ground state of Ce^{3+} ion is located above the valence band top with enough large energy gap, which means Ce^{3+} can act as a deep hole trap. Also, Ce^{3+}-doped $Y_3Al_2Ga_3O_{12}$ shows $5d$–$4f$ green luminescence. The lowest $5d_1$ level is located below the bottom of CB with an appropriate energy gap, and the $4f$–$5d_1$ absorption is located in the blue light region due to the strong crystal field. Thus, this phosphor can be photoionizaed by blue light with the support of thermal energy. Ce^{3+}-doped $Y_3Al_2Ga_3O_{12}$ is one of the good candidates of blue light chargeable persistent phosphors.

From the VRBE diagram, Sm^{3+}, Eu^{3+}, Yb^{3+}, Sc^{3+}, Ti^{3+}, V^{3+}, and Cr^{3+} have the possibility to be electron traps. This is because those divalent states are located below the CB bottom as shown in Figure 6.8. Considering the electron trap depth between 0.5 and 1.0 eV, it is predicted that the red region shown along the right *y*-axis is the suitable range as an electron trap for the persistent luminescence at room temperature. Figure 6.9 shows the thermoluminescence (TL) glow curves, which give information of the trap depth of YAGG:Ce^{3+} with different codopant ions [11, 53, 55]. The TL glow curves are clearly changed by changing the codopant ions, which shows that these codopants form different electron traps (Figure 6.9). There is a slight energetic difference between the trap depth estimated by the VRBE diagram and the TL glow curves. However, it is efficient enough to screen candidates of electron traps using VRBE diagram (Figure 6.8). Based on the TL glow curves, the YAGG:Ce^{3+} codoped with Cr^{3+}, Sc^{3+}, and

Yb^{3+} are considered to be suitable as a persistent phosphor at ambient temperature because the TL glow peak temperature is located around 300 K.

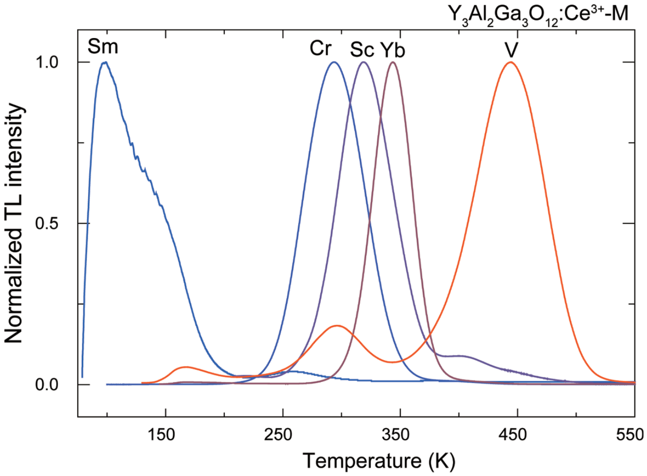

Figure 6.9: Thermoluminescence glow curves of $Y_3Al_2Ga_3O_{12}$:Ce^{3+} with different electron traps [8] (reproduced from Ref. [8] with permission from the Chemical Society of Japan).

All of $Y_3Al_2Ga_3O_{12}$:Ce^{3+}–M^{3+} (M = Cr, Sc, Yb) samples show Ce^{3+} green persistent luminescence. The prepared YAGG:Ce^{3+}–Cr^{3+} persistent phosphors are shown in Figure 6.10a, b. The YAGG:Ce^{3+}–Cr^{3+} ceramics shows better persistent luminescence intensity for tens of minutes compared with the $SrAl_2O_4$:Eu^{2+}–Dy^{3+} powder under white LED illumination. When the Cr^{3+} of codopant is changed to the Yb^{3+} with a slightly deeper trap depth, super long persistent luminescence for more than 5 days after blue LED excitation was achieved as shown in Figure 6.10d. The deeper Yb traps give the slower detrapping rate and extend the persistent duration [55].

Also, the luminescence color of Ce^{3+}-doped garnet phosphors can be tuned by changing the crystal field splitting using different host compositions. The substitution of Lu for Y in YAGG gives blue shifting for Ce^{3+} luminescence and the substitution of Gd for Y site gives redshifting by enhancing the distortion of dodecahedral site [2, 26]. Utilizing the crystal field splitting, bluish green and yellow-to-orange persistent luminescence were successfully developed in the series of (Lu, Y, Gd)$_3Al_2Ga_3O_{12}$:Ce^{3+}–Cr^{3+} as shown in Figure 6.10c [11, 12, 15, 16].

In order to discuss the persistent luminescence properties, persistent luminescence (PersL) spectrum and persistent luminescence excitation (PersLE) spectrum should be measured. The PersL spectrum is the plot of persistent luminescence intensity as a function of wavelength or energy and the PersLE spectrum is the plot of the persistent luminescence intensity at a certain time after ceasing excitation as a function of charging wavelength. Figure 6.11a and b shows the set of general photoluminescence (PL) and PL

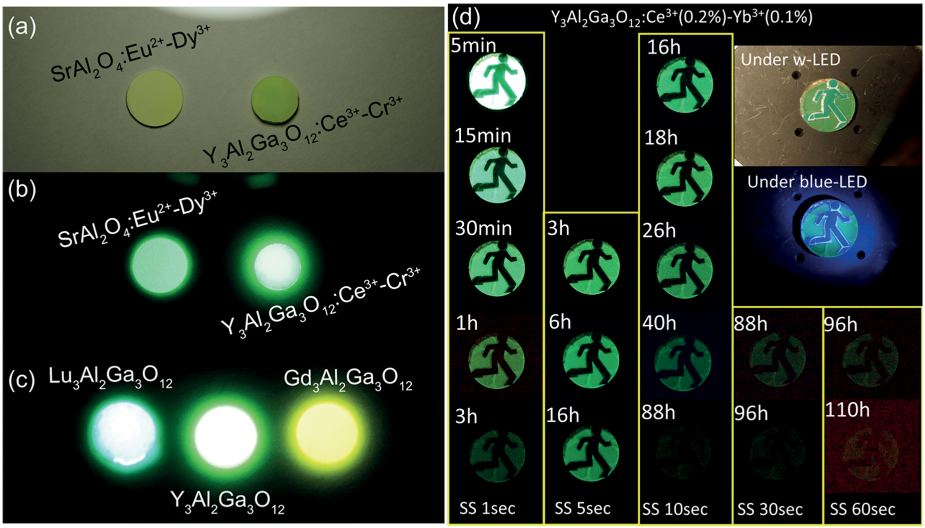
(a)
$SrAl_2O_4$:Eu^{2+}-Dy^{3+}
$Y_3Al_2Ga_3O_{12}$:Ce^{3+}-Cr^{3+}
(b)
$SrAl_2O_4$:Eu^{2+}-Dy^{3+}
$Y_3Al_2Ga_3O_{12}$:Ce^{3+}-Cr^{3+}
(c) $Lu_3Al_2Ga_3O_{12}$
$Gd_3Al_2Ga_3O_{12}$
$Y_3Al_2Ga_3O_{12}$
(d) $Y_3Al_2Ga_3O_{12}$:Ce^{3+}(0.2%)-Yb^{3+}(0.1%)
5min
15min
30min
1h
3h
SS 1sec
3h
6h
16h
SS 5sec
16h
18h
26h
40h
88h
SS 10sec
Under w-LED
Under blue-LED
88h
96h
SS 30sec
96h
110h
SS 60sec

Figure 6.10: (a) Image of $Y_3Al_2Ga_3O_{12}$:Ce^{3+}–Cr^{3+} ceramics and $SrAl_2O_4$:Eu^{2+}–Dy^{3+} powder compact under white-LED illumination and (b) 5 min after excitations ceased, and (c) image of Ce–Cr-doped $Lu_3Al_2Ga_3O_{12}$, $Y_3Al_2Ga_3O_{12}$, and $Gd_3Al_2Ga_3O_{12}$ just after excitations ceased (reproduced from ref. [11] with the permission of AIP Publishing). (d) Photograph of as-made $Y_3Al_2Ga_3O_{12}$:Ce^{3+}–Yb^{3+} transparent ceramics under white LED and blue LED and at different times after blue LED excitation (reprinted with permission from ref. [55], Copyright 2018, American Chemical Society).

excitation(PLE) spectra and the set of the PersL and PersLE spectra in YAGG:Ce^{3+}–Cr^{3+} persistent phosphors [11]. A strong PersLE band is observed in the blue region from 400 to 500 nm in the PersLE spectrum of $Y_3Al_2Ga_3O_{12}$:Ce^{3+}–Cr^{3+} (Figure 6.11b), which indicates that this persistent phosphor is able to be charged by the blue LED as well as the white-LED illumination.

In order to check the charging route, the photocurrent excitation (PCE) spectrum, which is the plot of photocurrent as a function of excitation wavelength, is a powerful tool. In the PCE spectrum of $Y_3Al_2Ga_3O_{12}$:Ce^{3+}, the Ce^{3+}:$4f$–$5d_1$ and $4f$–$5d_2$ (the second lowest $5d$ level) are observed at around 420 and 350 nm, respectively. These results show the electrons are excited to the conduction band from the Ce^{3+} ion through the 5d excited states. Based on the results of both the PersLE spectrum and the PCE spectrum, the charging process of this persistent phosphor by blue light is mainly caused by the excitation to Ce^{3+}:$5d_1$ and the electron transfer to the conduction band.

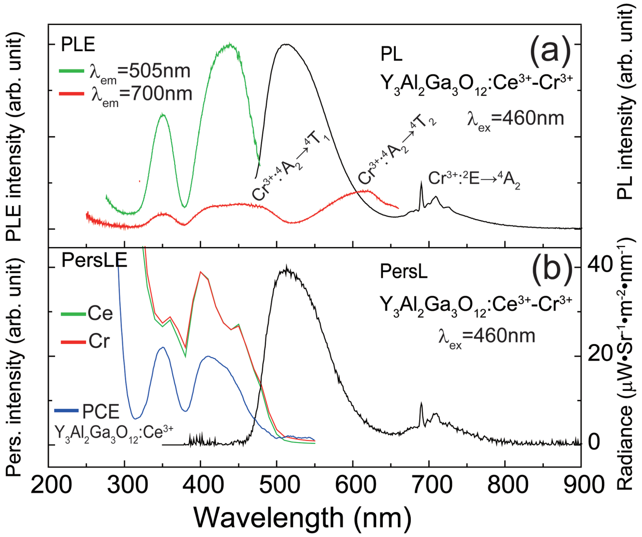

Figure 6.11: (a) PL and PLE and (b) PersL, PersLE, and PCE spectra of $Y_3Al_2Ga_3O_{12}$:Ce^{3+}–Cr^{3+} [8, 11] (reproduced from ref. [11] with the permission of AIP Publishing).

6.5.3 Pr^{3+}- and Tb^{3+}-doped persistent phosphors

Based on the VRBE of Figure 6.8, Pr^{3+} and Tb^{3+} can also act as hole traps, leading to good persistent luminescence centers [18]. Different for Ce^{3+}:5*d*–4*f* luminescence, both Pr^{3+} and Tb^{3+} show several sharp luminescence peaks attributed by the 4*f*–4*f* transitions in the visible range. Figure 6.12 shows several VRBE diagrams of rare earth aluminum gallium garnets $Lu_3Al_5O_{12}$(LuAG), $Y_3Al_5O_{12}$(YAG), $Y_3Al_2Ga_3O_{12}$ (YAGG), $Y_3Ga_5O_{12}$ (YGG), and $Gd_3Ga_5O_{12}$ (GGG) [18, 26]. Because the Pr^{3+} and Tb^{3+} ground states are located deeply apart from the bottom of conduction band, the GGG with the lowest CB bottom energy among these garnet compounds is suitable to get the small activation energy for charging process. On the other hand, the electron traps of Yb^{3+} and Cr^{3+} that works well in YAGG may not act as a good electron trap in the GGG host because of the shallow trap depth. In the GGG host, a deeper Eu^{3+} electron trap becomes suitable (Figure 6.12). As another advantage, Gd-based materials can be attracted by a permanent magnet due to the large magnetic moments, which means that the spatial location of Gd-based persistent phosphors can be controlled magnetically.

In order to check the electron traps by Eu^{3+}, the TL glow curves of the GGG samples were measured (Figure 6.13a, b). Although both GGG:Tb^{3+} and GGG:Pr^{3+} samples show weak TL glow peaks, an intense TL glow peak is observed around ambient temperature in the Eu^{3+}-codoped GGG:Tb^{3+} and GGG:Pr^{3+} [18]. This result indicates that the Eu^{3+} ions act as identical electron traps in both samples. Actually, strong persistent luminescence

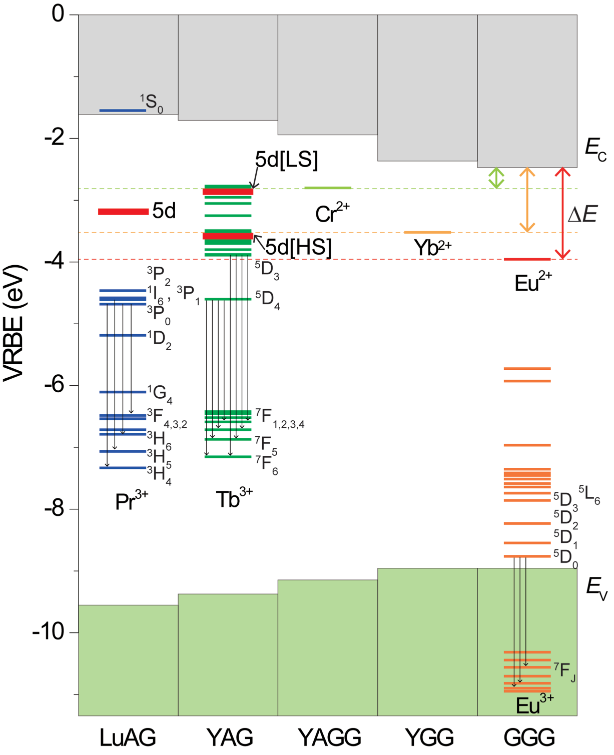

Figure 6.12: Stacked VRBE diagram of several garnets [18] (reproduced from ref. [18] with the permission of Wiley).

was observed in the GGG:Pr^{3+}–Eu^{3+} and Tb^{3+}–Eu^{3+} samples. The persistent color of GGG: Tb^{3+}–Eu^{3+} is blue and that of GGG:Pr^{3+}–Eu^{3+} is reddish white as shown in Figure 6.13c. By doping with Pr^{3+} and Tb^{3+} as luminescence centers simultaneously, the persistent luminescence color changes to pure white as shown in Figure 6.13c due to the mixing of the blue persistent luminescence from Tb^{3+} and the red persistent luminescence from Pr^{3+}.

Due to the paramagnetic center of the Gd^{3+} ion ($4f^7$), the $Gd_3Ga_5O_{12}$ is also paramagnetic with high susceptibility. Figure 6.13d shows the schematic diagram of the experimental procedure to drag powder phosphors in water. The powder sample of GGG:Pr^{3+}–Tb^{3+}–Eu^{3+} were dispersed in water and charged by the Hg lamp. When the magnet is fixed on the wall of the quartz cell by plastic tape and the dispersed powder in water is stirred again, the powders are dragged around the magnet. As a result, persistent luminescence was observed at the bottom and near the magnet as shown in Figure 6.13e.

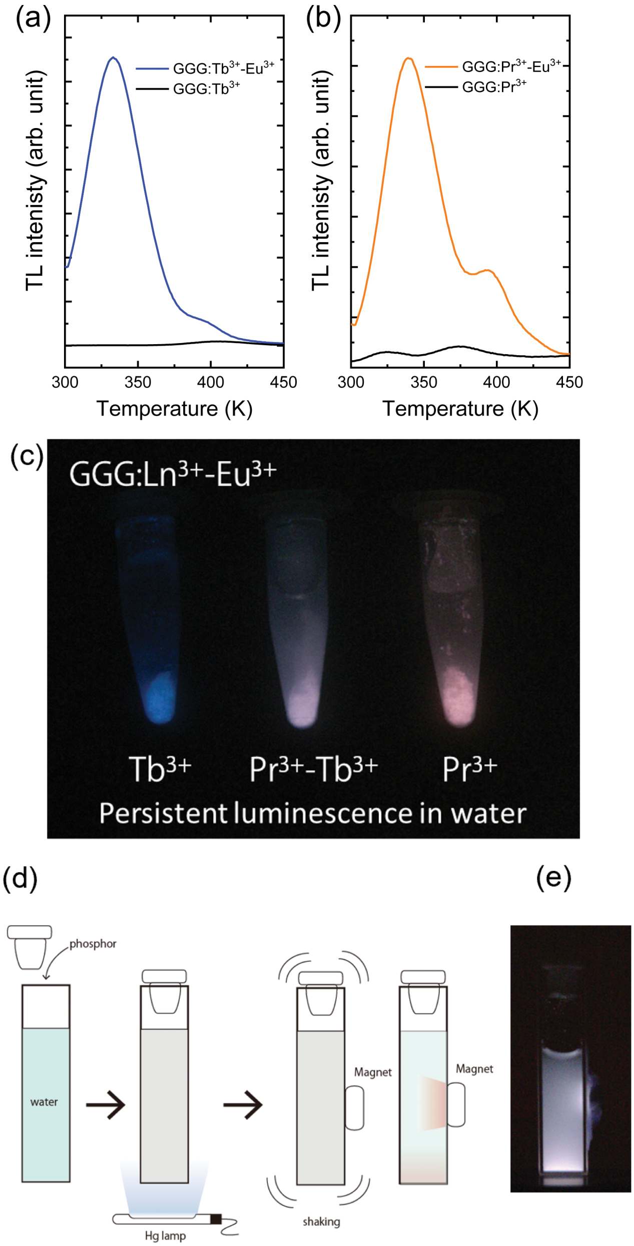

Figure 6.13: Thermoluminescence glow curves of (a) $Gd_3Ga_5O_{12}$:Tb^{3+} and Tb^{3+}–Eu^{3+} and (b) $Gd_3Ga_5O_{12}$:Pr^{3+} and Pr^{3+}–Eu^{3+}. (c) Images of persistent luminescence for the $Gd_3Ga_5O_{12}$ compounds with Tb^{3+}–Eu^{3+}, Pr^{3+}–Tb^{3+}–Eu^{3+}, and Pr^{3+}–Eu^{3+} in water. (d) Experimental procedure to demonstrate that the magnet drags the $Gd_3Ga_5O_{12}$:Pr^{3+}–Tb^{3+}–Eu^{3+} persistent phosphors in water, and (e) photograph of cool white persistent phosphors dragged by magnet [18] (reproduced from ref. [18] with the permission of Wiley).

6.5.4 Cr^{3+} deep red persistent phosphors

While the Cr^{3+} ion is one of the good electron traps for the garnet compounds such as $Y_3Al_2Ga_3O_{12}$, it also acts as the hole trap because the Cr^{3+} ground state is located within bandgap as shown in Figure 6.8. Thus, there is the possibility that Cr^{3+} singly doped garnet compounds show persistent luminescence without codopants. Also the Cr^{3+} ion in an octahedral site shows red sharp luminescence line due to the ^2E–$^4A_2$ transition in the high crystal field and deep red broad luminescence band due to the $^4T_2$–$^4A_2$ transition in the weak crystal field. Controlling the crystal field strength, the luminescence wavelength can be changed. The left figure of Figure 6.14 shows the PL spectra of Cr^{3+}-doped various garnet compounds [21]. In the PL spectra, several sharp lines (^2E–$^4A_2$) and broad band ($^4T_2$–$^4A_2$) are observed in the range between 650 and 950 nm. These luminescence intensity ratios are changed by a garnet composition which varies the crystal field of Cr^{3+} in the octahedral site of the garnet structure. The right figure of Figure 6.14 shows the PersL spectra [21]. All the samples show persistent luminescence, which has the same spectral shape as PL. The persistent luminescence spectra are located in the first biological window. Therefore, it is a promising candidate as a luminescent probe for bioimaging applications.

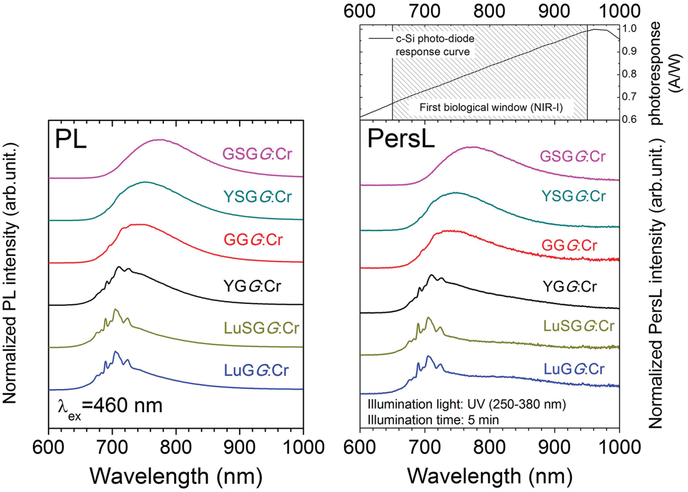

Figure 6.14: PL and PersL spectra of Cr^{3+}-doped $Gd_3Sc_2Ga_3O_{12}$(GSGG), $Y_3Sc_2Ga_3O_{12}$(YSGG), $Gd_3Ga_5O_{12}$ (GGG), $Y_3Ga_5O_{12}$(YGG), $Gd_3Ga_5O_{12}$(GGG), $Lu_3Sc_2Ga_3O_{12}$(LuSGG), and $Lu_3Ga_5O_{12}$(LuGG). (inset) Response curve of c-Si photodiode with first biological window [21] (reproduced from ref. [21] with the permission of Wiley).

6.5.5 Er^{3+}, Nd^{3+} near-infrared persistent phosphors

There are persistent phosphors caused by energy transfer from the persistent luminescent center with high photon energy to another luminescent center that originally does not show persistent luminescence. Physically, if the luminescence energy transfer occurs in the PL spectrum, the persistent energy transfer also occurs. It is known that Nd^{3+} and Er^{3+} ions are excellent NIR luminescence centers. However, it is difficult to be deep hole trap because these energy levels are located within VB or just above VB top in the garnet compounds as shown in Figure 6.8. In order to obtain the NIR persistent luminescence of Er^{3+} and Nd^{3+} in the garnets, the persistent energy transfer is the only way. Er^{3+} and Nd^{3+} have 4*f* energy levels also in the visible range, and the developed YAGG:Ce^{3+}–Cr^{3+} persistent phosphors can be a suitable donor of the persistent energy transfer because of very broad persistent luminescence band around 510 nm as shown in Figure 6.11.

Figure 6.15a shows the PL spectra of YAGG:Ce–Cr and YAGG:Nd–Ce–Cr ceramics and the diffuse reflectance of the YAGG:Nd ceramic [23]. In the diffuse reflectance of the YAGG:Nd, the absorption bands ($^4I_{9/2} \rightarrow {}^2G_{3/2}, {}^4G_{7/2}, {}^2G_{7/2}, {}^4G_{5/2}$) of Nd^{3+} are observed in the range between 450 and 600 nm, which overlaps with the 5*d*–4*f* luminescence band of Ce^{3+} in the YAGG host. Thus, the energy transfer process from Ce^{3+} to Nd^{3+} is expected. From the comparison between the PL spectra of YAGG:Ce–Cr and YAGG:Nd–Ce–Cr, the Ce^{3+}: 5*d*–4*f* luminescence intensity decreases and additional PL lines at around 880, 1,064, and 1,335 nm, owing to the Nd^{3+}: $^4F_{3/2} \rightarrow {}^4I_{9/2}$, $^4I_{11/2}$, and $^4I_{13/2}$, respectively, appear by codoping with Nd^{3+}. It is obvious that the energy transfer occurs between Ce^{3+} and Nd^{3+}, and the persistent energy transfer should also exist. Figure 6.15b shows PersL spectra of the YAGG:Nd–Ce–Cr samples. Similar to the PL spectrum, the Nd^{3+} 4*f*–4*f* persistent luminescence lines are observed from 800 to 1,500 nm in addition to Ce^{3+} and Cr^{3+} persistent luminescence band in the visible range. Also the persistent radiance of the YAGG: Nd–Ce–Cr phosphor is over two times higher in the NIR region than that of the widely used $ZnGa_2O_4$:Cr^{3+} red persistent phosphor at 60 min after ceasing the excitation due to an efficient persistent energy transfer. The YAGG: Nd–Ce–Cr NIR persistent phosphors are expected to be applied to in vivo bioimaging probe because of the matching with the NIR-I (650–950 nm) and NIR-II (1,000–1,400 nm) biological windows.

This kind of persistent energy transfer is also caused between Ce^{3+} and Er^{3+} because Er^{3+} has an absorption transition of $^4I_{15/2} \rightarrow {}^4S_{3/2}$ peaking at 555 nm[22]. Also, Er^{3+} has strong NIR luminescence due to the $^4I_{13/2} \rightarrow {}^4I_{15/2}$ transition around 1,550 nm which is located in the third bioimaging window (NIR-III, approximately from 1,500 to 1,800 nm). Therefore, YAGG:Er–Ce–Cr shows excellent NIR persistent luminescence in the NIR-III window. Figure 6.16a and b shows persistent luminescence decay curves with luminance and NIR photon radiance values of YAGG:Er–Ce–Cr and reference samples after ceasing blue light illumination. The luminance of YAGG:Er–Ce–Cr is lower than that of YAGG:Ce–Cr. Figure 6.16c and d shows the images of persistent luminescence for YAGG:Ce–Cr and YAGG:Er–Ce–Cr taken by a general digital camera and a SWIR (the short-wave infrared, ~900–1,700 nm) camera, respectively. Although visible persistent luminescence is observed in both YAGG:Ce–Cr and YAGG:Nd–Ce–Cr samples, NIR persistent luminescence was detected only in YAGG:Er–Ce–Cr. These results suggest that the persistent energy transfer occurs from Ce^{3+} to Er^{3+}. From the persistent luminescence spectrum, the NIR persistent luminescence is confirmed to be caused by the Er^{3+}:$^4I_{13/2} \rightarrow {}^4I_{15/2}$. Figure 6.16b shows the persistent luminescence curves with NIR photon radiance for $ZnGa_2O_4$:Cr^{3+} and YAGG:Er–Ce–Cr. The NIR photon radiance of the YAGG:Er–Ce–Cr sample for the NIR-III window at 10 min after ceasing the blue light excitation is over two times higher than that of the widely used deep red persistent phosphor $ZnGa_2O_4$:Cr^{3+} for the NIR-I window.

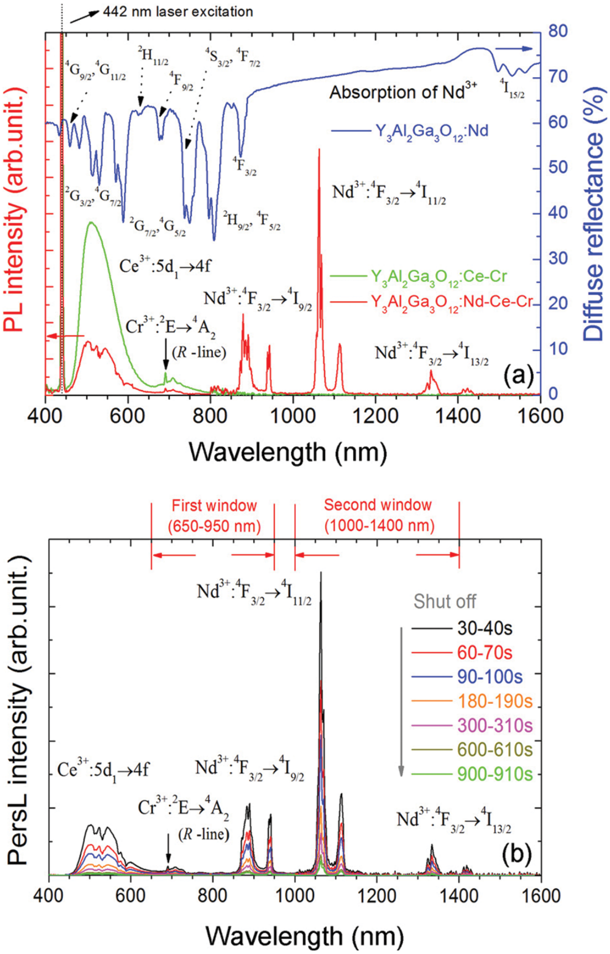

Figure 6.15: (a) PL spectra of the YAGG:Ce–Cr and YAGG:Nd–Ce–Cr ceramics as well as the diffuse reflectance of the YAGG:Nd ceramic and (b) PersL spectra of the YAGG:Nd–Ce–Cr ceramics (integrating time: 10 s) [23] (reproduced from ref. [23] with the permission of AIP Publishing).

The series of garnet persistent phosphors covers the visible to NIR-I, II, III luminescence wavelength region with excellent persistent luminescence intensity by controlling carrier traps and energy transfer process. These various unique persistent luminescence properties are enabled by the solubility of metal ions as luminescence center and carrier trapping center and the tunability of host composition for garnet compounds.

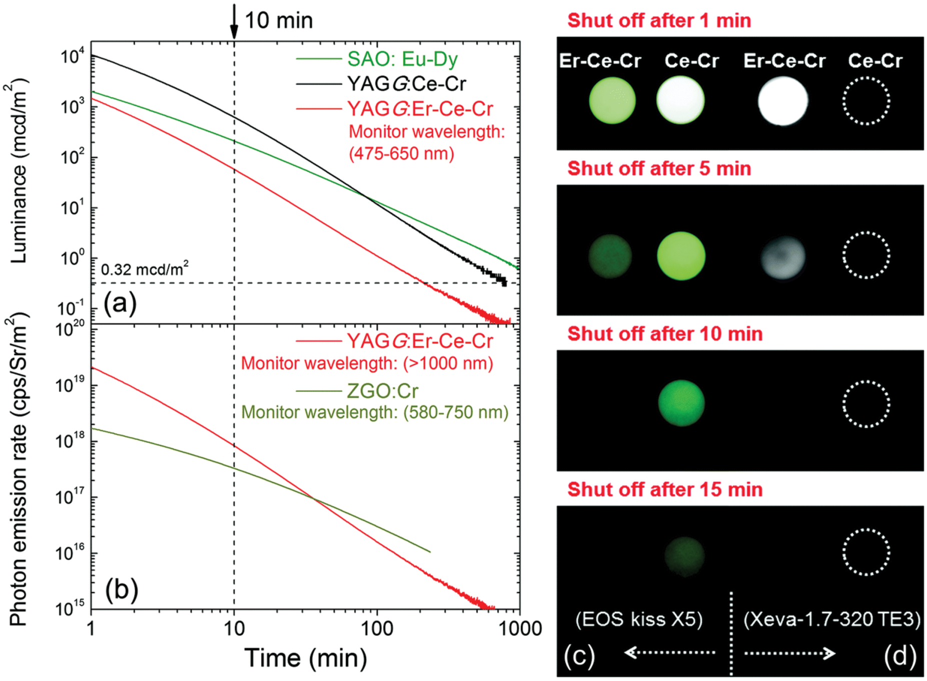

Figure 6.16: Persistent luminescence decay curves of the YAGG:Er–Ce–Cr ceramic sample: (a) luminance monitoring Ce^{3+} emission (YAGG:Ce–Cr and $SrAl_2O_4$:Eu–Dy ceramic samples as references) and (b) photon emission rate monitoring Er^{3+} emission ($ZnGa_2O_4:Cr^{3+}$ ceramic sample as a reference); and photo images of the YAGG:Ce–Cr and YAGG:Er–Ce–Cr ceramic samples after blue LED (455 nm, 1 W output) illumination for 5 min: (c) this is taken by a digital camera (EOX kiss X5) with exposure time of 1 s, ISO value of 1,600, aperture value (*F*-value) of 5.0, and (d) by a SWIR camera (Xeva-1.7–320 TE3) with integrating time of 0.04 s [22] (reproduced from Ref. [22] with permission from the Royal Society of Chemistry).

References

[1] G. Blasse, A. Bril, A new phosphor for flying-spot cathode-ray tubes for color television: Yellow-emitting $Y_3Al_5O_{12}$–Ce^{3+}, Appl. Phys. Lett. 11 (1967) 53.

[2] Z. Xia, A. Meijerink, Ce^{3+}-Doped garnet phosphors: Composition modification, luminescence properties and applications, Chem. Soc. Rev. 46 (2017) 275.

[3] J.E. Geusic, H.M. Marcos, L.G.V. Uitert, Laser oscillations in Nd-doped yttrium aluminum, yttrium gallium and gadolinium garnets, Appl. Phys. Lett. 4 (1964) 182.

[4] A. Ikesue, T. Kinoshita, K. Kamata, K. Yoshida, Fabrication and optical properties of high-performance polycrystalline Nd:YAG ceramics for solid-state lasers, J. Am. Ceram. Soc. 78 (1995) 1033.

[5] G.N.A. De Guzman, M.-H. Fang, C.-H. Liang, Z. Bao, S.-F. Hu, R.-S. Liu, [INVITED] Near-infrared phosphors and their full potential: A review on practical applications and future perspectives, J. Lumin. 219 (2020) 116944.

[6] Z. Jia, C. Yuan, Y. Liu, X.-J. Wang, P. Sun, L. Wang, H. Jiang, J. Jiang, Strategies to approach high performance in Cr^{3+}-doped phosphors for high-power NIR-LED light sources, Light Sci. Appl. 9 (2020) 86.

[7] J. Ueda, Analysis of optoelectronic properties and development of new persistent phosphor in Ce^{3+}-doped garnet ceramics, J. Ceram, Soc. Jpn. 123 (2015) 1059.

[8] J. Ueda, How to design and analyze persistent phosphors? Bull. Chem. Soc. Jpn. 94 (2021) 2807.

[9] J. Ueda, K. Aishima, S. Nishiura, S. Tanabe, Afterglow luminescence in Ce^{3+}-doped $Y_3Sc_2Ga_3O_{12}$ ceramics, Appl. Phys. Express 4 (2011) 042602.

[10] J. Ueda, K. Aishima, S. Tanabe, Temperature and compositional dependence of optical and optoelectronic properties in Ce^{3+}-doped $Y_3Sc_2Al_{3-x}Ga_xO_{12}$ (x=0, 1, 2, 3), Opt. Mater. (Amst.) 35 (2013) 1952.

[11] J. Ueda, K. Kuroishi, S. Tanabe, Bright persistent ceramic phosphors of Ce^{3+}-Cr^{3+}-codoped garnet able to store by blue light, Appl. Phys. Lett. 104 (2014) 101904.

[12] J. Ueda, K. Kuroishi, S. Tanabe, Yellow persistent luminescence in Ce^{3+} -Cr^{3+}-codoped gadolinium aluminum gallium garnet transparent ceramics after blue-light excitation, Appl. Phys. Express 7 (2014) 062201.

[13] J. Ueda, P. Dorenbos, A.J.J. Bos, K. Kuroishi, S. Tanabe, Control of electron transfer between Ce^{3+} and Cr^{3+} in the $Y_3Al_{5-x}Ga_xO_{12}$ host via conduction band engineering, J. Mater. Chem. C 3 (2015) 5642.

[14] J. Xu, J. Ueda, K. Kuroishi, S. Tanabe, Fabrication of Ce^{3+}-Cr^{3+} co-doped yttrium aluminium gallium garnet transparent ceramic phosphors with super long persistent luminescence, Scr. Mater. 102 (2015) 47.

[15] K. Asami, J. Ueda, S. Tanabe, Trap depth and color variation of Ce^{3+}-Cr^{3+} co-doped $Gd_3(Al,Ga)_5O_{12}$ garnet persistent phosphors, Opt. Mater. (Amst.) 62 (2016) 171.

[16] K. Asami, J. Ueda, M. Kitaura, S. Tanabe, Investigation of luminescence quenching and persistent luminescence in Ce^{3+} doped $(Gd,Y)_3(Al,Ga)_5O_{12}$ garnet using vacuum referred binding energy diagram, J. Lumin. 198 (2018) 418.

[17] J. Xu, J. Ueda, S. Tanabe, Novel persistent phosphors of lanthanide-chromium co-doped yttrium aluminum gallium garnet: Design concept with vacuum referred binding energy diagram, J. Mater. Chem. C 4 (2016) 4380.

[18] J. Ueda, S. Miyano, J. Xu, P. Dorenbos, S. Tanabe, Development of white persistent phosphors by manipulating lanthanide ions in gadolinium gallium garnets, Adv. Photon. Res. 2 (2021) 2000102.

[19] J. Xu, J. Ueda, S. Tanabe, Design of deep-red persistent phosphors of $Gd_3Al_{5-x}Ga_xO_{12}$:Cr^{3+} transparent ceramics sensitized by Eu^{3+} as an electron trap using conduction band engineering, Opt. Mater. Express 5 (2015) 963.

[20] J. Xu, J. Ueda, Y. Zhuang, B. Viana, S. Tanabe, $Y_3Al_{5-x}Ga_xO_{12}$:Cr^{3+} : A novel red persistent phosphor with high brightness, Appl. Phys. Express 8 (2015) 042602.

[21] J. Xu, J. Ueda, S. Tanabe, Toward tunable and bright deep-red persistent luminescence of Cr^{3+} in garnets, J. Am. Ceram. Soc. 100 (2017) 4033.

[22] J. Xu, D. Murata, J. Ueda, S. Tanabe, Near-infrared long persistent luminescence of Er^{3+} in garnet for the third bio-imaging window, J. Mater. Chem. C 4 (2016) 11096.

[23] J. Xu, S. Tanabe, A.D. Sontakke, Near-infrared multi-wavelengths long persistent luminescence of Nd^{3+} ion through persistent energy transfer in Ce^{3+}, Cr^{3+} co-doped $Y_3Al_2Ga_3O_{12}$ for the first and second bio-imaging windows, J. Ueda, Appl. Phys. Lett. 107 (2015) 081903.

[24] G. Menzer, Zeitschrift Für Kristallographie – Cryst. Mater. 69 (1929) 300.

[25] K. Momma, F. Izumi, J. Appl. Crystallogr. 44 (2011) 1272.

[26] J. Ueda, S. Tanabe, Review of luminescent properties of Ce^{3+}-doped garnet phosphors: New insight into the effect of crystal and electronic structure, Opt. Mater.:X 1 (2019) 100018.

[27] F. Euler, J.A. Bruce, Oxygen coordinates of compounds with garnet structure, Acta Crystallogr. 19 (1965) 971.

[28] R.J. Lang, The spectrum of trebly ionized cerium, Can. J. Res. 14a (1936) 127.

[29] P. Dorenbos, 5d-level energies of Ce^{3+} and the crystalline environment. I. Fluoride compounds, Phys. Rev. B 62 (2000) 15640.

[30] P. Dorenbos, 5d-level energies of Ce^{3+} and the crystalline environment. II. Chloride, bromide, and iodide compounds, Phys. Rev. B 62 (2000) 15650.

[31] P. Dorenbos, 5d-level energies of Ce^{3+} and the crystalline environment. III. Oxides containing ionic complexes, Phys. Rev. B 64 (2001) 125117.

[32] P. Dorenbos, 5d-level energies of Ce^{3+} and the crystalline environment. IV. Aluminates and “simple” oxides, J. Lumin. 99 (2002) 283.

[33] P. Dorenbos, A review on how lanthanide impurity levels change with chemistry and structure of inorganic compounds, ECS J. Solid State Sci. Technol. 2 (2013) R3001.

[34] P. Dorenbos, Electronic structure and optical properties of the lanthanide activated $RE_3(Al_{1-x}Ga_x)_5O_{12}$ (RE=Gd, Y, Lu) garnet compounds, J. Lumin. 134 (2013) 310.

[35] P. Dorenbos, Relating the energy of the $[Xe]5d^1$ configuration of Ce^{3+} in inorganic compounds with anion polarizability and cation electronegativity, Phys. Rev. B 65 (2002) 235110.

[36] P. Dorenbos, Optical basicity, interpreted by means of Ce^{3+} 5d level spectroscopy in ionic crystals, J. Non Cryst. Solids 324 (2003) 220.

[37] J.A. Duffy, M.D. Ingram, Use of thallium(I), lead(II), and bismuth(III) as spectroscopic probes for ionic -covalent interaction in glasses, J. Chem. Phys. 52 (1970) 3752.

[38] J.A. Duffy, M.D. Ingram, Establishment of an optical scale for Lewis basicity in inorganic oxyacids, molten salts, and glasses, J. Am. Chem. Soc. 93 (1971) 6448.

[39] J.A. Duffy, M.D. Ingram, New correlation between s -p spectra and the nephelauxetic ratio β: Applications in molten salt and glass chemistry, J. Chem. Phys. 54 (1971) 443.

[40] J.A. Duffy, Optical basicity analysis of glasses containing trivalent scandium, yttrium, gallium and indium, Phys. Chem. Glasses 46 (2005) 500.

[41] P. Dorenbos, Crystal field splitting of lanthanide $4f^{n-1}5d$-levels in inorganic compounds, J. Alloys Compd. 341 (2002) 156.

[42] J.L. Wu, G. Gundiah, A.K. Cheetham, Structure-property correlations in Ce-doped garnet phosphors for use in solid state lighting, Chem. Phys. Lett. 441 (2007) 250.

[43] J. Xu, S. Tanabe, Persistent luminescence instead of phosphorescence: History, mechanism, and perspective, J. Lumin. 205 (2019) 581.

[44] P. Dorenbos, Systematic behaviour in trivalent lanthanide charge transfer energies, J. Phys.: Condens. Matter 15 (2003) 8417.

[45] P. Dorenbos, A.H. Krumpel, E. van der Kolk, P. Boutinaud, M. Bettinelli, E. Cavalli, Lanthanide level location in transition metal complex compounds, Opt. Mater. (Amst.) 32 (2010) 1681.

[46] P. Dorenbos, Modeling the chemical shift of lanthanide 4f electron binding energies, Phys. Rev. B 85 (2012) 165107.

[47] P. Dorenbos, E.G. Rogers, Vacuum referred binding energies of the lanthanides in transition metal oxide compounds, ECS J. Solid State Sci. Technol. 3 (2014) R150.

[48] E.G. Rogers, P. Dorenbos, Vacuum referred binding energy of the single 3d, 4d, or 5d electron in transition metal and lanthanide impurities in compounds, ECS J. Solid State Sci. Technol. 3 (2014) R173.

[49] P. Dorenbos, The nephelauxetic effect on the electron binding energy in the $4f^q$ ground state of lanthanides in compounds, J. Lumin. 214 (2019) 116536.

[50] P. Dorenbos, [INVITED] Improved parameters for the lanthanide $4f^q$ and $4f^{q-1}5d$ curves in HRBE and VRBE schemes that takes the nephelauxetic effect into account, J. Lumin. 222 (2020) 117164.

[51] P. Dorenbos, Ce^{3+} 5d-centroid shift and vacuum referred 4f-electron binding energies of all lanthanide impurities in 150 different compounds, J. Lumin. 135 (2013) 93.

[52] E.G. Rogers, P. Dorenbos, Vacuum energy referred $Ti^{3+}/^{4+}$ donor/acceptor states in insulating and semiconducting inorganic compounds, J. Lumin. 153 (2014) 40.

[53] J. Ueda, A. Hashimoto, S. Takemura, K. Ogasawara, P. Dorenbos, S. Tanabe, Vacuum referred binding energy of 3d transition metal ions for persistent and photostimulated luminescence phosphors of cerium-doped garnets, J. Lumin. 192 (2017) 371.

[54] B. Qu, R. Zhou, L. Wang, P. Dorenbos, How to predict the location of the defect levels induced by 3d transition metal ions at octahedral sites of aluminate phosphors, J. Mater. Chem. C 7 (2019) 95.

[55] J. Ueda, S. Miyano, S. Tanabe, Formation of deep electron traps by Yb3+ codoping leads to super-long persistent luminescence in Ce^{3+}-doped yttrium aluminum gallium garnet phosphors, ACS Appl. Mater. Interfaces 10 (2018) 20652.

Gabrielle A. Mandl, Gabriella Tessitore, Steven L. Maurizio,
John A. Capobianco

Chapter 7
Luminescent nanoparticles for bioimaging applications

Luminescent nanoparticle-based imaging probes have risen to the forefront of advancements in bioimaging due to their unique optical and physical properties. The ability to modify the surfaces of these materials to achieve biocompatibility, targeting, and sensing capabilities combined with the photostability of these materials has paved the way for optical and anatomical imaging advancements. Lanthanide and transition metal-doped nanoparticles are of particular interest for their applications in near-infrared (NIR), upconversion, and persistent luminescence imaging. Herein, the fundamental properties of nanomaterials exhibiting traits to facilitate these three imaging techniques are discussed.

7.1 Introduction

Bioimaging refers to all imaging techniques related to the observation of biological structure and/or function, including but not limited to microscopy-based techniques [1–3]. Together, these technologies are capable of generating complex images from the anatomical level all the way down to subcellular components. These techniques have been employed to diagnose and treat patients as well as advance our understanding of fundamental biological functions. Each of these imaging techniques has benefited from, or requires, a contrast agent to increase signal-to-noise ratios and/or differentiate between healthy and diseased tissues. In order to accurately diagnose disease or observe biological functioning, it is imperative that the means through which the structure and/or function are observed does not alter or interfere with the specimen [2]. Thus, a primary goal of researchers developing contrast agents is to do so without significantly altering the specimen.

Traditional small molecule-based contrast agents have been approved for clinical use for anatomical imaging techniques such as computed tomography (CT) and magnetic resonance imaging (MRI) and *ex vivo* histopathological imaging also commonly relies on the use of small molecule probes to diagnose abnormalities in tissue samples [1]. Despite the advances that have been made using small molecule contrast agents, there are still drawbacks that hinder the advancement of imaging techniques such as their photostability and broad excitation and emission bands [2–5]. Optical imaging techniques, in which light in the visible and NIR regions are used to generate images

https://doi.org/10.1515/9783110607871-007

at both the subcellular and anatomical levels, have advanced significantly in terms of improved detection, resolution, and multiplexing abilities due to the introduction of luminescent nanoparticles for increasing contrast.

Luminescent nanomaterials have a distinct advantage over their bulk and micro-counterparts, as they are in a size range (typically sub-100 nm along a single dimension) that facilitates cellular uptake as well as the ability to target and accumulate in different subcellular compartments [6]. Furthermore, their surface chemistry is highly versatile and can allow for a wide array of chemical functionalizations, imparting nearly infinite possibilities for targeting and stability purposes. Also, coupling of luminescent nanoparticles for optical imaging with other techniques has been investigated [7–9].

One of the primary advantages of nanoparticles over small molecule probes lies in the ability to conjugate multiple different targeting moieties to the surface of nanoparticles. Typically, small molecule contrast agents are specific to the identification of a single biomarker and require different excitation energies to obtain a signal [10]. In contrast, the conjugation of multiple targeting moieties to a single nanoparticle can enable the simultaneous detection of multiple biomarkers using a single excitation wavelength. The simplicity and versatility of systems which rely on a single excitation wavelength is highly advantageous for clinical applications, as this limits the cost of acquiring sophisticated imaging systems as well as the time required to obtain results for each biomarker.

Luminescent nanoparticles used for bioimaging ideally possess a combination of five main properties: (1) a large Stokes or anti-Stokes shift to minimize autofluorescence and background noise, (2) robust luminescence which is highly stable and resistant to photobleaching to facilitate long-term tracking of the probes, (3) have narrow emission bands to allow for multiplexed imaging, (4) functionalizable surfaces that facilitate targeting of specific organs or subcellular components depending on the application, and (5) exert minimal toxicity and sample-altering effects on the specimen [1–3, 5, 6, 10–12]. These properties are necessary to design nanoparticles that can be used to safely and accurately observe the nuances of cellular functioning that have advantages over single molecule probes. The development of nanoparticles which possess a combination of two or more of these properties is believed to generate advancements which cannot be achieved with conventional small molecule fluorophores [11, 13]. For a more in-depth understanding of the requirements at the cellular level, there are several publications on the subject [1, 13, 14].

The advent of some recently developed optical microscopy techniques has taken advantage of a variety of unique luminescence properties exhibited by several types of luminescent nanomaterials including, but not limited to, their luminescence lifetime, excitation and emission wavelengths, nonlinear luminescence, and narrow emission bands. For example, fluorescence lifetime imaging microscopy (FLIM) utilizes the luminescence lifetime of fluorophores to generate images with a high signal-to-noise ratio. Since the luminescence lifetimes of biological fluorophores are quite short (on the order of several nanoseconds) [3], luminescent nanoparticles with lifetimes on the order of microseconds to milliseconds, such as lanthanide-doped nanoparticles, are ideal probes for generating background-free images through this technique. Several review articles that discuss advances in optical microscopy techniques at length are present in the literature [1, 5, 11, 15–17].

Herein, we will focus the discussion on three avenues in which luminescent nanoparticles have advanced microscopy-based bioimaging techniques: NIR imaging, upconversion imaging, and persistent luminescence imaging utilizing transition metal and lanthanide ion-doped nanoparticles. A thorough discussion of the premise of each technique and the fundamental luminescence properties that have been utilized to generate advancements in these techniques will be provided.

7.2 Near-infrared luminescence: the role of the biological windows

To utilize nanoparticles for optical bioimaging, the primary consideration is the excitation and emission wavelengths of the nanoparticles. This is because only light in the NIR region is minimally transparent to biological systems and can pass through tissues and other cellular components with greater efficiency. Ultraviolet and most visible light (<600 nm) can cause cellular damage or can induce intrinsic luminescence processes in lipids and proteins, known as autofluorescence [18]. This makes these wavelengths unsuitable for optical bioimaging applications as much of the light will be attenuated by the biological system itself. For wavelengths >600 nm, however, there are other concerns that must be addressed to maximize the efficiency of the intended probes.

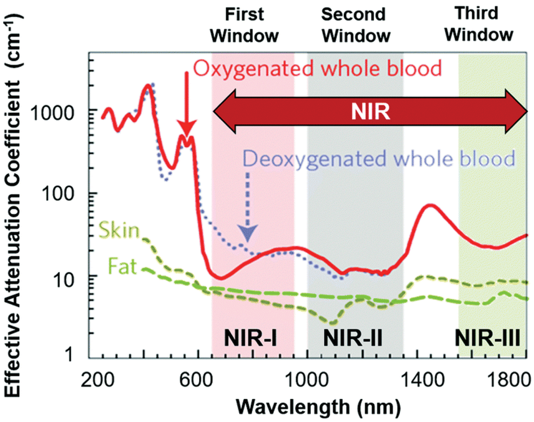

Figure 7.1: Graphical depiction of the biological window as a function of wavelength and attenuation coefficient (reproduced from Ref. [21] with permission from the Royal Society of Chemistry).

In the red to NIR regions of light, there are only specific wavelengths that are ideal for optical bioimaging, which are known as the biological windows (Figure 7.1). The first window lies roughly between 650 and 950 nm, where there is minimal absorption from biological systems [19, 20]. However, this window still suffers from trace autofluorescence, making detection signal-to-noise ratios a challenge with nanoprobes that do not have overwhelmingly efficient luminescence. Rather, the use of the second window, between approximately 1,000 and 1,350 nm, and the third window, between 1,550 and 1,870 nm, is more feasible for nanoparticle-based optical imaging [21, 22]. Local absorption maxima from water prevent the use of light in between the three windows. Moreover, the second and third windows, although more effective than the first window due to reduced scattering, suffer from their own uncertainties in efficiency. This is because of the variation in absorption of oxygenated and deoxygenated blood as well as other hemoglobin derivatives, which changes the transmittance of NIR light within these windows, making quantitative bioimaging techniques difficult. Regardless of these limitations, however, numerous extensive studies have fully exploited these biological windows and produce effective optical imaging probes using nanomaterials.

Strong signal-to-noise ratios are necessary for accurate optical imaging to produce resolved and distinguishable signals [15]. For this reason, the narrow emission bands of lanthanide ions have piqued the interest of researchers due to their characteristic signals that are easily distinguishable both by the shape of their emission bands as well as their relatively long lifetimes [23]. When doped in nanomaterials, they pose as viable probes for use in optical imaging, with the further possibility to functionalize the nanoparticle surface. The simplest of such systems is Nd^{3+}-doped $NaYF_4$ nanoparticles, with excitation and emission bands within the first biological window [24]. With excitation bands between 800 nm and 850 nm from the $^4I_{9/2} \rightarrow {}^4F_{5/2}$, $^4F_{3/2}$, and $^2H_{9/2}$ transitions, Nd^{3+} exhibits efficient photoluminescence emissions between 850 nm and 950 nm from the $^4F_{3/2} \rightarrow {}^4I_{9/2}$ radiative transition [25]. This emission band spans ≈ 80 nm in the cubic-phase $NaYF_4$ host due to the Stark splitting of the involved levels, resulting in five sublevels of the $^4I_{9/2}$ ground state and two sublevels of the $^4F_{3/2}$ excited state of Nd^{3+} [26]. This is in contrast to organic dyes like indocyanine green and IR-820, which have emission bands spanning over 100 nm, which limits their use in applications involving multiple luminescence probes [27]. These two excited state sublevels of Nd^{3+} ($\Delta E \approx 60\ \text{cm}^{-1}$) are thermally linked, meaning their relative population is temperature-dependent and has been studied in potential nanothermometry applications. Nd^{3+}-doped nanoparticles can also be exploited as a luminescence-based, noninvasive thermometer to provide valuable insight on the temperature of a given biological system.

While singly doped Nd^{3+} nanoparticles provide reliable luminescence in the first biological window, there are certain limitations that arise when the excitation and emission wavelengths are in the same region. Scattered and reflected excitation light will interfere with the camera or detector, increasing the background noise at the intended spectral region of the nanoprobe's luminescence. While applying excitation band-pass filters to the detector is a valid method to minimize this in laboratory experimental settings, the practicality of this approach in real-world settings is limited. Rather, the use of multiple lanthanide dopants has become a more common method to prevent excitation interference by exciting nanoparticles in one biological window and recording emissions from a different window. This relies on Förster resonance energy transfer (FRET), where the two dopants have resonant energy levels (similar gaps in energy between states) [28]. By exciting the first dopant (known as a sensitizer), the ion will transfer its energy to the second dopant (known as the activator) rather than relaxing radiatively. This has been thoroughly studied with doubly Nd^{3+}, Yb^{3+}-doped nanoparticles. Once again, exciting Nd^{3+} with ≈800 nm light populates the $^4F_{5/2}$ excited state. However, rather than emitting from the lower Nd^{3+} levels, the energy is nonradiatively transferred to Yb^{3+} through the $^4F_{3/2}(Nd^{3+}) + {}^2F_{7/2}(Yb^{3+}) \rightarrow {}^4I_{9/2}(Nd^{3+}) + {}^2F_{5/2}(Yb^{3+})$ mechanism [29, 30]. The excited Yb^{3+} ion can then emit via the radiative $^2F_{5/2} \rightarrow {}^2F_{7/2}$ transition at ≈1,000 nm. By exciting in the first biological window and recording nanoparticle emissions from the second biological window, minimization of background noise on the detector is achieved, and these nanoparticles have been thoroughly studied for use in optical bioimaging [31].

Besides Yb^{3+}, other NIR emitting lanthanide ions have also been explored for use in optical bioimaging. Examples include the $^5I_6 \rightarrow {}^5I_8$ transition of Ho^{3+} (in the first biological window at ≈1,180 nm) or the $^4I_{13/2} \rightarrow {}^4I_{15/2}$ transition of Er^{3+} (in the third biological window at ≈1,550 nm) [32]. With the emissions from lanthanide ions spanning all three biological windows, their versatility has attracted the interest of the scientific community to exploit their luminescence properties in various imaging techniques.

While the range of possible emission wavelengths gives lanthanide-doped nanoparticles a promise in the field of bioimaging, they still suffer from a major limitation in efficiency. The absorption cross sections and radiative probability from the forbidden nature of $4f \rightarrow 4f$ transitions significantly limit the use of lanthanide ions [33]. Many approaches exist, however, to maximize the luminescence intensities of these probes despite their inherently weak nature. To improve the luminescence efficiency of these nanoparticles, dyes can be grafted to their surface with higher absorption coefficients than the lanthanide ions doped in the material itself. This relies on the positively charged surface of fluoride host nanoparticles, which allows negatively charged functional groups of efficient dyes to be electrostatically linked. Direct excitation of the dyes, rather than the ions, serves to improve the absorption of incident light of the overall nanoprobe. This is then followed by energy transfer to the lanthanide dopants inside, similar to the FRET processes that transfer energy between lanthanide ions.

Indocyanine green is an organic dye with a strong, allowed, singlet transition with an absorption band between 700 and 860 nm (absorption cross section of 10^{-16} cm^{-2}) [34]. Furthermore, the sulfonate groups on indocyanine green have a very strong affinity to the surface of fluoride nanoparticles, allowing for effective linking on the surface [35]. Because this dye absorbs in the same region as Nd^{3+}, but has a substantially stronger absorption cross section (Nd^{3+}: 10^{-20} cm^{-2}), grafting it on the surface of Nd^{3+}-doped nanoparticles can facilitate the population of the Nd^{3+} excited states more efficiently than Nd^{3+} alone. From there, co-doping the nanoparticles with other lanthanides (as described above) will improve the luminescence intensities of the activator ion. Other NIR dyes, such as IR-806, can also be used in a similar fashion [36]. As long as the dye in question has negatively charged functional groups (most commonly sulfonate and carboxylate) and resonant energy levels with the lanthanide ions, they can enhance the luminescence processes of these nanoparticles by improving the absorption of the incident light and facilitating the population of the lanthanide excited states through FRET.

Implementing NIR-emissive lanthanide-doped nanoparticles in optical imaging applications offers many benefits to current techniques. For example, their sharp emission bands, spanning multiple biological windows into the longer wavelength NIR region of light, allows for potential improvements to signal detection. Moreover, the positively charged surface of fluoride nanoparticles allows for surface functionalization with dyes or targeting molecules. This can act to improve the luminescence efficiency of the system itself or allow a more defined tuning of the system for a specific application. While much work remains to achieve optimally efficient compositions for bioimaging probes, and the in vivo biodistribution of these nanoparticles is still not thoroughly understood, the groundwork and theory behind these nanosystems have shown great promise in improving optical imaging in nanomedicine.

7.3 Upconverting nanoparticles

Upconversion has been one of the fastest growing fields with the most significant achievements of all luminescence mechanisms to date. Considering that persistent phosphors were developed during the nineteenth century [37, 38], and other linear luminescence mechanisms useful for imaging were well known by then, upconversion luminescence is the most recently discovered [39]. The study of this nonlinear mechanism started around 1959, when Bloembergen theorized the possibility to achieve an infrared detector by using visible upconversion luminescence, which could be detected by a photomultiplier tube [40]. Unfortunately, the initial idea to use Er^{3+} ions to achieve upconversion luminescence was proven to be too inefficient for the NIR laser powers available at the time. In 1965, the use of Yb^{3+} ions to sensitize Er^{3+} emissions was proposed in silica glasses, with the scope of obtaining NIR-pumped visible-emitting lasers [41, 42]. The mechanism of the observed upconversion was further investigated by Auzel in 1966 in Yb^{3+}–Er^{3+} and Yb^{3+}–Tm^{3+} systems, which provided the first description of upconversion luminescence as we know it today [39, 43, 44].

Fascination over this anti-Stokes mechanism began for purposes considerably different from their application in imaging. However, the possibility to use upconverting nanoparticles in biological imaging is the main reason for their developments. The switch to bioimaging as a possible application for upconverting materials started with their miniaturization at the nanoscale. At the beginning of this millennium, several research groups developed synthesis routes to obtain monodisperse and efficient upconverting nanoparticles [45–52]. These methods yielded dispersions of colloidal nanoparticles in different media, which was essential for their biological application [53–56]. Further techniques to improve their biocompatibility, stability in water and biological media, and luminescence efficiency lead to the exponential growth of the publications in the field of upconverting nanoparticles for biological imaging.

We provide in the following discussion the rationale behind the exponential growth of publications relative to such an interesting subcategory of luminescent nanomaterials. From the mechanism to the most common and efficient ions to be used for bioimaging, this section covers the evolution of upconverting nanoparticles from their first use in bioimaging to their recent applications in super-resolution imaging. Most of the following discussion presents examples from the literature relative to lanthanide-doped upconverting nanoparticles since these nanomaterials have been extensively investigated. Examples of the use of transition metal ions (Mn^{2+} and Fe^{3+}) are also discussed with respect to the possibility to shift or enhance the upconversion efficiencies in nanomaterials. Purely transition metal ion-doped materials are not presented, due to the low upconversion efficiency of such materials.

7.4 Upconversion mechanisms

Upconversion luminescence is a nonlinear process involving the absorption of multiple photons of low energy to produce higher energy emissions (anti-Stokes luminescence). This general definition, however, does not explain how this phenomenon occurs nor the parameters required to obtain it. Figure 7.2 shows the main luminescence mechanisms within ions in upconverting nanoparticles. Alternative luminescence mechanisms have been reported in crystals and glasses, but their low efficiency even in these bulk materials led to their possible exclusion from the most relevant processes occurring in nanomaterials. In principle, the absorption of lower energy photons in any wavelength can lead to upconversion, as for example the upconversion of Er^{3+} under excitation of photons in the red spectral region [57]. However, for applications in biological imaging, excitation of the nanoparticles in the NIR region is the most desirable, due to the lower scattering from tissues and, consequently, higher penetration depth [58, 59]. Thus, we limit our report to nanoparticles which can be excited within the NIR region, which are the most promising for bioimaging.

Two main upconversion mechanisms can be distinguished, depending on the presence or absence of a sensitizer [39, 44]. Sensitizer ions are employed to efficiently absorb the NIR excitation photons and transfer their energy to the activator ions, which are utilized to emit higher energy photons. When both absorption and emission occur within a single species of ion, that is, between ions which are all the same, the process is known as ESA , shown in Figure 7.2. Due to the intrinsic low absorption

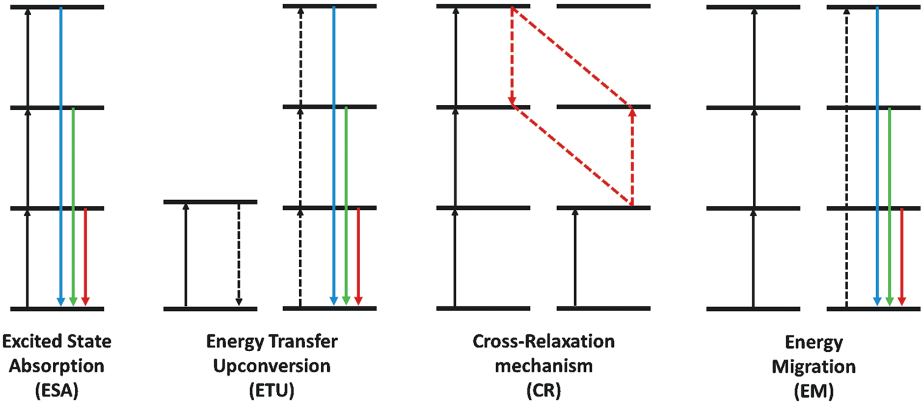

Figure 7.2: Main population and depopulation mechanisms involved in upconversion luminescence at the nanoscale. Emissions can occur after absorption of multiple photons within a single ion (ESA) or between two ions, a sensitizer absorbing the energy and transferring it to an activator, which undergoes luminescence (ETU). Between populated levels, other involved mechanisms redistributing the photons within ions are cross relaxations (CRs) and energy migration (EM), both of which are energy transfer processes.

coefficient of the majority of the ions which can undergo upconversion luminescence, the efficiency of ESA is also limited. In order to enhance the upconversion efficiency, the same activator ions can be coupled to ions which are characterized by higher absorption coefficients and emission stability in the NIR region, that is, longer decay times. With respect to the intrinsic decay time of the involved NIR states, it is paramount to consider that energy transfer between ions is a function of the decay time of the sensitizer [28, 60]. Therefore, sensitizers with intrinsically long decay times and relatively high absorption coefficients of the NIR populated levels and resonance with the activator intermediate states must be chosen. When upconversion occurs by coupling a sensitizer and an activator, the process is known as ETU, shown in Figure 7.2.

A graphical description of two additional upconversion mechanisms that are paramount for the understanding of luminescence dynamics in upconverting nanoparticles is reported in Figure 7.2. CR and EM occur within ions by transferring the energy of a populated state through different paths. These two mechanisms can occur in other luminescent materials than upconverting nanoparticles. Nevertheless, they are particularly favored in these nanoparticles, considering that the probability of CR and EM to occur strongly depends on the concentration of the dopant ions, generally higher in upconverting materials (around 20% sensitizer ions). Moreover, CR is also favored by the resonance between successive energy levels in activator ions, which is one of the requirements to achieve upconversion, as discussed later in this section.

In CR mechanisms, two excited states of two ions are populated and the resonant energy gap between states allows for the depopulation of one state to achieve the population of the other. In contrast, in the case of EM, only the excited states of one ion are populated, and the excited states of nearby ions are populated directly by transferring energy within states of equal energy. Both the processes involve energy transfer and are favored by the same conditions which favor ETU. The simultaneous occurrence of these mechanisms and their relative weight with respect to each other determines the overall upconversion efficiency and the relative emission efficiency. This is an important factor to consider because the efficiency of an emission is not only determined by its probability with respect to the number of absorbed photons (following the logic of more photons required, less probable the emissions). This probability is a combination of the probability to reach the state via the absorption of multiple photons and also the probability to achieve the depopulation or further population of the considered emitting state by CRs and EMs. As a consequence, high energy emissions which are not efficient in one material can become predominant in another material, depending on the influence of these other mechanisms in the luminescence dynamics.

First, the concept of multiple photon absorption suggests a temporal succession of steps, which requires the right timing. This “timing parameter” to achieve efficient upconversion luminescence resides in the stability of the intermediate states, that is, their intrinsic decay time. Intermediate states characterized by long decay times (metastable) allow for the successive absorption of an additional photon before the emission from the same state can occur. Since both population and depopulation occur simultaneously, the probability to achieve the population of higher energy states is higher if the intermediate states are metastable. Consequently, ions characterized by metastable intermediate low energy states can provide the required stability to achieve such a successive absorption process.

The energy gaps between consecutive levels in activator ions are also of the utmost importance, as previously mentioned. If the energy of the incident NIR photons does not overlap perfectly with the energy gaps, two scenarios are possible. If the energy of the incident photon is greater than the energy gaps, there would be an excess of energy that will correspond to a loss, that is, reduced efficiency of the process. If the energy of the incident photon is smaller than the energy gaps between consecutive levels in the activator ions, the population of these states requires additional energy, which can still be obtained to achieve the upconversion process only if small enough to be bridged by phonons (thermal energy from the host material). Also, in this case, the efficiency of the upconversion luminescence can be severely affected by the absence of resonance of the activator energy levels with the incident NIR light. For the same reason, the resonance between the energy levels of the sensitizer and activator also significantly affects the efficiency of upconversion luminescence.

Finally, the possible quenching effects of ligand and solvent molecules should be considered to avoid further depletion of the luminescence efficiencies. Ligand or solvent quenching occurs via energy transfer from an ion in an excited state to the resonant vibrational modes of the molecule [61]. The resonance with the vibrational mode of the molecules depends on the nature of the solvent and the ion. Each system can be studied to verify the presence of such quenching, or energy transfer can be limited by the core-shell approach [55, 62, 63]. Considering these luminescence mechanisms, the requirements for each ion and their involvement in the upconversion efficiency, the ions which are best suited for biological applications are presented. The ions are reported based on their role as sensitizers (Section 7.4.1) or activators (Section 7.4.2) and their reported applications (Section 7.4.3).

7.4.1 Excitation

Considering the limited absorption cross sections of the lanthanide ions, in particular, in the NIR region, the options available for the sensitizer ions are limited to the most commonly encountered Yb^{3+} and Nd^{3+} ions. The Yb^{3+} ions were originally employed to enhance the efficiency of upconversion in co-doped materials [39, 43, 44]. The excitation of Yb^{3+} ions can be obtained in a relatively broad range around 970–980 nm, which are the most common values due to the availability of excitation sources in this region. The most common examples in the literature include this ion as sensitizer both for historical reasons and the proven enhanced efficiency of the co-doped materials.

As previously discussed, the use of Nd^{3+} can shift the excitation wavelength to a more convenient region around 800 nm, within the first biological window [31, 34, 64, 65]. When Nd^{3+} ions are used as a sensitizer, they are commonly coupled to Yb^{3+} ions, incorporated into core-shell structures to separate the two sensitizers. NIR excitation at around 800 nm is efficiently absorbed by Nd^{3+} ions in one of the shells and transferred to Yb^{3+} in another shell and from Yb^{3+} to the activator ion in the core. The several steps required to achieve the upconversion luminescence result in lower efficiencies than the systems co-doped with only Yb^{3+}. However, the advantage in exciting the nanoprobes at this wavelength in which the heating effects of the incident light are minimal is a distinct advantage when dealing with biological media.

Some transition metal ions have been proven to sensitize upconversion luminescence when coupled with Yb^{3+} sensitizer ions. The most common example is the $Fe^{3+}/Yb^{3+}/Er^{3+}$ combination, in which it has been proven that the presence of Fe^{3+} enhances the upconversion efficiency through enhanced sensitization [66]. This enhancement is still reduced with respect to other methods described in Section 7.2 such as dye-sensitized upconversion.

7.4.2 Emission

Although several ions can undergo upconversion luminescence, the intrinsically low efficiencies of the upconversion process limit the choice to the few most efficient activators. Considering the even lower efficiencies of these luminescent materials at the nanoscale, in particular in aqueous and biological media, the possibilities are severely limited. The most common activator ions in nanomaterials are Er^{3+}, Tm^{3+}, Ho^{3+}, and

Pr^{3+}, also in combination with other ions such as Mn^{2+}, Tb^{3+}, Eu^{3+}, Sm^{3+}, and Dy^{3+} [62, 67–69]. Multishell structures are often described in the literature with the aim to separate the optically active ions, avoiding the quenching from their reciprocal interactions, while obtaining tunable emission colors [67–69]. For application in biological imaging, the tunability of the emission of the main activator to the red and NIR region is particularly interesting, due to the higher penetration depth of light in this region [58, 59].

The choice of sensitizers is limited to those previously discussed (Nd^{3+} and Yb^{3+}), while the choice of activators depends on the desired application. For in vitro imaging, the thickness and contents of the cellular medium limit the absorption of the emitted light, which can be in any region of the visible or NIR spectrum. Considering the higher efficiency of systems co-doped with Er^{3+}, Tm^{3+}, or Ho^{3+}, it is convenient to use these ions together with Yb^{3+} as sensitizer. The use of additional ions, even in multiple-shell structures, is usually accompanied by a loss of upconversion efficiency and is only useful in bioimaging when red or NIR emissions have to be enhanced, as is the case small animal imaging, as will be discussed shortly. The main UV and visible emissions of these three ions consist of the Er^{3+} green ($^2H_{11/2},{}^4S_{3/2} \rightarrow {}^4I_{15/2}$) and red ($^4F_{9/2} \rightarrow {}^4I_{15/2}$) emissions around 520, 540, and 675 nm; the Tm^{3+} UV ($^1I_6 \rightarrow {}^3H_6,{}^3F_4$; $^1D_2 \rightarrow {}^3H_6$), blue ($^1D_2 \rightarrow {}^3F_4$; $^1G_4 \rightarrow {}^3H_6$), and red ($^1G_4 \rightarrow {}^3F_4$), around 300, 325, 350, 450, 475, and 650 nm; and the Ho^{3+} green ($^5F_4$, $^5S_2 \rightarrow {}^5I_8$) and red ($^5F_5 \rightarrow {}^5I_8$) emissions around 540 and 650 nm, respectively. The NIR emissions of these ions can be achieved both by upconversion and photoluminescence as described in Section 7.2. The most efficient upconverting materials at the bulk and nanoscale are those co-doped with Yb^{3+}/Er^{3+}. The perfect resonance of the sensitizer/activator levels and metastability of the activator intermediate states are unique among the lanthanide ions. These two factors result in the highest quantum efficiencies for these materials [70, 71].

The emissions of all the three reported activators are achieved mainly by ETU, with CR and EM phenomena altering the incident photon distribution in the co-doped materials. For Er^{3+}, the source of the emission from the $^4F_{9/2}$ state is still under debate since it appears that it can arise by both ETU and a CR mechanism involving the green emitting states [72–74]. Red and NIR emissions are favored at high concentrations due to such CR mechanisms. For Tm^{3+}, several CR mechanisms occur simultaneously and strongly determine the efficiency of each single emission [75, 76]. The UV-emitting states are predominantly populated by CR rather than ETU, considering the scarce resonance of the energy gap between the $^1G_4$ and $^1D_2$ state with the Yb^{3+} energy gap. A series of CR mechanisms further depopulate the UV and visible emitting states in favor of NIR emitting states, resulting in concentration quenching of the UV and visible emissions. Finally, Ho^{3+} is affected by back-transfer due to CR from the Ho^{3+} emitting states to Yb^{3+} ions. Such CR mechanisms must be considered when planning the optimal dopant concentration based on the required emission.

The presence of such CR mechanisms results in the possibility to manipulate the ratio between emissions by altering the dopant concentrations, but, even more interesting for imaging, the tunability of the emission color with the time [67, 77–79]. Concentration quenching due to CR processes results in a shortening of the decay time of the involved emissions [77]. Each single emission can then be imaged based on the time at which it occurs, by gating the detector, as further discussed in the next section. Moreover, the succession of emissions is directly dependent on the successive absorption of photons and their involvement in CR and energy transfer pathways, leading to a possible differentiation of different emissions based on the intrinsic decay times of upconverting nanoparticles [67, 68, 79]. As reported in Figure 7.3, energy transfer mechanisms can also be exploited to achieve time-tunable emission from different ions, with the potential to image different emissions at different times [67]. These aspects are particularly interesting in view of the possibility to achieve single-particle imaging, as discussed in the next session.

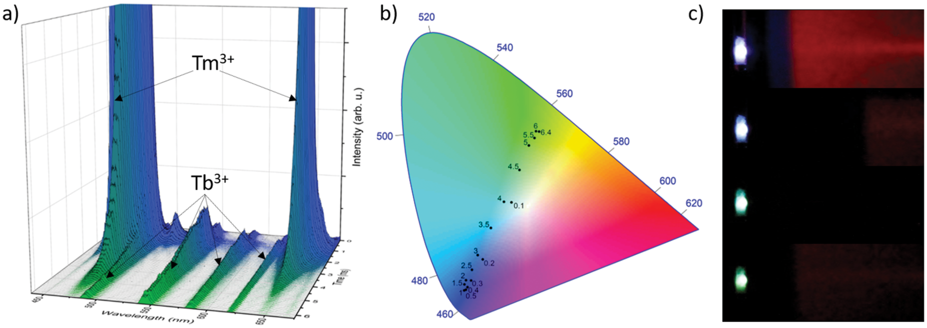

Figure 7.3: (a) Time-resolved spectra of core-shell nanoparticles β-NaGdF$_4$: 1% Tm^{3+}, 49% Yb^{3+}/β-NaGdF$_4$: 10% Tb^{3+} powder samples under a 976 nm pulsed laser. The emissions from Tb^{3+} and Tm^{3+} are indicated by arrows for clarity and occur due to energy transfer from Tm^{3+} to Tb^{3+}, determining a time-tunability of the emission. (b) CIE diagram as a function of time (in milliseconds). (c) Photographs of the color-tunable emissions from blue (Tm^{3+}) to green (Tb^{3+}). An NIR card shows the excitation source (reprinted from Ref. [67] with permission from John Wiley and Sons).

Independently of the host, EM between Yb^{3+} ions has been reported to considerably affect the upconversion luminescence efficiency, as concentration quenching by EM to surface-trap states involving these ions is the main cause of the lower quantum efficiencies of upconverting nanomaterials [61, 72]. To improve the low quantum yield due to such a phenomenon, growth of an inert shell to protect the activator-containing core is still considered one of the only options. The concern of concentration quenching of Yb^{3+} ions cannot be avoided through any other means than the use of a core-shell structure. This is due to the inherent need to dope the material with a high concentration of Yb^{3+} to achieve a more efficient absorption of NIR light.

When a higher penetration depth of the emitted light is required, as in small animal imaging, emissions in the red and NIR region are required. With respect to the possibility to achieve stronger red emissions in upconverting nanoparticles, both CR mechanisms or the use of additional red-emitting activator ions can be manipulated to achieve the desired outcome. Depending on the concentration of the activator ion, the red emissions of the three main reported activator ions can be enhanced by varying the CR efficiency. When multiple ions are used, as by coupling Yb^{3+}/Er^{3+} or Tm^{3+} with Eu^{3+} or Mn^{2+}, the red emissions from these ions can be beneficial in small animal imaging [68, 80, 81]. Engineering of the required nanoprobes is necessary to avoid interference of the ions with one another, which can lead to quenching of the luminescence. The applications described in the next section benefit from the unique features of these activator ions.

7.4.3 Bioimaging applications

Several examples were provided in the literature for lanthanide-doped upconverting nanoparticles, mainly based on the efficient and biocompatible fluoride hosts [8, 23, 82]. One of the major advantages in using upconverting nanoparticles in biological imaging is the absence of autofluorescence from cells and tissues due to the used NIR excitation source [9, 54, 83, 84]. When using nanoprobes which require high energy excitation (UV region), molecules and proteins present in biological media can fluoresce with emissions in the visible region (autofluorescence), which results in high noise signals in the collected images, low resolution, and decreased contrast.

Due to the positively charged surface of fluoride host nanoparticles, these structures can be functionalized with targeting and sensing molecules, allowing for optical imaging that provides information about the environment of the nanosystem. Similar to the dye sensitization processes discussed previously to enhance NIR imaging, grafting photosensitive molecules through negatively charged functional groups can produce a nanoparticle system that varies in spectroscopic properties depending on the ligand's surroundings. However, rather than relying on energy transfer *from* the dye to enhance the nanoparticle's luminescence, the lanthanide dopants can transfer energy *to* the surface molecules. This is particularly effective in lanthanide-doped materials due to multiple characteristic emission bands that are sometimes at drastically different wavelengths. For example, Neutral red is a dye with a strong absorption band in the blue/green regions of light [85]. The absorption coefficient of this dye varies with pH. By functionalizing Er^{3+}-doped upconverting nanoparticles with neutral red, the observed green emission will be quenched by this dye to a different extent depending on the pH of the probe's environment. In contrast, the red emission intensity of Er^{3+} will remain unchanged since the dye is completely transparent to red light. Therefore, using the red transition as an internal standard, the ratio of the Er^{3+} red and green emissions will be characteristic of the pH of the nanoprobe's environment, which is useful in cancer diagnosis where malignant cells are known to be more acidic [86]. Dye functionalization can extend to bioassays and biomarkers as well, exploiting dyes such as rhodamine-B or Alexa Fluor 680 which are resonant with Er^{3+} transitions, to interact with phospholipase D or folate-binding proteins for in vitro diagnostics, for example [87, 88].

Considering the diffraction limitation in resolution in optical microscopy, it is paramount to limit any further depletion of resolution during imaging of biological species. In this regard, upconverting nanoparticles excited with NIR sources guarantee the absence of autofluorescence, with resulting higher signal-to-noise ratios and clearer images. Such a strong advantage over other nanoprobes for bioimaging explains the great success of these materials and the possibility to achieve imaging of single nanoparticles [77, 89–92].

The possibility of observing single nanoparticles in a medium provides interesting opportunities. First, the nanoparticle can be visualized and tracked during internalization [93], providing meaningful insights into the complex mechanisms of nanoparticle uptake and internalization from the blood stream [13, 94–98]. The contrast of the image can be improved by the already discussed absence of autofluorescence due to the reduction in background noise. Finally, the possibility to manipulate the position of the upconverting nanoparticles by optical trapping (or optical tweezers) [99, 100], with the same NIR source responsible for their excitation has been demonstrated and can be a distinct advantage in image-guided therapy [92].

As also stated before, the possibility to achieve single-particle tracking of upconverting nanoparticles, together with their unique optical properties, allows for enhancing the resolution of imaging with optical microscopes. The resolution of a microscope, also defined as the possibility to distinguish overlapping objects, can be obtained by dividing the wavelength of the exciting source by twice the numerical aperture of the used focusing lenses. Therefore, the resolution of a microscope equipped with a certain NIR excitation source cannot be changed and is commonly on the order of magnitude of hundreds of nanometers. By using an upconverting nanoprobe, the possibility to track and distinguish single particles in diluted media is a distinct advantage. However, further improvements are required to allow discrimination of the same nanoparticles in concentrated or biological media, with the resolution of optical microscopes the major limitation.

The advent of super-resolution microscopy, also known as nanoscopy, completely revolutionized the field of optical microscopy, yielding a significant improvement in image resolution [101–104]. The idea from which this field originated is to manipulate the emissions from luminescent probes to achieve a selective emission of some objects, while others are not emitting. Such a process reduces the overlapping of the emissions from the different probes, making it possible to discern different probes through the analysis of multiple images. The most common technique reported in conjunction with upconverting nanoparticles is stimulated emission depletion. In this super-resolution microscopy technique, two light sources are required to irradiate a sample: one excites the nanoprobes, while the second depletes their emission in a specific spatial region. By collecting multiple images of the emitting and depleted objects, a full reconstruction of the single overlapping objects is possible, with resolutions one order of magnitude lower than the one determined by the diffraction limit.

With respect to the use of upconverting nanoparticles in nanoscopy, upconverting nanoparticles doped with Tm^{3+} have proven interesting for such applications [105, 106].

An efficient way to achieve excitation/depletion of an emission in Tm^{3+}-doped upconverting materials was presented [106]. Based on the same principle by which lasers operate, an emission from a certain level can be depleted if the lower level, which gets populated if the emission occurs, is populated. In other words, to achieve the population inversion required for the operation of lasers, the lower energy level has to be continuously depopulated, and populating this level results in the depletion of the emission.

The provided example involves the use of $NaGdF_4$:Yb^{3+},Tm^{3+} upconverting nanoparticles, which result in the known upconversion luminescence spectra when excited by a 975 nm source [105]. The Tm^{3+} emissions from the $^1D_2$ state were depleted by the population of the lower energy levels ($^3F_{2,3}$ and $^3H_4$) by the use of a depleting 810 nm laser, which results in the population of NIR emitting levels via CR. A resolution of 66 nm was achieved, and the nanoprobe was tested for use in super-resolution immunofluorescence microscopy of the cytoskeleton in HeLa cells. The nanoprobes were functionalized with poly(acrylic acid) and an antibody to achieve a targeted bonding with the cytoskeleton, as in Figure 7.4 [105]. The incredible improvements in resolution by using these nanoprobes are definitely promising and deserve further investigation.

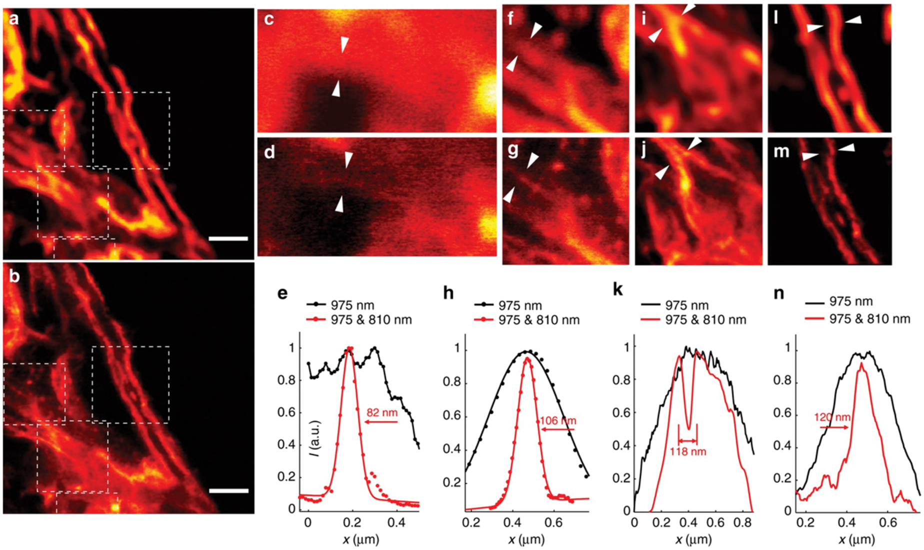

Figure 7.4: Immunofluorescence of cell cytoskeleton with antibody-conjugated upconverting nanoparticles: (a) confocal microscopy imaging of upconversion under 975 nm excitation in HeLa cancer cells; (b) super-resolution images (under 975 nm and 810 nm irradiation, as exciting and depleting sources, respectively) of the same area in (a). Scale bars are 2 μm. (c)–(n) Magnified areas marked by white-dotted squares in (a) and (b) and line profile analyses; images in (c), (f), (i), and (l) are taken from the white-dotted squares in (a); images in (d), (g), (j), and (m) are taken from the white-dotted squares in (b). (e), (h), (k), and (n) point spread function in the areas indicated by arrow heads in (c) and (d), (f) and (g), (i), and (j), and (l) and (m), respectively (reprinted with permission from Ref. [104] by the Creative Commons Attribution 4.0 International License from Springer Nature Publishing Group).

Combining the possibility to achieve imaging of single particles and the obtained promising results for application of upconverting nanoparticles for super-resolution microscopy will, in perspective, allow for the imaging and tracking of single particle with a resolution in the nanoscale. Considering the complicated interactions of nanomaterials within the human body, it is paramount to precisely determine the fate of these nanoparticles, in particular with respect to their use in nanomedicine. First examples of this combination were reported to determine the 2D and 3D trajectories of upconverting nanoparticles in tumoral spheroids [93]. By coupling single-particle tracking to super-resolution, novel insights into the mechanisms of uptake in tumors were obtained, opening new interesting perspectives.

7.5 Persistent luminescence imaging

Persistent luminescence, also referred to as afterglow, long-persistent luminescence, and phosphorescence are described by the continued emission of light after excitation has ceased [107]. It can also be thought of as a luminescent material which has an extremely long luminescence decay time, on the order of seconds to days. Knowledge of these “glow in the dark” materials dates back centuries, though complete understanding of the mechanisms through which the persistent luminescence phenomenon occurs is still disputed today [107–109]. However, it has been well-established that persistent luminescence requires the presence of two species: a trapping center and a luminescence center. Trapping centers, often called “traps,” are formed as the result of the presence of defects in the crystalline host material. Defects such as *f*-centers, interstitials, oxygen vacancies, and intentionally introduced dopant ions are known to serve as trapping centers in a variety of persistent luminescence materials [108, 110–113]. When a material is excited with the appropriate wavelength of light, charge carriers can be trapped at these defect sites. The trapping centers continue to fill with electrons or holes as the material is charged. Once excitation has ceased, trapped charge is then released and recombines at a luminescence center, which then emits light, giving rise to the persistent luminescence effect. With regard to bioimaging, persistent luminescence has a distinct advantage over luminescent materials which need to be excited in situ. Most luminescent materials need constant excitation to provide emissions which can be detected and harnessed for imaging. This often results in the simultaneous excitation of biological fluorophores, giving rise to autofluorescence, which is deleterious for high-quality image acquisition, as previously discussed. The premise of persistent luminescence imaging is to charge the material prior to introduction to the specimen, such that in situ excitation is completely avoided, allowing for very high signal-to-noise ratios [12]. Furthermore, materials which exhibit persistent luminescence on the order of several hours to days can be extremely useful for long-term tracking of biodistribution of nanoparticles and cell metastasis [114–116]. The main luminescent properties which need to be optimized for achieving high-quality persistent luminescence imaging are the charging time, the persistent luminescence duration, the brightness of persistent luminescence, and finally, the emission wavelength.

7.5.1 Charging and persistent luminescence duration

A major avenue of materials science is dedicated toward trap-depth engineering in order to facilitate more intense and longer persistent luminescence. The trap depth typically refers to how far above or below the trap state resides with respect to the valence and conduction bands, respectively. It should also be noted, however, that some detrapping mechanisms occur through the overlapping of potential energy wells or quantum tunneling processes and avoid the conduction and valence bands entirely [117]. Charge carriers (electrons and holes) can be released from traps via thermal and optical stimulation, the energy of which depends on the trap depth. If a trap is too shallow, all of the charge will be released quickly, leading to little or no persistent luminescence. In contrast, if a trap is too deep, there is not enough thermal energy at room temperature to facilitate charge release and observe persistent luminescence. Typically, distributions of traps are ideal, such that charge can be slowly released from deeper traps into shallower traps, which can then result in recombination at the luminescence center to generate long-lasting persistent luminescence. Additionally, in some cases, light can be used to stimulate the release of the charge carriers from the traps. This is known as optically stimulated luminescence (OSL). OSL can often be obtained after persistent luminescence has ceased, allowing for the liberation of charges residing in traps that are too deep to be liberated thermally. This phenomenon is extremely useful for bioimaging, as it allows for the possibility to re-initiate persistent luminescence, which will be discussed later.

The vast majority of persistent luminescent host materials are based on complex oxides such as gallates, germanates, aluminates, and stannates [107, 108, 118]. Sulfide-based hosts are also renowned for facilitating efficient persistent luminescence, though their sensitivity to water has largely phased them out of use, and though surface passivation techniques like silica coating have been demonstrated to effectively overcome this obstacle [119, 120]. The relatively narrow bandgap of these materials mostly restricts charging of the phosphor through UV and sometimes X-ray excitation. Since the premise of persistent luminescence imaging is to charge the material prior to introduction to the specimen, the biological window is of no concern and UV excitation can easily be accomplished with commercially available lamps. However, should the material need to be recharged in situ, UV excitation can be a significant obstacle owing to the lack of tissue penetration and potential for cellular damage. X-ray excited phosphors and phosphors which exhibit OSL under red or NIR excitation after persistent luminescence have been developed for this purpose [121–123]. The ability to recharge the phosphor in situ enables researchers to continue long-term tracking experiments using persistent luminescence phosphors that may have intense but relatively short luminescence durations.

It is most common for persistent luminescence to follow an exponential or hyperbolic decay, meaning that luminescence intensity drops off rapidly followed by a slower decay which indeed can last for hours or days [113, 117]. Thus, the initial signal-to-noise ratio may be extremely high and then steadily decrease. Future generations of persistent luminescence phosphors should aim to exhibit intense persistent luminescence for a duration that is greater than the time it takes for the nanoprobe to be uptaken by cells or to localize and accumulate at the desired target. Again, materials which can be re-excited in situ become increasingly more attractive in these situations, as a high signal-to-noise ratio can be repeatedly re-obtained.

7.5.2 Biological considerations

While the complex oxide hosts have been successfully used for persistent luminescence imaging, there are a few potential drawbacks with regard to their clinical application. First, it should also be noted that there is significant difficulty in producing oxide-based nanoparticles with a high degree of size and morphological purity; this can be especially problematic if luminescence intensity is size-dependent, as many immunofluorescence imaging techniques utilize luminescence intensity for quantification purposes [1, 6]. Additionally, irregularly shaped particles, especially those which have sharp angles, can potentially damage tissues as they travel through healthy vasculature and may be less efficiently uptaken by cells [6].

Despite the concerns raised with the morphology of complex oxide materials, zinc gallates and gallogermantes doped with Cr^{3+} have been well-studied in terms of short and long-term toxicity and reveal no major toxicological concerns [116, 124–126]. In fact, persistent luminescence from these materials has been used to study their biological effects in mice, illustrating the usefulness of the persistent luminescence in studying bio-nanointeractions [125]. Additionally, clever efforts have been made toward obtaining red persistent luminescence in already known biocompatible hosts such as tricalcium phosphate, owing to its presence in bone [127].

To address the concerns regarding nanoparticle uniformity, there is considerable interest in developing materials which exhibit persistent luminescence in ternary fluoride hosts, such as $NaYF_4$, $NaLuF_4$, and $NaGdF_4$, as these materials are well-known hosts for upconversion and produce highly uniform nanoparticles under facile conditions with little to no toxicity concerns [8, 128]. Relatively few examples of persistent luminescent nanomaterials based on fluoride hosts exist, and none have been studied for persistent luminescence imaging yet, but those which have been published do show impressive promise [129–132].

7.5.3 Emission

As previously stated, a major advantage of this technique is the wavelength of light required to excite the luminescent material does not need to fall within the biological window, as tissue penetration is irrelevant when charging these materials. The emission wavelength, however, still needs to be tailored for detection in situ, as the emitted light must be able to penetrate tissues to facilitate efficient detection and signal acquisition. Thus, the concern of the biological windows cannot be entirely avoided and this still restricts the use of certain persistent luminescence materials to specific applications. Persistent luminescence nanoparticles which emit in the red and NIR are of particular interest for in vivo imaging due to their ability to penetrate tissues efficiently, while visible wavelengths can be used for in vitro cellular imaging techniques.

The most commonly utilized luminescent activators are lanthanide ions (Ce^{3+}, Pr^{3+}, Nd^{3+}, Sm^{3+}, Eu^{2+}, Tb^{3+}, Dy^{3+}, Er^{3+}, Tm^{3+}, and Yb^{3+}) and transition metal ions such as Cr^{3+} and $Mn^{2+/4+}$ [107–109, 118]. Various combinations of these ions have been employed to achieve persistent luminescence of many different wavelengths and luminescence durations. It is worth noting that emission bands from the $4f \rightarrow 4f$ transitions of lanthanide ions are significantly narrower than emissions from transition metal ions; thus, lanthanide-doped nanoparticles have more promise when considering the ease of signal deconvolution in multiplexed imaging techniques. However, the parity-allowed transitions observed from transition metal ions typically result in greater emission intensity than the forbidden $4f \rightarrow 4f$ emissions of lanthanides. Thus, a trade-off must be considered between the necessities for signal detection intensity versus deconvolution capability.

7.5.4 Applications

7.5.4.1 Blue and green persistent luminescence imaging

Blue and green persistent luminescence is most often obtained from Eu^{2+}/Dy^{3+}-doped nanoparticles, in which the luminescence is obtained from Eu^{2+} [108, 118]. Emissions from Eu^{2+} are highly dependent on the crystal field and typically only silicates and aluminates are found to facilitate Eu^{2+} persistent luminescence, though others certainly exist [118, 119]. It should be noted that the emission wavelength of Eu^{2+} is highly dependent on the surrounding crystal field; thus, it is common to see Eu^{2+} emissions reported as blue, green, and sometimes even red. A more in-depth discussion on persistent luminescence from Eu^{2+} doped compounds can be found in the literature [118].

The Eu^{2+}/Dy^{3+} combination is most useful for in vitro imaging, as the issue of tissue penetration is minimized. Nanoparticles utilizing this persistent luminescence combo have been successfully demonstrated for high-sensitivity analyte detection in lateral-flow assays, fluorescence lifetime imaging, and in vivo imaging, among others [133–135]. Of note, persistent luminescence of a complex silicate doped with the Eu^{2+}/Dy^{3+} combination was utilized for FLIM to be able to live-image intracellular caspase-3 activity, a marker for apoptosis [134]. Fluorescein isothiocyanate conjugated to a peptide, DNA, or aptamer and then conjugated to the nanoparticles was used as a FRET-based "on-off" switch in which the activation of luminescence from fluorescein isothiocyanate (in the presence of biomarker targets) and decrease in luminescence intensity of the persistent luminescence could be used to both detect and image cellular functioning. Furthermore, signal changes were found to be more sensitive using the persistent luminescence-FLIM technique in comparison to fluorescence-based confocal microscopy, illustrating the attractiveness of the technique. This study represents an elegant example of how the use of nanoparticles for surface functionalization combined with persistent luminescence and lifetime imaging, as well as luminescence from conventional organic fluorophores, can be used to bring about advancements in bioimaging technologies.

7.5.4.2 Red and near-infrared persistent luminescence imaging

With regard to red and NIR persistent luminescence, Cr^{3+}-doped gallates have been the most widely studied and applied, especially in the gallogermanate hosts [109, 136]. Persistent luminescence from Cr^{3+} is obtained from either the $^2E \rightarrow {}^4A_2$ transition or the $^4T_2 \rightarrow {}^4A_2$ transition, both of which give rise to emissions around the 690–800 nm region. Nanomaterials utilizing Mn^{2+} as the luminescent center can be observed to give green, red, or NIR persistent luminescence depending on the crystal field the ion is doped into [108]. Mn^{4+}, which exhibits emissions in the 650–800 nm range, is also renowned as an alternative to Cr^{3+}, as it can also be doped into fluorides as well as oxides [137]. Cr^{3+}-doped materials were the first to be used for NIR-persistent luminescence imaging in 2007 [115] and represent the vast majority of nanomaterials studied for persistent luminescence imaging purposes [109]. Interestingly, persistent luminescence from Cr^{3+}-doped materials can be activated with X-rays in some hosts, in addition to the commonly used UV excitation wavelengths between 250 and 365 nm. The use of X-ray excitation is particularly interesting when considering the potential need for in situ recharging of the phosphor, as was demonstrated with $ZnGa_2O_4{:}Cr^{3+}$ nanoparticles in which re-activation of the phosphors using low-energy X-ray excitation was achieved at a depth of 2 cm inside of a Kunming mouse, with persistent luminescence detectable for 1 h before re-excitation was needed [121]. Nanoparticles which can be re-excited via NIR irradiation have also demonstrated great achievements though NIR irradiation penetrates tissues to a significantly lesser extent [129, 138, 139].

Some of the most impressive advancements in imaging techniques using red persistent luminescence phosphors have come from the engineering of nanoparticles that allow for persistent luminescence imaging in combination with other imaging techniques such as MRI, CT, and FLIM among others [134, 140–142]. The imaging sensitivity achieved due to the lack of background noise in persistent luminescence optical imaging, combined with the spatial resolution achieved in MRI using nanoparticles as contrast agents brings forth a great deal of information which can be obtained using a single, multimodal contrast agent. Persistent luminescence nanoparticles containing Cr^{3+} have been conjugated to superparamagnetic iron oxide nanoparticles to obtain T_2-weighted MRI contrast and have also been conjugated to gadolinium complexes to obtain T_1-weighted MRI contrast [140, 141]. The absence of need for an in situ luminescence excitation source greatly simplifies the possibility of obtaining optical images while MRI is being performed. The balance between the dose of nanoparticles needed to achieve acceptable contrast in MRI as well as optical luminescence should be tailored to achieve results that give meaningful information from both techniques without jeopardizing the results of one or the other.

Materials utilizing dopants such as Yb^{3+}, Nd^{3+}, and Er^{3+} to obtain NIR persistent luminescence have also shown significant promise, as the longer-wavelength emissions from Yb^{3+} (976 nm), Nd^{3+} (800 nm, 1.0 and 1.3 μm), and Er^{3+} (1.5 μm) have greater tissue penetration capability than Cr^{3+}-doped materials [143–144]. Finally, the use of NIR-emissive nanoparticles for imaging, while promising, is also dependent on the continued improvement in detector technologies to facilitate imaging in the third biological window.

7.6 Conclusions and outlook

Luminescent nanoparticles doped with transition metal and lanthanide ions have been demonstrated in a myriad of applications, proving their incredible potential for advancing the bioimaging field. The potential for their use in both cellular and anatomical imaging stems from the wide variety of emissions they possess, which span the UV, visible, and NIR regions. However, the absorption and scattering of light by proteins, water, hemoglobin, and other biomolecules restrict the use of luminescent nanoparticles. The three biological windows (650–950, 1,000–1,350, and 1,550–1,870 nm) provide the greatest opportunity for optical imaging, as these regions exhibit minimal interaction with water and biomolecules. Thus, a significant amount of attention has been focused on developing nanomaterials which emit within these windows.

With regard to photoluminescence, Yb^{3+} and Nd^{3+}-doped nanoparticles can both be excited by and exhibit emissions in the NIR. The conjugation of NIR-absorbing dyes such as indocyanine green can be conjugated to the surface of lanthanide-doped fluoride nanoparticles, increasing their absorption efficiency through the antenna effect. These ions can also serve as sensitizers for upconversion luminescence, in which the sequential absorption of low energy photons populates these ions, and their energy is transferred to activator ions such as Er^{3+}, Tm^{3+}, and Ho^{3+} to populate metastable excited states and result in the emission of higher-energy photons. Upconverting nanoparticles can be regarded as the fastest-advancing luminescent nanoprobes, owing to their unique nonlinear luminescence properties that make it possible to avoid autofluorescence in bioimaging. Advancements in their design have made it possible to prove their applicability in breaking past the diffraction limit of resolution in optical microscopy techniques, bringing about the advent of super-resolution microscopy.

The absolute necessity to eliminate the background noise associated with autofluorescence in conventional optical microscopy techniques has brought about the development of persistent luminescence nanoparticles designed for use in bioimaging. These nanoparticles are preirradiated with high energy excitation that charges them, such that when excitation has ceased luminescence from these materials continues for seconds to days. The persistent luminescence nanoparticles can then be introduced to the specimen and imaged without an excitation source present, greatly enhancing the signal-to-noise ratios achieved in fluorescence microscopy. Complex oxide-based materials such as silicates, aluminates, germanates, and gallates are the most widely encountered hosts, which are most-often doped with lanthanide ions such as Eu^{2+} and Dy^{3+} to obtain blue or green persistent luminescence or transition metals such as Cr^{3+} to obtain red and NIR persistent luminescence. The ability to recharge these materials in situ has also made it possible to perform long-term nanoparticle tracking experiments to visualize nano-biointeractions and the onset of apoptosis, for example.

The developments made in upconversion, persistent luminescence, and NIR optical imaging have been combined with other imaging techniques such as MRI, CT, and lifetime imaging, making it possible to achieve multimodal imaging that provides a wealth of information in terms of diagnosis and biological functioning. Furthermore, the ability to functionalize the surface of nanoparticles with a nearly infinite number of small molecules that can stabilize and/or target biomarkers makes it possible to create complex nanoprobes that are able to have multiple capabilities within a single nanoprobe.

The potential for these materials is still evolving, as advancements in luminescence efficiency, detector technologies, and imaging resolutions are continually being made. Future efforts should be focused on developing nontoxic, photostable, highly efficient luminescent materials that ideally emit within the biological windows. The advantage of nanoparticles over small molecules definitively lies in the possibility to functionalize their surface and provide multimodal diagnostic and imaging capabilities; the effects of the functionalization of these nanoparticles and their fate at both an anatomical and subcellular level are still yet to be fully understood, though their future in biotechnological advancements is definitely bright.

References

[1] C. Vonesch, F. Aguet, J.L. Vonesch, M. Unser, The colored revolution of bioimaging, IEEE Signal Process. Mag. 23 (2006) 20–31.

[2] M.S. Ghamsari, State of the Art in Nano-bioimaging, InTech (2018).

[3] M.A. Hahn, A.K. Singh, P. Sharma, S.C. Brown, B.M. Moudgil, Anal. Bioanal. Chem. 399 (2011) 3–27.

[4] J. Wang, Q. Ma, Y. Wang, H. Shen, Q. Yuan, Recent progress in biomedical applications of persistent luminescence nanoparticles, Nanoscale 9 (2017) 6204–6218.

[5] S. Sreedharan, R. Tiwari, D. Tyde, S.O. Aderinto, S.K. Pramanik, A. Das, J.A. Thomas, Nanocarriers used as probes for super-resolution microscopy, Mater. Chem. Front. Advance Article 5 (2021) 1268–1282.

[6] S. Behzadi, V. Serpooshan, W. Tao, M.A. Hamaly, M.Y. Alkawareek, E.C. Dreaden, D. Brown, A.M. Alkilany, O.C. Farokhzad, M. Mahmoudi, Cellular uptake of nanoparticles: Journey inside the cell, Chem. Soc. Rev. 46 (2017) 4218–4244.

[7] Q. Liu, M. Chen, Y. Sun, G. Chen, T. Yang, Y. Gao, X. Zhang, F. Li, Multifunctional rare-earth self-assembled nanosystem for tri-modal upconversion luminescence /fluorescence /positron emission tomography imaging, Biomaterials 32 (2011) 8243–8253.

[8] D.M. Samhadaneh, G.A. Mandl, Z. Han, M. Mahjoob, S.C. Weber, M. Tuznik, D.A. Rudko, J.A. Capobianco, U. Stochaj, Evaluation of lanthanide-doped upconverting nanoparticles for in vitro and in vivo applications, ACS Appl. Bio Mater. 3 (2020) 4358–4369.

[9] M.V. DaCosta, S. Doughan, Y. Han, U.J. Krull, Anal. Chim. Acta 832 (2014) 1–33.

[10] Y.W. Wang, N.P. Reder, S. Kang, A.K. Glaser, J.T.C. Liu, Nanotheranostics 1 (2017) 369–388.

[11] F.W. Pratiwi, C.W. Kuo, B.-C. Chen, P. Chen, Recent advances in the use of fluorescent nanoparticles for bioimaging, Nanomedicine 14 (2019) 1759–1769.

[12] S. Wu, Y. Li, W. Ding, L. Xu, Y. Ma, L. Zhang, Nano-Micro Lett. 12 (2020).

[13] P. Foroozandeh, A.A. Aziz, Nanoscale Res. Lett. 13 (2018) 1–12.

[14] S. Siddique, J.C.L. Chow, Application of nanomaterials in biomedical imaging and cancer therapy, Nanomaterials 10 (2020) 1700.

[15] G.D. Luker, K.E. Luker, Optical imaging: Current applications and future directions, J. Nucl. Med. 49 (2008) 1–4.

[16] M.H.Y. Cheng, Y. Mo, G. Zheng, Nano versus molecular: Optical imaging approaches to detect and monitor tumor hypoxia, Adv. Healthc. Mater. 10 (2021) 2001549.

[17] G. Pirovano, S. Roberts, S. Kossatz, T. Reiner, Optical imaging modalities: Principles and applications in preclinical research and clinical settings, J. Nucl. Med. 61 (2020) 1419–1427.

[18] M. Monici, Cell and tissue autofluorescence research and diagnostic applications, Biotechnol. Annu. Rev. 11 (2005) 227–256.

[19] A.M. Smith, M.C. Mancini, S. Nie, Bioimaging: Second window for in vivo imaging, Nat. Nanotechnol. 4 (2009) 710–711.

[20] R.R. Anderson, J.A. Parrish, The optics of human skin, J. Invest. Dermatol. 77 (1981) 13–19.

[21] E. Hemmer, P. Acosta-Mora, J. Méndez-Ramos, S. Fischer, Optical nanoprobes for biomedical applications: shining a light on upconverting and near-infrared emitting nanoparticles for imaging, thermal sensing, and photodynamic therapy, J. Mater. Chem. B 5 (2017) 4365–4392.

[22] Y.T. Lim, S. Kim, A. Nakayama, N.E. Stott, M.G. Bawendi, J.V. Frangioni, Selection of quantum dot wavelengths for biomedical assays and imaging, Mol. Imaging 2 (2003) 50–64.

[23] R. Naccache, Q. Yu, J.A. Capobianco, The fluoride host: Nucleation, growth, and upconversion of lanthanide-doped nanoparticles, Adv. Opt. Mater. 3 (2015) 482–509.

[24] D. Wawrzynczyk, A. Bednarkiewicz, M. Nyk, W. Strek, M. Samoc, Neodymium(iii) doped fluoride nanoparticles as non-contact optical temperature sensors, Nanoscale 4 (2012) 6959–6961.

[25] J.M. Meijer, L. Aarts, B.M. Van Der Ende, T.J.H. Vlugt, A. Meijerink, Downconversion for solar cells in YF_3: Nd^{3+}, Yb^{3+}, Phys. Rev. B – Condens. Matter Mater. Phys. 81 (2010) 035107.

[26] S. Hüfner, Optical Spectra of Transparent Rare Earth Compounds, Academic Press (1978).

[27] A. Fernandez-Fernandez, R. Manchanda, T. Lei, D.A. Carvajal, Y. Tang, S.Z.R. Kazmi, A.J. McGoron, Comparative study of the optical and heat generation properties of IR820 and indocyanine green, Mol. Imaging 11 (2012) 7290.2011.00031.

[28] T. Förster, Zwischenmolekulare Energiewanderung und Fluoreszenz, Ann. Phys. 437 (1948) 55–75.

[29] M. Tan, F. Li, N. Cao, H. Li, X. Wang, C. Zhang, D. Jaque, G. Chen, Accurate in vivo nanothermometry through NIR-II lanthanide luminescence lifetime, Small 16 (2020) 2004118.

[30] D.H. Ortgies, M. Tan, E.C. Ximendes, B. Del Rosal, J. Hu, L. Xu, X. Wang, E. Martín Rodríguez, C. Jacinto, N. Fernandez, G. Chen, D. Jaque, Lifetime-Encoded Infrared-Emitting Nanoparticles for in Vivo Multiplexed Imaging, ACS Nano 12 (2018) 4362–4368.

[31] C. Cao, M. Xue, X. Zhu, P. Yang, W. Feng, F. Li, Energy transfer highway in Nd^{3+}-sensitized nanoparticles for efficient near-infrared bioimaging ACS Appl. Mater. Interfaces 9 (2017) 18540–18548.

[32] A. Skripka, A. Benayas, R. Marin, P. Canton, E. Hemmer, F. Vetrone, Double rare-earth nanothermometer in aqueous media: Opening the third optical transparency window to temperature sensing, Nanoscale 9 (2017) 3079–3085.

[33] J.W. Stouwdam, M. Raudsepp, F.C.J.M. Van Veggel, Colloidal nanoparticles of Ln^{3+}-doped LaVO4: Energy transfer to visible- and near-infrared-emitting lanthanide ions, Langmuir 21 (2005) 7003–7008.

[34] W. Shao, G. Chen, A. Kuzmin, H.L. Kutscher, A. Pliss, T.Y. Ohulchanskyy, P.N. Prasad, Tunable narrow band emissions from dye-sensitized core/shell/shell nanocrystals in the second near-infrared biological window, J. Am. Chem. Soc. 138 (2016) 16192–16195.

[35] H.T.T. Duong, Y. Chen, S.A. Tawfik, S. Wen, M. Parviz, O. Shimoni, D.J. Ab, Systematic investigation of functional ligands for colloidal stable upconversion nanoparticles†, RSC Adv. 8 (2018) 4842–4849.

[36] X. Wu, Y. Zhang, K. Takle, O. Bilsel, Z. Li, H. Lee, Z. Zhang, D. Li, W. Fan, C. Duan, E.M. Chan, C. Lois, Y. Xiang, G. Han, Dye-sensitized core/active shell upconversion nanoparticles for optogenetics and bioimaging applications, ACS Nano 10 (2016) 1060–1066.

[37] C.J. Milner, Sulphide phosphors and the zone theory of solids, Trans. Faraday Soc. 35 (1939) 101–111.

[38] G. Swati, V.V. Jaiswal, D. Haranath, Spectroscopy of Lanthanide Doped Oxide Materials, Elsevier Inc. (2019), pp. 393–425.

[39] F. Auzel, History of upconversion discovery and its evolution, J. Lumin. 223 (2020) 116900.

[40] N. Bloembergen, Solid state infrared quantum counters, Phys. Rev. Lett. 2 (1959) 84–85.

[41] H.W. Gandy, R.J. Ginther, J.F. Weller, Laser oscillations in erbium activated silicate glass, Phys. Lett. 16 (1965) 266–267.

[42] E. Snitzer, R. Woodcock, Yb^{3+} single bond sign Er^{3+} glass laser, Appl. Phys. Lett. 6 (1965) 45–46.

[43] F. Auzel, Upconversion and anti-stokes processes with f and d ions in solids, Chem. Rev. 104, 1 (2004) 139–174.

[44] F. Auzel, Upconversion processes in coupled ion systems, J. Lumin. 45 (1990) 341–345.

[45] S. Heer, K. Kömpe, H.-U. Güdel, M. Haase, Highly efficient multicolour upconversion emission in transparent colloids of lanthanide-doped NaYF4 nanocrystals, Adv. Mater. 16 (2004) 2102–2105.

[46] A. Aebischer, S. Heer, D. Biner, K. Krämer, M. Haase, H.U. Güdel, Visible light emission upon near-infrared excitation in a transparent solution of nanocrystalline β-$NaGdF_4$: Yb^{3+}, Er^{3+}, Chem. Phys. Lett. 407 (2005) 124–128.

[47] J.F. Suyver, A. Aebischer, D. Biner, P. Gerner, J. Grimm, S. Heer, K.W. Krämer, C. Reinhard, H.U. Güdel, Novel materials doped with trivalent lanthanides and transition metal ions showing near-infrared to visible photon upconversion, Opt. Mater. (Amst). 27 (2005) 1111–1130.

[48] J.-C. Boyer, F. Vetrone, L.A. Cuccia, J.A. Capobianco, Synthesis of colloidal upconverting NaYF 4 nanocrystals doped with Er^{3+}, Yb^{3+} and Tm^{3+}, Yb^{3+} via thermal decomposition of lanthanide trifluoroacetate precursors, J. Am. Chem. Soc. 128 (2006) 7444–7445.

[49] R. Naccache, F. Vetrone, V. Mahalingam, L.A. Cuccia, J.A. Capobianco, Controlled synthesis and water dispersibility of hexagonal phase NaGdF 4: Ho^{3+}/Yb^{3+} nanoparticles, Chem. Mater. 21 (2009) 717–723.

[50] F. Vetrone, R. Naccache, V. Mahalingam, C.G. Morgan, J.A. Capobianco, Upconverting nanoparticles: The active-core/active-shell approach: A strategy to enhance the upconversion luminescence in lanthanide-doped nanoparticles (Adv. Funct. Mater. 18/2009), Adv. Funct. Mater. 19 (2009) 2924–2929.

[51] P. Ptacek, H. Schäfer, K. Kömpe, M. Haase, Crystal phase control of luminescing α-$NaGdF_4$: Eu^{3+} and β-$NaGdF_4$: Eu^{3+} nanocrystals, Adv. Funct. Mater. 17 (2007) 3843–3848.

[52] T. Rinkel, J. Nordmann, A.N. Raj, M. Haase, Ostwald-ripening and particle size focussing of sub-10 nm NaYF4 upconversion nanocrystals, Nanoscale 6 (2014) 14523–14530.

[53] M. Haase, H. Schäfer, Upconverting nanoparticles, Angew. Chemie – Int. Ed. 50 (2011) 5808–5829.

[54] A.M. Ibarra-Ruiz, D.C. Rodríguez Burbano, J.A. Capobianco, Photoluminescent nanoplatforms in biomedical applications, Adv. Phys. X 1 (2016) 194–225.

[55] G. Tessitore, G.A. Mandl, M.G. Brik, W. Park, J.A. Capobianco, Recent insights into upconverting nanoparticles: Spectroscopy, modeling, and routes to improved luminescence, Nanoscale 11 (2019) 12015–12029.

[56] C. Li, J. Lin, Rare earth fluoride nano-/microcrystals: synthesis, surface modification and application, J. Mater. Chem. 20 (2010) 6831.

[57] J. Zhang, Z. Hao, J. Li, X. Zhang, Y. Luo, G. Pan, Observation of efficient population of the red-emitting state from the green state by non-multiphonon relaxation in the Er^{3+}-Yb^{3+} system, Light Sci. Appl. 4 (2015) e239.

[58] P. Taroni, A. Pifferi, A. Torricelli, D. Comelli, R. Cubeddu, In vivo absorption and scattering spectroscopy of biological tissues, Photochem. Photobiol. Sci. 2 (2003) 124–129.

[59] H. Zhang, D. Salo, D.M. Kim, S. Komarov, Y.-C. Tai, M.Y. Berezin, Penetration depth of photons in biological tissues from hyperspectral imaging in shortwave infrared in transmission and reflection geometries, J. Biomed. Opt. 21 (2016) 126006.

[60] D.L. Dexter, A theory of sensitized luminescence in solids, J. Chem. Phys. 21 (1953) 836–850.

[61] F.T. Rabouw, P.T. Prins, P. Villanueva-Delgado, M. Castelijns, R.G. Geitenbeek, A. Meijerink, Quenching pathways in $NaYF_4$: Er^{3+}, Yb^{3+} upconversion nanocrystals, ACS Nano 12 (2018) 4812–4823.

[62] M. Haase, H. Schäfer, Upconverting nanoparticles, Angew. Chemie Int. Ed. 50 (2011) 5808–5829.

[63] F. Vetrone, J.A. Capobianco, Lanthanide-doped fluoride nanoparticles: luminescence, upconversion, and biological applications, Int. J. Nanotechnol. 5 (2008) 1306–1339.

[64] Y.F. Wang, G.Y. Liu, L.D. Sun, J.W. Xiao, J.C. Zhou, C.H. Yan, Nd^{3+}-sensitized upconversion nanophosphors: Efficient in vivo bioimaging probes with minimized heating effect, ACS Nano 7 (2013) 7200–7206.

[65] Q. Zhu, T. Sun, M.N. Chung, X. Sun, Y. Xiao, X. Qiao, F. Wang, Yb^{3+}-sensitized upconversion and downshifting luminescence in Nd^{3+} ions through energy migration, Dalt. Trans. 47 (2018) 8581–8584.

[66] J. Tang, L. Chen, J. Li, Z. Wang, J. Zhang, L. Zhang, Y. Luo, X. Wang, Selectively enhanced red upconversion luminescence and phase/size manipulation via Fe^{3+} doping in NaYF4: Yb, Er nanocrystals, Nanoscale 7 (2015) 14752–14759.

[67] G. Tessitore, S.L. Maurizio, T. Sabri, J.A. Capobianco, Intrinsic time-tunable emissions in core -shell upconverting nanoparticle systems, Angew. Chemie Int. Ed. 58 (2019) 9742–9751.

[68] S. Wen, J. Zhou, K. Zheng, A. Bednarkiewicz, X. Liu, D. Jin, Advances in highly doped upconversion nanoparticles, Nat. Commun. 9 (2018) 2415.

[69] X. Liu, Y. Wang, X. Li, Z. Yi, R. Deng, L. Liang, X. Xie, D.T.B. Loong, S. Song, F.A. Di, H. All, H. Zhang, L. Huang, X. Liu, Binary temporal upconversion codes of Mn^{2+}-activated nanoparticles for multilevel anti-counterfeiting, Nat. Commun. 8 (2017) 1–7.

[70] J.-C. Boyer, F.C.J.M. Van Veggel, Absolute quantum yield measurements of colloidal $NaYF_4$: Er^{3+}, Yb^{3+} upconverting nanoparticles, Nanoscale 2 (2010) 1417–1419.

[71] K.W. Krämer, D. Biner, G. Frei, H.U. Güdel, M.P. Hehlen, S.R. Lüthi, Hexagonal sodium yttrium fluoride based green and blue emitting upconversion phosphors, Chem. Mater. 16 (2004) 1244–1251.

[72] M.Y. Hossan, A. Hor, Q. Luu, S.J. Smith, P.S. May, M.T. Berry, Explaining the nanoscale effect in the upconversion dynamics of β-$NaYF_4$: Yb^{3+}, Er^{3+} core and core-shell nanocrystals, J. Phys. Chem. C 121 (2017) 16592–16606.

[73] R.B. Anderson, S.J. Smith, P.S. May, M.T. Berry, Revisiting the NIR-to-visible upconversion mechanism in β-$NaYF_4$: Yb^{3+}, Er^{3+}, J. Phys. Chem. Lett. 5 (2014) 36–42.

[74] P. Villanueva-Delgado, K.W. Krämer, R. Valiente, M. de Jong, A. Meijerink, Modeling blue to UV upconversion in β-NaYF: Tm^{3+}, Phys. Chem. Chem. Phys. 18 (2016) 27396–27404.

[75] S.L. Maurizio, G. Tessitore, G.A. Mandl, J.A. Capobianco, Luminescence dynamics and enhancement of the UV and visible emissions of Tm^{3+} in $LiYF_4$: Yb^{3+}, Tm^{3+} upconverting nanoparticles, Nanoscale Adv. 1 (2019) 4492–4500.

[76] Y. Lu, J. Zhao, R. Zhang, Y. Liu, D. Liu, E.M. Goldys, X. Yang, P. Xi, A. Sunna, J. Lu, Y. Shi, R.C. Leif, Y. Huo, J. Shen, J.A. Piper, J.P. Robinson, D. Jin, Tunable lifetime multiplexing using luminescent nanocrystals, Nat. Photonics 8 (2014) 32–36.

[77] E. Messina, E. Cavallaro, A. Cacciola, M. Antonia, I. Iatì, P.G. Gucciardi, F. Borghese, P. Denti, R. Saija, G. Compagnini, M. Meneghetti, V. Amendola, O.M. Marag, Plasmon-enhanced optical trapping of gold nanoaggregates with selected optical properties, ACS Nano 5, 2 (2011) 905–913.

[78] G. Tessitore, S.L. Maurizio, T. Sabri, C.D. Skinner, J.A. Capobianco, Multiemission Particle Velocimetry: The Key Role of Intrinsic Lifetime Dynamics from Upconverting Nanosystems in Multiemission Particle Velocimetry (Adv. Mater. 42/2020), Adv. Mater. 32 (2020) 2070316.

[79] G.A. Sobral, M.A. Gomes, J.F.M. Avila, J.J. Rodrigues, Z.S. Macedo, J.M. Hickmann, M.A.R.C. Alencar, Tailoring red-green-blue emission from Er^{3+}, Eu^{3+} and Tb^{3+} doped Y2O3 nanocrystals produced via PVA-assisted sol-gel route, J. Phys. Chem. Solids 98 (2016) 81–90.

[80] G. Tessitore, A.-V. Mudring, K.W. Krämer, Luminescence and energy transfer in β-$NaGdF_4$: Eu^{3+}, Er^{3+} nanocrystalline samples from a room temperature synthesis, New J. Chem. 42 (2018) 237–245.

[81] A. Gnach, T. Lipinski, A. Bednarkiewicz, J. Rybka, J.A. Capobianco, Chem. Soc. Rev. 44 (2015) 1561–1584.

[82] J. Zhou, Z. Liu, F. Li, Upconversion nanophosphors for small-animal imaging, Chem. Soc. Rev. 41 (2012) 1323–1349.

[83] X. Liu, C.-H. Yan, J.A. Capobianco, Photon upconversion nanomaterials, Chem. Soc. Rev. 44 (2015) 1299–1301.

[84] R.J. Meier, J.M.B. Simbuürger, T. Soukka, M. Schaüferling, Background-free referenced luminescence sensing and imaging of pH using upconverting phosphors and color camera read-out, Anal. Chem. 86 (2014) 5535–5540.

[85] B.A. Webb, M. Chimenti, M.P. Jacobson, D.L. Barber, Dysregulated pH: A perfect storm for cancer progression, Nat. Rev. Cancer 11 (2011) 671–677.

[86] Y. Cen, Y.M. Wu, X.J. Kong, S. Wu, R.Q. Yu, X. Chu, Phospholipid-modified upconversion nanoprobe for ratiometric fluorescence detection and imaging of phospholipase D in cell lysate and in living cells, Anal. Chem. 86 (2014) 7119–7127.

[87] R. Arppe, L. Mattsson, K. Korpi, S. Blom, Q. Wang, T. Riuttamäki, T. Soukka, Homogeneous assay for whole blood folate using photon upconversion, Anal. Chem. 87 (2015) 1782–1788.

[88] S. Wu, G. Han, D.J. Milliron, S. Aloni, V. Altoe, D.V. Talapin, B.E. Cohen, P.J. Schuck, Non-blinking and photostable upconverted luminescence from single lanthanide-doped nanocrystals, Proc. Natl. Acad. Sci. U. S. A. 106 (2009) 10917–10921.

[89] D.J. Gargas, E.M. Chan, A.D. Ostrowski, S. Aloni, M.V.P. Altoe, E.S. Barnard, B. Sanii, J.J. Urban, D.J. Milliron, B.E. Cohen, P.J. Schuck, Engineering bright sub-10-nm upconverting nanocrystals for single-molecule imaging, Nat. Nanotechnol. 9 (2014) 300–305.

[90] A.D. Ostrowski, E.M. Chan, D.J. Gargas, E.M. Katz, G. Han, P.J. Schuck, D.J. Milliron, B.E. Cohen, Controlled synthesis and single-particle imaging of bright, sub-10 nm lanthanide- doped upconverting nanocrystals, ACS Nano 6 (2012) 2686–2692.

[91] X. Wu, G. Chen, J. Shen, Z. Li, Y. Zhang, G. Han, Upconversion nanoparticles: A versatile solution to multiscale biological imaging, Bioconjug. Chem. 26 (2015) 166–175.

[92] K. Shin, Y.H. Song, Y. Goh, K.T. Lee, Two-dimensional and three-dimensional single particle tracking of upconverting nanoparticles in living cells, Int. J. Mol. Sci. 20 (2019) 1424.

[93] R. Palomba, A.L. Palange, I.F. Rizzuti, M. Ferreira, A. Cervadoro, M.G. Barbato, C. Canale, P. Decuzzi, Modulating phagocytic cell sequestration by tailoring nanoconstruct softness, ACS Nano 12, 2 (2018) 1433–1444.

[94] G. Fullstone, J. Wood, M. Holcombe, G. Battaglia, Modelling the transport of nanoparticles under blood flow using an agent-based approach, Sci. Rep. 5 (2015) 1–13.

[95] P. Rees, J.W. Wills, M.R. Brown, C.M. Barnes, H.D. Summers, The origin of heterogeneous nanoparticle uptake by cells, Nat. Commun. 10 (2019) 1–8.

[96] P.A. Rojas-Gutierrez, D. Bekah, J. Seuntjens, C. Dewolf, J.A. Capobianco, Cellular uptake, cytotoxicity and trafficking of supported lipid-bilayer-coated lanthanide upconverting nanoparticles in alveolar lung cancer cells, ACS Appl. Bio Mater. 2 (2019) 4527–4536.

[97] V. Belli, D. Guarnieri, M. Biondi, F. Della Sala, P.A. Netti, Dynamics of nanoparticle diffusion and uptake in three-dimensional cell cultures, Colloids Surf. B Biointerfaces 149 (2017) 7–15.

[98] P. Haro-González, B. Del Rosal, L.M. Maestro, E. Martín Rodríguez, R. Naccache, J.A. Capobianco, K. Dholakia, J.G. Solé, D. Jaque, Optical trapping of NaYF4: Er^{3+}, Yb^{3+} upconverting fluorescent nanoparticles, Nanoscale 5 (2013) 12192–12199.

[99] P. Rodríguez-Sevilla, H. Rodríguez-Rodríguez, M. Pedroni, A. Speghini, M. Bettinelli, J.G. Solé, D. Jaque, P. Haro-González, Assessing single upconverting nanoparticle luminescence by optical tweezers, Nano Lett. 15 (2015) 5068–5074.

[100] E. Betzig, Single molecules, cells, and super-resolution optics (Nobel Lecture), Angew. Chemie Int. Ed. 54 (2015) 8034–8053.

[101] S.W. Hell, Nanoscopy with focused light (Nobel Lecture), Angew. Chemie Int. Ed. 54 (2015) 8054–8066.

[102] T.J. Gould, S.T. Hess, J. Bewersdorf, Optical nanoscopy: From acquisition to analysis, Annu. Rev. Biomed. Eng. 14 (2012) 231–254.

[103] B. Huang, M. Bates, X. Zhuang, Super-resolution fluorescence microscopy, Annu. Rev. Biochem. 78 (2009) 993–1016.

[104] Q. Zhan, H. Liu, B. Wang, Q. Wu, R. Pu, C. Zhou, B. Huang, X. Peng, H. Ågren, S. He, Achieving high-efficiency emission depletion nanoscopy by employing cross relaxation in upconversion nanoparticles, Nat. Commun. 8 (2017) 1–11.

[105] Y. Liu, Y. Lu, X. Yang, X. Zheng, S. Wen, F. Wang, X. Vidal, J. Zhao, D. Liu, Z. Zhou, C. Ma, J. Zhou, J.A. Piper, P. Xi, D. Jin, Amplified stimulated emission in upconversion nanoparticles for super-resolution nanoscopy, Nature 543 (2017) 229–233.

[106] K. Van Den Eeckhout, D. Poelman, P.F. Smet, Persistent luminescence in non-Eu^{2+}-doped compounds: A review, Materials (Basel). 6 (2013) 2789–2818.

[107] Y. Li, M. Gecevicius, J. Qiu, Chem. Soc. Rev. 45 (2016) 2090–2136.

[108] S.K. Singh, RSC Adv. 4 (2014) 58674–58698.

[109] H.F. Brito, J. Holsa, T. Laamanen, M. Lastusaari, M. Malkamaki, L.C.V. Rodrigues, Persistent luminescence mechanisms: Human imagination at work, Opt. Mater. Express 2 (2012) 371–381.

[110] K. Kirakci, P. Kubát, K. Fejfarová, J. Martinčík, M. Nikl, K. Lang, X-ray inducible luminescence and singlet oxygen sensitization by an octahedral molybdenum cluster compound: A new class of nanoscintillators, Inorg. Chem. 55, 2 (2016) 803–809.

[111] D. Jaque, C. Richard, B. Viana, K. Soga, X. Liu, J. García Solé, Inorganic nanoparticles for optical bioimaging, Adv. Opt. Photonics 8 (2016) 1.

[112] C. Richard, T. Maldiney, Q. Le Masne De Chermont, J. Seguin, N. Wattier, G. Courties, F. Apparailly, M. Bessodes, D. Scherman, Adv. Intell. Syst. Comput. 120 (2012) 37–53.

[113] T. Maldiney, M.U. Kaikkonen, J. Seguin, Q. Le Masne, D. Chermont, M. Bessodes, K.J. Airenne, S. Ylä-Herttuala, D. Scherman, C. Richard, In vitro targeting of avidin-expressing glioma cells with biotinylated persistent luminescence nanoparticles, Bioconjug. Chem. 23 (2012) 472–478.

[114] Q.L.M. De Chermont, C. Chanéac, J. Seguin, F. Pellé, S. Maîtrejean, J.P. Jolivet, D. Gourier, M. Bessodes, D. Scherman, Nanoprobes with near-infrared persistent luminescence for in vivo imaging, Proc. Natl. Acad. Sci. U. S. A. 104 (2007) 9266–9271.

[115] J.M. Liu, D.D. Zhang, G.Z. Fang, S. Wang, Erythrocyte membrane bioinspired near-infrared persistent luminescence nanocarriers for in vivo long-circulating bioimaging and drug delivery, Biomaterials 165 (2018) 39–47.

[116] A. Vedda, M. Fasoli, Tunneling recombinations in scintillators, phosphors, and dosimeters, Radiat. Meas. 118 (2018) 86–97.

[117] K. Van den Eeckhout, P.F. Smet, D. Poelman, Persistent luminescence in Eu^{2+}-doped compounds: A review, Materials (Basel). 3 (2010) 2536–2566.

[118] D.C. Rodríguez Burbano, S.K. Sharma, P. Dorenbos, B. Viana, J.A. Capobianco, Persistent and photostimulated red emission in CaS: Eu^{2+}, Dy^{3+} nanophosphors, Adv. Opt. Mater. 3 (2015) 551–557.

[119] D.C. Rodríguez Burbano, E.M. Rodríguez, P. Dorenbos, M. Bettinelli, J.A. Capobianco, J. Mater. Chem. C. 2 (2014) 228–231.

[120] Z. Xue, X. Li, Y. Li, M. Jiang, H. Liu, S. Zeng, J. Hao, X-ray-activated near-infrared persistent luminescent probe for deep-tissue and renewable in vivo bioimaging, ACS Appl. Mater. Interfaces 9 (2017) 22132–22142.

[121] L. Song, P.P. Li, W. Yang, X.H. Lin, H. Liang, X.F. Chen, G. Liu, J. Li, H.H. Yang, Low-dose X-ray activation of W(VI)-doped persistent luminescence nanoparticles for deep-tissue photodynamic therapy, Adv. Funct. Mater. 28 (2018) 1707496.

[122] F. Liu, W. Yan, Y.J. Chuang, Z. Zhen, J. Xie, Z. Pan, Photostimulated near-infrared persistent luminescence as a new optical read-out from Cr^{3+}-doped LiGa5O8, Sci. Rep. 3 (2013) 1554.

[123] H. Liu, F. Ren, X. Zhou, C. Ma, T. Wang, H. Zhang, Q. Sun, Z. Li, Ultra-sensitive detection and inhibition of the metastasis of breast cancer cells to adjacent lymph nodes and distant organs by using long-persistent luminescence nanoparticles, Anal. Chem. 91 (2019) 15064–15072.

[124] G. Ramírez-García, S. Gutiérrez-Granados, M.A. Gallegos-Corona, L. Palma-Tirado, F. d'Orlyé, A. Varenne, N. Mignet, C. Richard, M. Martínez-Alfaro, Long-term toxicological effects of persistent luminescence nanoparticles after intravenous injection in mice, Int. J. Pharm. 532 (2017) 686–695.

[125] Y.J. Li, X.P. Yan, Synthesis of functionalized triple-doped zinc gallogermanate nanoparticles with superlong near-infrared persistent luminescence for long-term orally administrated bioimaging, Nanoscale 8 (2016) 14965–14970.

[126] A. Bessière, A. Lecointre, R.A. Benhamou, E. Suard, G. Wallez, B. Viana, How to induce red persistent luminescence in biocompatible Ca 3(PO4)2, J. Mater. Chem. C 1 (2013) 1252–1259.

[127] A. Gnach, T. Lipinski, A. Bednarkiewicz, J. Rybka, J.A. Capobianco, Chem. Soc. Rev. 44 (2015) 1561–1584.

[128] D. Van der Heggen, D.R. Cooper, M. Tesson, J.J. Joos, J. Seuntjens, J.A. Capobianco, P.F. Smet, Optically stimulated nanodosimeters with high storage capacity, Nanomaterials 9 (2019) 1127.

[129] D.R. Cooper, J.A. Capobianco, J. Seuntjens, Radioluminescence studies of colloidal oleate-capped β-Na(Gd,Lu)F4: Ln^{3+} nanoparticles (Ln = Ce, Eu, Tb), Nanoscale 10 (2018) 7821–7832.

[130] G.A. Mandl, D. Van der Heggen, D.R. Cooper, J.J. Joos, J. Seuntjens, P.F. Smet, J.A. Capobianco, On a local (de-)trapping model for highly doped Pr^{3+} radioluminescent and persistent luminescent nanoparticles, Nanoscale 12 (2020) 20759–20766.

[131] Y. Hu, Y. Yang, X. Zhang, X. Wang, X. Li, Y. Li, T. Li, H. Zhang, X-ray-excited super-long green persistent luminescence from Tb_{3+} monodoped β-NaYF 4, J. Phys. Chem. C 124 (2020), 24940–24948.

[132] L. Zhan-Jun, Z. Hong-Wu, S. Meng, S. Jiang-Shan, F. Hai-Xia, A facile and effective method to prepare long-persistent phosphorescent nanospheres and its potential application for in vivo imaging, J. Mater. Chem. 22 (2012) 24713–24720.

[133] L. Zhang, J. Lei, J. Liu, F. Ma, H. Ju, Persistent luminescence nanoprobe for biosensing and lifetime imaging of cell apoptosis via time-resolved fluorescence resonance energy transfer, Biomaterials 67 (2015) 323–334.

[134] A.N. Danthanarayana, E. Finley, B. Vu, K. Kourentzi, R.C. Willson, J. Brgoch, A multicolor multiplex lateral flow assay for high-sensitivity analyte detection using persistent luminescent nanophosphors, Anal. Methods 12 (2020) 272–280.

[135] I.P. Machado, C.C.S. Pedroso, J.M. de Carvalho, V.D.C. Teixeira, L.C.V. Rodrigues, H.F. Brito, A new path to design near-infrared persistent luminescence materials using Yb^{3+}-doped rare earth oxysulfides, Scr. Mater. 164 (2019) 57–61.

[136] J. Du, D. Poelman, Near-infrared persistent luminescence in Mn^{4+} doped perovskite type solid solutions, Ceram. Int. 45 (2019) 8345–8353.

[137] S.-Q. Wu, C.-X. Yang, X.-P. Yan, A dual-functional persistently luminescent nanocomposite enables engineering of mesenchymal stem cells for homing and gene therapy of glioblastoma, Adv. Funct. Mater. 27 (2017) 1604992.

[138] Y. Gao, R. Li, W. Zheng, X. Shang, J. Wei, M. Zhang, J. Xu, W. You, Z. Chen, X. Chen, Broadband NIR photostimulated luminescence nanoprobes based on CaS: Eu^{2+}, Sm^{3+} nanocrystals, Chem. Sci. 10 (2019) 5452–5460.

[139] E. Teston, Y. Lalatonne, D. Elgrabli, G. Autret, L. Motte, F. Gazeau, D. Scherman, O. Clément, C. Richard, T. Maldiney, Design, properties, and in vivo behavior of superparamagnetic persistent luminescence nanohybrids, Small 11 (2015) 2696–2704.

[140] A. Abdukayum, C.X. Yang, Q. Zhao, J.T. Chen, L.X. Dong, X.P. Yan, Gadolinium complexes functionalized persistent luminescent nanoparticles as a multimodal probe for near-infrared luminescence and magnetic resonance imaging in vivo, Anal. Chem. 86 (2014) 4096–4101.

[141] Y.C. Lu, C.X. Yang, X.P. Yan, Radiopaque tantalum oxide coated persistent luminescent nanoparticles as multimodal probes for in vivo near-infrared luminescence and computed tomography bioimaging, Nanoscale 7 (2015) 17929–17937.

[142] J. Xu, D. Murata, J. Ueda, S. Tanabe, Near-infrared long persistent luminescence of Er^{3+} in garnet for the third bio-imaging window, J. Mater. Chem. C 4 (2016) 11096–11103.

[143] Z. Zou, C. Wu, X. Li, J. Zhang, H. Li, D. Wang, Y. Wang, Near-infrared persistent luminescence of Yb^{3+} in perovskite phosphor, Opt. Lett. 42 (2017) 4510.

[144] J. Xu, D. Murata, J. Ueda, S. Tanabe, 1.5μm persistent luminescence of Er^{3+} in Gd3Al5-xGaxO12 (GAGG) garnets via persistent energy transfer in: M.J. Digonnet, S. Jiang (Eds.), Optical Components and Materials XVI, SPIE-Intl Soc Optical Eng, Vol. 10914, (2019), p. 2.

Veeramani Rajendran, Ho Chang, Ru-Shi Liu

Chapter 8
Transition metal ion-based phosphors for LED applications

8.1 Introduction

Transition metals (TM) are fascinating chemical elements that we use in our everyday life. They find application in food, convenience tools, cutlery tools, transportation, and communication technology. In general, forty chemical elements are considered TM elements; their atomic numbers range from 21 (scandium) to 30 (zinc), from 39 (yttrium) to 48 (cadmium), from 71 (lutetium) to 80 (mercury), and from 103 (lawrencium) to 112 (copernicium). However, the TM elements with atomic numbers from 21 (scandium) to 30 (zinc) are widely investigated because of their great potential. TM ions act as a bridge between the two sides of the periodic table. TM ions also tend to exhibit more than one oxidation number by losing the outer 4*s* electrons and gaining or losing some *d* electrons in the outer shell. Hence, the electronic configuration of TM ions is $1s^2 2s^2 2p^6 3s^2 3p^6 3d^n 4s^2$, where n ($1 \leq n \leq 10$) stands for the number of 3*d* electrons in the outer shell. These electrons in the unfilled outer shell are what make TM ions interesting optical active centers in the semiconductor industry. Moreover, the large ionic radius and the unshielded outer shell of the TM ions make them more susceptible to different coordinating environments and anion types. This unshielded effect produces pronounceable electron–lattice coupling in TM ions. As a result, TM ions can exhibit both broad and sharp optical transition bands, unlike rare-earth ions.

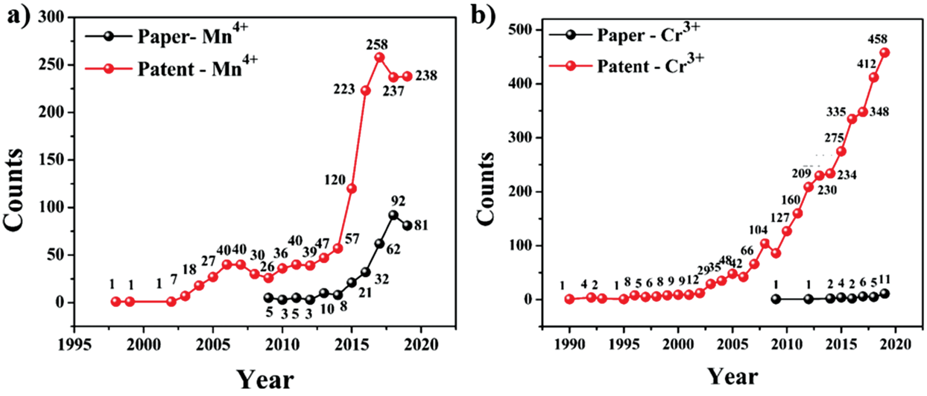

Figure 8.1: Results of the search for Derwent Innovation patents and publications by using the keyword phrases (a) “Mn^{4+} and phosphor and light-emitting diode” and (b) “Cr^{3+} and phosphor and light-emitting diode” (accessed on Dec. 22, 2019).

https://doi.org/10.1515/9783110607871-008

Mn^{4+} and $Cr^{3+}$are well-known TM ions used as activators for red and infrared phosphors for light-emitting diode (LED) applications. The Derwent Innovations search engine is used to uncover details of a patent and of a paper publication by using the relevant keywords. Figure 8.1a shows the number of patents and papers published that was generated by the search using the combined keywords "Mn^{4+}," "phosphors," and "light-emitting diode" [1]. The number of patent publications increased from 1 in 2007 to more than 258 in 2017. Similarly, the number of papers published increased from 5 in 2011 to over 92 in 2018. The number of patents and publications differed over the years, indicating that the technology had fully matured within a year. In other words, Mn^{4+} was widely investigated by both the academe and the industry in 2017 and 2018.

Cr^{3+} is known for its use in Ruby laser in 1960, followed by a series of various crystals, for tunable solid-state laser. The number of patent publications, as generated by the search using the keywords "Cr^{3+}," "phosphors," and "light-emitting diode," has steadily increased from 1988 onward (Figure 8.1b) [1]. The number of papers published is 32, signifying the recent advancement of Cr^{3+} in LED applications. Similarly, the number of paper publications has progressively increased. Moreover, the difference in the counts of patents and papers is large because of the high demand for Cr^{3+} in the industry.

Each TM has unique properties. Hence, TMs can be used in various applications. Mn^{4+} and Cr^{3+} are the TMs largely used in LEDs for various purposes, such as lighting, plant growth, optical thermometry, and spectroscopy. Given that TM ions act as phosphors in LED devices, the main ideas behind their spectroscopy in various crystal systems must be understood. Hence, this chapter reviews the fundamentals of the luminescence mechanisms of TM ions. Furthermore, the possible applications of Mn^{4+} and Cr^{3+} are briefly discussed.

8.2 Fundamentals of luminescence mechanism

In inorganic phosphors for light-emitting materials, the combined effects of nephelauxetic effect and crystal field splitting are inevitably encountered. "Nephelauxetic" is a Greek word that means "cloud expansion." The nephelauxetic effect denotes the delocalization of central metal ion orbitals due to the establishment of chemical bonds with the surrounding ligands. In TM ions such as Mn^{4+} and Cr^{3+}, the electrons in the outer *d* orbitals of the central metal ions expand the interaction time with the *p* and *s* orbitals of the ligands, which eventually reduces the interelectron repulsion force within the *d* shell (Figure 8.2). The occurrence of interelectron repulsions is quantified by the values of Racah parameter terms (*A*, *B*, and *C*). In addition, the nephelauxetic effect is responsible for the variations in the energy states between the different energy states in d^3 configurations. On the basis of optical spectroscopy of several crystal systems, Brik et al. [2] proposed a new parameter $\beta = \sqrt{(B/B_0)^2 + (C/C_0)^2}$ for the determination of ^2E_g and ^1E_g states as a linear function. Here, B and C (B_0 and C_0) are the

Racah parameters of the free state and ions in a crystal, respectively. Remarkably, fluoride-based crystal systems always experience a weak nephelauxetic effect because of the high ionic bond features. As a result, fluoride-based systems always shift the states of ^2E_g and ^1E_g to high energies. However, the nephelauxetic effect is elevated in other crystal systems because of the presence of more covalent oxides, chlorides, and bromides, which ultimately shift the energy states to low energies. The order of the nephelauxetic effect between the ligands is as follows:

$$S^{2-} > I^- > Br^- > CN^- > Cl^- > N^{3-} > O^{2-} > F^-$$

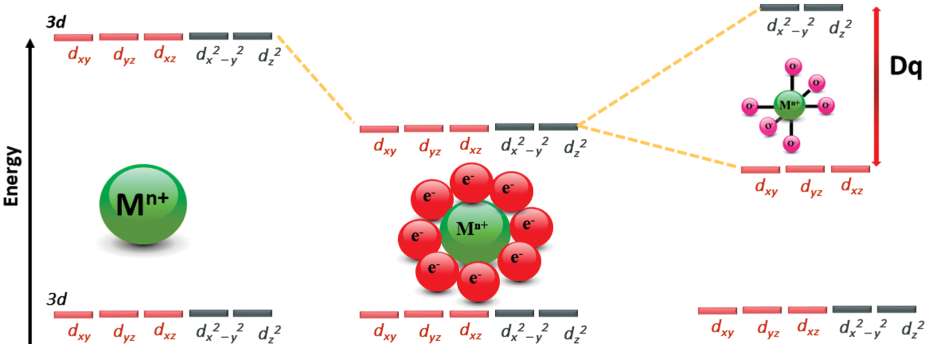

Figure 8.2: Schematic of the nephelauxetic effect and the crystal field theory in 3*d* orbital interactions.

Crystal field theory (or ligand field theory) (CFT) describes symmetry deviations around the central metal ion in crystals. In CFT, metal ions and ligands are assumed to be point charges, and their interactions are purely electrostatic, but this is not the case in practice. In general, the electrostatic field around the central metal ion is spherical, indicating that the energies of electrons in degenerated 3*d* orbitals are uniform. By contrast, the degenerated 3*d* orbitals split into different energy levels when the electrostatic field deviates from the spherical. In other words, the energy levels of the 3*d* degenerated orbitals split into multiple levels according to the surrounding coordinating environment with the ligands. Splitting patterns should be determined quantitatively in examining the nature and the number of energy states involved in the system. For example, the 3*d* degenerated orbitals in the octahedral coordination in Figure 8.2 split into two energy levels, namely, t_{2g} (d_{xy}, d_{yz}, d_{xz}) and e_g $(d_z{}^2, d_{x}{}^2{}_{-y}{}^2)$ with low and high energies, respectively. However, the splitting patterns are the opposite in tetrahedral coordination: e_g $(d_z{}^2, d_{x}{}^2{}_{-y}{}^2)$ acquires high energies whereas t_{2g} (d_{xy}, d_{yz}, d_{xz}) attains low energies. The crystal field strength can be quantified using the following equation:

$$D_q = \frac{ze^2r^4}{6R^5} \tag{8.1}$$

where Dq is the crystal field strength, z is the anion valence, e is the electron charge, r is the radius of the d wave function, and R is the distance between the central ion and the ligands. Equation (8.1) indicates that crystal field strength is inversely proportional to the distance between the central metal ion and the ligands. Moreover, delocalization and splitting of the d orbitals vary for different crystal systems and ligands for the same TM ion activators. Hence, a proper host should be selected and the length of the chemical bonds should be adjusted accordingly to obtain pronounced effects.

8.3 Tanabe–Sugano diagram

In crystalline solids, TM ions lose two 4s and several 3d electrons in the outer shell orbitals. Therefore, the unfilled 3d outer shell owns variable oxidation states, ranging from +1 to +6. The electronic state of the 3d electrons, primarily formed by the Coulombic interactions in the unfilled outer shell, is greatly affected because of the interference by the nearest surrounding environment. Hence, the energy state of electrons splits into different energy levels because of the surrounding environment in the host crystalline system. The occurrence of electronic transitions between the energy levels changes the spectral light energy from ultraviolet to infrared. The number of energy states allowed for each transition metal, as determined by the Pauli exclusion principle, is listed in Table 8.1, with an irreducible representation for each ground term in an octahedral symmetry. Each term symbol represents the degeneracy of the electron configurations shown in Table 8.2. “T” represents triply degenerate and asymmetrically occupied state, whereas “E” denotes doubly degenerate and asymmetrically occupied state. “A” and “B” indicate a nondegenerate and symmetrically occupied state, respectively.

Table 8.1: Number of states for d electrons with the relevant electronic configurations and irreducible representation of the ground-state terms, in octahedral symmetry.

Electron configuration	**Number of states**	**Number of LS terms**	**Ground term**	**Irreducible representation of ground terms in octahedral symmetry**
d^1, d^9	10	1	^{2}D	$^2T_{2g}$ (d^1), ^2E_g (d^9)
d^2, d^8	45	5	^{3}F	$^3T_{1g}$ (d^2), $^3A_{2g}$ (d^8)
d^3, d^7	120	8	^{4}F	$^4A_{2g}$ (d^3), $^4T_{1g}$ (d^7 weak field) + ^2E_g (d^7 strong field)
d^4, d^6	210	16	^{5}D	^5E_g (d^4 weak field) + $^3T_{1g}$ (d^7strong field), $^5T_{2g}$ (d^6 weak field) + $^1A_{1g}$ (d^6 strong field)
d^5	252	16	^{6}S	$^6A_{1g}$ (weak field), $^2T_{2g}$ (strong field)

In 1954, Yukito Tanabe and Satoru Sugano studied the energy levels of the splitting of TM ions in different complexes [3]. They proposed a diagram (now famously called the Tanabe–Sugano [T–S] diagram) for *d–d* transition that depicts the relationship between the energy and the interaction strength of TM ions with the surrounding ligands. This diagram is commonly used as an analysis tool for studying the energy level splitting of TM ions. It is a straightforward two-axis diagram, with increasing values of energy levels and crystal field strength in the vertical and horizontal axes, respectively. Unlike the Orgel diagram, the T–S diagram considers the degeneracy of rotational energy states of the electron configurations, making it more qualitative than the former. Hence, the T–S diagram can be applied to both high-spin and low-spin systems and also to anticipate the crystal field requisites for the changeover, from high-spin to low-spin complexes. However, seven distinct T–S diagrams are required for analyzing specific electronic configurations.

Table 8.2: Degeneracy states with the possible electronic configurations.

State	Definition	Examples
T	Designates a triply degenerate asymmetrically state	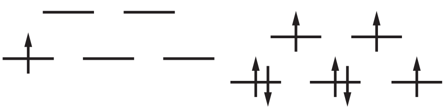
E	Designates a doubly degenerate asymmetrically occupied state	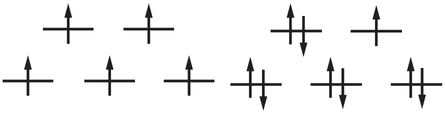
A or B	Designates a nondegenerate state. Each set of levels in an A or B state in symmetrically occupied state	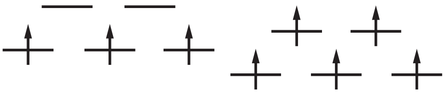

Two T–S diagrams, namely, d^3 – octahedral and d^7 – tetrahedral, are briefly discussed in this section. Electron transition processes that occur between the ground and the excited states are governed by definite selection rules and the absorption of light with a specific wavelength. The straightforward selection rule is the parity selection rule. According to the Born–Oppenheimer approximation, the transition process of electrons is considerably faster than the moment of nuclei [4]. Hence, the total wave function can be simply written as

$$\boldsymbol{\Psi}(r,R)=\Psi_{\mathrm{e}}(r,\mathrm{Re})\Psi_{\mathrm{v}}(R)\Psi_{\mathrm{r}}(R) \tag{8.2}$$

where $\Psi(r, R)$ is the total wave function; and $\Psi_{\mathrm{e}}(r, \mathrm{Re})$, $\Psi_{\mathrm{v}}(R)$, and $\Psi_{\mathrm{r}}(R)$ are the electronic, vibrational, and rotational wave functions, respectively. An electric dipole moment is called an optically allowed transition if it experiences some changes during the transition process. Otherwise, the transition is known to be parity forbidden. For TM elements, the two selection rules for electron transition processes are spin-selection and Laporte selection rules.

The spin-selection rule states that the electron transition process is an allowed transition ($S = 0$) when it occurs between two excited states with the same spin multiplicity. Violation of this rule results in less transition probability. For spin-allowed d–d transition, phosphors show a broad emission spectrum, whereas for spin-forbidden d–d transition, the emission spectrum is narrow or a sharp line [5].

The Laporte rule states that the probability of an allowed electron transition from a gerade state to an ungerade state is high for structures with central symmetry. The transition is forbidden or the probability to transition from a gerade state to another gerade state or from an ungerade state to another ungerade state is low.

The transition process obeys the following equation:

$$\int \Psi_e \, \hat{\mu} \, \Psi_g d\tau; \; \hat{\mu} = \vec{q}.\vec{r} \tag{8.3}$$

where Ψ_e and Ψ_g are the wave functions of the two states involved in the transition, and $\hat{\mu}$ is the transition moment operator (an odd function). If the integral value from this equation is equal to zero, the transition is forbidden [6, 7].

8.3.1 Tanabe–Sugano diagram of d^3 configuration

The T–S diagram of d^3 electronic configuration is shown in Figure 8.3a. $^4A_{2g}$ is the ground state of the ion, whereas ^2E_g and $^4T_{2g}$ are the first energy states on the high (right) and low crystal field (left) sides of the diagram, respectively, with a centerline Dq/B at ~ 2.3 (intermediate). The same spin multiplicities of the first excited states on the left-hand side ($^4T_{2g}$) possess the same spin multiplicity number (superscript 4) as the ground state ($^4A_{2g}$). Hence, the resultant emission spectrum results in a wider distribution of light by following spin-allowed transitions, according to the spin-selection rule (weak crystal field). On the right-hand side (high crystal field), $^2E_{2g}$ is the possible first excited state with a different spin multiplicity number (superscript 2), implying that the spin-selection rule is no longer valid; the resultant emission spectrum will follow spin-forbidden transitions and results in a narrow or a line-emission spectrum. Another important feature is the crystal field value of ~ 2.3 because it is the cross-point of the triplet and the doublet energy states. The point where energy states with different spin multiplicities are mixed eventually results in both types of transition natures (i.e., spin-forbidden and spin-allowed). The wide distribution of the emission spectrum is more desirable for the detection of multiple compounds in near-infrared spectroscopy applications [8]. Hence, a proper host with a weak crystal field value must be identified. Alternatively, the crystal field value should be shifted toward the left side by applying tuning strategies. Cr^{3+}-doped oxide and fluoride hosts are preferred over other TM ions

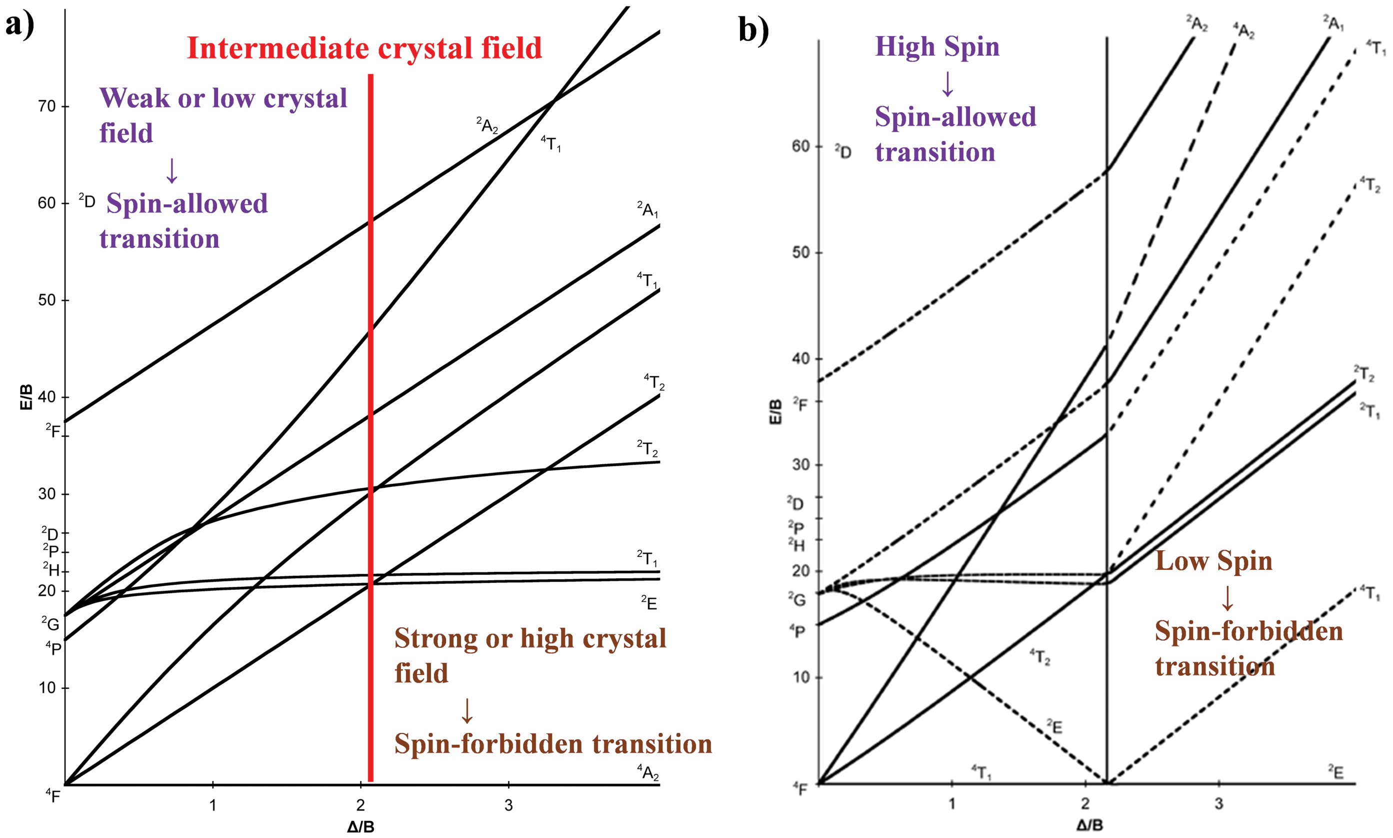

Figure 8.3: Tanabe–Sugano diagram: (a) d^3 electronic configuration and (b) d^7 electronic configuration.

in designing near-infrared light because of their wider range of crystal field strengths. However, Mn^{4+} in fluorides experiences a weak nephelauxetic effect because of the ionic character of the host. Hence, the resultant emission spectrum will always result in a spin-forbidden transition from $^2E_g \rightarrow {}^4A_{2g}$, regardless of the crystal field strength.

8.3.2 Tanabe–Sugano diagram of d^7 configuration

Unlike octahedral complexes, tetrahedral complexes usually do not possess an inversion center. Hence, the Laporte selection rule cannot be applied to tetrahedral complexes. Moreover, transitions in tetrahedral complexes are more intense than in other complexes. The splitting pattern of d orbitals in tetrahedral and octahedral complexes is an inverse phenomenon. In tetrahedral complexes, doublet states (e_g) of $d_{x^2-y^2}$ and d_{z^2} occupy low energy levels, whereas triplet states (t_{2g}) of d_{xy}, d_{yz}, and d_{xz} occupy high energy levels. Except for the presence of empty n orbitals (n holes) in tetrahedral complexes, configuration symmetry in tetrahedral complexes is almost similar to that in octahedral complexes. Hence, the T–S diagram of octahedral $d^{10\text{-}n}$ can be used to describe d^n tetrahedral complexes. For example, Cr^{3+} has three electrons in the valence shell. Hence, the octahedral coordination environment of Cr^{3+} can be explained using the d^3 T–S diagram, whereas the tetrahedral coordination environment of Cr^{3+} can be described using the d^7 (d^{10-n}, $n = 3$) T–S diagram [9]. In most cases, the crystal system of near-infrared phosphors has both octahedral and tetrahedral coordination for Cr^{3+} incorporation. Although the luminescence in tetrahedral coordination is forbidden, some other systems have been reported. Moreover, researchers commonly explain tetrahedral coordination by using the d^3 octahedral T–S diagram. Hence, a short introduction about the d^7 T–S diagram is provided in this section (Figure 8.3b). At the critical point of $Dq/B = \sim 2.2$, TM ions attain new ground-state electronic configurations because of the changes in the arrangement of electron spin (from high to low spin). At the low crystal field value of $Dq/B < \sim 2.2$, crystal field splitting energy is very low with a high spin electronic configuration. Hence, the transitions are mostly spin-allowed. In other words, the possible first excited state ($^4T_{2g}$) and the second excited state ($^4A_{2g}$) own the same spin value of 4, as the ground state ($^4T_{1g}$). Nevertheless, the ground state becomes ^2E_g for high crystal field values of $Dq/B > \sim 2.2$. The high crystal field splitting energy leads to a low spin electronic configuration. Moreover, charge-transfer band (CTB) transitions (the transfer of an electron from the central cation to anion) between the d orbitals have to be considered for intense absorptions.

8.4 Mn-activated phosphors

Among TMs, Mn is the second most abundant element in the Earth’s crust, next to iron. The different oxidation states of Mn make this element an interesting activator for luminescent materials. Oxidation states, combined with features of local coordination and distribution in the host crystal system, determine the luminescence properties of Mn. For example, Mn in the divalent state produces green emission, whereas it provides red emission in the tetravalent state. Moreover, Mn^{2+} in octahedral coordination symmetry produces an orange-to-red emission, whereas Mn^{2+} in tetrahedral sites emits green emission [10]. However, Mn^{4+} is known for red emission in white LEDs and backlight applications. On the basis of the types of ligands, Mn^{4+}-activated phosphors are classified into three broad categories, namely, oxides, fluorides, and oxyfluorides.

8.4.1 Mn^{4+}-activated oxide phosphors

Mn^{4+}-activated oxide phosphors are chemically and thermally stable compounds, with excellent quantum efficiency, and require an uncomplicated synthesis procedure. Quantum efficiency is the quantitative measurement of the luminescent performance of phosphors. A high quantum efficiency contributes to a superior performance of pc-LED devices. Mn^{4+}-activated oxide phosphors can be classified into germanates, aluminates, titanates, pyrosilicates, phosphates, and zirconates (Table 8.3). Among these types, Mn-activated oxide phosphors produce emissions with a wavelength greater

Table 8.3: Mn^{4+}-activated oxide phosphors and their luminescence properties.

Phosphors	Crystal system	Emission peak (nm)	Reference
$Li_2Ge_4O_9$:Mn^{4+}	Orthorhombic, $Pca2_1$	660–670	[12]
$LiNaGe_4O_9$:Mn^{4+}	Orthorhombic, $Pca2_1$	660–670	[12]
Mg_2GeO_4:Mn^{4+}	Orthorhombic, *Pmnb*	660	[13]
$SrAl_{12}O_{19}$:Mn^{4+}	Hexagonal, $P6_3/mmc$	655	[14]
$LiAl_5O_8$:Mn^{4+}	Cubic, *Fd*-3*m*	680	[15]
$CaAl_{12}O_{19}$:Mn^{4+}	Cubic, *Ia*-3*d*	658	[16]
Li_5AlO_4:Mn^{4+}	Cubic, $P4_332$	680	[17]
$Sr_2MgAl_{22}O_{36}$:Mn^{4+}	Hexagonal, *P*-6*m*2	658	[18]
$CaAl_4O_7$:Mn^{4+}	Hexagonal, $P6_3/mmc$	656	[19]
$LaAlO_3$:Mn^{4+},Ge^{4+}	Rhombohedral, *R*-3*c*	731	[20]
$SrLaAlO_4$:Mn^{4+}	tetragonal , *I4/mmm*	714	[21]
$CaAl_2O_4$:Mn^{4+}	Monoclinic, *P*121/*n*1	658	[22]
$Sr_4Al_{14}O_{25}$:Mn^{4+}	Orthorhombic, *Pmm*	652	[23]
$SrMgAl_{10}O_{17}$:Mn^{4+}	Hexagonal, $P6_3/mmc$	660	[24]
$CaMg_2Al_{16}O_{27}$:Mn^{4+}	Hexagonal, *P*6*mc*	655	[25]
$LaAlO_3$:Mn^{4+},Ge^{4+}	Rhombohedral, *R*3*m*	698	[26]
$GdAlO_3$:Mn^{4+},Ge^{4+}	Orthorhombic	698	[26]
$SrAl_4O_7$:Mn^{4+}	Orthorhombic, *C*2/*c*	656	[27]
Li_2MgTiO_4	Cubic, *Fm*-3*m*	600–800 (678)*	[28]
$Li_2Mg_3SnO_6$	Cubic, *Fm*-3*m*	600–790 (670)*	[29]
$Li_2MgTi_3O_8$	Cubic, $P4_132$	600–800 (678)*	[30]

*Values enclosed in parentheses represent centered emissions.

than 650 nm. Thus, Mn-activated oxide phosphors are near-infrared emitters, and are beyond the sensitivity of the human eye [11].

Mn^{4+}-activated germanate-based oxide phosphors were predominantly produced as deep-red phosphors in the 1940s. Germanate-based oxide phosphors ($3.5MgO_{0.5}MgF_2$. GeO_2) were used as commercial red phosphors in the 1960s. However, most germanate-based oxide phosphors that are activated by Mn^{4+} produce a narrow emission (within 660–670 nm), which is beyond the visible red region of the electromagnetic spectrum [31]. Hence, Mn^{4+}-activated germanate-based oxide phosphors are extensively utilized as color conversion materials in red-light phototherapy applications, fluorescent lamps for inducing plant growth, and in high-pressure mercury lamps. Other Mn^{4+}-activated germanate-based oxide phosphors, such as Ba_2GeO_4:Mn^{4+} [32], Li_2MgGeO_4:Mn^{4+} [33], $LiAlGe_2O_6$:Mn^{4+} [34], $LiGdGe_2O_6$:Mn^{4+} [34], Sr_2GeO_4:Mn^{4+} [35], $LiNaGe_4O_9$:Mn^{4+} [12], and $Li_2Ge_4O_9$:Mn^{4+} [12], also produce deep-red emissions.

Aluminate-based oxide phosphors are widely used host lattice materials for Mn^{4+} activation. Most Mn^{4+}-activated aluminate-based oxides can be effectively excited by near-UV and blue light to emit red and deep-red light. This property makes this type of oxide an interesting system for numerous optical spectroscopy studies. The phenomenon of zero-phonon, along with the characteristic Stokes and anti-Stokes sidebands, is generally noticeable in most aluminate-based oxide phosphors, regardless of the crystal system. However, the number of vibration modes that contribute to the emission intensity differs. $CaAl_{12}O_{19}$:Mn^{4+} is the most prominent phosphor die, with a centered emission at 658 nm, which is close to visible red light [36]. Two strategies are employed to enhance the luminescence intensity of $CaAl_{12}O_{19}$:Mn^{4+}. The first strategy involves accelerating the crystal growth by using the synergetic effects of CaF_2 and MgF_2 fluxes. The second strategy requires chemical modification by mixing it with GeO_2, MgO, and monovalent ions of Li^+, Na^+, and K^+ [37–39]. Other fascinating aluminate oxide-based phosphors, such as $Sr_2MgAl_{22}O_{36}$:Mn^{4+} [18], $SrAl_4O_7$:Mn^{4+} [31], $SrAl_2O_4$:Mn^{4+} [22], $CaAl_2O_4$:Mn^{4+} [22], $Sr_4Al_{14}O_{25}$: Mn^{4+} [23], $CaMg_2Al_{16}O_{27}$:Mn^{4+} [25], $CaYAlO_4$:Mn^{4+} [40], and $SrMgAl_{10}O_{17}$:Mn^{4+} [24], have also been reported (Table 8.3).

Mn^{4+}-activated titanium metal-based oxide phosphors are better than other oxide phosphors because of its stability. These phosphors mostly have a spinel or rock-salt structure (Table 8.3). In spinel structures, Mn^{4+} always occupies the octahedral units of Ti^{4+} because of the close ionic radius – Ti^{4+} (0.605 Å) to Mn^{4+} (0.53 Å) – in octahedral coordination and the exact valence state [41]. Moreover, lattice contraction and the shifting of X-ray diffraction peaks toward high angles are generally feasible. Mn^{4+}-activated titanium metal-based oxide phosphors always exhibit broadband asymmetric deep-red emission that is centered at approximately 670–680 nm, owing to the dipole transitions of Mn^{4+} from $^2E \rightarrow {}^4A_2$. In general, the emission spectrum of Mn^{4+}-activated titanium metal-based oxide phosphors does not show the typical feature of zero-photon line with Stokes and anti-Stokes sidebands. Hence, the emission spectrum does not contain any inflection point or sharp clear peaks of the zero-phonon line – a possible criteria of Mn^{4+}-activated titanium metal-based oxide phosphors. Mg_2TiO_4:Mn^{4+} is prepared via the sol–gel method, with red emission at 655 nm [42]. Several compounds with interesting crystal and spectroscopic features have been synthesized via chemical modifications of this parent composition. For instance, $Li_2MgTiO_4:Mn^{4+}$ (1 mol of Mg is substituted with 2 mol of Li) crystallizes in cubic systems with three different octahedral sites for Mn^{4+} [28].

Several other oxide systems are activated by Mn^{4+} ions. Some of the most interesting and important oxide phosphors are listed in Table 8.3. Mn^{4+}-activated $MgAl_2Si_2O_8$, with a series of co-doped lanthanide ions (Gd^{3+}, Lu^{3+}, Eu^{3+}, Yb^{3+}, Pr^{3+}, Nd^{3+}, Tb^{3+}, Er^{3+}, Tm^{3+}, Dy^{3+}, Sm^{3+}, and Ho^{3+}), reportedly produces red emission higher than 660 nm [43–46].

8.4.2 Mn^{4+}-activated fluoride phosphors

Mn^{4+}-activated fluoride compounds are known for their interesting optical luminescence properties. These compounds are ideal candidates for warm white LEDs as red phosphors. The standard chemical formula of Mn^{4+}-activated fluoride phosphors is $A_2BF_6:Mn^{4+}$, where A is a monovalent cation (Li, Na, K, Rb, K, or Cs) and X is a tetravalent cation (Ti, Si, Ge, Zr, or Sn). Another well-known standard chemical formula is $BaMF_6:Mn^{4+}$, where M can be Si, Ge, Sn, or Ti. In general, Mn^{4+}-activated fluoride compounds have a narrow-band red emission, with fluctuations at the centered emission position of ~ 630–632 nm. In the T–S diagram, the difference in energy between the excited states of ^2E_g and $^4T_{2g}$ is independent of the crystal field strength. Hence, the variations in the emission position are chiefly due to the bond length between the central metal ion and the ligands. High ionic compounds usually possess a short distance that decreases the nephelauxetic effect and increases the Racah parameter B. As a result, the ^2E energy state in fluorides shifts upward. Hence, the ^2E energy state of fluorides is observable in both photoluminescence excitation and photoluminescence emission spectrum, unlike that of oxides and garnets [47, 48]. Thus, the emission from $^2E \rightarrow {}^4A_2$ is spin-forbidden. By contrast, the absorption and emission, with respect to $^4A_2 \rightarrow {}^2T_1$ and $^2T_1 \rightarrow {}^4A_2$ transitions, are clearly parity and spin-forbidden. Hence, the excitation and emission spectra of Mn^{4+}-activated fluoride phosphors are difficult to observe. However, the origin of $^2T_1$ usually lies at ~ 0.1 eV above the ^2E origin [49]. Consequently, the absorption peak of $^4A_2 \rightarrow {}^2T_1$ must coincide with the absorption and emission peaks of $^2E \rightarrow {}^4A_2$. Therefore, the emission intensity of $^2E \rightarrow {}^4A_2$ can be enhanced by the electron transfer from $^2T_1$ to ^2E in fluoride phosphors.

Notably, spin–orbit coupling caused by lattice vibrations (dynamic strains) mixes the $^4A_2$, ^2E, $^2T_2$, and $^4T_2$ states, thus transforming spin-forbidden transitions $^2E \rightarrow {}^4A_2$ into allowed transitions. Lattice vibrations in the octahedral-coordinated Mn^{4+} sites are supposed to have six independent frequency modes. These modes are subdivided into Raman-active modes: ν_1 (a_{1g}; stretch), ν_2 (e_g; stretch), and ν_5 (t_{2g}; bend); infrared-active modes: ν_3 (t_{1u}; stretch) and ν_4 (t_{1u}; bend); and silent mode: ν_6 (t_{2u}; bend) [49]. The photoluminescence emission of Mn^{4+}-activated fluoride phosphors has sharp emission peaks, accompanied by Stokes and anti-Stokes ν_3, ν_4, and ν_6 phonons. Likewise, Mn^{4+}-activated fluoride phosphors have typical very broad excitation bands of $^4A_2\rightarrow{}^4T_1$ and $^4A_2\rightarrow{}^4T_2$ with several bends. Aside from these typical excitation bands, other transition bands, such as $^4A_2 \rightarrow {}^2A_1$, $^4A_2 \rightarrow {}^2T_2$, $^4A_2 \rightarrow {}^2T_1$, and $^4A_2 \rightarrow {}^4T_1$ (^4P), are also possible. A charge-transfer band (CTB) can also be observed in this spectral region.

K_2SiF_6:Mn^{4+} is a remarkable red-emission phosphor (Table 8.4). It can be prepared via several techniques, such as wet chemical etching method, cation exchange reaction, hydrothermal method, coprecipitation method, and microwave irradiation method, as well as by a large-scale facile synthesis method that does not use hydrogen fluoride (HF) solution. Each synthesis method produces unique surface morphological features. These features affect the luminescence properties and performance of these types of phosphors. Based on the spectroscopic features, the intensity of the zero-phonon line is directly dependent on the crystal structure. Mn^{4+}-activated fluoride materials with low crystal symmetry exhibit a high-intensity zero-phonon line. In the A_2BF_6:Mn^{4+} system, ZPL emission intensity

Table 8.4: Mn^{4+}-activated fluoride phosphors and their luminescence properties.

Phosphor	Structure	ZPL emission	EX (nm)	EM (nm)	Reference
$(NH_4)_2SiF_6$	Cubic, *Fm*3*m*	L	472	633	[51]
$(NH_4)_2TiF_6$	Trigonal, *P*-3 *m*1	L	472	633	[51]
$(NH_4)_2GeF_6$	Trigonal, *P*-3 *m*1	L	472	633	[51]
$(NH_4)_2SnF_6$	Trigonal, *P*-3 *m*1	L	472	633	[51]
Na_2SiF_6	Trigonal, *P*321	H	460	627	[52, 53]
Na_2TiF_6	Trigonal, *P*321	H	465	627	[53]
Na_2TiF_6	Trigonal, *P*-3 *m*1	H	465	627	[53]
Na_2GeF_6	Trigonal, *P*321	H	465	627	[53]
Na_2SnF_6	Tetragonal, $P4_2/mnm$	L	470	626	[54]
K_2SiF_6	Cubic, *Fm*3*m*	L	460	632	[55]
K_2TiF_6	Trigonal, *P*-3 *m*1	L	468	632	[56]
K_2GeF_6	Trigonal, *P*-3 *m*1	L	475	632	[50, 57]
K_2GeF_6	Trigonal, $P6_3\ mc$	H	475	632	[50]
$K_2SnF_6.6H_2O$	Orthorhombic, *Fddd*	H	470	630	[58]
K_3ZrF_7	Cubic, *Fm*3*m*	H	482	633	[59]
Rb_2SiF_6	Cubic, *Fm*3*m*	L	450	630	[60]
Cs_2SiF_6	Cubic, *Fm*3*m*	L	460	633	[61]
Cs_2TiF_6	Trigonal, *P*-3 *m*1	L	474	632	[62]
Cs_2GeF_6	Cubic, *Fm*3*m*	L	460	633	[61]
Cs_2SnF_6	Trigonal, *P*-3 *m*1	L	470	632	[54]
$KNaSiF_6$	Orthorhombic, *Pmna*	H	460	629	[63, 64]
$BaSiF_6$	Trigonal, $R\bar{3}m$	L	466	632	[65, 66]
$BaTiF_6$	Trigonal, $R\bar{3}m$	L	466	630	[67]
$BaGeF_6$	Trigonal, $R\bar{3}m$	L	460	634	[68]
$BaSnF_6$	Trigonal, $R\bar{3}$	L	480	640	[69]
$ZnSiF_6\cdot 6H_2O$	Trigonal, $R\bar{3}$	L	470	630	[70, 71]
$ZnGeF_6\cdot 6H_2O$	Trigonal, $R\bar{3}$	L	470	630	[71]

increases in the order of cubic ($K_2SiF_6:Mn^{4+}$) > orthorhombic ($KNaSiF_6:Mn^{4+}$) > trigonal ($Na_2SiF_6:Mn^{4+}$) [11]. However, this order does not apply to $BaMF_6:Mn^{4+}$, where M can be a Si, Ge, Sn, or Ti system. For instance, $BaSiF_6:Mn^{4+}$, $BaTiF_6:Mn^{4+}$, $BaGeF_6:Mn^{4+}$, $ZnSiF_6:Mn^{4+}$, and $ZnGeF_6:Mn^{4+}$ phosphors do not exhibit strong zero-phonon lines, unlike $K_2SiF_6:Mn^{4+}$ (Table 8.4). Moreover, a low-symmetry crystal structure with the apparent splitting of emission peaks (ν_3, ν_4, ν_6) is often observed in fluoride phosphors. $K_2GeF_6:Mn^{4+}$ is another interesting type of red phosphor because of its structural evolution and luminescence. $K_2GeF_6:Mn^{4+}$ can structurally evolve from hexagonal crystal systems with a space group of $P\bar{3}m1$ to $P6_3mc$ and can be gradually changed into cubic crystal systems with a space group of $Fm3m$ by simply varying the processing temperature from 400 to 500 °C [50].

8.5 White LEDs for lighting applications

High-brightness blue LEDs revolutionized the lighting sector because they have low energy consumption, long lifetime, and are environmentally friendly. The blue LED also triggers several approaches for generating white light for lighting. On the basis of the red–green–blue (RGB) combinations, white light can be achieved by incorporating three LEDs that independently emit RGB colors. Alternatively, a single LED with two or more inorganic phosphors can also be used to obtain white light [72]. In particular, the single LED chip can be a blue LED based on InGaN or an ultraviolent LED that serves as an excitation source. Hence, this fabrication strategy is called phosphor-converted white LEDs (pc-WLEDs). Compared to other LED designs, pc-WLEDs offer a higher luminous flux, a satisfactorily correlated color temperature (CCT), and a good efficacy. Hence, traditional lighting sources, such as incandescent bulbs and mercury luminescence lamps, have been replaced by white LEDs.

Commercial white light used to be based on a combination of a blue LED and a yellow light-emitting $Y_3Al_5O_{12}:Ce^{3+}$ yellow phosphor. However, these pc-white LEDs do not cover the red region of the visible light spectrum and they also possess a high CCT. As a consequence, these pc-white LEDs suffer from poor color rendering index, especially R9. Color rendering index is the ability of a light source to distinguish colors. In general, the color rendering index is denoted as Ra, which is the average of $R1$ to $R8$. Ra represents the classical colors of typical environments and common objects. $R9$ evaluates the reproduction of red, and is also defined as a special color rendering index. Thus, red phosphors are needed in fabricating white light sources with a high color rendering index (CRI > 90) and a warm temperature (2,700–4,700 K) [73].

Two types of red phosphors are commonly selected for fabricating warm white LEDs: Mn^{4+}-activated fluoride phosphors and Eu^{2+}-activated phosphors. Based on the price of the starting precursors, Mn^{4+} is the ideal choice. In general, warm white LEDs are fabricated using a blue LED chip (InGaN) with commercial $Y_3Al_5O_{12}:Ce^{3+}$ (yellow phosphor) and Mn^{4+}-activated fluoride phosphors. Warm pc-WLEDs are evaluated on the basis of efficacy (lmW^{-1}), CCT (K), *Ra*, and chromaticity coordinates. For practical applications, chromaticity coordinate values are the points that are specified based on their application needs. Lian *et al.* [74] prepared $A_2GeF_6:Mn^{4+}$ (A = Na, K, Rb, Cs) phosphors via a two-step precipitation–cation exchange route for LED lighting applications. They fabricated a warm wLED by using $Cs_2GeF_6:0.03Mn^{4+}$ and blue LED (~465 nm). The warm wLED had a low CCT of 3,385 K and a high correlated color index *Ra* of 90.5. Zhou et al. [75] used $Cs_2ZrF_6:Mn^{4+}$ to fabricate warm wLED with a CCT of 3,469 K CCT and an *Ra* of 82.4 at a driving current of 20 mA. Yang et al. [76] achieved an *Ra* of 93.1 and a CCT of 3,373 K at a driving current of 20 mA by using $Cs_2HfF_6:Mn^{4+}$ red phosphors. Liu and coworkers [77] achieved an *Ra* of 81 and a CCT of 3,556 K by using commercial YAG: Ce^{3+} and blue LED (455 nm). They also evaluated the performance of wLED by using commercial YAG:Ce^{3+} or aluminate green phosphors (GAL535, Intematix). $K_2SiF_6:Mn^{4+}$, prepared in an HF-free environment, achieved a CCT of 3,334 K and an *Ra* of 88.91 [78].

8.6 White LEDs for backlighting applications

Technological improvements have increased consumer demand for LED display products, such as televisions, smartphones, personal computers, mobile tablets, and car navigators with excellent image quality and color saturation. The traditional cold cathode-fluorescence lamps (CCFL) have been replaced by pc-wLEDs. Compared to CCFLs, pc-wLEDs allow the image display devices to be made thinner, lighter, brighter, and more colorful. The Commission International de l'Eclairage (CIE) chromaticity diagram (Figure 8.4) is used to quantify the quality of light colors. The CIE diagram specifies the colors that are visible to the human eye in terms of hue and saturation. The upper curve of the diagram resembles a clean rainbow of violet–indigo–blue–green–yellow–orange–red colors. The colors in this curve represent natural colors. By comparison, the bottom straight lines are called magenta lines, which are a mixture of red and violet. In practical applications, combinations of blue and red or violet and red produce purple, magenta, or pink.

In general, the colors on the curve edge are purer than those inside the curve. At the center, white is a balanced mixture of other colors. The straight line that connects any two points or colors in the CIE results in an in-between color (color lies in the straight line) or a point instead of individual colors. For instance, a mixture of yellow and blue produces white, and a mixture of red and green gives yellow. Mixing of colors in different proportions can also result in in-between colors that are stronger or closer, according to the proportion. Likewise, the involvement of three-color or *n*-color mixtures produces a triangle instead of a straight line in the bicolor system. The triangle is also called the color gamut. A tricolor mixture resembles the final color at the center of the triangle. In the tricolor system, the color enclosed by the triangle is reproducible,

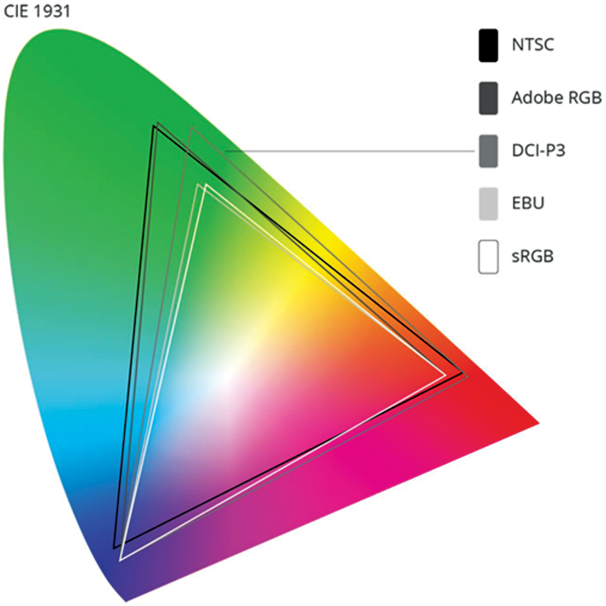

Figure 8.4: Commission International de l'Eclairage (CIE) 1931 with various standards.

indicating that a wide color triangle (or wide color gamut) can generate more precise colors than a narrow color gamut. Hence, a wide color gamut is the ultimate goal for backlighting applications.

Different standards of color gamut, such as sRGB, Adobe RGB, National Television Standards Committee (NTSC), European Broadcasting Union, and DCI-P3 color space (defined by the Society of Motion Pictures and Television Engineers), are based on different applications. NTSC covers a wider color gamut and is more commonly used. Trigroup pc-WLEDs already cover a color gamut greater than 90% of NTSC (CIE 1976), whereas conventional CCFLs have a color gamut of ~ 75% only. By contrast, the color gamut of quantum dot backlight systems is greater than 100% of NTSC because of their narrower full width at half maximum (*fwhm*). Nevertheless, the complicated synthesis procedure and the quantum dot instability render quantum dot backlight systems underdeveloped. Aside from *fwhm*, several parameters, such as quantum efficiency, emission peak position, decay time, and thermal and chemical stability, have to be considered in choosing phosphors for use in wLED backlights.

Green phosphors usually used in practical applications are β-sialon:Eu^{2+} because of their narrow *fwhm* and high quantum efficiency. By contrast, $CaAlSiN_3$:Eu^{2+} and K_2SiF_6:Mn^{4+} are the red phosphors commonly utilized for backlighting. Nevertheless, the broad emission spectrum and the excitation spectrum overlap of β-sialon:Eu^{2+} emission make the Mn^{4+}-activated fluoride phosphor K_2SiF_6:Mn^{4+} a promising candidate for enhancing the color mimicking and brightness of LED backlighting. General Electric (GE) reported that post-treated K_2SiF_6:Mn^{4+}, centered at 631 nm, can achieve a performance greater than 10%, compared with Eu^{2+}-doped nitride red phosphors under the GE Tri-GainTM Technology [79]. Wang et al. [80] achieved a brightness of 91–95 lm/W (driving current of 120 mA) and a color gamut of 86% and 94%–96% with respect to NTSC CIE 1931 and CIE 1976, respectively. Oh et al. [81] achieved brightness of 105 lm/W (driving current of 60 mA) and a color gamut of 86.4% with respect to NTSC CIE 1931 by using K_2SiF_6:Mn^{4+} and $SrGa_2S_4$:Eu^{2+} as red and green phosphors, respectively. Yeo et al. [82] obtained a similar value of 96.5% by employing green-emitting $SrGa_2S_4$:Eu^{2+} and K_2SiF_6:Mn^{4+} red phosphors, which were prepared via a redox reaction with three sharp emissions at 615, 630, and 650 nm under 465 nm excitation. Zhou et al. [83] investigated the potential of short-time decay of Mn^{4+}-activated A_2NaScF_6 (A = K, Rb, Cs) red phosphors for backlighting. They used InGaN blue LED (~455 nm) and β-SiAlON green phosphor in fabricating the device. At 20 mA driving current, K_2NaScF_6:Mn^{4+}, Rb_2NaScF_6:Mn^{4+}, and Cs_2NaScF_6:Mn^{4+} covered a wide color gamut of 105.6%, 108.4%, and 105.6%, respectively, with respect to NTSC CIE 1931. As an alternative to $SrGa_2S_4$:Eu^{2+} and β-sialon:Eu^{2+} green phosphors, Song *et al.* [84] synthesized $MgAl_2O_4$:Mn^{2+} green phosphors and obtained a color gamut of 116% with respect to NTSC CIE 1931, in combination with K_2SiF_6:Mn^{4+}. Zhu *et al.* [85] also synthesized novel $Sr_2MgAl_{22}O_{36}$:Mn^{2+} green phosphors and combined them with K_2SiF_6:Mn^{4+} red phosphors to fabricate wLEDs with a color gamut of 127%, with respect to NTSC CIE 1931.

8.7 Near-infrared LED

Infrared light is the broad spectrum of invisible light located between the visible and the microwave regions of the electromagnetic spectrum. Researchers have several misconceptions about the classification of infrared light. Infrared light has two global classifications (Table 8.5) [8], International Commission on Illumination classification based on photon energy and the International Organization for Standardization 20473 based on wavelength. The design and fabrication techniques for phosphor-converted near-infrared LEDs (pc-NIR LEDs) follow the same principle as those for white LEDs. In brief, pc-NIR LED is the optoelectronic device that contains a semiconductor chip for emitting primary radiations and phosphor conversion materials to convert primary radiations (mostly blue light at 450 nm) into secondary radiations (near-infrared light) [8, 86].

Radiant flux or radiant power is the most straightforward tool for evaluating the performance of pc-NIR LEDs. Radiant flux is a measure of the amount of radiant energy emitted from the radiant source per unit time and described in W, mW, or μW. In general, radiant power is directly proportional to the input operating current. Therefore, a high operating input leads to a high output power from the device. Hence, radiant power at a fixed operating current must be measured to compare and evaluate the real performance of NIR phosphors. Aside from operating current, the

Table 8.5: Classification of infrared regions.

	CIE classification		ISO 20473
	Wavelength (nm)	**Photon energy (THz)**	**Wavelength (nm)**
Near IR, NIR	700–1,400	215–430	780–3,000
Mid-IR, MIR	1,400–3,000	100–215	3,000–5,000
Far IR, FIR	3,000 nm to 0.1 mm	3–100	5,000–10,000

size of pc-NIR LEDs should also be considered. Photoconversion efficiency is an indirect indicator of the performance of pc-NIR LED devices. Photoconversion efficiency is expressed as the ratio of output power to input power. Photoconversion efficiency quantifies the down-conversion capability of the absorbed blue photons in NIR photons [87]. In general, radiant flux is inversely proportional to photoconversion efficiency. NIR phosphors, with a high radiant flux at a high operating current, always achieve a low photoconversion efficiency. Hence, innovative approaches must be developed to increase the radiant flux of pc-NIR LED devices without compromising the photoconversion efficiency [8, 88].

8.8 Cr-doped oxide phosphors

The *d* orbitals of Cr^{3+} ions are highly susceptible to the surrounding environment and ligands. Hence, they can be tuned to achieve variable crystal strengths by changing the host atoms and the neighboring coordination environment. In general, Cr^{3+} produces a broad light emission spectrum for a weak crystal field strength, whereas a strong crystal field strength gives a narrow or line emission spectrum. However, the crystal field strength of Cr^{3+} ions is intermediate in most cases. Thus, Cr^{3+} ions can exhibit both a narrow and a broad light spectrum – a most interesting and unique luminescence characteristic for optical applications [89].

Aside from the famous ruby crystal, Al_2O_3:Cr^{3+}, several chemical systems have been reported for laser applications and other uses. Several important chemical systems are listed in Table 8.6. The relationship between the crystal system and its crystal field strength for selecting the proper host system according to application requirements is depicted in Figure 8.5.

Table 8.6: Cr^{3+}-activated oxide phosphors and their luminescence properties.

Phosphor	Incorporation site	Crystal system	Emission range (nm)	Centered emission (nm)	Dq/B	Reference
$Y_3Ga_5O_{12}$	Ga^{3+}(VI)	Cubic	650–1,000	613	2.56	[88]
$Gd_3Ga_5O_{12}$	Ga^{3+}(VI)	Cubic	650–1,000	627	2.53	[88]
$Lu_3Ga_5O_{12}$	Ga^{3+}(VI)	Cubic	650–1,000	599	2.67	[88]
$Y_3Sc_2Ga_3O_{12}$	Ga^{3+}/Sc^{3+}(VI)	Cubic	650–1,000	629	2.52	[88]
$Gd_3Sc_2Ga_3O_{12}$	Ga^{3+}/Sc^{3+}(VI)	Cubic	650–1,000	641	2.43	[88]
$Lu_3Sc_2Ga_3O_{12}$	Ga^{3+}/Sc^{3+}(VI)	Cubic	650–1,000	603	2.64	[88]
$Ca_2LuZr_2Al_3O_{12}$ – (I)	Al^{3+}(VI)	Cubic	650–850	813	2.39	[90]
$Ca_2LuZr_2Al_3O_{12}$ – (II)	Ca^{2+}/Lu^{3+}(VIII)	Cubic	650–850	754	1.92	[90]
(La, Lu)$_3Ga_5O_{12}$	Ga^{3+}(VI)	Cubic	700–950	833	2.39	[91]
$Y_3Ga_5O_{12}$	Ga^{3+}(VI)	Cubic	700–950	740	2.55	[91]
$CaY_2Mg_2Ge_3O_{12}$	–	Cubic	700–800	695*,710, 720, 740	2.47	[92]
$MgGa_2O_4$	Ga^{3+}(VI)	Spinel	650–770	–	2.78	[93]
$MgAl_2O_4$	Ga^{3+}(VI)	Spinel	650–770	–		
$ZnGa_2O_4$	Ga^{3+}(VI)	Spinel	–	–	–	[94]
$Zn_3(Al_{0.8}Ga_{0.2})_2Ge_2O_{10}$	Ga^{3+}(VI)/ Al^{3+}(VI)	Spinel	–	721	2.47	[95]
$BaAl_2O_4:Cr^{3+}$	Al^{3+}(VI)/ Al^{3+}(IV)	Spinel	–	701, 705	3.4	[96]
$LiGa_5O_8$	Ga^{3+}(VI)	Inverse spinel	–	715*	3.0	[97]
$Zn_{(2-x)}Al_{2x}Sn_{(1-x)}O_4$ ($x = 0–0.4$)	Zn^{2+}/Sn^{4+}(VI)	Inverse spinel	650–1,200	800	2.292–3.066	[98]
$Zn_3(Al_{0.8}Ga_{0.2})_2Ge_2O_{10}$	Al^{3+}/Ga^{3+}(VI)	Spinel	600–900	721	2.47	[95]
$LaSr_2Ga_{11}0_{20}$	Ga^{3+}(VI)	Monoclinic	–	693*	2.26	[99]
$LiSc(WO_4)_2$	Sc^{3+}(VI)	Monoclinic	–	1,111*	2.51	[100]
$MgWO_4$	Mg^{2+}(VI)	Monoclinic	850–1,350	993.6	2.577	[101]

Table 8.6 (continued)

Phosphor	Incorporation site	Crystal system	Emission range (nm)	Centered emission (nm)	Dq/B	Reference
$NaAl(WO_4)_2$	Al^{3+}(VI)	Monoclinic	700–1,150	815	2.51	[102]
$Sr_8MgLa(PO_4)_7$	Mg^{2+}(VI)	Monoclinic	700–1,000	848	2.07	[103]
$NaScSi_2O_6$	Sc^{3+}(VI)	Monoclinic	650–950	840	1.82	[104]
$KTiOPO_4$	Ti^{4+}(VI)	Orthorhombic	700–1,000	833	2.31	[105]
$KIn(MoO_4)_2$	In^{3+}(VI)	Orthorhombic	800–1,200	891	2.03	[106]
$RbIn(MoO_4)_2$	In^{3+}(VI)	Orthorhombic	800–1,200	998	1.94	[106]
$Na_3Ce(PO_4)_2$	Ce^{3+}(VI)	Orthorhombic	700–1,050	860	2.21	[107]
$Sc_2(MoO_4)_3$	Al^{3+}/Sc^{3+}(VI)	Orthorhombic	750–1,200	880	2.32	[108]
$(Sr_{1-x}Ca_x)Sc_2O_4$ ($x = 0–1.0$)	Sc^{3+}(VI)	Orthorhombic	700–1,000	860	2.1–1.95	[109]
$Bi_2Ga_4O_9$	Ga^{3+}(VI)	Orthorhombic	–	702*, 710*, 800	2.31	[110]
$LaMgAl_{11}O_{19}$	Al^{3+}(VI)	Hexagonal	–	692*	2.90	[111]
$La_3Ga_{5.5}Nb_{0.5}O_{14}$	Ga^{3+}(VI)/ Ga^{3+}(IV)	Hexagonal	600–1,300	730, 1,030	2.5	[112]
$MgSrAl_{11}O_{17}$	Al^{3+}(VI)	Hexagonal	–	690*	2.67	[113]
$BaZr_{0.93}Si_3O_9$	Zr^{4+}(VI)	Hexagonal	700–1,000	792–815	2.1	[114]
$SrGa_{12}O_{19}$	Ga^{3+}(VI)/ Ga^{3+}(IV)/ Ga^{3+}(V)	Hexagonal	650–950	750	2.51	[115]

*R line.

8.8.1 Cubic crystal system

The cubic crystal system or garnet structure system is generally known by the chemical formula $A_3B_5O_{12}$. The framework of the crystal structure is usually composed of units of octahedral B cations [BO_6] and tetrahedral B cations [BO_4] with the A cations located between the spaces in a dodecahedral fashion [AO_8]. In the garnet system, anions are the oxygen atoms, and each anion is identically bonded with a single unit of BO_6 and BO_4, and two units of AO_8. In most NIR phosphors, B cations are trivalent Al^{3+} and Ga^{3+} ions, whereas A cations are trivalent Y^{3+}, Lu^{3+}, Gd^{3+}, and Lu^{3+} ions. The choice of cations also varies. Through incorporation, Cr^{3+} impurity ions will prefer to occupy BO_6 than BO_4

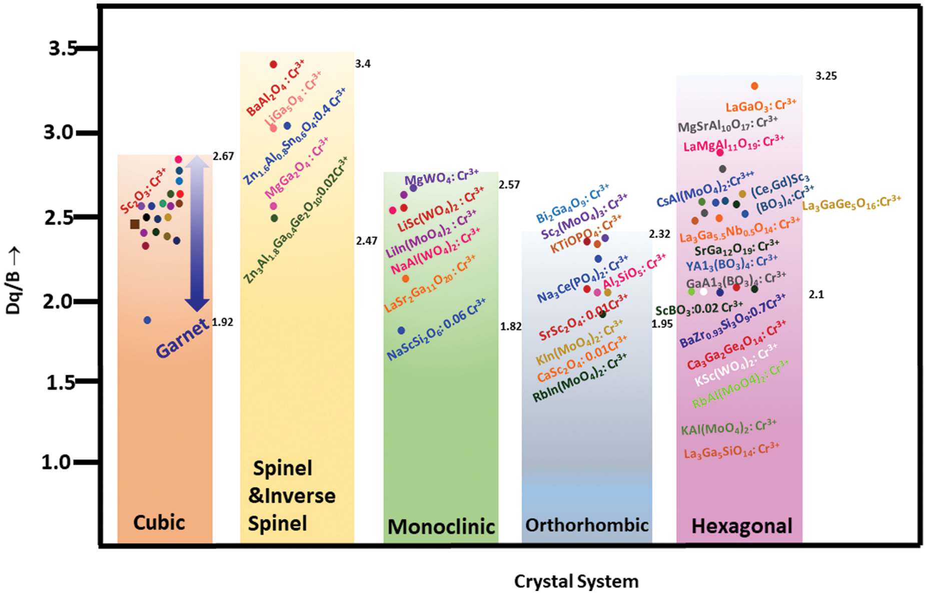

Figure 8.5: Classification of host systems for Cr^{3+} on the basis of crystal structure and *Dq*/*B*.

because the crystal field splitting energy of Cr^{3+} into octahedral units (0.6 *Dq*) is higher than that in tetrahedral units (0.4 *Dq*). The cubic crystal system exhibits a tunable crystal field value (*Dq*/*B*) of ~ 2.56–2.67, according to the type of cations (Table 8.6 and Figure 8.5). Yttrium gallium garnet ($Y_3Ga_5O_{12}$) has a *Dq*/*B* value of ~ 2.47, whereas yttrium aluminum garnet ($Y_3Al_5O_{12}$) has a *Dq*/*B* value of ~ 2.38, indicating that the replacement of large ionic B cations (Ga = 0.62 Å) by small ionic cations (Al = 0.535 Å) will shift the crystal field value toward the right side of the T–S diagram. Simultaneously, an increase in the crystal field will result in a blue shift in the emission spectrum. By contrast, the substitution of the original B cations by large ionic atoms will reduce the crystal field value due to the occurrence of redshift in the emission spectrum. The crystal field value (~2.53, $Gd_3Ga_5O_{12}$:Cr^{3+}) is reduced (~2.43, $Gd_3Sc_2Ga_3O_{12}$:Cr^{3+}) by the substitution of Sc^{3+} (ionic radius of −0.745 Å) (Table 8.6). Similar results are observed when A cations are changed in the dodecahedral units. For example, the *Dq*/*B* value of $Y_3Ga_5O_{12}$:Cr^{3+} is ~ 2.56. However, the *Dq*/*B* value decreases to 2.67 and 2.53 because of the alteration of the Y^{3+} cations (1.019 Å) by small ionic cations (Lu^{3+} = 0.977 Å) and large ionic cations (Gd^{3+} = 1.053 Å), respectively.

8.8.2 Spinel and inverse spinel structures

Spinel and inverse spinel structures are cubic-type packed crystal systems, with the general formula of MN_2O_4, where *M* indicates divalent cations (Zn and Mg) and *N* denotes trivalent cations (Al and Ga). The main difference between the spinel and the inverse spinel structures is the occupation of cations in unit cells. In spinel structures, divalent cations occupy 1/8 of the tetrahedral sites, whereas trivalent cations occupy 1/8 of the octahedral sites. An interesting characteristic of the inverse spinel structures is that octahedral sites are occupied by trivalent cations and one-half of the divalent cations, whereas tetrahedral sites contain the remaining half of the divalent cations. This arrangement allows a versatile substitution of the divalent and trivalent cations in octahedral sites with a similar geometrical ionic size. However, solving the crystal structure for real occupancy and concentration of impurity ions or dopants is cumbersome. Inverse spinel crystal structures are the primary choice for NIR-persistent luminescence because this type of structure allows the possible generation of intrinsic and antisite defects. The versatile substitution potential allows crystal field tuning to a large extent. Like cubic systems, gallate-based NIR systems offer a lower crystal field value than aluminate-based systems, that is, the Dq/B value of $MgGa_2O_4$ and $MgAl_2O_4$ is 2.78 and 3.32, respectively [93]. By contrast, the crystal field value in inverse spinel systems can be adjusted by doping tetravalent cations in octahedral sites. This type of inequivalent valence substitution (Ge^{4+} substitution for Ga^{3+} atoms) is another advantage in designing superior NIR-persistent luminescence phosphors that do not affect the crystal lattice. $ZnGa_2O_4$:Cr^{3+} has a crystal field value of ~3.32 [94]. Chemical composition tuning of crystal structures via successful substitution of tetravalent cations achieves a crystal field value of ~ 2.47 [95]. Calculations of Dq/B vary for different studies, but the difference is not remarkable.

8.8.3 Hexagonal crystal systems

Two crystal systems (hexagonal and trigonal systems) and two Bravais lattice systems (rhombohedral and hexagonal systems) are included in the family of hexagonal structures. These systems are characterized by concurrent 120° angles of three equilateral or horizontal axes with the vertical axes being perpendicular to one another. These systems are part of a complex crystal family with no generalized chemical formula. However, most tungstates, silicates, molybdates, and borates have hexagonal crystal systems. The framework is typically a layered structure with alternate cation layers of tetrahedral and octahedral coordination. Hexagonally structured compounds doped with Cr^{3+} ions achieve Dq/B values of 2.1–2.9. Most chemical compounds that are listed in Figure 8.5 and Table 8.6 possess a Dq/B value closer to the intermediate crossing point. Hence, these chemical compounds exhibit the characteristic R line embedded in the broadband distribution of emission (within 600–1,000 nm). Another interesting feature of the hexagonal crystal systems is the number of crystallographic sites and the successful substitution of Cr^{3+} ions in these sites. For instance, $La_3Ga_{5.5}Nb_{0.5}O_{14}$ contains disordered octahedral coordinated sites and ordered tetrahedrally coordinated sites for the luminescence of Cr^{3+} [112]. The photoluminescence emission spectrum of $La_3Ga_{5.5}Nb_{0.5}O_{14}$:$Cr^{3+}$ also displays two emission peaks at 730 and 1,030 nm, which can be ascribed to $^4T_2 \rightarrow ^4A_2$ spin-allowed transition. Moreover, Cr^{3+} ions in disordered octahedral coordination sites experience longer decay times and stronger crystal fields than Cr^{3+} ions in ordered tetrahedral sites. $SrGa_{12}O_{19}$ contains tetrahedron, hexahedron, and octahedron coordinated sites for the incorporation of Cr^{3+} ions. At 425 nm excitation, $SrGa_{12}O_{19}$:Cr^{3+} exhibits several narrow emission peaks over the broad emission band of 650–950 nm [115].

8.8.4 Monoclinic crystal systems

Monoclinic crystal systems are structured by three unequal length axes, in which one unequal axis is perpendicular to the other two axes. These systems are generally a twofold symmetry crystal system, with a rotation of 180° along the perpendicular axis. Tungstate-based compounds are the most used compounds for Cr^{3+} activation, with an NIR luminescence of not less than 1,000 nm. Most monoclinic-structured compounds have a Dq/B value less than or almost equal to the intermediate value. Thus, monoclinic-structured compounds experience weak or intermediate crystal fields most of the time. Hence, the monoclinic crystal system will always result in a broadband emission spectrum with an average distribution of 650–1,100 nm.

8.8.5 Orthorhombic crystal systems

Orthorhombic crystal systems resemble stretched cubic lattices along one direction in the form of a rectangular prism with a rectangular base. Hence, three crystallographic axes are distinct and occur at a 90° angle. These systems are also twofold symmetry crystal systems with a rotation of 180° along the *c*-axis. The framework of these systems is made up of tetrahedral units of cations along the *c*-direction, ordered in a chain and two tetrahedral units connected by commonly shared anions. The octahedral unit of cations is positioned between these tetrahedral units and shares the anion atoms with the tetrahedral units. Phosphates and tungstates belong to this system (Figure 8.5 and Table 8.6). Thus, these compounds experience a weak crystal field value of less than the crossing point (~2.3). Hence, most Cr^{3+}-activated orthorhombic-structured compounds show the broadest emission spectrum of NIR luminescence within 600–1,200 nm).

8.9 Cr-doped fluoride phosphors

Cr^{3+}-activated fluoride host phosphors are a special class of optical materials because their spectroscopy properties have been rarely investigated. Although the spectroscopy of Cr^{3+} have been comprehensively studied since the 1930s, few fluoride host compounds, such as K_3AlF_6:Cr^{3+} [116], K_3GaF_6:Cr^{3+} [116], Cs_2NaAlF_6:Cr^{3+} [117], Cs_2NaGaF_6:Cr^{3+} [118], $LiCaAlF_6$:Cr^{3+} [119], and $LiSrAlF_6$:Cr^{3+} [119], have been reported for the luminescence of Cr^{3+}. Red lines or ruby line emissions in Cr^{3+}-activated oxide phosphors are often unavoidable. Nevertheless, some oxide phosphors do not exhibit this phenomenon. By contrast, Cr^{3+}-activated fluoride hosts always exhibit a broadband emission within 700–950 nm without any sharp peaks or red line emissions. The main concept behind this observation is that the energy inequality relation in fluoride hosts is $E(^2E)_{\mathrm{ZPL}} > E(^4T_2)_{\mathrm{ZPL}}$. By contrast, the energy inequality relation in oxide hosts can fit any of the following relations: $E(^2E)_{\mathrm{ZPL}} \sim E(^4T_2)_{\mathrm{ZPL}}$, $E(^2E)_{\mathrm{ZPL}} \geq E(^4T_2)_{\mathrm{ZPL}}$, and $\mathrm{E}(^2E)_{\mathrm{ZPL}} < E(^4T_2)_{\mathrm{ZPL}}$. Hence, the emission of Cr^{3+} in fluoride hosts is from spin-allowed $^4T_{2g} \rightarrow {}^4A_{2g}$ transitions [120].

Lee et al. [116] synthesized two NIR-emitting K_3AlF_6:Cr^{3+} and K_3GaF_6:Cr^{3+} phosphors via coprecipitation routes for NIR spectroscopy applications. Both phosphors are crystallized in the cubic system with a space group of *Fm*3*m*. At 442 nm excitation, K_3AlF_6:Cr^{3+} and K_3GaF_6:Cr^{3+} show broadband emission within 650–950 nm centered at 750 nm because of the spin-allowed $^4T_2 \rightarrow {}^4A_2$ transitions. Although both samples exhibit a weak crystal field, the gallate fluoride K_3GaF_6:Cr^{3+} ($Dq/B = 1.89$) achieves a higher splitting value than aluminate fluoride ($Dq/B = 1.94$), suggesting that the characteristics of spin-allowed transitions are affected by the nature of the host atoms and the coordination environment. Apart from the characteristic emission profile, the Fano-antiresonance between $^2E/^2T_1$ and quasicontinuous, vibronically coupled $^4T_2$ levels can be interpreted as two dips at 610 and 645 nm in the excitation spectrum. Although fluoride compounds have an in-built nature of broadband emission, the value of their radiant flux is 7–8 mW with an input power of 1.05 W, which is inferior to the performance of oxide host systems for NIR applications.

Yu et al. [121] synthesized monoclinic Na_3AlF_6:Cr^{3+} phosphors via the hydrothermal method. Regardless of the excitation wavelength (282, 420, and 580 nm), Na_3AlF_6:1% Cr^{3+} displays a broadband NIR emission of 640–850 nm centered at 720 nm because of the spin-allowed transitions. The observation of red shift from 715 to 745 nm as the concentration of activator (Cr^{3+}) increases is debatable. The redshift may be due to the perturbation effects of crystal field strength on $^4T_2$ (^4F) spin-allowed states or severe reabsorption within the 650–710 nm range. Nevertheless, the emission profile and the redshift matched with the active bands of phototherapy (613–623, 667–683, and 750–772 nm). In addition, pc-NIR LEDs fabricated using commercial InGaN for excitation produce bright deep-red like Color Hex Color Codes of #960000 at a constant current (drive voltage of 2.72 V and drive current of 14 mA). Hence, pc-NIR LEDs with Cr^{3+}-activated fluoride compounds are an alternative to rare-earth-doped phosphors for phototherapy.

8.10 Applications of NIR LEDs

8.10.1 NIR spectroscopy

NIR spectroscopy is a well-known analytical tool for characterizing a wide range of materials, including organic and inorganic compounds. However, the commercial NIR spectroscopy instruments are massive and mostly limited to laboratory research purposes. Over the last few decades, advancements in microelectromechanical systems have allowed the design and development of miniature spectrometers capable of onsite and in-field analyses [8, 86]. The development of miniature NIR spectrometers for complete consumer end utilization may take a few more decades. In reducing the size of traditional spectrometers, the first critical activity is light source selection. Light sources influence the quality of spectroscopy operation and instrument specifications, specifically size and lifetime. Tungsten lamps mainly employ light sources in traditional spectrometers, but they require auxiliary parts such as a glass envelope for heat dissipation, a DC power supply, and heating time for spectral stability. The other commercial NIR light sources of laser diodes suffer from the narrow spectrum and electrical housing arrangements. These factors must be considered in searching for alternative light sources for miniature spectrometers. pc-NIR LEDs are emerging as alternative light sources for miniature spectrometers because of their compact size, low power consumption, and long lifetime. Although several NIR light-emitting phosphors have been developed, most NIR systems possess line or narrow light spectral distributions that make them unsuitable for spectroscopy applications. Several broadband NIR phosphors developed for NIR spectroscopy applications are listed in Table 8.7.

OSRAM announced that smartphones can be used to analyze daily food samples by integrating them with NIR LED chips that can emit broad spectral distributions of NIR light. OSRAM also launched two NIR LED products (SFH 4735 and SFH4776) with an NIR wavelength of 650–1,050 nm [128, 129]. The IR LED technology can also be extended to healthcare products for blood analysis and endoscopy [130, 131]. For instance, IR LEDs can be incorporated in biopsy surgery needles, which can be easily used by physicians in performing spectral tumor diagnostics [122].

8.10.2 Plant growth

The photoreceptors in plants absorb light energy from the Sun to synthesize nutrients. Hence, plant growth can be accelerated by providing a proper artificial lighting environment. The primary photoreceptors in plants are chlorophyll *a* and chlorophyll *b*, which absorb blue (425–175 nm) and red light (625–675 nm) in the visible light spectrum to drive photosynthesis. Photosynthesis normally occurs in the green pigments of chlorophyll. Plant uses carbon dioxide, water, and light to manufacture nutrients for their growth and release oxygen as a byproduct. The phytochrome photoreceptors

Table 8.7: Cr^{3+}-activated near-infrared phosphors developed for NIR spectroscopy applications.

Phosphor	Incorporated site	Crystal system	Emission (nm)	FWHM (nm)	Input current (mA)	NIR power (mW)	Efficiency (%)	Year	Reference
$Lu_3Al_5O_{12}$:0.05Ce^{3+}, 0.5% Cr^{3+} + Bi-doped GeO_2 glass	Ga^{3+}(VI)	Cubic	500–850 + 1,000–1,600	–	100	47	–	2017	[122]
$La_3Ga_{4.95}GeO_{14}$:0.05 Cr^{3+}	Ga^{3+}(VI) Ga^{3+}/Ge^{4+}(IV)	Trigonal	600–1,200	330	350	18.2	76.59	2018	[123]
$Ca_2LuZr_2Al_3O_{12}$:0.08 Cr^{3+}	Ga^{3+}(VI)/ Lu^{3+}(VIII)	Cubic	650–850	117	20	2.448	4.1	2018	[90]
$ScBO_3$:0.02 Cr^{3+}	Sc^{3+}(VI)	Rhombohedral	700–950	120	120	26	7	2018	[124]
$YAl_3(BO_3)_4$:0.04 Cr^{3+}, 0.01 Yb^{3+} + $NaScSi_2O_6$:0.06 Cr^{3+}	Al^{3+}(VI) +Sc^{3+}(VI)	Trigonal + Monoclinic	650–850, 980, + 750–950	–	100	26	8.6	2018	[104]
$Ca_2LuHf_2Al_3O_{12}$:0.08Cr^{3+}	–	Cubic	700–1,000	–	100	46.09	15.75	2019	[125]
$La_3GaGe_5O_{16}$: 0.06 Cr^{3+}	Ga^{3+}(VI)	Triclinic	650–1,050	–	350	43.1	52.5	2019	[126]
$La_3GaGe_5O_{16}$: 0.06 Cr^{3+}, 0.03 Gd^{3+}	Ga^{3+}(VI)	Triclinic	650–1,050	–	350	56.3	60.6	2019	[126]
$La_3GaGe_5O_{16}$: 0.06 Cr^{3+}, 0.03 Gd^{3+}, 0.05 Sn^{4+}	Ga^{3+}(VI)	Triclinic	650–1,050	–	350	65.2	68.27	2019	[126]
$LiInSi_2O_6$:Cr^{3+}	In^{3+}(VI)	Monoclinic	700–1,100	143	210	51.6	17.2	2019	[127]

in plants absorb the infrared light for photomorphogenic functions, including germination, flowering, and fruiting. P_r and P_{fr} are the two interconvertible forms of phytochrome that absorb red light (660 nm) and NIR light (730 nm), respectively. P_r is inactive and exists in darkness. After absorbing the red light, P_r is converted into the active P_{fr}. P_{fr} is again converted into the inactive P_r by absorbing the NIR light. P_{fr} is then translocated to the nucleus and induces changes in plants [132–134].

When numerous plants grow under a canopy or nearby, they always compete for light, especially for the red and the NIR light because most of NIR light is reflected by the adjacent vegetative plants, whereas the red light is absorbed by the top plant layers. Hence, plants in the lower parts of the canopy receive only small amounts of infrared light and red light. To overcome this competition for light, plants usually have two opposing strategies: shade avoidance and shade tolerance [135]. Shade avoidance occurs due to the enrichment of the infrared light (high R/NR ratio) and is generally observed in flowering plants. During the initial stages of seed germination, the ability to avoid shade results in elongation, expansion of the leaf lamina, and a decrease in root development. By contrast, changes due to shade avoidance are rapid and reversible [136, 137]. Dicotyledonous plants exhibit shade tolerance. The shade tolerance effect occurs due to the low R/NR ratios and results in stem elongation. The photomorphogenic changes induced by shade tolerance are decreased leaf growth, reduced branching, and increased apical dominance [138, 139].

8.10.3 Optical thermometry

Optical thermometry uses light as a medium to convey temperature information. Compared to other recognized systems, such as infrared pyrometer and electronic thermometers, luminescence-based optical thermometry measurements are more accurate (i.e., free from electromagnetic interference). Moreover, optical thermometry allows localized measurements because optical thermometers are compact. Optical thermometers can be designed in terms of reflectance, fluorescence, decay lifetime, and absorption. The construction of optical thermometry on the basis of the fluorescence intensity ratio method has recently become widespread. This technique is widely applied because of its high spatial resolution and high detection sensitivity. A system with two excited states that are in thermal equilibrium is the primary criterion for temperature measurements because variations in environmental parameters affect the quantum yield and ensure identical Boltzmann PL intensity distributions because of its fast population renormalization. TM ions, especially Cr^{3+}, are the most preferred because of the two possible excited states, namely, ^2E and $^4T_2$, from the ground state, $^4A_2$. Besides, light emission from these states can be tuned and controlled according to the crystal field strength. A suitable crystalline host with desirable properties must be selected to obtain optical thermometers with excellent performance. Crystalline hosts with an intermediate or weak crystal field strength are the most preferred for optical thermometry applications. NIR FIR-based optical thermometry is suitable for biomedical applications because of its deep tissue penetration and minimal autofluorescence, for example, real-time measurement of temperature of tissues in hyperthermia [109, 110, 140–144].

8.11 Future perspectives

The reduction in the size of LEDs has revolutionized the lighting industry, specifically the LED display technology. Mini- and micro-LEDs are the next generation of LED light sources for backlighting. Micro-LEDs are less than 100 μm in size, whereas mini-LEDs are 100–200 μm in size. However, the development of micro-LEDs must overcome the challenge of mass transfer in real-time production. Consequently, mini-LEDs are investigated as an alternative source for backlighting. The main advantage of reducing the size of LEDs is the attainment of better dimming features. Each micro-LED/mini-LED acts as a self-emitting pixel and enhances the contrast ratio with less energy consumption. In general, conventional phosphors that utilize LEDs are several micrometers in size with an uneven size distribution, high light-scattering effects, and low packing density. However, the same conventional phosphors that are in several nanometers in size can overcome these difficulties with the combined advantages of mini-LED and micro-LED dimming technologies. Cr^{3+}-activated NIR oxide phosphors with the chemical composition of $ZnGa_2O_4:Cr^{3+}$ or $ZnGa_2O_4:Sn^{4+}$ are integrated into mini-NIR LED technologies, with a radiant flux of 3.3 mW at an operating current of 45 mA [145]. NIR light-emitting mini-LED devices may also be applied in various fields, such as theranostics, photobiomodulation, and biosensing.

References

[1] Available at: https://clarivate.com/derwent/solutions/derwent-innovation/. Accessed: Accessed on Dec 22, 2019.

[2] M.G. Brik, S. Camardello, A.M. Srivastava, N.M. Avram, A. Suchocki, Spin-forbidden transitions in the spectra of transition metal ions and nephelauxetic effect, ECS J. Solid State Sci. Technol. 5 (2015) R3067–R3077. 10.1149/2.0091601jss.

[3] Y. Tanabe, S. Sugano, On the absorption spectra of complex ions II, J. Phys. Soc. Jpn. 9 (1954) 766–779. doi: 10.1143/JPSJ.9.766.

[4] J.M. Combes, P. Duclos, R. Seiler, The Born-Oppenheimer approximation, in: G. Velo, A. S. Wightman (Eds.), Rigorous Atomic and Molecular Physics, Springer, Boston, MA (1981), pp. 185–213.

[5] P. Atkins, T. Overton, Shriver and Atkins' Inorganic Chemistry, Oxford University Press, USA (2010).

[6] H. Tippins, Charge-transfer spectra of transition-metal ions in corundum, Phys. Rev. B 1 (1970) 126–135. doi: 10.1103/PhysRevB.1.126.

[7] B.R. Hollebone, Subduced selection rules for vibronic transitions in d^3 octahedral complexes, Theory. Chim. Acta 56 (1980) 45–60. doi: 10.1007/BF00716679.

[8] V. Rajendran, H. Chang, R.S. Liu, (INVITED) Recent progress on broadband near-infrared phosphors-converted light emitting diodes for future miniature spectrometers. Opt. Mater. X (2019) 1 100011. doi: 10.1016/j.omx.2019.100011.

[9] S. Sugano, Multiplets of Transition-metal Ions in Crystals, in: S. Sugano, Y. Tanabe, H. Kamimura (Eds.), Multiplets of Transition-Metal Ions in Crystals, Academic Press, New York and London (1970).

[10] Z. Zhou, N. Zhou, M. Xia, M. Yokoyama, H.B. Hintzen, Research progress and application prospects of transition metal Mn^{4+}-activated luminescent materials, J. Mater. Chem. C 4 (2016) 9143–9161. doi: 10.1039/C6TC02496C.

[11] H.D. Nguyen, R.S. Liu, Narrow-band red-emitting Mn^{4+}-doped hexafluoride phosphors: Synthesis, optoelectronic properties, and applications in white light-emitting diodes, J. Mater. Chem. C 4 (2016) 10759–10775. doi: 10.1039/C6TC03292C.

[12] R. Suzuki, J. Kunitomo, Y. Takahashi, K. Nakamura, M. Osada, N. Terakado, et al., Mn-doped $LiNaGe_4O_9$ as a rare-earth free phosphor: Impact of Na-substitution on emission in tetragermanate phase, J. Ceram. Soc. Jpn. 123 (2015) 888–891. doi: 10.2109/jcersj2.123.888.

[13] S. Kawakita, H. Kominami, K. Hara, Preparation and photoluminescence properties of Mn-doped deep red emitting phosphor under blue to near ultraviolet excitations, Physica Status Solidi C 12 (2015) 805–808. doi: 10.1002/pssc.201400323.

[14] L. Wang, Y. Xu, D. Wang, R. Zhou, N. Ding, M. Shi, et al., Deep red phosphors $SrAl_{12}O_{19}$: Mn^{4+}, M(M = Li^+, Na^+, K^+, Mg^{2+}) for high colour rendering white LEDs, Physica Status Solidi A 210 (2013) 1433–1437. doi: 10.1002/pssa.201228815.

[15] B.D. McNicol, G.T. Pott, Luminescence of Mn ions in ordered and disordered $LiAl_5O_8$, J. Lumin. 6 (1973) 320–334. doi: 10.1016/0022-2313(73)90027-6.

[16] H. Jeong, S. Kim, K. Lee, J. Jeong, T. Yoo, M. Kwon, et al., Optical properties of white organic light-emitting devices fabricated utilizing a mixed $CaAl_{12}O_{19}$: Mn^{4+} and $Y_3Al_5O_{12}$: Ce^{3+} color conversion layer, J. Nanosci. Nanotechnol. 13 (2013) 4394–4397. 10.1166/jnn.2013.7003.

[17] W.Z. Yan, L. Lin, Y.H. Chen, M. Yin, New red long afterglow aluminate materials doped with Mn^{4+}, Chin. J. Lumin. 29 (2008) 114.

[18] R. Cao, M. Peng, E. Song, J. Qiu, High efficiency Mn^{4+} doped $Sr_2MgAl_{22}O_{36}$ red emitting phosphor for white LED, ECS J. Solid State Sci. Technol. 1 (2012) R123–R126. doi: 10.1149/2.022204jss.

[19] J. Park, G. Kim, Y.J. Kim, Luminescent properties of $CaAl_4O_7$ powders doped with Mn^{4+} ions, Ceram. Int. 39 (2013) S623–S626. 10.1016/j.ceramint.2012.10.149.

[20] A.M. Srivastava, M.G. Brik, Crystal field studies of the Mn^{4+} energy levels in the perovskite, $LaAlO_3$, Opt. Mater. 35 (2013) 1544–1548. doi: 10.1016/j.optmat.2013.03.021.

[21] Y. Zhydachevskii, A. Suchocki, A. Pajączkowska, A. Kłos, A. Szysiak, A. Reszka, Spectroscopic properties of Mn^{4+} ions in $SrLaAlO_4$, Opt. Mater. 35 (2013) 1664–1668. doi: 10.1016/j.optmat.2013.04.028.

[22] R. Cao, F. Zhang, C. Cao, X. Yu, A. Liang, S. Guo, et al., Synthesis and luminescence properties of $CaAl_2O_4$: Mn^{4+} phosphor, Opt. Mater. 38 (2014) 53–56. doi: 10.1016/j.optmat.2014.10.002.

[23] M. Peng, X. Yin, P.A. Tanner, C. Liang, P. Li, Q. Zhang, et al., Orderly-layered tetravalent manganese-doped strontium aluminate $Sr_4Al_{14}O_{25}$: Mn^{4+}: An efficient red phosphor for warm white light emitting diodes, J. Am. Ceram. Soc. 96 (2013) 2870–2876. doi: 10.1111/jace.12391.

[24] R. Cao, K.N. Sharafudeen, J. Qiu, Enhanced luminescence in $SrMgAl_xO_{17\pm\delta}$: YMn^{4+} composite phosphors, Spectrochim. Acta, A Mol. Biomol. Spectrosc. 117 (2014) 402–405. doi: 10.1016/j.saa.2013.08.025.

[25] B. Wang, H. Lin, J. Xu, H. Chen, Y. Wang, $CaMg_2Al_{16}O_{27}$:Mn^{4+}-based red phosphor: A potential color converter for high-powered warm W-LED, ACS Appl. Mater. Interfaces 6 (2014) 22905–22913. doi: 10.1021/am507316b.

[26] Y. Li, Y.-Y. Li, K. Sharafudeen, G.P. Dong, S.F. Zhou, Z.J. Ma, et al., A strategy for developing near infrared long-persistent phosphors: Taking $MAlO_3$: Mn^{4+},Ge^{4+}(M = La, Gd) as an example, J. Mater. Chem. C 2 (2014) 2019–2027. doi: 10.1039/C3TC32075H.

[27] R. Cao, Q. Xiong, W. Luo, D. Wu, X. Fen, X. Yu, Synthesis and luminescence properties of efficient red phosphors $SrAl_4O_7$: Mn^{4+},R^+(R^+=Li^+, Na^+, and K^+) for white LEDs, Ceram. Int. 41 (2015) 7191–7196. doi: 10.1016/j.ceramint.2015.02.047.

[28] Y. Jin, Y. Hu, H. Wu, H. Duan, L. Chen, Y. Fu, et al., A deep red phosphor Li_2MgTiO_4: Mn^{4+} exhibiting abnormal emission: Potential application as color converter for warm w-LEDs, Chem. Eng. J. 288 (2016) 596–607. doi: 10.1016/j.cej.2015.12.027.

[29] R. Cao, J. Zhang, W. Wang, Z. Hu, T. Chen, Y. Ye, et al., Preparation and photoluminescence characteristics of $Li_2Mg_3SnO_6$: Mn^{4+} deep red phosphor, Mater. Res. Bull. 87 (2017) 109–113. doi: 10.1016/j.materresbull.2016.11.031.

[30] S. Zhang, Y. Hu, H. Duan, Y. Fu, M. He, An efficient, broad-band red-emitting $Li_2MgTi_3O_8$: Mn^{4+} phosphor for blue-converted white LEDs, J. Alloys Compd. 693 (2017) 315–325. doi: 10.1016/j.jallcom.2016.09.203.

[31] L. Thorington, Temperature dependence of the emission of an improved manganese-activated magnesium germanate phosphor, JOSA 40 (1950) 579–583. 10.1364/JOSA.40.000579.

[32] R. Cao, W. Luo, Q. Xiong, S. Jiang, Z. Luo, J. Fu, Synthesis and photoluminescence properties of Ba_2GeO_4: Mn^{4+} novel deep red-emitting phosphor, Chem. Lett. 44 (2015) 1422–1424. doi: 10.1246/cl.150578.

[33] R. Cao, D. Ceng, X. Yu, S. Guo, Y. Wen, G. Zheng, Synthesis and luminescence properties of novel deep red emitting phosphors Li_2MgGeO_4: Mn^{4+}, Funct. Mater. Lett. 8 (2015) 1550046. doi: 10.1142/S1793604715500460.

[34] R. Cao, W. Luo, Q. Xiong, A. Liang, S. Jiang, Y. Xu, Synthesis and luminescence properties of novel red phosphors $LiRGe_2O_6$: Mn^{4+} (R= Al or Ga), J. Alloys Compd. 648 (2015) 937–941. doi: 10.1016/j.jallcom.2015.07.080.

[35] W. Shen, Y. Liu, Z. Wang, Synthesis and photo-luminescent properties of new red phosphor $SrGe_4O_9$: Mn^{4+}, Mater. Lett. 161 (2015) 140–143. doi: 10.1016/j.matlet.2015.08.091.

[36] T. Murata, T. Tanoue, M. Iwasaki, K. Morinaga, T. Hase, Fluorescence properties of Mn^{4+} in $CaAl_{12}O_{19}$ compounds as red-emitting phosphor for white LED, J. Lumin. 114 (2005) 207–212. doi: 10.1016/j.jlumin.2005.01.003.

[37] W. Shu, L. Jiang, S. Xiao, X. Yang, J. Ding, GeO_2 dopant induced enhancement of red emission in $CaAl_{12}O_{19}$: Mn^{4+} phosphor, Mat. Sci. Eng.: B 177 (2012) 274–277. doi: 10.1016/j.mseb.2011.12.016.

[38] Y. Li, Z. Xiao, L. Xu, Y. Zou, M. Guo, Fluorescence enhancement mechanism in phosphor $CaAl_{12}O_{19}$: Mn^{4+} Modified with alkali-chloride, IET Micro Nano Lett. IET 8 (2013) 254–257. 10.1049/mnl.2012.0809.

[39] Y. Pan, G. Liu, Influence of Mg^{2+} on luminescence efficiency and charge compensating mechanism in phosphor $CaAl_{12}O_{19}$: Mn^{4+}, J. Lumin. 131 (2011) 465–468. doi: 10.1016/j.jlumin.2010.11.014.

[40] Y. Chen, M. Wang, J. Wang, M. Wu, C. Wang, A high color purity red emitting phosphor $CaYAlO_4$: Mn^{4+} for LEDs, J. Solid State Light. 1 (2014) 1–8. doi: 10.1186/s40539-014-0015-4.

[41] R.D. Shannon, Revised effective ionic radii and systematic studies of interatomic distances in halides and chalcogenides, Acta Crystallogr. 32 (1976) 751–767. doi: 10.1107/S0567739476001551.

[42] T. Ye, S. Li, X. Wu, M. Xu, X. Wei, K. Wang, et al., Sol–gel preparation of efficient red phosphor Mg_2TiO_4: Mn^{4+} and XAFS investigation on the substitution of Mn^{4+} for Ti^{4+}, J. Mater. Chem. C 1 (2013) 4327–4333. doi: 10.1039/C3TC30553H.

[43] N.O. Kalaycioglu, E. Çırçır, Red phosphors in $MgAl_2Si_2O_8$ doping with Mn^{4+}, Gd^{3+} and Lu^{3+} and host-sensitized luminescence properties, J. Therm. Anal. Calorim. 111 (2013) 273–277. doi: 10.1007/s10973-012-2248-z.

[44] E. Çırçır, N.O. Kalaycioglu, Host-sensitized phosphorescence of Mn^{4+}, Eu^{3+}, and Yb^{3+} in $MgAl_2Si_2O_8$, J. Therm. Anal. Calorim. 110 (2012) 1179–1183. doi: 10.1007/s10973-011-2118-0.

[45] E. Öztürk, N. Ozpozan Kalaycioglu, Mn^{4+}-, Tb^{3+}, $^{4+}$-, and Er^{3+}-activated red phosphors in the $MgAl_2Si_2O_8$ system, J. Therm. Anal. Calorim. 115 (2014) 573–577. doi: 10.1007/s10973-013-3277-y.

[46] E. Öztürk, N.K. Ozpozan, S. Dayan, Novel red-emitting phosphors, $(Mg_{(1-x-y)}xDy_y)Al_2Si_2O_8$ and $(Mg_{(1-x-y)}Mn_xTm_y)Al_2Si_2O_8$, J. Therm. Anal. Calorim. 117 (2014) 573–578. doi: 10.1007/s10973-014-3791-6.

[47] M.G. Brik, S. Camardello, A.M. Srivastava, N.M. Avram, A. Suchocki, Spin-forbidden transitions in the spectra of transition metal ions and nephelauxetic effect, ECS J. Solid State Sci. Technol. 5 (2016) R3067–R3077. doi: 10.1149/2.0091601jss.

[48] S. Adachi, Crystal-field and Racah parameters of Mn^{4+} ion in red and deep red-emitting phosphors: Fluoride versus oxide phosphor, J. Lumin. 218 (2020) 116829. doi: 10.1016/j.jlumin.2019.116829.

[49] S. Adachi, Photoluminescence properties of Mn^{4+}-activated oxide phosphors for use in white-LED applications: A review, J. Lumin. 202 (2018) 263–281. doi: 10.1016/j.jlumin.2018.05.053.

[50] L.L. Wei, C.C. Lin, Y.Y. Wang, M.H. Fang, H. Jiao, R.S. Liu, Photoluminescent evolution induced by structural transformation through thermal treating in the red narrow-band phosphor K_2GeF_6: Mn^{4+}, ACS Appl. Mater. Interfaces 7 (2015) 10656–10659. doi: 10.1021/acsami.5b02212.

[51] Y.K. Xu, S. Adachi, Photoluminescence and Raman scattering spectra in $(NH_4)_2XF_6$: Mn^{4+}(X = Si, Ge, Sn, and Ti) red phosphors, J. Electrochem. Soc. 159 (2011) E11–E17. doi: 10.1149/2.026201jes.

[52] H.D. Nguyen, C.C. Lin, M.H. Fang, R.S. Liu, Synthesis of Na_2SiF_6: Mn^{4+}red phosphors for white LED applications by co-precipitation, J. Mater. Chem. C 2 (2014) 10268–10272. doi: 10.1039/C4TC02062F.

[53] Z. Wang, Y. Liu, Y. Zhou, Q. Zhou, H. Tan, Q. Zhang, et al., Red-emitting phosphors Na_2XF_6: Mn^{4+}(X = Si, Ge, Ti) with high colour-purity for warm white-light-emitting diodes, RSC Adv. 5 (2015) 58136–58140. doi: 10.1039/C5RA10568D.

[54] Y. Arai, S. Adachi, Optical properties of Mn^{4+}-activated Na_2SnF_6 and Cs_2SnF_6 red phosphors, J. Lumin. 131 (2011) 2652–2660. doi: 10.1016/j.jlumin.2011.06.042.

[55] R. Kasa, S. Adachi, Red and deep red emissions from cubic K_2SiF_6: Mn^{4+} and hexagonal K_2MnF_6 synthesized in $HF/KMnO_4/KHF_2/Si$ solutions, J. Electrochem. Soc. 159 (2012) J89. doi: 10.1149/2.005204jes.

[56] L. Lv, Z. Chen, G. Liu, S. Huang, Y. Pan, Optimized photoluminescence of red phosphor K_2TiF_6: Mn^{4+} synthesized at room temperature and its formation mechanism, J. Mater. Chem. C 3 (2015) 1935–1941. doi: 10.1039/C4TC02097A.

[57] L.L. Wei, C.C. Lin, M.H. Fang, M.G. Brik, S.F. Hu, H. Jiao, et al., Low-temperature co-precipitation approach to synthesize fluoride phosphors K_2MF_6: Mn^{4+}(M= Ge, Si) for white LED applications, J. Mater. Chem. C 3 (2015) 1655–1660. doi: 10.1039/C4TC02551B.

[58] Y. Arai, S. Adachi, Photoluminescent properties of $K_2SnF_6\cdot H_2O$: Mn^{4+} hydrate phosphor, J. Electrochem. Soc. 158 (2011) J81–J85. doi: 10.1149/1.3532784.

[59] H. Tan, M. Rong, Y. Zhou, Z. Yang, Z. Wang, Q. Zhang, et al., Luminescence behaviour of Mn^{4+} ions in seven coordination environments of K_3ZrF_7, Dalton Trans. 45 (2016) 9654–9660. doi: 10.1039/C6DT01693F.

[60] M.H. Fang, H.D. Nguyen, C.C. Lin, R.S. Liu, Preparation of a novel red Rb_2SiF_6: Mn^{4+} phosphor with high thermal stability through a simple one-step approach, J. Mater. Chem. C 3 (2015) 7277–7280. doi: 10.1039/C5TC01396H.

[61] Y. Arai, S. Adachi, Optical transitions and internal vibronic frequencies of $MnF_6{}^{2-}$ ions in Cs_2SiF_6 and Cs_2GeF_6 red phosphors, J. Electrochem. Soc. 158 (2011) J179–J183. doi: 10.1149/1.3576124.

[62] Q. Zhou, Y. Zhou, Y. Liu, Z. Wang, G. Chen, J. Peng, et al., A new and efficient red phosphor for solid-state lighting: Cs_2TiF_6: Mn^{4+}, J. Mater. Chem. C 3 (2015) 9615–9619. doi: 10.1039/C5TC02290H.

[63] S. Adachi, H. Abe, R. Kasa, T. Arai, Synthesis and properties of hetero-dialkaline hexafluorosilicate red phosphor $KNaSiF_6$:Mn^{4+}, J. Electrochem. Soc. 159 (2011) J34–J37. doi: 10.1149/2.064202jes.

[64] Y. Jin, M.H. Fang, M. Grinberg, S. Mahlik, T. Lesniewski, M.G. Brik, et al., Narrow red emission band fluoride phosphor $KNaSiF_6$: Mn^{4+} for warm white light-emitting diodes, ACS Appl. Mater. Interfaces 8 (2016) 11194–11203. doi: 10.1021/acsami.6b01905.

[65] D. Sekiguchi, J.I. Nara, S. Adachi, Photoluminescence and Raman scattering spectroscopies of $BaSiF_6$: Mn^{4+} red phosphor, J. Appl. Phys. 113 (2013) 183516. doi: 10.1063/1.4803880.

[66] Y. Zhou, Q. Zhou, Y. Liu, Z. Wang, H. Yang, Q. Wang, Hydrothermal synthesis and luminescent properties of $BaTiF_6$: Mn^{4+} red phosphor for LED backlighting, Mater. Res. Bull. 73 (2016) 14–20. doi: 10.1016/j.materresbull.2015.08.022.

[67] X. Jiang, Z. Chen, S. Huang, J. Wang, Y.A. Pan, Red phosphor $BaTiF_6$: Mn^{4+}: Reaction mechanism, microstructures, optical properties, and applications for white LEDs, Dalton Trans. 43 (2014) 9414–9418. doi: 10.1039/C4DT00781F.

[68] Q. Zhou, Y. Zhou, Y. Liu, L. Luo, Z. Wang, J. Peng, et al., A new red phosphor $BaGeF_6$: Mn^{4+}: Hydrothermal synthesis, photo-luminescence properties, and its application in warm white LED devices, J. Mater. Chem. C 3 (2015) 3055–3059. doi: 10.1039/C4TC02956A.

[69] R. Hoshino, T. Nakamura, S. Adachi, Synthesis and photoluminescence properties of $BaSnF_6$: Mn^{4+} red phosphor, ECS J. Solid State Sci. Technol. 5 (2016) R37. doi: 10.1149/2.0151603jss.

[70] R. Hoshino, S. Adachi, Optical spectroscopy of $ZnSiF_6\cdot 6H_2O$: Mn^{4+} red phosphor, J. Appl. Phys. 114 (2013) 213502. doi: 10.1063/1.4836896.

[71] M. Kubus, D. Enseling, T. Jüstel, H.J. Meyer, Synthesis and luminescent properties of red-emitting phosphors: $ZnSiF_6\cdot 6H_2O$ and $ZnGeF_6\cdot 6H_2O$ doped with Mn^{4+}, J. Lumin. 137 (2013) 88–92. doi: 10.1016/j.jlumin.2012.12.038.

[72] J.J.L. Leano, M.H. Fang, R.S. Liu, Critical review-narrow-band emission of nitride phosphors for light-emitting diodes: Perspectives and opportunities, ECS J. Solid State Sci. Technol. 7 (2017) R3111. doi: 10.1149/2.0161801jss.

[73] M.H. Fang, J.L. Leaño Jr, L. RS, Control of narrow-band emission in phosphor materials for application in light-emitting diodes, ACS Energy Lett. 3 (2018) 2573–2586. doi: 10.1021/acsenergylett.8b01408.

[74] H. Lian, Q. Huang, Y. Chen, K. Li, S. Liang, M. Shang, et al., Resonance Emission Enhancement (REE) for narrow band red-emitting A_2GeF_6: Mn^{4+} (A= Na, K, Rb, Cs) phosphors synthesized via a precipitation–cation exchange route, Inorg. Chem. 56 (2017) 11900–11910. doi: 10.1021/acs.inorgchem.7b01890.

[75] Q. Zhou, H. Tan, Y. Zhou, Q. Zhang, Z. Wang, J. Yan, et al., Optical performance of Mn^{4+} in a new hexa-coordinated fluorozirconate complex of Cs_2ZrF_6, J. Mater. Chem. C 4 (2016) 7443–7448. doi: 10.1039/C6TC02254E.

[76] Z. Yang, Q. Wei, M. Rong, Z. Yang, Z. Wang, Q. Zhou, et al., Novel red-emitting phosphors A_2HfF_6: Mn^{4+}(A= Rb^+, Cs^+) for solid-state lighting, Dalton Trans. 46 (2017) 9451–9456. doi: 10.1039/C7DT01842H.

[77] H. Zhu, C.C. Lin, W. Luo, S. Shu, Z. Liu, Y. Liu, et al., Highly efficient non-rare-earth red emitting phosphor for warm white light-emitting diodes, Nat. Commun. 5 (2014) 1–10. doi: 10.1038/ncomms5312.

[78] L. Yang, S. Wang, Y. Wang, J. Wang, Narrow-band red-emitting phosphor K_2SiF_6: Mn^{4+}: HF-free synthesis, surface modification, and application for warm white LEDs, ChemistrySelect 4 (2019) 3891–3897. doi: 10.1002/slct.201900988.

[79] J.E. Murphy, F. Garcia-Santamaria, A.A. Setlur, S. Sista, 62.4: PFS, K_2SiF_6: Mn^{4+}: The red-line emitting LED phosphor behind GE's TriGain Technology™ Platform, in: SID Symposium Digest of Technical Papers, Wiley Online Library (2015). doi: 10.1002/sdtp.10406.

[80] L. Wang, X. Wang, T. Kohsei, K.I. Yoshimura, M. Izumi, N. Hirosaki, et al., Highly efficient narrow-band green and red phosphors enabling wider color-gamut LED backlight for more brilliant displays, Opt. Express 23 (2015) 28707–28717. doi: 10.1364/OE.23.028707.

[81] J.H. Oh, H. Kang, M. Ko, Y.R. Do, Analysis of wide color gamut of green/red bilayered freestanding phosphor film-capped white LEDs for LCD backlight, Opt. Express 23 (2015) A791–A804. doi: 10.1364/OE.23.00A791.

[82] B.E. Yeo, Y.S. Cho, Y.D. Huh, Synthesis and photoluminescence properties of a red-emitting phosphor, K_2SiF_6: Mn^{4+}, for use in three-band white LED applications, Opt. Mater. 51 (2016) 50–55. doi: 10.1016/j.optmat.2015.11.014.

[83] Y.Y. Zhou, E.H. Song, M.G. Brik, Y.J. Wang, T. Hu, Z.G. Xia, et al., Non-equivalent Mn^{4+} doping into A_2NaScF_6 (A = K, Rb, Cs) hosts toward short fluorescence lifetime for backlight display application, J. Mater. Chem. C 7 (2019) 9203–9210. doi: 10.1039/C9TC02564B.

[84] E.H. Song, Y.Y. Zhou, Y. Wei, X.X. Han, Z.R. Tao, R.L. Qiu, et al., A thermally stable narrow-band green-emitting phosphor $MgAl_2O_4$: $Mn^{2+}$for wide color gamut backlight display application, J. Mater. Chem. C 7 (2019) 8192–8198. doi: 10.1039/C9TC02107H.

[85] Y. Zhu, Y. Liang, S. Liu, H. Li, J. Chen, Narrow-band green-emitting $Sr_2MgAl_{22}O_{36}$:Mn^{2+} phosphors with superior thermal stability and wide color gamut for backlighting display applications, Adv.Opt. Mater. 7 (2019) 1801419. doi: 10.1002/adom.201801419.

[86] G.N.A. De Guzman, M.H. Fang, C.H. Liang, Z. Bao, S.F. Hu, R.S. Liu, Near-infrared phosphors and their full potential: A review on practical applications and future perspectives, J. Lumin. 219 (2020) 116944. doi: 10.1016/j.jlumin.2019.116944.

[87] R. Filippo, E. Taralli, M. Rajteri, LEDs: Sources and intrinsically bandwidth-limited detectors, Sensors 17 (2017) 1673. doi: 10.3390/s17071673.

[88] J. Xu, J. Ueda, S. Tanabe, Toward tunable and bright deep-red persistent luminescence of Cr^{3+} in garnets, J. Am. Ceram. Soc. 100 (2017) 4033–4044. doi: 10.1111/jace.14942.

[89] Y. Zhuang, Y. Katayama, J. Ueda, S. Tanabe, A brief review on red to near-infrared persistent luminescence in transition-metal-activated phosphors, Opt. Mater. 36 (2014) 1907–1912. doi: 10.1016/j.optmat.2014.05.035.

[90] L. Zhang, S. Zhang, Z. Hao, X. Zhang, G.H. Pan, Y. Luo, et al., A high efficiency broad-band near-infrared $Ca_2LuZr_2Al_3O_{12}$: Cr^{3+} garnet phosphor for blue LED chips, J. Mater. Chem. C 6 (2018) 4967–4976. doi: 10.1039/C8TC01216D.

[91] B. Struve, G. Huber, The effect of the crystal field strength on the optical spectra of Cr^{3+} in gallium garnet laser crystals, Appl. Phys. B 36 (1985) 195–201. doi: 10.1007/BF00704574.

[92] H. Örücü, J. Collins, B. Di Bartolo, Photoluminescence spectroscopy of Cr^{3+} in $CaY_2Mg_2Ge_3O_{12}$, J. Appl. Phys. 108 (2010) 103101. doi: 10.1063/1.3510508.

[93] N. Basavaraju, S. Sharma, A. Bessière, B. Viana, D. Gourier, K.R. Priolkar, Red persistent luminescence in $MgGa_2O_4$: Cr^{3+}- a new phosphor for in vivo imaging, J. Phys. D: Appl. Phys. 46 (2013) 375401. doi: 10.1088/0022-3727/46/37/375401.

[94] A. Bessière, S.K. Sharma, N. Basavaraju, K.R. Priolkar, L. Binet, B. Viana, et al., Storage of visible light for long-lasting phosphorescence in chromium-doped zinc gallate, Chem. Mater. 26 (2014) 1365–1373. doi: 10.1021/cm403050q.

[95] Q. Bai, S. Zhao, L. Guan, Z. Wang, P. Li, Z. Xu, Design and control of the luminescence of Cr^{3+}-doped phosphors in the near-infrared i region by fitting the crystal field, Cryst. Growth Des. 18 (2018) 3178–3186. doi: 10.1021/acs.cgd.8b00273.

[96] V. Singh, R. Chakradhar, J. Rao, J.J. Zhu, Studies on red-emitting Cr^{3+} doped barium aluminate phosphor obtained by combustion process, Mater. Chem. Phys. 111 (2008) 143–148. doi: 10.1016/j.matchemphys.2008.03.033.

[97] V. Singh, R.V.S.S.N. Ravikumar, G. Sivaramaiah, J.L. Rao, S.H. Kim, Investigations of the optical and EPR properties of $LiGa_5O_8$: Cr^{3+} phosphor, Mater. Res. Bull. 61 (2015) 183–188. doi: 10.1016/j.materresbull.2014.09.092.

[98] Y. Li, Y. Li, R. Chen, K. Sharafudeen, S. Zhou, M. Gecevicius, et al., Tailoring of the trap distribution and crystal field in Cr^{3+}-doped non-gallate phosphors with near-infrared long-persistence phosphorescence, NPG Asia Mater. 7 (2015) 180–180. doi: 10.1038/am.2015.38.

[99] A. Luci, T. Castrignanò, U.M. Grassano, M. Casalboni, A.A. Kaminskii, Optical properties of $LaSr_2Ga_{11}O_{20}$ crystals containing Cr^{3+}, Phys. Rev. B: Condens. Matter 51 (1995) 1490–1494. doi: 10.1103/PhysRevB.51.1490.

[100] Y.R. Shen, M. Grinberg, J. Barzowska, K.L. Bray, J. Hanuza, P.J. Dereń, The effect of pressure on luminescence properties of Cr^{3+} ions in $LiSc(WO_4)_2$ crystals – Part I: Pressure dependent emission lineshape, J. Lumin. 116 (2006) 1–14. doi: 10.1016/j.jlumin.2005.02.010.

[101] L. Li, Y. Yu, G. Wang, L. Zhang, Z. Lin, Crystal growth, spectral properties and crystal field analysis of Cr^{3+}: $MgWO_4$.cryst, Eng. Comm. 15 (2013) 6083–6089. doi: 10.1039/C3CE40483H.

[102] I. Nikolov, X. Mateos, F. Güell, J. Massons, V. Nikolov, P. Peshev, et al., Optical properties of Cr^{3+}: $NaAl(WO_4)_2$ crystals, a new candidate for broadband laser applications, Opt. Mater. 25 (2004) 53–58. doi: 10.1016/S0925-3467(03)00216-7.

[103] B. Malysa, A. Meijerink, T. Jüstel, Temperature dependent photoluminescence of Cr^{3+} doped $Sr_8MgLa(PO_4)_7$, Opt. Mater. 85 (2018) 341–348. doi: 10.1016/j.optmat.2018.09.001.

[104] Q. Shao, H. Ding, L. Yao, J. Xu, C. Liang, Z. Li, et al, Broadband near-infrared light source derived from Cr^{3+}-doped phosphors and a blue LED chip, Opt. Lett. 43 (2018) 5251–5254. doi: 10.1364/OL.43.005251.

[105] E.V. Pestryakov, V. Petrov, A. Volkov, V. Maslov, Spectroscopic properties of Cr^{3+} ions in KTP single crystals, in: XI Feofilov Symposium on Spectroscopy of Crystals Activated by Rare-Earth and Transition Metal Ions, International Society for Optics and Photonics (2002).

[106] K. Hermanowicz, J. Hanuza, M. Maczka, P. Deren, E. Mugenski, H. Drulis, et al., Optical properties of chromium (III) in MIIn $(MoO_4)_2$ hosts, where MI= Li, Na, K, Rb, Cs, J. Phys.: Condens. Matter 13 (2001) 5807. doi: 10.1088/0953-8984/13/25/307.

[107] P. Godlewska, A. Matraszek, L. Macalik, S.M. Kaczmarek, T. Skibiński, K. Hermanowicz, et al., Structural, optical and EPR studies of Cr^{3+} doped $Na_3Ce(PO_4)_2$ orthophosphate, J. Alloys Compd. 606 (2014) 124–131. doi: 10.1016/j.jallcom.2014.03.163.

[108] G. Wang, Z. Lin, L. Zhang, Y. Huang, G. Wang, Spectral characterization and energy levels of Cr^{3+}: $Sc_2(MoO_4)_3$ crystal, J. Lumin. 129 (2009) 1398–1400. doi: 10.1016/j.jlumin.2009.07.012.

[109] B. Malysa, A. Meijerink, W. Wu, T. Jüstel, On the influence of calcium substitution to the optical properties of Cr^{3+} doped $SrSc_2O_4$, J. Lumin. 190 (2017) 234–241. doi: 10.1016/j.jlumin.2017.05.030.

[110] M. Back, E. Trave, J. Ueda, S. Tanabe, Ratiometric optical thermometer based on dual near-infrared emission in Cr^{3+}-doped bismuth-based gallate host, Chem. Mater. 28 (2016) 8347–8356. doi: 10.1021/acs.chemmater.6b03625.

[111] V. Singh, G. Sivaramaiah, J. Rao, S. Kim, EPR and optical investigations of $LaMgAl_{11}O_{19}$: Cr^{3+} phosphor, Mater. Res. Bull. 60 (2014) 397–400. doi: 10.1016/j.materresbull.2014.08.038.

[112] Y. Li, S. Ye, Q. Zhang, Ultra-broadband near-infrared luminescence of ordered–disordered multi-sited Cr^{3+} in $La_3Ga_{5.5}Nb_{0.5}O_{14}$: Cr^{3+}, J. Mater. Chem. C 2 (2014) 4636–4641. doi: 10.1039/C4TC00243A.

[113] V. Singh, R.P.S. Chakradhar, J.L. Rao, S.H. Kim, EPR and luminescence studies of Cr^{3+} doped $MgSrAl_{10}O_{17}$ phosphor synthesized by a low-temperature solution combustion route, J. Lumin. 154 (2014) 328–333. doi: 10.1016/j.jlumin.2014.03.035.

[114] X. Wu, D. Xu, W. Li, T. Wang, L. Cao, J. Meng, Synthesis and luminescence of novel near-infrared emitting $BaZrSi_3O_9$: Cr^{3+} phosphors, Lumin 32 (2017) 1554–1560. doi: 10.1002/bio.3359.

[115] J. Xu, D. Chen, Y. Yu, W. Zhu, J. Zhou, Y. Wang, Cr^{3+}: $SrGa_{12}O_{19}$: A broadband near-infrared long-persistent phosphor, Chem. Asian J. 9 (2014) 1020–1025. doi: 10.1002/asia.201400009.

[116] C. Lee, Z. Bao, M.H. Fang, T. Lesniewski, S. Mahlik, M. Grinberg, et al., Chromium(III)-doped fluoride phosphors with broadband infrared emission for light-emitting diodes, Inorg. Chem. 59 (2020) 376–385. doi: 10.1021/acs.inorgchem.9b02630.

[117] L.P. Sosman, A.D. Tavares Jr, R.J.M. da Fonseca, T. Abritta, N.M. Khaidukov, Study of optical properties of Cr^{3+} ions in Cs_2NaAlF_6 single crystals, Solid State Commun. 114 (2000) 661–665. doi: 10.1016/S0038-1098(00)00107-1.

[118] RJM da Fonseca, A.D. Tavares, P.S. Silva, T. Abritta, N.M. Khaidukov, Investigation of Cr^{3+} ions in Cs_2NaGaF_6 single crystals by optical spectroscopy, Solid State Commun. 110 (1999) 519–524. doi: 10.1016/S0038-1098(99)00008-3.

[119] N. Barnes, S. Benson, F. Duarte, C. Freed, D. Harris, R. Sze, et al., Tunable Lasers Handbook, Academic, San Diego (1995), pp. 219–291.

[120] S. Adachi, Photoluminescence spectroscopy and crystal-field parameters of Cr^{3+} ion in red and deep red-emitting phosphors, ECS J. Solid State Sci. Technol. 8 (2019) R164–R168. doi: 10.1149/2.0061912jss.

[121] D. Yu, Y. Zhou, C. Ma, J.H. Melman, K.M. Baroudi, M. LaCapra, et al., Non-rare-earth Na_3AlF_6: Cr^{3+} phosphors for far-red light-emitting diodes, ACS Appl. Electron. Mater. 1 (2019) 2325–2333. doi: 10.1021/acsaelm.9b00527.

[122] D. Hayashi, A.M.V. Dongen, J. Boerekamp, S. Spoor, G. Lucassen, J. Schleipen, A broadband LED source in visible to short-wave-infrared wavelengths for spectral tumor diagnostics, Appl. Phys. Lett. 110 (2017) 233701. doi: 10.1063/1.4985015.

[123] V. Rajendran, M.H. Fang, G.N.D. Guzman, T. Lesniewski, S. Mahlik, M. Grinberg, et al., Super broadband near-infrared phosphors with high radiant flux as future light sources for spectroscopy applications, ACS Energy Lett. 3 (2018) 2679–2684. 10.1021/acsenergylett.8b01643.

[124] Q. Shao, H. Ding, L. Yao, J. Xu, C. Liang, J. Jiang, Photoluminescence properties of a $ScBO_3$: Cr^{3+} phosphor and its applications for broadband near-infrared LEDs, RSC Adv. 8 (2018) 12035–12042. doi: 10.1039/C8RA01084F.

[125] L. Zhang, D. Wang, Z. Hao, X. Zhang, G. Pan, H. Wu, et al., Cr^{3+}-doped broadband NIR garnet phosphor with enhanced luminescence and its application in NIR spectroscopy, Adv. Optical Mater. 7 (2019) 1900185. doi: 10.1002/adom.201900185.

[126] V. Rajendran, T. Lesniewski, S. Mahlik, M. Grinberg, G. Leniec, S.M. Kaczmarek, et al., Ultra-broadband phosphors converted near-infrared light emitting diode with efficient radiant power for spectroscopy applications, ACS Photonics 6 (2019) 3215–3224. doi: 10.1021/acsphotonics.9b01086.

[127] X. Xu, Q. Shao, L. Yao, Y. Dong, J. Jiang, Highly efficient and thermally stable Cr^{3+}-activated silicate phosphors for broadband near-infrared LED applications, Chem. Eng. J. 383 (2020) 123108. doi: 10.1016/j.cej.2019.123108.

[128] K. Cleveland Broadband IR LED from Osram opto semiconductors enables food analytics applications, in: LEDs Magazine, and Business/Energy/Technology Journalist Nov 21, 2016, https://www.ledsmagazine.com/ugc/2016/11/21/worlds-first-broadband-infrared-led-from-osram.3.leftinheritedbottom_standard.html.

[129] M. Halper Osram's latest infrared LED identifies what's in your food, in: LEDs Magazine, and Business/Energy/Technology Journalist Sep 11, 2018, https://www.ledsmagazine.com/articles/2018/09/osram-s-latest-infrared-led-identifies-what-s-in-your-food.html.

[130] S. Tragl, D. Eisert, S. Lange, N. Kaufmann, A. Martin, K. Bergenek Radiation-Emitting Optoelectronic Component, A1 W (Ed.), OSRAM OPTO SEMICONDUCTORS GMBH German-[DE] (2016).

[131] V. Rajendran, M.H. Fang, R.S. Liu, H. Chang, K.M. Lu, L. Yan-Shen, et al., Phosphor, Method for Preparing Phosphor, Optoelectronic Component, and Method for Producing Optoelectronic Component, States U (Ed.), Google Patents, United States (2019).

[132] Y. Xu, Nature and source of light for plant factory, in: Plant Factory Using Artificial Light, Elsevier (2019), pp. 47–69. doi: 10.1016/B978-0-12-813973-8.00002-6.

[133] V.D. Kreslavski, D.A. Los, F.J. Schmitt, S.K. Zharmukhamedov, V.V. Kuznetsov, S.I. Allakhverdiev, The impact of the phytochromes on photosynthetic processes, BBA – Bioenergetics 1859 (2018) 400–408. doi: 10.1016/j.bbabio.2018.03.003.

[134] S.D. Gupta, A. Dutta Agarwal, Light Emitting Diodes for Agriculture, Springer Nature Singapore Pte Ltd (2017).

[135] G. Morelli, I. Ruberti, Light and shade in the photocontrol of arabidopsis growth, Trends Plant Sci. 7 (2002) 399–404. doi: 10.1016/S1360-1385(02)02314-2.

[136] Q. Meng, N. Kelly, E.S. Runkle, Substituting green or far-red radiation for blue radiation induces shade avoidance and promotes growth in lettuce and kale, Environ. Exp. Bot. 162 (2019) 383–391. doi: 10.1016/j.envexpbot.2019.03.016.

[137] Y. Park, E.S. Runkle, Far-red radiation promotes growth of seedlings by increasing leaf expansion and whole-plant net assimilation, Environ. Exp. Bot. 136 (2017) 41–49. doi: 10.1016/j.envexpbot.2016.12.013.

[138] H.Y. Yuan, S. Saha, A. Vandenberg, K.E. Bett, Flowering and growth responses of cultivated lentil and wild Lens germplasm toward the differences in red to far-red ratio and photosynthetically active radiation, Front. Plant Sci. 8 (2017). doi: 10.3389/fpls.2017.00386.

[139] P. Kalaitzoglou, W. van Ieperen, J. Harbinson, M. van der Meer, S. Martinakos, K. Weerheim, et al., Effects of continuous or end-of-day far-red light on tomato plant growth, morphology, light absorption, and fruit production, Front. Plant Sci., 10 (2019). doi: 10.3389/fpls.2019.00322.

[140] M. Back, J. Ueda, M.G. Brik, T. Lesniewski, M. Grinberg, S. Tanabe, Revisiting Cr^{3+}-doped $Bi_2Ga_4O_9$ spectroscopy: Crystal field effect and optical thermometric behavior of near-infrared-emitting singly-activated phosphors, ACS Appl. Mater. Interfaces 10 (2018) 41512–41524. doi: 10.1021/acsami.8b15607.

[141] J. Ueda, M. Back, M.G. Brik, Y. Zhuang, M. Grinberg, S. Tanabe, Ratiometric optical thermometry using deep red luminescence from $^4T_2$ and ^2E states of Cr^{3+} in $ZnGa_2O_4$ host, Opt. Mater. 85 (2018) 510–516. doi: 10.1016/j.optmat.2018.09.013.

[142] Q. Wang, Z. Liang, J. Luo, Y. Yang, Z. Mu, X. Zhang, et al., Ratiometric optical thermometer with high sensitivity based on dual far-red emission of Cr^{3+} in $Sr_2MgAl_{22}O_{36}$, Ceram. Int. 46 (2020) 5008–5014. doi: 10.1016/j.ceramint.2019.10.241.

[143] B. Malysa, A. Meijerink, T. Jüstel, Temperature dependent Cr^{3+} photoluminescence in garnets of the type $X_3Sc_2Ga_3O_{12}$(X= Lu, Y, Gd, La), J. Lumin. 202 (2018) 523–531. doi: 10.1016/j.jlumin.2018.05.076.

[144] B. Malysa, A. Meijerink, T. Jüstel, Temperature dependent photoluminescence of Cr^{3+} doped $Sr_8MgLa(PO_4)_7$, Opt. Mater. 85 (2018) 341–348. doi: 10.1016/j.optmat.2018.09.001.

[145] W.T. Huang, C.L. Cheng, Z. Bao, C.W. Yang, K.M. Lu, C.Y. Kang, et al., Broadband Cr^{3+}, Sn^{4+}-doped oxide nanophosphors for infrared mini light-emitting diodes, Angew. Chem. Int. Ed. 58 (2019) 2069–2072. doi: 10.1002/anie.201813340.

Florian Baur, Thomas Jüstel

Chapter 9

UV-emitting phosphors: from fundamentals to applications

9.1 Historical introduction

Ultraviolet (UV)-emitting phosphors were researched as early as the first quarter of the twentieth century, focusing mainly on Tl^{+}-, Bi^{3+}-, and Pb^{2+}-activated phosphors [1]. In the 1950s, Ce^{3+} was found to show emission in the UV range in many hosts such as $Ca_3(PO_4)_2$. In the early 1970s, it was discovered that Pr^{3+} can show emission in the UV as a result of radiative 5*d*–4*f* transitions [2]. In 1979, the first report on $SrB_4O_7:Eu^{2+}$ with an emission maximum at 368 nm was published, showing that Eu^{2+} emission can be shifted to the UV range in specific hosts [3]. That phosphor has been used in tanning lamps since the 1990s to increase the relative UV-A emission intensity.

Originally, cathode ray tubes, Hg discharge, or Xe_2^* excimer lamps were used to excite these phosphors. With the advent of a wider range of excimer discharge sources and, in particular, UV-emitting LEDs, the choice of excitation wavelengths grew and allowed the use of a larger number of UV-emitting phosphors. This chapter provides an overview of the primary UV radiation sources for excitation and the main UV-emitting phosphors that can be used for conversion.

9.2 UV radiation sources

Downconversion, that is, the conversion of high-energy, short-wavelength radiation into lower energy, that is, longer wavelength radiation is the most common mechanism of luminescence. Therefore, to excite UV-emitting phosphors, a source is required that emits primary radiation with a wavelength shorter than that of the UV-emitting phosphor in question. For the sake of energy efficiency, the difference in wavelength between excitation and emission should be as small as possible, since the difference in radiative energy is lost to the luminescence process. In addition to the source's efficiency, the wavelength of its emission is an important criterion. There are three major types of UV sources: Hg low-pressure discharge, excimer discharge, and light-emitting diodes (LEDs) which are discussed in the following paragraphs.

https://doi.org/10.1515/9783110607871-009

9.2.1 Hg low-pressure discharge lamps

Low-pressure mercury discharge lamps operate at a pressure of typically less than 10 mbar and employ the noble gases argon or neon as filling or buffer gas. A high voltage is applied between a heated cathode and the anode in the lamp, resulting in the thermal emission of electrons from the cathode. Due to the low partial pressure of Hg in these lamps, narrow line emission is observed with almost no broadening or reabsorption. The main emission lines of Hg in these lamps are at 185.0 and 253.7 nm, respectively, that is, in the UV-C spectral region. The primary emission can be either used directly or it can be converted into UV-B or UV-A radiation. In order to be able to use the 185 nm emission, the lamp's tube must not exhibit any absorption in this range, which is ensured by using high-purity silica as the tube material. The UV-C output of conventional low-pressure Hg lamps decreases with increasing temperature because the Hg vapor pressure varies with temperature. The highest output efficiency is usually observed at around 40 °C.

Amalgam lamps that circumvent this problem to some degree by using an amalgam such as (In,Hg) or (Au,Hg) that serves as a reservoir for Hg in the lamp have been developed. If the Hg vapor pressure is too high, the amalgam will absorb some of the Hg, while a low vapor pressure will cause the amalgam to release Hg into the gas phase. Such lamps achieve the highest UV output efficiency at temperatures around 100 °C and provide much greater overall temperature stability of the UV output. Amalgam lamps can contain a larger amount of Hg than conventional Hg discharge lamps of similar size and therefore allow a higher power density of about 2–3 W/cm.

A disadvantage of these types of lamps is the use of toxic mercury and the poor switchability and temperature stability. The Minamata convention, signed by 137 countries so far (as of 2021), regulates the use of mercury worldwide. From 2020, the production and sale of Hg discharge lamps will be severely restricted and Hg-free alternatives must be used. The poor switchability of discharge lamps in general is a problem in applications where the lamp is only used for short periods of time such as disinfection.

9.2.2 Dielectric barrier Xe excimer discharge lamps

Xe excimer discharge lamps are vacuum UV (VUV)-emitting radiation sources. Dielectric barrier discharge (DBD) lamps operate on the principle of generating plasma by applying an alternating electrical field with a frequency of around 30 kHz and an initial voltage of several kilovolts. In the plasma excited Xe dimers, so-called excimers (Xe_2^*) are formed. Upon returning to the ground state, the Xe excimers predominantly show emission at 172 nm (2nd continuum) and at 152 nm (1st continuum). In most lamps, the 172 nm emission is dominating the spectrum, and the 152 nm emission is only observed in significant intensity if the Xe pressure is below ambient pressure. Typical values for the operating pressure of 172 nm-emitting lamps are between 250 and 600 mbar.

Usually, the primary radiation of a Xe excimer lamp is not used directly, but converted into longer wavelength radiation by means of a phosphor coating. For a choice of respective phosphors, please see Section 9.5. If the primary emission of the excimer lamp is to be used, the lamp's tube consists of pure silica glass which is sufficiently transparent in the VUV to UV-C region.

9.2.3 Other excimer discharges ($KrCl^*$, $XeBr^*$, and $XeCl^*$)

The fundamental working principle of the DBD lamp can also be applied to other excited moieties. Instead of an excited dimer, or excimer, excited heterodimers, or exciplexes, are formed. Please note that frequently the name "excimer" is used for these compounds. Prominent examples are $KrCl^*$, $XeBr^*$, and $XeCl^*$, which arise from lamp fillings of a noble gas and a halogen. Table 9.1 lists commonly used excimers with the respective reactants and peak emission wavelength.

Table 9.1: Various common excimers used in DBD lamps with the reactants and the peak emission wavelength.

Excimer	Reactants	Peak emission (nm)
KrI^*	$Kr + I_2$	191
ArF^*	$Ar + F_2$	193
$KrCl^*$	$Kr + Cl_2$	222
KrF^*	$Kr + NF_3$	248
$XeBr^*$	$Xe + Br_2$	282
$XeCl^*$	$Xe + Cl_2$	308

Of these, specifically the $KrCl^*$ excimer has gained much attention in recent years due to the apparent property of the 222 nm radiation to effectively inactivate germs while not causing harm in the human or animal skin since the radiation will be fully absorbed in the outmost layer of dead skin cells [4]. This would enable the use of such lamps for disinfection purposes in the presence of humans for prolonged periods of time and higher power densities. However, as of today, UV radiation in that spectral region is not treated differently by law than UV-C radiation in general. The respective laws might be adapted though to reflect the presumed lower hazard of radiation damage.

9.2.4 Inorganic (Al,Ga)N and (In,Ga)N LEDs

LEDs are now used in many areas where conventional UV sources such as incandescent lamps or discharge lamps dominated the market a decade or two ago. This is due to their high efficiency, low-voltage drive, long lifetime, low price, high power density, and small size [5]. However, LEDs are still less commonly used in the UV range because their efficiency in this spectral region is low compared to conventional sources such as discussed in the previous sections [6].

In terms of their emission wavelength, the III–V semiconductors have a natural limit set by AlN's band gap of about 6.0 eV, which corresponds to an emission wavelength of 210 nm. GaN has a band gap of 3.4 eV, which corresponds to a wavelength of 360 nm. Therefore, solid solutions of (Al,Ga)N can be used to achieve emission bands between 210 and 360 nm. The efficiency of such LEDs is low, especially for short wavelength UV-C [7]. Recent reports have demonstrated a wall-plug efficiency of 0.37% for a 230–237 nm LED. Commercially available LED types can reach efficiencies of up to 10% for emission in the UV-C range between 260 and 280 nm [8]. For UV-A LEDs, the efficiency is much higher and already reaches 70%.

UV-C radiation puts a high demand on all parts of the LED, especially the encapsulation which is usually made of silicon or epoxy resin. These materials show declining transparency when damaged by the radiation. The lifetime of UV-emitting LEDs is therefore considerably shorter than that of other types of LEDs. For UV-C emitting LEDs, a significant decrease in output power has been observed after only 2,000 h of operation. Due to the lower photon energy, UV-A LEDs have a much longer lifetime of more than 8,000 h. However, sufficient cooling is essential to ensure that the LED can operate at high efficiency over longer periods of operation.

In 2021, the price of UV LEDs in $\$ \text{ mW}^{-1}$ is still relatively high, but has seen a steep decline from around $\$1{,}000 \text{ mW}^{-1}$ in the early 2000s to less than $\$1 \text{ mW}^{-1}$ in 2019. Based on this observation, it is reasonable to assume that the market share of UV LEDs will continue to increase. However, the fundamental limit of III–V semiconductors of 210 nm emission wavelength will prevent LEDs from being used as primary emitters in this range for the foreseeable future.

9.3 Fundamentals of UV-emitting phosphors

9.3.1 Host materials

Compounds that can be considered as host materials for UV phosphors must meet certain criteria. It is generally accepted that the activator ground state and excited state must be located within the band gap of the host material. Otherwise, quantum efficiency is low due to energy migration through the conduction band. While this is true for all solid-state phosphors, it places additional requirements on the host materials for UV phosphors because the energy gap between the ground state and the excited state is large. The VUV spectral range (100–200 nm) corresponds to 6–12 eV, and the energy of UV-A radiation (315–380 nm) still amounts to 3–4 eV. Thus, to ensure with reasonable certainty that neither the ground nor excited state of the activator is in the valence or conduction band, the host material should have a wide band gap of at least 5 eV for UV-A-emitting phosphors and about 10 eV for VUV-emitting phosphors. Oxide compounds that generally meet this criterion include silicates, phosphates, borates, and aluminates. Transition metal oxides usually have smaller band gaps due to the low-lying unoccupied *d* orbitals. Fluorides often have large band gaps, with MgF_2 and LiF exhibiting band gaps of more than 11 eV.

In addition, a suitable host compound must have sufficient stability to high-energy radiation. In the case of orthosilicates, it has been found that high energy radiation can cause the release of an electron from an $[SiO_4]^{4-}$ tetrahedron. This electron can be trapped and localized or move freely through the material to reduce a cation to a lower oxidation state. A similar mechanism has been observed in phosphates, leading to the formation of P^{4+} [9]. These defects cause competing absorption and thus quenching and. Therefore, a decrease of the photoluminescence quantum yield of the phosphor is observed. Table 9.2 lists a number of potential host compounds for UV emission and their respective band gap.

Table 9.2: Selected compounds suitable for use as phosphor hosts with their approximate band gap in eV and corresponding transition wavelength in nm.

Host compound	Band gap (eV)	Band gap (nm)
$BaSi_2O_5$	6.0	207
Y_2SiO_5	6.4	194
YBO_3	7.0	177
$Y_3Al_5O_{12}$	7.3	170
$LaMgAl_{11}O_{19}$	7.5	165
Lu_2SiO_5	7.5	165
$Y_2Si_2O_7$	7.6	163
$Lu_3Al_5O_{12}$	7.8	159
$Lu_2Si_2O_7$	7.8	159
YPO_4	8.0	155
$LuPO_4$	8.2	151
$LaPO_4$	8.6	145
CaF_2	12.0	105

9.3.2 Activator ions

The requirements on the activator ions are similar to those placed on activators in general: a high absorption in the chosen excitation region, high probability of radiative transition versus nonradiative transition, and emission in the desired UV spectral region. Furthermore, the oxidation state of the activator must be stable toward photoionization. A constraint specific to UV-emitting activators is the requirement for high stability towards ionizing radiation. During operation, the phosphor is constantly irradiated by the primary emission from the excitation source. It is well-known that this can lead to degradation of the phosphor host. Usually, oxidation of an atom occurs and the released electron can either occupy a site in the crystal as a color center or bind to another atom. Thus, the activator ion has to have a stable valence state to prevent both oxidation and reduction by ionizing radiation.

In general, an activator for emission in the UV has to exhibit a large energy gap between the electronic states involved in the radiative transition [10]. In many activators that show *s*–*p* or 4*f*–5*d* luminescence, the energy gap between the states is too small even in the free ion. Since the energy distance between the states is largest for the free ion and is decreased due to crystal field and nephelauxetic effect in a phosphor host this renders them fundamentally unsuitable for luminescence in the UV range.

Simplified energy level diagrams of s^2 ions and $4f^n$ ions are presented in Figure 9.1 [11]. The $4f^n$ rare earth cations can exhibit 5*d*–4*f* luminescence as well as 4*f*–4*f* luminescence. The 5*d* band is often at sufficiently high energy to result in UV emission due to the respective 5*d*–4*f* transition. However, most trivalent rare earth ions possess a large number of 4*f* states that consequently have only a small energy separation between them, resulting in emission in the visible range.

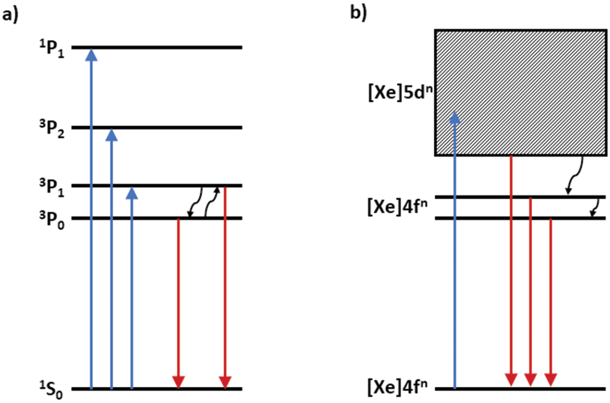

Figure 9.1: Schematic energy level diagram of (a) an s^2 ion and (b) a $4f^n$ ion with the excitation transitions (blue arrow), radiative transitions (red arrows), and nonradiative transitions (black arrows).

In conclusion, the result is a limited choice of activators as listed in Table 9.3. Thallium (Tl) and lead (Pb) are toxic and therefore problematic for commercial application. Hence, most UV-emitting phosphors that have widespread use rely on Bi^{3+}, Pr^{3+}, Ce^{3+}, or Eu^{2+} as activators. Figure 9.2 depicts the excitation spectra of various UV-emitting phosphors. The excitability in the various UV regions determines which excitation source is most suitable for a specific phosphor. The different peaks in the excitation spectrum correspond to transitions of the activator ion and in most cases of overlapping band gap transitions of the host. Excitation via the band gap usually results in a decreased intensity, however.

Table 9.3: List of selected activators with typical excitation and emission ranges in the UV.

Activator ion	**Excitation range**	**Emission range**	**Transition type**	**Energy gap 4f–5d (free ion, cm^{-1})**
Nd^{3+}	VUV	VUV	4*f*–5*d*	72,100
Tl^{+}	UV-C	UV-C to UV-A	6*s*–6*p*	–
Bi^{3+}	VUV to UV-A	UV-C to UV-A	6*s*–6*p*	–
Pr^{3+}	VUV to UV-A	UV-C to UV-A	4*f*–5*d*	61,580
Pb^{2+}	UV-C to UV-A	UV-C to UV-A	6*s*–6*p*	–
Gd^{3+}	UV-C	UV-B	4*f*–4*f*	95,200
Ce^{3+}	UV-C to UV-A	UV-B to UV-A	5*f*–5*d*	49,340
Tm^{3+}	UV-C to UV-B	UV-A	4*f*–5*d*	78,600
Eu^{2+}	UV-B to UV-A	UV-A	4*f*–5*d*	34,000

Note: The specific wavelength depends on the choice of host and can also be located outside the UV range. Free ion energies were taken from Dorenbos [12, 13].

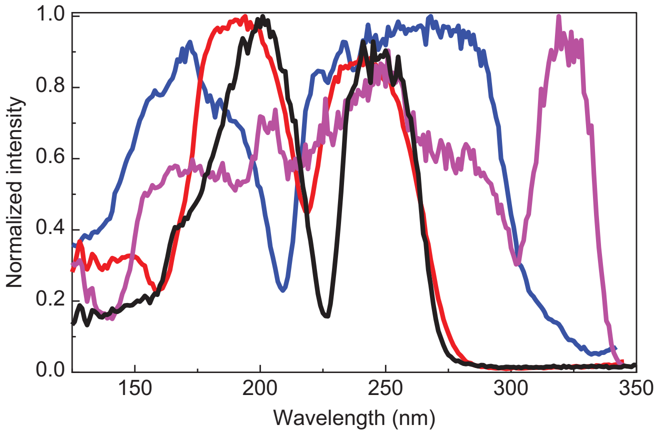

Figure 9.2: Excitation spectra of $LaMgAl_{11}O_{19}:Ce^{3+}$ (blue line), $BaSi_2O_5:Pb^{2+}$ (red line), $Sr_2MgSi_2O_7:Pb^{2+}$ (black line), and $YPO_4:Ce^{3+}$ (magenta line).

9.4 UV phosphors for Hg discharge lamps

To obtain a continuous spectrum from a low-pressure Hg discharge lamp, the primary line emission has to be converted by means of a phosphor. The prominent Hg emission line is located at 253.7 nm and hence can be used to excite downconversion photoluminescence in the UV-B and UV-A region. For UV-C-emitting phosphors the 185.0 nm line of Hg can be utilized. Combining both phosphors for 185.0 and 253.7 nm excitation in a single lamp is challenging as the latter type of phosphor will reabsorb the UV-C emission of the former which decreases overall efficiency. If solely UV-C-emitting phosphors are used, the corresponding lamp spectrum will show both the emission of the phosphor and the 253.7 nm line of Hg, that is, a quasi-continuous spectrum.

9.4.1 UV-A and UV-B phosphors

The most prominent activators for conversion of the 253.7 nm line of Hg to UV-B and UV-A radiation are Ce^{3+}, Pb^{2+}, and Bi^{3+}. By the thorough choice of the host, the luminescence properties can be controlled to closely match the desired characteristics. Figure 9.3(a) shows the emission, excitation, and reflection spectrum of $LaMgAl_{11}O_{19}:Ce^{3+}$. The excitation maximum lies around 275 nm, but the band is broad enough to allow efficient excitation with a low-pressure Hg discharge. As depicted in Figure 9.3(b), $YPO_4:Ce^{3+}$ has similar emission properties, albeit with excitation peaking at 250 nm and therefore a better match for the primary Hg discharge emission. In $YPO_4:Ce^{3+}$, the two emission bands of Ce^{3+} are discernible; they are caused by transitions to $^2F_{7/2}$ and $^2F_{5/2}$ states of Ce^{3+}. The structures observed in the excitation band are due to transitions to the various 5*d* states and overlapping band gap transitions of the host (cf. Table 9.2).

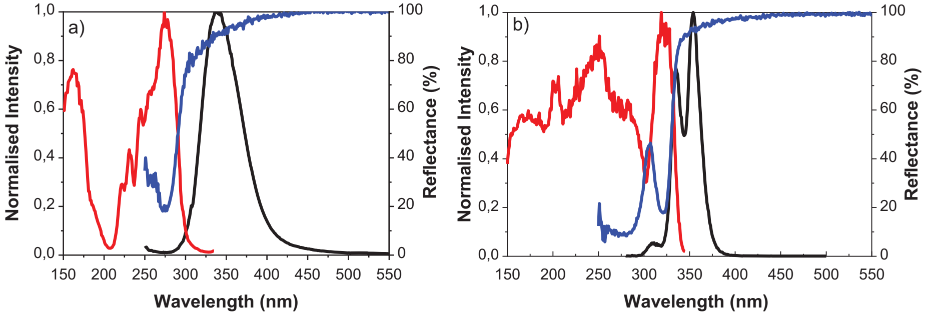

Figure 9.3: Emission (black lines), excitation (red lines), and reflection spectrum (blue lines) of (a) $LaMgAl_{11}O_{19}:Ce^{3+}$ (λ_{ex} = 160 nm, λ_{em} = 345 nm) and (b) $YPO_4:Ce^{3+}$ (λ_{ex} = 160 nm, λ_{ex} = 354 nm).

In Figure 9.4, the spectra of two Pb^{2+}-activated UV-A-emitting phosphors are presented. The underlying 6*s*–6*p* transitions result in a larger Stokes Shift than in case of Ce^{3+}. Therefore, the phosphors can be excited with high efficiency with a Hg discharge without reabsorption and the full-width at half-maximum (FWHM) of the bands is larger. The larger Stokes Shift, however, usually leads to an inferior quantum efficiency. Legislature concerning hazardous substances makes the commercial use of substances containing lead more difficult or even impossible, and Pb^{2+}-activated phosphors will not play a role in commercial UV radiation sources in the near future.

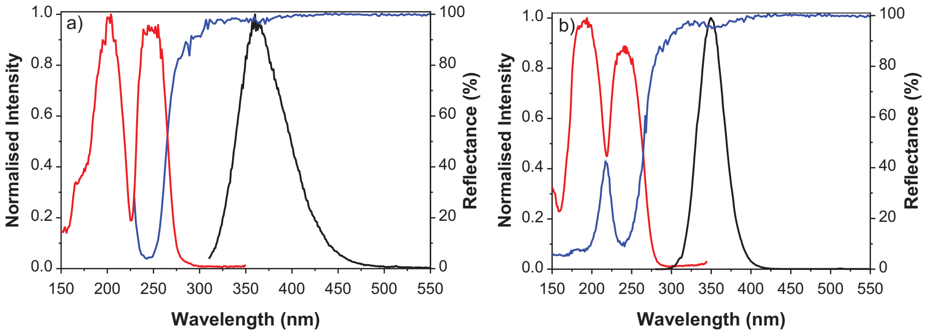

Figure 9.4: Emission (black lines), excitation (red lines), and reflection spectrum (blue lines) of (a) $Sr_2MgSi_2O_7:Pb^{2+}$ (λ_{ex} = 250 nm, λ_{em} = 362 nm) and (b) $BaSi_2O_5:Pb^{2+}$ (λ_{ex} = 192 nm, λ_{ex} = 349 nm).

9.4.2 UV-B and UV-C phosphors for 185.0 nm line conversion

Figure 9.5 depicts the spectra of two UV-B-emitting phosphors, namely, $Lu_3Al_5O_{12}:Gd^{3+}$ and $Lu_3Al_5O_{12}:Bi^{3+},Gd^{3+}$. Due to its half-filled 4*f* shell, Gd^{3+} only exhibits a large number of 4*f* states; however, only a few 4*f*–4*f* transitions are located in the suitable range below 70,000 cm^{-1}. These transitions have a small absorption cross-section due to their spin- and parity-forbidden nature. However, the excitation spectrum in Figure 9.5(a) demonstrates that Gd^{3+} can be excited via the 185.0 nm line of Hg via the band gap of the host. The emission generated by the $^6P_{7/2}$ to $^8S_{7/2}$ transition of Gd^{3+} is in the form of a line at 311 nm without any overspill to other spectral regions. That makes Gd^{3+} a good choice for a highly brilliant UV-B radiation source. $Lu_3Al_5O_{12}:Bi^{3+}$ is another example of a UV-B phosphor that can be excited via the 185.0 nm Hg line. It can be excited via the host or the 6*s*–6*p* transition at 275 nm. Furthermore, by co-doping Bi^{3+} and Gd^{3+} into the host, Bi^{3+} will act as a sensitizer for Gd^{3+} as depicted in Figure 9.5(b). The

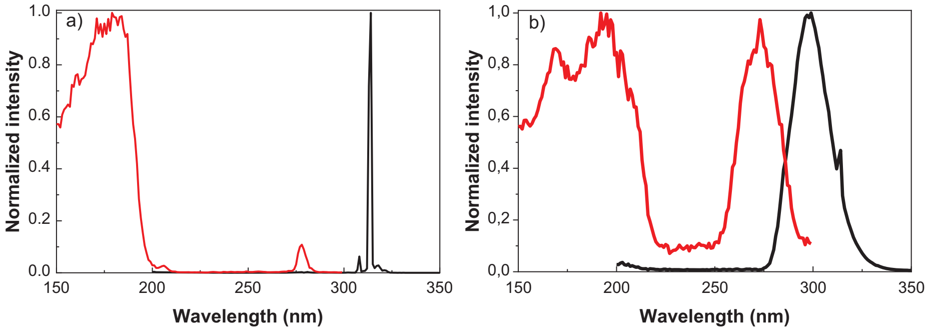

Figure 9.5: Emission (black lines) and excitation (red lines) spectrum of (a) $Lu_3Al_5O_{12}:Gd^{3+}$ (λ_{ex} = 160 nm, λ_{em} = 311 nm) and (b) $Lu_3Al_5O_{12}:Bi^{3+}$, Gd^{3+} (λ_{ex} = 160 nm, λ_{ex} = 300 nm).

emission consists of the 6*p*–6*s* band of Bi^{3+}, centered at 300 nm, and the aforementioned 311 nm line of Gd^{3+}. By adjusting the Bi^{3+} and Gd^{3+} concentrations, the relative intensity of the 300 nm band and the 311 nm line can be controlled.

9.5 UV phosphors for excimer discharge lamps

Driven by the advances in plasma display panel (PDP) technology and Hg-free fluorescent lamps, the interest on highly efficient VUV phosphors is steadily growing since the end of the twentieth century. While the PDP technology has been widely replaced by LED backlit LC or OLED displays, the need for an Hg-free UV radiation source is considered more important today than in recent decades as the Minamata convention placed a ban on Hg discharge lamps for many applications. Thus, despite the lower efficiency of Xe excimer discharge lamps compared to conventional Hg fluorescent lamps they can be considered the main viable alternative for UV radiation sources with a primary emission wavelength shorter than 200 nm. The III–V semiconductor LEDs have a minimal emission wavelength of about 210 nm, constituted by the band gap of pure AlN.

Xe excimer discharge lamps can thus be used as Hg-free UV radiation sources by the application of UV-emitting, VUV-excitable phosphors. Such lamps could generate an arbitrary spectrum in the 190–400 nm range rendering them applicable for disinfection, purification, and photochemistry purposes. To that end, efficient and stable UV-C, UV-B, and UV-A phosphors have to be developed.

9.5.1 UV-C-emitting phosphors

Figure 9.6 depicts the emission spectra of three different Pb^{2+}-activated phosphors. The peak emission wavelength depends strongly on the host and can be further modulated by preparing solid solutions such as $(Ca,Mg)SO_4:Pb^{2+}$. These phosphors can be efficiently excited via the 172 nm VUV radiation of a Xe excimer discharge. However, they suffer from somewhat sensitivity towards water and have been found to incorporate Xe upon prolonged operation in such lamps.

Bi^{3+} is a suitable alternative to Pb^{2+} as an activator for UV-C-emitting phosphors. Figure 9.7 depicts the emission spectra of $LuPO_4:Bi^{3+}$ and $YPO_4:Bi^{3+}$ upon excitation with 172 nm Xe excimer radiation. The emission bands exhibit a comparatively narrow FWHM and the phosphors show a very good chemical stability and physical stability toward ionizing radiation.

As a third alternative Pr^{3+} is widely utilized. Pr^{3+} can show emission from both 5d-4f transitions and 4f-4f transitions, the former manifest themselves in the form of bands in the UV region, whereas the latter result in lines in the visible range. The relative intensity of these two types of transitions is a function of the host and strongly

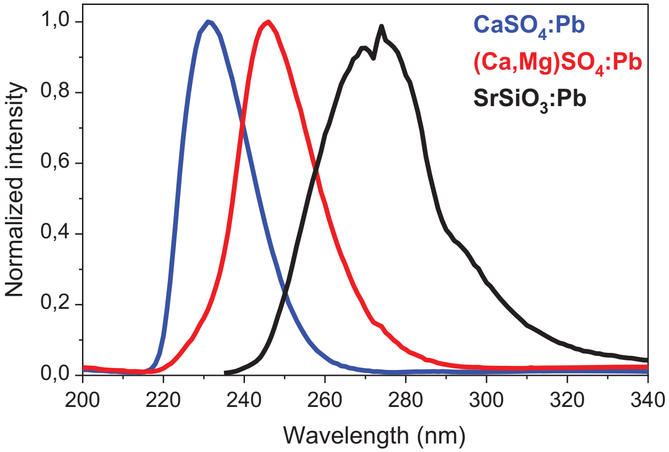

Figure 9.6: Emission spectra of $CaSO_4$:Pb^{2+} (blue line), (Ca,Mg)SO_4:Pb^{2+} (red line), and $SrSiO_3$:Pb^{2+} (black line) upon 172 nm excitation.

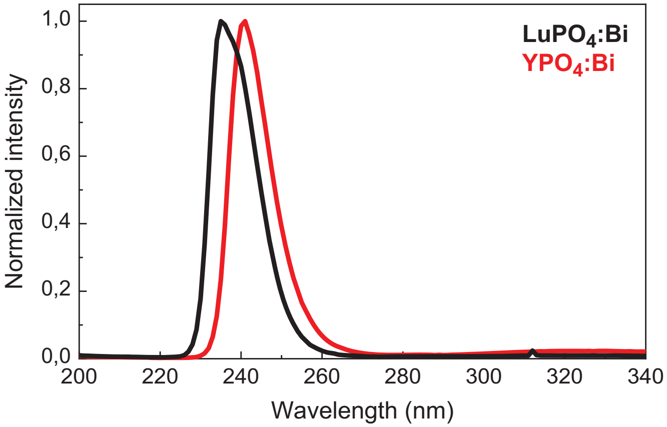

Figure 9.7: Emission spectra of $LuPO_4$:Bi^{3+}(0.5%) (blue line) and YPO_4:Bi^{3+}(0.5%) (red line) upon 172 nm excitation.

influenced by the position of the 5d band relative to the 4*f* levels. Phosphates are well known hosts for Pr^{3+} to produce UV-C emission. In Figure 9.8, the emission spectra of $LaPO_4$:Pr^{3+} and $LuPO_4$:Pr^{3+} are depicted. The peak wavelength is shifted to lower energy in $LuPO_4$:Pr^{3+} (Figure 9.8b) due to the stronger ligand field acting on the Pr^{3+} as a consequence of the shorter Pr–O distance in that host. Furthermore, the electron–phonon coupling is less pronounced in that host, resulting in a more distinct structure of the emission band.

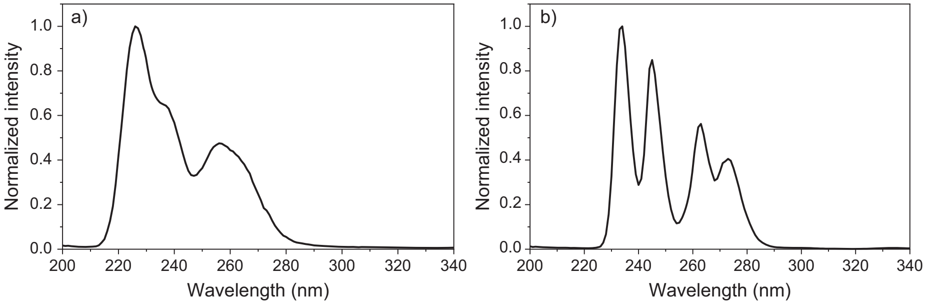

Figure 9.8: Emission spectra of $LaPO_4:Pr^{3+}$ (a) and $LuPO_4:Pr^{3+}$ (b) upon 172 nm excitation.

9.5.2 VUV phosphors

Photoluminescence in the VUV is rarely observed with one of the few examples being $YPO_4:Nd^{3+}$ or $LuPO_4:Nd^{3+}$. Here, the 5*d*–4*f* is at sufficiently high energy to show luminescence, while in most hosts Nd^{3+} will solely yield 4*f*–4*f* emission in the NIR region. Figure 9.9 shows the excitation and emission spectrum of $YPO_4:Nd^{3+}$. The narrow bands at 190, 240, and 280 nm arise from transitions from the 5d band to various 4f states, namely to $^4I_{9/2}$, ^4F_j, and ^2H_j [14]. The phosphor can be excited with the 172 nm primary emission of a Xe excimer lamp, however, with the excitation maxima being located at 160 and 180 nm.

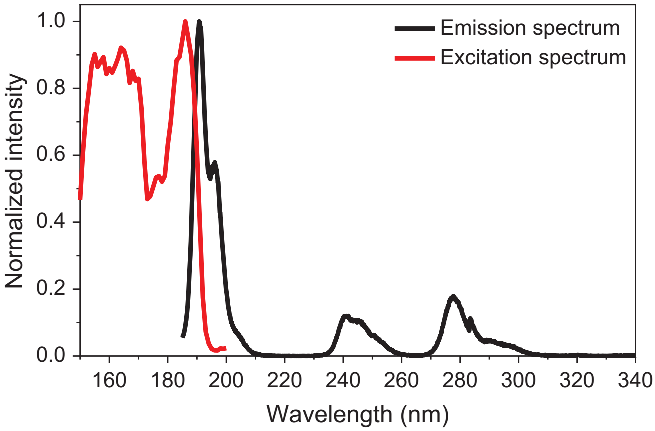

Figure 9.9: Emission spectrum (black line, λ_{ex} = 172 nm) and excitation spectrum (red line, λ_{em} = 240 nm) of $YPO_4:Nd^{3+}$ (1%).

9.5.3 Light yield

The suitability of a phosphor for use in Xe excimer lamps depends on the quantum efficiency and the absorption at the primary emission wavelength of the Xe_2* excimers at 172 nm. The product of these two values is the light yield, an important indicator for the efficiency of a phosphor in a device. Table 9.4 lists a selection of UV-emitting phosphors with the respective excitation and emission maxima and the light yield upon 172 nm excitation.

Table 9.4: Various UV-emitting phosphors with the respective excitation and emission maxima and the light yield upon excitation at 172 nm.

Phosphor	Excitation band maxima (nm)	Emission band maxima (nm)	Light yield upon 172 nm excitation
$YPO_4:Nd^{3+}$	160, 190	190	90%
$LaPO_4:Pr^{3+}$	165, 200	225	70%
$YPO_4:Pr^{3+}$	160, 190	233	70%
$YPO_4:Bi^{3+}$	170	241	90%
$(Ca,Mg)SO_4:Pb^{2+}$	170	245	80%
$LuBO_3:Pr^{3+}$	240	257	50%
$YBO_3:Pr^{3+}$	240	261	50%
$Y_2SiO_5:Pr^{3+}$	170, 245	270	20%
$SrSiO_3:Pb^{2+}$	170, 235	275	80%
$LaMgAl_{11}O_{19}:Gd^{3+}$	170, 275	311	90%
$LaPO_4:Ce^{3+}$	170, 270	320	90%
$YPO_4:Ce^{3+}$	170, 270	335, 355	55%
$LaMgAl_{11}O_{19}:Ce^{3+}$	170, 275	340	90%

9.6 UV Phosphors for (Al,Ga)N LEDs

(Al,Ga)N LEDs show emission between 210 and 360 nm, depending on the Al:Ga ratio. It is narrow, with an FWHM of around 10 nm, so if a continuous, broad spectrum in the UV is desired, the primary emission of the semiconductor chip has to be converted by means of a phosphor layer. Since the emission of the LED chip can be adjusted with relative ease compared to the discharge sources, a broader choice of phosphors is available for excitation by an LED. Predominantly, Ce^{3+} or Pr^{3+} can be used as activators.

Figure 9.10 shows the optical spectra of $LaMgAl_{11}O_{19}:Ce^{3+}$, a UV-emitting phosphor with a quantum efficiency of more than 95%. The excitation maximum is located at 275 nm, not matching the primary emission of the Hg and excimer discharge sources. However, the phosphor is an excellent candidate for use in (Al,Ga)N LEDs, as the primary emission of the semiconductor can be adjusted to that wavelength. In combination, a broad and continuous spectrum from the UV-C to the UV-A can be produced.

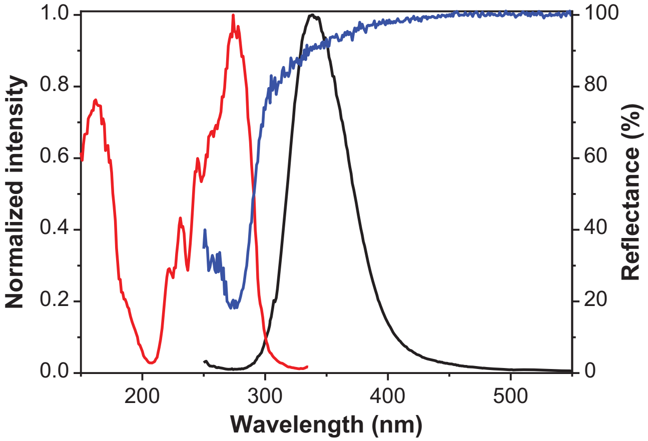

Figure 9.10: Excitation (red line, λ_{em} = 345 nm), emission (black line, λ_{ex} = 160 nm), and reflection (blue line) spectrum of $LaMgAl_{11}O_{19}:Ce^{3+}$.

9.7 Application areas of UV radiation sources

9.7.1 Disinfection

As the name indicates, ionizing radiation has such high energy, that all kind of chemical bonds can be activated or even broken. This finding can be used for efficient disinfection by damaging the RNA or DNA of microorganisms. For a log-4 reduction, that is, a survival rate of microorganisms of 0.0001, a UV-C dose of 2–5 mJ/cm^2 is deemed sufficient. The specific dose depends on the wavelength of the radiation, the type of microorganism, and geometrical factors.

Studies showed that radiation around 220 nm is harmful to microorganisms, while it is not able to penetrate the layer of dead cells that covers the skin and eye of humans and higher animals. That would allow such radiation to be used for disinfection purposes in the presence of humans, such as in offices or malls [15, 16]. The radiation can be generated by various sources, for example, excimer lamps with or without phosphor conversion or (Al,Ga)N LEDs with a primary emission wavelength of 220 nm. Currently, only sources utilizing the KrCl* excimer discharge are available commercially. Since it also emits radiation with slightly longer wavelength, it requires the use of filters to single out the 222 nm radiation of KrCl* [17].

9.7.2 Water treatment

Water treatment comprises disinfection and breakdown of harmful chemical contaminants. Purification via UV radiation has the advantage of being nontoxic and fast [18]. When attempting to purify water, it is mandatory to ensure that the decomposition products of the contaminants are not harmful in themselves. The aim is complete mineralization, i.e. decomposition of organic matter to inorganic compounds such as CO_2, H_2O, or N_2. Single bonds between carbon atoms have an energy of 347 kJ/mol and triple bonds one of 839 kJ/mol, while the 253.7 nm photons have an energy of 4.7 MJ/mol [19]. These photons provide enough energy to break most bonds in organic molecules, but the overall UV dose has to be high enough to provide sufficient photons to cleave each individual bond. A fraction of the UV photons is absorbed or scattered before reaching the contaminant, further reducing the effective UV dose. Since molecules tend to break at selective positions and undergo specific rearrangements upon irradiation, the decomposition products can be highly reactive themselves. That makes it hard to estimate what dose and type of radiation is required for complete mineralization and usually a bioassay is performed. Typical values are in the range of 30–300 mJ/cm^2 of 253.7 nm radiation.

9.7.3 Photopolymerization

Polymers are often synthesized via chain-growth polymerization. To initiate the chain-growth, an unsaturated monomer has to be activated. The initiation transforms a monomer into a radical or ion that will bond with another monomer, which in turn will become a radical or ion. The energy required for initiation can be supplied thermally, chemically, or via radiation, that is, photopolymerization. Typically, photoinitiation is used in dentistry for fillings or for the hardening of photoresist in photolithography.

9.7.4 Photochemistry

The topics discussed earlier can be summarized as photochemistry. These are chemical reactions subsequent to the absorption of radiation from the UV to the IR range. The radiation is absorbed, after which the molecule is in an excited state. In the excited state the molecule can undergo chemical reactions that will not occur in the ground state. Such reactions include isomerization of benzene to fulvene and benzvalene, the formation of HCl from Cl_2 and H_2 or photochlorination of organic molecules. Photosynthesis in plants is another example of photochemistry. Furthermore, it is widely used in inorganic chemistry. Here, the radiation excites an electron to the valence band. The resulting electron-hole pair can start redox reactions by either supplying an electron or taking an electron up. For example, irradiation of a suspension of TiO_2 and water with UV radiation results in the formation of highly reactive radicals as depicted in Figure 9.11.

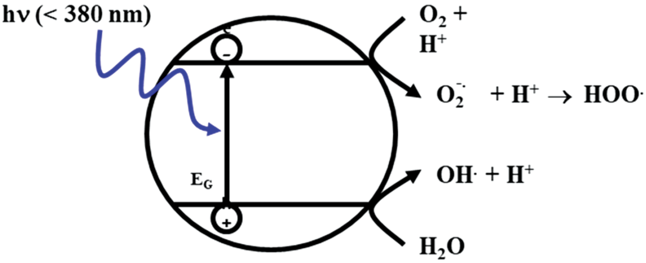

Figure 9.11: Illustration of the generation of OH· and HOO· radicals upon UV irradiation of TiO_2 in contact with H_2O.

Photochemistry can also be used for water splitting to generate H_2 and O_2 by a mechanism similar to that shown for TiO_2. The excited electrons have sufficient energy to reduce 4 H^+ to 2 H_2 and the respective holes in the valence band can oxidize 2 O^{2-} to O_2.

9.8 Conclusions and outlook

As discussed in this chapter, UV radiation is generated either directly, for example, by a gas discharge, or by conversion of higher energy radiation to lower energy radiation. The disadvantage of this so-called down-conversion is the inherent energy loss in converting a high-energy photon to a low-energy one and the need for a source of high-energy radiation such as VUV or UV-C to generate UV-B or UV-A radiation. An alternative is upconversion, in which two low-energy photons are converted into one high-energy photon. This process allows the use of primary sources that emit visible or even NIR radiation, such as (In,Ga)N or (In,Ga)(P,As) LEDs which are inexpensive and small compared to conventional VUV and UV-C sources.

$NaYF_4:Yb^{3+},Tm^{3+}$ shows upconversion emission in the UV-A region around 350 nm when excited at 980 nm. The underlying process is energy-transfer upconversion, that is, Yb^{3+} absorbs NIR radiation at 980 nm, followed by simultaneous energy transfer from two Yb^{3+} to one Tm^{3+} [20, 21]. Visible to UV upconversion has been observed in phosphors such as $Y_2SiO_5:Pr^{3+}$, $Lu_7O_6F_9:Pr^{3+}$, or $Lu_3(Ga,Al)_5O_{12}:Pr^{3+}$. Pr^{3+} shows upconversion upon excitation of the $^3P_0 \rightarrow {}^3H_4$ transition at 488 nm. The upconversion emission is due to a 5*d*–4*f* transition in the UV-B at 300–400 nm [22–24]. Currently known upconversion phosphors have relatively low quantum efficiencies of less than 5%. Such phosphors can be used for applications where low emission intensities are acceptable, e.g. in medicine or analytics.

Dedicated research on persistent UV luminescence is underway. Such luminescent materials can be used in medical imaging or to attack tumors. Several phosphors are known to exhibit persistent luminescence in the UV range, such as $LiYGeO_4:Bi^{3+}$ or $LiScGeO_4:Bi^{3+}$ [25, 26].

In addition, the efficiency of UV-emitting LEDs is expected to increase further. Assuming a similar development as in the visible range, it would be conceivable for LEDs to become the dominant technology in the UV range. For wavelengths shorter than 210 nm, however, excimer discharge lamps or the conversion of cathode or x-rays by scintillators are likely to remain the only viable alternative.

References

[1] F. Seitz, Interpretation of the properties of Alkali Halide-thallium phosphors, J. Chem. Phys. 6 (1938) 150–162. https://doi.org/10.1063/1.1750216.

[2] W.W. Piper, J.A. DeLuca, F.S. Ham, Cascade fluorescent decay in Pr3+-doped fluorides: Achievement of a quantum yield greater than unity for emission of visible light, J. Lumin. 8 (1974) 344–348. https://doi.org/10.1016/0022-2313(74)90007-6.

[3] K. Machida, G. Adachi, J. Shiokawa, Luminescence properties of Eu(II)-borates and Eu2+- activated Sr-Borates, J. Lumin. 21 (1979) 101–110. https://doi.org/10.1016/0022-2313(79)90038-3.

[4] M. Buonanno, D. Welch, I. Shuryak, D.J. Brenner, Far-UVC light (222 nm) efficiently and safely inactivates airborne human coronaviruses, Sci. Rep. 10 (2020) 10285. https://doi.org/10.1038/s41598-020-67211-2.

[5] H. Amano, R. Collazo, C.D. Santi, S. Einfeldt, M. Funato, J. Glaab, S. Hagedorn, A. Hirano, H. Hirayama, R. Ishii, Y. Kashima, Y. Kawakami, R. Kirste, M. Kneissl, R. Martin, F. Mehnke, M. Meneghini, A. Ougazzaden, P.J. Parbrook, S. Rajan, P. Reddy, F. Römer, J. Ruschel, B. Sarkar, F. Scholz, L.J. Schowalter, P. Shields, Z. Sitar, L. Sulmoni, T. Wang, T. Wernicke, M. Weyers, B. Witzigmann, Y.-R. Wu, T. Wunderer, Y. Zhang, The 2020 UV emitter roadmap, J. Phys. D: Appl. Phys. 53 (2020) 503001. https://doi.org/10.1088/1361-6463/aba64c.

[6] N. Susilo, S. Hagedorn, D. Jaeger, H. Miyake, U. Zeimer, C. Reich, B. Neuschulz, L. Sulmoni, M. Guttmann, F. Mehnke, C. Kuhn, T. Wernicke, M. Weyers, M. Kneissl, AlGaN-based deep UV LEDs grown on sputtered and high temperature annealed AlN/sapphire, Appl. Phys. Lett. 112 (2018) 41110. https://doi.org/10.1063/1.5010265.

[7] M. Kumar, Advances in UV-A and UV-C LEDs and the applications they enable, in: J.K. Kim, M.R. Krames, M. Strassburg (Eds.), Proceedings Volume 10940, Light-Emitting Devices, Materials, and Applications; 1094008 (2019), https://doi.org/10.1117/12.25, SPIE, San Francisco, United States (02.02.2019–07.02.2019), p. 7.

[8] N. Susilo, E. Ziffer, S. Hagedorn, L. Cancellara, C. Netzel, N.L. Ploch, S. Wu, J. Rass, S. Walde, L. Sulmoni, M. Guttmann, T. Wernicke, M. Albrecht, M. Weyers, M. Kneissl, Improved performance of UVC-LEDs by combination of high-temperature annealing and epitaxially laterally overgrown AlN/sapphire, Photon. Res. 8 (2020) 589. https://doi.org/10.1364/PRJ.385275.

[9] M. Broxtermann, T. Jüstel, Photochemically induced deposition of protective alumina coatings onto UV emitting phosphors for Xe excimer discharge lamps, Mater Res Bull. 80 (2016) 249–255. https://doi.org/10.1016/j.materresbull.2016.04.008.

[10] A.B. Gawande, R.P. Sonekar, S.K. Omanwar, Synthesis and PL study of UV emitting phosphor KCa4 (BO3)3:Pb2+, J. Lumin. 149 (2014) 200–203. https://doi.org/10.1016/j.jlumin.2014.01.044.

[11] H.F. Folkerts, G. Blasse, Luminescence of Pb2+ in several calcium borates, J. Mater. Chem. 5 (1995) 273. https://doi.org/10.1039/JM9950500273.

[12] P. Dorenbos, The $4f^n \leftrightarrow 4f^{n-1}5d$ transitions of the trivalent lanthanides in halogenides and chalcogenides, J. Lumin. 91 (2000) 91–106. https://doi.org/10.1016/S0022-2313(00)00197-6.

[13] P. Dorenbos, Energy of the first 4f7→4f65d transition of Eu2+ in inorganic compounds, J. Lumin. 104 (2003) 239–260. https://doi.org/10.1016/S0022-2313(03)00078-4.

[14] J. Pejchal, M. Nikl, K. Fukuda, N. Kawaguchi, T. Yanagida, Y. Yokota, A. Yoshikawa, V. Babin, Doubly doped BaY2F8: Er, Nd VUV scintillator, Radiat Meas. 45 (2010) 265–267. https://doi.org/10.1016/j.radmeas.2009.10.017.

[15] M. Buonanno, D. Welch, D.J. Brenner, Exposure of human skin models to KrCl excimer lamps: The impact of optical filtering†, Photochem. Photobiol. 97 (2021) 517–523. https://doi.org/10.1111/php.13383.

[16] E. Eadie, P. O'Mahoney, L. Finlayson, I.R.M. Barnard, S.H. Ibbotson, K. Wood, Computer modeling indicates dramatically less DNA damage from Far-UVC krypton chloride lamps (222 nm) than from sunlight exposure, Photochem. Photobiol. 97 (2021) 1150–1154. https://doi.org/10.1111/php.13477.

[17] B. Ma, P.M. Gundy, C.P. Gerba, M.D. Sobsey, K.G. Linden, UV inactivation of SARS-CoV-2 across the UVC spectrum: KrCl* excimer, mercury-vapor, and light-emitting-diode (LED) sources, Appl. Environ. Microbiol. 87 (2021) e0153221. https://doi.org/10.1128/AEM.01532-21.

[18] K. Song, M. Mohseni, F. Taghipour, Application of ultraviolet light-emitting diodes (UV-LEDs) for water disinfection: A review, Water Res. 94 (2016) 341–349. https://doi.org/10.1016/j.watres.2016.03.003.

[19] E.L. Cates, J.-H. Kim, Bench-scale evaluation of water disinfection by visible-to-UVC upconversion under high-intensity irradiation, J. Photochem. Photobiol. B. 153 (2015) 405–411. https://doi.org/10.1016/j.jphotobiol.2015.10.021.

[20] X. Wang, X. Liu, H. Zhu, G. Zhang, X. Li, C.-Y. Tang, W.-C. Law, X. Zhao, Near infrared to ultraviolet upconversion nanocomposite for controlling the permittivity of polyspiropyran shell, Polym Test. 94 (2021) 107042. https://doi.org/10.1016/j.polymertesting.2020.107042.

[21] J. Wu, H. Zheng, X. Liu, B. Han, J. Wei, Y. Yang, UVC upconversion material under sunlight excitation: LiYF(4):Pr 3+, Opt. Lett. 41 (2016) 792–795. https://doi.org/10.1364/OL.41.000792.

[22] J. Wu, Y. Song, B. Han, J. Wei, Z. Wei, Y. Yang, Synthesis and characterization of UV upconversion material Y 2 SiO 5: Pr3+ Li + /TiO 2 with enhanced the photocatalytic properties under a xenon lamp, RSC Adv. 5 (2015) 49356–49362. https://doi.org/10.1039/C5RA06416C.

[23] E.L. Cates, A.P. Wilkinson, J.-H. Kim, Visible-to-UVC upconversion efficiency and mechanisms of $Lu_7O_6F_9Pr^{3+}$ and Y_2SiO_5: Pr^{3+}ceramics, J. Lumin. 160 (2015) 202–209. https://doi.org/10.1016/j.jlumin.2014.11.049.

[24] P. Pues, M. Laube, S. Fischer, F. Schröder, S. Schwung, D. Rytz, T. Fiehler, U. Wittrock, T. Jüstel, Luminescence and up-conversion of single crystalline $Lu_3Al_5O_{12}$:Pr^{3+}, J. Lumin. 234 (2021) 117987. https://doi.org/10.1016/j.jlumin.2021.117987.

[25] J. Shi, X. Sun, S. Zheng, X. Fu, Y. Yang, J. Wang, H. Zhang, Super-long persistent luminescence in the ultraviolet A region from a Bi 3+ -doped LiYGeO 4 phosphor, Adv. Opt. Mater. 7 (2019) 1900526. https://doi.org/10.1002/adom.201900526.

[26] Z. Zhou, P. Xiong, H. Liu, M. Peng, Ultraviolet-A persistent luminescence of a Bi3+-activated LiScGeO4 material, Inorg. Chem. 59 (2020) 12920–12927. https://doi.org/10.1021/acs.inorgchem.0c02007.

Philippe Boutinaud, Enrico Cavalli

Chapter 10

Metal-to-metal charge transfer involving Pr^{3+} or Tb^{3+} ions in transition metal oxides and its consequences on the luminescence behaviors

10.1 Introduction

The interest toward the luminescent inorganic solids is constantly growing since more than forty years, in parallel with the development of the technologies in which they can be utilized. The assessment of the application perspectives of these materials requires a deep knowledge of the de-excitation pathways, in terms of energy level structure and involved mechanisms. In many cases, the luminescence is generated by active ions introduced as dopants into wide bandgap (mostly oxide or fluoride) lattices. The host effects on the emission properties are usually interpreted as generated by interactions of electrostatic nature: crystal field, electron–phonon coupling, energy transfer (host sensitization) processes, and so on. In many cases, however, the emission dynamics cannot be fully accounted for by considering the host lattice and the optical center as distinct and weakly coupled entities, and stronger types of interactions, involving electron transfer phenomena, must be taken into account. These interactions give rise to the formation of excited states, known as charge transfer (CT) states (CTSs) that can play a role in the emission kinetics by introducing supplementary absorption and de-excitation channels. Systematic studies on the CTSs have provided information interesting not only for understanding the emission properties of the single material, but also for developing general models that rationalize the behavior of the "doping ion + host matrix" system by considering it as a whole, and offer new tools for predicting its properties and for the design of new compounds. The aim of this section is to give a brief overview of how the phenomenon occurs in luminescent materials and of how the state of the art in this connection has evolved along the years.

A metal-to-metal CT (MMCT) forms when an excitation radiation induces an electron transfer from a metal donor to a metal acceptor of different nature. According to IUPAC, a CT occurring between metal ions of same nature is referred to as an intervalence CT (IVCT).

The phenomenon, known since longtime and covering practically all classes of inorganic compounds, has its most evident effect on the absorption spectra and then on the color properties of several materials (minerals, pigments, salts, etc.). It accounts in fact for the presence of intense bands not ascribable to isolated optical centers [1].

https://doi.org/10.1515/9783110607871-010

Concerning the luminescence properties, the effects of MMCT states are relevant in oxidic lattices containing a d^0 transition metal ion having electron acceptor properties, that is, easy to reduce (V^{5+}, Mo^{6+}, Ti^{4+}, etc.), activated with ions having electron donor properties, easy to oxidize, like Ce^{3+}, Pr^{3+}, Tb^{3+}, Bi^{3+}, or Sb^{3+}. The formation of MMCT excited states was initially considered detrimental on the emission properties since introducing efficient nonradiative depletion channels for the emitting levels. This aspect was well evidenced in studies on the luminescence quenching in YVO_4:Tb^{3+} [2, 3], carried out in the latest 1960s. Systems in which the MMCT state exhibits emission properties, like YVO_4:Bi^{3+} [4, 5], were considered rather exceptional. This point of view started to change after a paper on rare-earth-doped scheelite and fergusonite crystals was published in 1973 [6], in which quenching pathways of some emission lines based on the so-called virtual recharge mechanism were proposed. The approach, rather original at the time, did not have great success and it was also contested [7]. More than 20 years therefore went by before this mechanism was taken in the due consideration and extensively investigated to account for the selective quenching of the emission from certain excited levels in oxide materials doped with lanthanide ions. Particular interest, precisely, was addressed to the possibility of isolating the $^1D_2$ red luminescence from the $^3P_0$ emission features in Pr^{3+}-doped materials, in the perspective of replacing the more expensive Eu^{3+} ion in red emitting phosphors. After some initial misinterpretations of the experimental evidences [8], the $^3P_0 \rightarrow {}^1D_2$ nonradiative decay was systematically analyzed by considering all possible involved mechanisms and a model based on the formation of an MMCT (denoted improperly as IVCT in the papers) state in the emission dynamics was proposed in YVO_4:Pr^{3+} [9] and $CaTiO_3$:Pr^{3+} [10]. At the same period, the same process was identified in $LiTaO_3$:Pr^{3+} [11] and $LiNbO_3$:Pr^{3+} [12] and described based on the formation of excitons trapped at the Pr^{3+} sites. These impurity-trapped excitons consist of a hole localized at the Pr^{3+} ion (forming formally a Pr^{4+} center) and an electron in the lattice conduction band bounded by the long-range Coulomb potential of the trapped hole. This description was confirmed simultaneously in $CaTiO_3$:Pr^{3+} by using photostimulated electron spin resonance [13]. This process supposes that the orbitals that compose the bottom of the lattices conduction band have a prominent d metal character, which is in general fulfilled in d^0 transition metal oxidic hosts like titanates, vanadates, niobates, tantalates, and tungstates [14–26].

Subsequent systematic investigations allowed to assess a correlation between the energy positions of the Pr^{3+}-to-metal CT states and the electronic properties of the metal oxidic lattices, leading to an empirical model whose validity was extended to analogous lattices doped with Tb^{3+}.

The existence and the role of these CT states were convincingly supported by emission studies as a function of the temperature and of the pressure. Concomitantly, the physical interpretation the Pr^{3+}/Tb^{3+}-to-d^0 metal CT transition allowed the development of a model for the determination of the position of the energy levels of the rare earth ions relative to the bandgap of the host materials, with interesting consequences from both theoretical and applicative points of view.

10.2 Luminescence quenching induced by the MMCT state in Pr^{3+}- and Tb^{3+}-doped oxides

10.2.1 The model and its evolution: Pr^{3+}-doped lattices

The energy level structure of Pr^{3+} is shown in Figure 10.1. The visible emission of this ion mainly originates in the $^3P_0$ and $^1D_2$ states. The first emits in the blue (→ $^3H_4$), green (→ $^3H_5$), and red (→ $^3H_6$), whereas the second emits in the red (→ $^3H_4$). The study of the Pr^{3+} emission properties in $CaTiO_3$:Pr^{3+} [10, 13] and YVO_4:Pr^{3+} [9] and related isostructural $CaZrO_3$:Pr^{3+} and YPO_4:Pr^{3+} compounds, respectively, constituted the starting point for the "renaissance" of the virtual recharge mechanism and its evolution toward a more consistent formulation. Upon UV or near-UV excitation, $CaTiO_3$:Pr^{3+} and YVO_4:Pr^{3+} showed single red emission from the $^1D_2$ level, indicating a very efficient $^3P_0$ – $^1D_2$ nonradiative relaxation. This phenomenon was not observed in $CaZrO_3$:Pr^{3+} and YPO_4:Pr^{3+} (Figure 10.1), in the latter, the (partial) quenching of $^3P_0$ emission occurs *via* multiphonon relaxation [27, 28].

In addition, the excitation spectrum of $CaTiO_3$:Pr^{3+} and YVO_4:Pr^{3+} evidenced a band, or a shoulder, in correspondence of the low energy side of the host absorption, whose intensity depended on the doping level but that was not ascribable to isolated Pr^{3+} ions (Figure 10.2). The presence of this extra excitation was concluded to be responsible for the efficient quenching of otherwise emitting $^3P_0$ state and for the concomitant prominent red $^1D_2 \rightarrow {}^3H_4$ emission in these compounds.

The processes potentially involved in the $^3P_0$ – $^1D_2$ radiationless relaxation were systematically examined: cross-relaxation pathways, multiphonon relaxation, intersystem crossing from low-lying $4f^15d^1$ states, and it was concluded that none of them could be responsible of the $^3P_0$ quenching. It was then proposed to ascribe this band to an absorption of the type Pr^{3+} ($4f^2$), M^{n+} (d^0) → Pr^{4+}($4f^1$), $M^{(n-1)+}$ (d^1) with $M^{n+} = Ti^{4+}$ or V^{5+} in these cases, with concomitant formation of a CTS, improperly denoted as IVCT in the original papers and renamed as MMCT in this review. This process is favored by the tendency of the trivalent praseodymium to oxidize, in agreement with the low value of the E°($M^{4+} \rightarrow M^{3+}$) reduction potential relative to the other trivalent rare-earth ions (except Ce^{3+} and Tb^{3+}) [29].

The presence of the MMCT state can strongly alter the excited state dynamics of the Pr^{3+} ion by introducing quenching pathways for its emitting levels, depending on its energy position relative to the $4f$ levels, as shown in Figures 10.2 and 10.3. The possibility of a selective quenching of the $^3P_0$ blue-green in favor of the $^1D_2$ red emission was considered attractive in the perspective to develop red-emitting phosphors based on the Pr^{3+} ion as a possible substitute of the more expensive Eu^{3+}, and then systematically investigated.

Systematic studies were then carried out on d^0 transition metal oxides activated with Pr^{3+}, like titanates, vanadates, niobates, and tantalates [30–33], to define a

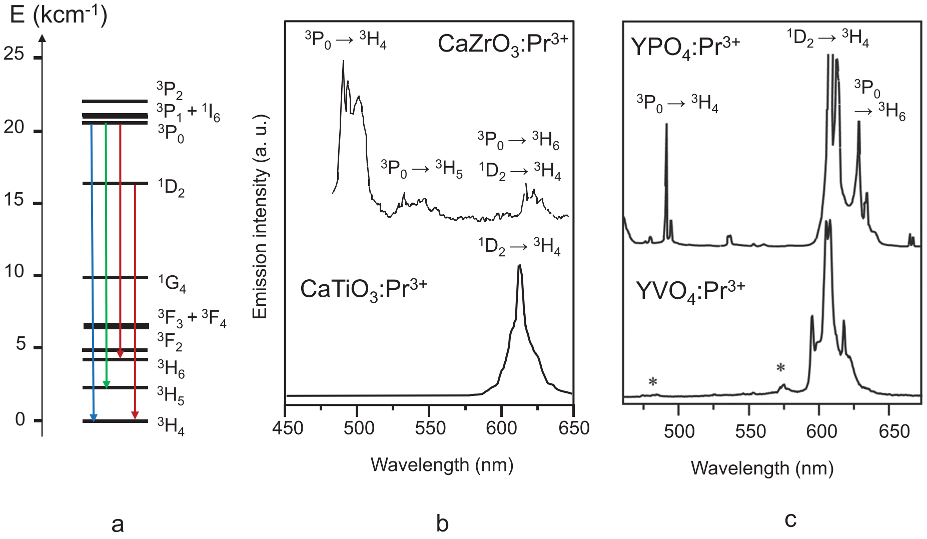

Figure 10.1: (a) Energy level scheme of Pr^{3+}. (b) Emission spectra of $CaZrO_3:Pr^{3+}$ and $CaTiO_3:Pr^{3+}$ (upon excitation at 254 nm) (redrawn with permission from [10], Copyright 2004, Elsevier). (c) Emission spectra of $YPO_4:Pr^{3+}$ and $YVO_4:Pr^{3+}$ (upon excitation at 450 and 320 nm, respectively. * denotes emission lines from residual Dy^{3+} traces) (redrawn with permission from [9], Copyright 2004, AIP Publishing).

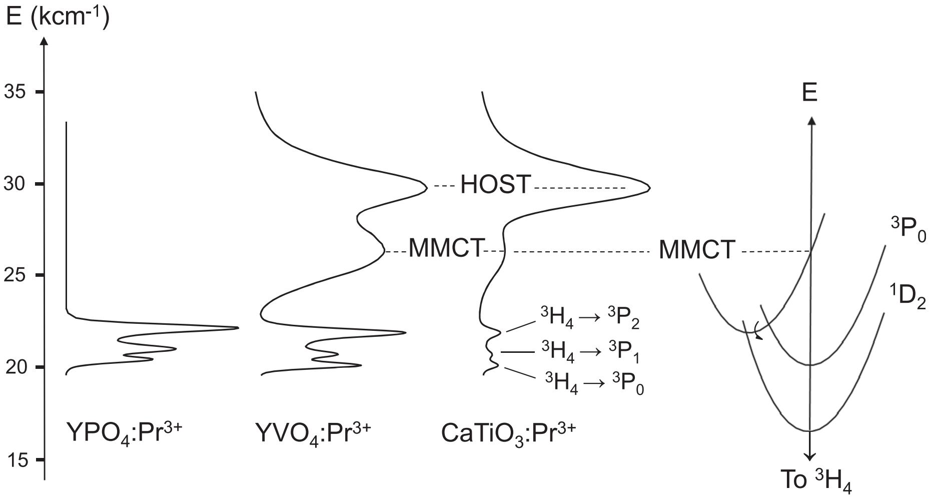

Figure 10.2: Excitation spectra of the red Pr^{3+} emission (em = 610 nm) in $YPO_4:Pr^{3+}$, $YVO_4:Pr^{3+}$, and $CaTiO_3:Pr^{3+}$ and configurational coordinate scheme showing the quenching pathway of the $^3P_0$ level (redrawn with permission from [9], Copyright 2004, AIP Publishing and [10], Copyright 2004, Elsevier).

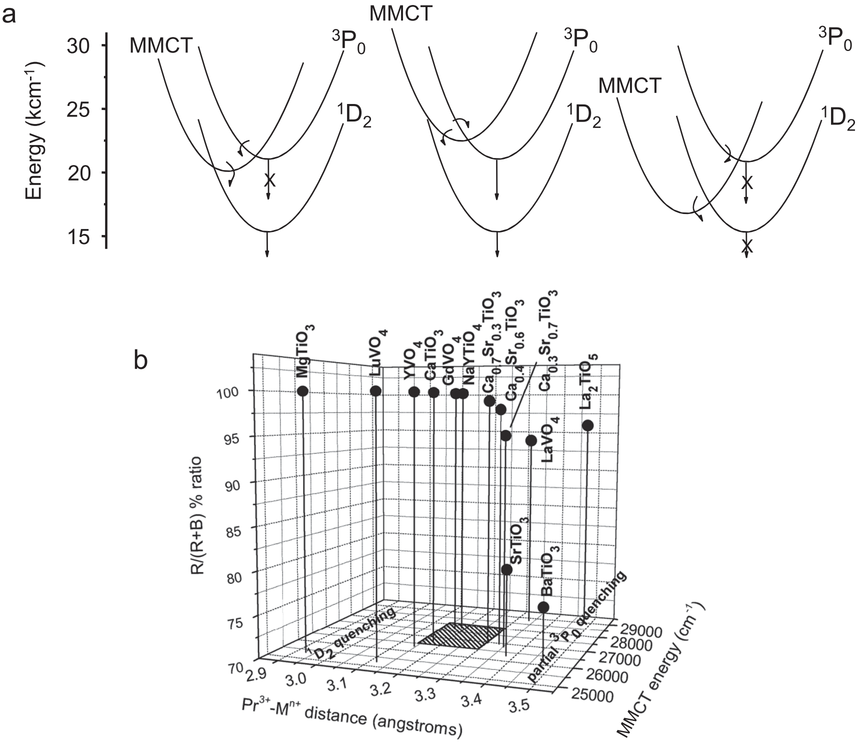

Figure 10.3: (a) Simplified single configurational coordinate diagrams showing the effect of the position of the MMCT state on the population of the $^3P_0$ and $^1D_2$ emitting states in Pr^{3+}-doped lattices (adapted with permission from [33], Copyright 2006, Elsevier). (b) Variation of the $R/(R+B)$ intensity ratio between the red (R) and blue (B) emission bands as a function of the shortest Pr^{3+}–M^{n+} distance ($M^{n+} = Ti^{4+}$ or V^{5+}) and of the MMCT band energy (adapted with permission from [30], Copyright 2006, Elsevier).

predictive criterion for the quenching of the $^3P_0$ emission. In this context, it was demonstrated in the case of vanadates and titanates that the intensity ratio $R/(R+B)$ between the red (R) $^1D_2 \rightarrow {}^3H_4$ emission and the sum (red (R) $^1D_2 \rightarrow {}^3H_4$ + blue (B) $^3P_0 \rightarrow {}^3H_4$) visible luminescence is correlated with both MMCT energy position and Pr^{3+}–M^{n+} ($M^{n+} = Ti^{4+}$ or V^{5+}) shortest distance in the lattice (Figure 10.3).

The MMCT energy position (intended as excitation edge) was then related to the nature of the metal acceptor, expressed in terms of optical electronegativity in the frame of the model firstly elaborated by Jørgensen [34–36] and successively revisited by Qiang [37]. It was observed that the MMCT energy position varies linearly with the ratio between the optical electronegativity $\chi_{opt}(M^{n+})$ of the d^0 lattice cation M^{n+}, and the shortest Pr^{3+}–M^{n+} distance, $d(Pr^{3+}–M^{n+})$ (Figure 10.4, [33]).

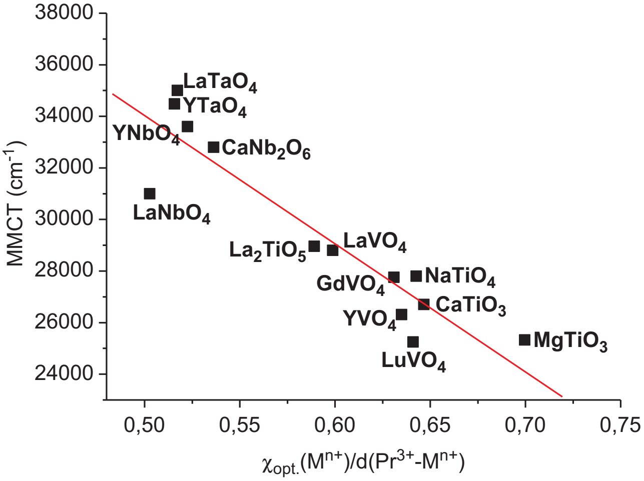

Figure 10.4: Variation of the MMCT energy *vs.* the ratio between the optical electronegativities of the d^0 M^{n+} lattice cations and the shortest Pr^{3+}–M^{n+} distances (adapted with permission from [33], Copyright 2006, Elsevier).

Correspondingly, a mathematical expression was formulated [38], expressed here in eV:

$$\mathrm{MMCT}\left(\mathrm{Pr}^{3+},\mathrm{eV}\right)=7.29-6.17\frac{\chi_{\mathrm{opt}}\left(\mathrm{M}^{n+}\right)}{d\left(\mathrm{Pr}^{3+}-\mathrm{M}^{n+}\right)} \tag{10.1}$$

This expression has phenomenological meaning only but allowed for the first time to predict the position of the MMCT band from the structural properties of the host lattices, within an uncertainty amounting ±0.4 eV. This uncertainty is explained for a large part by the fact that the used values of optical electronegativites were originally introduced for octahedrally coordinated transition metals in hexahalides and not basically adapted for oxidic systems.

Successively, this empirical Pr^{3+}-to-d^0 transition metal CT model was revisited in the frame of the chemical shift model of P. Dorenbos [39, 40] and with the introduction of more accurate values of electronegativities, to lay the foundations for the development of a physical model for the MMCT states.

Following this new approach, the MMCT energy (in eV) is now calculated using [41]

$$\mathrm{MMCT}\left(\mathrm{Pr}^{3+},\mathrm{eV},A\right)=\mathrm{VRBE}\left(\mathrm{Pr}^{3+},4f^{2},A\right)-k(A)\frac{\chi_{\mathrm{CN}'}\left(\mathrm{M}^{n+}\right)}{d\left(\mathrm{Pr}^{3+}-\mathrm{M}^{n+}\right)} \tag{10.2}$$

where VRBE(Pr^{3+}, $4f^2$, A) is the vacuum-referred binding energy of an electron located in the $4f^2$ ($^3H_4$) ground state of Pr^{3+} in a given host lattice (A). Note that the absolute value of this energy is taken in (10.2). $\chi_{\mathrm{CN}'}(\mathrm{M}^{n+})$ is the electronegativity of the host metal ion as calculated by [42]

$$\chi_{\mathrm{CN}'}(\mathrm{M}^{n+}) = \frac{0.105n^*}{r(\mathrm{M}^{n+})}\sqrt{\frac{I_m}{13.6}} + 0.863 \qquad (10.3)$$

where n^* is the effective principal quantum number and I_m is the ultimate ionization energy of the considered cation. CN' and $r(\mathrm{M}^{n+})$ are, respectively, the coordination number and ionic radius of M^{n+} in the lattice as picked up in [43]. As defined by eq. (10.3), the electronegativities are directly proportional to the effective nuclear charge carried by M^{n+} in the host lattice.

$d(\mathrm{Pr}^{3+}-\mathrm{M}^{n+})$ is the shortest Pr^{3+}–M^{n+} distance corrected for the ionic radii mismatch existing between Pr^{3+} and the substituted host lattice cation X, obtained as $d(\mathrm{Pr}^{3+}-\mathrm{M}^{n+}) = d(X-\mathrm{M}^{n+}) + \frac{1}{2}\left[r(\mathrm{Pr}^{3+}) - r(X)\right]$, where $d(X-\mathrm{M}^{n+})$ is the shortest X–M^{n+} distance obtained directly from the crystal structure of the host lattice and $r(\mathrm{Pr}^{3+})$ and $r(X)$ are the ionic radii of the cations in the lattice obtained from [43]. $k(A)$ is a constant pertaining to the host lattice (A) (tabulated in Table 10.1 for a selection of d^0-based metal oxide lattices) obtained by plotting the experimental CT excitation energies against $\frac{\chi_{\mathrm{CN}'}(M^{n+})}{d(\mathrm{Pr}^{3+}-M^{n+})}$ (Figure 10.5).

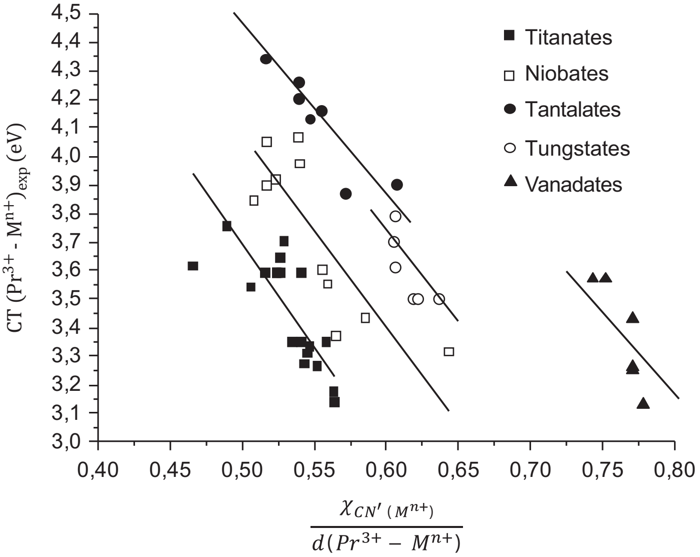

Figure 10.5: Experimental $\mathrm{Pr}^{3+} \rightarrow \mathrm{M}^{n+}$ CT energies against $\chi_{\mathrm{CN}'}(\mathrm{M}^{n+})/d(\mathrm{Pr}^{3+}-\mathrm{M}^{n+})$ for Pr^{3+} in d^0 transition metal oxides. The solid lines result from fitting using eq. (10.4) and data given in Table 10.1 (reproduced with permission from [41], Copyright 2019, Elsevier).

The vacuum-referred binding energy of an electron in the $4f^2$ shell of Pr^{3+} is given by [39]

$$\mathrm{VRBE}\left(\mathrm{Pr}^{3+},\, 4f^2,\, A\right) = -24.92 + \frac{18.05 - U(A)}{0.777 - 0.035U(A)} - U(A) + 3.4 \tag{10.4}$$

with $U(A)$ being the Coulomb repulsion energy of the host lattice. This value was determined within an accuracy of ≈ ±0.1 eV as the binding energy difference between the Eu^{2+} ($4f^7$) and Eu^{3+} ($4f^6$) ground states [44–46] and conveniently accounts for the effect of the environment around a lanthanide dopant in the solid. Values of $U(A)$ can be retrieved in [47–49] for many lattices. Some are given in Table 10.1 for d^0 transition metal oxides based on the procedure reported in [41].

Table 10.1: Values of $U(A)$, $k(A)$, and VRBE(Pr^{3+}, $4f^2$, A) for Pr^{3+}-containing titanates, niobates, tantalates, tungstates, molybdates, and vanadates.

Host lattice (*A*)	**$U(A)$**	**$\chi_{CN'}(M^{n+})$**	**$k(A)$**	**VRBE(Pr^{3+}, $4f^2$, A)**
Titanates, CN' =6	6.7	1.73	7.21	−7.30
Niobates, CN' =6	6.8	1.86	6.81	−7.45
Tantalates, CN' =6	6.8	1.925	5.97	−7.45
Tungstates, CN' =6	6.9	2.17	6.42	−7.60
Tungstates, CN' =4	7.1	2.596	–	−7.9
Molybdates, CN' =4	7.05	2.506	–	−7.82
Vanadates, CN' =4	7.0	2.46	5.73	−7.75

All energies in eV. Adapted with permission from [41], Copyright 2019, Elsevier.

The rationalized Pr^{3+}-to-d^0 transition metal CT model was tested on more than 50 d^0 transition metal-based oxidic compounds in which the MMCT transition ($\mathrm{CT}(\mathrm{Pr}^{3+}\text{–}M^{n+})_{\mathrm{exp}}$) has been identified and was demonstrated to predict the MMCT energies with an accuracy of ±0.1 to ±0.15 eV, depending on the considered family of host materials; see Table 10.2.

This quenching process opens attractive perspectives in terms of spectral tuning either by varying temperature, as it will be discussed below, or by manipulating the chemical composition of the cation neighborhood of Pr^{3+}, either changing the nature of the d^0 metal acceptor (i.e., changing its electronegativity) or changing the nature of the doping site (i.e., changing all interatomic distances) with the aim to adjust the $R/(R+B)$ intensity ratio at will. This is illustrated in Figure 10.6 for the $Ca_{1-x}Sr_xTiO_3:Pr^{3+}$ solid solution [92].

10.2.2 Tb^{3+}-doped lattices

The energy level scheme of Tb^{3+} is presented in Figure 10.7. Like Pr^{3+}, Tb^{3+} has two visible luminescent states: $^5D_3$, whose main emission lines are in the blue region and $^5D_4$, whose main emission lines are in the green region. Compared with Pr^{3+} levels, $^5D_4$ is located approximately at the same energy as $^3P_0$, whereas $^5D_3$ is about 5,500 cm^{-1} higher in energy. In many Tb^{3+}-doped compounds, the $^5D_3$ emission is quenched at the benefit of the green-emitting $^5D_4$ levels by means of an efficient cross-relaxation process subject that the Tb^{3+} doping rate is high enough in the compound. It is noteworthy that Tb^{3+} has a redox behavior comparable to Pr^{3+}, and its emission properties in d^0 transition metal oxides are influenced by the formation of a Tb^{3+} $(4f^8)$, M^{n+} $(d^0) \rightarrow Tb^{4+}(4f^7)$, $M^{(n-1)+}$ (d^1) state in a similar way. However, the energy level scheme of Tb^{3+} does not contain levels below $^5D_4$ that could be fed by crossover to the CT state, as it occurs for the $^1D_2$ level of Pr^{3+}. Therefore, a too low-positioned Tb-to-d^0 metal CT state results in strong quenching of the green $^5D_4$ emission at room temperature, as, for instance, in titanate perovskites (see Figure 10.7) or in YVO_4:Tb^{3+} [3, 93]. In comparison, YPO_4:Tb^{3+} 0.5% shows emission from both $^5D_3$ and $^5D_4$ levels at room temperature, indicating that the Tb-related CT state does not form in this compound or is present at too high energies to interfere with the relaxation process [51].

Equation (10.2) can be adapted to the case of Tb^{3+} as follows:

$$\mathrm{MMCT}\left(\mathrm{Tb}^{3+},\mathrm{eV},A\right)=\mathrm{VRBE}\left(\mathrm{Tb}^{3+},4f^8,A\right)-k(A)\,\frac{\chi_{\mathrm{CN}'}(\mathrm{M}^{n+})}{d\left(\mathrm{Tb}^{3+}-\mathrm{M}^{n+}\right)} \qquad (10.5)$$

with $\mathrm{VRBE}\left(\mathrm{Tb}^{3+},\ 4f^8,\ A\right)=\mathrm{VRBE}\left(\mathrm{Pr}^{3+},\ 4f^2,\ A\right)+\Delta E\left(4f^8,4f^2\right)$, where $\Delta E\left(4f^8,4f^2\right)$ is the energy difference between $4f^8$ and $4f^2$ ground states of Tb^{3+} and Pr^{3+}. This value was estimated at 0.18 eV in [94, 95] but recently revised in [40, 96] to a value amounting zero that we will retain here. We list in Table 10.3 a few data available for Tb^{3+} in d^0 transition metal oxides.

The data are scarcer compared to Pr^{3+} and the lowest excitation is in general not ascribed to $Tb^{3+} \rightarrow M^{n+}$ CT but more often to $4f^8 \rightarrow 4f^7 5d^1$ transitions. However, it is shown in Table 10.3 that several of the lowest excitations in d^0 metal complex oxides are reproduced by eq. (10.5) within $<\pm0.15$ eV. This suggests the usefulness to closely examine the spectral assignments in these cases.

Table 10.2: Structural and electronic properties of Pr^{3+}-doped transition metal oxides.

Host lattice (*A*)	**Doping site *X***	$\frac{\chi_{CN'}(M^{n+})}{d(Pr^{3+}-M^{n+})}$	**CT $(Pr^{3+}–M^{n+})_{exp.}$**	**CT $(Pr^{3+}– M^{n+})_{calc.}$**	***R*/(*R*+*B*) @ 300 K**	**ΔE_q**
$MgTiO_3$	Mg	0.565	3.14 [30]	3.23	1^{un} (0.2 mol% Pr^{3+})	–
$Lu_{1/2}Na_{1/2}TiO_3$	Lu	0.565	3.17 [50]	3.23	1 (0.2 mol% Pr^{3+})	0.57 [50]
$Y_{1/2}Na_{1/2}TiO_3$	Y	0.553	3.26 [50]	3.32	1 (0.2 mol% Pr^{3+})	0.67 [50]
$Gd_{1/2}Na_{1/2}TiO_3$	Gd	0.544	3.28 [50]	3.38	1 (0.2 mol% Pr^{3+})	0.72 [50]
$CaTiO_3$	Ca	0.546	3.31 [13]	3.36	1 (0.2 mol% Pr^{3+})	0.49 [51]
$SrTiO_3$	Sr	0.522	No data [30]	3.53	0.8 (0.2 mol% Pr^{3+})	–
$Na_{1/2}Bi_{1/2}TiO_3$	Na, Bi	0.533	3.35^{un} [52]	3.60	–	0.41 [52]
$K_{1/2}Bi_{1/2}TiO_3$	K, Bi	0.530	3.64^{un} [52]	3.48	–	0.47 [52]
$Ca_3Ti_2O_7$	Ca(1)	0.540	3.35 [53]	3.40	1 (0.3 mol% Pr^{3+})	–
	Ca(2) ^{preferred}	0.558		3.27		
$Y_2Ti_2O_7$	Y	0.478	3.61 [54]*	3.94	1 (0.5 mol% Pr^{3+})	0.42 [54]
$La_2Ti_2O_7$	La(1)	0.524	3.59 [41, 55, 56]	3.52	≈ 0.9 (0.5 mol% Pr^{3+})	–
	La(2)	0.516		3.57		
	La(3)	0.524		3.52		
	La(4)	0.524		3.52		

La_2TiO_5	La(1)	0.503	3.59 [30]	3.40	0.96 (0.2 mol % Pr^{3+})	-
	La(2)	0.490		3.50		
$NaYTiO_4$	Y	0.535	3.35 [30]	3.44	1 (0.2 mol% Pr^{3+})	0.38 [57]
$NaGdTiO_4$	Gd	0.527	3.64 [58]	3.50	1 (0.1 mol% Pr^{3+})	0.62 [57]
Gd_2ZnTiO_6	Gd	0.547	3.33 [59]	3.35	0.9 (0.2 mol% Pr^{3+})	0.83 [59]
$Na_2La_2Ti_3O_{10}$	La	0.506	3.55 [60]	3.65	<0.4 (0.2 mol% Pr^{3+})	–
La_2MgTiO_6	La	0.529	3.70 [61]*	3.48	≈0.7 (0.5 mol% Pr^{3+})	0.4 [61]
$BaTi_4O_9$	Ba	0.490	3.75 [62]	3.77	1 (1 mol% Pr^{3+})	–
$NaCaTiNbO_6$	(Na,Ca)	0.563 (Ti) 0.606 (Nb)	3.57 [63] 3.1 (sh) [41]	3.39 3.32	1 (0.5 mol% Pr^{3+})	–
$LaTiNbO_6$	La	0.497 (Ti) 0.534 (Nb)	No data [64]	3.86 3.81	≈ 0.5 (0.8 mol% Pr^{3+})	–
$YNbTiO_6$	Y	0.519 (Ti) 0.558 (Nb)	3.61 [41]	3.70 3.64	1 (0.2 mol% Pr^{3+})	–
$LiNbO_3$	Li	0.587	3.43 [65]	3.46	1 (0.1 mol% Pr^{3+})	0.51 [65]
$NaNbO_3$	Na	0.557	3.60 [65]	3.66	≈ 0.8 (0.1 mol% Pr^{3+})	0.70 [65]
$K_{0.5}Na_{0.5}NbO_3$	Na $K^{preferred}$	0.545 0.576	3.37 [66]	3.73 3.52	<0.4 (0.5 mol% Pr^{3+})	–
$CaNb_2O_6$	Ca	0.539	3.97 [38] 3.87 [67, 68]	3.77	>0.8 (0.2 mol% Pr^{3+})	0.90 [38]

(continued)

Table 10.2 (continued)

Host lattice (*A*)	Doping site *X*	$\frac{\chi_{CN'}(M^{n+})}{d(Pr^{3+}-M^{n+})}$	CT (Pr^{3+}–M^{n+})$_{exp.}$	CT (Pr^{3+}– M^{n+})$_{calc.}$	*R*/(*R*+*B*) @ 300 K	ΔE_q
$Ca_2Nb_2O_7$	Ca(1)	0.561	3.92 [69] ≈ 3.70 (sh) [70]	3.62	>0.9 (0.5 mol% Pr^{3+})	–
	Ca(2)	0.570		3.56		
	Ca(3)	0.565		3.60		
	Ca(4)	0.540		3.77		
M'-$LuNbO_4$	Lu	0.521	4.06 [41] 4.2 [71]	3.90	>0.95 (0.2 mol% Pr^{3+})	–
M'-$YNbO_4$	Y	0.518	4.05 [38, 51]	3.92	>0.8 (0.2 mol% Pr^{3+})	0.56 [38]
M'-$GdNbO_4$	Gd	0.518	3.90 [49]	3.92	–	–
$LaNbO_4$	La	0.508	3.84 [32]	3.98	≈ 0.5 (0.2 mol% Pr^{3+})	–
$Ba_3ZrNb_4O_{15}$	Ba(1)^{preferred}	0.574	3.55 [72]	3.63	>0.9 (0.2 mol% Pr^{3+})	0.23 [72]
	Ba(2)	0.528		3.84		
$Ba_2NaNb_5O_{15}$	Ba_9 (A2 site)	0.540	3.31 [73] 3.37 [73] 3.59 [73]	3.77	>0.95 (0.5 mol% Pr^{3+})	–
	Na_{12} (A1 site)	0.558		3.65		
	C site preferred	0.642		3.06		
M'-$YTaO_4$	Y	0.539	4.15 [49] 4.27 [32]	4.23	≈0.85 (0.5 mol% Pr^{3+}) [74]	–

M'-$GdTaO_4$	Gd	0.539	4.20 [49]	4.23	≈ 0.85 (0.5 mol% Pr^{3+}) [74]	–
$LaTaO_4$	La	0.516	4.34 [32]	4.37	≈ 0.5 (0.2 mol% Pr^{3+})	–
$CaTa_2O_6$	Ca	0.555	4.16 [75]	4.13	<0.3 (5 mol% Pr^{3+})	–
$SrTa_2O_6$	Sr	0.547	4.13 [76]	4.18	–	–
$LiTaO_3$	Li	0.607	3.76 [11]	3.82	≈ 0.70 (0.4 mol% Pr^{3+})	–
$ZnTa_2O_6$	Zn	0.571	3.87 [77]	4.04	>0.9 (1 mol% Pr^{3+})	–
$LuVO_4$	Lu	0.778	3.13 [30]	3.29	1 (0.2 mol% Pr^{3+})	–
YVO_4	Y	0.771	3.26 [30]	3.33	1 (0.2 mol% Pr^{3+})	0.43 [51]
$GdVO_4$	Gd	0.771	3.25 [78] 3.42 [30]	3.33	1 (0.2 mol% Pr^{3+})	–
$LaVO_4$	La	0.743	3.57 [30]	3.49	0.94 (0.2 mol% Pr^{3+})	0.68 [51]
$Ca_9Y(VO_4)_7$	(Ca(1),Y(1))	0.769	3.57 [79, 41]	3.34	–	–
	(Ca(2),Y(2))	0.752		3.43		
	(Ca(3),Y(3))	0.781		3.27		
	Ca(4)	0.709		3.69		
$CaWO_4$	Ca	0.701	4.00 ^{un} [80] 4.40 ^{un} [49]	–	<0.4 (0.5 mol% Pr^{3+})	–
$BaWO_4$	Ba	0.679	4.60 ^{un} [49]	–	–	–
$PbWO_4$	Pb	0.688	3.70 ^{un} [49] 3.92 ^{un} [81]	–	–	–
$NaGd(WO_4)_2$	(Na,Gd)	0.699	3.75 ^{un} [82]	–	≈ 0.05 (0.5 mol% Pr^{3+})	–

(continued)

Table 10.2 (continued)

Host lattice (*A*)	**Doping site *X***	$\frac{\chi_{CN'}(M^{n+})}{d(Pr^{3+}-M^{n+})}$	**CT (Pr^{3+}–M^{n+})$_{exp.}$**	**CT (Pr^{3+}– M^{n+})$_{calc.}$**	***R*/(*R*+*B*) @ 300 K**	**ΔE_q**
$KLu(WO_4)_2$	Lu	0.606	3.61 [83]	3.70	1 (0.5 mol% Pr^{3+})	0.54 [83]
$KY(WO_4)_2$	Y	0.604	3.70 [83]	3.72	1 (0.5 mol% Pr^{3+})	0.54 [83]
$KGd(WO_4)_2$	Gd	0.606	3.79 [83]	3.70	1 (0.5 mol% Pr^{3+})	0.55 [83]
Y_2WO_6	Y(1)	0.618	3.50 [84]	3.63	1 (0.5 mol% Pr^{3+})	–
	Y(2)	0.622		3.60		
	Y(3)	0.636		3.51		
$NaLaMgWO_6$	La	0.631	4.13 [85]	3.55	<0.1 (7 mol% Pr^{3+})	–
$CaMoO_4$	Ca	0.677	3.75 ^{un} [86, 87]	–	≈ 0.6 (0.5 mol% Pr^{3+})	–
$SrMoO_4$	Sr	0.670	4.30 ^{un} [88, 89]	–	<0.4 (1 mol% Pr^{3+})	–
$BaMoO_4$	Ba	0.661	4.00 ^{un} [90]	–	–	–
$NaGd(MoO_4)_2$	Na/Gd	0.582	3.93 [91]	–	1 (0.5 mol% Pr^{3+})	0.56 [91]

sh, shoulder; un, uncertain; * assignment to $Pr^{3+} \rightarrow Ti^{4+}$ uncertain [41].

CT (Pr^{3+}–M^{n+})$_{exp.}$ and CT (Pr^{3+}–M^{n+})$_{calc.}$ pertain to experimental and calculated CT energies in eV using eq. (10.2). ΔE_q is the activation energy (in eV) that is required for the thermal quenching of $^1D_2$ emission; see Section 10.2.4. Adapted with permission from [41], Copyright 2019, Elsevier.

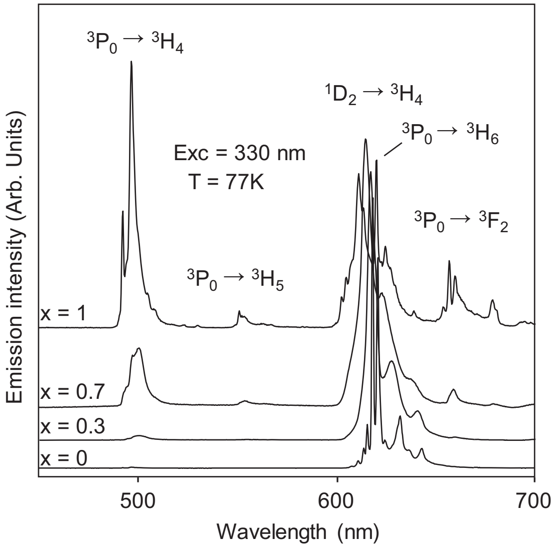

Figure 10.6: Emission spectra along the $Ca_{1-x}Sr_xTiO_3:Pr^{3+}$ series (reproduced with permission from [92], Copyright 2009, IOP Publishing).

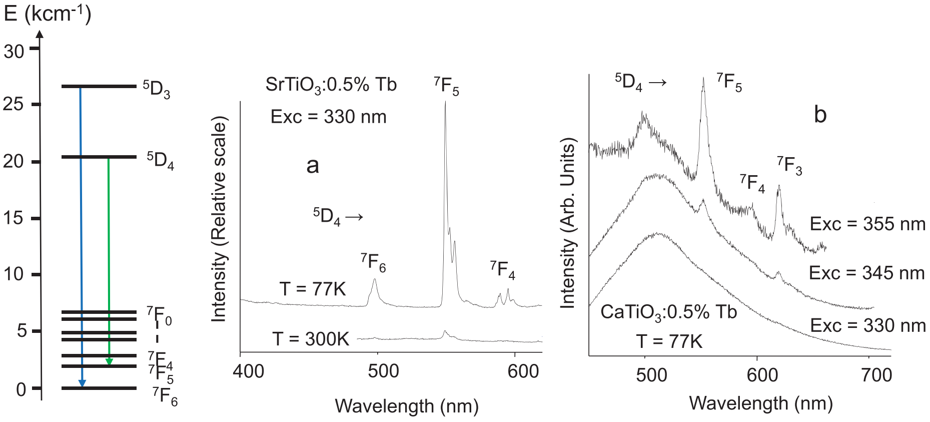

Figure 10.7: Energy level scheme of Tb^{3+} and emission spectra of $SrTiO_3:Tb^{3+}$ and $CaTiO_3:Tb^{3+}$ (unpublished results), evidencing the quenching effect of low-lying MMCT state on the Tb^{3+} luminescence.

10.2.3 The CT states and the location of the lanthanide impurity levels in transition metal complex compounds

In its primary interpretation, the formation of the $Pr^{3+}(Tb^{3+})$-to-d^0 metal CT state was ascribed to the interaction of the Ln^{3+} dopant (Pr^{3+} or Tb^{3+}) with a nearest neighbor host metal ion. As shown earlier, this "molecular vision" allows to account for several

Table 10.3: Structural and electronic properties of Tb^{3+}-containing transition metal oxides.

Host lattice (*A*)	Doping site *X*	$\frac{\chi_{CN'}(M^{n+})}{d(Tb^{3+}-M^{n+})}$	Lowest excitation	CT $(Tb^{3+}–M^{n+})_{calc.}$	Observed emission (*T*)	ΔE_q
$La_2Ti_2O_7$	La(1)	0.531	4.16 [97] ≈ 3.65 sh [97]*	3.47	$^5D_4$ (295 K)	0.17 [97]
	La(2)	0.523		3.53		
	La(3)	0.531		3.47		
	La(4)	0.531		3.47		
Gd_2MgTiO_6	Gd	0.569[a]	–	3.19	$^5D_4$ (295 K) [98]	–
$LiNbO_3$	Li	0.593	–	3.39	$^5D_4$ (12 K) [99]	–
$CaNb_2O_6$	Ca	0.546	3.95 [38]	3.73	$^5D_4$ (295 K)	0.75 [38]
$Ca_2Nb_2O_7$	Ca(1)	0.569	3.99 [100]	3.57	$^5D_4$ (295 K)	–
	Ca(2)	0.577		3.52		
	Ca(3)	0.573		3.55		
	Ca(4)	0.547		3.72		
M’-$YNbO_4$	Y	0.524	4 [38] 4.13 [101]	3.87	$^5D_4$ (295 K)	0.56 [38]
M’-$GdNbO_4$	Gd	0.524	3.7 [49]	3.87	$^5D_4$ (295 K) [102]	
M’-$LuNbO_4$	Lu	0.527	3.85 [103]	3.86	$^5D_4$ (295 K)	0.44 [103]
$LaNbO_4$	La	0.514	–	3.95	$^5D_4$ (295 K) [104, 105]	–

$InNbO_4$	In	0.527	4 [106]		3.86	$^5D_4$ (295 K)	–
M’-$YTaO_4$	Y	0.546	4^{un} [51] 4.7^{un} [108]		4.19	$^5D_3$ and $^5D_4$ (295 K) [107]	–
M’-$GdTaO_4$	Gd	0.546	4.2^{un} [49, 109]		4.19	$^5D_3$ and $^5D_4$ (295 K) [107–110]	–
$LuTaO_4$	Lu	0.550	–		4.16	$^5D_3$ & $^5D_4$ (295 K) [111]	–
$LaTaO_4$	La	0.522	4.6^{un} [108]		4.33	$^5D_4$ (295 K)	–
$LiTaO_3$	Li	0.614	–		3.78	[112]	–
$InTaO_4$	In	0.516	4 [106]		4.37	$^5D_4$ (295 K)	–
$GdVO_4$	Gd	0.781	3.29 [78]		3.27	$^5D_4$ (<295 K)	0.11 [78]
$LaVO_4$	La	0.753	3.81 [113]		3.43	$^5D_4$ (<295 K)	0.02 [78]
InVO4	In	0.695	–		3.77	Host (295 K) [106]	–
$CaWO_4$	Ca	0.710	4.00^{un} [114]	–		$^5D_3$ & $^5D_4$ (295 K) [114, 115]	0.68 [114]
$SrWO_4$	Sr	0.698	4.8^{un} [49]	–		$^5D_4$ (295 K) [116]	–
$BaWO_4$	Ba	0.687	4.60^{un} [49] 4.55^{un} [117]	–		$^5D_3$ & $^5D_4$ (295 K)	–
$PbWO_4$	Pb	0.696	4.6^{un} [49] 3.77^{un} [118]	–		$^5D_3$ & $^5D_4$ (295 K)	0.66 [119]
$KLu(WO_4)_2$	Lu	0.613	3.78 [83]		3.66	$^5D_4$ (295 K)	0.63 [83]
$KYb(WO_4)_2$	Yb	0.623	3.49 [83]		3.59	$^5D_4$ (295 K)	0.42 [120]
$KY(WO_4)_2$	Y	0.613	3.76 [121]		3.66	$^5D_4$ (295 K)	–

(continued)

Table 10.3 (continued)

Host lattice (*A*)	**Doping site *X***	$\frac{\chi_{CN'}(M^{n+})}{d(Tb^{3+}-M^{n+})}$	**Lowest excitation**	**CT** $(Tb^{3+}–M^{n+})_{calc.}$	**Observed emission (*T*)**	ΔE_q
Y_2WO_6	Y(1)	0.626	–	3.58	$^5D_4$ (295 K) [122]	–
	Y(2)	0.629		3.56		
	Y(3)	0.644		3.46		
$CaMoO_4$	Ca	0.685	3.75^{un} [86, 114, 116]	–	$^5D_4$ (295 K)	0.70 [114]
$SrMoO_4$	Sr	0.678	4.30^{un} [117, 118] 4.28^{un} [123]	–	$^5D_3$ & $^5D_4$ (295 K)	
$BaMoO_4$	Ba	0.669	4.00^{un} [119] 3.86^{un} [124]	–	$^5D_3$ & $^5D_4$ (295 K)	
$NaGd(MoO_4)_2$	Na/Gd	0.588	4.08 [91]	–	$^5D_4$ (295 K)	0.36 [91]

un, uncertain; * ascribed to Tb-to-d^0 metal CT in the present work.

[a] From the crystal structure reported in [125].

CT $(Tb^{3+} – M^{n+})_{calc.}$ pertains to calculated CT energies in eV using eq. (10.5). ΔE_q is the activation energy (in eV) that is required for the thermal quenching of $^5D_4$ emission; see Section 10.2.4.

experimental behaviors and to elaborate a reliable overview of the luminescence dynamics of the [Ln^{3+}–O^{2-}–M^{n+}] systems. Further interesting information can be obtained through an alternative approach, proposed firstly by P. Dorenbos, that considers the "host lattice + doping ion" system as a whole, in the awareness that its spectroscopic properties can be fully understood only if the position of the rare-earth energy levels relative to the bands of the host crystal is known. Moreover, the developed method exploits the systematic nature of the properties of the rare earth ions in order to extend to the whole series the knowledge acquired for only some of them (Pr^{3+} and Tb^{3+}), giving rise to a powerful tool for interpretative and predictive purposes. The basic principles of the method are summarized as follows:

- The metal-to-metal CT process is ascribed as an excitation from the ground state of the Pr^{3+} or Tb^{3+} to the conduction band of the host with the subsequent creation of a bound exciton connected to the formation of the Ln^{4+}–$M^{(n-1)+}$ pair (with n being the oxidation number of the d^0 metal ion).
- The energy of the corresponding CT band in the excitation spectrum provides information on the location of the Pr^{3+} and Tb^{3+} levels relative to the host bands.
- Using the "double seat" empirical model developed by Dorenbos et al., it is possible to predict the ground state level location for all trivalent lanthanides in the host. The model has been quantitatively formalized through the compilation of a set of parameters, ΔE_{Vf} (Ln^{3+}), indicating the difference between the energy position of the Ln^{3+} ground state with respect to that of Ce^{3+}, taken as a reference [45, 46].
- Since their energy level structures are relatively host insensitive, the complete energy level schemes for all trivalent rare-earth ions can be easily constructed based on the Dieke diagram.
- This information can be combined with that provided by the observation of the LMCT transition of Eu^{3+}, allowing locating the position of the Eu^{2+} ground state in the bandgap. It was observed that the energy difference between the Eu^{2+} and Pr^{3+} ground state is approximately constant [45].

Using this method, the energy level schemes of the Ln^{3+} ions in vanadates [78, 113], molybdates and tungstates [83, 94, 114, 126], titanates, niobates, and tantalates [94] have been determined; see for example, the energy level schemes obtained for trivalent lanthanides $CaWO_4$ and $CaMoO_4$ (Figure 10.8). As demonstrated in [40, 95, 96], the model is subject to continuous improvement.

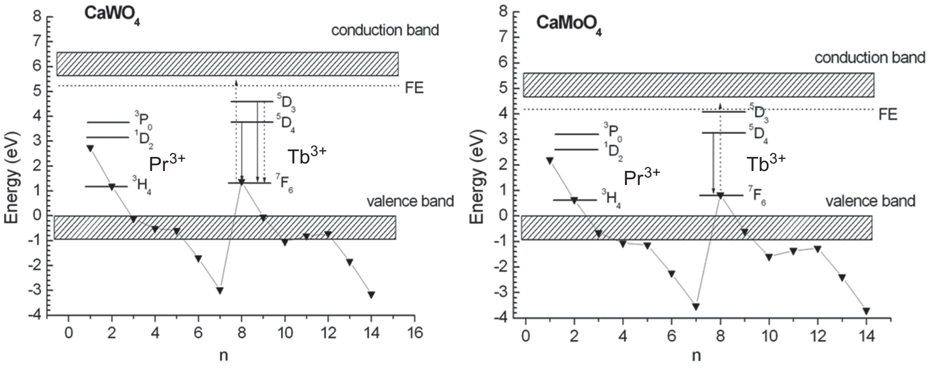

Figure 10.8: Position of the ground state energy along the Ln^{3+} series in $CaWO_4$ and $CaMoO_4$. *n* is the number of electrons in the 4*f* shell (reproduced with permission from [114], Copyright 2010, American Chemical Society).

10.2.4 Effect of temperature and application in optical thermometry

The effect of temperature can be examined based on simplified single coordinate configurational diagrams. In the case of Pr^{3+} and Tb^{3+} (Figure 10.9), only the emitting states of interest are drawn. States $^7F_6$, $^5D_4$, and $^5D_3$ relate to Tb^{3+} while states $^3H_4$, $^1D_2$, and $^3P_0$ relate to Pr^{3+}. $^3P_0$ and $^5D_4$ are taken at the same energy, for simplicity. For both cations, the MMCT state forms a Franck–Condon-shifted state that crosses the emitting states at points *A’*, *B’*, and *C’*. The bottom of this state is figured by point *D’*, and its crossover to the ground state ($^3H_4$ for Pr^{3+} or $^7F_6$ for Tb^{3+}) is figured by point *E*. It is worth noting here that no emission has been reported so far from either the Pr^{3+}-to-d^0 or Tb^{3+}-to-d^0

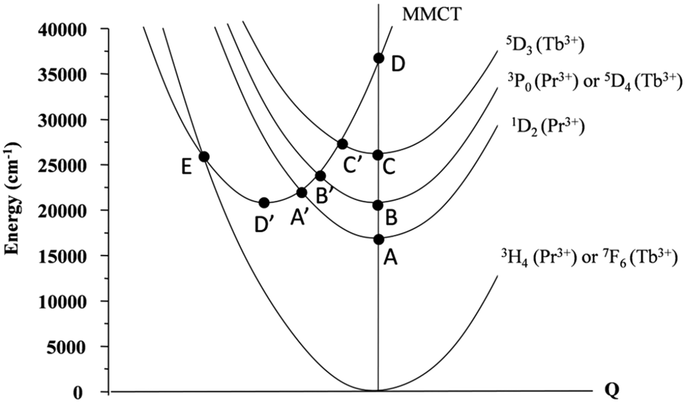
MMCT
5D3 (Tb3+)
3P0 (Pr3+) or 5D4 (Tb3+)
1D2 (Pr3+)
3H4 (Pr3+) or 7F6 (Tb3+)
Energy (cm-1)
40000
35000
30000
25000
20000
15000
10000
5000
0
Q
D
E
C’
C
B’
B
D’
A’
A

Figure 10.9: Single configurational coordinate diagram for the (Pr^{3+}, Tb^{3+})-MMCT system.

metal CT state, even at low temperature. After exciting the Pr^{3+} or Tb^{3+}-related CT states in direct (point *D*), fast radiationless relaxation takes place at point *D'*. From this point, $^1D_2$ and $^3P_0$ states of Pr^{3+} are populated with the necessary thermal assistance to overcome energy barriers $\Delta E_{D'A'}$ and $\Delta E_{D'B'}$, respectively, while $^5D_3$ and $^5D_4$ states of Tb^{3+} are fed with activation energies $\Delta E_{D'B'}$ and $\Delta E_{D'C'}$, respectively.

Let us now consider Pr^{3+} and Tb^{3+} separately. For Tb^{3+}, an activation energy $\Delta E_{CC'}$ allows thermal depopulation of $^5D_3$ at the benefit of $^5D_4$ by crossover to the CT state at point *C'*. $^5D_4$ is in turn depopulated by crossover to the CT state at point *B'* if a thermal energy larger than $\Delta E_{BB'}$ is provided to the system. Quenching occurs when point *E* is reached, that is, for an activation energy ΔE_{BE}. In the case of Pr^{3+}, $\Delta E_{BB'}$ represents the thermal energy that is required to depopulate $^3P_0$ at the benefit of $^1D_2$ by crossover to the CT state. As it will be reviewed further, this path is exploited for the design of Pr^{3+}-doped optical thermometers. A thermal energy corresponding to ΔE_{AE} will lead to the quenching of $^1D_2$. This process is possibly accompanied with the thermalization of $^3P_0$. The underlying presence of the $^1D_2$ state explains why the $^3P_0$ emission of Pr^{3+} is strongly quenched in several transition metal oxides (e.g., $CaTiO_3$), whereas the $^5D_4$ emission of Tb^{3+} is not even though these levels have similar energy [127] (Figure 10.7).

The thermal quenching of an emitting state by crossover to a Franck–Condon shifted state (here the MMCT state) is in general well reproduced in the approximation of a single energy barrier model by [128]

$$\frac{I(T)}{I(T_0)} = \frac{1}{1 + A\exp\left(-\frac{\Delta E_q}{kT}\right)} \tag{10.6}$$

where *I*(*T*) is the emission intensity estimated as the integrated area of the emission spectrum, $I(T_0)$ is the emission intensity at the reference temperature (usually 295 K), *A* is the ratio between the radiative rate and the attempt rate of the nonradiative process, with values typically in the range of 10^7–10^8, and ΔE_q is the activation energy that is required for the emission quenching. Some values are given in Tables 10.2 and 10.3. Figure 10.10 shows, for the sake of example, the temperature evolution of the $^5D_3$ emission in $CaWO_4$:Tb^{3+} and of the $^5D_4$ emission in $CaMoO_4$:Tb^{3+}, well reproduced using eq. (10.6) [114].

The efficient thermal quenching due to the crossover to the MMCT state has recently been conveniently exploited in the field of the optical temperature sensing. The working principle of these materials is based on the temperature evolution of the ratio of the luminescence from two thermally coupled levels of active ions like $^2H_{11/2}$, $^4S_{3/2}$ levels of Er^{3+}, or phonon-assisted energy transfer processes between rare-earth ions, for instance, Nd^{3+} and Yb^{3+} [129]. The performances of these materials are expressed in terms of absolute temperature sensitivity S_a and relative temperature sensitivity S_r:

$$S_a = \left|\frac{\delta(\mathrm{FIR})}{\delta T}\right| = \frac{\Delta E_q}{kT^2} C \exp\left(-\frac{\Delta E_q}{kT}\right) \tag{10.7}$$

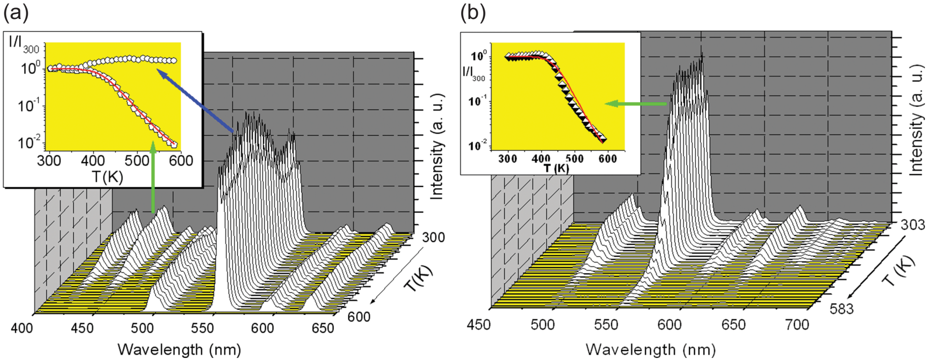

Figure 10.10: Emission spectra of $CaWO_4$:Tb^{3+} (a) and $CaMoO_4$:Tb^{3+} (b) measured in the 300–600 K temperature range. The temperature behaviors of the integrated intensities of the 440 nm ($^5D_3$) and 550 nm ($^5D_4$) bands are reported in the inset. The red line represents the fit by means of eq. (10.6) (reproduced with permission from [114], Copyright 2010, American Chemical Society).

$$S_r = 100\left|\frac{1}{\mathrm{FIR}}\frac{\delta(\mathrm{FIR})}{\delta T}\right| = 100\frac{\Delta E_q}{kT^2}\frac{C\exp\left(-\frac{\Delta E_q}{kT}\right)}{D + C\exp\left(-\frac{\Delta E_q}{kT}\right)} \tag{10.8}$$

where C and D are adjustable parameters that depend on the considered system.

A strategy based on the thermal depopulation of Pr^{3+} or Tb^{3+} states by crossover to an MMCT was recently proposed, and its higher efficiency with respect to the abovementioned approaches was demonstrated. Several single Pr^{3+}-doped or Pr^{3+}, Tb^{3+} co-doped systems have been developed and characterized as optical thermometers, as shown in Table 10.4. Single Pr^{3+}-doped systems exploit the temperature dependence of the ($^1D_2 \to {}^3H_4$)/($^3P_0 \to {}^3H_4$) intensity ratio, that is, FIR(Pr^{3+}) = I($^1D_2$)/I($^3P_0$). Referring to Figure 10.9, $\Delta E_q = \Delta E_{BB'(Pr3+)}$ is the key factor that accounts for the thermal depopulation of $^3P_0$ at the benefit of $^1D_2$ in the abovementioned equations. In doubly Pr^{3+},Tb^{3+}-doped systems, the temperature sensing is provided by the intensity ratio of the red ($^1D_2 \to {}^3H_4$) line of Pr^{3+} and green ($^5D_4 \to {}^7F_5$) line of Tb^{3+}, that is, FIR(Pr^{3+}, Tb^{3+}) = I($^1D_2$)/I($^5D_4$). The quenching, in this case, mostly affects the green Tb^{3+} emission because $\Delta E_{BB'(Tb3+)} < \Delta E_{AA'}$. It comes that $\Delta E_q = \Delta E_{BB'(Tb3+)}$ in the abovementioned equations.

10.2.5 Effect of hydrostatic pressure

Steady-state and time-resolved emission measurements on different host lattices activated with Tb^{3+} or Pr^{3+} were carried out in conditions of high hydrostatic pressure up to 315 kbar using a diamond anvil cell [67, 68, 86, 115, 120, 134–138], and the MMCT model (properly reformulated) was applied in order to interpret the effect of the

Table 10.4: Pr^{3+} and Tb^{3+}-to-d^0 metal-based optical thermometers, maximal values of S_a and S_r, and working range of the optical thermometer.

Compound	Dopant	Working temperature range (K)	S_a (K^{-1})	S_r (%/K)	Reference
$CaTiO_3$	Pr^{3+}	298–473	0.026	7.69	[130]
$Ba_{0.7}Sr_{0.3}TiO_3$	Pr^{3+}	290–513		1.62	[131]
La_2MgTiO_6	Pr^{3+}	303–543	0.054	1.31	[132]
		77–500	0.072	1.28	[61]
$La_2Ti_3O_9$	Pr^{3+},Tb^{3+}	303–423	0.156	3.47	[91]
$Na_2La_2Ti_3O_{10}$	Pr^{3+}	303–543	0.4	1.96	[132]
Gd_2ZnTiO_6	Pr^{3+}	293–433	0.63	1.67	[59]
		433–593	0.096[a]	1.48[a]	
$Y_2Ti_2O_7$	Pr^{3+}	289–573	0.098	5.25	[54]
$Gd_2Ti_2O_7$	Pr^{3+}	289–573	0.081	4.62	[54]
$LaVO_4$	Pr^{3+},Tb^{3+}	303–443	0.193	5.3	[91]
$K_{1/2}Na_{1/2}NbO_3$	Pr^{3+}	293–456	0.353	3.62	[66]
$YNbO_4$	Pr^{3+}	303–543	0.105	1.56	[132]
$LuNbO_4$	Pr^{3+},Tb^{3+}	283–493	0.024	1.26	[133]
$NaGd(MoO_4)_2$	Pr^{3+},Tb^{3+}	303–483	0.097	2.05	[91]
$NaLu(MoO_4)_2$	Pr^{3+},Tb^{3+}	303–423	0.061	2.51	[91]
$NaLu(WO_4)_2$	Pr^{3+},Tb^{3+}	583–783	0.075	1.45	[91]

[a] From fluorescence lifetime of $^1D_2$ state.

pressure on the luminescence properties. The evolution of the emission features with increasing pressure can be reliably accounted for by considering that the pressure induces a downshift of the MMCT state with respect to the lanthanide levels, as a consequence of the shortening of the Pr^{3+}(Tb^{3+})–M^{n+} distance.

As shown in Figure 10.11 for the case of $CaWO_4$:Pr^{3+}, the pressure evolution of the luminescence spectrum can be properly accounted for based on a single configurational coordinate in which the representative parabola of the MMCT state is progressively lowered [136]. This MMCT-related control of the intensity, spectral position, and lifetime of the Pr^{3+} or Tb^{3+} emission lines with pressure is potentially exploitable for designing pressure-sensitive luminescence probes.

10.3 Summary

CTSs formed between oxidizable dopants like Pr^{3+} or Tb^{3+} and closed-shell transition metals in oxidic lattices have deep influence on the optical properties by creating new relaxation channels that either quench or promote luminescence. These properties have opened new horizons toward the development of ultrasensitive optical thermometers or tunable phosphors, potentially excitable in the near-UV spectral region. In this review, we make an inventory of the existing compounds and introduce semiempirical

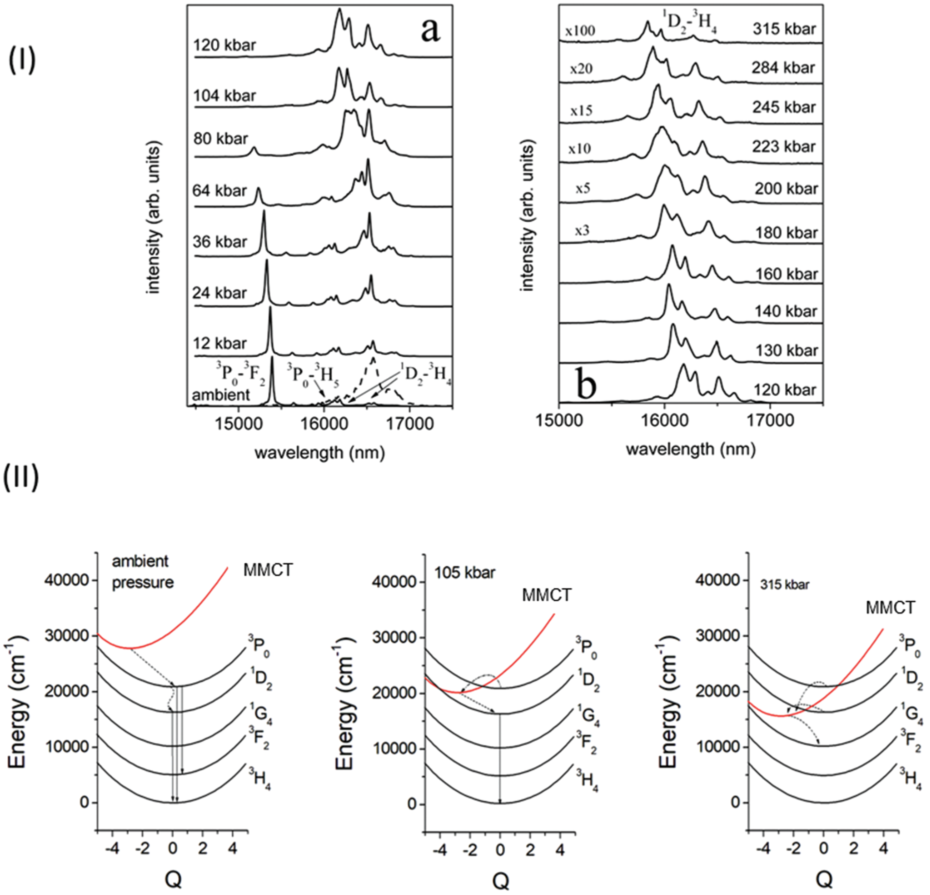

Figure 10.11: (I) Pressure dependence of the $CaWO_4$:Pr^{3+} emission measured upon 473 nm excitation. (a) 1–120 kbar range (dashed line: time resolved spectrum of the $^1D_2$ emission); (b) 120–315 kbar range (reproduced with permission from [136], Copyright 2012, Elsevier). (II) Single configurational coordinate scheme of $CaWO_4$:Pr^{3+} at ambient pressure, at 105 kbar and at 315 kbar. The radiative and nonradiative transitions are indicated by solid and dashed arrows, respectively (adapted with permission from [136], Copyright 2012, Elsevier).

methods for calculating the excitation energy of these CTSs based on the structural characteristics of the host lattices. These easy-to-use tools pave the way toward the design of new Pr^{3+}- or Tb^{3+}-doped compounds with original optical properties.

References

[1] G. Blasse, Optical electron transfer between metal ions and its consequences, Struct. Bond 76 (1991) 153–187.

[2] G. Blasse, A. Bril, Investigations of Tb^{3+}-activated phosphors, Philips Res. Rep. 22 (1967) 481–504.

[3] R.G. DeLosh, T.Y. Tien, E.F. Gibbins, P.J. Zacmanides, H.L. Stadler, Strong quenching of Tb^{3+} emission by Tb-V interaction in YPO_4-YVO_4, J. Phys. Chem. 53 (1970) 681–685. https://doi.org/10.1063/1.1674044.

[4] G. Blasse, A. Bril, Investigations on Bi^{3+}-activated phosphors, J. Chem. Phys. 48 (1968) 217–222. https://doi.org/10.1063/1.1667905.

[5] R. Moncorgé, G. Boulon, Investigation of the absorption and emission properties along with energy transfer in pure and Bi^{3+}-doped YVO_4, J. Lumin. 18, 19 (1979) 376–380. https://doi.org/10.1016/0022-2313(79)90144-3.

[6] E.G. Reut, A.I. Ryskin, Virtual recharge: Mechanism of radiationless transition in scheelite and fergusonite type crystals doped with rare-earth ions, Phys. Stat. Sol. (a) 17 (1973) 47–57. https://doi.org/10.1002/pssa.2210170103.

[7] C. De Mello Donegá, A. Meijerink, G. Blasse, Non-radiative relaxation processes of the Pr^{3+} ion in solids, J. Phys. Chem. Solids 56 (1995) 673–685. https://doi.org/10.1016/0022-36979400183-9.

[8] P.T. Diallo, P. Boutinaud, R. Mahiou, J.C. Cousseins, Red luminescence in Pr^{3+}-doped calcium titanates, Phys. Stat. Sol. (a) 160 (1997) 255–263. https://doi.org/10.1002/1521-396X(199703)160:1<255::AID-PSSA255>3.0.CO;2-Y.

[9] P. Boutinaud, R. Mahiou, E. Cavalli, M. Bettinelli, Excited state dynamics of Pr^{3+} in YVO_4 crystals, J. Appl. Phys. 96 (2004) 4923–4929. https://doi.org/10.1063/1.1797551.

[10] E. Pinel, P. Boutinaud, R. Mahiou, What makes the luminescence of Pr^{3+} different in $CaTiO_3$ and in $CaZrO_3$?, J. Alloys Comp. 380 (2004) 202–206. https://doi.org/10.1016/j.jallcom.2004.03.048.

[11] W. Gryk, D. Dyl, W. Ryba-Romanowski, M. Grinberg, Spectral properties of $LiTaO_3 : Pr^{3+}$under high hydrostatic pressure, J. Phys.: Condens. Matter 17 (2005) 5381–5396. https://doi.org/10.1088/0953-8984/17/35/006.

[12] W. Gryk, D. Dyl, M. Grinberg, M. Malinowski, High pressure photoluminescence study of Pr^{3+} doped $LiNbO_3$, Phys. Stat. Sol. (c) 2 (2005) 188–191. https://doi.org/10.1002/pssc.200460142.

[13] P. Boutinaud, E. Pinel, M. Dubois, A.P. Vink, R. Mahiou, UV-to-red relaxation pathway in $CaTiO_3 : Pr^{3+}$, J. Lumin. 111 (2005) 69–80. https://doi.org/10.1016/j.jlumin.2004.06.006.

[14] S. Saha, T.P. Sinha, A. Mookerjee, First principles study of electronic structure and optical properties of $CaTiO_3$, Eur. Phys. J. B 18 (2000) 207–214. https://doi.org/10.1007/s100510070050.

[15] Z. Huang, J. Feng, W. Pan, Theoretical investigations of the physical properties of zircon-type YVO_4, J. Solid State Chem. (2012) 42–48. https://doi.org/10.1016/j.jssc.2011.10.050.

[16] Z. Huang, L. Zhang, J. Feng, X. Cui, W. Pan, Electronic, elastic and optical properties of zircon GdVO4 investigated from experiments and LSDA+U, J. Alloys Comp. 538 (2012) 56–60. https://doi.org/10.1016/j.jallcom.2012.05.103.

[17] L. Sun, X. Zhao, Y. Li, P. Li, H. Sun, X. Cheng, W. Fan, First-principles studies of electronic, optical and vibrational properties of $LaVO_4$ polymorph, J. Appl. Phys. 108 (2010) 093519. https://doi.org/10.1063/1.3499308.

[18] I.L.V. Rosa, M.C. Oliveira, M. Assis, M. Ferrer, R.S. André, E. Longo, M.F.C. Gurgel, A theoretical investigation of the structural and electronic properties of orthorhombic $CaZrO_3$, Ceram. Int. 41 (2015) 3069–3074. https://doi.org/10.1016/j.ceramint.2014.10.149.

[19] R.I. Egletis, S. Piskunov, First principles calculations of $SrZrO_3$ bulk and ZrO_2-terminated (001) surface F centers, Comput. Condens. Matter 7 (2016) 1–6. https://doi.org/10.1016/j.cocom.2016.04.002.

[20] M. Hossain, First-principles study on the structural, elastic, electronic and optical properties of $LiNbO_3$, Heliyon 5 (2019) e01436. https://doi.org/10.1016/j.heliyon.2019.e01436.

[21] H. Shi, Z. Zou, Photophysical and photocatalytic properties of $ANbO_3$ (A = Na,K) photocatalysts, J. Phys. Chem. Solids 73 (2012) 788–792. https://doi.org/10.1016/j.jpcs.2012.01.026.

[22] T.L. Lim, M. Nazarov, T.L. Yoon, L.C. Low, M.N.A. Fauzi, First-principles LDA+U calculations and luminescence study of $YNbO_4$, Phys. Scr. 89 (2014) 095102. https://doi.org/10.1088/0031-8949/89/9/095102.

[23] F.Y. Yan, Z.G. Liu, J.H. Ouyang, M.F. Yan, First principles calculations of water dissociation on the oxygen-deficient (010) surface of fergusonite-type $LaNbO_4$ crystal, Int. J. Hydrogen Energy 39 (2014) 1457–1462. https://doi.org/10.1016/j.ijhydene.2013.11.018.

[24] T.L. Lim, M. Nazarov, T.L. Yoon, L.C. Low, M.N.A. Fauzi, X-ray diffraction experiments, luminescence measurements and first-principles GGA+U calculations on $YTaO_4$, Comput. Mater. Sci. 77 (2013) 13–18. https://doi.org/10.1016/j.commatsci.2013.03.042.

[25] F.K.F. Oliveira, M.C. Oliveira, L. Gracia, R.L. Tranquilin, C.A. Paskocimas, F.V. Motta, E. Longo, J. Andrés, M.R.D. Bomio, Experimental and theoretical study to explain the morphology of $CaMoO_4$ crystals, J. Phys. Chem. Solids 114 (2018) 141–152. https://doi.org/10.1016/j.jpcs.2017.11.019.

[26] L.S. Cavalcante, V.M. Longo, J.C. Sczancoski, M.A.P. Almeida, A.A. Batista, J.A. Varela, M.O. Orlandi, E. Longo, M.S. Li, Electronic structure, growth mechanism and photoluminescence of $CaWO_4$ crystals, CrystEngComm. 14 (2012) 853–868. https://doi.org/10.1039/c1ce05977g.

[27] X. Zhou, Y. Deng, S. Jiang, G. Xiang, L. Li, X. Tang, X. Luo, Y. Pang, Y. Huang, Investigation of energy transfer in Pr^{3+}, Yb^{3+} co-doped phosphate phosphor : The role of $^3P_0$ and $^1D_2$, J. Lumin. 209 (2019) 45–51. https://doi.org/10.1016/j.jlumin.2019.01.010.

[28] J. Collins, M. Geen, M. Bettinelli, B. Di Bartolo, Dependence of cross-relaxation on temperature and concentration from the $^1D_2$ level of Pr^{3+} in YPO_4, J. Lumin. 132 (2012) 2626–2633. https://doi.org/10.1016/j.jlumin.2012.04.027.

[29] B. Johansson, Energy position of 4f levels in rare-earth metals, Phys. Rev. B 20 (1979) 1315–1327. https://doi.org/10.1103/PhysRevB.20.1315.

[30] P. Boutinaud, R. Mahiou, E. Cavalli, M. Bettinelli, Luminescence properties of Pr^{3+} in titanates and vanadates: Towards a criterion to predict $^3P_0$ emission quenching, Chem. Phys. Lett. 418 (2006) 185–188. https://doi.org/10.1016/j.cplett.2005.10.120.

[31] E. Pinel, P. Boutinaud, R. Mahiou, Using a structural criterion for the selection of red-emitting oxide-based compounds containing Pr^{3+}, J. Alloys Comp. 374 (2004) 165–168. https://doi.org/10.1016/j.jallcom.2003.11.084.

[32] P. Boutinaud, E. Pinel, M. Oubaha, R. Mahiou, E. Cavalli, M. Bettinelli, Making red emitting phosphors with Pr^{3+}, Opt. Mater. 28 (2006) 9–13. https://doi.org/10.1016/j.optmat.2004.09.027.

[33] P. Boutinaud, R. Mahiou, E. Cavalli, M. Bettinelli, Red luminescence induced by intervalence charge transfer in Pr^{3+}-doped compounds, J. Lumin. 122-123 (2007) 430–433. https://doi.org/10.1016/j.jlumin.2006.01.198.

[34] R. Reisfeld, C.K. Jørgensen, Lasers and Excited States of Rare Earths, Springer-Verlag (1977), p. 45.

[35] C.K. Jørgensen, Electron transfer spectra, Prog. Inorg. Chem. 12 (1970) 101–158. https://doi.org/10.1002/9780470166130.ch2.

[36] C.K. Jørgensen, Modern Aspects of Ligand Field Theory, North-Holland Publishing Co (1971).

[37] S. Qiang, Optical electronegativity of lanthanide ions, in: G. Xu, et al. (Eds.), Proceedings of the Second International Conference on Rare-Earth Development and Applications, Vol. 2, International Academic Publishers, Beijing, China (1991), pp. 765–769.

[38] P. Boutinaud, E. Cavalli, M. Bettinelli, Emission quenching induced by intervalence charge transfer in Pr^{3+}- or Tb^{3+}-doped $YNbO_4$ and $CaNb_2O_6$, J. Phys.: Condens. Matter 19 (2007) 386230. https://doi.org/10.1088/0953-8984/19/38/386230.

[39] P. Dorenbos, Modeling the chemical shift of lanthanide 4f electron binding energies, Phys. Rev. B 85 (2012) 165107. https://doi.org/10.1103/PhysRev.85.165107.

[40] P. Dorenbos, Determining binding energies of valence-band electrons in insulators and semiconductors via lanthanide spectroscopy, Phys. Rev. B 87 (2013) 035118. https://doi.org/10.1103/PhysRevB.87.035118.

[41] P. Boutinaud, Rationalization of the Pr^{3+}- to-transition metal charge transfer model: Application to the luminescence of Pr^{3+} in titano-niobates, J. Lumin. 214 (2019) 116557. https://doi.org/10.1016/j.jlumin.2019.116557.

[42] K. Li, D. Xue, Estimation of electronegativity values of elements in different valence states, J. Phys. Chem. A 110 (2006) 11332–11337. https://doi.org/10.1021/jp062886k.

[43] R.D. Shannon, Revised effective ionic radii and systematic studies of interatomic distances in halides and chalcogenides, Acta Cryst. A 32 (1976) 751–767. https://doi.org/10.1107/S0567739476001551.

[44] P. Dorenbos, Systematic behaviour in trivalent lanthanide charge transfer energies, J. Phys.: Condens. Matter 15 (2003) 8417–8434. https://doi.org/10.1088/0953-8984/15/49/018.

[45] P. Dorenbos, The Eu^{3+} charge transfer energy and the relation with the band gap of compounds, J. Lumin. 111 (2005) 89–104. https://doi.org/10.1016/j.jlumin.2004.07.003.

[46] P. Dorenbos, Lanthanide charge transfer energies and related luminescence, charge carrier trapping, and redox phenomena, J. Alloys Comp. 488 (2009) 568–573. https://doi.org/10.1016/j.jallcom.2008.09.059.

[47] R.H. Awater, P. Dorenbos, The Bi^{3+} 6s and 6p electron binding energies in relation to the chemical environment of inorganic compounds, J. Lumin. 184 (2017) 221–231. https://doi.org/10.1016/j.jlumin.2016.12.021.

[48] P. Dorenbos, Ce^{3+} 5d-centroid shift and vacuum referred 4f-electron binding energies of all lanthanide impurities in 150 different compounds, J. Lumin. 135 (2013) 93–104. https://doi.org/10.1016/j.jlumin.2012.09.034.

[49] E.G. Rogers, P. Dorenbos, Vacuum referred binding energy of the single 3d,4d or 5d electron in transition metal and lanthanide impurities in compounds, ECS J. Sol. State Sci. Technol. 3 (2014) R173–R184. https://doi.org/10.1149/2.0121410jss.

[50] P. Boutinaud, L. Sarakha, R. Mahiou, P. Dorenbos, Y. Inaguma, Intervalence charge transfer in perovskite titanates $R_{1/2}Na_{1/2}TiO_3$: Pr^{3+}(R = La, Gd, Y, Lu), J. Lumin. 130 (2010) 1725–1729. https://doi.org/10.1016/j.jlumin.2010.03.040.

[51] P. Boutinaud, P. Putaj, R. Mahiou, E. Cavalli, A. Speghini, M. Bettinelli, Quenching of lanthanide emission by intervalence charge transfer in crystals containing closed shell transition metal ions, Spectrosc. Lett. 40 (2007) 209–220. https://doi.org/10.1080/00387010701247019.

[52] P. Boutinaud, E. Cavalli, R. Velchuri, M. Vithal, Luminescence properties of $K_{1/2}Bi_{1/2}TiO_3$: $Pr^{3+}$and $Na_{1/2}Bi_{1/2}TiO_3$: Pr^{3+}, J. Phys. Condens. Matter 24 (2012) 075502. https://doi.org/10.1088/0953-8984/24/7/075502.

[53] X.H. Fan, J.C. Zhang, M. Zhang, C. Pan, X. Yan, W.P. Han, H.D. Zhang, Y.Z. Long, X. Wang, Piezoluminescence from ferroelectric $Ca_3Ti_2O_7$: Pr^{3+}long-persistent phosphor, Opt. Express 25 (2017) 14238–14246. https://doi.org/10.1364/OE.25.014238.

[54] R. Lei, X. Luo, Z. Yuan, H. Wang, F. Huang, D. Deng, S. Xu, Ultrahigh-sensitive optical temperature sensing in Pr^{3+}: $Y_2Ti_2O_7$based on diverse thermal response from trap emission and Pr^{3+} red luminescence, J. Lumin. 205 (2019) 440–445. https://doi.org/10.1016/j.jlumin.2018.09.029.

[55] P.T. Diallo, P. Boutinaud, R. Mahiou, Anti-Stokes luminescence and site selectivity in $La_2Ti_2O_7$: Pr^{3+}, J. Alloys Comp. (2002) 341139–341143. https://doi.org/10.1016/S0925-83880200098-1.

[56] P.T. Diallo, P. Boutinaud, R. Mahiou, J.C. Cousseins, Luminescence properties of $(La,Pr)_2Ti_2O_7$, J. Alloys Comp. 275-277 (1998) 307–310. https://doi.org/10.1016/S0925-83889800324-7.

[57] S. Zhang, H. Liang, Y. Liu, Temperature-sensitive fluorescence of $NaRETiO_4$: Pr^{3+}(RE = Y, Gd) based on the intervalence charge transfer between Pr^{3+} and Ti^{4+}, J. Appl. Phys. 115 (2014) 073511. https://doi.org/10.1063/1.4865960.

[58] S. Zhang, H. Liang, C. Liu, Increased $^1D_2$ red emission of Pr^{3+} in $NaGdTiO_4$: Pr^{3+}due to temperature-assisted host sensitization and its color variation, J. Phys. Chem. C 117 (2013) 2216–2221. https://doi.org/10.1021/jp3120258.

[59] Y. Gao, Y. Chen, T. Hu, Z. Ji, H. Lin, J. Xu, Y. Wang, Broadening the valid temperature range of optical thermometry through dual-mode design, J. Mater. Chem. C 6 (2018) 11178–11183. https://doi.org/10.1039/C8TC03851A.

[60] J. Lin, B. Yan, Rare earth titanates ceramics $Na_2La_2Ti_3O_{10}$: $Pr^{3+}$and $RE_2Ti_2O_7$: Pr^{3+}(RE = Gd, Y): Sol-gel synthesis, characterization and luminescence, J. Mater. Sci: Mater. Electron. 22 (2011) 672–678. https://doi.org/10.1007/s10854-010-0194-8.

[61] R. Shi, L. Lin, P. Dorenbos, H. Liang, Development of a potential optical thermometric material through photoluminescence of Pr^{3+} in La_2MgTiO_6, J. Mater. Chem. C 5 (2017) 10737–10745. https://doi.org/10.1039/C7TC02661G.

[62] L. Tian, S. Mho, Z. Jin, Luminescence properties of red-emitting praseodymium-activated $BaTi_4O_9$ phosphor, J. Lumin. 129 (2009) 797–800. https://doi.org/10.1016/j.jlumin.2009.02.016.

[63] D. Xu, P. Yu, L. Tian, Luminescence properties of Pr^{3+} and Bi^{3+} co-doped $NaCaTiNbO_6$ phosphor for red-LEDs, J. Rare Earths 36 (2018) 243–247. https://doi.org/10.1016/j.jre.2017.07.013.

[64] X. Qi, C.M. Liu, C.C. Kuo, Pr^{3+}-doped $LaTiNbO_6$ as s single phosphor for white LEDs, J. Alloys Comp. 492 (2010) L61–L63. https://doi.org/10.1016/j.jallcom.2009.11.188.

[65] P. Boutinaud, L. Sarakha, R. Mahiou, $NaNbO_3$:Pr^{3+}, a new red phosphor showing persistent luminescence, J .Phys.: Condens. Matter 21 (2009) 025901. https://doi.org/10.1088/0953-8984/21/2/025901.

[66] W. Tang, S. Wang, Z. Li, Y. Sun, L. Zheng, R. Zhang, B. Yang, W. Cao, M. Yu, Ultrahigh-sensitive optical temperature sensing based on ferroelectric Pr^{3+}-doped $(K_{0.5}Na_{0.5})NbO_3$, Appl. Phys. Lett. 108 (2016) 061902. https://doi.org/10.1063/1.4941669.

[67] S. Mahlik, M. Grinberg, A.A. Kaminskii, M. Bettinelli, P. Boutinaud, Luminescence of $Ca(NbO_3)_2$: Pr^{3+}at ambient and high hydrostatic pressure, J. Lumin. 129 (2009) 1219–1224. https://doi.org/10.1016/j.jlumin.2009.06.002.

[68] S. Mahlik, M. Grinberg, A.A. Kaminskii, M. Bettinelli, P. Boutinaud, Luminescence of $Ca(NbO_3)_2$: Pr^{3+}:Pr^{3+} and self-trapped exciton emission, Rad. Measur. 45 (2010) 288–291. https://doi.org/10.1016/j.radmeas.2010.01.023.

[69] J. Geng, Y. Chen, G. Gu, L. Tian, Tunable white-light-emitting $Sr_{2-x}Ca_xNb_2O_7$: Pr^{3+}phosphor by adjusting the concentration of Ca^{2+} ion, Opt. Mater. 36 (2014) 1093–1096. https://doi.org/10.1016/j.optmat.2014.01.009.

[70] C. Wu, Y. Li, H. Gong, J. Gao, Z. Wang, Niobium-oxygen octahedral and oxygen interstitial emissions in calcium niobate matrix and its color manipulation via doping with Pr^{3+}, AIP Adv. 7 (2017) 025019. https://doi.org/10.1063/1.4977967.

[71] C. Liu, F. Pan, Q. Peng, W. Zhou, R. Shi, L. Zhou, J. Zhang, J. Chen, H. Liang, Excitation wavelength dependent luminescence of $LuNbO_4$: Pr^{3+}– Influences of intervalence charge transfer and host sensitization, J. Phys. Chem. C 120 (2016) 26044–26053. https://doi.org/10.1021/acs.jpcc.6b09806.

[72] G. Zhu, Z. Li, C. Wang, X. Wang, F. Zhou, S. Xin, Novel red-emitting phosphor $Ba_3ZrNb_4O_{15}$: Pr^{3+}:the structure, characteristic photoluminescence property and thermal quenching behavior

investigation, Mater. Res. Bull. 104 (2018) 173–178. https://doi.org/10.1016/j.materresbull.2018.04.018.

[73] E. Cavalli, G. Calestani, F. Mezzadri, R. Faoro, M. Tonelli, P. Boutinaud, Structural effects on the emission properties of Pr^{3+}-doped $Ba_2NaNb_5O_{15}$ crystals, J. Phys. D: Appl. Phys. 43 (2010) 455404. https://doi.org/10.1088/0022-3727/43/45/455404.

[74] L.L. Noto, S.S. Pitale, M.A. Gusowki, O.M. Ntwaeaborwa, J.J. Terblans, H.C. Swart, Luminescent dynamics of Pr^{3+} in $MTaO_4$ hosts (M = Y, La or Gd), J. Lumin. 145 (2014) 907–913. https://doi.org/10.1016/j.jlumin.2013.09.026.

[75] L.L. Noto, M.L. Chitambo, O.M. Ntwaeaborwa, H.C. Swart, The greenish-blue emission and thermoluminescence properties of $CaTa_2O_6$: Pr^{3+}, J. Alloys Comp. 589 (2014) 88–93. https://doi.org/10.1016/j.jallcom.2013.11.185.

[76] L.L. Noto, M.Y.A. Yagoub, O.M. Ntwaeaborwa, H.C. Swart, Persistent photoluminescence emission from $SrTa_2O_6$: Pr^{3+}phosphor prepared at different temperatures, Ceram. Intern. 41 (2015) 8828–8836. https://doi.org/10.1016/j.ceramint.2015.03.112.

[77] L.L. Noto, M.L. Chitambo, O.M. Ntwaeaborwa, H.C. Swart, Photoluminescence and thermoluminescence properties of Pr^{3+}-doped $ZnTa_2O_6$ phosphor, Powder Technol. 247 (2013) 147–150. https://doi.org/10.1016/j.powtec.2013.07.012.

[78] A.H. Krumpel, E. van der Kolk, E. Cavalli, P. Boutinaud, M. Bettinelli, P. Dorenbos, Lanthanide 4f-level location in AVO_4 : Ln^{3+}(A = La,Gd,Lu) crystals, J. Phys.: Condens. Matter 21 (2009) 115503. https://doi.org/10.1088/0953-8984/21/11/115503.

[79] S. Cao, Y. Ma, C. Quan, W. Zhu, K. Yang, W. Yin, G. Zheng, M. Wu, Z. Sun, Photoluminescence properties of $Ca_9Y(VO_4)_7$ and $Ca_9Y_{0.95}Ln_{0.05}(VO_4)_7$ (Ln^{3+} = Eu^{3+}, Sm^{3+}, Pr^{3+}), J. Alloys Comp. 487 (2009) 346–350. https://doi.org/10.1016/j.jallcom.2009.07.139.

[80] E. Cavalli, P. Boutinaud, M. Grinberg, Luminescence dynamics in $CaWO_4$: Pr^{3+}powders and single crystals, J. Lumin. 169 (2016) 450–453. https://doi.org/10.1016/j.jlumin.2014.10.069.

[81] E. Auffray, M. Korjik, T. Shalapska, S. Zazubovich, Photoluminescence and excited states dynamics in $PbWO_4$: Pr^{3+}crystals, J. Lumin. 154 (2014) 381–386. https://doi.org/10.1016/j.jlumin.2014.05.012.

[82] A. Durairajan, D. Thangaraju, S. Moorthy Babu, M.A. Valente, Luminescence characterization of sol-gel derived Pr^{3+}-doped $NaGd(WO_4)_2$ phosphors for solid state lighting applications, Mater. Chem. Phys. 179 (2016) 295–303. https://doi.org/10.1016/j.matchemphys.2016.05.042.

[83] P. Boutinaud, M. Bettinelli, F. Diaz, Intervalence charge transfer in Pr^{3+} and Tb^{3+}-doped double tungstate crystals $KRE(WO_4)_2$ (RE = Y, Gd, Yb, Lu), Opt. Mater. 32 (2010) 1659–1663. https://doi.org/10.1016/j.optmat.2010.04.025.

[84] Q. Wang, G. Zhu, Y. Li, Y. Wang, Photoluminescent properties of Pr^{3+} activated Y_2WO_6 for light emitting diodes, Opt. Mater. 42 (2015) 385–389. https://doi.org/10.1016/j.optmat.2015.01.032.

[85] B. Han, Y. Dai, J. Zhang, X. Wang, W. Shi, H. Shi, $NaLaMgWO_6$:Pr^{3+}: A novel blue-light excitable red-emitting phosphor for white light-emitting diodes, J. Lumin. 196 (2015) 275–280. https://doi.org/10.1016/j.jlumin.2017.12.050.

[86] S. Mahlik, M. Behrendt, M. Grinberg, E. Cavalli, M. Bettinelli, High pressure luminescence spectra of $CaMoO_4$: Ln^{3+}(Ln = Pr, Tb), J. Phys.: Condens. Matter 25 (2013) 105502. https://doi.org/10.1088/0953-8984/25/10/105502.

[87] E. Cavalli, F. Angiuli, P. Boutinaud, R. Mahiou, Optical spectroscopy and excited state dynamics of $CaMoO_4$: Pr^{3+}, J. Solid State Chem. 185 (2012) 136–142. https://doi.org/10.1016/j.jssc.2011.11.004.

[88] W. Wu, Y. Xuan, Y. J-N, J. Xie, Influence of praseodymium doping concentration on the structural and optical properties of strontium molybdate crystals, Res. Chem. Intermed. 41 (2015) 2479–2488. https://doi.org/10.1007/s11164-013-1362-2.

[89] F. Chun, B. Zhang, H. Su, H. Osman, W. Deng, W. Deng, H. Zhang, X. Zhao, W. Yang, Preparation and luminescent properties of self-organized broccoli-like $SrMoO_4$: Pr^{3+}superparticles, J. Lumin. 190 (2017) 69–75. https://doi.org/10.1016/j.jlumin.2017.05.028.

[90] X. He, M. Guan, Z. Li, T. Shang, N. Lian, Q. Zhou, Enhancement of fluorescence from $BaMoO_4$: Pr^{3+} deep-red-emitting phosphor via codoping Li^+ and Na^+ Ions, J. Am. Ceram. Soc. 94 (2011) 2483–2488. https://doi.org/10.1111/j.1551-2916.2011.04382.x.

[91] Y. Gao, F. Huang, H. Lin, J. Zhou, J. Xu, Y. Wang, A novel optical thermometry strategy based on diverse thermal response from two intervalence charge transfer states, Adv. Funct. Mater. 26 (2016) 3139–3145. https://doi.org/10.1002/adfm.201505332.

[92] P. Boutinaud, L. Sarakha, E. Cavalli, M. Bettinelli, P. Dorenbos, R. Mahiou, About red afterglow in Pr^{3+} doped titanate perovskites, J. Phys. D: Appl. Phys. 42 (2009) 045106. https://doi.org/10.1088/0022-3727/42/4/045106.

[93] G. Blasse, A. Bril, Photoluminescent efficiency of phosphors with electronic transitions in localized centers, J. Electrochem. Soc. 115 (1968) 1067–1075. https://doi.org/10.1149/1.2410880.

[94] P. Dorenbos, A.H. Krumpel, E. van der Kolk, P. Boutinaud, M. Bettinelli, E. Cavalli, Lanthanide level location in transition metal complex compounds, Opt. Mater. 32 (2010) 1681–1685. https://doi.org/10.1016/j.optmat.2010.02.021.

[95] P. Dorenbos, Charge transfer bands in optical materials and related defect level location, Opt. Mater. 69 (2017) 8–22. https://doi.org/10.1016/j.optmat.2017.03.061.

[96] P. Dorenbos, Improved parameters for the lanthanide 4fq and 4fq-15d curves in HRBE and VRBR schemes that takes the nephelauxetic effect into account, J. Lumin. 222 (2020) 117164. https://doi.org/10.1016/j.jlumin.2020.117164.

[97] H. Zhang, G. Li, Y. Zhu, S. Liu, K. Li, Y. Liang, Color tuning and white light emission in a single-phased $La_2Ti_2O_7$: Tb^{3+}phosphor, J. Alloys Comp. 798 (2019) 800–809. https://doi.org/10.1016/j.jallcom.2019.05.306.

[98] J. Xie, N. Ding, X. Li, W. Huang, H. Yang, J. Wang, L. Wang, Q.T. Zhang, Luminescence properties of double perovskite Gd_2MgTiO_6 : Tb^{3+}phosphors by solid state reaction method, J. Mater. Sci: Mater. Electron. 30 (2019) 17923–17932. https://doi.org/10.1007/s10854-019-02146-7.

[99] E.R. Alvarez, R.F. Sosa, I. Földvari, K. Polgar, A. Peter, A.F. Munoz, Co-emission of Tb^{3+} and Eu^{3+} ions in $LiNbO_3$: Tb^{3+},Eu^{3+}single crystals, Phys. Stat. Sol. (c) 4 (2007) 826–829. https://doi.org/10.1002/pssc.200673849.

[100] J. Xian, S. Yi, Y. Deng, L. Zhang, X. Hu, Y. Wang, Synthesis and photoluminescence properties of Ln^{3+} (Ln^{3+}=Tb^{3+}, Dy^{3+}, Sm^{3+}, Er^{3+})-doped $Ca_2Nb_2O_7$ phosphors, Physica B 483 (2016) 19–25. https://doi.org/10.1016/j.physb.2015.12.022.

[101] A. Bril, W.L. Wanmaker, R.E. Schuil, International Symposium on Luminescence, Munich, 1965, Verlag Karl Thiemig K. G., Munich (1966), p. 310.

[102] X. Xiao, B. Yan, Synthesis and luminescent properties of novel $RENbO_4$: Ln^{3+}(RE = Y, Gd, Lu; Ln = Eu, Tb) micro-crystalline phosphors, J. Non-Cryst. Solids 351 (2005) 3634–3639. https://doi.org/10.1016/j.jnoncrysol.2005.09.018.

[103] M.H. Im, Y.J. Kim, Energy transfer and multiple photoluminescence of $LuNbO_4$ co-doped with Eu^{3+} and Tb^{3+}, Mater. Res. Bull. 112 (2019) 399–405. https://doi.org/10.1016/j.materresbull.2019.01.009.

[104] K. Li, Y. Zhang, X. Li, M. Shang, H. Lian, J. Lin, Host-sensitized luminescence in $LaNbO_4$: Ln^{3+}(Ln^{3+} = Eu^{3+}/Tb^{3+}/Dy^{3+}) with different emission colors, Phys. Chem. Chem. Phys. 17 (2015) 4283–4292. https://doi.org/10.1039/C4CP03894K.

[105] H. Huang, T. Wang, H. Zhou, D. Huang, Y. Wu, G. Zhou, J. Hu, J. Zhan, Luminescence, energy transfer and up-conversion mechanisms of Yb^{3+} and Tb^{3+} co-doped $LaNbO_4$, J. Alloys Comp. 702 (2017) 209–215. https://doi.org/10.1016/j.jallcom.2017.01.246.

[106] P. Botella, F. Enrichi, A. Vomiero, J.E. Munoz-Santiuste, A.B. Garg, A. Arvind, F.J. Manjon, A. Segura, D. Errandonea, Investigation of the luminescence properties of $InMO_4$ (M = V^{5+},Nb^{5+},Ta^{5+}) crystals doped with Tb^{3+} or Yb^{3+} rare earth ions, ACS Omega 5 (2020) 2148–2158. https://doi.org/10.1021/acsomega.9b02862.

[107] B. Li, Z. Gu, J. Lin, Z.M. Su, Photoluminescence of Eu^{3+}-activated $GdTaO_4$ with both M type and M′ type structures, J. Mater. Sci. 35 (2000) 1139–1143. https://doi.org/10.1023/A:1004767916006.

[108] G. Blasse, A. Bril, Luminescence phenomena in compounds with fergusonite structure, J. Lumin. 3 (1970) 109–131. https://doi.org/10.1016/0022-2313(70)90011-6.

[109] M.J.J. Lammers, G. Blasse, Energy transfer phenomena in Tb^{3+}-activated gadolinium tantalate ($GdTaO_4$), Mater. Res. Bull. 19 (1984) 759–768. https://doi.org/10.1016/0025-5408(84)90033-3.

[110] H. Zhang, Y. Wang, L. Xie, Luminescent properties of Tb^{3+} activated $GdTaO_4$ with M and M′ type structure under UV–VUV excitation, J. Lumin. 130 (2010) 2089–2092. https://doi.org/10.1016/j.jlumin.2010.05.032.

[111] G. Blasse, J. Dirksen, L.H. Brixner, M.K. Crawford, Luminescence of materials based on $LuTaO_4$, J. Alloys Comp. 209 (1994) 1–6. https://doi.org/10.1016/0925-83889491069-3.

[112] M. Nikl, R. Morlotti, C. Magro, R. Bracco, Emission and storage properties of $LiTaO_3$: Tb^{3+}phosphor, J. Appl. Phys. 79 (1996) 2853–2856. https://doi.org/10.1063/1.361279.

[113] A. Krumpel, E. van der Kolk, P. Dorenbos, P. Boutinaud, E. Cavalli, M. Bettinelli, Energy level diagram for lanthanide-doped lanthanum orthovanadate, Mater. Sci. Eng. B 146 (2008) 114–120. https://doi.org/10.1016/j.mseb.2007.07.074.

[114] E. Cavalli, P. Boutinaud, R. Mahiou, M. Bettinelli, P. Dorenbos, Luminescence dynamics in Tb^{3+}-doped $CaWO_4$ and $CaMoO_4$ crystals, Inorg. Chem. 49 (2010) 4916–4921. https://doi.org/10.1021/ic902445c.

[115] S. Mahlik, E. Cavalli, M. Amer, P. Boutinaud, Energy levels in $CaWO_4$: Tb^{3+}at high pressure, Phys. Chem. Chem. Phys. 17 (2015) 32341–32346. https://doi.org/10.1039/C5CP05442G.

[116] J. Liao, B. Qiu, H. Wen, J. Chen, W. You, Hydrothermal synthesis and photoluminescence of $SrWO_4$: Tb^{3+}novel green phosphor, Mater. Res. Bull. 44 (2009) 1863–1866. https://doi.org/10.1016/j.materresbull.2009.05.013.

[117] J. Lin, Z. Zeng, Q. Ma, Q. Wang, Y. Zhang, Effects of multiple irradiations on luminescent materials and energy savings – A case study for the synthesis of $BaMO_4$: Ln^{3+} (M = W, Mo; Ln = Eu, Tb) phosphors, Energy 64 (2014) 551–556. https://doi.org/10.1016/j.energy.2013.11.026.

[118] A. Nosenko, L. Kostyk, L. Koslovs'ka, Some peculiarities of the luminescence of the lead tungstate crystals, J. Lumin. 90 (2000) 49–53. https://doi.org/10.1016/S0022-23139900606-7.

[119] K.W. Meert, J.J. Joos, D. Poelman, P.F. Smet, Investigation of the quenching of Tb^{3+} doped scheelites, J. Lumin. 173 (2016) 263–273. https://doi.org/10.1016/j.jlumin.2015.12.045.

[120] S. Mahlik, F. Diaz, P. Boutinaud, Pressure-induced luminescence quenching in $KY(WO_4)_2$: Pr^{3+}, Opt. Mater. 74 (2017) 41–45. https://doi.org/10.1016/j.optmat.2017.04.002.

[121] S. Schwung, D. Rytz, B. Heying, U. Rodewald, P. Niehaus, D. Enseling, T. Jüstel, R. Pöttgen, The crystal structure and luminescence quenching of poly- and single-crystalline KYW_2O_8: Tb^{3+}, J. Lumin. 166 (2015) 289–296. https://doi.org/10.1016/j.jlumin.2015.05.052.

[122] R. van Deun, D. Ndagsi, J. Liu, I. van Driessche, K. van Hecke, A.M. Kaczmarek, Dopant and excitation wavelength dependent color-tunable white light-emitting Ln^{3+}: Y_2WO_6materials (Ln^{3+} = Sm, Eu, Tb, Dy), Dalton Trans. 44 (2015) 15022–15030. https://doi.org/10.1039/C5D2112J.

[123] S.W. Park, B.K. Moon, J.H. Jeong, J.S. Bae, J.H. Kim, Crystal structure, electronic structure, and photoluminescent properties of $SrMoO_4$: Tb^{3+}phosphors, Mater. Res. Bull. 70 (2015) 403–411. https://doi.org/10.1016/j.materresbull.2015.04.066.

[124] Y.S. Cho, Y.D. Huk, Preparation and optical properties of green-emitting $BaMoO_4$: Tb^{3+}, Na^+ nanophosphors for transparent displays, Electron. Mater. Lett. 10 (2014) 1185–1189. https://doi.org/10.1007/s13391-014-4143-1.

[125] D.A. Landinez Tellez, D. Martinez Buitrago, R. Cardona, E.W. Barrera, J. Roa-Rojas, Crystalline structure, magnetic response and electronic properties of RE_2MgTiO_6 (RE=Dy, Gd) double perovskites, J. Mol. Struct. 1067 (2014) 205–209. https://doi.org/10.1016/j.molstruc.2014.03.041.

[126] E. Cavalli, P. Boutinaud, M. Bettinelli, P. Dorenbos, The excited state dynamics of $KLa(MoO_4)_2$: Pr^{3+}:From a case study to the determination of the energy levels of rare earth impurities relative to the bandgap in oxidising host lattices, J. Sol. State. Chem. 181 (2008) 1025–1031. https://doi.org/10.1016/j.jssc.2008.02.007.

[127] M. Shivram, K.M. Girish, H.B. Premakumar, S.C. Prashantha, H.P. Nagaswarupa, K. Channakeshavalu, H. Nagabhushana, K.R. Vishnu Mahesh, NUV excited luminescence studies of Tb^{3+} in $CaTiO_3$ nanophosphor for wLEDs, Mater. Todays Proceed. 4 (2017) 11720–11726. https://doi.org/10.1016/j.matpr.2017.09.088.

[128] C.W. Struck, W.H. Fonger, Thermal quenching of Tb^{+3}, Tm^{+3}, Pr^{+3}, and Dy^{+3} $4f^n$ emitting states in La_2O_2S, J. Appl. Phys. 42 (1971) 4515–4516. https://doi.org/10.1063/1.1659809.

[129] X. Wang, Q. Liu, Y. Bu, C.S. Liu, T. Liu, X. Yan, Optical temperature sensing of rare-earth ion doped phosphors, RSC Adv. 5 (2015) 86219–86236. https://doi.org/10.1039/C5RA16986K.

[130] X. Tian, C. Wang, J. Wen, S. Lian, C. Ji, Z. Huang, Z. Chen, H. Peng, S. Wang, J. Li, J. Hu, Y. Peng, High temperature sensitivity phosphor based on an old material: Red emitting H_3BO_3 flux assisted $CaTiO_3$: Pr^{3+}, J. Lumin. 214 (2019) 116528. https://doi.org/10.1016/j.jlumin.2019.116528.

[131] T. Wei, N. Haiyong, Z. Qiuhong, D. Jianhong, Novel optical temperature sensor based on emission in Pr^{3+} doped ferroelectric $Ba_{0.7}Sr_{0.3}TiO_3$, RSC Adv. 8 (2018) 23996–24001. https://doi.org/10.1039/C8RA04228D.

[132] Y. Gao, F. Huang, H. Lin, J. Xu, Y. Wang, Intervalence charge transfer state interfered Pr^{3+} luminescence: A novel strategy for high sensitive optical thermometry, Sens Actuat. B 243 (2017) 137–143. https://doi.org/10.1016/j.snb.2016.11.143.

[133] Y. Wu, H. Suo, X. Zhao, Z. Zhou, C. Guo, Self-calibrated optical thermometer $LuNbO_4$: Pr^{3+}/Tb^{3+}based on intervalence charge transfer transitions, Inorg. Chem. Frontiers 5 (2018) 2456–2461. https://doi.org/10.1039/C8QI00755A.

[134] S. Mahlik, M. Grinberg, E. Cavalli, M. Bettinelli, P. Boutinaud, High pressure evolution of YVO_4: Pr^{3+} luminescence, J. Phys.: Condens. Matter 21 (2009) 105401. https://doi.org/10.1088/0953-8984/21/10/105401.

[135] S. Mahlik, M. Grinberg, E. Cavalli, M. Bettinelli, High pressure luminescence spectra of $CaMoO_4$: Pr^{3+}, J. Phys.: Condens. Matter 24 (2012) 215402. https://doi.org/10.1088/0953-8984/24/21/215402.

[136] S. Mahlik, M. Behrendt, M. Grinberg, E. Cavalli, M. Bettinelli, Pressure effects on the luminescence properties of $CaWO_4$: Pr^{3+}, Opt. Mater. 34 (2012) 2012–2016. https://doi.org/10.1016/j.optmat.2012.02.011.

[137] S. Mahlik, E. Cavalli, M. Bettinelli, M. Grinberg, Luminescence of $CaWO_4$: $Pr^{3+}$and $CaWO_4$: Tb^{3+}at ambient and high hydrostatic pressures, Rad. Meas. 56 (2013) 1–5. https://doi.org/10.1016/j.radmeas.2013.03.019.

[138] S. Mahlik, F. Diaz, P. Boutinaud, Luminescence quenching in $KYb(WO_4)_2$: Tb^{3+}:an example of temperature-pressure equivalence, J. Lumin. 191 (2017) 18–21. https://doi.org/10.1016/j.jlumin.2017.02.007.

Alok M. Srivastava, Mikhail G. Brik, William W. Beers

Chapter 11
Luminescence of Bi^{3+} in oxides with perovskite structures

11.1 Introduction

Luminescence of ions with the $d^{10}s^2$ electronic configuration has had a long history of investigations and has played an important role in the development of fluorescent lamp phosphors and scintillators [1, 2]. The family of alkali halide materials activated with impurity ions with the ns^2 electronic ground-state configuration has been extensively studied, both by experimental and theoretical techniques [3]. Tl^+ ($5d^{10}6s^2$)-activated CsI is a well-known scintillator with a high light yield that is used in X-ray imaging applications [2]. The self-activated $Bi_4Ge_3O_{12}$ (BGO) with Bi^{3+} ($5d^{10}6s^2$) ion finds application as detectors of gamma rays in PET scanners [2]. The calcium halophosphate phosphor activated with Sb^{3+} ($4d^{10}5s^2$) and Mn^{2+} was introduced in the marketplace after the Second World War, and it revolutionized global lighting [1]. The Sn^{2+} ($4d^{10}5s^2$) is an efficient activator ion in several fluorescent lamp phosphors [1]. It is, thus, not too surprising that there remains a continual interest in investigating the spectroscopic properties of ns^2 ions in solids.

It is a daunting task to review the entire subject of ns^2 ion luminescence in solids. Recent literature is indicative of considerable research activity that is aimed at developing new hosts for the Bi^{3+} ion, in order to produce innovative materials for various applications such as scintillators, persistent phosphors with high storage capacity, phosphors for light-emitting diodes (LEDs), solar down conversion, and bioimaging, to name a few [4]. More importantly, in recent years, researchers have been productive in determining the underlying reasons for the behavior of Bi^{3+} ion luminescence in solids [5, 6]. These advancements of the fundamental understanding, which will be discussed in this chapter, can serve as a practical guide to innovative materials for various applications.

The complex and diverse behavior of the Bi^{3+} ion luminescence in solids arises from the fact that it depends greatly on the coordination polyhedron and chemical bonding, which affects the energy position of the excited states and the Stokes shift of emission. Metal-to-metal charge transfer (MMCT) is often observed when the Bi^{3+} ion is introduced in lattices containing nd^0 cations. The ns^2 ions often show a tendency to form pairs or clusters when introduced as impurity ions in certain solids, and this will be discussed in the context of the Bi^{3+} ion luminescence in this chapter. Since the literature reports a huge number of host lattices with Bi^{3+} as the active ion, it will be impossible for us to cover them in any meaningful manner. Instead, we will primarily focus on the optical properties of the Bi^{3+} ion in the family of materials that adopt the

https://doi.org/10.1515/9783110607871-011

orthorhombic perovskite (A*B*O$_3$) and the double perovskite (A$_2$*BB*$'$O$_6$) crystal structures. The vast variation in optical properties, which is observed in these compounds, will serve to illustrate the structure–optical property relationship that determines the behavior of Bi^{3+} ion luminescence with varying chemical composition, when the crystal structure is maintained. More specifically, we will focus on localized ($^3P_{0,1}$→$^1S_0$)-to-delocalized (D-level or MMCT) emission of the Bi^{3+} ion in the perovskites and on the luminescence from Bi^{3+} ion pairs. The properties of luminescence that develop under these three mechanisms are vastly different.

The aim of this chapter is to show how systematic experiments can provide adequate data to map out the evolution of various transitions in the Bi^{3+} ion luminescence as a function of the chemical composition in a family of materials that crystallize in the orthorhombic perovskite structure. First-principles calculations have been recently conducted to provide further understanding of the Bi^{3+} ion luminescence in these perovskites. Extending the discussions to other compounds will serve to shed light on the understanding of the mechanisms that determine the behavior of the Bi^{3+} ion in solids.

11.2 Energy level scheme and the optical transitions

Figure 11.1 shows some of the optical transitions that can occur when the Bi^{3+} ion is substituted in a host lattice. The figure represents a schematic view of the optical transitions with respect to the intrinsic bands of the host crystal (valence and conduction bands). The ground level of the free ion, which has the 6*s*^{2} electronic configuration, is $^1S_0$ (singlet), and the lowest excited configuration 6*s*6*p* leads to the three triplet levels $^3P_0$, $^3P_1$, $^3P_2$, and a singlet level $^1P_1$. This energy level structure is schematically represented in Figure 11.1a. In the excitation spectrum of the Bi^{3+} ion, the $^1S_0$→$^3P_1$ transition (A-band) which is spin-forbidden appears as a strong band because this transition becomes allowed as a result of spin-orbit coupling between $^3P_1$ and $^1P_1$ levels. The $^1S_0$→$^1P_1$ transition (C-band) is a fully allowed transition, whereas the $^1S_0$→$^3P_2$ transition (B-band) is forbidden, but can be vibronically induced. The intensity of the B-band is not expected to be high. The $^1S_0$→$^3P_0$ transition is both spin- and orbital-forbidden and is not observed in the excitation spectrum. The emission spectrum, after excitation into the A-band, corresponds to the localized $^3P_{0,1}$→$^1S_0$ transition; at low temperatures, the metastable $^3P_0$ level is the emitting state, whereas at higher temperatures, emission from the $^3P_1$ state occurs [7].

In some solids, the Bi^{3+} excited levels are located within the conduction band, and the resulting emission is very different from the localized $^3P_{0,1}$→$^1S_0$ transition. In the literature, the resulting optical transition has been identified as emission from the D-level, as luminescence originating from an impurity trapped excitonic level due to photoionization of the Bi^{3+} ion, and as emission from the MMCT. This is shown in Figure 11.1(b). As we will demonstrate, relative to the localized Bi^{3+} $^3P_{0,1}$→$^1S_0$ transition, the D-level emission is

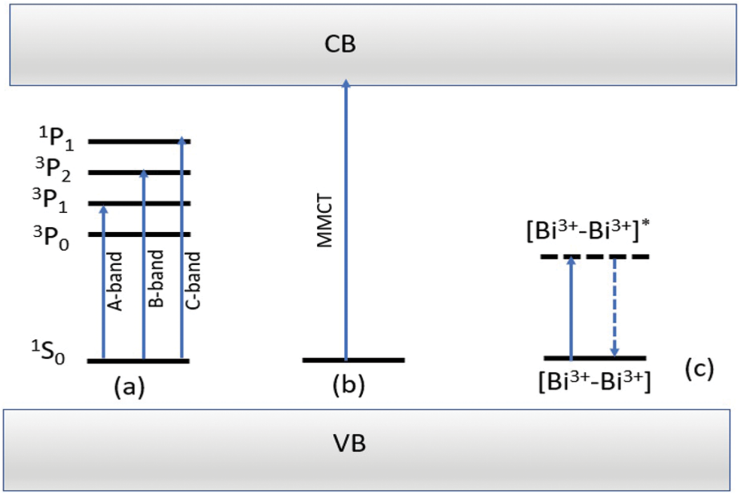

Figure 11.1: The various optical transitions of the Bi^{3+} ion when incorporated in a host lattice. The VB and CB represent the valence and conduction bands of the host: (a) represents the energy level structure of the Bi^{3+} ion when the ground and excited levels are within the band gap. In this case, the emission corresponds to the localized $^3P_{0,1}\rightarrow{}^1S_0$ transition: (b) represents the situation when the excited levels lie in the conduction band. In this case, a metal-to-metal charge transfer (MMCT) transition occurs, and the luminescence corresponds to the delocalized emission from the D-level: (c) signifies Bi–Bi ion pair absorption and luminescence.

usually characterized by (1) larger Stokes shift; (2) lower emission energy; and (3) larger full width at half maxima (FWHM) of the emission bands.

In addition to the localized and delocalized emission, there is also the possibility of luminescence from pairs or clusters of Bi^{3+} ions in the host lattice. This is schematically shown in Figure 11.1(c). In some crystals with high concentrations of Bi^{3+} ions, new excitation and emission bands appear in the luminescence spectrum due to paired or clustered ions. The luminescence occurs at lower energy and is broader than the emission from the isolated Bi^{3+} ions.

When the Bi^{3+} $^1S_0$ ground level is above the valence band maxima (VBM), it can act as a hole trap, so that the ground state can also be represented by the couple "Bi^{3+}–Bi^{4+}." Similarly, when the excited $^3P_{0,1}$ state is below the conduction band minima (CBM), the Bi^{3+} ion can act as an electron trap, which can be represented by the charge transfer state, "Bi^{2+}–Bi^{3+}" [6].

Yet another transition that can occur is the ligand to Bi^{3+} charge transfer. The corresponding transition should terminate at the empty *p* orbitals, and the energy of this transition should locate the Bi^{2+} ground state within the band gap of the compound. It has been observed in compounds such as LaOBr, $K_4Bi_2Br_{10}\cdot 4H_2O$, and Rb_3BiBr_6 [8, 9].

11.3 Luminescence of Bi^{3+} in the orthorhombic perovskites

Srivastava and coworkers have presented systematic studies of the Bi^{3+} ion luminescence in several orthorhombic perovskite-structured compounds: $LaGaO_3$ [10], $CaB^{4+}O_3$ (B = Zr, Sn) [11], $GdAlO_3$ [12] and $SrB^{4+}O_3$ (B = Zr, Sn) [13]. Luminescence data pertaining to the orthorhombic perovskite, $LaInO_3$, is available in the literature [14]. These compounds offer the possibility of studying the optical properties as the luminescence changes from localized to delocalized emission. An understanding of the factors that cause the different behaviors of the Bi^{3+} ion can be important in defining parameters relevant to the rational design of new Bi^{3+}-based optical materials for various applications. This was the motivation behind the fundamental studies conducted by Srivastava and coworkers on these perovskites. The reports have stimulated several additional experimental and computational studies on the Bi^{3+} luminescence in these perovskites, which will be discussed in this chapter.

11.3.1 Crystal structure

In the cubic ABO_3 perovskites, the A cations are present in a 12-fold coordination, and the B cations are in an octahedral (6-fold) coordination. In orthorhombic perovskite, a cooperative rotation of the BO_6 octahedral groups along the cubic [1 1 0] axis yields the orthorhombic $GdFeO_3$ (space group Pbnm) structural type [15]. The space group is given as *Pnma* or *Pbnm*, depending on the choice of axis system. The octahedral tilting reduces the coordination of the A cation from 12 in cubic perovskites (AO_{12}) to 8 (AO_8; 2 × O(1) and 6 × O(2)) [15]. The two kinds of oxygen anions [O (1) and O (2)] occupy the 4*c* and 8*d* sites, respectively.

11.3.2 Luminescence of Bi^{3+} in $CaB^{4+}O_3$ (B = Zr, Hf, Ti)

The luminescence of Bi^{3+} in these isostructural perovskites is of interest, since the evolution of the spectroscopic properties of the Bi^{3+} ion can be tracked with the electronic configuration of the B cation, because the three compounds have the same A cation (Ca^{2+}). The electronic configurations of the B site cations in these perovskites are as follows: Zr^{4+} ($[Kr]4d^05s^0$), Hf^{4+} ($[Xe]4f^{14}5d^06s^0$) and Sn^{4+}($[Kr]4d^{10}5s^0$). Generally, the ns^2 ions should have a reducing character because of the lone electron pairs. Therefore, in the presence of cations with empty orbitals that are energetically close to the $6s^2$ orbital, a low-energy MMCT can be anticipated (Figure 11.1b).

In these perovskites, the Bi^{3+} substitutes at the Ca^{2+} site that is best regarded as 4-fold antiprism coordination [15]. The ionic radii difference between $^{VIII}Ca^{2+}$ (1.12 Å) and $^{VIII}Bi^{3+}$ (1.17 Å) is slight [16]. According to first-principles calculations [17], the mean bond lengths change by less than 0.002 Å when Bi^{3+} substitutes for Ca^{2+} in $CaTiO_3$ and $CaZrO_3$ but decreases by 0.015 Å in $CaSnO_3$. Additionally, the substitution of Bi^{3+} ions on Ca^{2+} sites requires charge compensation. Since the perovskite structure cannot tolerate interstitial ions, the compensation, probably, takes place by the creation of Ca vacancies. Thus, two Ca^{2+} ions are replaced by two Bi^{3+} ions plus a Ca^{2+} cation vacancy. This mode of compensation is verified by theoretical studies which also find that the vacancy and Bi^{3+} center do not associate to influence the spectroscopic properties of the Bi^{3+} ion [17].

In Table 11.1, we have assembled the Bi^{3+} optical properties in these perovskites that are important to our discussions.

Table 11.1: Optical properties of Bi^{3+} in $(Ca,Sr)B^{4+}O_3$ (B = Zr, Sn, Ti) perovskites.

Perovskite	Excitation peak (eV)	Emission peak (eV)	Stokes shift (eV)	FWHM (eV)	E^{ex} (eV)	Nature	Reference
$CaZrO_3$	4.02	3.19	0.83	0.32	6.05	$^3P_{0,1}\rightarrow{}^1S_0$	[11]
	3.89	3.10	0.79				[19]
$CaSnO_3$	4.10	3.64	0.46	–	4.90	$^3P_{0,1}\rightarrow{}^1S_0$	[19]
	4.07	2.74	1.33	0.66		MMCT	[11]
$CaTiO_3$	3.65	2.10	1.51	–	3.72	MMCT	[19]
$SrZrO_3$	4.09	2.87	1.22	0.42	5.80	$^3P_{0,1}\rightarrow{}^1S_0$	[13]
$SrSnO_3$	4.13	3.21	0.92	0.26	4.55	$^3P_{0,1}\rightarrow{}^1S_0$	[13]
	4.13	2.82	1.31	–		MMCT	

Ca(Zr, Sn, Hf)O$_3$:Bi^{3+}: In Figure 11.2, the excitation and emission spectra of $CaZrO_3$: Bi^{3+} acquired at T = 15 K are exhibited [11]. The excitation and emission bands peak at 304 nm (4.02 eV) and at 388 nm (3.19 eV), respectively. The Stokes shift is 0.83 eV, and the FWHM of the emission band is 0.32 eV. In Figure 11.3, the low-temperature emission spectrum of $CaSnO_3$:Bi^{3+} is exhibited [11]. At T = 10 K, the emission spectrum is dominated by an emission band peaking near 450 nm (2.75 eV). The Stokes shift of emission is large, 1.33 eV. The FWHM of this emission band is 0.66 eV. A very weak band on the short wavelength side can be additionally discerned in the emission spectrum. This is assigned to emission from the localized $^3P_{0,1}$ level. Relative to $CaZrO_3$, the Bi^{3+} ion luminescence in $CaSnO_3$ is markedly different. Not shown is the excitation spectrum which exhibits two bands peaking at 260 nm (4.77 eV) and 303 nm (4.1 eV), respectively [11].

The different emission spectra of Bi^{3+} in $CaZrO_3$ and $CaSnO_3$ are intriguing and are a most striking result. This difference can be rationalized as follows: The Bi^{3+} luminescence

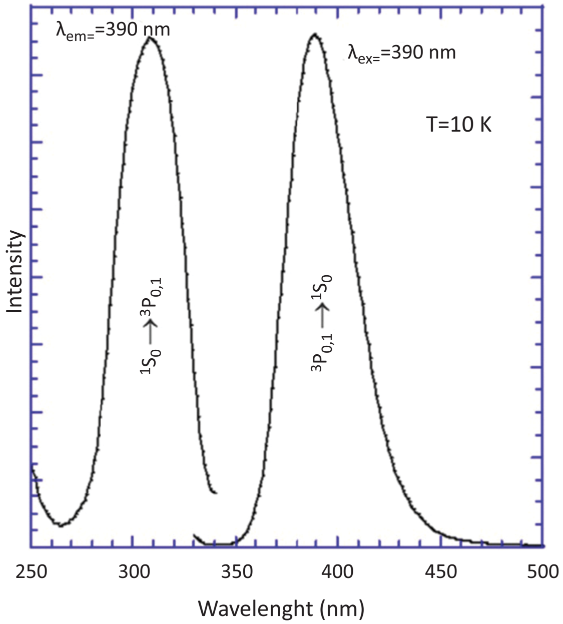

Figure 11.2: Excitation (λ_{em} = 390 nm) and emission (λ_{ex} = 300 nm) spectrum of $CaZrO_3$:Bi^{3+} at T = 10 K (reproduced with permission from Ref. [11]).

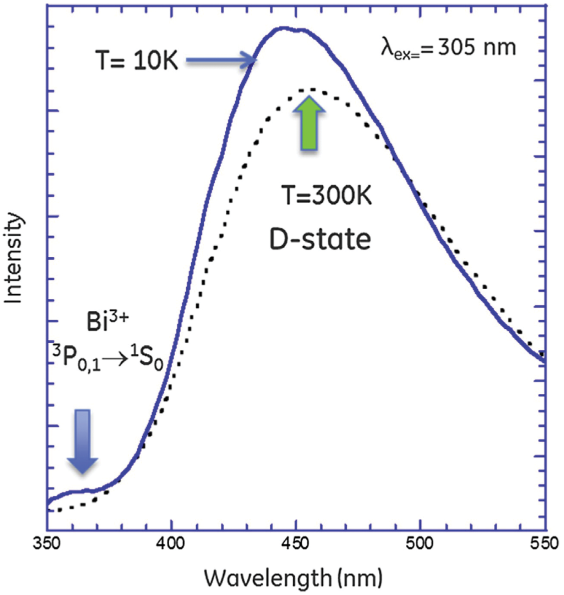

Figure 11.3: The room- (T = 300 K; dotted line) and low-temperature (T = 10 K; solid line) emission (λ_{ex} = 305 nm) spectra of $CaSnO_3$:Bi^{3+} at T = 10 K (reproduced with permission from Ref. [11]).

in $CaZrO_3$ is characterized by a small Stokes shift (<1 eV) and a narrow (FWHM) emission band. Therefore, it is prudent to assign this to the localized $^3P_{0,1} \rightarrow {}^1S_0$ emission transition. The large Stokes shift in $CaSnO_3$ coupled with considerably broadened emission band in the visible signals an emission of a different origin. The luminescence is attributed to optical transition from the D-level to the Bi^{3+} ground level ($^1S_0$).

These data clearly show that the nature of Bi^{3+} emission depends sensitively on the electronic configuration of the B^{4+} cation. To understand the role played by the B^{4+} cation in determining the optical properties of the embedded activator ions, it is necessary to determine, quantitatively, the electronic properties of the host lattice in the absence of the activator ions. We begin by examining the $CaSnO_3$:Bi^{3+} system. The electronic properties of $CaSnO_3$ have been calculated by means of density functional theory [18]. The density-of-states (DOS) calculation shows the presence of oxygen 2*p* orbitals at the top of the valence band (VB). The bottom of the conduction band (CB) showed the presence of Sn *s* and *p* orbitals.

As previously stated, the luminescence of $CaSnO_3$:Bi^{3+} corresponds to emission from the D-level. Therefore, in $CaSnO_3$, the MMCT emission band involves an electron transfer between the Bi^{3+} $^1S_0$ ground level ($6s^2$) and the empty Sn^{4+} $5s^0$ level that constitutes the bottom of the conduction band. This is possible because the Sn^{4+} can be easily reduced, and the Bi^{3+} can be easily oxidized to Bi^{5+}. The MMCT can be written as $Bi^{3+} + Sn^{4+} \rightarrow Bi^{5+} + Sn^{2+}$. Tthis may also be represented as $Bi^{3+} + Sn^{4+} \rightarrow Bi^{4+} + Sn^{3+}$ but would leave the valence state unclear: Bi^{4+} ($6s^1$) versus Bi^{5+} ($6s^0$); however, if the Bi 6*s* electron is delocalized, the oxidation state could be given as Bi^{4+}. The calculated energy of this emission transition is 2.86 eV relative to the experimental value of 2.75 eV [17]. At low temperature, the emission spectrum shows the presence of a very weak band near 360 nm (3.44 eV), which is assigned to the localized emission from the $^3P_0$ level (Figure 11.3) [11]. An accurate determination of the emission energy and Stokes shift was made by acquiring the emission spectrum excited by synchrotron radiation at low temperatures (9 K) [19]. The broad band emission spectrum was resolved into two Gaussians, which located the $^3P_{0.1} \rightarrow {}^1S_0$ emission transition at 3.76 eV. The resulting Stokes shift of 0.46 eV is much smaller than that for the Bi^{3+} emission in $CaZrO_3$ [19].

The mechanism of the Bi^{3+} ion luminescence in $CaSnO_3$ is the following: At low temperature, excitation into the $^3P_1$ level results in relaxation to $^3P_0$ level from which the UV emission with very weak intensity originates. At room temperature, a thermally activated ionization becomes efficient, resulting in emission exclusively from the D-level. However, at all temperatures, the D-level emission is strongly favored over localized emission because the Bi^{3+} excited level is near the bottom of the host conduction band.

A schematic single configuration coordinate diagram representing the situation in the stannate and zirconate perovskites is exhibited in Figure 11.4(a) and (b), respectively. In the case of $CaZrO_3$, the localized excited level is well below the D-level (Figure 11.4(b)), while in $CaSnO_3$, the two levels are close in energy (Figure 11.4(a)). The small energy separation between the D-level and the $^3P_{0,1}$ level is responsible for the occurrence of D-level emission at all temperatures in $CaSnO_3$.

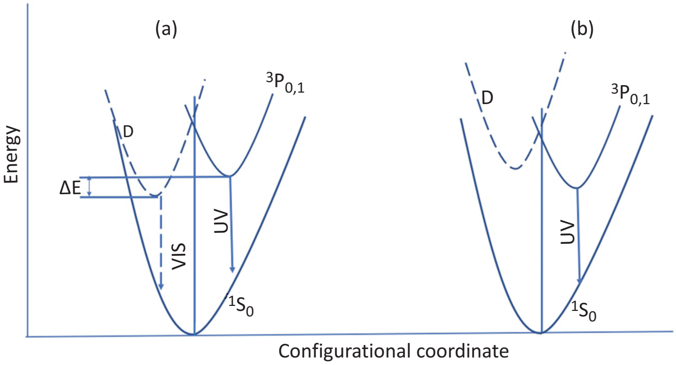

Figure 11.4: A schematic configuration coordinate diagram representing the difference between the luminescence of (a) $CaSnO_3$ and (b) $CaZrO_3$ perovskites (see text for details).

Back et al. [19] have conducted a detailed study of the luminescence properties of Bi^{3+} in these perovskites. The temperature dependence of the Bi^{3+} luminescence in $CaSnO_3$ was measured in the 20–600 K temperature range. The luminescence thermal quenching temperature, T_{50}, defined as the point where the integrated intensity has fallen to 50% of its low temperature value, was determined to be 225 K. Interestingly, two different activation energies are required to describe the quenching of the emission intensity, indicating two different quenching processes.

Back et al. [19] also measured the vacuum ultraviolet excitation spectrum of $CaSnO_3{:}Bi^{3+}$ at low temperatures ($T = 9$ K). The excitation spectrum resulting from monitoring emission from the D-level ($\lambda_{em} = 460$ nm) shows the A-band and the host lattice excitation band. In agreement with the UV excitation spectrum of Srivastava [11], the intensity of the host lattice band in the VUV (5–7 eV) is high, indicating efficient energy transfer from the host to the Bi^{3+} ion. Further, the A-band was resolved into two Gaussians that placed the $^1S_0 \rightarrow {}^3P_1$ and the MMCT transition at 4.22 and 4.03 eV, respectively [19]. The calculated and experimental energies of the MMCT transition in the three perovskites are assembled in Table 11.2. The calculated values are from Refs. [17, 19], which adopt the first-principles and semiempirical methodologies,

Table 11.2: Calculated and experimental MMCT and A-band (energies in $CaB^{4+}O_3$ (B = Zr, Sn, Ti) perovskites .

Perovskite	E_c(MMCT)[a]	E_c(MMCT)[b]	E_{exp}(MMCT)[b]	E_A
$CaZrO_3$	5.19	4.08	4.15	4.10
$CaSnO_3$	3.78	3.84	4.22	4.03
$CaTiO_3$	3.05	3.76	3.31	–

(a) and (b) are data from refs. [17] and [19], respectively.

respectively. The energy (experimental) of the A-band is also given. The calculated MMCT energy, 3.78–3.84 eV, is lower than the energy of the A-band in $CaSnO_3$:Bi^{3+}.

In contrast to $CaSnO_3$, the D-level is not active in the emission spectrum of $CaZrO_3$:Bi^{3+} [11]. The thermal quenching temperature of $T_{50} = 380$ K is much higher than that of D-level emission in the stannate perovskite, suggesting that T_{50} depends on the nature of the emission transition. As in the stannate perovskite, two different emission quenching processes are operative in the zirconate compound [19].

We now consider the excitation spectrum of $CaZrO_3$:Bi^{3+}. Srivastava's measurement of the $CaZrO_3$:Bi^{3+} excitation spectrum at $T = 15$ K placed the spin-forbidden ${}^1S_0 \rightarrow {}^3P_1$ transition (A-band) at 304 nm (4.02 eV) [11]. In the synchrotron-acquired data of $CaZrO_3$:Bi^{3+}, the lowest energy excitation band (A-band) was broadened on the high energy side, which indicated the presence of an overlapping band. A Gaussian decomposition placed the A-band at 3.89 eV and the MMCT transition at 4.15 eV. The calculated MMCT energy is 4.08 eV/5.19 eV (Table 11.2). The measurement also located the spin-allowed C-band (${}^1S_0 \rightarrow {}^1P_1$) at 5.70 eV. The host lattice excitation band was placed near 234 nm (5.3 eV). The emission intensity is strongly reduced to about 6 eV, which is in the region of host lattice absorption. This implies that unlike $CaSnO_3$, energy transfer from the host to the Bi^{3+} ion is inefficient in the zirconate perovskite.

The room-temperature spectroscopic properties of Bi^{3+} in $CaHfO_3$ have been reported in reference [20]. The excitation and emission spectra are very similar to those found for the $CaZrO_3$ perovskite (see Table 11.1). The emission is due to the localized ${}^3P_{0,1} \rightarrow {}^1S_0$ transition. There is no contribution of emission from the D-level in the room-temperature luminescence spectrum.

We now consider the behavior of Bi^{3+} in the orthorhombic perovskite, $CaTiO_3$. The spectroscopic properties of pristine $CaTiO_3$ show an excitation and emission maximum at 3.97 eV (312 nm) and 2.68 eV (463 nm), respectively [19, 21]. The Stokes shift is 1.29 eV. Upon Bi^{3+} activation, a broad excitation band on the low energy side of the host excitation band is observed. The electronic band structure of $CaTiO_3$ shows that the top of the VB is composed of the oxygen $2p$ orbitals, while the $3d^0$ orbitals of Ti^{4+} compose the bottom of the conduction band [22]. Therefore, the broad band observed in the excitation spectrum of Bi^{3+}-activated $CaTiO_3$ is assigned to an MMCT transition between the Bi^{3+} $6s^2$ orbital (${}^1S_0$) and the empty Ti^{4+} $3d$ orbital. The VUV spectra acquired at $T = 9$ K locates the MMCT excitation and emission bands at 350 nm (3.65 eV) and 580 nm (2.14 eV), respectively [19]. The Stokes shift is 1.5 eV. The absence of localized emission indicates that the ${}^3P_{0,1}$ levels lie within the conduction band of $CaTiO_3$ (Figure 11.1b). The interpretation of the Bi^{3+} excitation spectrum in $CaTiO_3$ is relatively free from the evasiveness because the lowest energy transition corresponds to the MMCT transition [23]. Recently, it has been suggested that both the localized A-band and the MMCT are emitting in the room-temperature luminescence of $CaTiO_3$:Bi^{3+} [24]. The emission band is resolved into two Gaussians at 2.185 and 2.35 eV, respectively.

11.3.3 Thermal quenching of the Bi^{3+} luminescence in the perovskites

A short discussion on the thermal quenching temperature is appropriate here. Back et al. have determined thermal quenching temperature of $T_{50} = 140$ K in $CaTiO_3:Bi^{3+}$ [19]. Therefore, T_{50} increases in the sequence $CaTiO_3$ (140 K; D-level) < $CaSnO_3$ (225 K; D-level) < $CaZrO_3$ (380 K; $^3P_{0,1}$). The Stokes shifts of the D-level emission in $CaTiO_3$ (1.55 eV) and $CaSnO_3$ (1.52 eV) are very nearly the same. Therefore, the Stokes shift is not responsible for the considerably lower T_{50} of $CaTiO_3$, relative to $CaSnO_3$. A possible reasoning can be advanced to explain the T_{50} differences. The energy of the MMCT excitation transition in $CaSnO_3$ (4.22 eV) is higher than in $CaTiO_3$ (3.65 eV). In a configuration coordinate model, it is easy to show that under the assumption of the shape and equilibrium distance of the configuration, coordinate curves do not change with the crystal structure; the activation energy for thermal quenching will increase with increasing energy of the MMCT excitation transition energy [25]. Therefore, a higher T_{50} can be anticipated in $CaSnO_3$, based on the higher energy of the MMCT transition.

Compounds such as $LuVO_4:Bi^{3+}$, Eu^{3+} that involve sensitization of the Eu^{3+} luminescence by the "Bi^{3+}–V^{5+}" MMCT transition are explored for applications in lighting devices, such as the modern-day LEDs [26]. The main reason is that the addition of Bi^{3+} shifts the absorption to longer wavelengths. However, the MMCT transitions usually exhibit low efficiencies at room temperature to be useful, commercially. Considerable fundamental explorations have been performed on $YVO_4:Bi^{3+}$ to understand the behavior of the "Bi^{3+}–V^{5+}" MMCT transition [27, 28]. The thermal quenching temperature of the isolated $[VO_4]^{3-}$ moiety in YPO_4 is very high, $T_{50} = 680$ K [29]. However, the T_{50} of the MMCT transition in $YVO_4:Bi^{3+}$is much lower, about 400 K [29]. While $YVO_4:Eu^{3+}$ is a commercial red phosphor that is applied in high-pressure mercury vapor lamps, the efficiency of this phosphor decreases with addition of Bi^{3+} [30, 31]. Therefore, the addition of Bi^{3+} to these vanadates is detrimental to the performance of the phosphor.

There is one remarkable example in which an ns^2 ion increases the thermal quenching temperature of the intrinsic host emission. The host is $CaWO_4$ containing isolated $[WO_4]^{2-}$ moiety, and the ns^2 ion is Pb^{2+} [29]. The T_{50} of the intrinsic blue luminescence of $CaWO_4$ is 380 K. Addition of 1% Pb^{2+} shifts the emission to yellow and increases T_{50} to 650 K, a remarkable result. As stated by Blasse, this effect does not occur with the addition of Ba^{2+} to $CaWO_4$; therefore, the modified emission and the higher quenching temperature must be in nature a "Pb^{2+}–W^{6+}" MMCT transition [29]. At Pb^{2+} concentrations greater than 0.01, concentration quenching of the emission is observed.

11.3.4 The VRBE scheme of Bi^{3+} in perovskites

The placement of the Bi^{3+} $^1S_0$ ground state and the $^3P_{0,1}$ excited state relative to the top of the valence band and the bottom of the conduction band is attained by constructing the VRBE (vacuum-referred binding energy) scheme that was developed by Dorenbos for lanthanides [32] and extended to Bi^{3+} [6, 33]. The VRBE scheme for Bi^{3+} in CaMO_3 (M = Zr, Sn, Ti) has been determined in two independent studies [17, 19].

The VRBEs of the Bi^{3+} 6*s* orbital and that of the valence band maxima (VBM) of the hosts and as calculated by the first-principles methodology are summarized in Table 11.3 [17]. In these orthorhombic perovskites, the Bi^{3+} $6s^2$ ground level is located above the top of the valence band. Therefore, the Bi^{3+} ion can act as a hole trap in the three perovskites. This is usually the case for the Bi^{3+} ion in solids; the ground state is either above or slightly overlapping with the top of the valence band. For $CaSnO_3$, $CaZrO_3$, and $CaTiO_3$, the VRBEs of −8.12, −7.83, and −7.56 eV are calculated. The VRBE of the electron in the 6*s* ground level is driven by the "Bi–ligand" covalent mixing (nephelauxetic effect). The data indicate that the electron in the Bi^{3+} ground level is most strongly bonded in $CaSnO_3$ and least in $CaTiO_3$. Only in the case of $CaZrO_3$ can the excited $^3P_{0,1}$ level act as an electron trapping level, since this level lies within the band gap [17].

Table 11.3: The VRBE of the valence band top and the $Bi^{3+1}S_0$ ground level (E($^1S_0$)) in Ca$B^{4+}O_3$ (B = Zr, Sn, Ti) [17].

Perovskite	VBM	$E(^1S_0)$
$CaZrO_3$	−8.95	−7.83
$CaSnO_3$	−9.51	−8.12
$CaTiO_3$	−8.55	−7.56

11.3.5 The luminescence of Bi^{3+} in $Sr(Sn,Zr)O_3$

In these orthorhombic perovskites, the band gaps are lower than those of the corresponding Ca compounds. Therefore, it is of interest to determine the influence of band-gap narrowing on the optical properties of the Bi^{3+} ion.

In $SrZrO_3$:Bi^{3+}, the broad excitation and emission bands peak at 303 nm (4.09 eV) at 432 nm (2.87 eV), respectively (T = 10 K). The Stokes shift is 1.22 eV, and the FWHM of the emission band is 0.42 eV (Table 11.1) [13]. Recalling that the localized emission of Bi^{3+} (as in $CaZrO_3$) is characterized by emission in the UV with a small Stokes shift (<1 eV) and FWHM of 0.35 eV or less, the Bi^{3+} luminescence in $SrZrO_3$ was assigned by Srivastava to D-level emission involving the activator Bi^{3+} and the host lattice Zr^{4+} cation (Table 11.1). However, a recent reexamination shows the previous assignment to be incorrect and reassigns the Stokes shifted emission to the localized $^3P_{0,1} \rightarrow {}^1S_0$ transition [34]. The host lattice exciton formation energy of $SrZrO_3$ is 5.8 eV [35]. Relative to $CaZrO_3$, the band-gap narrowing still supports luminescence-localized emission.

The luminescence of $SrSnO_3$:Bi^{3+} is temperature-dependent [13]. The excitation and emission spectra at T = 10 K and the emission spectrum at T = 200 K are exhibited in Figure 11.5. For λ_{em} = 390 nm and at T = 10 K, the excitation spectrum is dominated by a broad band centered at 300 nm (4.13 eV). A weaker broad band centered near 270 nm (4.59 eV) is also observed. This corresponds to the host lattice absorption. At $T = 10$ K, the emission spectrum ($\lambda_{em} = 300$ nm) is dominated by a broad band centered near 387 nm (3.20 eV; UV). The Stokes shift is 0.93 eV. The FWHM of the UV band is 0.26 eV. Even at low temperatures, there is evidence of an additional emission band at longer wavelengths. When the temperature is increased to $T = 200$ K, the intensity of the UV band decreases in favor of a new emission band that is centered near 435 nm (2.85 eV; VIS) (Figure 11.5). The excitation spectra (not shown) of the UV and VIS bands practically coincide, with the exception that the host lattice band (at 270 nm) is quenched at $T = 200$ K. The Stokes shift of VIS emission band is roughly 1.28 eV (Table 11.1). The UV band peaking at 387 nm (3.20 eV) in the $T = 10$ K emission spectrum is attributed to the localized $^3P_{0,1} \rightarrow {}^1S_0$ emission transition.

The visible emission band, which gains an intensity at the expense of the UV band as the temperature is increased, is assigned to emission form the D-level (Figure 11.5). This emission is characterized by a large Stokes shift of emission (>1 eV) and increased bandwidth. The quenching of the UV emission ($^3P_{0,1}$) with increasing temperature is through thermal activation into the D-level, because the excitation spectrum resulting from monitoring the UV and D-emission is the same. This implies that the two emission bands must originate from the same excited state of the Bi^{3+} ion. To summarize, in $SrSnO_3$, the energy separation between the D-level and the $^3P_{0,1}$ level is sufficiently

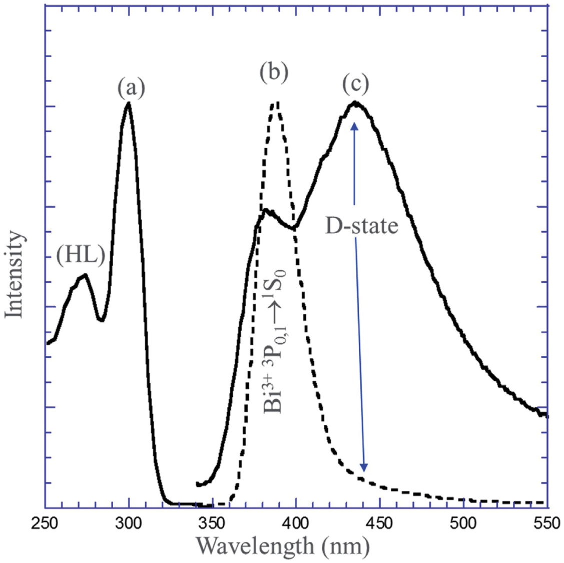

Figure 11.5: The excitation ($T = 10$ K; $\lambda_{em} = 390$ nm) and emission spectrum ($\lambda_{ex} = 300$ nm) of $SrSnO_3$: (a) excitation spectrum, $\lambda_{em} = 390$ nm, $T = 10$ K; (b) emission spectrum, $\lambda_{ex} = 300$ nm, $T = 10$ K; and (c) emission spectrum, $\lambda_{ex} = 300$ nm, $T = 200$ K. The host lattice band in the excitation spectrum is identified as HL (reproduced with permission from Ref. [13]).

large for the $^3P_{0,1}$ state to radiate at low temperatures. A thermally activated process switches the emission from the $^3P_{0,1}$ to the D-state at elevated temperatures.

11.3.6 Nature of (Ca,Sr)$B^{4+}O_3$:Bi^{3+} emission in relation to the host band gap

In this section, we explore the relationship between the host band gap and the prevalence of emission from the two different excited levels ($^3P_{0,1}$ and D) of the Bi^{3+} ion. In Table 11.1 are listed the energies of the host exciton creation energy (E^{ex}) from which the band-gap energy can be obtained ($E_g \sim E^{ex} \times 1.08$) [35]. Figure 11.6 is a schematic representation of the optical transitions observed in the perovskites in relation to E^{ex}.

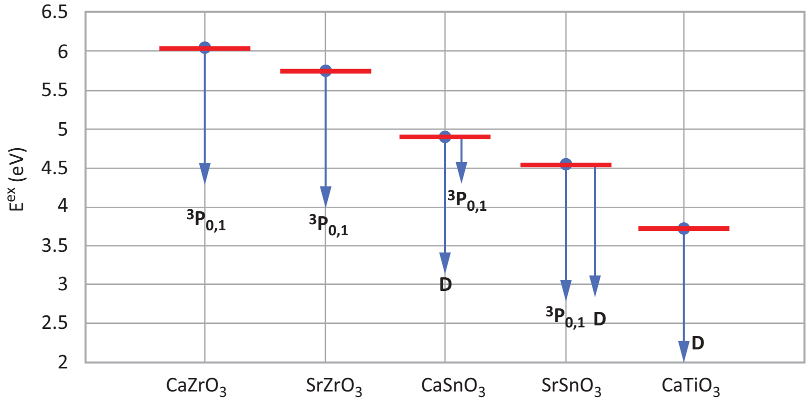

Figure 11.6: Schematic representation of the optical transitions observed in the perovskites in relation to E^{ex}.

Figure 11.6 shows that the luminescence from the localized $^3P_{0,1}$ level is observed in $CaZrO_3$ and $SrZrO_3$, with $E^{ex} = 6.05$ and 5.80 eV, respectively. In $CaTiO_3$, with $E^{ex} = 4.90$ eV, the $^3P_{0,1}$ level lies in the conduction band. The resulting luminescence originates from the D-level. In contrast to emission from the $^3P_{0,1}$ or D-levels, radiative emission from both these levels is observed in the stannate compounds that have E^{ex} intermediate between the zirconate and titanate perovskites. The difference between $CaSnO_3$ and $SrSnO_3$ lies in the placement of the $^3P_{0,1}$ relative to the D-level. In $CaSnO_3$, the localized and the D-level are close in energy, and emission from the D-level dominates at all temperatures. In $SrSnO_3$, the energy difference between the $^3P_{0,1}$ and D-level is increased so that a potential barrier must be overcome by thermal energy to induce D-level emission with strong intensity. The $^3P_{0,1}$ is the dominant emissive level at low temperatures, and a thermally activated process switches the emission from $^3P_{0,1}$ to D-level at elevated temperatures. The contrasting behavior of the Bi^{3+} luminescence in $CaSnO_3$ and $SrSnO_3$ is interesting and indicates that the energy barrier (activation energy) depends on the ionic radii of the host lattice. Since the ionic size of $^{viii}Sr^{2+}$ (1.26 Å) > $^{viii}Ca^{2+}$ (1.17 Å), the activation energy increases with increasing ionic radii of the host cation where the Bi^{3+} substitutes. Interestingly, this is in contrast to the behavior of the Pb^{2+} ion in alkaline earth carbonates with the aragonite structure where emission from D-level takes precedence with increasing ionic radii of the host cation [36].

A point of interest pertains to $CaTiO_3$, where the conduction band, which is composed of the Ti^{4+} empty 3*d* band (π*), lies at low enough energy ($E^{ex} = 3.85$ eV) that electrons can be introduced into them by chemical substitution. For example, substituting La^{3+} on Ca^{2+} sites makes $CaTiO_3$ an *n*-type conductor [37]. Thus, the fact that the Bi^{3+} $^3P_{0,1}$ level lies in the host lattice conduction band is not surprising. Similarly, $SrTiO_3$ can be made into an *n*-type conductor by substitution of La for Sr. However, it is difficult to reduce $SrZrO_3$ and $SrHfO_3$, because the respective 4*d* and 5*d* bands lie at too high an energy [38]. The luminescence of Bi^{3+} in $SrZrO_3$ is, indeed, from the localized $^3P_{0,1}$ level.

The VRBE scheme of titanate hosts indicates that titanates generally have conduction band at or below −3 eV relative to the vacuum level. As a result, the excited $^3P_{0,1}$ level of the Bi^{3+} ion lies in the conduction band of titanates, such as $CaTiO_3$. An exception, which we will discuss, is the Bi^{3+} luminescence in the double perovskite, La_2MgTiO_6. In this compound, luminescence from the localized $^3P_{0,1}$ is observed.

11.3.7 Luminescence of Bi^{3+} in $LnB^{3+}O_3$ (Ln = Y, Gd, La; *B* = Al, Ga, In) orthorhombic perovskites

The Bi^{3+} optical properties in these perovskites that are important to our discussions are assembled in Table 11.4. Results of first-principles calculations pertaining to the luminescence of Bi^{3+} in these perovskites are available in the literature [39].

Table 11.4: Optical properties of Bi^{3+} in $LnB^{3+}O_3$ (Ln = Y, Gd, La; *B* = Al, Ga, In) perovskites.

Perovskite	Excitation peak (eV)	Emission peak (eV)	Stokesshift (eV)	FWHM (eV)	E^{ex} (eV)	Nature	Reference
$YAlO_3$	4.24	3.76	0.67	0.27	7.96	$^3P_{0,1}\rightarrow{}^1S_0$	[40]
$GdAlO_3$	4.27	~3.72	~0.55	~0.30	7.40	$^3P_{0,1}\rightarrow{}^1S_0$	[12]
	4.27	2.58	1.69	0.82	7.40	Ion pair	
$LaGaO_3$	4.02	3.28	0.74	0.28	5.67	$^3P_{0,1}\rightarrow{}^1S_0$	[10]
$LaInO_3$	3.76	2.86	0.89	0.42	4.77	$^3P_{0,1}\rightarrow{}^1S_0$	[14]

$YAlO_3$:Bi^{3+}: The spectroscopic properties of this system are reported by Krasnikov et al. [40]. The excitation and emission bands peak at 280 nm (4.42 eV) and 330 nm (3.76 eV), respectively. The Stokes shift is 0.66 eV, and the emission half-width is 0.27 eV, which is typical of the localized $^3P_{0,1}\rightarrow{}^1S_0$ emission transition in these perovskites The first-principles calculations place the MMCT at 6.84 eV, which is higher relative to the energy position of the A-band [39]. It is also proposed by Dorenbos that the band in the excitation spectrum at ~ 6.5 eV is due to the MMCT transition [33].

$LaGaO_3$:Bi^{3+}: The luminescence of $LaGaO_3$:Bi^{3+} was reported by Jacquier et al. [41]. It was later investigated by Srivastava with the goal of resolving whether there was any influence of Ga^{3+} with nd^{10} electronic configuration on the behavior of Bi^{3+} ion [10]. At $T = 15$ K, the excitation and emission spectra peaked at 308 nm (4.02 eV) and 378 nm (3.33 eV), respectively. The half-width of the emission band is 0.28 eV. The Stokes shift is 0.74 eV. With a Stokes shift of less than 1 eV and a narrow band FWHM, the emission is assigned to the localized $^3P_{0,1}\rightarrow{}^1S_0$ transition.

The assignment of the excitation band is more complicated. The main low energy band is assigned to the $^1S_0\rightarrow{}^3P_1$ transition. First-principles calculations reproduce the energy of the A-band transition [39]. However, the energy of the MMCT has not been calculated. Boutinaud has developed an empirical model to locate the energies of the A-band and the MMCT (D-band) of the Bi^{3+} ion in oxides [23]. His analysis predicts the $Bi^{3+}\rightarrow La^{3+}$ and $Bi^{3+}\rightarrow Ga^{3+}$ MMCT at 5.16 eV (240 nm) and 4.13 eV (300 nm), respectively. In the work of Jacquier et al., the A-band in the excitation spectrum has been decomposed into three Gaussian components centered at 3.96, 4.12, and 4.29 eV [41]. These components are assigned to the crystal field splitting of the Bi^{3+} $^3P_1$ level in a C_1 site symmetry. Alternatively, and following the Boutinaud model, the band at 4.12 eV can be assigned to the $Bi^{3+}\rightarrow Ga^{3+}$ MMCT.

In the excitation spectrum of $LaGaO_3$:Bi^{3+}, the band at shorter wavelength (240 nm or 5.16 eV) has been tentatively assigned to the spin-allowed $^1S_0 \rightarrow {}^1P_1$ (C-band) excitation transition [41]. This excitation band is decomposed into two Gaussian components centered at approximately 5 and 5.4 eV. The energy of the C-band (E_C) can be calculated from the energy of the A-band (E_A) via the equation [42]:

$$E_C = 3.236 + 2.290(E_A - 2.972)^{0.856}$$

This equation would locate the C-band at 5.62 eV (220 nm). Therefore, the band near 5.4 eV can be assigned to C-band, although the $Bi^{3+}\rightarrow La^{3+}$ MMCT is also anticipated near 5.2 eV. Further, the host lattice exciton creation energy is 5.67 eV (220 nm) [39]. Thus, it is possible that the high energy band is a combination of the host lattice absorption, MMCT, and the C-band. If the $Bi^{3+}\rightarrow Ga^{3+}$ MMCT in $LaGaO_3$ is located at 4.13 eV, then that would place it above the $^3P_{0,1}$ state. Therefore, the MMCT will relax into the A-band resulting in emission from the localized $^3P_{0,1}\rightarrow{}^1S_0$ transition upon A-band excitation.

$LaInO_3$: Bi^{3+}: The luminescence of Bi^{3+} in $LaInO_3$ was investigated by Van Steensel et al. [14]. They reported the excitation and emission bands peaking at 340 nm (3.65 eV) and 420 nm (2.95 eV) and a Stokes shift of 0.69 eV. We digitized their spectral data and determined the excitation and emission band to peak at 330 nm (3.75 eV) and 437 nm (2.84 eV), respectively. The Stokes shift is 0.91 eV and the emission half-width is 0.25 eV. The behavior of the luminescence is characteristic of $^3P_{0,1} \rightarrow {}^1S_0$ emission transition. The calculated energy of the MMCT from the first-principles calculation is 4.33 eV or 286 nm [39]. This is consistent with the value predicted by the Boutinaud model [23]. Since the band gap of $LaInO_3$ is 4.55 eV [43], the MMCT would overlap with the host lattice absorption. Hence, the observed broad band in the excitation spectrum is due to the localized $^1S_0 \rightarrow {}^3P_1$ transition. It is of interest to note that despite the low band gap, the luminescence of Bi^{3+} emanates from the $^3P_{0,1}$ level.

$GdAlO_3$:Bi^{3+}: The Bi^{3+} ion behavior in $GdAlO_3$ was measured as a function of concentration because the luminescence showed the presence of Bi^{3+} ion pair [12]. This is unlike the other perovskites previously discussed. The luminescence data was acquired on samples with the compositions $(Gd_{1-x}Bi_x)AlO_3$, where $x = 0.01$ and 0.05. In the sample with $x = 0.01$, the emission spectrum acquired at room temperature exhibited two bands: a high-energy emission band in the ultraviolet with very low intensity centered near 333 nm (3.72 eV) and a low energy visible band (VIS) peaking near 480 nm (2.58 eV) with FWHM of 0.82 eV. In the sample with $x = 0.05$, the VIS band peaks near 495 nm (2.50 eV) with FWHM of 0.90 eV. Therefore, increasing the Bi^{3+} concentration broadens the visible emission band and displaces the emission peak to longer wavelengths (lower energy). The excitation spectra for both UV and VIS emission transitions are nearly identical and peaking near 290 nm.

The assignment of the weak UV emission to the $^3P_{0,1} \rightarrow {}^1S_0$ emission transition is straightforward. The dependence of the visible emitting band on the Bi^{3+} concentration suggests that this emission is due to Bi^{3+} ion pair in the $GdAlO_3$ lattice. The tendency of the ns^2 ions to form pairs or clusters is well established in the literature. It is with interest that we note that the first-principles calculations show that the tendency of Bi^{3+} pair formation in $GdAlO_3$ is no different than that in $YAlO_3$ [39]. Therefore, any ion pair must be present in exceedingly low concentration. Nevertheless, the luminescence due to ion pair is observed in $GdAlO_3$. The reason is traceable to energy transfer and migration process [39]. Upon excitation into the A-band, energy is transferred from the Bi^{3+} to the Gd^{3+} ^6P level, since the UV emission overlaps with Gd^{3+} absorption. Energy migration over the Gd^{3+} sublattice is eventually transferred to the "(Bi^{3+}–Bi^{3+})" ion pair level, resulting in the VIS emission. This energy transfer process is not possible in $YAlO_3$.

While on the subject of Bi^{3+} ion pairs in solids, it is prudent to discuss the Bi^{3+} luminescence in (Y, Lu)PO_4. The phosphate crystallizes in the tetragonal zircon structure in which the Ln ions occur in a dodecahedral coordination of oxygen ions (coordination number = 8), and there is a single site for the Bi^{3+} ion to substitutionally replace the Ln^{3+} ion.

A history of the Bi^{3+} luminescence in YPO_4 is provided by Dorenbos [6]. Blasse observed a broad band emission centered near 335 nm (3.7 eV), with a corresponding excitation band at ~ 230 nm (5.4 eV) [44]. This was further confirmed in an investigation pertaining to the influence of In^{3+} (d^{10} ion) on the Bi^{3+} luminescence in YPO_4 by van de Craats and Blasse [45]. Jüstel et al. [46] reported on the room-temperature luminescence of YPO_4:Bi^{3+}. An intense broad band near 240 nm (5.16 eV) and another broad band with much weaker intensity near 320 nm (3.87 eV) were observed. Boutinaud had tentatively assigned the long wavelength band to a Bi → Y^{3+} MMCT [6], and a later work by Cavalli et al. [27] reached the following conclusions: (1) a clear-cut assignment of the low energy band to a charge transfer emission is not possible; and (2) the low-energy band is composed of at least two components that may involve emission from Bi^{3+} pairs and D-level.

Srivastava et al. investigated the concentration dependence of the Bi^{3+} emission in (Y, Lu)PO_4 [47]. The room-temperature emission spectrum was composed of two bands centered near 240 and 320 nm, respectively (Figure 11.7). The intensity of the low-energy band increases with increasing Bi^{3+} concentration, at the expense of the intensity of the high-energy band. With this observation, the high-energy emission band was assigned to the localized $^3P_{0,1}\rightarrow{}^1S_0$ emission transition, whereas pairs or clusters of Bi^{3+} ions were held responsible for the low-energy emission band. The excitation spectra, when the probe emission wavelength is tuned for 240 and 320 nm bands, practically coincide with the excitation spectrum of the 335 nm emission band being broader and peaking at slightly longer wavelength. The two excitation bands peak at 5.32 and 5.5 eV. The former is assigned to the $^1S_0\rightarrow{}^3P_1$ (A-band) transition of the isolated Bi^{3+} ion and the latter to the Bi^{3+} ion pair.

Considerable work has been done by Dorenbos in establishing the absolute location of the Bi^{3+} energy levels relative to the intrinsic bands of the host crystal. Luminescence under X-ray excitation established the Bi^{2+} ground state within the band gap of YPO_4, and it was determined that the (Bi^{2+}-Bi^{3+}) charge transfer couple was below the $^3P_1$ excited level [48]. As argued by Dorenbos, in this case, an intervalence charge transfer transition (IVCT) can occur in which, upon A-band excitation of a Bi^{3+} ion, there is an electron transfer to a neighboring Bi^{3+} ion that forms a "Bi^{4+}–Bi^{2+}" charge transfer level [49]. The radiative decay of this level is the ion pair emission, as observed in YPO_4. Recent first-principles calculations reproduce the energy of the localized and pair emission and identify the (pair) excited state as "Bi^{3+}–Bi^{3+}" rather than "Bi^{2+}–Bi^{4+}" [50]. These studies confirm the assignment of the low-energy emission band to the presence of Bi^{3+} pairs in the (Y, Lu)PO_4 lattice, as suggested in reference [47]. It also explains the emission quenching of the isolated Bi^{3+} ion (A-band) with increasing Bi^{3+} concentration in favor of the ion pair emission that has been observed in Refs. [47, 48].

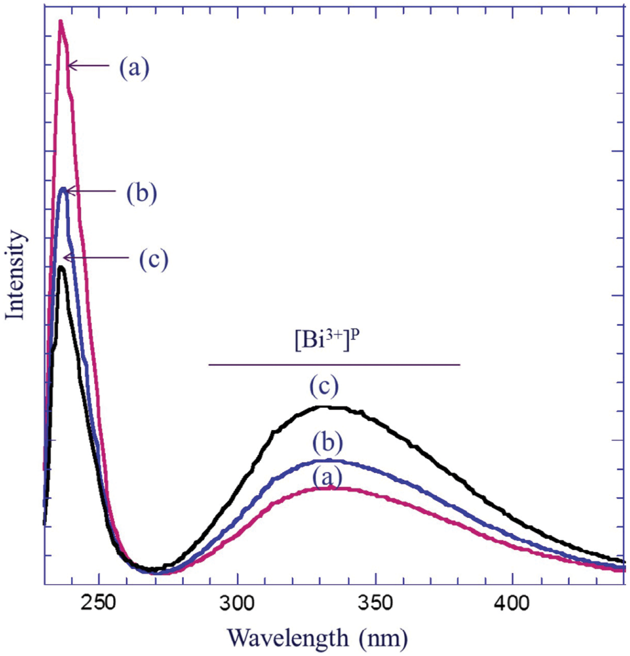

Figure 11.7: Room-temperature emission spectra of $(Y_{1-x}\,Bi_x)PO_4$ as a function of Bi^{3+} concentration: (a) $x = 0.005$, (b) $x = 0.01$, and (c) $x = 0.02$ ($\lambda_{ex} = 225$ nm) (reproduced with permission from Ref. [47]).

11.3.8 Nature of $\mathrm{Ln}B^{3+}\mathrm{O}_3$:$\mathrm{Bi}^{3+}$ emission in relation to the host band gap

As mentioned in Section 11.3.4, we explore the relationship between the optical properties of Bi^{3+} ion in relation to the band gap of the $\mathrm{Ln}B\mathrm{O}_3$ perovskites. Compared to the behavior of Bi^{3+} in (Ca,Sr)$B\mathrm{O}_3$, the absence of emission from the D-level at all temperatures in $\mathrm{Ln}B\mathrm{O}_3$ perovskites is surprising. For example, $LaInO_3$ with a lower band gap than $CaSnO_3$ supports localized $^3P_{0,1}$ emission, whereas with $E^{ex} = 4.90$ eV, the stannate perovskite supports luminescence from the D-level. The bottom of the conduction band in $CaSnO_3$, $LaGaO_3$, and $LaInO_3$ is composed of the *n*s orbitals of Sn^{4+}, Ga^{3+} and In^{3+} ions [39]. The "$6s^2$–ns^0" charge transfer is active in $CaSnO_3$ but not in $LaGaO_3$ and $LaInO_3$ perovskites. The VRBE scheme for these perovskites shows the $^3P_{0,1}$ level lies in the conduction band of $CaSnO_3$ and at −1.24 and −0.54 eV below the CBM in $LaGaO_3$ and $LaInO_3$, respectively. The lower than CBM location of the $^3P_{0,1}$ level in $LaInO_3$ induces the localized emission. The absence of D-level emission implies that the activation energy for the crossover is high, so that the $^3P_{0,1}$ emission is not quenched in favor of emission from the D-level. In the literature, $LaInO_3$:Bi^{3+} has been reported to emit efficiently at room temperature.

What imposes localized emission versus charge transfer emission is a point of interest that should be investigated further. Comparing the Bi^{3+} ion luminescence in isostructural $(Ca,Sr)SnO_3$ and $La(In,Ga)O_3$ rules out the band gap as being a decisive factor. We may speculate that in $(Ca,Sr)BO_3$, where charge compensation is required, the local strain around the dopant ion, coupled with coulombic interaction between dopant and vacancy, pushes the excited level to near the conduction band edge in a low band-gap material, such as $CaSnO_3$. In the $LaInO_3$ perovskite with lower band gap, this is impeded, since there is no charge imbalance. However, it should be emphasized that the first-principles calculations suggest negligible interaction between the Bi^{3+} and the charge-compensating defect in $CaBO_3$.

Lou et al. showed that the excitation and emission energies were linearly correlated with the host band gap in $LnBO_3$ perovskites [39]. Data in Table 11.1 shows that this relationship is not observed in the $(Ca,Sr)BO_3$ family of perovskites.

11.3.9 The absolute energy location of the Bi^{3+} energy levels relative to the intrinsic bands of the orthorhombic perovskite hosts

The VRBE scheme for Bi^{3+} in $LnMO_3$ (Ln = Gd, La, Y; M = Al, Ga, In) is constructed in ref. [39]. In all cases, the VRBEs of the Bi^{3+} 6*p* orbital is flat and around −4 eV. However, the VRBEs of the CBM of the hosts vary from −1.5 to −3.8 eV. The shift of the conduction band is what determines the electron trapping properties of the Bi^{3+} ion, in these orthorhombic perovskites [39].

The VRBE of the $6s^2$ ground level shows that the aluminates ($YAlO_3$ and $GdAlO_3$) have stronger electron binding energy than the perovskites with B cation of $nd^{10}ns^0$ electronic configuration ($LaInO_3$ and $LaGaO_3$).

11.4 The luminescence of Bi^{3+} in zirconate compounds

Of particular interest is the discussion on the luminescence of Bi^{3+} in zirconate compounds, in the context of the emission from the D-level. In the previous section, we stated that the MMCT is not active in $CaZrO_3$ and in $SrZrO_3$. A cursory literature survey indicates that there has been very little experimental work that has been directed towards exploring the MMCT transition between the Bi^{3+} and Zr^{4+} ions in solids. The extensive listing of inorganic compounds by Boutinaud contains only two compounds where the Bi^{3+} emission has been examined in zirconates, $CaZrO_3$ and $La_2Zr_2O_7$ [23]. The $La_2Zr_2O_7$ compound adopts the cubic pyrochlore structure in which the Bi^{3+} ion substitutes for the La ions, which are coordinated to eight oxygen ions. In contrast to $CaZrO_3$ and $SrZrO_3$, the Bi^{3+} luminecence in the pyrochlore reveals emission from both the $^3P_{0,1}$ and the D-levels, and it is useful to briefly discuss the nature of Bi^{3+} luminescence in $La_2Zr_2O_7$.

Srivastava and Beers investigated the photoluminescence and the excitation spectra of $La_2Zr_2O_7$:Bi^{3+} in the temperature range of 15–300 K [51]. At low temperatures, the emission consists of two bands, one in the ultraviolet (UV; 385 nm) and the other in the visible (VIS; 515 nm). A complex, thermally activated intensity exchange between the two bands was observed. For details, the reader is referred to reference [51]. The UV emission is attributed to the localized transition and the visible luminescence to the MMCT between the activator Bi^{3+} and the Zr^{4+} ($4d^0$) cations of the host lattice.

The excitation spectrum contains a low-energy band at 4.27 eV that was assigned to the A-band, and a high energy band at 5.06 eV, which was tentatively assigned to the MMCT. The work of Boutinaud [23] and Dorenbos [33] confirm this band as being due to the MMCT transition. Returning to the emission spectrum, an analysis by Dorenbos also suggests that the VIS band could be due to the presence of Bi^{3+}–Bi^{3+} pairs, as we have discussed in the case of the perovskite, $GdAlO_3$:Bi^{3+} [49]. Boutinaud empirical model that identifies the transition associated with such pairs seems to confirm this assignment [52]. Therefore, the luminescence of $La_2Zr_2O_7$:Bi^{3+} is composed of emission from the localized ($^3P_{0,1}$) level, from delocalized D-level, and from Bi^{3+}–Bi^{3+} pair level. Hence, this compound is especially noteworthy and should be subjected to further investigations. The host lattice exciton energy of $La_2Zr_2O_7$ is around 6 eV, which is close to that of $CaZrO_3$ (6.05 eV) and slightly higher than that of $SrZrO_3$ (5.80 eV). Nevertheless, the Bi^{3+} luminescence in the zirconate pyrochlore is dominated by emission from the D-level.

The VRBE diagram for $La_2Zr_2O_7$:Bi^{3+} shows the $^1S_0$ ground level just above the top of the valence band and the $^3P_{0,1}$ excited level near the excitonic level of the host [33]. This explains the complicated temperature dependence of emission, since the $^3P_1$ electron can become delocalized into Zr^{4+}-dominated conduction band via a thermally activated process. Since the structure of $A_2B_2O_7$ pyrochlore can be perceived as an A_2O network interpenetrating the BO_3 framework, the MMCT can be regarded as the hole residing on the $(La,Bi)_2O$ sublattice and the electron in the ZrO_3 framework. The VIS luminescence is caused by recombination of this electron and the hole.

It is also useful to consider the behavior of the Bi^{3+} ion that distinguishes the MMCT emission from emission due to Bi^{3+} ion pair. A particularly noticeable difference between the emitting levels of Bi^{3+} pairs and MMCT is in their coupling with the localized $^3P_{0,1}$ state. In $La_2Zr_2O_7$, there is a clear exchange in intensity between the MMCT and $^3P_{0,1}$ level, which is similar to what has been observed in $CdCl_2$:Pb^{2+} [53]. For example, UV and VIS emissions were also observed in the luminescence spectrum of the pyrochlore, $Y_2Sn_2O_7$:Bi^{3+} [54]. The UV band was assigned to the localized $^3P_{0,1}\rightarrow{}^1S_0$ (A-band) transition. A temperature induced intensity exchange between the two emitting states was not observed. What was of importance is that the Bi^{3+} concentration had a significant effect on the emission spectrum. The effect of increasing Bi^{3+} concentration in $Y_2Sn_2O_7$ was to increase the intensity of the VIS band at the expense of the UV band. Therefore, the VIS band was assigned to Bi^{3+} pairs/clusters in the pyrochlore lattice. This is similar to the behavior of the Bi^{3+} ion in (Y, Lu)PO_4, which was previously discussed.

The excitation spectrum of the Bi^{3+} UV and VIS bands in $Y_2Sn_2O_7$ differed slightly. The main band at 280 nm (4.43 eV) was assigned to the $^1S_0 \rightarrow {}^3P_1$ (A-band) transition. The excitation spectrum for the VIS band peaked at only slightly longer wavelength. It should be mentioned that more complex (or bigger clusters) of Bi–Bi ions were also observed in the spectroscopic data of $Y_2Sn_2O_7$:Bi^{3+}. For example, a sample with five percent Bi substitution gives an additional weak excitation and emission band peaking near 325 nm (3.82 eV) and 620 nm (2.00 eV), respectively [54].

11.5 Luminescence of Bi^{3+} in the titanates with emphasis on the double perovskite Ln_2MgTiO_6

It was discussed in a previous section that the CBM in titanates are composed of the Ti^{4+} 3*d* orbitals. Usually, the CBM of titanates is at low energies, so that the Bi^{3+} $^3P_{0.1}$ level lies in the conduction band. This is the case in $CaTiO_3$ and $Y_2Ti_2O_7$ (pyrochlore structure), where the emission is due to the Bi^{3+}–Ti^{4+} MMCT transition [55]. For $Y_2Ti_2O_7$, the VRBE scheme shows the $^1S_0$ level to be located just above the VBM and the excited state lies in the conduction band [33]. Therefore, it was anticipated that localized $^3P_{0,1} \rightarrow {}^1S_0$ emission transition would not be observed in titanates [33].

Srivastava et al. investigated the Bi^{3+} luminescence in the ordered perovskite, La_2MgTiO_6 [56]. They had anticipated the Bi^{3+} $^3P_{0,1}$ excited level to lie in the conduction band. However, the experimental results were consistent with the model of the electronic structure in which the Bi^{3+} $^3P_{0,1}$ excited level lies below the host conduction band. It was this energy structure which permitted the first observation of luminescence from the localized Bi^{3+} $^3P_{0,1}$ excited level in a titanate host lattice. The luminescence of La_2MgTiO_6:Bi^{3+} is discussed in the following.

The double perovskite, La_2MgTiO_6, crystallizes in the monoclinic system with the space group $P2_1/n$. The *B*-site contains the [-Mg^{2+}–O^{2-} Ti^{4+}-] linkages, which isolates the TiO_6 octahedron; there are alternating MgO_6 and TiO_6 corner-sharing octahedral moieties. The La^{3+} is in 8-fold coordination that is similar to the coordination in the orthorhombic perovskites that were discussed previously.

In Table 11.5, we have assembled the spectroscopic data for the Bi^{3+} ion in a few isostructural double perovskite compounds containing the Ti^{4+} ion on one of the *B*-sites. If we compare the Stokes shift and the FWHM obtained from the low temperature spectroscopic data with those reported in Tables 11.1 and 11.4 for the orthorhombic ABO_3 perovskites, we find compelling evidence for assigning the emission to the localized $^3P_{0,1} \rightarrow {}^1S_0$ transition. The Stokes shift and the FWHM of this transition in these compounds at low temperatures range from 0.5 to 0.8 eV and from 0.26 to 0.35 eV.

The spectroscopic data for the other double perovskites in Table 11.5 are those reported in the archival literature and measured at room temperature. The Stokes shift and FWHM in the double perovskites are all indicative of localized emission transition. This is good evidence that the excited state of Bi^{3+} is located below the CBM. Therefore, unlike $CaTiO_3$ and $Y_2Ti_2O_7$, the double perovskites represented by the general formula, $LnBTiO_6$, are the first titanate compounds that support the localized emission of the Bi^{3+} ion.

It was also of interest to determine if the CBM of La_2MgTiO_6 was composed of the Ti^{4+} 3*d* orbitals. Therefore, the composition of all electronic bands of La_2MgTiO_6 was analyzed and assigned with the help of the DOS diagrams. It was indeed established that the CBM was mainly composed of the Ti 3*d* states [56].

We also wish to point out that the Stokes shift of the Bi^{3+} emission in Ln_2BTiO_6 is influenced by the Ln cations. For example, replacement of the larger La by the smaller Gd in Ln_2ZnTiO_6 decreases the Stokes shift from 0.50 to 0.36 eV. The relation that the Stokes shift of emission increases with increasing ionic radii of the host cation is frequently observed in the luminescence of Bi^{3+} ion [10].

Table 11.5: Optical properties of Bi^{3+} in $Ln(Mg, Zn)TiO_6$ double perovskites.

Perovskite	Excitation peak (eV)	Emission peak (eV)	Stokes shift (eV)	FWHM (eV)	*T* (K)	Reference
La_2MgTiO_6	3.65	2.88	0.77	0.34	15	[56]
La_2ZnTiO_6	3.54	3.04	0.50	0.52	300	[57]
Gd_2MgTiO_6	3.31	2.88	0.43	0.23	300	[58]
Gd_2ZnTiO_6	3.31	2.95	0.36	0.28	300	[59]

11.6 Conclusions

In focusing our attention on the orthorhombic perovskites (ABO_3) and double perovskite compounds, we have shown how systematic experiments can unravel factors that affect the Bi^{3+} ion luminescence in solids. Three types of luminescence are distinguished in these perovskites: localized from the $^3P_{0,1}$ level, delocalized from the D-level, and from ion pair. Clear examples of transition from localized to delocalized behavior occur in the $CaB^{4+}O_3$ and $SrB^{4+}O_3$ perovskites that are dependent on the electronic configuration of the B^{4+} cation. For example, replacement of Zr^4 ($4d^0$) by Sn^{4+} ($4d^{10}$) in $CaB^{4+}O_3$ changes the luminescence from the localized $^3P_{0,1}$ state to delocalized D-level, partially as a result of band-gap narrowing. While $SrZrO_3$ shows localized emission, both localized and D-level emissions are found in $SrSnO_3$. The stannate perovskites have lower band-gap energy than the corresponding zirconate compounds. The low CBM of $CaTiO_3$ (Ti^{4+}; $3d^0$) ensure that the excited state of Bi^{3+} lies in the conduction band. Therefore, it appears that in these perovskites, localized emission from the $^3P_{0,1}$ level requires a certain value of the band gap.

The behavior of the Bi^{3+} ion is completely different in the $\mathrm{Ln}B^{3+}\mathrm{O}_3$ (Ln = Y, Gd, La; B = Al, Ga, In) orthorhombic perovskites. In every case the luminescence corresponds to localized $^3P_{0,1}\rightarrow{}^1S_0$ emission transition. The localized emission is also found in $LaInO_3$ with narrower band gap than the stannate perovskites. Clearly, the $^3P_{0,1}$ level is stabilized, relative to the D-level in these perovskites. Energy transfer and migration process is responsible for finding Bi^{3+} ion pair in $GdAlO_3$.

The results of the more rigorous approaches such as the semiempirical models and first-principles calculations are in support of the simple approach, which identifies and differentiates the transitions based on the Stokes shift of emission, FWHM (localized vs delocalized), and the dependence of luminescence on the Bi^{3+} ion concentration (ion pair luminescence). However, these rigorous approaches further advance our fundamental understanding by identifying overlapping transitions in the excitation and emission spectrum that may escape notice, when probing the luminescence by the simple method. The fundamental reason for the dominance of Bi^{3+} ion pair emission in solids such as YPO_4 and $Y_2Sn_2O_7$ should be explored further. Systematic research should be pursued in Bi^{3+} ion luminescence in zirconate and hafnate compounds. Finally, surprises are still possible, as the observation of localized emission in the titanate host lattice with the double perovskite structure ($\mathrm{Ln}_2B\mathrm{TiO}_6$) demonstrates.

References

[1] K.H. Butler, Fluorescent Lamp Phosphors, Pennsylvania State University Press, University Park (1980).
[2] G. Blasse, B.C. Grabmier, Luminescent Materials, Springer Verlag (1994).
[3] P.W.M. Jacob Alkali, Halide crystals containing impurity ions with the ns^2 ground-state electronic configuration, Phys. Chem. Solids. 52 (1991) 3547. https://doi.org/10.1016/0022-3697(91)90059-9.
[4] H.-T. Sun, J. Zhou, J. Qiu, Recent advances in bismuth activated photonic materials, Prog. Mater. Sci. 64 (2014) 1–72. http://dx.doi.org/10.1016/j.pmatsci.2014.02.002.
[5] A. Kransnikov, E. Mihokova, M. Nikl, S. Zazubovich, Y. Zhydachevskyy, Luminescence spectroscopy and origin of luminescence centers in bi-doped materials, Crystals. 10 (2020) 208. https://doi.org/10.3390/cryst10030208.
[6] P. Dorenbos, Electronic structure of bi-activated luminescent compounds and pure bismuth photocatalytic compounds, ECS J. Solid State Sci. Technol. 10 (2021) 086002. https://doi.org/10.1149/2162-8777/ac19c610(2021)086002.
[7] G. Boulon, J. Phys. 32 (1972) 333.
[8] A. Wolfert, G. Blasse, Luminescence of Bi^{3+}-Activated LaOBr, a system with emission from a different state, J. Lumin. 33 (1985) 213–236. https://doi.org/10.1016/0022-2313(85)90019-5.
[9] C.W.M. Timmermans, G. Blasse, The Luminescence of $K_4Bi_2Br_{10} \cdot 4\,H_2O$ and Rb_3BiBr_6 Single Crystals, Phys. Status Solidi. B. 118 (1983) 353–361. https://doi.org/10.1002/pssb.2221180141.

[10] A.M. Srivastava, Luminescence of Bi^{3+} in $LaGaO_3$, Mat. Res. Bull. 34 (1999) 1391–1396. https://doi.org/10.1016/S0025-5408(99)00149-X.

[11] A.M. Srivastava, Luminescence of Bi^{3+} in the orthorhombic perovskites $CaB^{4+}O_3$ (B^{4+}=Zr, Sn): Crossover from localized to D-state emission, Opt. Mat. 58 (2016) 89–92. https://doi.org/10.1016/j.optmat.2016.03.045.

[12] A.M. Srivastava, H.A. Comanzo, The ultraviolet and visible luminescence of Bi^{3+} in the orthorhombic perovskite, $GdAlO_3$, Opt. Mat. 63 (2017) 118–121. https://doi.org/10.1016/j.optmat.2016.05.042.

[13] A.M. Srivastava, Luminescence of Bi^{3+} in the orthorhombic perovskites, $SrB^{4+}O_3$(B^{4+} =Zr, Sn), Opt. Mat. 72 (2017) 313–315. https://doi.org/10.1016/j.optmat.2017.06.026.

[14] L.I. van Steensel, S.G. Bokhove, A.M. van de Craats, J. de Blank, G. Blasse, The luminescence of Bi^{3+} in $LaInO_3$ and some other perovskites, Mat. Res. Bull. 30 (1995) 1359–1362. https://doi.org/10.1016/0025-5408(95)00129-8.

[15] R.P. Liferovich, R.H. Mitchel, A structural study of ternary lanthanide orthoscandate perovskites, J. Solid St. Chem. 177 (2004) 2188–2197. https://doi.org/10.1016/j.jssc.2004.02.025.

[16] R.D. Shannon, Revised effective ionic radii and systematic studies of interatomie distances in halides and chalcogenides, Acta Cryst. A. 32 (1976) 751–767. https://doi.org/10.1107/S0567739476001551.

[17] B. Lou, J. Wen, J. Cai, -Y.-Y. Yeung, M. Yin, C.-K. Duan, First-principles study of Bi^{3+}-related luminescence and traps in the perovskites $CaMO_3$ (M = Zr, Sn, Ti), Phys. Rev. B. 103 (2021) 075109. https://doi.org/10.1103/PhysRevB.103.07510.

[18] J.M. Henriques, E.W.S. Caetano, V.N. Freire, J.A.P. da Costa, E.L. Albuquerque, Structural, electronic, and optical absorption properties of orthorhombic $CaSnO_3$ through ab initio calculations, J. Phys. Condens. Matter. 19 (2007) 106214–106223. doi: 10.1088/0953-8984/19/10/106214.

[19] M. Back, J. Ueda, J. Xu, K. Asami, L. Amidani, E. Trave, S. Tanabe, Uncovering the origin of the emitting states in Bi^{3+}-Activated $CaMO_3$ (M = Zr, Sn, Ti) Perovskites: Metal-to-metal charge transfer versus s−p transitions, J. Phys. Chem. C. 123 (2019) 4677–14688. https://doi.org/10.1021/acs.jpcc.9b03940.

[20] A.A. Setlur, A.M. Srivastava, The nature of Bi^{3+} luminescence in garnet, Opt. Mat. 29 (2006) 410–415. https://doi.org/10.1016/j.optmat.2005.09.076.

[21] P. Boutinaud, E. Cavalli, R. Mahiou, Photon conversion in Bi^{3+}/Pr^{3+}-codoped $CaTiO_3$, J. Phys. Condens. Matter. 24 (2012) 295502. https://doi.org/10.1088/0953-8984/24/29/295502.

[22] K.C. Bhamu, A. Dashora, G. Arora, B.L. Ahuja, Nature of bonding in $CaTiO_3$ and $SrTiO_3$: A compton scattering study, Radiat. Phys. Chem. 81 (2012) 728–734. https://doi.org/10.1016/j.radphyschem.2012.04.010.

[23] P. Boutinaud, Revisiting the spectroscopy of the Bi^{3+} Ion in oxide compounds, Inorg. Chem. 52 (2013) 6028–6038. https://doi.org/10.1021/ic400382k.

[24] P. Boutinaud, On the spectroscopy of Bi^{3+} in d^{10} post-transition metal oxides, J, Lumin. 223 (2020) 117219. https://doi.org/10.1016/j.jlumin.2020.117219.

[25] G. Blasse, A. Bril, Photo luminescent efficiency of phosphors with electronic transitions in localized centers, J. Electrochem. Soc. 115 (1968) 1067. https://doi.org/10.1149/1.2410880.

[26] X. Zhang, Z. Zhu, Z. Guo, F. Mo, Z.-C. Wu, A zero-thermal-quenching and color-tunable phosphor $LuVO_4$: Bi^{3+}, Eu^{3+} for NUV LEDs, Dyes Pigm. 156 (2018) 67–73. https://doi.org/10.1016/j.dyepig.2018.03.071.

[27] E. Cavalli, F. Angiuli, F. Mezzadri, M. Trevisani, M. Bettinelli, P. Boutinaud, M.G. Brik, Tunable luminescence of Bi^{3+} -doped $YP_xV_{1-x}O_4$ ($0 \le x \le 1$), J. Phys. Condens. Matter. 26 (2014) 385503. doi: 10.1088/0953-8984/26/38/385503.

[28] V. Tsiumraa, A. Zhyshkovych, T. Malyi, Y. Chornodolskyy, V. Vistovskyy, S. Syrotyuk, Y. Zhydachevskyy, A. Suchocki, A. Voloshinovskii, Opt. Mater. 89 (2019) 480–487. https://doi.org/10.1016/j.optmat.2019.01.071.

[29] G. Blasse, Classical phosphors: A Pandora's box, J. Lumin. 72-74 (1997) 129–134.

[30] S.Z. Toma, F.F. Mikus, J.E. Mathers, Energy transfer and fluorescence processes in Bi and Eu activated YVO_4, J. Electrochem. Soc. 114 (1967) 953. https://doi.org/10.1149/1.2426788.

[31] E. Cavalli, F. Angiuli, A. Belletti, P. Boutinaud, Luminescence spectroscopy of YVO_4: Ln^{3+},Bi^{3+} (Ln^{3+} = Eu^{3+}, Sm^{3+}, Dy^{3+}) phosphors, Opt. Mater. 36 (2014) 1642. https://doi.org/10.1016/j.optmat.2013.12.020.

[32] P. Dorenbos, Lanthanide 4f-electron binding energies and the nephelauxetic effect in wide band gap compounds, J. Lumin. 136 (2013) 122–129. https://doi.org/10.1016/j.jlumin.2012.11.030.

[33] R.H.P. Awater, P. Dorenbos, The Bi^{3+} 6s and 6p electron binding energies in relation to the chemical environment of inorganic compounds, J. Lumin. 184 (2017) 221–231. https://doi.org/10.1016/j.jlumin.2016.12.021.

[34] A.M. Srivastava, M.G. Brik, W.W. Beers, W. Cohen, unpublished data

[35] E.G. Rogers, P. Dorenbos, Vacuum referred binding energy of the single 3d, 4d, or 5d electron in transition metal and lanthanide impurities in compounds, ECS J. Solid State Sci. Technol. 3 (2014) R173. https://doi.org/10.1149/2.0121410jss.

[36] H.F. Folkerts, G. Blasse, Two types of luminescence from Pb2+ in alkaline earth carbonates with the aragonite structure, J. Phys. Chem Solids. 57 (1996) 303.

[37] T. Bak, J. Nowotny, C.C. Sorrell, M.F. Zhou, E.R. Vance, Charge transport in $CaTiO_3$: I. electrical conductivity, J. Mater. Sci. Mater. Electron. 15 (2004) 635–644. https://doi.org/10.1023/B:JMSE.0000038917.73334.92.

[38] J.B. Goodenough, Electronic and ionic transport properties and other physical aspects of perovskites, Rep. Prog. Phys. 67 (2004) 1915–1993. http://iopscience.iop.org/0034-4885/67/11/R01.

[39] B. Lou, J. Wen, L. Ning, M. Yin, C.-G. Ma, C.-K. Duan, Phys. Rev. 104 (2021) 115101. doi: 10.1103/PhysRevB.104.115101.

[40] A. Krasnikov, L. Lipińska, E. Mihokova, M. Nikl, T. Shalapska, A. Suchocki, S. Zazubovich, Y. Zhydachevskii, Time-resolved photoluminescence and excited state structure of Bi^{3+} center in $YAlO_3$, Opt. Mater. 36 (2014) 1705–1708. https://doi.org/10.1016/j.optmat.2014.01.030.

[41] B. Jacquier, G. Boulon, G. Sallavuard, F. Gaume-Mahn, Bi^{3+} center in a lanthanum gallate phosphor, J. Solid St. Chem. 4 (1972) 374–378. https://doi.org/10.1016/0022-4596(72)90152-1.

[42] L. Wang, Q. Sun, Q. Liu, J. Shi, Investigation and application of quantitative relationship between sp energy levels of Bi^{3+} ion and host lattice, J, Solid St. Chem. 191 (2012) 142–146. https://doi.org/10.1016/j.jssc.2012.03.015.

[43] W. Aggoune, K. Irmscher, D. Nabok, C. Vona, S.B. Anooz, Z. Galazka, M. Albrecht, C. Drax, Fingerprints of optical absorption in the perovskite $LaInO_3$: Insight from many-body theory and experiment, Phys. Rev. B. 103 (2021) 115105. doi: 10.1103/PhysRevB.103.115105.

[44] G. Blasse, A. Bril, Investigations on Bi^{3+}-Activated Phosphors, J. Chem. Phys. 48 (1968) 217. https://doi.org/10.1063/1.1667905.

[45] A.M. van de Craats, G. Blasse, The influence of d^{10} ions on the luminescence of bismuth(III) in solids, Mat. Res. Bull. 31 (1996) 381–387. https://doi.org/10.1016/0025-5408(96)00017-7.

[46] T. Jüstel, P. Huppertz, W. Mayr, D.U. Wiechert, Temperature-dependent spectra of YPO_4: Me(Me=Ce, Pr, Nd, Bi), J. Lumin. 106 (2004) 225–233. https://doi.org/10.1016/j.jlumin.2003.10.004.

[47] A.M. Srivastava, S.J. Camardello, Concentration dependence of the Bi^{3+} luminescence in $LnPO_4$ (Ln = Y^{3+}, Lu^{3+}), Opt. Mat. 39 (2015) 130–133. https://doi.org/10.1016/j.optmat.2014.11.011.

[48] R.H.P. Awater, L.C. Niemeijer-Berghuijs, Pieter Dorenbos, Luminescence and charge carrier trapping in YPO_4: Bi, Opt. Mat. 66 (2017) 351–355. https://doi.org/10.1016/j.optmat.2017.02.032.

[49] R.H.P. Awater, P. Dorenbos, Towards a general concentration quenching model of Bi^{3+} luminescence, J. Lumin. 188 (2017) 487–489. http://dx.doi.org/10.1016/j.jlumin.2017.05.011.

[50] Z. Feng, B. Lou, M. Yin, Y.-Y. Yeung, H.-T. Sun, C.-K. Duan, First-principles study of Bi3+-Related luminescence and electron and hole traps in (Y/Lu/La)PO_4, Inorg. Chem. 60 (7) (2021) 4434–4446. doi: 10.1021/acs.inorgchem.0c03217.

[51] A.M. Srivastava, W.W. Beers, On the impurity trapped exciton luminescence in La2Zr2O7: Bi3+, J. Lumin. 81 (1999) 293–300. https://doi.org/10.1016/S0022-2313(99)00004-6.

[52] P. Boutinaud, On the luminescence of Bi3+ pairs in oxidic compounds, J. Lumin. 197 (2018) 228–232. https://doi.org/10.1016/j.jlumin.2018.01.052.

[53] B. Moine, C. Pedrini, V. Ghiordanescu, An emission and kinetic study of the impurity-trapped exciton in $CdCl_2$: Pb^{2+} 1994, J. Phys. Condens. Matter. 6. 4093. https://iopscience.iop.org/article/10.1088/0953-8984/6/22/008.

[54] A.M. Srivastava, On the luminescence of Bi^{3+} in the pyrochlore $Y_2Sn_2O_7$, Mat. Res. Bull. 37 (2002) 745–751. https://doi.org/10.1016/S0025-5408(02)00688-8.

[55] A.M. Srivastava, H.A. Comanzo, S.J. Camaradello, On the “Bi3+–Ti4+” charge transfer transition in the pyrochlore $Y_2Ti_2O_7$: Bi^{3+}, Opt. Mat. 48 (2015) 31–35. https://doi.org/10.1016/j.optmat.2015.07.020.

[56] A.M. Srivastava, H.A. Comanzo, M.G. Brik, Luminescence of Bi^{3+} in the double perovskite, La_2MgTiO_6, Opt. Mat. 75 (2018) 809–813. https://doi.org/10.1016/j.optmat.2017.11.031.

[57] J. Wanga, R. Leib, S. Zhao, F. Huang, D. Deng, X. Shiqing, H. Wang, Color tunable Bi^{3+}/Eu^{3+} co-doped La_2ZnTiO_6 double perovskite phosphor for dual-mode ratiometric optical thermometry, J. Alloys Compound. 881 (2021) 160601. https://doi.org/10.1016/j.jallcom.2021.160601.

[58] P. Gao, P. Dong, Z. Zhou, Q. Li, H. Li, Z. Zhou, M. Xia, P. Zhang, Enhanced luminescence and energy transfer performance of double perovskite structure Gd_2MgTiO_6: Bi^{3+},Mn^{4+} phosphor for indoor plant growth LED lighting, Ceram. Int. 47 (2021) 16588–16596. https://doi.org/10.1016/j.ceramint.2021.02.230.

[59] C. Ji, Z. Huang, J. Wen, J. Zhang, X. Tian, H. He, L. Zhang, T.-H. Huang, W. Xie, Y. Peng, Blue-emitting Bi-doped double perovskite Gd_2ZnTiO_6 phosphor with near-ultraviolet excitation for warm white light-emitting diodes, J. Alloys. Comps. 788 (2019) 1127–1136. https://doi.org/10.1016/j.jallcom.2019.02.279.

Index

Δf/f$_0$ 124
β-diketonate complexes 41
β-diketone ligands 48
τ_{avg} 121
3–*j* symbols 24–25
4*f* electrons 34
4*f*–4*f* intensities 26, 40
4*f*–4*f* oscillator strengths 30
4*f*–4*f* transitions 19, 28

activator ion 160
AlN 224
aluminate fluoride 207
amalgam lamps 222
angular overlap model 32, 63, 72–73, 78, 83
anti-Stokes 160–161, 194
anti-Stokes luminescence 6
asymmetry 33
Au^0 MPs 116
Au^0 particles 118
autofluorescence 157–158, 167

bioimaging 160, 168
biological windows 158–159, 173
bioluminescence 2
biopsy surgery needles 208
blue 126
blue LED 197
body-centered cubic 132
bond overlap model 20, 44
boroselenate glass ceramics 121

C 1*s* 118
candoluminescence 2
canopy 210
cathodoluminescence 2
cavities 116, 121
Ce^{3+} 12, 135
chalcogenide oxide 115
charge factors 46–47
charge transfer states 239
charge-transfer band 192
chemical environment 42
chemical shift model 141
chemical stability 199
chemiluminescence 2
chlorophyll *a* 208
chlorophyll *b* 208
cloud expansion 186
color gamut 198
color mimicking 199
color rendering index 197
Commission International de l'Eclairage 198
components of lifetime 118
concentration quenching 165
contrast agent 175
contrast ratio 211
conversion materials 194
coordination compounds 40
coordination polyhedra 46
coordination polyhedron 41
core-shell structure 166
core-shell structures 164
correlated color temperature 197
Coulombic interactions 188
covalency 32, 38, 125
covalency contributions 50
covalency effects 45, 52
covalency model 40
covalency of bonds 33
Cr^{3+} 7, 186
cross relaxation 162
crossing point 206
cryoluminescence 2
crystal field 126
crystal field potential 67–69, 71–72
crystal field splitting 136
crystal field strength 207
crystal field theory 187
crystal structure 97
crystalloluminescence 3
$Cs_2AgBiBr_6$ 105
$Cs_2AgBiCl_6$ 105
$Cs_2InBr_5{\cdot}H_2O$ 109
Cs_2InCl_5 104
$Cs_2NaBiCl_6$ 105
Cs_2SnCl_6 101
Cs_2TeCl_6 100
Cs_2ZnCl_4 100
Cs_2ZrCl_6 101
$Cs_3Bi_2I_9$ 102
$Cs_3Cu_2I_5$ 103, 108

https://doi.org/10.1515/9783110607871-012

Cs_3InCl_6 104
Cs_3MnBr_5 103, 108
$Cs_3Sb_2I_9$ 102
$Cs_4CdSb_2Cl_{12}$ 105
$CsCu_2I_3$ 103
$CsMnCl_3{\cdot}2H_2O$ 103
$CsSnBr_3$ 98
$CsSnX_3$ 98

daily food samples 208
decay curves 120
decay time 116
decomposition 235
deep red broad luminescence 148
deep-red emission 194
defects 120, 170
degeneracy 188
degenerated 3*d* orbitals 187
degree of covalence 31
Derwent Innovations 186
descriptor of covalency 50
detection sensitivity 210
detrapping 140
detrapping mechanisms 171
device 200
Dieke diagram 10
diffraction pattern 119
diffractogram 118
dimensionality 94
dimming 211
dipole moment operator 38
dipole moments 37
dipole operator 28
dipole strength 42
disinfection 230, 234
disordered octahedral 205
distortion 139
dodecahedral site 131
double perovskite halide 104
doublet states 192
down-conversion capability 201
driving current 200
dye-sensitized upconversion 164
dynamic coupling 21, 27

edge dislocation 120
EDS 120
effect of the pressure on the luminescence 261
efficacy 197
electric dipole moment 189
electric dipole moments 39
electric dipole operator 24, 26
electrochemiluminescence 2
electroluminescence 2
electromagnetic interference 210
electron trap 142
electronegativity 137
electronic transitions 50
electron–lattice coupling 185
elemental composition 120
emission spectrum 190
energy inequality relation 207
energy level schemes of the Ln^{3+} ions 257
energy migration 162
energy shifting 137
energy transfer 159, 166
energy transfer upconversion 162
Eu^{2+} 12
Eu^{3+} 10
excimer 223
excimer lamps 221, 233–234
excited state absorption 161
experimental intensity parameters 40

Fano-antiresonance 207
Fermi velocity 124
fluorescence 2
fluorescence lifetime imaging microscopy 174
fluoride environment 43
fluoride host nanoparticles 159, 167
forced electric dipole 21, 25
Förster resonance energy transfer 159
fractoluminescence 3
Franck–Condon principle 4
free cavities 120
free volume fraction 121
frequency modes 195
FRET 159

gallate fluoride 207
garnet structure 131
Gd3Ga5O12 145
geometry 63–66, 71–74, 80–82
gerade 190
glass matrices 40
glasses 34
green 126
green band 127

green emission 193
ground term 188

healthcare products 208
HF-free environment 198
Hg discharge 221–222, 227–228, 230
Hg-free UV radiation source 230
high-spin 189
Ho^{3+} ions 116
hole trap 142
holmium ions 115, 123
host effects on the emission properties 239
hue and saturation 198
hypersensitive 123
hypersensitive transitions 27

images 120
imperfections 120
infrared-active modes 195
InGaN 197
inorganic matrices 40, 42
inorganic systems doped 42
intensity components 123
intensity parameters 44, 50
interelectron repulsion 186
International Commission on Illumination 200
International Organization for Standardization 20473 200
inversion center 192
ionizing radiation 230
irreducible tensor operator 24

J-O theory 33
JOYSpectra 45–46
JOYSpectra web platform 20, 44–45, 52
Judd-Ofelt parameters 19
Judd–Ofelt intensity parameters 25, 44
Judd–Ofelt theory 20, 23

Kapton wafer 118
$KrCl^*$ 223
Krönecker delta 29

$LaMgAl_{11}O_{19}:Ce^{3+}$ 228
lanthanide 19
lanthanide complexes 36, 53
lanthanide compounds 38, 51
lanthanide ion spectroscopy 30
lanthanide materials 53
lanthanide trihalide 35
lanthanide trihalides 33
lanthanide-doped nanoparticles 159–160
lanthanide-doped upconverting nanoparticles 161
lanthanides 10
Laporte selection 190
Laporte’s rule 19, 52
Laporte’s rule relaxation 50
layered structure 205
lead free 93
least-square fitting 120
lifetime components 121
ligand field Hamiltonian 21
ligand field parameters 25
ligand field theory 63, 72–73, 85, 88
ligand-to-metal charge transfer 39
light source selection 208
light-emitting diode 186
local environment 33
low-pressure mercury discharge lamps 222
low-spin 189
$Lu_3Al_5O_{12}:Bi^{3+},Gd^{3+}$ 229
$Lu_3Al_5O_{12}:Gd^{3+}$ 229
$Lu_3(Ga,Al)_5O_{12}:Pr^{3+}$ 236
luminance 19, 149
luminescence 1
luminescence dynamics 162–163
luminescence properties 120
luminescence thermal quenching temperature 278
luminescent materials 19
luminescent nanomaterials 161
luminescent sensors 109
luminous flux 197
$LuPO_4:Bi^{3+}$ 230
$LuPO_4:Nd^{3+}$ 232
$LuPO_4:Pr^{3+}$ 231
lyoluminescence 2

magnetic dipole 21, 27
magnitude of Ω_2 125
matrix elements 26
mechanoluminescence 2
metal halide perovskite 93
metal-to-metal charge transfer 271
metastable 163
Minamata convention 222
mini- and micro-LEDs 211

miniature spectrometers 208
MMCT 239
– metal-to-metal charge transfer 239
– MMCT energy position 243
– physical model 244
Mn^{4+} 7, 186
model core potential 39
molecular orbital 107
molecular vibrations 37
morphology 172
MRI 174
multiphoton absorption 25
multireference spin–orbit configuration 39

nanocrystal
– NC 95
nanoscopy 168
nanosized defects 117, 120
narrow emission 194
near-infrared 100, 157, 192
nephelauxetic effect 31–32, 187
NIR lasers 116
NIR-I 149
NIR-II 149
NIR-III 149
NIR-persistent luminescence 205
noble metal ions 116
Noether's theorem 64

OA bands 123
OA spectra 122
open-shell configurations 38
opposite parity states 26
optical absorption spectra 117
optical basicity 137
optical bioimaging 157, 159
optical imaging 167
optical imaging probes 158
optical microscopy 168
optical temperature sensing 259
optical transition bands 185
optical trapping 168
optically active ions 165
optically stimulated luminescence 171
orange 126
orange radiations 124
ordered tetrahedrally 205
Ortec PAL system 118
oscillating dipoles 29
oscillating electric field 27
oscillator strength 38–39
oscillator strengths 52
overlap integrals 48
overlap polarizability 45, 49
oxide glasses 34

PAL decay profiles 121
parity selection rule 189
PBSG system 117
persistent energy transfer 149
persistent luminescence 143
persistent luminescence excitation 143
persistent luminescence imaging 170, 174
phonon losses 122
phosphate 34
phosphorescence 2
phosphors 186
photochemistry 230
photochlorination 235
photoconversion efficiency 201
photocurrent excitation 144
photoluminescence 2
photomorphogenic function 210
photon radiance 149
photophysical properties 32–33
photoreceptors 208
phototherapy 194
piezoluminescence 2
PL efficiency 116, 122
PL spectrum 126
point charges 187
point group symmetry 33
polarizabilities 29, 31
polarizability 28, 137
polarization components 23
positron annihilation 116
Pr^{3+} 241
– emission properties 241
– energy level structure 241
– Pr^{3+}-containing transition metal oxide 248
– Pr^{3+}-to-d^0 transition metal CT 244
– quenching of $^3P_0$ emission 241
precipitation–cation exchange route 198
pseudo-multipolar field 38
pseudo-quadrupole mechanism 38
purify water 235

quantum efficiencies 165
quantum efficiency 4, 126, 193
quantum tunneling 171
quantum yield 3, 166
quasicontinuous 207

Racah parameters 187
radiant flux 200
radiant power 200
radioluminescence 3
Raman-active modes 195
Rb_2CuX_3 103
$Rb_7Bi_3Cl_{16}$ 102
$Rb_7Sb_3Cl_{16}$ 102
red emission 193
redshift 204
refractive index 42, 44
relativistic effective core 39
residual phase 120
rock-salt structure 194
ruby crystal 201

scintillation 110
Se^{4+} ions 118
selection rules 19, 21
selenate 115
selenium oxide 115
self-trapped excitons
– STE 106
SEM photograph 120
sensitizers 116
SeO_2 glass system 115
sequential atomic layers 132
Se–O–Se linkages 124
shade avoidance 210
shade tolerance 210
shared edge 133
shielding effect 123
silicate glasses 34
simple overlap model 20, 24
single configuration coordinate model 4
single crystal 95
single-particle tracking 168, 170
Sinha's parameter 32
sol–gel method 195
sonoluminescence 3
spatial resolution 210
spectrochemical series 71, 78–79, 81, 85
spin multiplicities 190
spin-allowed 190
spin-forbidden transition 192
spin-selection 190
spin–orbit coupling 195
Stark components 25
Stark-to-Stark transitions 30, 42
stimulated emission depletion 168
Stokes 194
Stokes rule 4
Stokes shift 4, 228
super-resolution microscopy 168, 170
surface plasmon resonance 116, 123
symmetry 33, 63–66, 69–72, 74–75, 79–80, 82, 84, 86, 125
synergetic effects 194
syntheses 95
s–*p* 106

Tanabe–Sugano 189
Tb^{3+} 247
– emission properties 247
– energy level scheme 247
– Tb^{3+}-containing transition metal oxides 254
TEM photographs 120
thermal analysis 117
thermal analysis) 117
thermal effects 38, 52
thermal feature 36
thermal quenching 280
thermoluminescence 2, 142
tiny crystallites 120
TiO_2 235
tissue penetration 171, 173
tolerance rule 94
transition dipole moment 39
transition metal ions 161, 173
trap depth 140, 171
trap-depth engineering 171
trapping 140
trapping center 170
triboluminescence 3
tricolor mixture 198
trigonal 205
trihalide complexes 35
triplet states 192
tungstate 206
twofold symmetry 206

ungerade 190
upconversion 236
upconversion efficiency 165
upconversion luminescence 160, 163–164
upconversion mechanisms 161
upconverting nanoparticles 166
UV dose 235
UV-A 222
UV-A-emitting phosphors 225
UV-B 222
UV-C 222
UV-emitting phosphors 221

vacancies 120
vacuum-referred binding energy) scheme 281
valence shell orbitals 29
vibration modes 194
vibrational frequencies 37
vibrational frequency 36
vibronic mechanism 50
vibronic mechanisms 21
voids 120
VUV-emitting radiation sources 222

white light-emitting devices
– WLED 108
Wigner–Eckart theorem 24
Wybourne parameters 68–72, 74

XeCl 223
X-ray excitation 174
X-ray excited phosphors 171
X-ray photoelectron spectra 117
XRD patterns 118

Y_2SiO_5:Pr^{3+} 236
$Y_3Al_5O_{12}$ 131
YPO_4:Bi^{3+} 230
YPO_4:Nd^{3+} 232
yttrium aluminum garnet 204
yttrium gallium garnet 204

zero-phonon 194
zero-phonon line 6
zigzag curves 141